NATIONAL TECHNICAL UNIVERSITY OF ATHENS

School of Civil Engineering

Institute of Structural Analysis & Antiseismic Research

AN ACCURATE AND COMPUTATIONALLY EFFICIENT THREE DIMENSIONAL NONLINEAR MODEL FOR THE ANALYSIS OF LARGE-SCALE RC STRUCTURES SUBJECTED TO CYCLIC AND DYNAMIC LOADING CONDITIONS

DOCTORAL DISSERTATION

For the title of Doctor of Philosophy in Engineering submitted in the school of civil Engineering, National Technical University of Athens

CHRISTOS MOURLAS

SUPERVISING PROFESSOR:
MANOLIS PAPADRAKAKIS

ATHENS
JANUARY 2019

ΕΘΝΙΚΟ ΜΕΤΣΟΒΙΟ ΠΟΛΥΤΕΧΝΕΙΟ

ΣΧΟΛΗ ΠΟΛΙΤΙΚΩΝ ΜΗΧΑΝΙΚΩΝ

ΕΡΓΑΣΤΗΡΙΟ ΣΤΑΤΙΚΗΣ & ΑΝΤΙΣΕΙΣΜΙΚΩΝ ΕΡΕΥΝΩΝ

ΑΝΑΠΤΥΞΗ ΤΡΙΣΔΙΑΣΤΑΤΩΝ ΠΡΟΣΟΜΟΙΩΜΑΤΩΝ ΓΙΑ ΤΗΝ ΑΝΑΛΥΣΗ ΚΑΤΑΣΚΕΥΩΝ ΜΕΓΑΛΗΣ ΚΛΙΜΑΚΑΣ ΑΠΟ ΟΠΛΙΣΜΕΝΟ ΣΚΥΡΟΔΕΜΑ ΚΑΤΑΠΟΝΟΥΜΕΝΩΝ ΣΕ ΑΝΑΚΥΚΛΙΖΟΜΕΝΗ ΚΑΙ ΔΥΝΑΜΙΚΗ ΦΟΡΤΙΣΗ

ΔΙΔΑΚΤΟΡΙΚΗ ΔΙΑΤΡΙΒΗ

για τον Επιστημονικό Τίτλο του Διδάκτορα Μηχανικού υποβληθείσα στη Σχολή Πολιτικών Μηχανικών του Εθνικού Μετσόβιου Πολυτεχνείου

ΧΡΗΣΤΟΣ ΜΟΥΡΛΑΣ

ΕΠΙΒΛΕΠΩΝ ΚΑΘΗΓΗΤΗΣ:
ΜΑΝΟΛΗΣ ΠΑΠΑΔΡΑΚΑΚΗΣ

ΑΘΗΝΑ
ΙΑΝΟΥΑΡΙΟΣ 2019

NATIONAL TECHNICAL UNIVERSITY OF ATHENS

School of Civil Engineering
Institute of Structural Analysis & Antiseismic Research

AN ACCURATE AND COMPUTATIONALLY EFFICIENT THREE DIMENSIONAL NONLINEAR MODEL FOR THE ANALYSIS OF LARGE-SCALE RC STRUCTURES SUBJECTED TO CYCLIC AND DYNAMIC LOADING CONDITIONS

DOCTORAL DISSERTATION

For the title of Doctor of Philosophy in Engineering submitted in the school of civil Engineering, National Technical University of Athens

CHRISTOS MOURLAS

Advisory Committee:

1. Manolis Papadrakakis
   Professor Emeritus N.T.U.A
   (Supervisor)
2. Konstantinos Spiliopoulos
   Professor N.T.U.A
3. Vissarion Papadopoulos
   Associate Professor N.T.U.A

Examination Committee:

1. Manolis Papadrakakis
   Professor Emeritus N.T.U.A
   (Supervisor)
2. Konstantinos Spiliopoulos
   Professor N.T.U.A
3. Vissarion Papadopoulos
   Associate Professor N.T.U.A
4. George Markou
   Associate Professor
   University of Pretoria
5. Constantine C. Spyrakos
   Professor N.T.U.A
6. Evangelos Sapountzakis
   Professor N.T.U.A
7. Michalis Fragiadakis
   Assistant Professor N.T.U.A

NATIONAL TECHNICAL UNIVERSITY OF ATHENS

School of Civil Engineering
Institute of Structural Analysis & Antiseismic Research

AN ACCURATE AND COMPUTATIONALLY EFFICIENT THREE DIMENSIONAL NONLINEAR MODEL FOR THE ANALYSIS OF LARGE-SCALE RC STRUCTURES SUBJECTED TO CYCLIC AND DYNAMIC LOADING CONDITIONS

DOCTORAL DISSERTATION

For the title of Doctor of Philosophy in Engineering submitted in the school of civil Engineering,
National Technical University of Athens

SPECIAL ACKNOWLEDGEMENT

This dissertation was performed under the co-supervision of
Associate Professor George Markou,
Faculty of EBIT, Department of Civil Engineering, University of Pretoria, South Africa.

UNIVERSITEIT VAN PRETORIA
UNIVERSITY OF PRETORIA
YUNIBESITHI YA PRETORIA

Dedicated to my parents,
my brother and my sister

Acknowledgements

I must begin by expressing my sincere gratitude to my supervisor Professor Manolis Papadrakakis for providing me with the opportunity to work with state of the art research subjects on engineering problems that use the Finite Element Method. His scientific guidance, his continuous support and confidence he has shown to me, helped me in all the time of research and writing of this thesis. I consider myself privileged working with him and I will always be grateful.

I wish to express my heartiest gratitude to my co-supervisor Associate Professor George Markou, for providing me the opportunity to work with him throughout the complete process of completing the doctoral dissertation. He also provided me the source code of the software ReConAn which was developed during his Ph.D dissertation. His precious suggestions and encouragement are the main reasons of completing my dissertation and for this reason I will always be grateful.

Following, I would like to thank Professor Michail Kotsovos and Professor Konstantinos Spiliopoulos for their helpful discussion and scientific comments. Their valuable comments and suggestions contributed to the improvement of the quality of this Dissertation.

Additionally I would like to thank Professor Michail Kotsovos, Professor Konstantinos Spiliopoulos, Professor Panayiotis Carydis, Professor Panagiotis Kotronis, Assistant Professor Yannis Koutroumanos, Dr. George Lykidis, Dr. Ilias Gkimousis and Dr. Martin Poljansek for providing the experimental data of the analysis of RC structural members.

I would also express my gratitude to Associate Professor Vissarion Papadopoulos, Assistant Professor Michalis Fragkiadakis, Assistant Professor George Stefanou and Assistant Professor Vassilis Papapanikolaou for their suggestions during the Ph.D Dissertation. Furthermore, I would like to thank the other members of my thesis committee Professor Constantine Spyrakos and Professor Evangelos Sapountzakis for their helpful discussions and scientific comments.

I would like to thank my friends and members of the research group Dimitris Giovannis, Giannis Kalogeris, Giannis Kapogianis, Odysseas Kokkinos, George Soimiris, Emmanuel Trypakis and Dimitris Tspaetis for their valuable comments and support during the preparation of this thesis. I would like to thank all my colleagues that worked in the research team of professor Manolis Papadrakakis for their helpful suggestions and comments thus maintaining a productive and pleasant environment.

Most of all, I would like to thank my parents, Panagiotis Mourlas and Athena Papadaki, my sister, Tina Mourla and my brother, Panagiotis Mourlas for their continuous encouragements, their selfless support which were the sustaining factors completing the Ph.D dissertation successfully.

Financial Support

The financial support provided by the European Research Council Advanced Grant "MASTER-Mastering the computational challenges in numerical modeling and optimum design of CNT reinforced composites" (ERC-2011-ADG 20110209) is gratefully acknowledged by the author.

Εκτεταμένη περίληψη στα ελληνικά (Extended Summary in Greek)

I. Εισαγωγή

Η προσομοίωση της περίπλοκης συμπεριφοράς του οπλισμένου σκυροδέματος όταν υποβάλλεται σε διαξονική ή τριαξονική ανακυκλική ένταση αποτελεί αντικείμενο έρευνας πολλών ερευνητών τις τελευταίες δεκαετίες. Το σκυρόδεμα είναι ένα ανομοιογενές σύνθετο υλικό όπου παρουσιάζει πολύπλοκη συμπεριφορά η οποία επηρεάζεται από της συνθήκες φόρτισης, την γεωμετρία διατομών και φορέα, ποσοστό οπλισμού και διαδικασία κατασκευής. Η αυξημένη πολυπλοκότητα των καταστατικών προσομοιωμάτων που αναπτύσσονται, οδηγεί σε μοντέλα που παρουσιάζουν μη ρεαλιστική συμπεριφορά καθώς και σε μοντέλα που δύσκολα εφαρμόζονται σε ευρύ φάσμα κατασκευών με διαφορετικές μηχανικές συμπεριφορές ώστε να ελεγχθεί κατάλληλα ο βαθμός αξιοπιστίας τους.

Τα καταστατικά μοντέλα που έχουν προταθεί στην βιβλιογραφία, βασίζονται στην θεωρία πλαστικότητας, στους νόμους της θερμοδυναμικής, στην θεωρία της θραυστομηχανικής και στον συνδυασμό τους. Η προσπάθεια να ενταχθούν οι ιδιότητες της συμπεριφοράς του σκυροδέματος στα παραπάνω εξιδανικευμένα μοντέλα δημιουργεί καταστατικά προσομοιώματα που εξαρτώνται από ένα πλήθος παραμέτρων που καθορίζουν την μη γραμμική συμπεριφορά του υλικού. Το κοινό χαρακτηριστικό που έχουν τα μοντέλα της βιβλιογραφίας που βασίζονται στις παραπάνω θεωρίες, είναι ότι δίνουν βαρύτητα στην συμπεριφορά του υλικού του σκυροδέματος μετά το πέρας της αντοχής του σε θλίψη ή εφελκυσμό. Συνεπώς ορίζεται ένα σύνολο παραμέτρων οι οποίες περιγράφουν τα χαρακτηριστικά της συμπεριφοράς του υλικού όπως πλαστιμότητα, παραμένουσα αντοχή σε θλίψη, εφελκυσμό, διάτμηση ρηγματωμένου σκυροδέματος και την παραμορφωσιακή χαλάρωση σε θλίψη και εφελκυσμό. Αυτές οι ιδιότητες δεν αποτελούν χαρακτηριστικά του υλικού του σκυροδέματος αλλά εξαρτώνται από τις ιδιαιτερότητες του προβλήματος που αναλύεται κάθε φορά. Συνεπώς, αυτός είναι ο λόγος όπου τα αριθμητικά μοντέλα τα οποία προσπαθούν να προσεγγίσουν την ρεαλιστική συμπεριφορά του σκυροδέματος καλύπτουν ένα περιορισμένο φάσμα προβλημάτων (π.χ. δοκούς, στύλους και τοιχία). Όσο αυξάνονται οι απαιτήσεις των αναλύσεων (ανακυκλιζόμενες και δυναμικές αναλύσεις) παρουσιάζονται αρκετά υπολογιστικά προβλήματα τα οποία καθιστούν δύσκολή την δημιουργία ενός εύρωστου υπολογιστικά μοντέλου. Συνεπώς ένα αριθμητικό προσομοίωμα που μπορεί να χρησιμοποιηθεί ευρέως, σε οποιονδήποτε φορέα από οπλισμένο σκυρόδεμα δεν υπάρχει διαθέσιμο στη διεθνή αγορά.

Τα χαρακτηριστικά της μη-γραμμικής συμπεριφοράς του σκυροδέματος εκφράζονται με διάφορες παραμέτρους που περιγράφουν την ρηγματωμένη συμπεριφορά του υλικού ή γενικότερα την κατάσταση στην οποία βρίσκεται μετά το πέρας της αντοχής, είτε σε θλίψη είτε σε εφελκυσμό. Οι ιδιότητες του υλικού καθώς έχει ρηγματωθεί εμφανίζονται και στην μεθοδολογία σχεδιασμού ενός φορέα από οπλισμένο σκυρόδεμα. Συνήθως, χρησιμοποιείται ένα σύστημα με δικτυώματα τα οποία αντιπροσωπεύουν τους μηχανισμούς αντίστασης του σκυροδέματος και γενικότερα περιγράφουν την μεταφορά των δυνάμεων από την περιοχή που ασκούνται στην στήριξη του φορέα. Ένα τέτοιο σύστημα φαίνεται στο Σχήμα 1 για την περίπτωση μιας αμφιέρειστης δοκού (EC2 [1]). Το σύστημα αυτό υπονοεί ότι αναπτύσσονται μηχανισμοί αντίστασης στο ρηγματωμένο σκυρόδεμα. Η ανάπτυξη διαγώνιων θλιπτήρων περιγράφει την ανάπτυξη δυνάμεων τριβής αντίστασης κατά μήκος της διεπιφάνειας των ρωγμών. Αυτός ο μηχανισμός όμως προϋποθέτει ότι δεν θα σχηματιστούν ρωγμές κάθετα στους διαγώνιους θλιπτήρες. Επίσης, σημαντικός παράγοντας στην μεταφορά της δύναμης στην στήριξη, αποτελεί και η συνεισφορά του ελκυστήρα που αντιπροσωπεύει τον διαμήκη

εφελκυόμενο οπλισμό. Αυτή η συνεισφορά προϋποθέτει το ότι στην οριακή κατάσταση, όπου ο χάλυβας έχει διαρρεύσει στην περιοχή του ρηγματωμένου σκυροδέματος, ο εφελκυόμενος οπλισμός δεν έχει χάσει την συνάφεια του με το σκυρόδεμα.

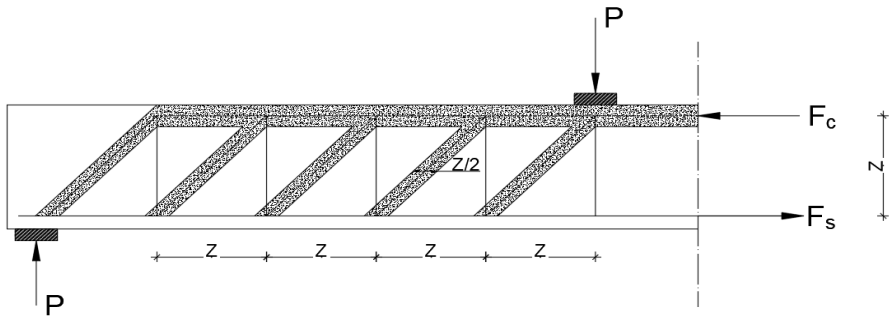

Σχήμα 1 Προσομοίωση αμφιέρειστης δοκού στην οριακή κατάσταση αστοχίας ως δικτύωμα.

Επιπλέον, η αστοχία του διαμήκη θλιπτήρα πραγματοποιείται όταν η θλιπτική παραμόρφωση του σκυροδέματος είναι ίση με ε_c=0.0035 (EC2 [1]) η οποία αντιστοιχεί σε θλιπτική αντοχή του σκυροδέματος ίση με $0.85f_c$ (όπου f_c είναι η αντοχή του σκυροδέματος σε μονοαξονική θλίψη). Παρόλα αυτά, έντονη ρηγμάτωση γίνεται ορατή όταν η θλιπτική παραμόρφωση είναι ίση με 0.002 και κατά συνέπεια το παραπάνω κριτήριο αστοχίας υποδηλώνει την παρουσία σημαντικής παραμένουσας δυσκαμψίας και αντοχής του ρηγματωμένου σκυροδέματος.

Η πειραματική συμπεριφορά δοκών από οπλισμένο σκυρόδεμα, έχει δείξει πως σε αρκετές περιπτώσεις εμφανίζεται ψαθυρή-διατμητική αστοχία πριν αναπτυχθεί πλήρως η καμπτική αντοχή της δοκού για την οποία σχεδιάστηκε. Επίσης, ψαθυρές μορφές αστοχίας έχουν εμφανιστεί και σε άλλους φορείς από οπλισμένο σκυρόδεμα μετά από ισχυρούς σεισμούς, όπως εμφανίζονται στο Σχήμα 2. Σε πολλές κολώνες από οπλισμένο σκυρόδεμα, εμφανίστηκε διατμητική αστοχία παραδόξως στο μέσο του ύψους τους (σε περιοχή που δεν θεωρείται κρίσιμη), ενώ η παραδοχή στερεού κόμβου από οπλισμένο σκυρόδεμα δεν φαίνεται να συνάδει με την έντονη ρηγμάτωση που εμφανίζεται σε αυτούς, όπως παρουσιάζεται στο Σχήμα 2β.

(a) (b)

Σχήμα 2(a) Αστοχία γέφυρας μετά τον σεισμό του Kobe στην Ιαπωνία το 1995, (b) Αστοχία των κόμβων και υποστυλωμάτων του κτιρίου (Sezen et al. 2000 [2]).

Όσον αφορά το σκυρόδεμα, είναι ένα ετερογενές υλικό του οποίου η συμπεριφορά επηρεάζεται σημαντικά από τριαξονικά φαινόμενα. Θλιπτικές τάσεις που αναπτύσσονται εκτός του επιπέδου της φόρτισης, οδηγούν σε σημαντική αύξηση της θλιπτικής αντοχής του υλικού (περίσφιξη) ενώ η ανάπτυξη εφελκυστικών τάσεων εκτός του επιπέδου της φόρτισης, οδηγεί σε πρόωρη αστοχία του φορέα. Συνεπώς η τριαξονική συμπεριφορά του σκυροδέματος δεν μπορεί να αγνοηθεί σε περίπτωση όπου θεωρούμε μία ρεαλιστική μόρφωση του καταστατικού προσομοιώματος υλικού. Επιπροσθέτως, ο φθιτός κλάδος που εμφανίζεται στη καμπύλη τάσεων-παραμορφώσεων όταν το δοκίμιο του σκυροδέματος υποβάλλεται σε μονοαξονική θλίψη, αποδίδεται στην αλληλεπίδραση μεταξύ του δοκιμίου και των πλακών φόρτισης όπως αναδεικνύεται και στο Σχήμα 3 [3] .

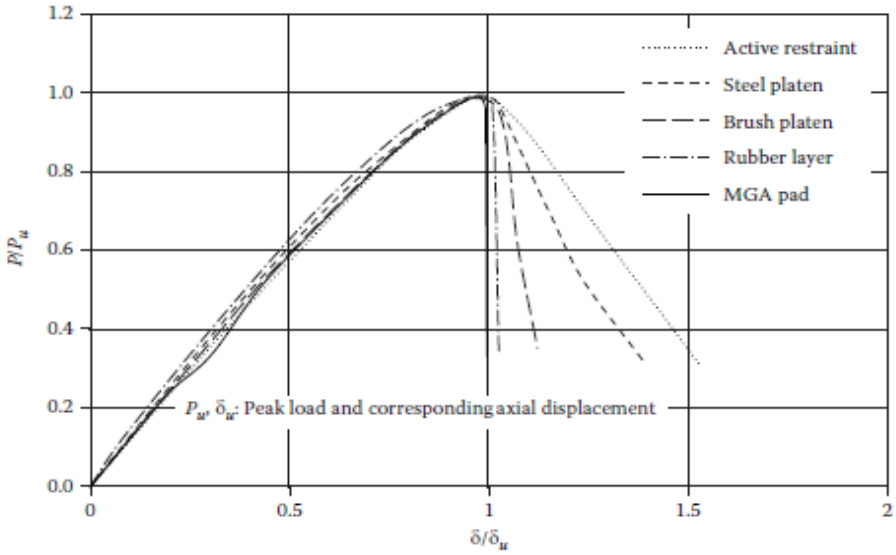

Σχήμα 3 Καμπύλη τάσης-ανηγμένης παραμόρφωσης για διάφορες συνοριακές συνθήκες της πειραματικής διάταξης (Kotsovos [3]*).*

Όσον αφορά το καταστατικό μοντέλο του υλικού, ένας κατάλληλος αλγοριθμικός σχεδιασμός πρέπει να αναπτυχθεί, ο οποίος θα βασίζεται στην τριαξονική συμπεριφορά του σκυροδέματος με βάση τα πειραματική συμπεριφορά του υλικού το οποίο θα παράγει ρεαλιστικά αριθμητικά αποτελέσματα με ελάχιστο υπολογιστικό κόστος. Επιπλέον, η επιλογή του κατάλληλου τύπου πεπερασμένων στοιχείων αποτελεί σημαντικό ρόλο στην ευστάθεια και ακρίβεια της υπολογιστικής διαδικασίας. Για παράδειγμα η υπόθεση Bernoulli η οποία χρησιμοποιείται συνήθως στα στοιχεία δοκού-υποστυλώματος δεν περιγράφει ρεαλιστικά την κατανομή των παραμορφώσεων της διατομής, ιδίως στην περίπτωση ενός ρηγματωμένου σκυροδέματος. Γενικότερα, τα στοιχεία δοκού δεν ενδείκνυνται για την προσομοίωση κατασκευών από οπλισμένο σκυρόδεμα όταν κυριαρχούν οι διατμητικές παραμορφώσεις, η ψαθυρή αστοχία με έντονη ρηγμάτωση και τα τριαξονικά φαινόμενα όπως η επιρροή της ανάπτυξης θλιπτικών ή εφελκυστικών τάσεων εκτός του επιπέδου φόρτισης.

Σκοπός της παρούσας έρευνας είναι η δημιουργία ενός ακριβούς και ρεαλιστικού αριθμητικού μοντέλου το οποίο να περιγράφει την τριαξονική συμπεριφορά του σκυροδέματος και το οποίο εν συνεχεία να μπορεί να χρησιμοποιηθεί για την προσομοίωση οποιασδήποτε κατασκευής από οπλισμένο σκυρόδεμα, καλύπτοντας όλες τις ιδιαιτερότητες των προβλημάτων σε επίπεδο υλικού. Η παρούσα εργασία αποσκοπεί στην δημιουργία ενός λογισμικού το οποίο θα έχει την ικανότητα να ξεπερνά τις υπολογιστικές δυσκολίες που έχουν παρουσιαστεί από

προηγούμενους ερευνητές έτσι ώστε να αποτελέσει ένα χρήσιμο εργαλείο για την προσομοίωση κατασκευών από οπλισμένο σκυρόδεμα.

Το προτεινόμενο καταστατικό μοντέλο περιγράφεται μέσω κατάλληλου αλγοριθμικού σχεδιασμού και βασίζεται στην ψαθυρότητα (άμεση απώλεια της φέρουσας ικανότητας όταν το υλικό ξεπεράσει τα όρια αντοχής του) του υλικού κάνοντας χρήση των καταστατικών σχέσεων που έχουν προκύψει από τριαξονική πειραματική διερεύνηση και παρουσιάζονται στο άρθρο [3]. Ένα βασικό προνόμιο του προτεινόμενου καταστατικού μοντέλου υλικού, είναι ότι χρειάζεται μόνο σαν μεταβλητή εισόδου την μονοαξονική αντοχή κυλινδρικού δοκιμίου του σκυροδέματος σε θλίψη f_c. Η ρηγμάτωση προσομοιώνεται με την μέθοδο της διανεμημένης ρηγμάτωσης (smeared crack approach) όπου με την μέθοδο αυτήν, η ρωγμή δεν αναπαρίσταται ως μια γεωμετρική ασυνέχεια αλλά αντ' αυτού μηδενίζονται οι ιδιότητες του υλικού στην διεύθυνση κάθετα αυτής. Συνεπώς, οι τάσεις που προκάλεσαν την ανάπτυξη της ρωγμής (που ικανοποίησαν το κριτήριο αστοχίας), μηδενίζονται στην διεύθυνση κάθετα στην ρωγμή και αναδιανέμονται εσωτερικά στις άλλες διευθύνσεις όπου το σκυρόδεμα είναι αρηγμάτωτο. Επιπλέον, ένα νέο κριτήριο κλεισίματος των ρωγμών προτάθηκε στην παρούσα εργασία το οποίο βοήθησε την ευστάθεια και ακρίβεια της υπολογιστικής διαδικασίας στην περίπτωση της ανακυκλιζόμενης φόρτισης ακόμα και σε περιπτώσεις όπου η ανακυκλική φόρτιση έφτανε τα όρια αντοχής του εξεταζόμενου φορέα.

Για την αριθμητική προσομοίωση του σκυροδέματος χρησιμοποιήθηκαν τρισδιάστατα 8-κομβικά ισοπαραμετρικά πεπερασμένα στοιχεία. Επιπροσθέτως, οι ράβδοι οπλισμού προσομοιώθηκα ως ενσωματωμένα διακριτά στοιχεία (embedded discrete elements) στο εσωτερικό των 8-κομβικών εξαεδρικών στοιχείων σκυροδέματος. Για τα στοιχεία του οπλισμού χρησιμοποιήθηκαν τα στοιχεία δοκού με την μέθοδο δυνάμεων (natural beam column flexibility based elements) και στοιχεία ράβδου. Η χρήση των στοιχείων δοκού για την προσομοίωση του οπλισμού των υπό ανάλυση φορέων, έδειξε ότι βοηθάει στην ευστάθεια της μη γραμμικής διαδικασίας ιδιαίτερα σε περιοχές όπου το σκυρόδεμα έχει έντονα ρηγματωθεί. Επίσης χρησιμοποιήθηκε ένας υβριδικός τρόπος διακριτοποίησης για κατασκευές μεγάλης κλίμακας από οπλισμένο σκυρόδεμα που αναπτύχθηκε στη δημοσίευση [4]. Σύμφωνα με τον υβριδικό τρόπο διακριτοποίησης HYMOD (Hybrid Modeling), το προτεινόμενο τρισδιάστατο λεπτομερές προσομοίωμα χρησιμοποιείται σε περιοχές όπου η συμπεριφορά του υλικού χαρακτηρίζεται ως διατμητική (διατμητικές παραμορφώσεις, έντονη ρηγμάτωση, ψαθυρή συμπεριφορά), όπως είναι οι περιοχές κόμβων, τοιχίων καθώς και τα άκρα κολώνων και δοκών. Οι περιοχές του σκυροδέματος που χαρακτηρίζονται από καμπτική συμπεριφορά (ενδιάμεσα τμήματα δοκών και κολώνων) διακριτοποιούνται με χρήση πεπερασμένων στοιχείων δοκού-υποστυλώματος (natural beam column flexibility based elements). Με αυτόν τον τρόπο, απομειώνεται σημαντικά το υπολογιστικό κόστος χωρίς σημαντικές επιπτώσεις στην ακρίβεια των αποτελεσμάτων. Θα πρέπει να αναφερθεί στο σημείο αυτό ό,τι το υβριδικό μοντέλο HYMOD χρησιμοποιήθηκε για την ανάλυση ενός τετραωρόφου κτιρίου σε ανακυκλιζόμενη φόρτιση και εξετάστηκαν εναλλακτικοί τρόποι ενίσχυσης της κατασκευής.

Είναι πολύ σημαντικό, ένα μοντέλο να μπορεί να προσομοιώσει τη μη γραμμική συμπεριφορά φορέων και μελών από οπλισμένο σκυρόδεμα έχοντας το ελάχιστο δυνατό υπολογιστικό κόστος ώστε να μπορέσει να επεκταθεί και για την προσομοίωση κατασκευών μεγάλης κλίμακας. Το προτεινόμενο μοντέλο χρησιμοποιήθηκε για την ανάλυση φορέων με διαφορετική μηχανική συμπεριφορά όπως τοιχία, δοκούς, κόμβους από οπλισμένο σκυρόδεμα που καταπονούνται σε ανακυκλιζόμενη φόρτιση και πολυώροφες κατασκευές. Η ανάλυση έδειξε ότι τα αποτελέσματα παρουσιάζουν ικανοποιητική ακρίβεια σε σύγκριση με τα πειραματικά αποτελέσματα με διαφορές μικρότερες του 10% όσον αφορά την φέρουσα ικανότητα του φορέα. Επιπλέον προτάθηκαν δύο νέες παράμετροι βλάβης οι οποίοι απομειώνουν την στιβαρότητα του σκυροδέματος και του οπλισμού λόγω έντονη ρηγμάτωσης

και του αριθμού του ανοιγοκλεισίματος των ρωγμών. Με αυτόν τον τρόπο το μοντέλο κατάφερε να προσομοιώσει ακριβέστερα την συμπεριφορά κατασκευών που υπόκεινται σε πολλαπλούς κύκλους φόρτισης καθώς και σε δυναμικές φορτίσεις. Τέλος τα αποτελέσματα έδειξαν ότι το μοντέλο προσομοίωσε χαρακτηριστικά όπως την απομείωση της δυσκαμψίας, της αντοχής και την στένωση του κύκλου υστέρησης (pinching effect).

II. Συνοπτική βιβλιογραφική ανασκόπηση

Αρκετά αριθμητικά μοντέλα για κατασκευές από οπλισμένο σκυρόδεμα, έχουν προταθεί στην διεθνή βιβλιογραφία. Μια συνοπτική παρουσίαση των αριθμητικών μοντέλων που έχουν αναπτυχθεί με χρονολογική σειρά παρατίθεται στο υποκεφάλαιο αυτό.

Ο Červenka [5] πρότεινε ένα ανελαστικό προσομοίωμα με χρήση επίπεδων τριγωνικών πεπερασμένων στοιχείων που καταπονούνται σε επίπεδη ένταση. Το καταστατικό προσομοίωμα είναι ελαστικό-πλαστικό σε θλίψη και ελαστικό-ψαθυρό σε εφελκυσμό. Αυτή η προσέγγιση ανέδειξε την ανάγκη της ακριβούς προσομοίωσης της συνάφειας μεταξύ του χάλυβα με το σκυρόδεμα και της διαδικασίας ρηγμάτωσης σε συνθήκες ανακυκλιζόμενης έντασης. Οι Darwin και Pecknold [6] πρότειναν μια συσχέτιση μεταξύ της διαξονικής με τη μονοαξονική απόκριση του σκυροδέματος μέσω της χρήσης μια ισοδύναμης μονοαξονικής παραμόρφωσης. Ανέπτυξαν ένα μη-γραμμικό καταστατικό νόμο υλικού για διαξονική ένταση και χρησιμοποίησαν τετρακομβικά ισοπαραμετρικά πεπερασμένα στοιχεία. Η ανάλυση έδειξε ρεαλιστικά αποτελέσματα όπως περιγράφηκε στην εργασία τους [6]. Οι Agrawal et al. [7] πρότειναν ένα ελαστοπλαστικό μοντέλο για το σκυρόδεμα και τον χάλυβα οπλισμού με σκοπό να προσομοιώσουν επαρκώς την επίπεδη συμπεριφορά του οπλισμένου σκυροδέματος όταν υποβάλλεται σε ανακυκλική φόρτιση. Σε μετέπειτα εργασία, οι Rule και Rowlands [8] ανέπτυξαν ένα μη γραμμικό μοντέλο χρησιμοποιώντας τριγωνικά πεπερασμένα στοιχεία επίπεδης παραμόρφωσης για να προβλέψουν την φέρουσα ικανότητα του φορέα από οπλισμένο σκυρόδεμα όταν αυτό υποβάλλεται σε ανακυκλική επίπεδη ένταση. Αυτή η μελέτη προτείνει τον χάλυβα οπλισμού να συνεισφέρει στη διατμητική δυσκαμψία του φορέα. Το μοντέλο αυτό χρησιμοποιήθηκε για την προσομοίωση ανακυκλιζόμενων υψίκορμων δοκών.

Εν συνεχεία, οι Ozbolt et al. [9] πρότειναν ένα μοντέλο μικροεπιπέδων (microplane model) χρησιμοποιώντας τετρακομβικά ισοπαραμετρικά στοιχεία επίπεδης έντασης με τα οποία περιέγραψαν την απόκριση κατασκευών από οπλισμένο σκυρόδεμα σε ανακυκλιζόμενες φορτίσεις. Οι Inoue et al. [10], παρουσίασαν ένα μη-γραμμικό μοντέλο πεπερασμένων στοιχείων για δυναμικές αναλύσεις τοιχίων προσομοιώνοντας χαρακτηριστικά της υστερητικής συμπεριφοράς του σκυροδέματος και του χάλυβα οπλισμού. Όπως αναφέρθηκε στην εργασία αυτή [10], χρησιμοποιήθηκαν τετρακομβικά ισοπαραμετρικά στοιχεία και τα αριθμητικά αποτελέσματα προσέγγισαν επαρκώς τα πειραματικά δεδομένα. Στην εργασία των Balan et al. [9], πρότειναν ένα 3D υποπλαστικό καταστατικό μοντέλο και όπως αναφέρουν και οι αρθρογράφοι, τα αριθμητικά αποτελέσματα ήταν ικανοποιητικά σε επίπεδο ακρίβειας. Ο Cela [11], περιέγραψε ένα βισκοπλαστικό νόμο που βασίζεται στο μοντέλο Drucker-Prager και προσομοίωσε δυναμικές αναλύσεις κατασκευών από οπλισμένο σκυρόδεμα με χρήση τετρακομβικών πεπερασμένων στοιχείων. Επίσης, ο Vecchio [12] πρότεινε ένα καταστατικό μοντέλο το οποίο βασίζεται στην θεωρία της θλιπτικού πεδίου (Modified Compressive Field Theory) και προσομοίωσε φορείς από οπλισμένο σκυρόδεμα με χρήση επίπεδων τετρακομβικών στοιχείων.

Στην δημοσίευση των Ile και Reynouard [13], προτείνετε ένα καταστατικό μοντέλο για προσομοίωση της ανακυκλικής συμπεριφοράς κατασκευών από οπλισμένο σκυρόδεμα θεωρώντας ότι το σκυρόδεμα υποβάλλεται σε επίπεδη ένταση χρησιμοποιώντας τετρακομβικά (2D) πεπερασμένα στοιχεία. Οι αρθρογράφοι αναφέρουν ότι τα αριθμητικά αποτελέσματα προσεγγίζουν ρεαλιστικά τα πειραματικά. Η παραμόρφωση της ρηγμάτωσης ορίστηκε με

χρήση θεωρίας της θραυστομηχανικής (Bazant και Oh [14]) συνδέοντας το μέγεθος των πεπερασμένων στοιχείων με την ενέργεια θραύσης. Οι Kwan και Billington [15], χρησιμοποίησαν οκτακοβικά πεπερασμένα στοιχεία επίπεδης έντασης ώστε να μελετήσουν την επιρροή του μοντέλου ρηγμάτωσης και τη μέθοδο προσομοίωσης της διατμητικής στιβαρότητας των ρωγμών της υστερητικής συμπεριφοράς του σκυροδέματος. Επιπλέον, οι Balan et al [16] παρουσίασαν ένα τρισδιάστατο μοντέλο χρησιμοποιώντας την ισοδύναμη μονοαξονική παραμόρφωση που είχαν προτείνει παλαιότερα οι Darwin και Pecknold [6] και με βάση την εργασία τους κατάφεραν να περιγράψουν επαρκώς την συμπεριφορά των κατασκευών σε μονοτονική και ανακυκλική φόρτιση. Το μοντέλο αυτό χρησιμοποιήθηκε και από τους Kwon και Spacone [17] οι οποίοι μελέτησαν την τριαξονική απόκριση δοκιμίων και δομικών μελών (κολώνες) από οπλισμένο σκυρόδεμα.

Οι Palermo και Vecchio [18], περιέγραψαν επαρκώς την φέρουσα ικανότητα των τοιχίων με βάση την θεωρία των θλιπτικού πεδίου (compression field theory) χρησιμοποιώντας τετρακομβικά και εξαεδρικά πεπερασμένα στοιχεία για 2D και 3D αναλύσεις αντίστοιχα, για συνθήκες ανακυκλιζόμενης έντασης. Εντός της εργασίας των Girard και Bastien [19], αναπτύχθηκε ένα τρισδιάστατο υποελαστικό καταστατικό μοντέλο το οποίο βασίζεται στις ισοδύναμες παραμορφώσεις των Darwin και Pecknold [6] για να προσομοιώσουν υποστυλώματα από οπλισμένο σκυρόδεμα λαμβάνοντας υπόψη την ολίσθηση των οπλισμών κατά τη διάρκεια ανακυκλιζόμενης φόρτισης. Σε αυτό το προσομοίωμα χρησιμοποιήθηκαν εξαεδρικά πεπερασμένα στοιχεία με είκοσι κόμβους. Οι Kwak και Kim [20], πρότειναν ένα αριθμητικό καταστατικό μοντέλο χρησιμοποιώντας τετρακομβικά πεπερασμένα στοιχεία για 2D αναλύσεις τοιχίων από οπλισμένο σκυρόδεμα υπό ανακυκλικές φορτίσεις. Επίσης, οι Au και Bai [21] παρουσίασαν ένα αριθμητικό μοντέλο που βασίζεται στη χρήση του τέμνοντος μέτρου ελαστικότητας (secant modulus approach) χρησιμοποιώντας τετρακομβικά (2D) πεπερασμένα στοιχεία με τα όποια προσομοίωσαν δοκούς από οπλισμένο σκυρόδεμα σε μονοτονικές και ανακυκλιζόμενες φορτίσεις. Επιπλέον το φαινόμενο ολίσθησης του χάλυβα οπλισμού προσομοιώθηκε με την χρήση στοιχείων επαφής (contact elements). Τα αριθμητικά αποτελέσματα έδειξαν ότι κατάφεραν να προσεγγίσουν ικανοποιητικά τις πειραματικές καμπύλες. Εν συνεχεία, στην ερευνητική δουλεία των He et al. [22], προτάθηκε ένα ενεργειακό μοντέλο χρησιμοποιώντας τετραεδρικά πεπερασμένα στοιχεία για 2D σε ανακυκλικές συνθήκες φόρτισης.

Σε μεταγενέστερη ερευνητική εργασία, οι To et al. [23] πρότειναν ένα αριθμητικό μη-γραμμικό μοντέλο στο οποίο διαχώρισαν τον όγκο του σκυροδέματος με ραβδόμορφα στοιχεία τα οποία ανάλογα με τη θέση τους, ακολουθούν ένα διαφορετικό καταστατικό νόμο (strut and tie model). Οι Eligenhousen et al. [10], μελέτησαν ένα αριθμητικό μοντέλο που βασίζεται στο μοντέλο των μικρορωγμών (microplane model) για την προσομοίωση 3D κόμβων από οπλισμένο σκυρόδεμα υπό ανακυκλιζόμενες φορτίσεις. Επιπλέον, προσομοίωσαν την ολίσθηση του οπλισμού θεωρώντας ένα ελατήριο που αντιπροσωπεύει τη μη-γραμμική μονοαξονική σχέση ολίσθησης. Η ερευνητική ομάδα των Melo et al. [24], χρησιμοποίησαν στοιχεία δοκού κατανεμημένης βλάβης για να προσομοιώσουν τη μη-γραμμική συμπεριφορά μιας δοκού δυο ανοιγμάτων από οπλισμένο σκυρόδεμα λαμβάνοντας υπόψη την ολίσθηση. Οι καμπύλες φέρουσας ικανότητας που προέκυψαν από το αριθμητικό μοντέλο τους συμπίπτουν ικανοποιητικά με τις πειραματικές καμπύλες. Οι Richard et al. [25], παρουσίασαν ένα σύνολο καταστατικών σχέσεων που περιγράφουν την μικρορηγμάτωση, την ολίσθηση του οπλισμού και μερική επαναφορά του υλικού σε επίπεδο δυσκαμψίας ώστε να συνθέσουν ένα 3D καταστατικό μοντέλο οπλισμένου σκυροδέματος. Στη δημοσίευση των Yuchuan et al. [26], αναπτύχθηκε ένα ανισότροπο μοντέλο βλάβης για την ανακυκλική συμπεριφορά κατασκευών οπλισμένου σκυροδέματος. Οι αριθμητικές εφαρμογές έδειξαν ρεαλιστικά αποτελέσματα.

Οι δημοσιεύσεις των Lykidis και Spiliopoulos [27, 28], παρουσίασαν ένα 3D αριθμητικό μοντέλο χρησιμοποιώντας εξαεδρικά πεπερασμένα στοιχεία 27 κόμβων. Η παραπάνω διαδικασία ανέδειξε την ανάγκη προσομοίωσης της σχέσης συνάφειας του οπλισμού. Το άρθρο Kotsovos [3], πρότεινε ένα μοντέλο υλικού το οποίο βασίστηκε στο μοντέλο των Kotsovos και Pavlovic [29] χρησιμοποιώντας εξαεδρικά πεπερασμένα στοιχεία 27 κόμβων και εξετάστηκε σε μονοτονικές, ανακυκλικές και δυναμικές φορτίσεις.

Στην παρούσα εργασία, προτείνεται μια ακριβείς τριαξονική προσομοίωση κατασκευών από οπλισμένο σκυρόδεμα που υποβάλλονται σε ανακυκλικές φορτίσεις. Το μοντέλο βασίζεται στην αριθμητική προσομοίωση που είχε προταθεί από τους Markou και Papadrakakis [30, 31]. Στην συνέχεια παρουσιάζεται ο αλγόριθμος που αναπτύχθηκε ο οποίος περιγράφει ένα τριαξονικό καταστατικό νόμο του υλικού για όταν υπόκειται σε ανακυκλιζόμενη ένταση.

III. Καταστατικό μοντέλο σκυροδέματος

Οι γενικευμένες σχέσεις τάσεων-ανηγμένων παραμορφώσεων μπορούν να διατυπωθούν αναλύοντας κάθε εντατική κατάσταση σε μια υδροστατική και μία αποκλίνουσα συνιστώσα, οι οποίες αντιπροσωπεύουν αντίστοιχα την ορθή και διατμητική οκταεδρική τάση. Για την προσομοίωση της μη γραμμικής συμπεριφοράς των σχέσεων σ_0-$\varepsilon_{0(h)}$, τ_0-$\gamma_{0(h)}$, χρησιμοποιούνται τα μέτρα συμπιεστότητας K και διάτμησης G καθώς και η εσωτερική τάση σ_{id} η οποία λαμβάνει υπόψη την σχέση μεταξύ τ_0-$\varepsilon_{0(d)}$ (όπου h και d αναφέρονται στην υδροστατική και αποκλίνουσα συνιστώσα, αντίστοιχα). Συνεπώς οι οκταεδρικές παραμορφώσεις που προκαλούνται από μια εξωτερικώς εφαρμοζόμενη εντατική κατάσταση $(\sigma_0$-$\tau_0)$ μπορούν να γραφτούν ως εξής:

$$\varepsilon_0 = \varepsilon_{0(h)} + \varepsilon_{0(d)} = (\sigma_0 + \sigma_{id}) / (3K_s) \tag{1}$$

$$\gamma_0 = \gamma_{0(d)} = \tau_0 / (2G_s) \tag{2}$$

Όπου K_s και G_s είναι οι τέμνουσες εκφράσεις των μέτρων συμπιεστότητας και διάτμησης αντίστοιχα. Σύμφωνα με την μέθοδο Newton-Raphson με έλεγχο μετατόπισης, σε κάθε επανάληψη οι παραμορφώσεις υπολογίζονται από τις επικόμβιες παραμορφώσεις. Στην συνέχεια οι τάσεις προσδιορίζονται χρησιμοποιώντας το καταστατικό μητρώο του υλικού όπως μορφώθηκε στο προηγούμενο βήμα αριθμητικής ανάλυσης. Πρέπει να αναφερθεί εδώ ότι με βάση την εργασία [31] η οποία υιοθετήθηκε εδώ, θεωρείται ότι το αρηγμάτωτο σκυρόδεμα συμπεριφέρεται ελαστικά σε χαμηλά επίπεδα έντασης και κατά συνέπεια το καταστατικό μητρώο υλικού παραμένει αμετάβλητο. Συγκεκριμένα, όταν η αποκλίνουσα τάση σε ένα αρηγμάτωτο σημείο ολοκλήρωσης είναι μικρότερη του 50% της αντίστοιχης οριακής αποκλίνουσας τάσης τ_{0u} τότε χρησιμοποιείται το ελαστικό καταστατικό μητρώο [31]. Σε αντίθετη περίπτωση το καταστατικό μητρώο του υλικού επαναϋπολογίζεται χρησιμοποιώντας τις εφαπτομενικές σχέσεις των μέτρων διόγκωσης και διάτμησης. Το ελαστικό καταστατικό μητρώο του υλικού έχει την παρακάτω μορφή:

$$\boldsymbol{D} = \begin{bmatrix} 2G+m & m & m & 0 & 0 & 0 \\ m & 2G+m & m & 0 & 0 & 0 \\ m & m & 2G+m & 0 & 0 & 0 \\ 0 & 0 & 0 & G & 0 & 0 \\ 0 & 0 & 0 & 0 & G & 0 \\ 0 & 0 & 0 & 0 & 0 & G \end{bmatrix} \tag{3}$$

Όπου $\mu = K - 2G/3$ και $K = K(\sigma_0,\tau_0)$, $G = G(\sigma_0,\tau_0)$.

Επιπλέον οι παραμορφώσεις και οι τάσεις διορθώνονται λαμβάνοντας υπόψη την ισοδύναμη υδροστατική τάση που εκφράζει την επιρροή της αποκλίνουσας τάσης στην ογκομετρική παραμόρφωση χρησιμοποιώντας τη Σχέση (1).

Το κριτήριο φόρτισης/αποφόρτισης ορίζεται με τη σύγκριση της τρέχουσας αποκλίνουσας τάσης με την αμέσως προηγούμενη αποκλίνουσα τάση (Kotsovos και Spiliopoulos [32]). Συνεπώς στην περίπτωση που η τρέχουσα αποκλίνουσα τάση είναι μικρότερη από την προηγούμενη, ο φορέας βρίσκεται σε κατάσταση αποφόρτισης. Το κριτήριο περιγράφεται ως εξης:

Φόρτιση: $\tau_0^{current} \geq \tau_0^{previous}$ (4a)

Αποφόρτιση: $\tau_0^{current} < \tau_0^{previous}$ (4b)

Η αποφόρτιση θεωρείται ότι γίνεται ελαστικά και γι' αυτό χρησιμοποιείται το ελαστικό καταστατικό μητρώο του υλικού. Κατά την διάρκεια της επαναφόρτισης, ομοίως χρησιμοποιείται το ελαστικό καταστατικό μητρώο μέχρι η αποκλίνουσα τάση του αντίστοιχου σημείου Gauss να φτάσει το 50% της οριακής της τιμής. Όταν αυτό το όριο ξεπεραστεί χρησιμοποιείται η Σχέση (3) ώστε να ληφθούν υπόψη οι μη-γραμμικότητες λόγω των μικρορωγμών. Το κριτήριο φόρτισης/αποφόρτισης εφαρμόζεται σε κάθε εσωτερική επανάληψη Newton-Raphson. Συνεπώς είναι αρκετά πιθανό ένα σημείο Gauss να βρίσκεται σε κατάσταση φόρτισης και αποφόρτισης μέσα σε ένα εξωτερικό βήμα επιβαλλόμενης μετατόπισης.

Όταν ικανοποιείται το κριτήριο αστοχίας, τότε ένα επίπεδο ρωγμής σχηματίζεται κάθετα της διεύθυνσης της κύριας εφελκυστικής τάσης. Η ρηγμάτωσης προσομοιώνεται με τη μέθοδο της διανεμημένης ρηγμάτωσης (smeared crack approach). Αυτό σημαίνει πως η στιβαρότητα που αντιστοιχεί στην διεύθυνση κάθετα της κύριας εφελκυστικής ρωγμής μηδενίζεται όπως φαίνεται στην παρακάτω σχέση:

$$\boldsymbol{D} = \begin{bmatrix} 2G_t + \mu & \mu & \mathbf{0} & 0 & 0 & 0 \\ \mu & 2G_t + \mu & \mathbf{0} & 0 & 0 & 0 \\ \mathbf{0} & \mathbf{0} & \mathbf{0} & 0 & 0 & 0 \\ 0 & 0 & 0 & G_t & 0 & 0 \\ 0 & 0 & 0 & 0 & \boldsymbol{\beta} G_t & 0 \\ 0 & 0 & 0 & 0 & 0 & \boldsymbol{\beta} G_t \end{bmatrix} \quad (5)$$

Επιπλέον, χρησιμοποιείται ο συντελεστής β, ο οποίος ονομάζεται συντελεστής διατήρησης της διατμητικής στιβαρότητας. Αυτή η παραμένουσα διατμητική στιβαρότητα οφείλεται στην αλληλεμπλοκή των αδρανών στο επίπεδο της ρωγμής. Επιπλέον η χρήση μη μηδενικής διατμητικής στιβαρότητας στο επίπεδο της ρωγμής, αποτελεί σημαντικό ρόλο κατά την αριθμητική επίλυση και την ευστάθεια του μοντέλου. Στην παρούσα εργασία, χρησιμοποιείται η τιμή β=0.05 η οποία υποδηλώνει πως μόνο το 5% της αρχικής διατμητικής δυσκαμψίας παραμένει μετά την ρηγμάτωση. Ομοίως, όταν σχηματιστεί μία δεύτερη ρωγμή στο υπό εξέταση σημείο, τότε και αυτή είναι κάθετη στη διεύθυνση της νέας κύριας εφελκυστικής τάσης η οποία μαζί με τη πρώτη ρωγμή επιτρέπουν στο σημείο ολοκλήρωσης να αναπτύξει δυσκαμψία μόνο κατά μία διεύθυνση. Αυτή η διεύθυνση συμπίπτει με την τομή των δυο επιπέδων των ρωγμών.

$$\boldsymbol{D}=\begin{bmatrix} \mathbf{0} & \mathbf{0} & \mathbf{0} & 0 & 0 & 0 \\ \mathbf{0} & 2G_t+\mu & 0 & 0 & 0 & 0 \\ \mathbf{0} & 0 & 0 & 0 & 0 & 0 \\ 0 & 0 & 0 & \boldsymbol{\beta} G_t & 0 & 0 \\ 0 & 0 & 0 & 0 & \beta G_t & 0 \\ 0 & 0 & 0 & 0 & 0 & \beta G_t \end{bmatrix} \tag{6}$$

Στο Σχήμα 4 φαίνεται μια διατομή στην οποία έχουν σχηματιστεί δύο ρωγμές. Συγκεκριμένα παρατηρούμε το επίπεδο της κάθε ρωγμής και τους αντίστοιχους άξονες. Οι άξονες *x΄,y΄,z΄* αναφέρονται στην ρωγμή 1, ενώ οι άξονες *x΄΄,y΄΄,z΄΄* αναφέρονται στη ρωγμή 2. Οι άξονες *z΄, z΄΄* είναι αντίστοιχα κάθετοι στο επίπεδο της ρωγμής 1 και 2. Τα καταστατικά μητρώα, που προκύπτουν από τις Σχέσεις (5) και (6), περιγράφουν την ανισότροπη συμπεριφορά του υλικού. Συνεπώς απαιτείται ο κατάλληλος μετασχηματισμός των μητρώων αυτών έτσι ώστε να εκφραστούν ως προς τους καθολικούς άξονες. Αυτό γίνεται με τον ακόλουθο μετασχηματισμό:

$$\boldsymbol{D_{gl}}=\boldsymbol{T}^{\boldsymbol{T}}\boldsymbol{D}\boldsymbol{T} \tag{7}$$

Όπου $\boldsymbol{T}$, το μητρώο μετασχηματισμού του *i*-άξονα από το τοπικό Καρτεσιανό σύστημα (*x΄, y΄, z΄*) στο καθολικό Καρτεσιανό σύστημα συντεταγμένων (*x, y, z*) όπως ορίζεται από τα αντίστοιχα συνημίτονα κατεύθυνσης (l_i, m_i, n_i). Το μητρώο μετασχηματισμού έχει την εξής μορφή:

$$\boldsymbol{T}=\begin{bmatrix} l_1^{\,2} & m_1^{\,2} & n_1^{\,2} & l_1m_1 & m_1n_1 & n_1l_1 \\ l_2^{\,2} & m_2^{\,2} & n_2^{\,2} & l_2m_2 & m_2n_2 & n_2l_2 \\ l_3^{\,2} & m_3^{\,2} & n_3^{\,2} & l_3m_3 & m_3n_3 & n_3l_3 \\ 2l_1l_2 & 2m_1m_2 & 2n_1n_2 & l_1m_2+l_2m_1 & m_1n_2+m_2n_1 & n_1l_2+n_2l_1 \\ 2l_3l_1 & 2m_3m_1 & 2n_3n_1 & l_3m_1+l_1m_3 & m_3n_1+m_1n_3 & n_3l_1+n_1l_3 \\ 2l_2l_3 & 2m_2m_3 & 2n_2n_3 & l_2m_3+l_3m_2 & m_2n_3+m_3n_2 & n_2l_3+n_3l_2 \end{bmatrix} \tag{8}$$

Τέλος, η τρίτη ρωγμή οδηγεί σε καταστατικό μητρώο του υλικού με μηδενικούς όρους και τις παραμένουσες διατμητικές δυσκαμψίες:

$$\boldsymbol{D}=\begin{bmatrix} 0 & 0 & 0 & 0 & 0 & 0 \\ 0 & \mathbf{0} & 0 & 0 & 0 & 0 \\ 0 & 0 & 0 & 0 & 0 & 0 \\ 0 & 0 & 0 & \beta G_t & 0 & 0 \\ 0 & 0 & 0 & 0 & \beta G_t & 0 \\ 0 & 0 & 0 & 0 & 0 & \beta G_t \end{bmatrix} \tag{9}$$

Όταν ανοίγει μια ρωγμή κάθετα στη διεύθυνση της κύριας εφελκυστικής τάσης σ_I, η εφελκυστική τάση που προκάλεσε την αστοχία στο σκυρόδεμα, τίθεται μηδέν και μετατρέπεται σε ισοδύναμες μη εξισορροπούμενες δυνάμεις οι οποίες κατανέμονται εσωτερικά στο περιβάλλον αρηγμάτωτο σκυρόδεμα. Συνεπώς, οι τάσεις υπολογίζονται από την παρακάτω εξίσωση:

$$\boldsymbol{\sigma_{Cr}} = \boldsymbol{T}^{-1}\begin{bmatrix} \sigma_1 = 0 \\ \sigma_2 \\ \sigma_3 \\ 0 \\ 0 \\ 0 \end{bmatrix} \tag{10}$$

Όπου $\boldsymbol{T}^{-1}$ είναι το αντίστροφο του μητρώου μετασχηματισμού εκφραζόμενο στο κύριο σύστημα αξόνων με βάση τη Σχέση (8). Σε όποια από τις δύο καταστάσεις κι αν βρίσκεται το σημείο Gauss (ρηγματωμένο-αρηγμάτωτο), οι διορθώσεις των τάσεων δίνουν μη εξισορροπούμενες εσωτερικές δυνάμεις, οι οποίες επανέρχονται στην επόμενη επανάληψη της διαδικασίας ως ένα νέο διάνυσμα εξωτερικών φορτίσεων.

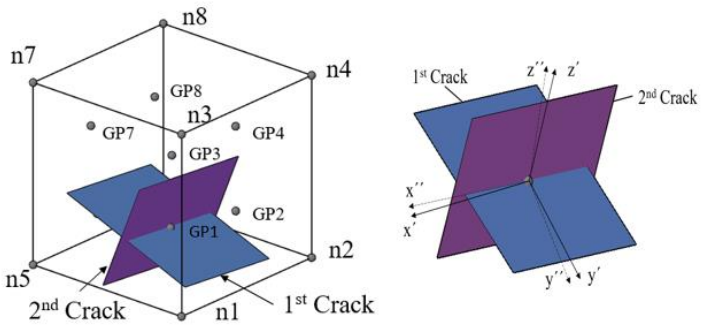

Σχήμα 4 Τοπικοί άξονες στην περίπτωση όπου έχουμε δυο ρωγμές σε ένα σημείο ολοκλήρωσης Gauss.

Το κλείσιμο των ρωγμών παίζει πολύ σημαντικό ρόλο στην μηχανική συμπεριφορά της κατασκευής, κυρίως στο πρώτο μισό κύκλο ανακυκλικής φόρτισης όπου καθορίζει την απομένουσα δυσκαμψία της κατασκευής η οποία θα ενεργοποιηθεί στο δεύτερο μισό κύκλο της ανακυκλικής φόρτισης. Η σύγκριση μεταξύ των αριθμητικών και πειραματικών αποτελεσμάτων έδειξε ότι οι παραμορφώσεις οι οποίες είναι κάθετα στο επίπεδο ρωγμής, μπορούν να αποκτήσουν μια χαμηλή τιμή με την οποία μπορεί να θεωρηθεί ότι έχουμε κλείσιμο ρωγμής. Η αναλυτική διερεύνηση που έγινε στην παρούσα εργασία έδειξε ότι κατά τη διάρκεια της αποφόρτισης, οι παραμορφώσεις οι οποίες είναι κάθετες στο επίπεδο ρωγμής παίρνουν μια αρκετά χαμηλή τιμή (όχι υποχρεωτικά αρνητική) σε σχέση με την παραμόρφωση η οποία προκάλεσε την αρχική ρηγμάτωση, όπου αριθμητικά η ρωγμή θεωρείτε ότι είναι ακόμη ανοικτή. Συνεπώς, προτείνεται ένα κριτήριο το οποίο καθορίζει τα ανεκτά όρια των παραμορφώσεων για τα οποία μπορούν να θεωρηθούν ότι οι ρωγμές είναι πρακτικά κλειστές. Το κριτήριο αυτό παίρνει την παρακάτω μορφή:

$$\varepsilon_i \leq a\varepsilon_{cr} \tag{11}$$

Όπου ε_i είναι η τρέχουσα παραμόρφωση που αναπτύσσεται στην i-διεύθυνση η οποία είναι κάθετη στο επίπεδο της ρωγμής και ε_{cr} είναι η παραμόρφωση που προκάλεσε την ρωγμάτωση. Η μεταβλητή a είναι ένας μειωτικός παράγοντας. Μετά από αριθμητική διερεύνηση, προέκυψε ότι όταν η ρωγμή σε ένα σημείο ολοκλήρωσης σχηματίζεται στο πρώτο επαυξητικό βήμα ενός κλάδου επιβαλλόμενης μετατόπισης, τότε το $\varepsilon_i \cong \varepsilon_{cr}$ όταν η κατασκευή επανέρχεται στην αρχική θέση ισορροπίας. Παράλληλα, όταν η ρωγμή ενός σημείου ολοκλήρωσης σχηματίζεται στο τελευταίο επαυξητικό βήμα ενός κλάδου επιβαλλόμενης μετατόπισης, τότε το $\varepsilon_i \cong 0$ όταν

η κατασκευή επανέρχεται στην αρχική θέση ισορροπίας. Σύμφωνα με τις παραπάνω παρατηρήσεις η παράμετρος *α* υπολογίζεται σύμφωνα με την παρακάτω σχέση:

$$a = 1 - \frac{\varepsilon_{cr}}{\varepsilon_{\max}} \tag{12}$$

Όπου ε_{max} είναι η μέγιστη τιμή της παραμόρφωσης που μπορεί να εμφανιστεί κάθετα στη διεύθυνση της ρωγμής σύμφωνα με την επιβαλλόμενη μετατόπιση. Θεωρείται ότι $\varepsilon_{cr} \approx n_{cr}\,\varepsilon$ και $\varepsilon_{max} \approx n_{tot}\,\varepsilon$ ("≈" λόγω της επιρροής της ισοδύναμης υδροστατικής τάσης σ_{id}), όπου n_{cr} και n_{tot} είναι ο αριθμός του βήματος στο οποίο εμφανίστηκε η ρωγμή και ο συνολικός αριθμός των βημάτων στο οποίο έχει διαιρεθεί ένας κλάδος επιβαλλόμενης μετατόπισης. Επιπλέον, ε είναι η παραμόρφωση που αντιστοιχεί σε κάθε επαυξητικό βήμα επιβαλλόμενης μετατόπισης. Έτσι, η Σχέση (12) παίρνει την εξής μορφή:

$$a = b - \frac{n_{cr}}{n_{tot}} \tag{13}$$

Όπου *b* είναι ο αριθμός του κλάδου επιβαλλόμενης μετατόπισης. Τέλος, για να αυξηθεί το όριο ανέχειας ούτως ώστε οι παραμορφώσεις να θεωρούνται εντός ορίων όπου οι ρωγμές κλείνουν κατά την αποφόρτιση, προστίθεται ο όρος $1/n_{tot}$ στην Σχέση (13):

$$a = b - \frac{n_{cr} - 1}{n_{tot}} \tag{14}$$

Οι μεταβλητές που συνθέτουν την παράμετρο *α* περιγράφονται στο Σχήμα 5 στην περίπτωση όπου n_{tot}=10.

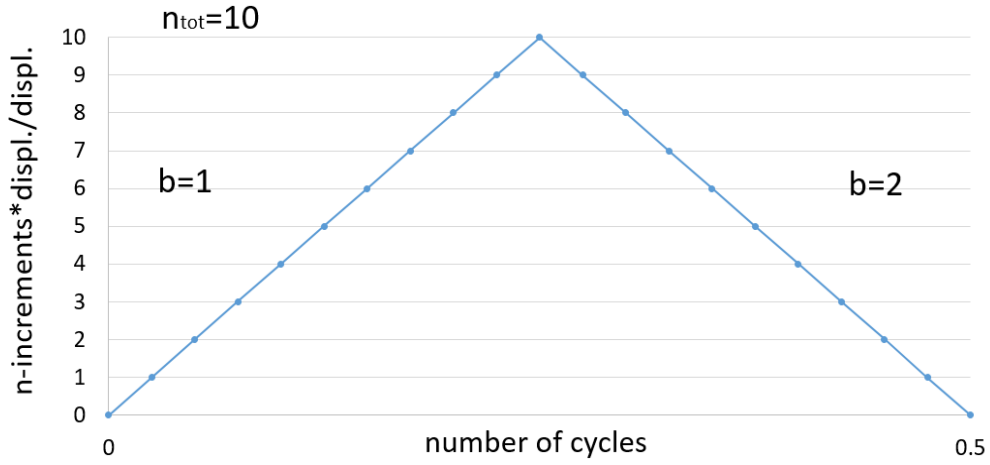

Σχήμα 5 Κανονικοποιημένη (διαιρεμένη με την επιβαλλόμενη μετατόπιση κάθε προσαυξητικού βήματος) συνάρτηση επιβαλλόμενης μετατόπισης σε μισό κύκλο φόρτισης.

Όταν η ρωγμή κλείσει, το ελαστικό καταστατικό μητρώο χρησιμοποιείται ώστε να υπολογιστούν οι τάσεις του προηγουμένως ρηγματωμένου σημείου ολοκλήρωσης στην επόμενη εσωτερική επανάληψη. Συνεπώς, οι τάσεις στη *i*-Newton-Raphson υπολογίζεται ως εξής:

$$\sigma^i = \sigma^{i-1} + D_{el}\Delta\varepsilon^i \tag{15}$$

Όταν το D_{el} υπολογίζεται από τη Σχέση (3) με $K=K_{el}(f_c)$ και $G=G_{el}(f_c)$ (Kotsovos και Pavlovic [29]), $\Delta\varepsilon^i$ είναι οι τρέχουσες παραμορφώσεις της i-επανάληψης και σ^{i-1} είναι οι τάσεις της (i-1)-επανάληψης στο ρηγματωμένο σημείο ολοκλήρωσης.

<u>Κριτήριο αστοχίας</u>

Η επιφάνεια αστοχίας που χρησιμοποιείται στο σκυρόδεμα, κάνοντας χρήση των οκταεδρικών τάσεων φαίνονται στο Σχήμα 6. Για να προσδιοριστεί η περιβάλλουσα αστοχίας, αρκεί να προβληθεί η επιφάνεια αστοχίας στο αποκλίνων επίπεδο, το οποίο είναι κάθετο στην διεύθυνση της σ_0. Η περιβάλλουσα καμπύλη μας δείχνει τα όρια της μέγιστης επιτρεπόμενης τιμής της μέγιστης αποκλίνουσας τάσης τ_{0u}. Η μέγιστη τιμή τ_{0u} υπολογίζεται από την υδροστατική τάση σ_0 και την γωνία θ. Η γωνία θ είναι η γωνία που σχηματίζει το διάνυσμα της αποκλίνουσας τάσης τ_0 με την προβολή οποιουδήποτε άξονα του συστήματος αξόνων των κυρίων τάσεων στο αποκλίνων επίπεδο. Η τιμή της τ_{0u} δίνεται από την παρακάτω σχέση:

$$\tau_{0u} = \frac{2\tau_{0c}(\tau_{0c}^2 - \tau_{0e}^2)\cos\theta + \tau_{0c}(2\tau_{0e} - \tau_{0c})\sqrt{4(\tau_{0c}^2 - \tau_{0e}^2)\cos^2\theta + 5\tau_{0e}^2 - 4\tau_{0c}\tau_{0e}}}{4(\tau_{0c}^2 - \tau_{0e}^2)\cos^2\theta + (2\tau_{0e} - \tau_{0c})^2} \tag{16}$$

για $60°<\theta<0°$.

Η επιφάνεια που περιγράφεται από την παραπάνω σχέση, είναι μια ομαλή κυρτή επιφάνεια της οποίας οι εφαπτόμενες είναι κάθετες στις διευθύνσεις των τάσεων τ_{0e} και τ_{0c} για θ=0° και θ=60°, αντίστοιχα. Στην παραπάνω σχέση είναι η έκφραση των Willam and Warnke [33] στην οποία έχουν παρεμβληθεί τα μεγέθη τ_{0e} και τ_{0c}.

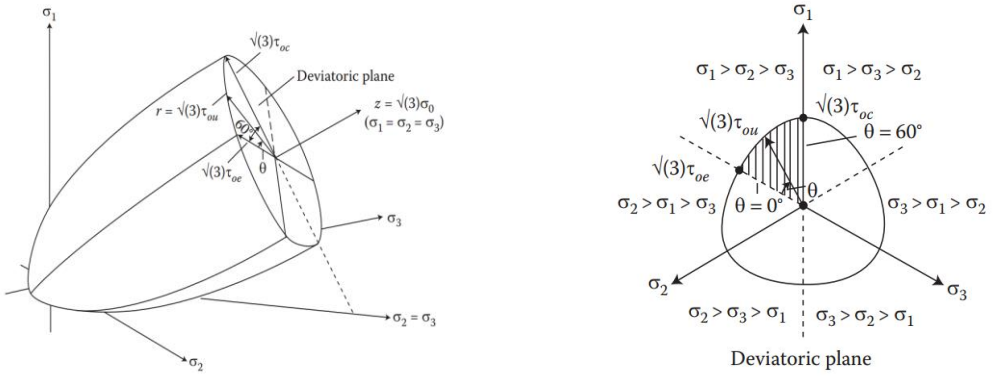

(a) (b)

Σχήμα 6 Σχηματική αναπαράσταση της επιφάνειας μέγιστης αντοχής (α) Προοπτικό στο χώρο των τάσεων (b) Εγκάρσια τομή της επιφάνειας αστοχίας με το αποκλίνων επίπεδο [3].

Οι αναλυτικές εκφράσεις των τ_{0e} και τ_{0c} προκύπτουν από την ανάλυση πειραματικών αποτελεσμάτων και δίνονται από τις παρακάτω σχέσεις:

$$\tau_{0c} / f_c = 0.944(\sigma_0 / f_c + 0.05)^{0.724} \tag{17}$$

$$\tau_{0e} / f_c = 0.633(\sigma_0 / f_c + 0.05)^{0.857} \tag{18}$$

Με τις παραπάνω σχέσεις, υπολογίζουμε τα μεγέθη σ_0, τ_{0e} και τ_{0c}, και με αυτόν τον τρόπο μπορούμε να καθορίσουμε πλήρως την επιφάνεια αστοχίας.

<u>Προτεινόμενη παράμετρος βλάβης σκυροδέματος</u>

Σε περιπτώσεις όπου η κατασκευή από οπλισμένο σκυρόδεμα υπόκειται σε ένα μεγάλο αριθμό ανακυκλίσεων ή σε δυναμική φόρτιση, είναι λογικό να υποθέσουμε ότι το ανοιγοκλείσιμο των ρωγμών αποτελεί έναν σημαντικό παράγοντα που συμβάλλει στην παραμένουσα βλάβη στο σκυρόδεμα κατά την διάρκεια της φόρτισης. Γενικότερα, η βλάβη που υφίσταται το σκυρόδεμα λόγω του ανοίγματος ή του κλεισίματος των ρωγμών καθορίζει και την υστερητική συμπεριφορά της κατασκευής.

Συνεπώς προτάθηκε μια παράμετρος βλάβης η οποία σχετίζεται με το μέγεθος της ρηγμάτωσης και τον αριθμό του ανοιγοκλεισίματος που καταγράφηκε σε κάθε ρωγμή κατά την διάρκεια της ανάλυσης. Για το μέγεθος της ρηγμάτωσης χρησιμοποιήθηκε η παράμετρος a (Σχέση (12)) η οποία εκφράζει το ποσοστό της παραμόρφωσης το οποίο αναπτύχθηκε κατά την διάρκεια ανοίγματος της ρωγμής μέχρι το κλείσιμο αυτής. Συνεπώς η παράμετρος a είναι ένα μέγεθος που εκφράζει το μέγεθος της ενέργειας που καταναλώνεται από την στιγμή που ανοίγει μια ρωγμή μέχρι το κλείσιμο της. Επιπλέον, το μέγεθος της παραμόρφωσης μιας ρωγμής στο επίπεδο αριθμητικής προσομοίωσης, αντιπροσωπεύει ένα σύνολο ρωγμών κοντά στο σημείο ολοκλήρωσης. Μετά από παραμετρική διερεύνηση, προτάθηκε η παρακάτω έκφραση της παραμέτρου βλάβης σκυροδέματος:

$$D_c = e^{-(1-a)/f_{cc}} = e^{-\left(1-\left(1-\frac{\varepsilon_{cr}}{\varepsilon_{\max}}\right)\right)/f_{cc}} = e^{-\left(\frac{\varepsilon_{cr}}{\varepsilon_{\max}}\right)/f_{cc}} \tag{19}$$

Όπου f_{cc} είναι ο αριθμός των ανοιγοκλεισιμάτων των ρωγμών. Όσο αυξάνεται ο αριθμός τον ανοιγοκλεισιμάτων f_{cc} καθώς και η παράμετρος a, η παράμετρος βλάβης D_c αυξάνεται. Η σχηματική απεικόνιση αυτής της συνάρτησης φαίνεται στο Σχήμα 7.

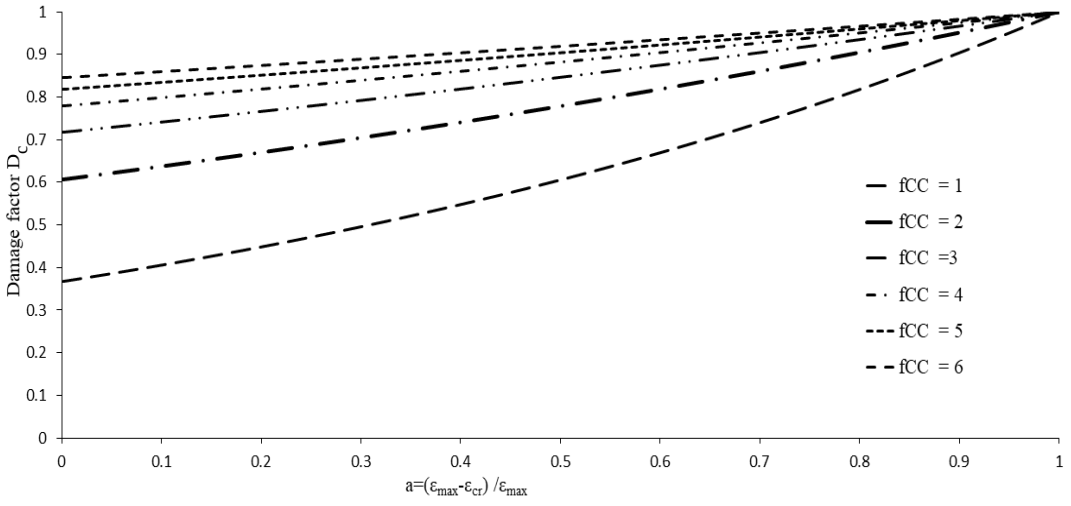

Σχήμα 7 Σχηματική απεικόνιση της παραμέτρου D_c συναρτήσει της παραμέτρου α και της f_{cc}.

Όταν ικανοποιείται το κριτήριο κλεισίματος της ρωγμής (Σχέση (11)) σε ένα σημείο ολοκλήρωσης Gauss Point (GP), ένα μέρος της δυσκαμψίας του χάνεται στο επίπεδο της ρωγμής ή οποία κλείνει. Υποθέτοντας ότι η ρωγμή η οποία κλείνει ήταν σχηματισμένη στον *x'*

άξονα και χρησιμοποιώντας τη Σχέση (19), το καταστατικό μητρώο του υλικού παίρνει την παρακάτω μορφή:(12)(12)

$$\boldsymbol{C}_l^{'}=\begin{bmatrix} a_n\cdot(1-D_c)\cdot(2G_t+\mu) & a_n\cdot(1-D_c)\cdot\mu & a_n\cdot(1-D_c)\cdot\mu & 0 & 0 & 0 \\ a_n\cdot(1-D_c)\cdot\mu & 2G_t+\mu & \mu & 0 & 0 & 0 \\ a_n\cdot(1-D_c)\cdot\mu & \mu & 2G_t+\mu & 0 & 0 & 0 \\ 0 & 0 & 0 & a_s\cdot(1-D_c)\cdot\beta\cdot G_t & 0 & 0 \\ 0 & 0 & 0 & 0 & a_s\cdot(1-D_c)\cdot\beta\cdot G_t & 0 \\ 0 & 0 & 0 & 0 & 0 & a_s\cdot(1-D_c)\cdot\beta\cdot G_t \end{bmatrix} \tag{20}$$

Οι παράμετροι a_n και a_s είναι σταθερές και ίσες με 0.25 και 0.125, αντίστοιχα. Οι τιμές αυτές έχουν προκύψει μετά από εκτενή παραμετρική διερεύνηση, συγκρίνοντας τα αριθμητικά με τα πειραματικά αποτελέσματα που προέρχονταν από την ανάλυση φορέων από οπλισμένο σκυρόδεμα σε ανακυκλική και δυναμική φόρτιση. Ομοίως, στην περίπτωση που κλείνουνε δύο ρωγμές και υποθέτοντας πως τα επίπεδα των ρωγμών είναι κάθετα στους άξονες *x'* και *y'* το καταστατικό μητρώο παίρνει την ακόλουθη μορφή:

$$\boldsymbol{C}_l^{''}=\begin{bmatrix} a_n\cdot(1-D_c)\cdot(2G_t+\mu) & a_n\cdot(1-D_c)\cdot\mu & a_n\cdot(1-D_c)\cdot\mu & 0 & 0 & 0 \\ a_n\cdot(1-D_c)\cdot\mu & a_n\cdot(1-D_c)\cdot(2G_t+\mu) & a_n\cdot(1-D_c)\cdot\mu & 0 & 0 & 0 \\ a_n\cdot(1-D_c)\cdot\mu & a_n\cdot(1-D_c)\cdot\mu & 2G_t+\mu & 0 & 0 & 0 \\ 0 & 0 & 0 & a_s\cdot(1-D_c)\cdot\beta\cdot G_t & 0 & 0 \\ 0 & 0 & 0 & 0 & a_s\cdot(1-D_c)\cdot\beta\cdot G_t & 0 \\ 0 & 0 & 0 & 0 & 0 & a_s\cdot(1-D_c)\cdot\beta\cdot G_t \end{bmatrix} \tag{21}$$

Οι Σχέσεις (20) και (21) περιγράφουν την ανισότροπη συμπεριφορά του σκυροδέματος στο τοπικό σύστημα και γι' αυτό απαιτείται ο κατάλληλος μετασχηματισμός των μητρώων με χρήση του μητρώου μετασχηματισμού της Σχέσης (8). Συνεπώς το μητρώο εκφρασμένου στο καθολικό σύστημα αξόνων υπολογίζεται από την ακόλουθη σχέση:

$$\boldsymbol{C}_g = \boldsymbol{T}^T\boldsymbol{C}_l\boldsymbol{T} \tag{22}$$

Οι τάσεις που αναπτύσσονται στο GP όταν ικανοποιείται το κριτήριο κλεισίματος της ρωγμής, υπολογίζεται από την παρακάτω σχέση:

$$\boldsymbol{\sigma}^i = \boldsymbol{\sigma}^{i-1} + \boldsymbol{C}_g\cdot\boldsymbol{\Delta\varepsilon}^i \tag{23}$$

Επιπροσθέτως, όταν σε ένα GP έχουν κλείσει όλες οι ρωγμές (θεωρείται αρηγμάτωτο) ενώ η παράμετρος *a* έχει τιμή ίση ή μεγαλύτερη του 0.5, τότε το καταστατικό μητρώο του υλικού υπολογίζεται σύμφωνα με την ακόλουθη εξίσωση:

$$\boldsymbol{C}_g{}' = (1-D_c)\cdot\boldsymbol{C}_g \tag{24}$$

Τα διαγράμματα ροής που περιγράφουν τον αλγόριθμο που αναπτύχθηκε για την περιγραφή του καταστατικού μοντέλου για ένα GP το οποίο είναι ρηγματωμένο ή αρηγμάτωτο φαίνονται στα Σχήματα 8, 9 και 10.

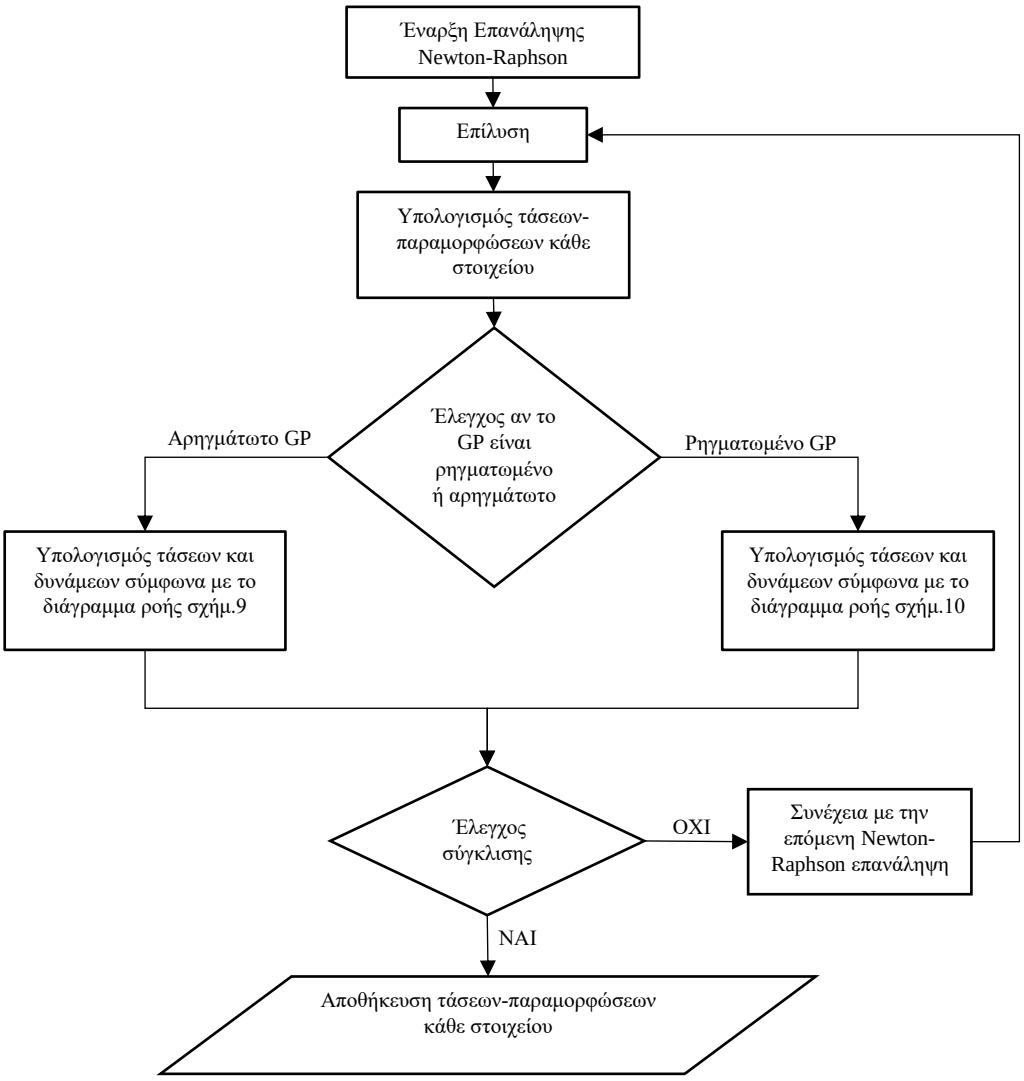

Σχήμα 8 Διάγραμμα ροής προτεινόμενου αλγορίθμου για το καταστατικό μοντέλο του σκυροδέματος.

IV. Καταστατικό μοντέλο χάλυβα οπλισμού

Για τα στοιχεία του οπλισμού χρησιμοποιήθηκε το μοντέλο των Menegotto και Pinto [34] το οποίο προσομοιώνει ρεαλιστικά τη συμπεριφορά του χάλυβα, συμπεριλαμβάνοντας το φαινόμενο Bauschinger. Η σχέση τάσεων παραμορφώσεων δίνεται από τον παρακάτω τύπο:

$$\sigma^* = b \cdot \varepsilon^* + \frac{(1-b)\cdot \varepsilon^*}{\left(1+\varepsilon^{*R}\right)^{\frac{1}{R}}} \tag{25}$$

όπου, $\varepsilon^* = (\varepsilon - \varepsilon_r)/(\varepsilon_0 - \varepsilon_r)$, $\sigma^* = (\sigma - \sigma_r)/(\sigma_0 - \sigma_r)$ και

$$R = R_0 - \frac{a_1 \xi}{\alpha_2 + \xi} \tag{26}$$

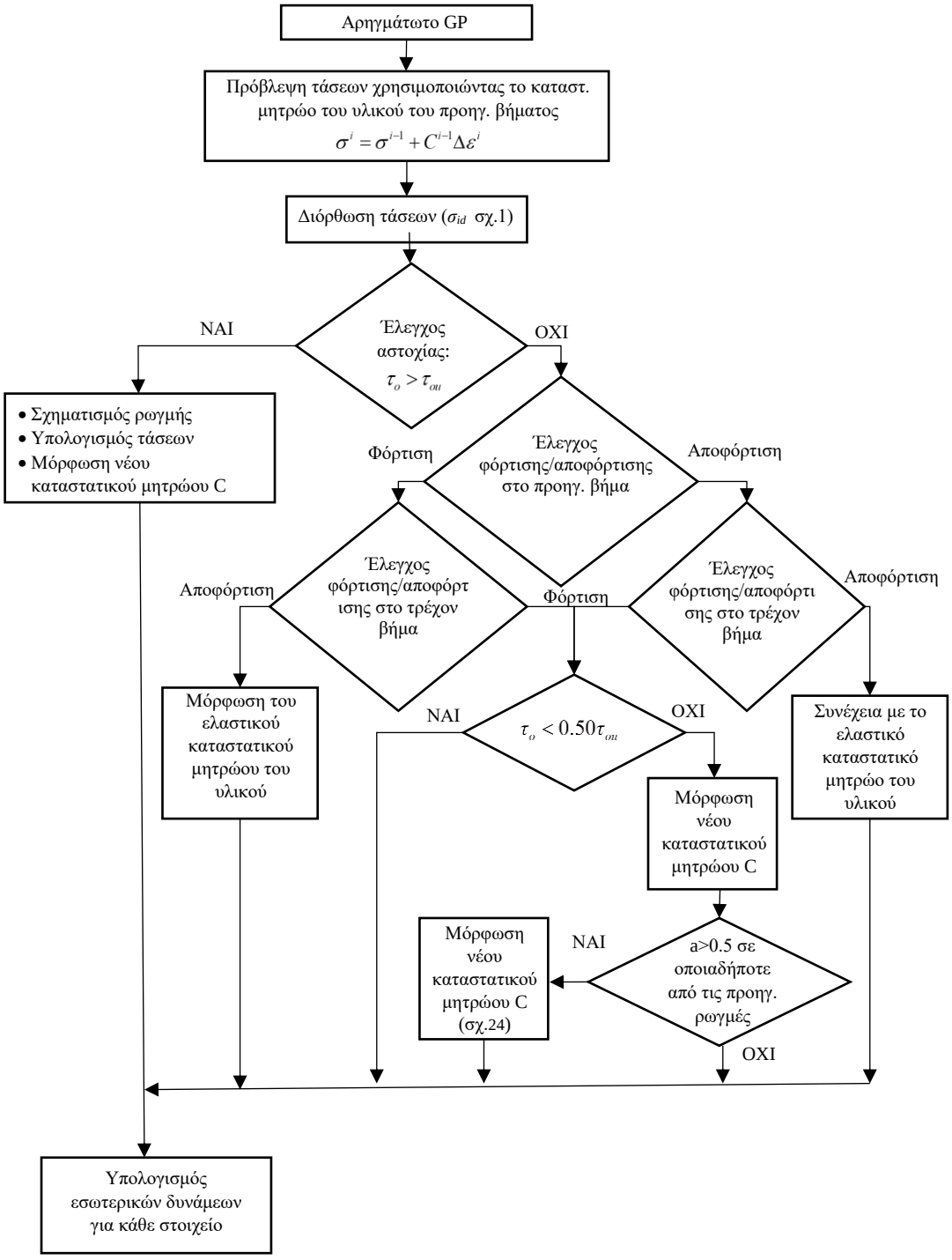

Σχήμα 9 Διάγραμμα ροής προτεινόμενου αλγορίθμου για το καταστατικό μοντέλο του σκυροδέματος για την περίπτωση ενός αρηγμάτωτου GP.

Η παράμετρος *b* είναι ίση με το πηλίκο E_0/E_t, όπου E_0 είναι το αρχικό μέτρο ελαστικότητας και E_t το μέτρο κράτυνσης του χάλυβα, σ_0 και ε_0 είναι η τάση και η παραμόρφωση αντίστοιχα του σημείου τομής των ασύμπτωτων ευθειών όπως φαίνεται στο Σχήμα 11. Όπου ε_r και σ_r είναι οι συντεταγμένες του σημείου στο οποίο πραγματοποιήθηκε η τελευταία αλλαγή της φοράς της φόρτισης. Η παράμετρος R είναι μια φθίνουσα συνάρτηση του ξ, το οποίο είναι η παραμορφωσιακή διαφορά όπως φαίνεται στο Σχήμα 11(a). Η παράμετρος R εκφράζει την

καμπυλότητα του τόξου συναρμογής, που καθορίζει το σχήμα της καμπύλης μετάβασης. Καθώς η παράμετρος αυτή αυξάνεται, η μετάβαση από τη μία ευθεία στην άλλη γίνεται πιο απότομη. Οι παράμετροι R_0, a_1 και a_2 προσδιορίζονται πειραματικά και οι τιμές που επιλέχθηκαν στην παρούσα διατριβή είναι 20, 18.5 και 0.15 αντίστοιχα.

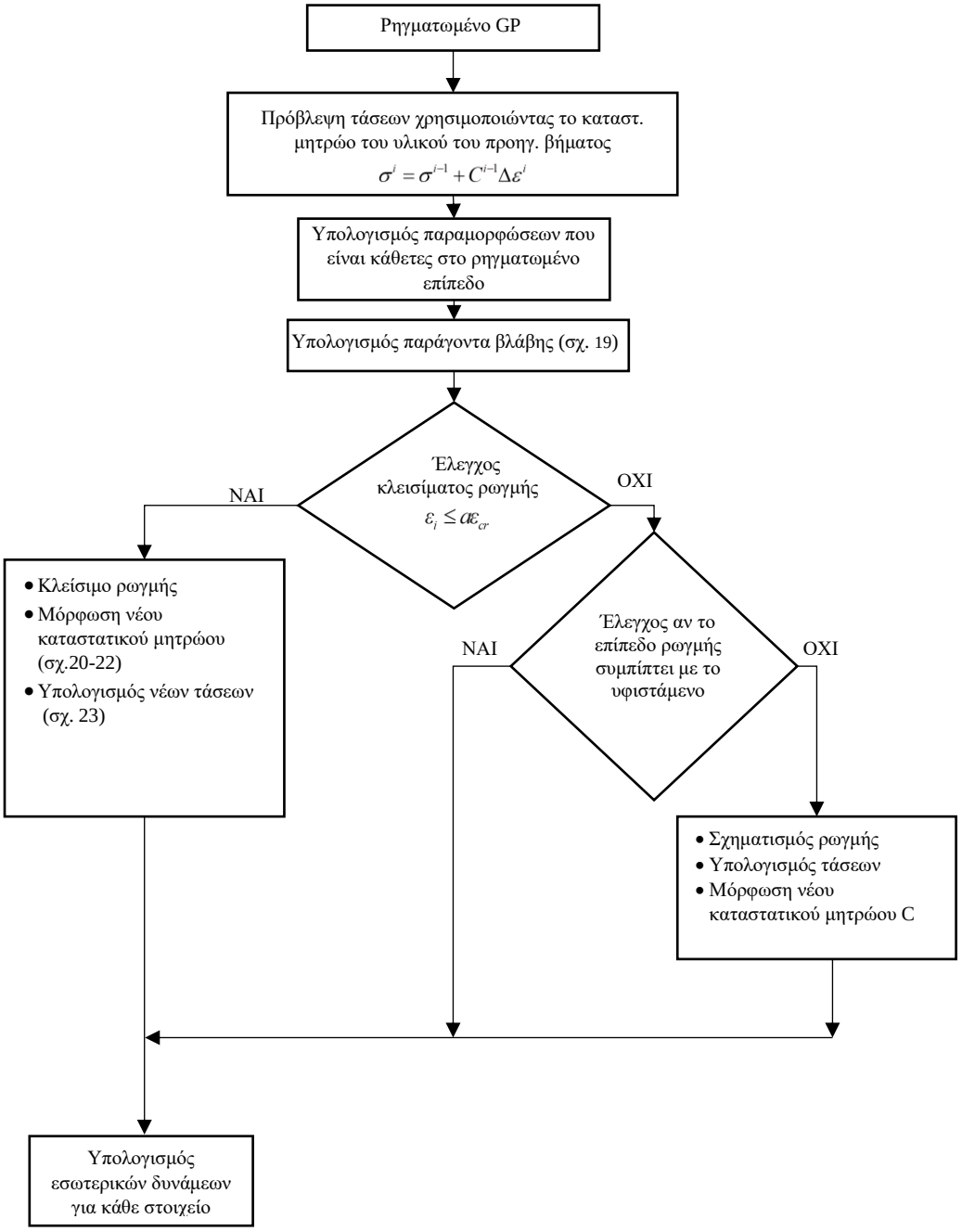

Σχήμα 10 Διάγραμμα ροής προτεινόμενου αλγορίθμου για το καταστατικό μοντέλο του σκυροδέματος για την περίπτωση ενός ρηγματωμένου GP.

<u>Προτεινόμενη παράμετρος βλάβης χάλυβα οπλισμού</u>

Σε φορείς που παρουσιάζουν έντονη διατμητική συμπεριφορά, η έντονη ρηγμάτωση του σκυροδέματος οδηγεί σε μεγάλη συγκέντρωση τάσεων στις ράβδους χάλυβα. Η μείωση της φέρουσας ικανότητας της κατασκευής σε περιοχές όπου παρουσιάζεται έντονη ρηγμάτωση επηρεάζει σημαντικά το μέγεθος των κύκλων υστέρησης που αναπτύσσει η κατασκευή στην εκάστοτε καταπόνηση.

Πειραματικά αποτελέσματα, έδειξαν πως οι κατασκευές από οπλισμένο σκυρόδεμα που παρουσιάζουν έντονες διατμητικές παραμορφώσεις (π.χ. τοιχία και κόμβοι), αναπτύσσουν σημαντικά φαινόμενα στένωσης των κύκλων υστέρησης (pinching effect) όταν η παραμόρφωση κατά την διάρκεια της ανακύκλισης πλησιάσει την τιμή μηδέν (αποφόρτιση). Η έντονη ρηγμάτωση καθώς και το πλήθος των ανοιγοκλεισιμάτων των ρωγμών συμβάλλουν σημαντικά στην έλλειψη συνάφειας του οπλισμού από το ρηγματωμένο σκυρόδεμα που τον περιβάλλει. Η επιρροή του ανοιγοκλεισίματος των ρωγμών στην στένωση των βρόχων υστέρησης (pinching effect) εξετάζεται πειραματικά στα άρθρα [35, 36]. Συνεπώς η στένωση των βρόγχων υστέρησης μπορεί να ληφθεί υπόψη μειώνοντας την συνεισφορά του χάλυβα του οπλισμού στην δυσκαμψία του φορέα λόγω έντονης ρηγμάτωσης. Αυτή η μείωση της συνεισφοράς του χάλυβα στην δυσκαμψία του φορέα, προσομοιώνει έμμεσα την έλλειψη συνάφειας του οπλισμού με το ρηγματωμένο σκυρόδεμα.

Το επίπεδο της ζημιάς του ρηγματωμένου σκυροδέματος μπορεί να υπολογιστεί με χρήση της παραμέτρου a (Σχέση (12)), όπως εξηγήθηκε στο υποκεφάλαιο III. Ο μέσος όρος όλων των παραμέτρων a που υπολογίστηκαν σε κάθε GP, εκφράζει ένα ποσοστό καταπόνησης του υλικού του στοιχείου. Δεδομένης της χρήσης του αλγόριθμου καταγραφής του αριθμού ανοιγοκλεισίματος ρωγμών, προτάθηκε η παράμετρος βλάβης για τον χάλυβα του οπλισμού με την παρακάτω μορφή:

$$D_s = \left[1 - a_{Element}\right] \tag{27}$$

Όπου:

$$a_{Element} = \frac{\sum_{1}^{ncr} a_i}{ncr} \text{ και } ncr \text{ είναι αριθμός των ρηγματωμένων GPs} \tag{28}$$

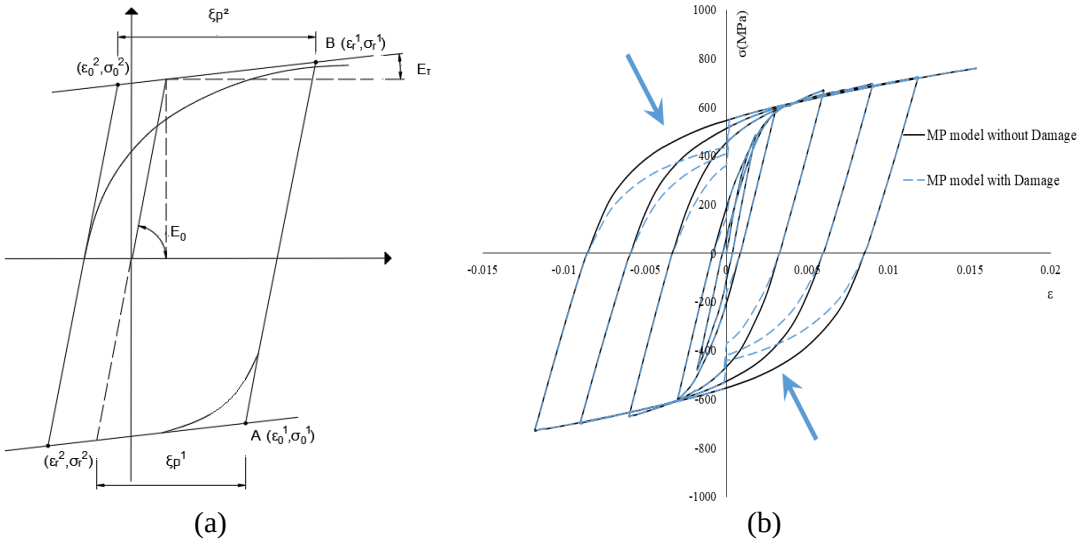

(a) (b)

Σχήμα 11 (α) Μοντέλο Menegotto-Pinto και (β) Τροποποιημένο Μοντέλο Menegotto-Pinto που λαμβάνει υπόψη του την μειωμένη συνεισφορά του χάλυβα οπλισμού λόγω ρηγμάτωσης.

Στην περίπτωση της αποφόρτισης, όταν η παραμόρφωση της κατασκευής φτάσει κοντά στο μηδέν, εφαρμόζεται μια μείωση της δυσκαμψίας του μέτρου ελαστικότητας του υλικού όπως περιγράφεται από τον παρακάτω τύπο:

$$E_s^{'} = (1 - D_s) E_s \tag{29}$$

Η Σχέση (29) εφαρμόζεται όταν $\sigma_s \cdot \varepsilon_s < 0$, που περιγράφει την περιοχή όπου οι ρωγμές τείνουν να κλείσουν και το φαινόμενο της στένωσης γίνεται αρκετά έντονο. Το τροποποιημένο καταστατικό μοντέλο του υλικού του χάλυβα φαίνεται στο Σχήμα 11(b).

V. Αριθμητική προσομοίωση με χρήση πεπερασμένων στοιχείων

Στην παρούσα διατριβή, χρησιμοποιήθηκαν τα εξαεδρικά ισοπαραμετρικά στοιχεία 8 και 20 κόμβων προκειμένου να προσομοιωθούν κατασκευές από οπλισμένο σκυρόδεμα. Ο χάλυβας οπλισμού προσομοιώνεται με ραβδωτά στοιχεία δικτυώματος (truss elements) ή με φυσικά στοιχεία δυνάμεων δοκού-υποστυλώματος (natural beam-column flexibility-based elements). Μέσω της χρήσης των στοιχείων δοκού, τα πεπερασμένα στοιχεία του οπλισμού συμβάλλουν στην διατμητική και καμπτική δυσκαμψία του φορέα και κυρίως παίζουν σημαντικό ρόλο στην αριθμητική ευστάθεια της μη-γραμμικής ανάλυσης [4]. Τα στοιχεία του οπλισμού προσομοιώνονται ως διακριτά στοιχεία ενσωματωμένα (embedded) στα εξαεδρικά στοιχεία σκυροδέματος. Με αυτόν τον τρόπο, δεν υπάρχει κάποιος περιορισμός στην διεύθυνση και στην θέση των στοιχείων του οπλισμού μέσα στο εξαεδρικό στοιχείο. Η σύνδεση των στοιχείων οπλισμού με τα αντίστοιχα εξαεδρικά στοιχεία επιτυγχάνεται μέσω επιβολής κινηματικών εξαρτήσεων. Στην περίπτωση ενός στοιχείου δικτυώματος, οι συνθήκες συμβιβαστότητας μεταξύ των ακραίων κόμβων του δικτυώματος και των αντίστοιχων κόμβων του εξαεδρικού στοιχείου επιβάλλονται μόνο μέσω των μεταφορικών βαθμών ελευθερίας. Όταν όμως χρησιμοποιείται ένα στοιχείο δοκού πρέπει να οριστεί η εξάρτιση των στροφών των κόμβων του στοιχείου δοκού με τις στροφές των εδρών του εξαεδρικού στοιχείου (Σχήμα 12).

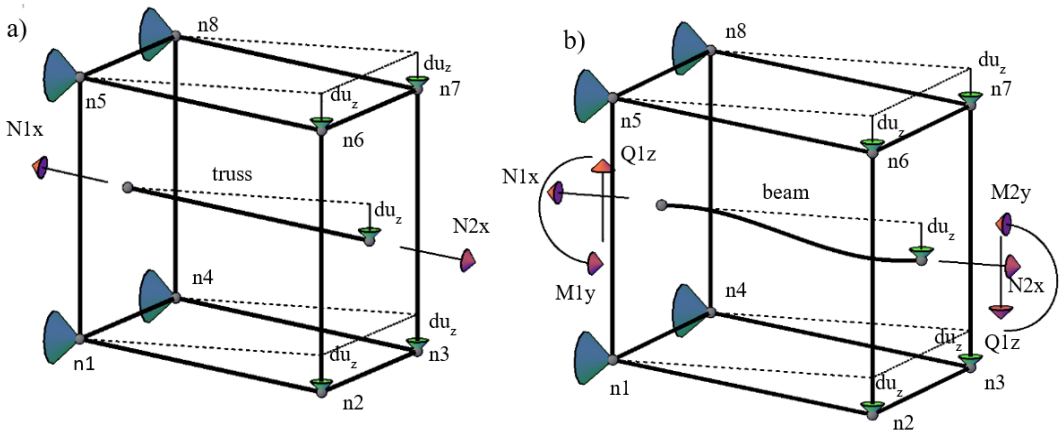

Σχήμα 12 Η απαραμόρφωτη και η παραμορφωμένη ενός ενσωματωμένου (εντός του εξαεδρικού) a) στοιχείου δικτυώματος (truss element) b) στοιχείο δοκού-υποστυλώματος (beam-column element)

<u>Υβριδικό μοντέλο προσομοίωσης HYMOD</u>

Σύμφωνα με το προτεινόμενο υβριδικό προσομοίωμα που παρουσιάστηκε από τους Markou και Papadrakakis [37], συνδυάζονται τα εξαεδρικά στοιχεία με στοιχεία δοκού-υποστυλώματος μέσω της επιβολής κινηματικών εξαρτήσεων. Οι κινηματικές εξαρτήσεις εφαρμόζονται στους κόμβους που βρίσκονται στην διεπιφάνεια $\boldsymbol{\Omega_i^1}$ των δυο τύπων πεπερασμένων στοιχείων (Σχήμα 13).

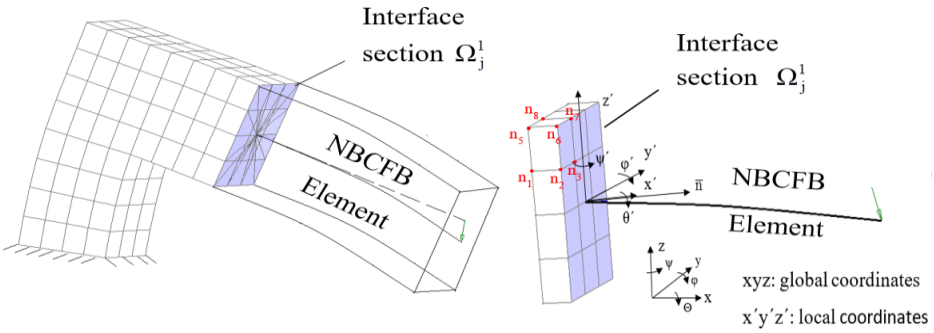

Σχήμα 13 Επιβαλλόμενες κινηματικές εξαρτήσεις από ένα δομικό στοιχείο δοκού πάνω στην διεπιφάνεια $\boldsymbol{\Omega_i^1}$

Συνεπώς οι περιοχές που παρουσιάζουν σημαντική διατμητική συμπεριφορά (όπως τοιχία και κόμβοι πλαισίων), προσομοιώνονται με την χρήση του τρισδιάστατου λεπτομερούς μοντέλου, ενώ οι περιοχές που παρουσιάζουν κυρίως καμπτική συμπεριφορά προσομοιώνονται με την χρήση στοιχείων δοκού-υποστυλώματος. Με αυτόν τον τρόπο μειώνονται οι βαθμοί ελευθερίας του φορέα και αντίστοιχα του υπολογιστικού κόστους της ανάλυσης χωρίς να μειώνεται η ακρίβεια της.

VI. Αριθμητικές εφαρμογές

<u>Εσωτερικός κόμβος πλαισίου υπό ανακυκλιζόμενη φόρτιση</u>

Ο εσωτερικός κόμβος που φαίνεται στο Σχήμα 14, υποβλήθηκε σε ανακυκλιζόμενη φόρτιση από τους Shiohara και Kusuhara [38] όπου εξετάστηκε η μηχανική συμπεριφορά του. Η μονοαξονική θλιπτική αντοχή του σκυροδέματος που χρησιμοποιήθηκε, είναι ίση με f_c = 28.3 MPa και η τάση διαρροής του χάλυβα οπλισμού είναι ίση με 456 MPa για τις ράβδους διαμέτρου 13 mm που βρίσκονται στο δοκάρι, ενώ οι ράβδοι που βρίσκονται στο υποστύλωμα παρουσιάζουν τάση διαρροής ίση με 357 MPa. Το μέτρο ελαστικότητας του χάλυβα που χρησιμοποιήθηκε είχε τιμή ίση με E_S = 176 GPa. Οι συνδετήρες αντίστοιχα έχουν 6 mm διάμετρο με τάση διαρροής ίση με 326 MPa και μέτρο ελαστικότητας ίσο με 151 GPa.

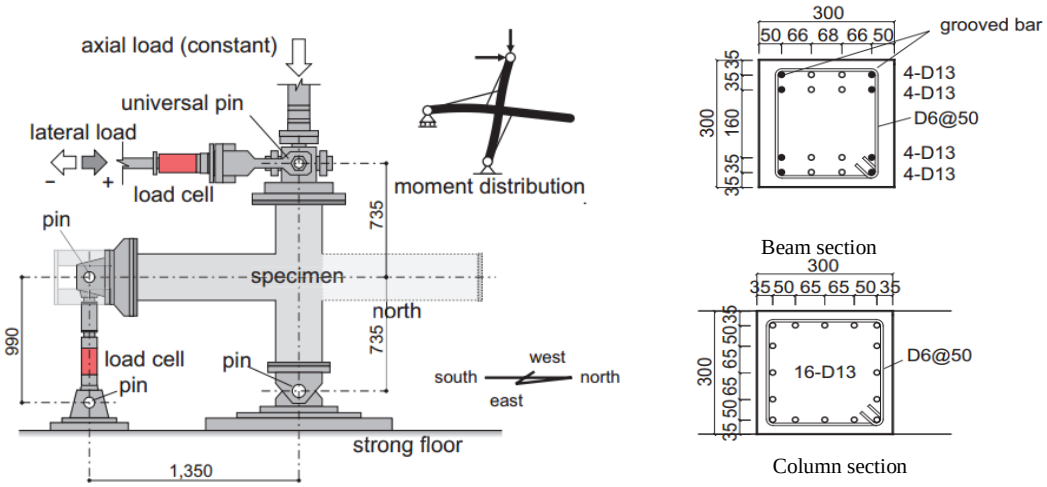

Σχήμα 14 Λεπτομέρειες γεωμετρίας και οπλισμού του εσωτερικού κόμβου πλαισίου [38]. *Διαστάσεις σε mm.*

Ο κόμβος υποβάλλεται σε ανακυκλιζόμενη φόρτιση όπως περιγράφεται στο πείραμα. Η ιστορία φόρτισης η οποία φαίνεται στο Σχήμα 15, αποτελείται από 15 κύκλους επιβαλλόμενης μετατόπισης.

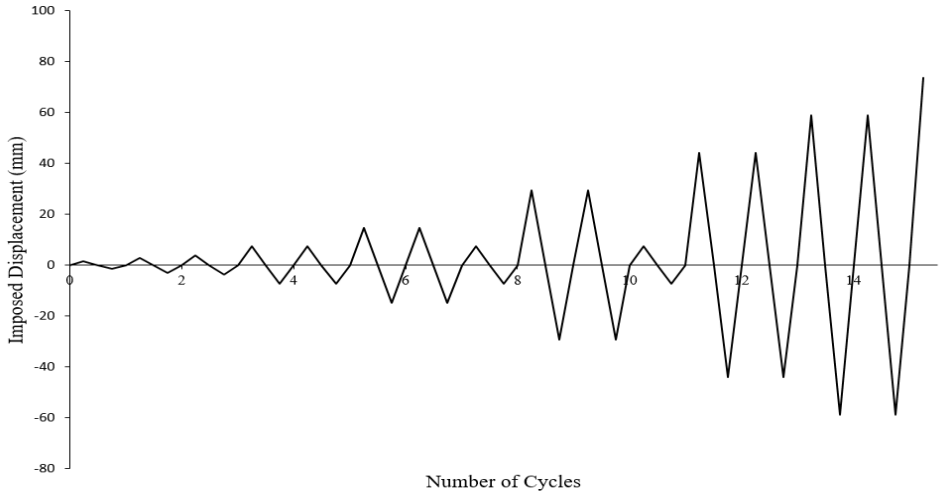

Σχήμα 15 Ιστορία φόρτισης σε μορφή επιβαλλόμενης μετατόπισης για τον εσωτερικό κόμβο πλαισίου.

Για την αριθμητική προσομοίωση χρησιμοποιήθηκαν 8-κομβικά εξαεδρικά πεπερασμένα στοιχεία και στοιχεία δοκού-υποστυλώματος για τον οπλισμό. Συνολικά χρησιμοποιήθηκαν 128 εξαεδρικά στοιχεία και 888 στοιχεία δοκού όπως απεικονίζεται στο Σχήμα 16. Στην άνω διατομή του υποστυλώματος επιβλήθηκαν οι μετατοπίσεις (ανακυκλιζόμενη φόρτιση όπως περιγράφεται από το Σχήμα 15) όπου παράλληλα ασκείται μια θλιπτική αξονική φόρτιση ίση με 216 kN όπως φαίνεται στο Σχήμα 16. Επιπροσθέτως, χρησιμοποιήθηκαν 8-κομβικα εξαεδρικά πεπερασμένα στοιχεία (κόκκινο χρώμα-Σχήμα 16) στις περιοχές των στηρίξεων και στην άνω ακραία διατομή του υποστυλώματος (όπου ασκούνται οι δυνάμεις) ώστε να προσομοιώσουν δύσκαμπτες μεταλλικές πλάκες (ελαστική συμπεριφορά υλικού χάλυβα) οι οποίες τοποθετούνται για να αποφευχθούν τοπικά φαινόμενα αστοχίας.

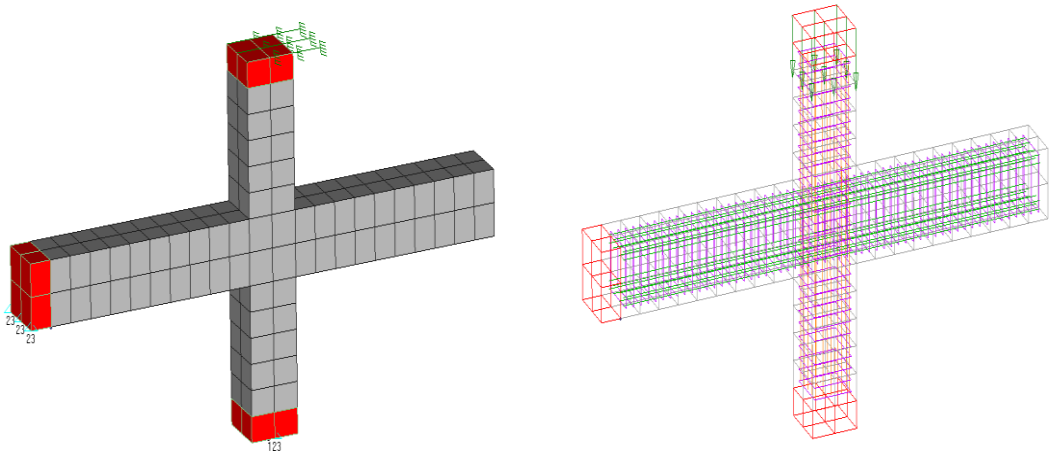

(a) (b)

Σχήμα 16 Εσωτερικός κόμβος πλαισίου. (α) Διακριτοποίηση σκυροδέματος και επιβολή μετατοπίσεων (β) διακριτοποίηση στοιχείων οπλισμού και επιβολή αξονικού φορτίου στην άνω διατομή υποστυλώματος.

Οι αριθμητικές καμπύλες ικανότητας συγκρίθηκαν με τα αντίστοιχα πειραματικά αποτελέσματα όπως φαίνεται στο Σχήμα 17. Τα αριθμητικά αποτελέσματα συμπίπτουν επαρκώς με τα πειραματικά όπου η δυσκαμψία και η αντοχή του φορέα που παρουσιάστηκε σε κάθε κύκλο υστέρησης, προσομοιώθηκαν με ικανοποιητική ακρίβεια. Σημειώνεται πως οι διαφορές μεταξύ της φέρουσας ικανότητας που παρουσιάζει το υποστύλωμα στους τελευταίους 6 κύκλους είναι κατά μέσο όρο γύρω στο 7.5% (4.6% για θετικά φορτία και -10.29% για τα αρνητικά φορτία). Επιπλέον, η αναλισκόμενη ενέργεια που προκύπτει από του αριθμητικούς βρόγχους υστέρησης φαίνεται να προσεγγίζει πολύ καλά την αντίστοιχη πειραματική. Οι διαφορές της αριθμητικής αναλισκόμενης ενέργειας σε σχέση με αυτές που υπολογίστηκαν από τους πειραματικούς βρόγχους υστέρησης στους τελευταίους 6 κύκλους είναι κατά μέσο όρο γύρω στο 20%. Επίσης, στο Σχήμα 17 παρουσιάζονται τα αριθμητικά αποτελέσματα χωρίς την χρήση της παραμέτρου βλάβης του χάλυβα του οπλισμού (Σχέση (29)). Όπως προκύπτει από τα αριθμητικά αποτελέσματα, το προτεινόμενο μοντέλο με την χρήση των δύο παραμέτρων βλάβης, προσομοιώνει ρεαλιστικά και την στένωση των βρόγχων υστέρησης. Κατά την διάρκεια της ανάλυσης, δεν παρουσιάστηκε διαρροή σε πολλές ράβδους οπλισμού όπου η πειραματικά καταγεγραμμένη έλλειψη της συνάφειας που εμφανίστηκε λόγω της έντονης διαγώνιας ρηγμάτωσης μέσα στην περιοχή του κόμβου προσομειώθηκε ικανοποιητικά από το προτεινόμενο μοντέλο. Το φαινόμενο της απώλειας αντοχής εντός του κόμβου που παρατηρήθηκε κατά την διάρκεια του πειράματος και καταγράφηκε κατά την αριθμητική ανάλυση, αναδεικνύει την αξία της προτεινόμενης παραμέτρου βλάβης του χάλυβα οπλισμού η οποία λαμβάνει υπόψη την απομειωμένη συνεισφορά του οπλισμού λόγω του ανοιγοκλεισίματος της ρηγμάτωσης.

Οι απαιτούμενες εσωτερικές επαναλήψεις Newton-Raphson, που χρειάστηκαν για να επιτευχθεί η σύγκλιση κάθε εξωτερικού βήματος (έλεγχος μετατόπισης-displacement control) απεικονίζονται στο Σχήμα 18, όπου χρησιμοποιήθηκε ένα ενεργειακό κριτήριο σύγκλισης με ανοχή σφάλματος ίσο με 10^{-4}. Όπως φαίνεται στο Σχήμα 18, 77% των εξωτερικών βημάτων χρειάστηκαν λιγότερο από 5 εσωτερικές επαναλήψεις, ενώ το 95% των εξωτερικών βημάτων χρειάστηκε λιγότερο από 10 εσωτερικές επαναλήψεις για την επίτευξη σύγκλισης.

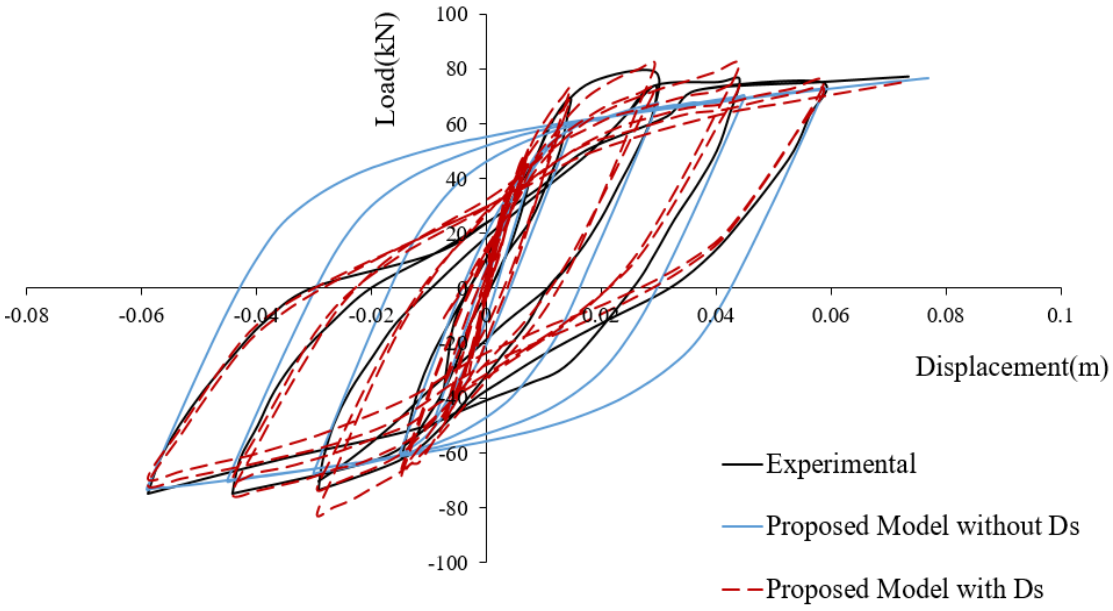

Σχήμα 17 Εσωτερικός κόμβος πλαισίου. Σύγκριση μεταξύ αριθμητικών και πειραματικών καμπυλών φορτίου-μετατόπισης.

Ο υπολογιστικός χρόνος για όλη την μη-γραμμική ανάλυση δίνεται στον Πίνακα 1, όπου χρειάστηκαν 173 δευτερόλεπτα για να επιλυθούν συνολικά 610 εξωτερικά βήματα, δεδομένο το οποίο αναδεικνύει την αποδοτικότητα της προτεινόμενης αριθμητικής μεθόδου.

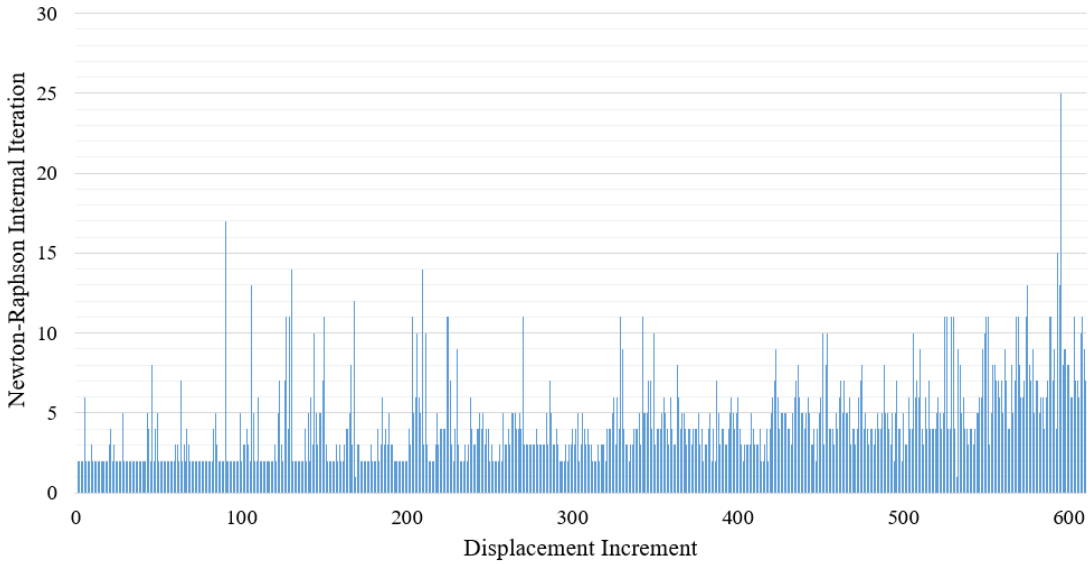

Σχήμα 18 Εσωτερικός κόμβος πλαισίου. Απαιτούμενος αριθμός εσωτερικών επαναλήψεων Newton-Raphson.

Πίνακας 1 Εσωτερικός κόμβος πλαισίου. Απαιτούμενος υπολογιστικός χρόνος για την μη-γραμμική ανάλυση.

Task	CPU Time (s)
Embedded rebar element mesh generation	0.1
Nonlinear incremental-iterative solution	173
Total Time	173.1

Υποστύλωμα υπό ανακυκλιζόμενη φόρτιση

Το υποστύλωμα U4 από οπλισμένο σκυρόδεμα που φαίνεται στο Σχήμα 19 υποβλήθηκε σε ανακυκλιζόμενη ένταση και εξετάστηκε από τους Saatcioglou και Ozcebe [39]. Η μονοαξονική θλιπτική αντοχή του σκυροδέματος που χρησιμοποιήθηκε, είναι ίση με f_c = 32 MPa και η τάση διαρροής του χάλυβα του οπλισμού είναι ίση με 438 MPa για τις ράβδους διαμέτρου 25 mm, ενώ οι ράβδοι διαμέτρου 10 mm έχουν τάση διαρροής ίση με 470 MPa. Οι λεπτομέρειες τις γεωμετρίας, του οπλισμού και η διακριτοποίηση που χρησιμοποιήθηκε για την ανάλυση απεικονίζονται στο Σχήμα 19.

Το υποστύλωμα U4, υποβλήθηκε σε ανακυκλιζόμενη φόρτιση όπως περιγράφεται από την ιστορία φόρτισης στο Σχήμα 20 (17 κύκλοι επιβαλλόμενης μετατόπισης). Παράλληλα μια θλιπτική δύναμη μεγέθους 600 kN ασκήθηκε στην άνω διατομή του υποστυλώματος. Ο φορέας διακριτοποιήθηκε με χρήση 8-κομβικών πεπερασμένων στοιχείων για το σκυρόδεμα ενώ για τον οπλισμό χρησιμοποιήθηκαν φυσικά στοιχεία δοκού-υποστυλώματος. Συνολικά χρειάστηκαν 24 εξαεδρικά στοιχεία και 120 στοιχεία δοκού-υποστυλώματος για να προσομοιώσουν την κατασκευή. Επιπλέον χρησιμοποιήθηκαν 8-κομβικά εξαεδρικά πεπερασμένα στοιχεία (μπλε χρώμα, Σχήμα 19) στις περιοχές της στήριξης και της άνω διατομής του στύλου όπου ασκούνται τα φορτία, ώστε να προσομοιώσουν μεταλλικές πλάκες (ελαστική συμπεριφορά) προς αποφυγή τοπικών φαινομένων αστοχίας.

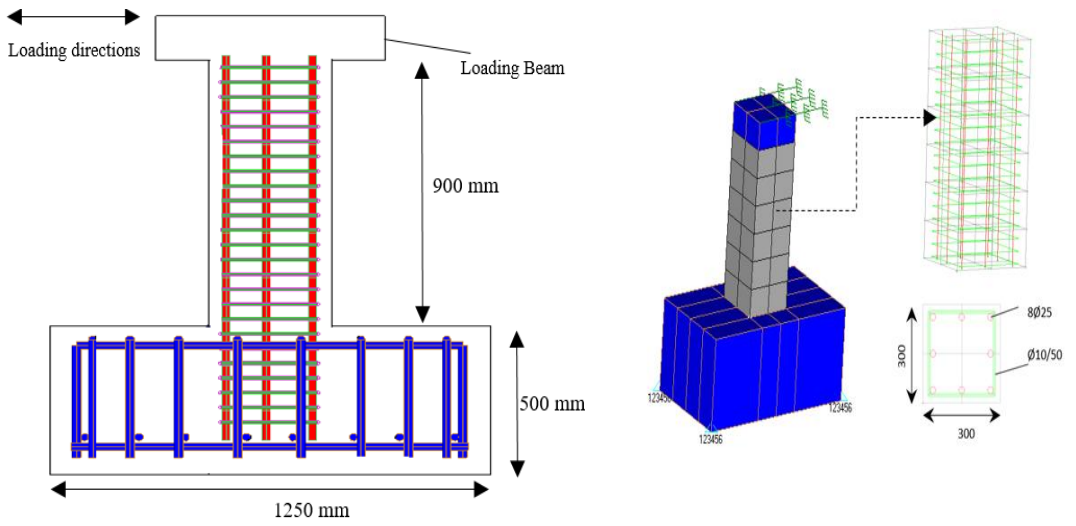

(a) (b)

Σχήμα 19 Υποστύλωμα U4. (a) Λεπτομέρειες γεωμετρίας και οπλισμού [39] *(b) Διακριτοποίηση φορέα.*

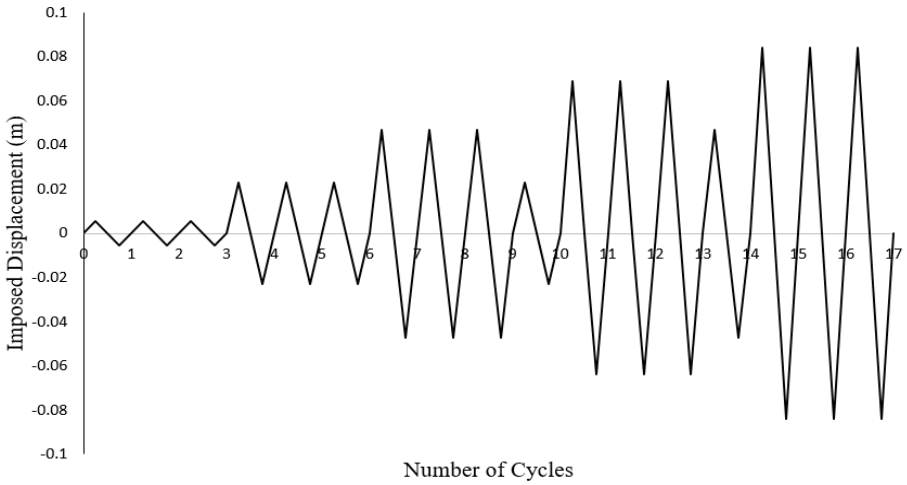

Σχήμα 20 Ιστορία φόρτισης σε μορφή επιβαλλόμενης μετατόπισης για υποστύλωμα U4.

Οι καμπύλες φορτίου-μετατόπισης που προέκυψαν από την αριθμητική ανάλυση συγκρίνονται με τα αντίστοιχα πειραματικά αποτελέσματα στο Σχήμα 21. Όπως προκύπτει από το διάγραμμα, τα αριθμητικά αποτελέσματα προσομοιώνουν με ικανοποιητική ακρίβεια τις πειραματικές καμπύλες.

Σημειώνεται πως οι διαφορές μεταξύ της φέρουσας ικανότητας που παρουσιάζει το υποστύλωμα στους τελευταίους 14 κύκλους είναι κατά μέσο όρο γύρω στο 11% (11.86% για θετικά φορτία και -10.12% για τα αρνητικά φορτία). Οι διαφορές της αριθμητικής αναλισκόμενης ενέργειας σε σχέση με αυτές που υπολογίστηκαν από τους πειραματικούς βρόγχους υστέρησης στους τελευταίους 9 κύκλους είναι κατά μέσο όρο 19%. Συνεπώς, οι υστερητικοί βρόγχοι προσομοιώνονται επαρκώς όσον αφορά την φέρουσα ικανότητα, την δυσκαμψία και την αναλισκόμενη ενέργεια.

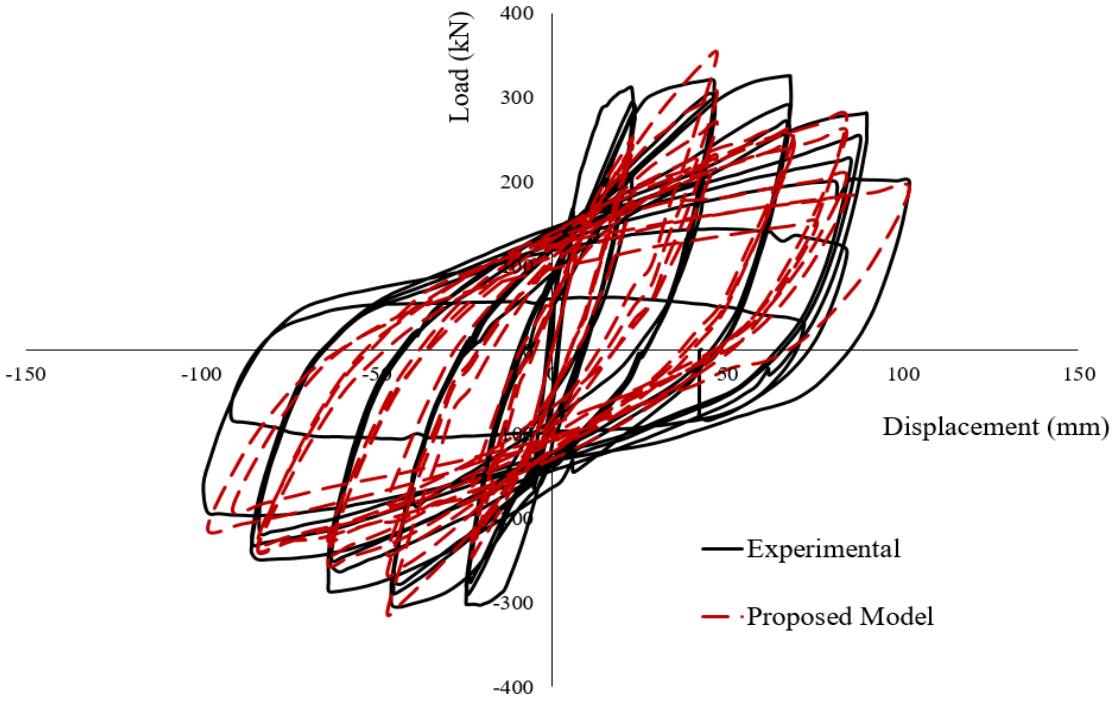

Σχήμα 21 Υποστύλωμα U4. Σύγκριση μεταξύ αριθμητικών και πειραματικών καμπυλών φορτίου-μετατόπισης.

Οι απαιτούμενες εσωτερικές επαναλήψεις Newton-Raphson, που χρειάστηκαν για να επιτευχθεί η σύγκλιση κάθε προσαυξητικού βήματος επιβαλλόμενης μετατόπισης κατά την διάρκεια της μη-γραμμικής ανακυκλικής ανάλυσης του υποστυλώματος U4, απεικονίζονται στο Σχήμα 22, όπου χρησιμοποιήθηκε ένα ενεργειακό κριτήριο σύγκλισης με ανοχή σφάλματος ίσο με 10^{-4}. Μετά από σχετική ανάλυση του Σχήμα 22, βρέθηκε ότι το 71% των εξωτερικών βημάτων χρειάστηκαν λιγότερο από 15 εσωτερικές επαναλήψεις για να συγκλίνουν. Ο υπολογιστικός χρόνος για όλη την μη-γραμμική ανάλυση δίνεται στον Πίνακα 2, όπου προκύπτει ότι χρειάστηκαν 95 δευτερόλεπτα για να επιλυθούν συνολικά 780 εξωτερικά βήματα το οποίο αναδεικνύει την αποδοτικότητα της προτεινόμενης αριθμητικής μεθόδου.

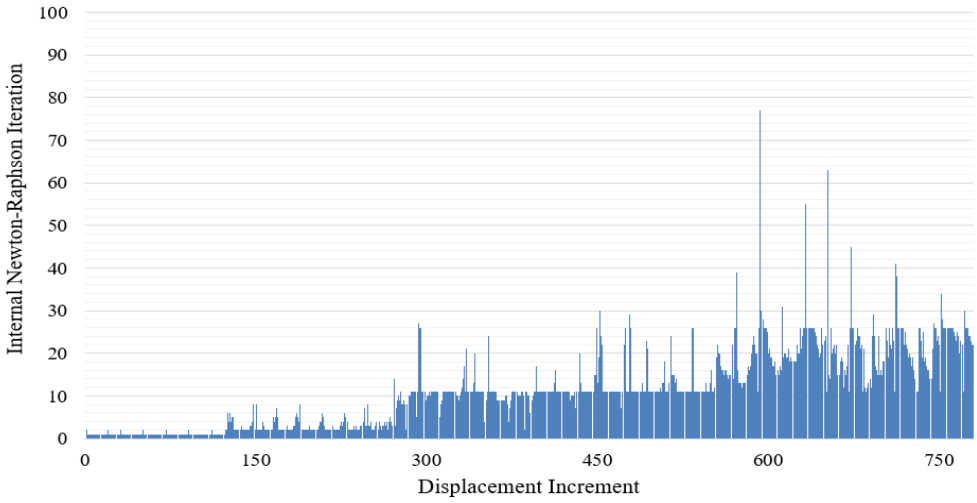

Σχήμα 22 Υποστύλωμα U4. Απαιτούμενος αριθμός εσωτερικών επαναλήψεων Newton-Raphson.

Πίνακας 2 Υποστύλωμα U4. Απαιτούμενος υπολογιστικός χρόνος για την μη-γραμμική ανάλυση.

Task	CPU Time (s)
Embedded rebar element mesh generation	0.02
Nonlinear incremental-iterative solution	94.3
Total Time	94.32

<u>Διώροφα πλαίσια υπό σεισμική φόρτιση</u>

Στην συνέχεια εξετάστηκαν δύο διώροφα πλαίσια (L30 και H30) από οπλισμένο σκυρόδεμα τα οποία υποβλήθηκαν σε δυναμική φόρτιση και εξετάστηκαν πειραματικά από τον Carydis [40]. Για την δυναμική ανάλυση χρησιμοποιήθηκε η μέθοδος Newmark με β=0.5 και γ=0.25 όπου β και γ είναι οι παράμετροι που ορίζουν την μεταβολή της επιτάχυνσης σε ένα χρονικό βήμα (μέθοδος μέσης επιτάχυνσης). Τα δύο πλαίσια (L30 και H30) σχεδιάστηκαν σύμφωνα με τους Ευρωκώδικες 2 και 8 για δύο επίπεδα πλαστιμότητας (Low-χαμηλή για το L30 και High-υψηλή για το H30). Οι λεπτομέρειες τις γεωμετρίας, του οπλισμού και η διακριτοποίηση που χρησιμοποιήθηκε για την ανάλυση απεικονίζονται στο Σχήμα 23. Η μονοαξονική θλιπτική αντοχή του σκυροδέματος που χρησιμοποιήθηκε, είναι ίση με f_c = 50 MPa και η τάση διαρροής του χάλυβα του οπλισμού είναι ίση με 500 MPa. Το συνολικό βάρος κάθε διώροφου πλαισίου ήταν 120 kN.

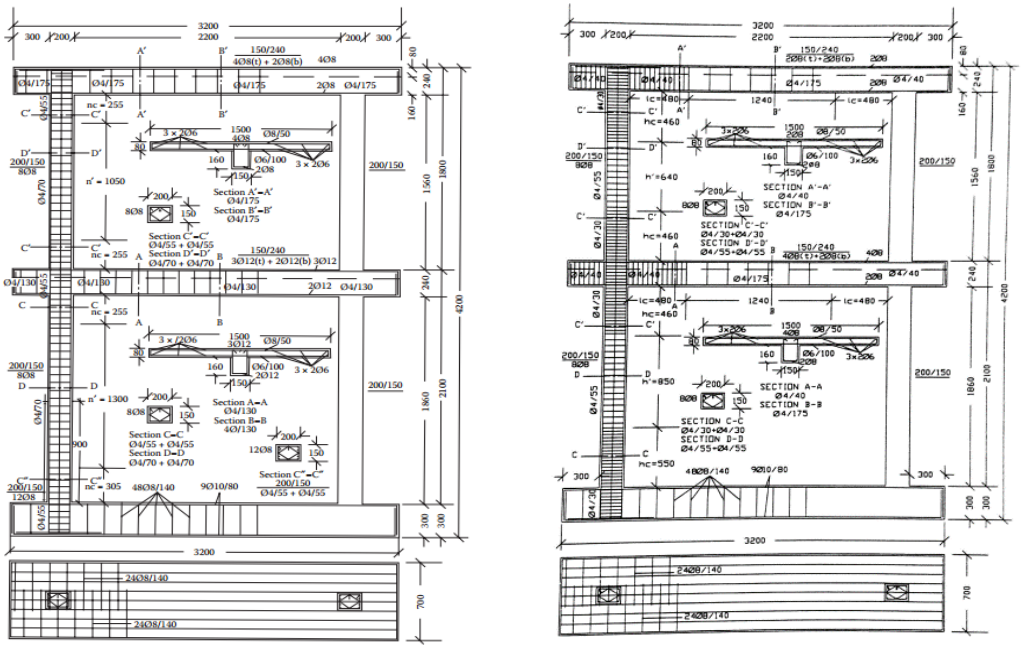

(a) (b)

Σχήμα 23 Λεπτομέρειες γεωμετρίας και οπλισμού για τα διώροφα πλαίσια (α) L30 και (b) H30. [40]

Το πλαίσιο L30 είναι σχεδιασμένο για πλαστιμότητα που αντιστοιχεί σε συντελεστή συμπεριφοράς q=2.5, ενώ το H30 για συντελεστή συμπεριφοράς q=5. Τα πλαίσια υποβλήθηκαν σε οριζόντια σεισμική φόρτιση η οποία ασκήθηκε στην βάση του αριθμητικού προσομοιώματος όπως φαίνεται στο Σχήμα 24 (πράσινο χρώμα). Η σεισμική φόρτιση ήταν ημιτονοειδούς μορφής όπως απεικονίζεται στο Σχήμα 25. Τα επιταχυνσιογραφήματα παρουσιάζουν μέγιστη επιτάχυνση μία έως και δύο φορές την επιτάχυνση σχεδιασμού η οποία ήταν ίση με 0.30g. Επιπλέον, για να γίνει αντιληπτό το μέγεθος της σεισμικής διέγερσης που επιβλήθηκε, στο Σχήμα 25 απεικονίζονται τα φάσματα απόκρισης απόλυτων επιταχύνσεων που

προκύπτουν από την σεισμική διέγερση (μέγιστη εδαφική επιτάχυνση ίση με 0.75g) μαζί με τα ελαστικά φάσματα σχεδιασμού (Ευρωκώδικας 8 [41], κατηγορία εδάφους Β). Οι μέγιστες φασματικές επιταχύνσεις που παρουσιάζονται στο πλαίσιο L30 είναι 2.164g και 4.374g για τα test1 και test2, αντίστοιχα. Επίσης, για το πλαίσιο H30, οι μέγιστες φασματικές επιταχύνσεις είναι 2.153g, 4.373g και 4.514g για τα test1, test2 και test3, αντίστοιχα.

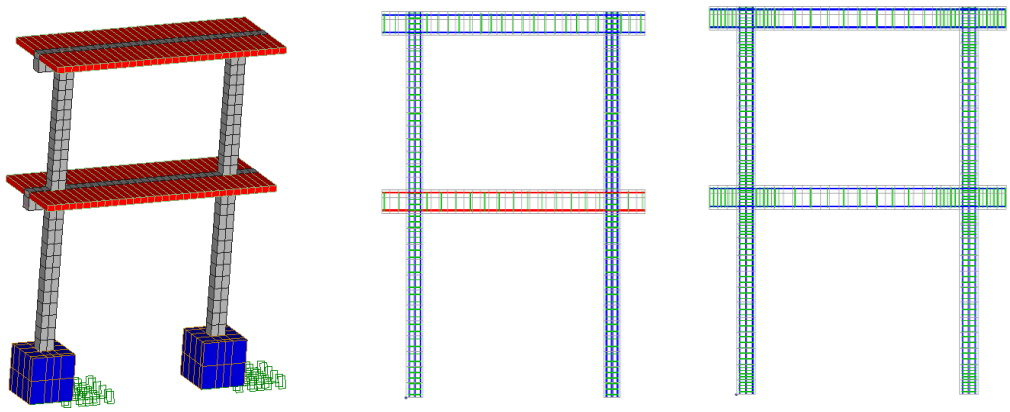

(a) (b)

Σχήμα 24 (αριστερά) Διακριτοποίηση του σκυροδέματος και (δεξιά) των στοιχείων οπλισμού για το διώροφο πλαίσιο (α) L30 και (b) H30.

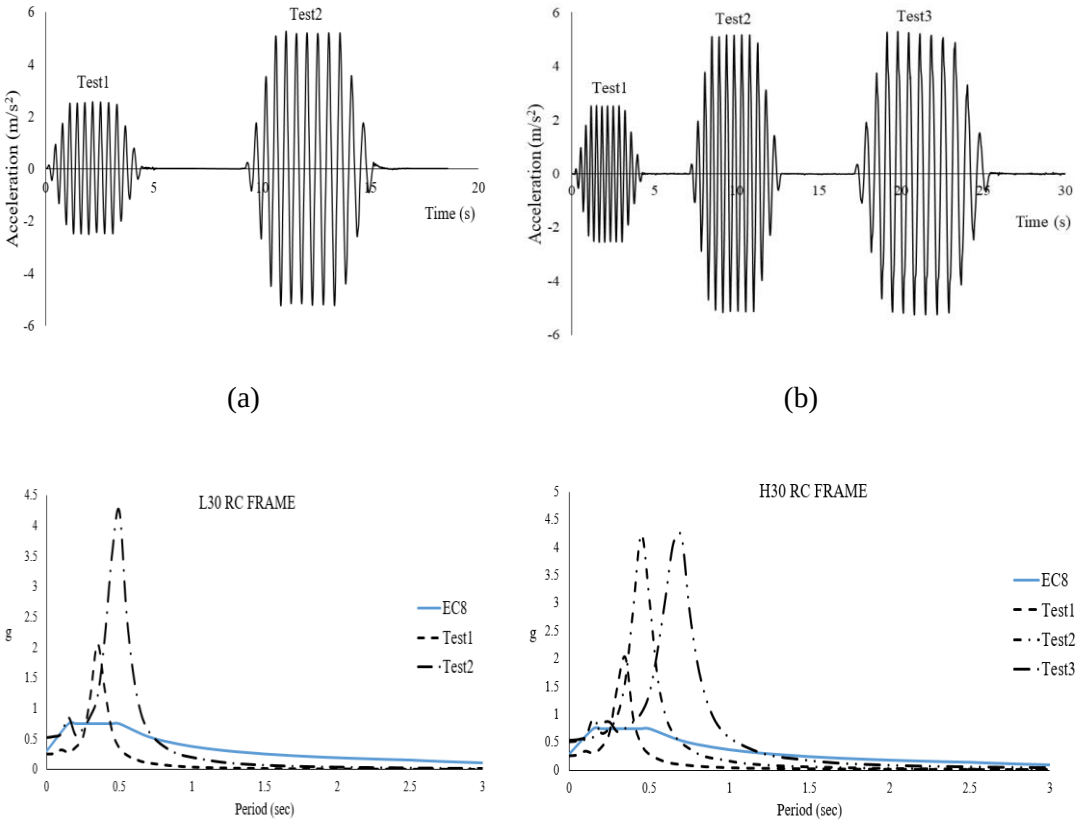

(a) (b)

(c) (d)

Σχήμα 25 Σεισμική διέγερση που επιβλήθηκε στα δοκίμια (α) L30 και (b) H30. Φασματικά διαγράμματα απόλυτων επιταχύνσεων για τις σεισμικές διεγέρσεις που ασκήθηκαν στα δοκίμια (α) L30 και (b) H30.

Ο φορέας διακριτοποιήθηκε με χρήση 8-κομβικών πεπερασμένων στοιχείων για το σκυρόδεμα ενώ για τον οπλισμό χρησιμοποιήθηκαν φυσικά στοιχεία δοκού-υποστυλώματος. Συνολικά χρειάστηκαν 224 εξαεδρικά στοιχεία για το σκυρόδεμα, ενώ 1,891 και 2,384 στοιχεία δοκού-υποστυλώματος για την προσομοίωση των ράβδων οπλισμού του L30 και H30, αντίστοιχα. Επιπλέον, χρησιμοποιήθηκαν 8-κομβικά εξαεδρικά πεπερασμένα στοιχεία (κόκκινο χρώμα-Σχήμα 24) για να προσομοιώσουν τις πλάκες από οπλισμένο σκυρόδεμα. Οι πλάκες προσομοιώθηκαν με τέτοιο τρόπο ώστε να έχουν ελαστική συμπεριφορά και ουσιαστικά έπαιξαν τον ρόλο της μάζας που τοποθετήθηκε στον κάθε όροφο. Τέλος, χρησιμοποιήθηκαν 8-κομβικά εξαεδρικά πεπερασμένα στοιχεία (μπλε χρώμα-Σχήμα 24) στις περιοχές της στήριξης ώστε να αποφευχθούν τοπικά φαινόμενα αστοχίας.

Για την δυναμική ανάλυση χρησιμοποιήθηκε χρονικό βήμα ίσο με $\Delta T = 0{,}007746$ s . Οι πρώτες δύο ιδιοσυχνότητες του μοντέλου L30, που υπολογίστηκαν στα πρώτα δευτερόλεπτα της ανάλυσης είχαν τιμή ίση με $f_1 = 2.93$ Hz και $f_2 = 9.7$ Hz οι οποίες είναι αρκετά κοντινές με αυτές που μετρήθηκαν πειραματικά ($f_{1exp} = 3.05$ Hz και $f_{2exp} = 9.8$ Hz). Ομοίως. οι ιδιοσυχνότητες του μοντέλου H30 ήταν ίσες με $f_1 = 3.11$ Hz και $f_2 = 14.31$ Hz ενώ αντίστοιχα οι πειραματικές τιμές ήταν $f_{1exp} = 3.28$ Hz και $f_{2exp} = 10.72$ Hz. Επιπλέον, χρησιμοποιήθηκε ένας σταθερός συντελεστής απόσβεσης ίσος με 2% για τον υπολογισμό της απόσβεσης κατά Rayleigh στο αριθμητικό μοντέλο L30, ώστε να ληφθούν υπόψη στην ανάλυση διάφοροι μηχανισμοί ανάλωσης ενέργειας που δεν προσομοιώθηκαν στο καταστατικό μοντέλο (όπως για παράδειγμα η ολίσθηση μεταξύ χάλυβα και σκυροδέματος και η ανάπτυξη τριβών στην διεπιφάνεια των ρωγμών). Θα πρέπει επίσης να αναφερθεί εδώ ό,τι για το αριθμητικό μοντέλο H30 δεν χρησιμοποιήθηκε ιξώδης απόσβεση ($\xi=0$).

Η απόκριση της κατασκευής υπό μορφής μετατοπίσεων των ορόφων η οποία προέκυψε από την αριθμητική ανάλυση συγκρίνεται με τα πειραματικά δεδομένα όπως απεικονίζεται στα Σχήματα 26-29. Όπως μπορεί εύκολα κανείς να παρατηρήσει, το αριθμητικό μοντέλο L30 προσομοιώνει επαρκώς την δυναμική συμπεριφορά της κατασκευής όσο αφορά τις μετατοπίσεις των ορόφων κατά την διάρκεια των test1 και test2. Ομοίως ρεαλιστική απόκριση προκύπτει και για το μοντέλο H30. Το αριθμητικό μοντέλο κατάφερε να παράγει ευσταθείς λύσεις για όλες τις χρονοϊστορίες (test1, test2 και test3). Συγκεκριμένα κατά την διάρκεια των test1 και test2, το αριθμητικό μοντέλο φαίνεται να παρουσιάζει την ίδια δυσκαμψία με τα πειραματικά αποτελέσματα, ενώ στην διάρκεια του test3 το αριθμητικό μοντέλο φαίνεται να έχει ελαφρός πιο δύσκαμπτη συμπεριφορά. Η απόκριση του πλαισίου H30 χαρακτηρίζεται από έντονη μη-γραμμικότητα όπου παρουσιάστηκε έντονη ρηγμάτωση, σημαντική αποφλοίωση του σκυροδέματος, διαρροή και θραύση ράβδων οπλισμού.

Εν κατακλείδι, παρόλο που η συμπεριφορά των πλαισίων παρουσίασε έντονα μη-γραμμικά χαρακτηριστικά, το προτεινόμενο μοντέλο κατάφερε να προσομοιώση επαρκώς την συμπεριφορά του φορέα σε όλη την χρονοϊστορία φόρτισης. Οι απαιτούμενες εσωτερικές επαναλήψεις Newton-Raphson, που χρειάστηκαν για να επιτευχθεί η σύγκλιση κάθε χρονικού βήματος κατά την διάρκεια της ανάλυσης των πλαισίων L30 και H30, απεικονίζονται στο Σχήμα 30. Για το μοντέλο L30, υπολογίστηκε ότι το 87% των εξωτερικών βημάτων χρειάστηκαν λιγότερο από 2 εσωτερικές επαναλήψεις για να συγκλίνουν, ενώ για το μοντέλο H30, 78% των εξωτερικών βημάτων χρειάστηκαν λιγότερο από 5 εσωτερικές επαναλήψεις. Αυτή η αύξηση των επαναλήψεων ώστε να επιτευχθεί η σύγκλιση, οφείλεται κυρίως στην έντονη μη-γραμμικότητα που παρουσιάζεται κατά την διάρκεια του test3, όπου παρουσιάστηκε αστοχία οπλισμών.

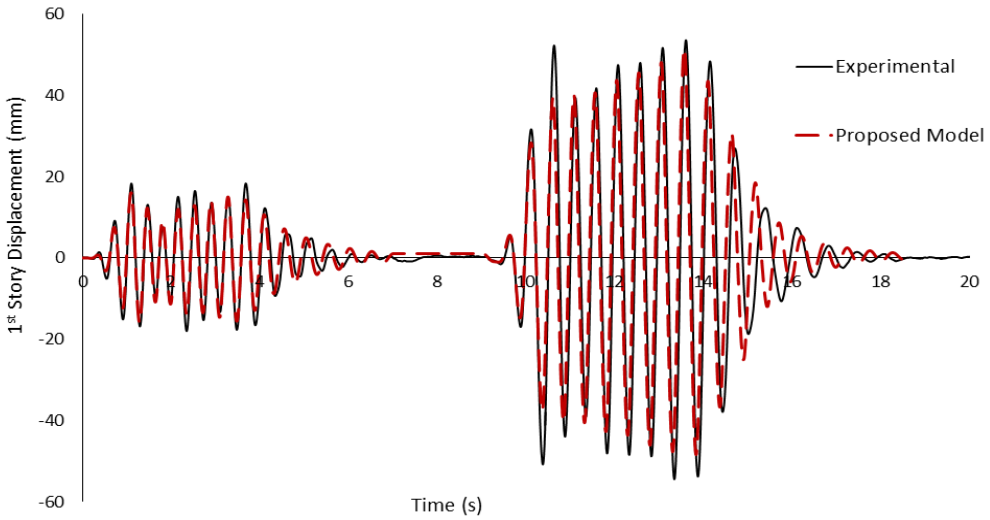

Σχήμα 26 Πλαίσιο L30. Σύγκριση μεταξύ αριθμητικής και πειραματικής απόκρισης υπό μορφής μετακινήσεων 1ου ορόφου.

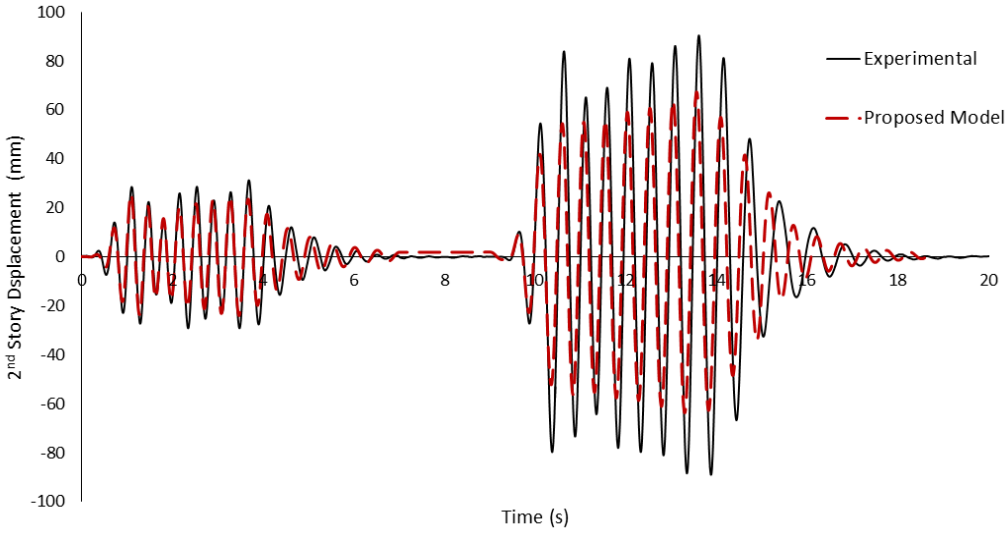

Σχήμα 27 Πλαίσιο L30. Σύγκριση μεταξύ αριθμητικής και πειραματικής απόκρισης υπό μορφής μετακινήσεων 2ου ορόφου.

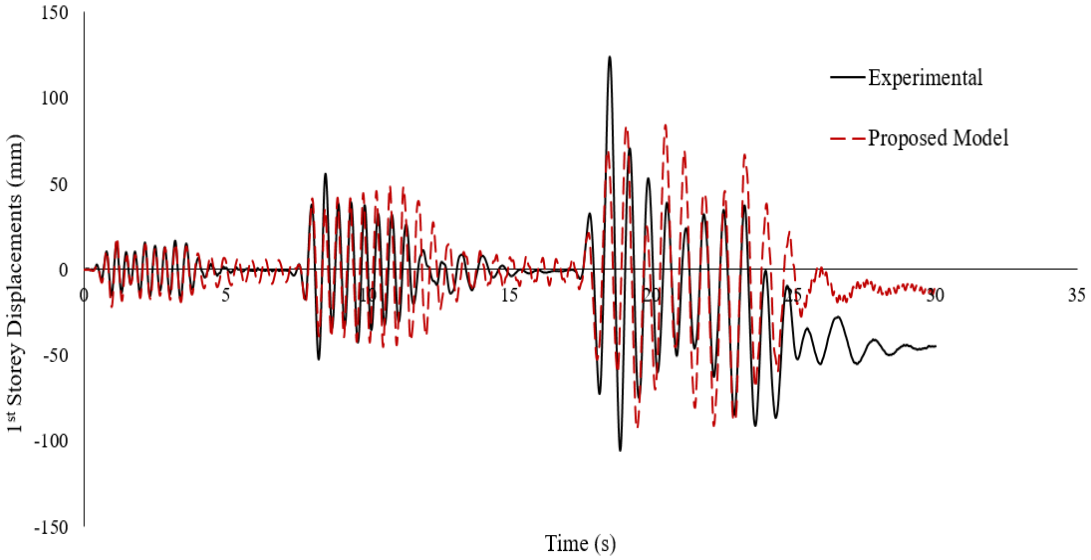

Σχήμα 28 Πλαίσιο H30. Σύγκριση μεταξύ αριθμητικής και πειραματικής απόκρισης υπό μορφής μετακινήσεων 1ου ορόφου.

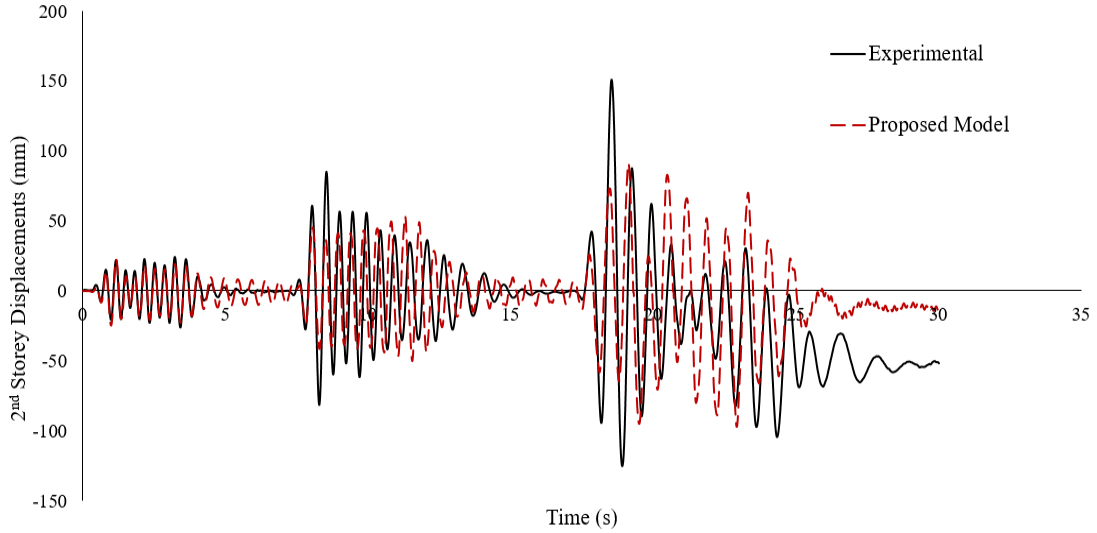

Σχήμα 29 Πλαίσιο H30. Σύγκριση μεταξύ αριθμητικής και πειραματικής απόκρισης υπό μορφής μετακινήσεων 2ου ορόφου.

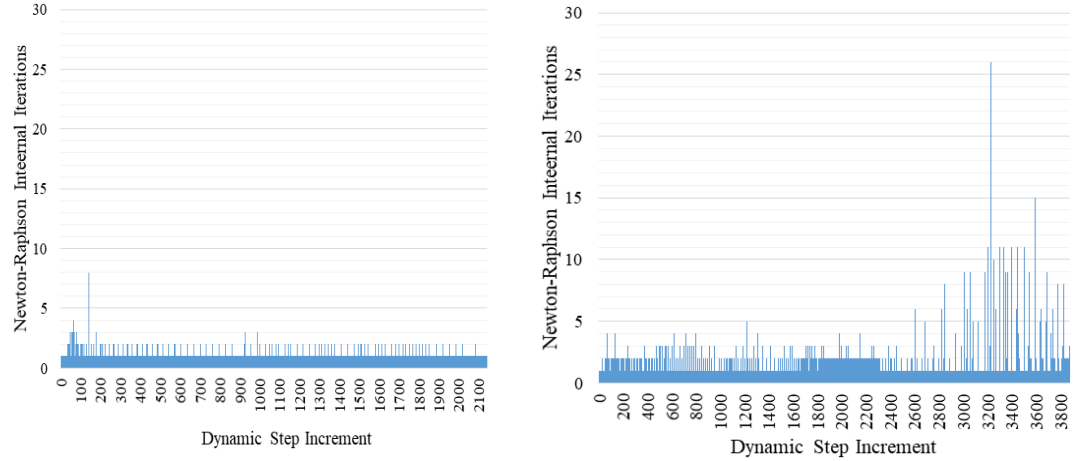

Σχήμα 30 Απαιτούμενος αριθμός εσωτερικών επαναλήψεων Newton-Raphson για τα μοντέλα (a) L30 και (b) H30.

Πίνακας 3 Απαιτούμενος υπολογιστικός χρόνος για την μη γραμμική ανάλυση για τα μοντέλα L30 και H30.

Task	L30	H30
	CPU Time (s)	CPU Time (s)
Embedded rebar element mesh generation	0.51	0.94
Nonlinear incremental-iterative solution	318.97	564.82
Total Time	319.48	565.76

Ο απαιτούμενος υπολογιστικός χρόνος για όλη την μη-γραμμική ανάλυση δίνεται στον Πίνακα 3, όπου προκύπτει ότι χρειάστηκαν 319.5 και 565.8 δευτερόλεπτα για να επιλυθούν συνολικά 2,041 και 3,826 εξωτερικά χρονικά βήματα για τα μοντέλα L30 και H30, αντίστοιχα. Το γεγονός αυτό, αναδεικνύει την υπολογιστική και αριθμητική ανωτερότητα της προτεινόμενης αριθμητικής μεθόδου.

Τέλος, στο Σχήμα 31 φαίνονται οι ρηγματώσεις που παρουσιάστηκαν στο τέλος του test3 του πλαισίου H30. Σύμφωνα με τις πειραματικές εικόνες ρηγμάτωσης, παρατηρείται πως οι ρωγμές ανοίγουν κυρίως στους κόμβους και στα υποστυλώματα. Οι ρωγμές στην βάση του πρώτου ορόφου φαίνονται να είναι πιο έντονες, φαινόμενο το οποίο συμφωνεί και τις ρωγμές του

αριθμητικού μοντέλου. Επίσης, εμφανίστηκε έντονη διαγώνια ρηγμάτωση στις περιοχές του κόμβου του πρώτου ορόφου.

Όπως είναι αναμενόμενο, τα αριθμητικά αποτελέσματα με την χρήση της διανεμημένης ρηγμάτωσης παρουσιάζουν πιο έντονη ρηγμάτωση από το πείραμα, στα υποστυλώματα του πλαισίου. Παρά ταύτα, η κατανομή της ρηγμάτωσης, η τοποθεσία και οι διευθύνσεις των ρωγμών (ιδιαίτερα των ρωγμών που παρουσιάζουν μεγάλο άνοιγμα) βρίσκονται σε συμφωνία με την πειραματική ρηγματωμένη απεικόνιση.

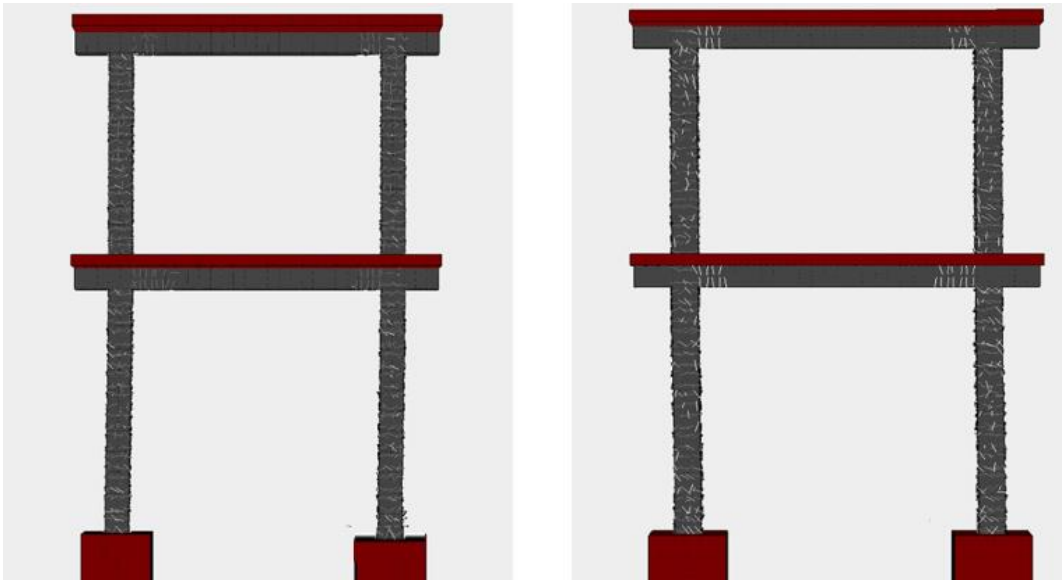

(a)

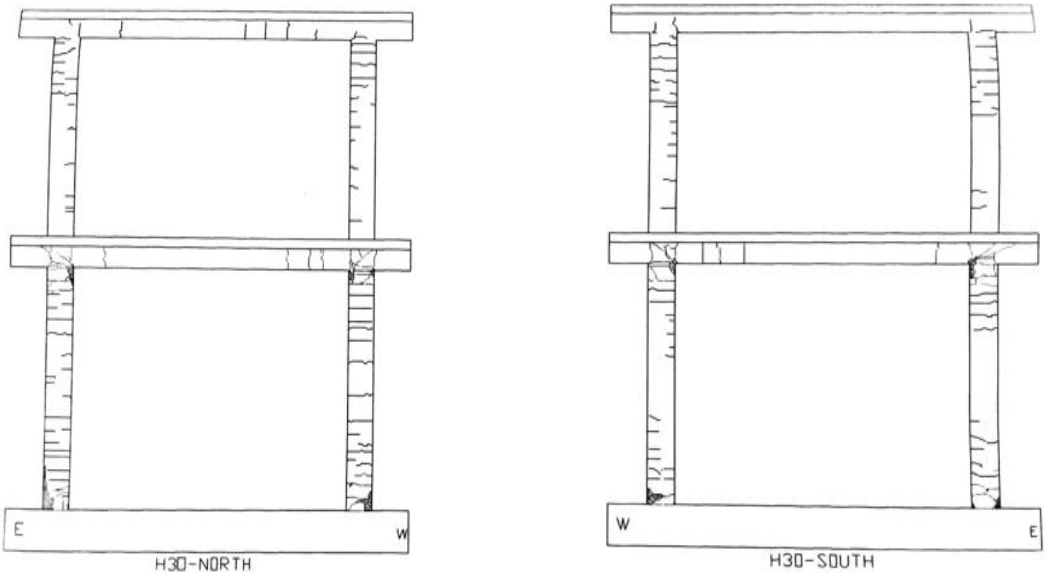

(b)

Σχήμα 31 Πλαίσιο H30. Σύγκριση μεταξύ (a) αριθμητικής και (b) πειραματικής [40] *αποτύπωσης της ρηγμάτωσης του φορέα στο τέλος της φόρτισης (test3).*

<u>Τετραώροφο κτίριο υπό ανακυκλιζόμενη φόρτιση</u>

Στην συνέχεια αναλύθηκε ένα τετραώροφο κτίριο από οπλισμένο σκυρόδεμα το οποίο μελετήθηκε πειραματικά στα πλαίσια του προγράμματος SERFIN [42]. Στο κτίριο αυτό εξετάζονται δυο μέθοδοι ενίσχυσης του κτιρίου μέσω της προσθήκης τοιχώματος από οπλισμένο σκυρόδεμα καθ' ύψος του κτιρίου και της ενίσχυσης με ινοπλισμένα πολυμερή από ίνες άνθρακα (CFRP) στην βάση του κτιρίου. Όπως περιγράφεται από τους Poljanšek et al. [42], το τετραώροφο κτίριο υποβλήθηκε σε ψευδό-δυναμική φόρτιση (pseudo-dynamic) και αποτελείται από δύο τετραώροφα παράλληλα πλαίσια τα οποία συνδέονται μονολιθικά με πλάκες πάχους 15 cm και τέσσερα δοκάρια (κάθετα του επιπέδου των πλαισίων) από οπλισμένο σκυρόδεμα σε κάθε όροφο όπως απεικονίζεται στο Σχήμα 32. Τα πλαίσια είναι τριών ανοιγμάτων με συνολικό μήκος 8.9 m. Τα κεντρικά ανοίγματα των πλαισίων είναι ενισχυμένα με την προσθήκη τοιχώματος μήκους 2.1 m. Η κατασκευή, έχει ύψος 12 m και η κάθετη απόσταση μεταξύ των πλαισίων είναι 6.25 m. Το κτίριο σχεδιάστηκε σύμφωνα με τον παλιό κώδικα της Κύπρου που προτάθηκε το 1970, ο οποίος αντικαταστάθηκε τώρα από τον Ευρωκώδικα (2003) [41]. Όσον αφορά τις ενισχύσεις, ο ΚΑΝΕΠΕ (2012) [43] είναι η καλύτερη υφιστάμενη επιλογή σε επίπεδο σχεδιαστικού κώδικα.

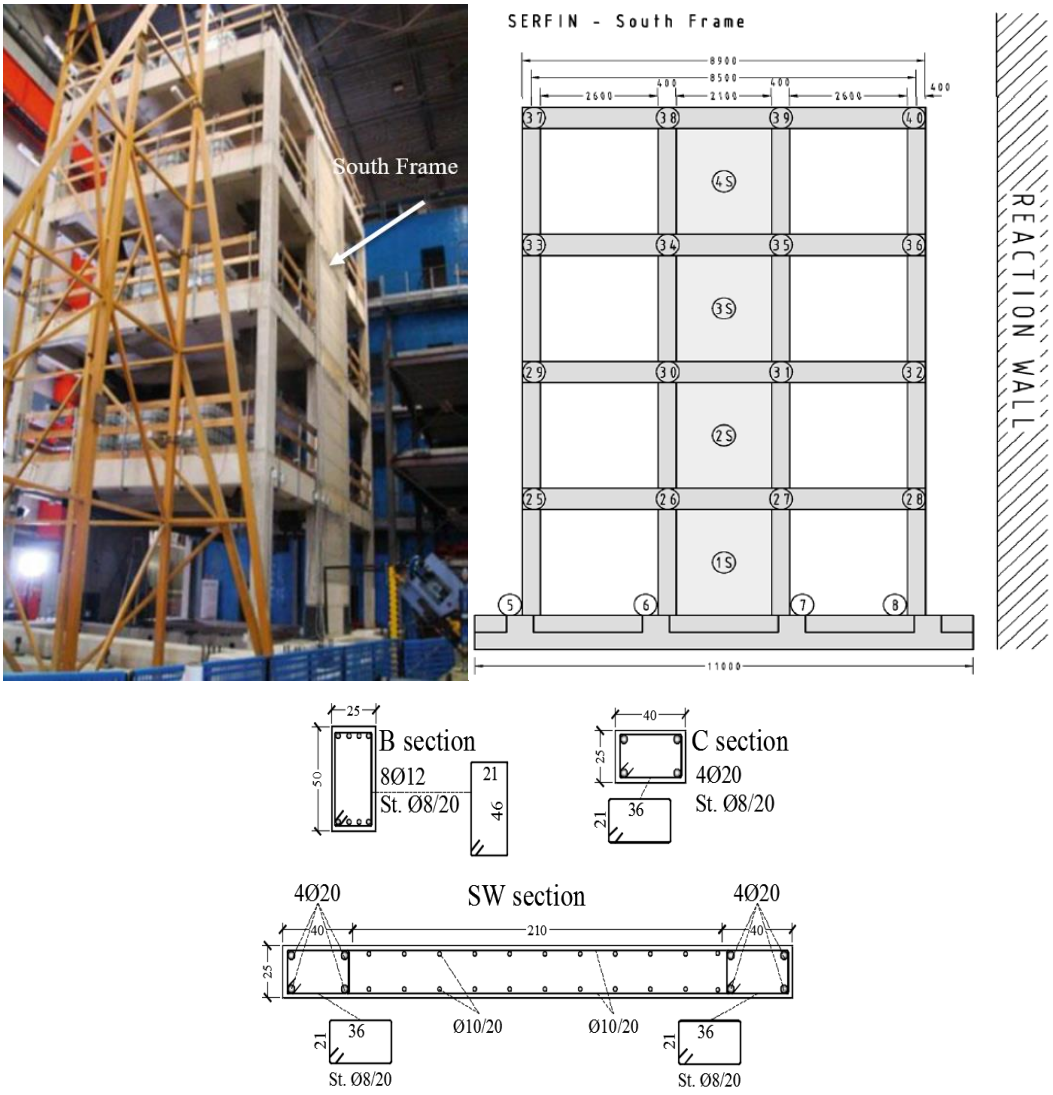

Σχήμα 32 Λεπτομέρειες γεωμετρίας και οπλισμού για το τετραώροφο κτίριο [42].

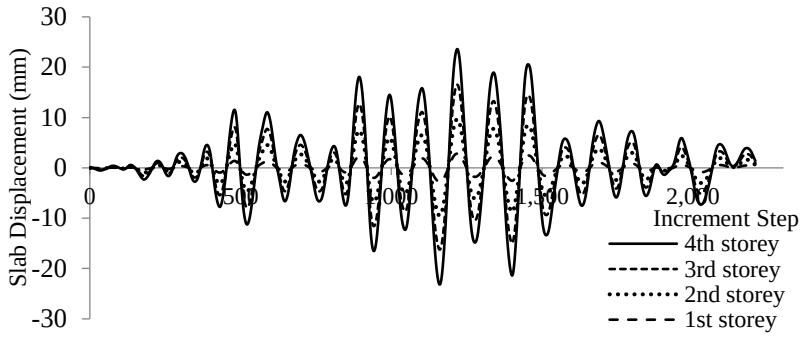

(a) 0.1g test

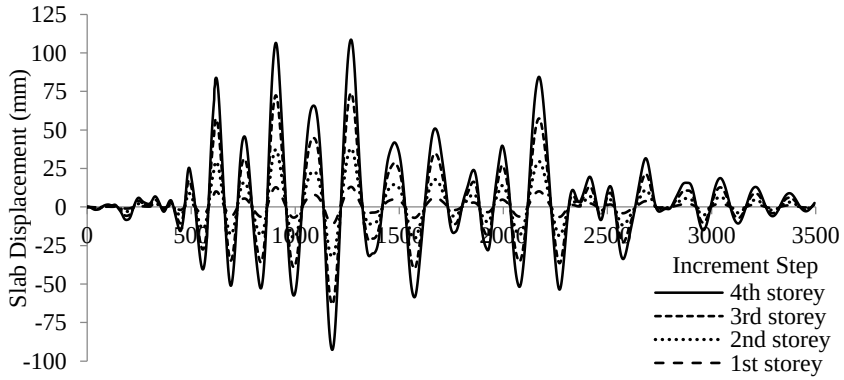

(b) 0.25g test

Σχήμα 33 Τετραώροφο κτίριο. Ιστορία φόρτισης σε μορφή επιβαλλόμενης μετατόπισης κάθε ορόφου.

Για την κατασκευή χρησιμοποιήθηκε σκυρόδεμα C20/25 με μέτρο ελαστικότητας E_c = 30 GPa και φαινόμενο βάρος ίσο με 25 kN/m^3. Οι ράβδοι οπλισμού που βρίσκονται εκτός του τοιχώματος παρουσίαζαν τάση διαρροής ίση με 400 MPa, ενώ ο οπλισμός του τοιχώματος είχε τάση διαρροής ίση με 450 MPa. Οι λεπτομέρειες της γεωμετρίας και του οπλισμού φαίνονται στο Σχήμα 32 (ενδεικτικά φαίνεται το τοίχωμα του πρώτου ορόφου του νότιου τοιχώματος). Να σημειωθεί ότι το νότιο τοίχωμα (South wall) προέβλεπε μικρότερο ποσοστό οπλισμού από το βόρειο σύμφωνα με την περιγραφή της πειραματικής διάταξης στο [42]. Σε κάθε όροφο θεωρείται ότι ασκείται μόνιμο φορτίο ίσο με 3 kN/m^2 και κινητό ίσο με 0.45 kN/m^2. Στα κατακόρυφα φορτία προστίθεται και το ίδιο βάρος της κατασκευής. Η οριζόντια φόρτιση ασκήθηκε σε κάθε όροφο με την μορφή επιβαλλόμενη μετατόπισης η οποία υπολογιζόταν σε κάθε βήμα μέσω της επίλυσης της διαφορικής εξίσωσης ισορροπίας ενός ισοδύναμου αναλυτικού μοντέλου (4 βαθμοί ελευθερίας) όπως περιγράφεται στο [42]. Για την επίλυση της διαφορικής εξίσωσης χρησιμοποιήθηκαν τα πρώτα 15 δευτερόλεπτα της κατακόρυφης συνιστώσας του Herzeg Novi (Montenegro 1979) επιταχυνσιογραφήματος έχοντας ως μέγιστη επιτάχυνση την τιμή 0.1g και 0.25g. Οι οριζόντιες μετατοπίσεις των ορόφων που αντιστοιχούν στα δυο αυτά επιταχυνσιογραφήματα (0.1g, 0.25g), επιβλήθηκαν στους ορόφους του αριθμητικού μοντέλο και απεικονίζονται στο Σχήμα 33.

Για την προσομοίωση του τετραώροφου κτιρίου, χρησιμοποιήθηκε η υβριδική μέθοδος διακριτοποίησης HYMOD όπου έγινε χρήση στοιχείων δοκού-υποστυλώματος για τα κυρίως καμπτόμενα μέλη (δοκοί και κολώνες) και εξαεδρικά στοιχεία με ενσωματωμένα στοιχεία δοκού για τους ράβδους οπλισμού (detailed modeling), για τα μέλη που παρουσιάζουν κυρίως διατμητική συμπεριφορά (συντελεστής απομείωσης δικτυώματος 1 - reduction level 1 [31]) όπως φαίνεται στο Σχήμα 34. Το υβριδικό μοντέλο κατάφερε να μειώσει τα στοιχεία κατά 39% και τους βαθμού ελευθερίας του κτιρίου κατά 48% σε σχέση με το μοντέλο που προβλέπει την

χρήση μόνο εξαεδρικών πεπερασμένων στοιχείων με ενσωματωμένα στοιχεία δοκού για τον οπλισμό (Full Hexa model), όπως φαίνεται από τον Πίνακα 4. Σημειώνεται πως τα μήκη των μελών δοκού και υποστυλώματος στο HYMOD μοντέλο όπου διακριτοποιήθηκαν με εξαεδρικά πεπερασμένα στοιχεία είχαν μέγεθος ίσο με 60 cm (δοκάρια εντός επιπέδου των πλαισίων), 70 cm (υποστυλώματα) και 100 cm (δοκάρια εκτός επιπέδου των πλαισίων). Σύμφωνα με τους Markou και Papadrakakis [31], το μήκος αυτών των περιοχών πρέπει να είναι ίσο με *h-2h* (όπου *h* το ύψος διατομής της δοκού ή του υποστυλώματος), ώστε να προσομοιώνεται ρεαλιστικά το μήκος των πλαστικών αρθρώσεων και κατ' επέκταση η μη-γραμμική συμπεριφορά των μελών όταν διακριτοποιούνται με την χρήση του προτεινόμενου υβριδικού δικτύου πεπερασμένων στοιχείων.

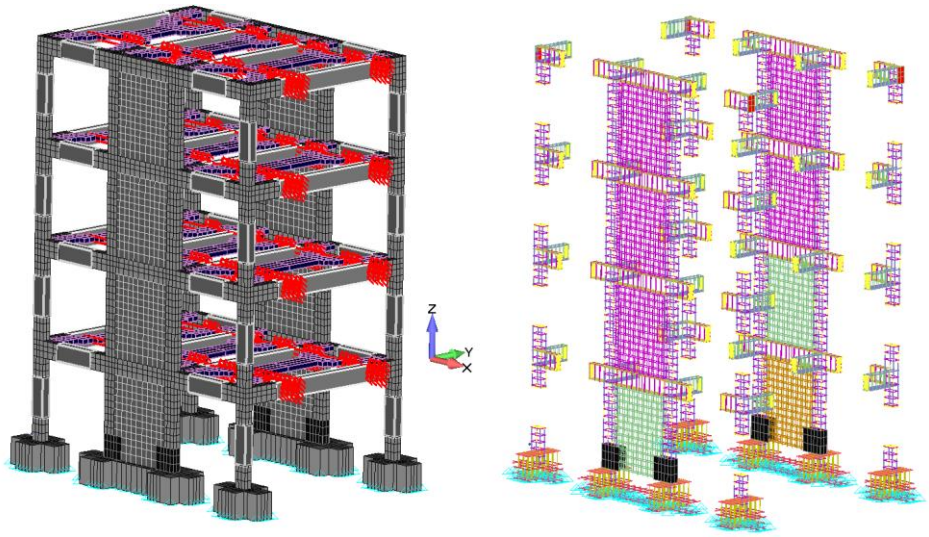

Σχήμα 34 Τετραώροφο κτίριο. (Αριστερά) Διακριτοποίηση σκυροδέματος και (Δεξιά) στοιχείων οπλισμού με χρήση υβριδικού δικτύου πεπερασμένων στοιχείων.

Πίνακας 4 Λεπτομέρειες της διακριτοποίησης που χρησιμοποιήθηκε για το αριθμητικό προσομοίωμα του τετραώροφου κτιρίου.

a/a	Model	Hexahedral Elements	Embedded Rebar Elements	RC NBCFB Elements	Hexa FE Reduction (%)	Embedded Rebar FE Reduction (%)	Overall FE Reduction (%)
1	Full Hexa	16,662	31,246	-	-	-	-
2	HYMOD	8,356	20,646	48	49.85	33.92	39.46
a/a	Model	Stiffness Matrix Size (Mb)	Reduction in Stiffness Matrix Size (%)		Dofs	Dofs Reduction (%)	
1	Full Hexa	1,000	-		85,191	-	
2	HYMOD	335	66.5		43,896	48.47	

Το μοντέλο θεωρεί ότι οι ράβδοι οπλισμού βρίσκονται σε πλήρη συνάφεια με το σκυρόδεμα και επίσης δεν χρησιμοποιήθηκαν οι παράγοντες βλάβης για την ανάλυση του τετραωρόφου κτιρίου. Επιπλέον, τα ινοπλισμένα πολυμερή από ίνες άνθρακα (CFRP) προσομοιώθηκαν με πρόσθετα 8-κομβικά εξαεδρικά πεπερασμένα στοιχεία τα οποία τοποθετήθηκαν στην ακριβή τους θέση (βάση τοιχωμάτων) όπως περιγράφεται στην πειραματική διάταξη. Τα χαρακτηριστικά των υλικών που χρησιμοποιήθηκαν για την αριθμητική προσομοίωση συνοψίζονται στον Πίνακα 5.

Πίνακας 5 Χαρακτηριστικά των υλικών που χρησιμοποιήθηκαν για το αριθμητικό προσομοίωμα του τετραώροφου κτιρίου.

Material	Young Modulus (GPa)	Hardening Modulus (GPa)	Yielding Stress / Tensile Strength* (MPa)	Compressive Strength (MPa)	Shear remaining strength β	Poisson Ratio	Ultimate Strain ε
Concrete	30	-	2*	20	0.2	0.2	-
Steel inside the Frame	190	2.1	400	-	-	0.3	15%
Steel inside the Infill Walls	190	2.1	450	-	-	0.3	15%
CFRP	100	-	1,000*	1,000	-	0.3	1%

Οι παραμορφώσεις που αναπτύχθηκαν στον φορέα στο τέλος της πρώτης φόρτισης (0.1g test, Σχήμα 33α) φαίνονται στο Σχήμα 35. Στις περιοχές του τοιχώματος και των κόμβων των πλαισίων αναπτύχθηκαν μεγαλύτερες παραμορφώσεις καθώς το σκυρόδεμα παρουσίασε έντονη ρηγμάτωση ενώ ο χάλυβας οπλισμού δεν παρουσίασε διαρροή (ελαστική συμπεριφορά). Επίσης το νότιο τοίχωμα (South wall) ανέπτυξε μεγαλύτερες παραμορφώσεις σε τοπικό επίπεδο εν συγκρίσει με το βόρειο (South wall) λόγω του μικρότερου ποσοστού οπλισμού που προέβλεπε ο σχεδιασμός του. Στην βάση των τοιχωμάτων αναπτύχθηκαν μικρές τάσεις-παραμορφώσεις λόγω της επιρροής των CFRP ενισχύσεων (έχουν οπτικά αφαιρεθεί από το Σχήμα 35) που συνέβαλλαν στην περίσφιξη και στην αύξηση της αντοχής του σκυροδέματος στις εν λόγω περιοχές.

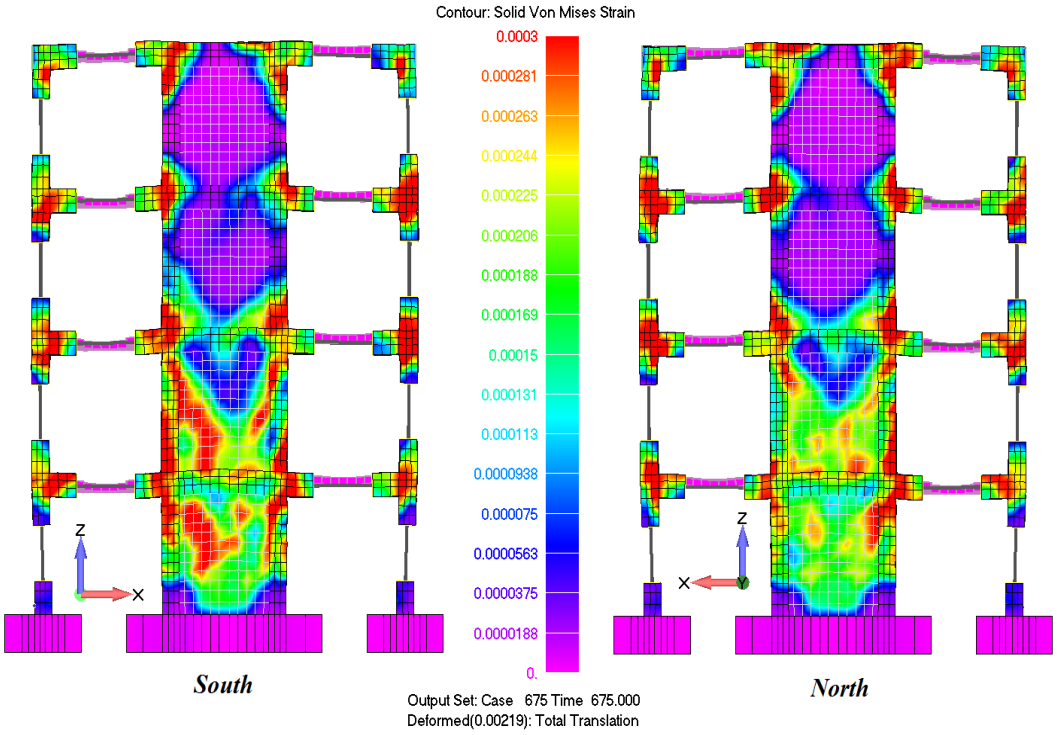

Σχήμα 35 Τετραώροφο κτίριο. Παραμορφώσεις (von Mises strain contour) που αναπτύχθηκαν μετά το τέλος της πρώτης φόρτισης (0.1g test)

Στο Σχήμα 36, φαίνεται η σύγκριση των αριθμητικών αποτελεσμάτων με τα πειραματικά δεδομένα μέσω των καμπυλών φορτίου-μετατόπισης. Όπως είναι εμφανές, το αριθμητικό

προσομοίωμα κατάφερε να προσομοιώσει με ακρίβεια την μέγιστη τέμνουσα βάσης που αναπτύχθηκε κατά την διάρκεια του πρώτου κύκλου φορτίσεων (0.1g test). Οι υστερετικοί βρόγχοι που προέκυψαν από το αριθμητικό προσομοίωμα φαίνονται να είναι πιο στενοί από τους αντίστοιχους πειραματικούς. Αυτή η διαφορά οφείλεται στο γεγονός ότι δεν έχει ληφθεί υπόψη η επιρροή του χρόνου κατά την διάρκεια του πειράματος (διάρκεια επιβολής της εκάστοτε παραμόρφωσης). Η μέγιστη θετική τέμνουσα βάσης, σύμφωνα με το αριθμητικό προσομοίωμα είχε τιμή ίση με 1,160 kN ενώ η αντίστοιχή πειραματική ήταν ίση με 1,152 kN (0.7% διαφορά). Ομοίως όσον αφορά την μέγιστη αρνητική τέμνουσα βάσης, η διαφορά μεταξύ αριθμητικής και πειραματικής καμπύλης ήταν 3% υπέρ της ασφαλείας.

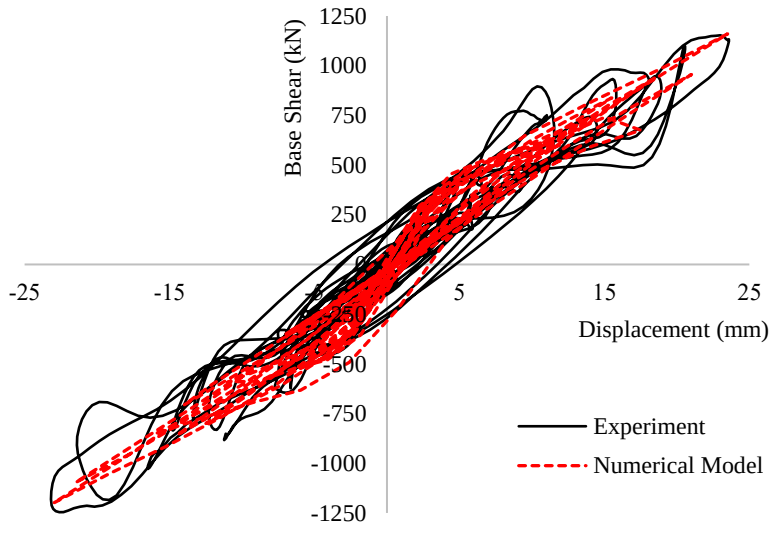

Σχήμα 36 Τετραώροφο κτίριο. Σύγκριση μεταξύ αριθμητικών και πειραματικών καμπυλών φορτίου-μετατόπισης πρώτης φόρτισης (0.1g test) .

Ο υπολογιστικός χρόνος για όλη την μη-γραμμική ανάλυση δίνεται στον Πίνακα 6, όπου χρειάστηκαν 15 ώρες και 30 λεπτά (19.7 δευτερόλεπτα κάθε εσωτερικό βήμα) για να επιλυθούν συνολικά 450 εξωτερικά βήματα και συνολικά 2,833 εσωτερικά βήματα. Ο μέσος όρος των εσωτερικών επαναλήψεων ήταν ίσος με 6.3, ενώ ο μέσος όρος του αριθμητικού σφάλματος (για να επιτευχθεί η σύγκλιση) ήταν ίσος με 1.01×10^{-5}. Το μέγεθος του αρχείου που περιείχε τα αποτελέσματα της ανάλυσης ήταν ίσο με 20.7 Gb το οποίο αναδεικνύει την αναγκαιότητα της χρήσης του υβριδικού δικτύου το οποίο απομείωσε σημαντικά το υπολογιστικό κόστος.

Πίνακας 6 Απαιτούμενος υπολογιστικός χρόνος για την μη γραμμική ανάλυση του τετραώροφου κτιρίου κατά την διάρκεια της πρώτης φόρτισης (0.1g test) .

Number of Displ. Incr. per loading cycle	Total Displ Incr. Solved	Total Internal Iter.	Average Num. Error	CPU Time Nonlinear Solution (hours)	Size of the Output File (Gb)
20	450	2,833	1.01×10^{-5}	15.5	20.7

Οι απαιτούμενες εσωτερικές επαναλήψεις Newton-Raphson, που χρειάστηκαν για να επιτευχθεί η σύγκλιση κάθε προσαυξητικού βήματος επιβαλλόμενης μετατόπισης κατά την διάρκεια της ανάλυσης τετραώροφου κτιρίου, απεικονίζονται στο Σχήμα 37. Όπως φαίνεται, 47,11% (212) των εξωτερικών βημάτων χρειάστηκαν λιγότερο από 5 εσωτερικές επαναλήψεις ενώ 77,33% (348) χρειάστηκαν λιγότερες από 10 για την επίτευξη σύγκλισης. Επίσης, μόνο 1.55% (7) των εξωτερικών επαναλήψεων χρειάστηκαν περισσότερες από 20 εσωτερικά βήματα για να επιτευχθεί η σύγκλιση.

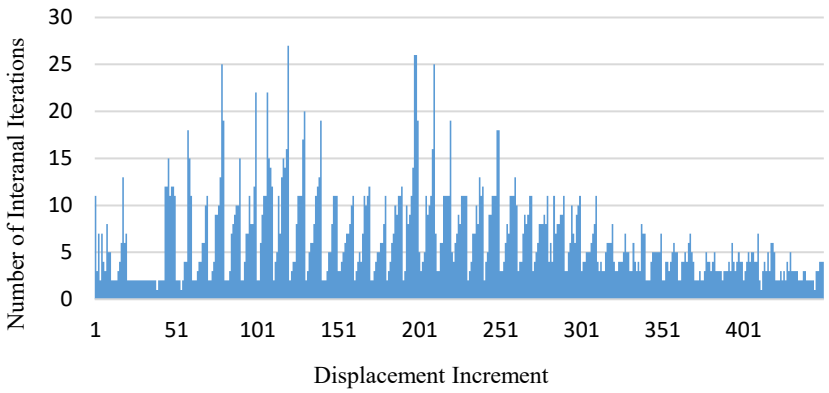

Σχήμα 37 Απαιτούμενος αριθμός εσωτερικών επαναλήψεων Newton-Raphson για το τετραώροφο κτίριο κατά την διάρκεια της πρώτης φόρτισης (0.1g test).

Η δεύτερη φόρτιση (0.25g test, Σχήμα 33) περιλαμβάνει 24 κύκλους με μέγιστη μετατόπιση ίση με 108 mm και 92 mm σε θετική και αρνητική κατεύθυνση αντίστοιχα. Η φόρτιση αυτή επιβλήθηκε ξεχωριστά στο αριθμητικό με τις αρχικές ελαστικές του ιδιότητες χωρίς να ληφθεί υπόψη η βλάβη που έχει υποστεί το μοντέλο από την πρώτη φόρτιση (0.1g test). Ο λόγος που έγινε αυτό, ήταν το αυξημένο υπολογιστικό κόστος που θα απαιτούσε η ανάλυση και τον δυο φορτίσεων διαδοχικά (0.1g, 0.25g). Οι καμπύλες τέμνουσας βάσης-μετατόπισης που προέκυψαν από τα αριθμητική ανάλυση (κόκκινη διακεκομμένη καμπύλη) συγκρίνονται με τα πειραματικά αποτελέσματα στο Σχήμα 39. Όπως ήταν αναμενόμενο, τα αριθμητικά αποτελέσματα παρουσιάζουν μια πιο δύσκαμπτη συμπεριφορά σε σύγκριση με την πειραματική συμπεριφορά επειδή δεν λήφθηκε υπόψη η βλάβη που είχε αναπτυχθεί από την πρώτη φόρτιση. Συνεπώς προστέθηκαν στην αρχή της υπάρχουσας φόρτισης, δύο κύκλοι επιβαλλόμενης μετατόπισης με μέγεθος 20 και 23 mm οριζόντιας μετατόπισης του τέταρτου ορόφου (μέγιστες μετατοπίσεις κατά την διάρκεια της πρώτης φόρτισης) για να αντιπροσωπεύσουν την πρώτη φάση φόρτισης.

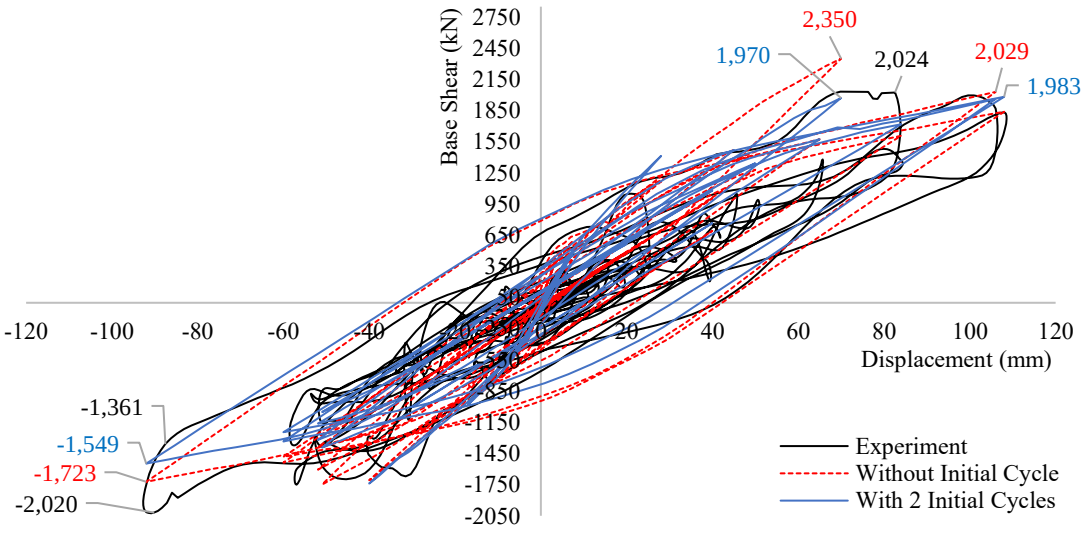

Σχήμα 38 Τετραώροφο κτίριο. Σύγκριση μεταξύ αριθμητικών και πειραματικών καμπυλών φορτίου-μετατόπισης δεύτερης φόρτισης (0.25g test) .

Τα αριθμητικά αποτελέσματα του μοντέλου με την τροποποιημένη φόρτιση (προσθήκη δύο κύκλων επιβαλλόμενης μετατόπισης) συγκρίνονται επίσης με τα πειραματικά στο Σχήμα 39 (μπλε συνεχόμενη καμπύλη). Το αριθμητικό μοντέλο προσομοιώνει αρκετά καλά την

πειραματική συμπεριφορά του φορέα με ακρίβεια 10% όσον αφορά την μέγιστη τέμνουσα βάσης (θετική και αρνητική) που αναπτύσσεται σε κάθε κύκλο φόρτισης, καταδεικνύοντας την αριθμητική ακρίβεια της προτεινόμενης μεθοδολογίας προσομοίωσης.

Οι παραμορφώσεις που αναπτύχθηκαν στον φορέα στο τέλος της δεύτερης φόρτισης (0.25g test, Σχήμα 33b) φαίνονται στο Σχήμα 39. Είναι προφανές, ότι οι παραμορφώσεις είναι αρκετά μεγαλύτερες από αυτές που προέκυψαν από την πρώτη φόρτιση (0.1g), αφού οι μετατοπίσεις που επιβλήθηκαν κατά την διάρκεια της δεύτερης φάσης φόρτισης ήταν σχεδόν πέντε φορές μεγαλύτερες σε σχέση με αυτές της πρώτης χρονοϊστορίας. Στις περιοχές του τοιχώματος και των κόμβων των πλαισίων, αναπτύχθηκαν μεγαλύτερες διατμητικές παραμορφώσεις και έντονη ρηγμάτωση του σκυροδέματος όπως φαίνεται από τα αριθμητικά αποτελέσματα, συμφωνώντας με τα πειραματικά αποτελέσματα [42].

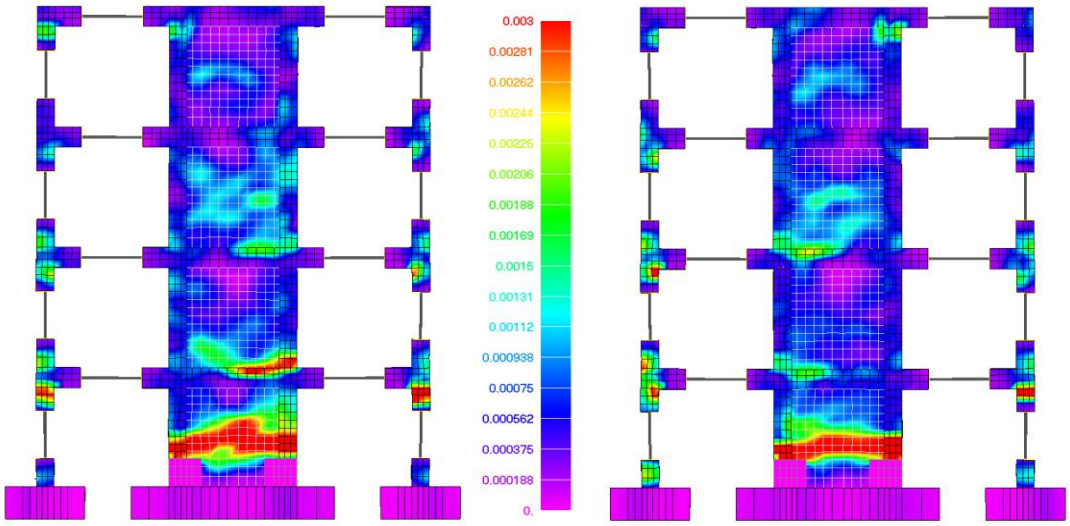

a. South Frame b. North Frame

Σχήμα 39 Τετραώροφο κτίριο. Παραμορφώσεις (von Mises strain contour) που αναπτύχθηκαν μετά το τέλος της δεύτερης φόρτισης (0.25g test)

Πίνακας 7 Απαιτούμενος υπολογιστικός χρόνος για την μη γραμμική ανάλυση του τετραώροφου κτιρίου κατά την διάρκεια της δεύτερης φόρτισης (0.25g test) .

Total Displ Incr. Solved	Total Internal Iter.	Average Numerical Error	CPU Time Nonlinear Solution (hours)	Other CPU Time (hours)	Size of the Output File (Gb)
1,560	7,504	8.92×10^{-6}	29.46	2.7	70.8

Ο υπολογιστικός χρόνος για όλη την μη-γραμμική ανάλυση δίνεται στον Πίνακα 7, όπου χρειάστηκαν 29 ώρες και 28 λεπτά (14.14 δευτερόλεπτα κάθε εσωτερικό βήμα) για να επιλυθούν συνολικά 1,560 εξωτερικά βήματα και συνολικά 7,504 εσωτερικά βήματα. Ο μέσος όρος των εσωτερικών επαναλήψεων ήταν ίσος με 4.81, ενώ ο μέσος όρος του αριθμητικού σφάλματος (για να επιτευχθεί η σύγκλιση) ήταν ίσος με 8.92×10^{-6}. Το μέγεθος του αρχείου που περιείχε τα αποτελέσματα της ανάλυσης ήταν ίσο με 70.8 Gb το οποίο για ακόμη μία φορά αναδεικνύει την αναγκαιότητα της χρήσης του υβριδικού δικτύου.

Οι απαιτούμενες εσωτερικές επαναλήψεις Newton-Raphson, που χρειάστηκαν για να επιτευχθεί η σύγκλιση κάθε προσαυξητικού βήματος επιβαλλόμενης μετατόπισης κατά την διάρκεια της ανάλυσης του τετραώροφου κτιρίου, απεικονίζονται στο Σχήμα 40. Όπως

προκύπτει από το Σχήμα 40, 68.5% (1,069) των εξωτερικών βημάτων χρειάστηκαν λιγότερο από 5 εσωτερικές επαναλήψεις ενώ 88,2% (1,376) χρειάστηκαν λιγότερες από 10. Μόνο ένα μηδαμινό 1.9% (30) των εξωτερικών επαναλήψεων χρειάστηκαν περισσότερες από 20 εσωτερικά βήματα για να επιτευχθεί η σύγκλιση.

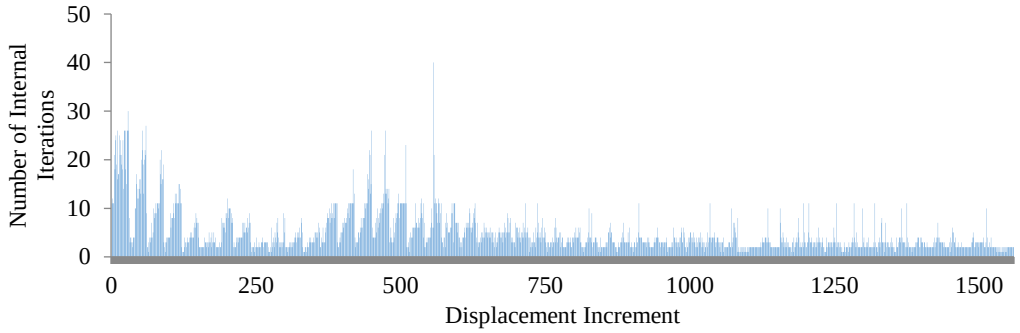

Σχήμα 40 Απαιτούμενος αριθμός εσωτερικών επαναλήψεων Newton-Raphson για το τετραώροφο κτίριο κατά την διάρκεια της δεύτερης φόρτισης (0.25g test).

Στην συνέχεια, εξετάστηκε η συνεισφορά του τοιχώματος ενίσχυσης σε σχέση με την αντοχή και πλαστιμότητα του τετραώροφου κτιρίου όπου διερευνήθηκε η επιρροή της προσθήκης τοιχώματος μόνο στο πρώτο όροφο ή στους πρώτους δύο ορόφους. Η διερεύνηση έγινε με βάση την ανάλυση του φορέα για την τελική ιστορία φόρτισης που οδηγεί το κτίριο στην αστοχία του ("funeral cycles"). Για σκοπούς περιορισμού του μεγέθους της περίληψης στα Ελληνικά, τα αποτελέσματα αυτά έχουν παραληφθεί. Τα αποτελέσματα αυτά έδειξαν πως η προσθήκη τοιχώματος σε όλους τους ορόφους διπλασιάζει την αντοχή του φορέα ενώ το μέγεθος των υστερητικών βρόγχων (καταναλισκόμενη ενέργεια) της οριακής ανακυκλικής φόρτισης ("funeral cycles") πενταπλασιάστηκε σε σχέση με τον φορέα που δεν προνοεί την χρήση τοιχίων ενίσχυσης. Η προσθήκη τοιχώματος στον πρώτο ή και στους πρώτους δύο ορόφους παρουσίασαν παρόμοια συμπεριφορά μεταξύ τους. Η αντοχή του φορέα ήταν γύρω στα 25% μικρότερη και η καταναλισκόμενη ενέργεια ήταν 2.4 φορές μικρότερη σε σύγκριση με τα αποτελέσματα του φορέα με το τοίχωμα που εκτείνεται σε όλους τους ορόφους του κτιρίου. Είναι σημαντικό να σημειωθεί ότι παρουσιάστηκαν σημαντικές τοπικές βλάβες και πρόωρη αστοχία του φορέα λόγω της ανισοκατανομής της δυσκαμψίας καθ' ύψος του κτιρίου στις περιπτώσεις που χρησιμοποιείται τοίχωμα μόνο στον πρώτο όροφο (τοπική αστοχία στους κόμβους μεταξύ πρώτου και δεύτερου ορόφου) ή στους πρώτους δύο ορόφους τοπική αστοχία στους κόμβους μεταξύ δεύτερου και τρίτου ορόφου).

VII. Συμπεράσματα και μελλοντική έρευνα

Το προτεινόμενο καταστατικό προσομοίωμα του σκυροδέματος κατάφερε να περιγράψει την συμπεριφορά του υλικού ως μια ψαθυρή μη-γραμμική συμπεριφορά που χαρακτηρίζεται από τριαξονικά φαινόμενα. Το αριθμητικό προσομοίωμα στηρίχθηκε σε ένα αλγοριθμικό σχεδιασμό ο οποίος διαχειρίστηκε το άνοιγμα και το κλείσιμο των ρωγμών με σκοπό να επιτευχθεί ακρίβεια στα αριθμητικά αποτελέσματα και ευστάθεια της υπολογιστικής διαδικασίας. Για τα στοιχεία του σκυροδέματος χρησιμοποιήθηκαν 8-κομβικά εξαεδρικά πεπερασμένα στοιχεία και η ρηγμάτωση προσομοιώθηκε με την χρήση της μεθόδου της διανεμημένης ρηγμάτωσης. Το προτεινόμενο κριτήριο κλεισίματος των ρωγμών έπαιξε κύριο ρόλο στην επίτευξη σύγκλισης της μη-γραμμικής ανάλυσης φορέων από οπλισμένο σκυρόδεμα που καταπονούνται σε ανακυκλιζόμενη και δυναμική φόρτιση. Αυτό αναδεικνύεται από το γεγονός ότι λίγες επαναλήψεις Newton-Raphson χρειάζονται για να επιτευχθεί η σύγκλιση ακόμα και σε περιπτώσεις που η φόρτισης φτάνει τα όρια αντοχής του φορέα.

Η προσθήκη δυο παραμέτρων βλάβης στο καταστατικό προσομοίωμα του σκυροδέματος και του χάλυβα του οπλισμού, προσομοίωσαν με σημαντική ακρίβεια (10% ακρίβεια στην φέρουσα ικανότητα των κατασκευών που μελετήθηκαν) την εξέλιξη της βλάβης και την επιρροή της στην μηχανική συμπεριφορά του φορέα κατά την διάρκεια στατικής ανακυκλιζόμενης και δυναμικής φόρτισης. Συγκεκριμένα προσομοιώθηκε η επιρροή του ανοίγματος-κλεισίματος των ρωγμών στην μείωση της αντοχής και δυσκαμψίας του φορέα κατά την διάρκεια της ανακύκλισης. Επιπλέον, η έντονη ρηγμάτωση επιφέρει σημαντική μείωση της συνάφειας του χάλυβα οπλισμού με το σκυρόδεμα. Αυτή η μείωση λήφθηκε έμμεσα υπόψη μέσω της προτεινόμενης παραμέτρου βλάβης του χάλυβα με την οποία προσομοιώθηκαν φαινόμενα στένωσης των υστερητηκικών βρόγχων (pinching effects).

Η χρήση των στοιχείων δοκού-υποστυλώματος (φυσικά στοιχεία δυνάμεων-NBCFB elements) για τις ράβδους οπλισμού έπαιξε επίσης καθοριστικό ρόλο στην ευστάθεια της υπολογιστικής διαδικασίας και στην ακρίβεια προσομοίωσης της συμπεριφορά των κατασκευών από οπλισμένο σκυρόδεμα. Η χρησιμοποίηση στοιχείων δικτυώματος για τον χάλυβα οπλισμού έδειξε ότι σε περιπτώσεις οριακής (επίπεδα έντασης ανώτερα της αντοχής σχεδιασμού του φορέα) ανακυκλιζόμενης ή δυναμικής φόρτισης οδηγεί την κατασκευή σε πρόωρη αστοχία. Αντιθέτως, συνιστάται η χρήση στοιχείων δοκού-υποστυλώματος για τον χάλυβα οπλισμού ακόμα και όταν η επιβαλλόμενη φόρτιση γίνεται διπλάσια από την φόρτιση σχεδιασμού του φορέα (διώροφα κτίρια) με την οποία εξασφαλίζεται σύγκλιση της μη-γραμμικής διαδικασίας σε περιπτώσεις έντονης ρηγμάτωσης.

Επιπλέον, η χρήση υβριδικού δικτύου πεπερασμένων στοιχείων σε ανακυκλικές φορτίσεις κατάφερε να απομειώσει σημαντικά το υπολογιστικό κόστος της ανάλυσης χωρίς να μειωθεί η ακρίβεια των αποτελεσμάτων. Το υβριδικό δίκτυο κατάφερε να προσομοιώσει επαρκώς ένα τετραώροφο κτίριο από οπλισμένο σκυρόδεμα το οποίο υποβλήθηκε σε ανακυκλιζόμενη φόρτιση. Η ανάλυση του τετραώροφου κτιρίου, έδωσε την δυνατότητα να διερευνηθεί η αποδοτικότητα της ενίσχυσης της κατασκευής με την προσθήκη τοιχώματος και την επιρροή των CFRP πλέγματος στην μηχανική συμπεριφορά του φορέα. Η ανάλυση μια κατασκευής σε μεγάλη κλίμακα (τετραώροφο κτίριο) που υποβάλλεται σε ανακυκλιζόμενη φόρτιση με χρήση τρισδιάστατων αριθμητικών προσομοιωμάτων συναντάται για πρώτη φορά στην υπάρχουσα βιβλιογραφία.

Ως μελλοντικός στόχος, τίθεται η χρήση του προτεινόμενου προσομοιώματος για την δυναμική ανάλυση των κατασκευών μεγάλης κλίμακας όπως πολυώροφα κτίρια και γέφυρες από οπλισμένο σκυρόδεμα. Κρίνεται επιβεβλημένη η χρήση του προτεινόμενου υβριδικού δικτύου πεπερασμένων στοιχείων για αυτές τις αναλύσεις καθώς και η ανάπτυξη αλγορίθμων παράλληλης επεξεργασίας όσον αφορά την επίλυση της ανάλυσης και την μόρφωση των μητρώων δυσκαμψίας θα αποφόρτωνε σημαντικά το απαιτούμενο υπολογιστικό κόστος.

Είναι σημαντικό επίσης να εξεταστούν φορείς από προεντεταμένο σκυρόδεμα, μεθοδολογία η οποία χρησιμοποιείται συχνά στην γεφυροποιία. Για να εξεταστεί πλήρως η συμπεριφορά αυτών των κατασκευών, θα πρέπει να προσομοιωθούν επιπλέον φαινόμενα ερπυσμού και συστολής ξήρανσης του σκυροδέματος. Επίσης, η ανάλυση της αλληλεπίδρασης εδάφους κατασκευής χρησιμοποιώντας τρισδιάστατα προσομοιώματα για την ανωδομή και για τα στοιχεία εδάφους, θα προσδώσει μεγαλύτερη ακρίβεια στην συμπεριφορά της κατασκευής υπό πραγματικές συνθήκες στήριξης.

Επιπροσθέτως, είναι σημαντικό να διερευνηθούν διάφοροι τρόποι ενίσχυσης κατασκευών από οπλισμένο σκυρόδεμα αφού εξεταστεί η αποδοτικότητά τους (χιαστοί μεταλλικοί σύνδεσμοι, μανδύες σκυροδέματος, χρήση ινοπλισμένων πολυμερών-FRP, προσθήκη ή εμφάντνωση τοιχωμάτων) με χρήση του προτεινόμενου αριθμητικού μοντέλου. Με αυτόν τρόπο μπορεί να

διερευνηθεί ο βέλτιστος τρόπος ενίσχυσης μιας κατασκευής ανάλογα με τα χαρακτηριστικά της (π.χ. γεωμετρία, καταπόνηση και υπάρχουσες βλάβες).

Τέλος, το προτεινόμενο αριθμητικό μοντέλο το οποίο στηρίζεται σε πειραματικές σχέσεις και σε ένα κατάλληλο αλγοριθμικό σχεδιασμό, πρέπει να συγκριθεί με άλλα θεωρητικά προσομοιώματα που στηρίζονται σε νόμους θερμοδυναμικής, πλαστιμότητας και θραυστομηχανικής. Με αυτόν τον τρόπο, θα φανερωθούν πλήρως τα πλεονεκτήματα και μειονεκτήματα της κάθε προσέγγισης όσον αφορά την ακρίβεια και την υπολογιστική απόδοση και θα γίνει η κατάλληλη βαθμονόμηση των παραμέτρων των διαφόρων μεθοδολογιών.

Preface

During the last decades, a progressive spread of the use of the finite element method has been occurred by professionals, engineering societies and construction firms. Although the FEM method is widely used, the objectivity of nonlinear finite element analysis is an open research subject through many fields in engineering community. The use of FEM software without possession of basic notions and assumptions about FEM and nonlinear modeling can give rise to many oversights and errors.

This is indicated by the fact that there are many FEM softwares like SAP2000, Abaqus, LS-DYNA, TNO DIANA, ANSYS, ATENA, ADINA, GT STRUDL, FEMAP with NXNastran, STAAD Pro, SEISMOSTRUCT that present different characteristics and assumptions about the nonlinear constitutive modeling, which makes it a difficult task for a numerical model to present the same response with the use of the above softwares. An engineer should never have blind confidence in the numerical results. On the contrary, he should have a useful skepticism of the output of the numerical model. It is the author's belief that the numerical modeling approaches should be able to simplify the real structures mechanic behavior into well-defined equivalent structural systems.

The non-linear finite element modeling of reinforced concrete has to provide a practical tool not only for researchers but for design office engineers. The non-linear analysis of RC structures can be used for the assessment of the strength, the level of damage and structures that are built according to previous codes. Furthermore, the non-linear FEM analysis can be used for the investigation of different types of retrofitting and its optimum design. Many constitutive models have been developed for the simulation of the behavior of reinforced concrete structures. There are many constitutive models which are based on plasticity theory, thermodynamic laws, fracture mechanics and the combinations of them. The main characteristic of these approaches, is that they use a uniaxial stress-strain relationships which place emphasis on stain-softening material properties. However, the accurate constitutive modeling of concrete needs to describe the behavior of concrete under multiaxial stress conditions. Experimental evidence shows that the post-cracking properties are characterized by uncertainty. The assumptions of brittle failure and the fact that the triaxial conditions can lead to an increase of the ductility of concrete when its strength is approached, are fundamental features of the realistic behavior of concrete.

The key characteristics of an accurate and computationally efficient non-linear FEM modeling of reinforced concrete structures are:

- Realistic assumptions that provide objectivity.
- Numerical stability during the nonlinear analysis.
- Ability to use the same constitutive modeling assumptions for different mechanical behaviors of RC structures.
- Ability to alleviate numerical limitation for simulating large-scale RC structures.

This thesis provide an accurate and efficient modeling approach for RC structures using the experimental evidence of triaxial tests which describe the brittle nature of concrete. The model uses the isoparametric hexahedral 8-noded elements to discretize concrete areas and the natural beam-column flexibility-based elements for the steel reinforcement. The steel-reinforcement rebars are modelled as embedded discrete elements inside the hexahedral concrete elements. The constitutive model follows an innovative algorithmic approach in order to take into account crack opening, crack closure, strength degradation, stiffness degradation and pinching effects. The model treats cracking with the smeared crack approach and the algorithm that describes the constitutive modeling, is based on the triaxial brittle behavior of concrete. It demonstrates its accuracy by comparing the numerical results with the experimental data of several structural

RC members subjected to cyclic loading. The proposed model manages to capture the behavior of RC members which different mechanical behavior under limit state conditions. The most important feature of the proposed method, is that it requires only the uniaxial compressive strength, the Poisson ratio and the Young modulus of elasticity of concrete as input parameters for every nonlinear analysis. This characteristic is a powerful advantage against other numerical models which provides objectivity. The model is enriched with new damage parameters which are defined during the analysis according to the level of crack opening and closure which causes the material of concrete and steel deterioration. Thus, the proposed procedure manages to capture phenomena such as strength and stiffness deterioration and pinching mechanisms during cyclic loading conditions.

The proposed method is combined with a hybrid modeling in order to simulate a 4-storey RC building under cyclic loading conditions. The use of 3D detailed modeling with the simulation of a full-scale structure is presented for the first time and demonstrates the computational efficiency of the model. Furthermore the model was found to be capable of capturing the dynamic behavior of RC structures with accuracy.

Several numerical investigation concerning modified crack-closure algorithms, different damage factors, mesh sensitivity analysis and different finite elements for concrete (8-node and 20-node hexahedral elements) and steel reinforcement (NBCFB and truss elements) are discussed. Last but not least, different retrofitting configurations for the 4-storey RC building are investigated indicating the capabilities of the proposed model providing knowledge of practical interest.

Table of Contents

Chapter 1. Introduction 1
1.1 General 1
1.2 Objectives of the Thesis 4
1.3 Layout of the Thesis 5
Chapter 2. The natural beam-column flexibility-based elements 8
2.1 Problems related to the numerical analysis of concrete structures 9
2.2 Natural mode approach 10
2.3 Natural modes for different finite elements 12
2.4 Beam-column elements for modeling RC structures 13
2.4.1 Lumped models 14
2.4.2 Distributed models 15
2.4.3 Displacement- and force-based elements 16
2.4.4 Beam-column model formulation incorporated in this work 19
Chapter 3. Proposed finite element modelling 26
3.1 Concrete elements 27
3.2 Steel reinforcement 30
3.3 Modeling of embedded rebar elements 30
3.4 Generating embedded rebars 33
3.5 Solution algorithms for static nonlinear analysis 35
3.6 Solution algorithms for dynamic nonlinear analysis 40
3.7 Solution algorithms for modal analysis 42
Chapter 4. 3D Constitutive behavior of concrete material 44
4.1 General 45
4.2 Concrete under uniaxial compression 45
4.3 Concrete under biaxial compression 49
4.4 Concrete under triaxial compression 50
4.5 Concrete under uniaxial tension 55
4.6 Concrete subjected to shear 56
4.7 Time dependent properties 57
4.7.1 Shrinkage 57
4.7.2 Creep 59
4.7.3 Rate of loading 60
4.8 3D Constitutive Modelling of Concrete Material 60
4.8.1 Elasticity-based models 61

4.8.2 Plasticity-based models 62
4.8.3 Damage mechanic models 64
4.8.4 Microplane models 65
4.8.5 Crack models 65
Chapter 5. Proposed constitutive modelling of concrete under cyclic loading conditions: State of the art and proposed algorithmic description of the model 78
5.1 State-of-the-art in modelling of RC structures under cyclic loading conditions 79
5.1.1 Elasticity based and Elastoplastic uniaxial constitutive laws 79
5.1.2 Equivalent uniaxial strain concept 81
5.1.3 Bounding surface models 83
5.1.4 Microplane models 84
5.1.5 Models based on the compression field theory 85
5.1.6 Elasticity based and Elastoplastic models combined with fracture energy based smeared crack approaches 86
5.1.7 Hybrid modelling with different constitutive laws in different regions 87
5.1.8 Damage models and coupling between plasticity and damage modeling 88
5.1.9 Discrete approaches 89
5.1.103D elasticity based constitutive laws based on CFP theory combined with smeared crack approach 90
5.2 Mathematical description of non-linear stress-strain concrete behavior based on Kotsovos and Pavlovic material model 91
5.2.1 Three-moduli approach 91
5.2.2 Internal-stress approach 92
5.2.3 Combined approach 97
5.3 Strength envelope for concrete 99
5.4 Proposed algorithmic approach of constitutive modelling of concrete under cyclic loading conditions 100
5.4.1 Constitutive model of Concrete 100
5.4.2 Behavior of uncracked concrete under cyclic conditions 101
5.4.3 Behavior of cracked concrete under cyclic conditions 103
5.4.4 Compressive failure of concrete 111
5.4.5 Constitutive model of steel reinforcement 111
Chapter 6. Numerical implementation for RC members under cyclic loading conditions 114
6.1 Introduction 115
6.1.1 Lefas and Kotsovos Shear Walls 115
6.1.2 Červenka Shear Wall W4 125
6.1.3 RC Frame Joints 130

6.2 Conclusions 138

Chapter 7. The hybrid modeling approach and numerical implementation to RC structures that undergo cyclic loading 140

7.1 Introduction 141

7.2 Hybrid modeling formulation – kinematical coupling of 1D and 3D finite elements. 142

7.3 Reduction Levels of HYMOD meshes 145

7.4 Numerical Results and Discussion 147

7.4.1 Del Toro Rivera RC Frame Joint 147

7.4.2 One-Storey RC Frame with a Shear Wall 160

7.4.3 Two-storey RC Frame with Shear Wall 165

7.5 Conclusions 170

Chapter 8. Simplified HYMOD non-linear simulations of a full-scale multistory retrofitted RC structure that undergoes multiple cyclic excitations – An infill RC wall retrofitting study 172

8.1 Introduction 173

8.2 Material Modeling 174

8.3 Experimental Data 176

8.4 Numerical Model, Results and Discussion 179

8.4.1 Finite Element Mesh 180

8.4.2 Analysis Results for the 0.1g Test 183

8.4.3 Analysis Results for the 0.25g Test 188

8.4.4 Analysis Results for the Final Loading Test 193

8.5 Numerical Investigation of Different Infill RC Wall Retrofitting Configurations 199

8.6 Conclusions 209

Chapter 9. Nonlinear static cyclic and dynamic analysis of RC structures considering damage factors 212

9.1 Introduction 213

9.2 Concrete and steel material constitutive models 214

9.3 Damage factor Dc for concrete 215

9.4 Damage factor Ds for steel reinforcement 217

9.5 Parametric investigation for defining constants a_n and a_s 221

9.6 Numerical Validation of the Proposed Model for Static Cyclic Analysis 224

9.6.1 RC Beam-Column Joint 224

9.6.2 RC Column 228

9.7 Numerical Validation of the Proposed Model for Dynamic Analysis 232

9.7.1 Two-Storey RC frames 232

9.7.2 RC frame 245

9.7.3 Three-storey, three-bay RC frame subjected to High Intensity Ground Motions 249
9.8 Conclusions 258
Chapter 10. Capturing the mechanical response of RC members with pinching effects..... 260
10.1 Pinching characteristics of RC structures..... 261
10.2 Modified steel reinforcement constitutive law. 266
10.3 Modified concrete constitutive law-concrete crushing..... 268
10.4 Numerical Implementations 268
10.4.1 RC Beam-Column Joint 269
10.4.2 RC Shear wall SW4 272
10.4.3 RC Column U1 Saatcioglou and Ozcebe 274
10.4.4 RC Beam-Column Joint with Severe Damage and Extreme Slippage..... 275
Chapter 11. Conclusions and Future work 280
11.1 Original contribution 281
11.2 Conclusions 282
11.3 Limitations of the proposed model..... 284
11.4 Future work 286
References 289

List of Figures

Chapter 1. Introduction

Fig. 1.1 Truss model of an RC beam. 2

Fig. 1.2 (a) Bridge collapse after the Kobe earthquake in Japan 1995, (b) Failure of beam column exterior joint joints (Sezen et al. 2000 [2]) 3

Chapter 2. The natural beam-column flexibility-based elements

Fig. 2.1 Strain modes for a beam finite element. [49] 13

Fig. 2.2 Beam element: (a) Euler Bernoulli beam theory, (b) Timoshenko beam theory. [50] 14

Fig. 2.3 Lumped models (a) Clough and Johnston [51], (b) Giberson [54] 15

Fig. 2.4 Distributed fiber beam model. [49] 16

Fig. 2.5 2D Beam finite element using the displacement based formulation. 16

Fig. 2.6 2D Beam finite element, that uses the force-based formulation. 17

Fig. 2.7 Natural rigid body modes for a 3D beam element. 19

Fig. 2.8 Generalized displacement and forces of flexibility based element. 20

Fig. 2.9 Flow chart of the full model state determination 23

Fig. 2.10 Flow chart of the element state determination 24

Chapter 3. Proposed finite element modelling

Fig. 3.1 Linear and quadratic finite elements and the representation of the 8-node hexahedral element in the natural coordinate system. 27

Fig. 3.2 Isoparameteric truss element in global and natural coordinate system and the shape functions in respect to the natural coordinate system. 30

Fig. 3.3 Embedded rebar elements under transverse deformation in the case of a) truss and b) beam element. 31

Fig. 3.4 (a) Master triangles of beam element nodes 1 and 2 (b) schematic representation of rotation θ.[4] 31

Fig. 3.5 Schematic representation of the possible locations of rebar nodes. (a) Three cases: (Left) Rebar node on hexahedral face, (middle) Rebar-hexahedral face intersection, (right) Rebar node inside hexahedral mesh. (b) Geometric constraint for the search of embedding rebars. [30] 34

Fig. 3.6 (α) Full Newton-Raphson incremental-iterative solution procedure (b) Modified Newton-Raphson iterative scheme [72] 36

Fig. 3.7 The snap-through behavior when force-control is performed. 37

Fig. 3.8 A system that presents snap-through and snap-back instabilities when load and displacement control are used respectively. 38

Fig. 3.9 Schematic representation of the Arc-Length method iterations. 40

Chapter 4. 3D Constitutive behavior of concrete material

Fig. 4.1 Behavior of concrete under cyclic uniaxial compression adapted from a) Karsan and Jirsa [86] and b) Sinha et al. [87]. 46

Fig. 4.2 Cylindrical concrete specimen. a) Boundary conditions effect under uniaxial compression and b) Stress paths for the central and the end zones cylinders under increasing uniaxial compression. [3] 47

Fig. 4.3 Different types of loading systems (Gerstle et al. [93]) 47

Fig. 4.4 Load-displacement curves for the cylinder specimens subjected to different test methods with uniaxial compressive strength a) $fc = 29MPa$, b) $fc = 50MPa$ ([3]) 48

Fig. 4.5 Schematic representation of crack-extension behavior of concrete cylinders under uniaxial compression. [3] 48

Fig. 4.6 Schematic representation of the experimental setup of a biaxial loading. (Li and Ren [95]) 49

Fig. 4.7 Biaxial compressive yield Surface for concrete for different (a) confining pressure (Kupfer et al. [96], Yin et al. [97] and Van Mier [98]), (b) compressive strength (Kupfer et al. [96]) 49

Fig. 4.8 Schematic representation of the experimental setup of a triaxial testing machine. (Launay and Gachon [99]) 50

Fig. 4.9 Schematic representation of the stages of the fracture process for concrete under compressive stress. [3] 52

Fig. 4.10 Stress-strain characteristics during the stages of fracture processing. (a) Linear material properties, (b) Internal stresses effect, (c) Void formation effect. [3] 54

Fig. 4.11 Stress-strain relationships (measured and predicted) for a typical concrete (with f_c=45 MPa) under (a) uniaxial and (b) triaxial compression. [3] 54

Fig. 4.12 Behavior of concrete under tensile stresses. [102] 55

Fig. 4.13 Stress-deformation response for concrete subjected to (a) cyclic tensile loading, (b) reversed cyclic loading. [104] 56

Fig. 4.14 Schematic representation of the mechanism “aggregate interlock” (a) crack morphology, (b) stresses that caused by the slip of the crack surfaces. (CEB [105]) 56

Fig. 4.15 Schematic representation of the mechanism “Dowell action” (a) crack morphology, (b) Dowel action-slip curves under cyclic loading conditions. [106] 57

Fig. 4.16 Schematic representation of changes in dimensions of cement pastes, mortars and concretes with moisture conditions. [107] 58

Fig. 4.17 Shrinkage strain components in (a) normal and (b) high-strength concrete [108]... 58

Fig. 4.18 Schematic representation of creep strain components. [108] 59

Fig. 4.19 Effect of strain rate on concrete (a) tensile, (b) compressive strength. [103] 60

Fig. 4.20 Schematic representation of the microstructure with the microplanes on which stress and strain components are developed. [121] 65

Fig. 4.21 Schematic representation of discrete crack modelling by nodal separation on adjacent elements. (CEB [105]) 66

Fig. 4.22 Schematic representation of remeshing methods for discrete crack approach proposed byMiguel [124]. 67

Fig. 4.23 Schematic representation of crack patterns in (a) RC shear wall [127] and (b) beam-column RC joint [3]. 68

Fig. 4.24 Schematic representation of the interaction of a cracked element (2) with the uncracked neighboring element (1) when the smeared crack approach is used [130]. 70

Fig. 4.25 (a) Bar length L with an axial tensile stress σ, (b) Stress-strain response of the bar with one finite element exceeding its tensile strength. [72] 71

Fig. 4.26 Schematic representation of cohesive zone in front of the crack tip [72]. 72

Fig. 4.27 Stress-displacement curves for (a) linear decohesion, (b) ductile solid and (c) a quasi-brittle solid [72]. 73

Fig. 4.28 Examples of discrete modelling of a RC beam and cylindrical concrete specimen ([140,141]). 74

Fig. 4.29 Three-dimensional crack branching at different time steps for the cases of non-adaptive (a-c) and adaptive methods (d-f). [147] 75

Fig. 4.30 Concrete slab under explosive loading using approximately 265,000 particles. [147] 75

Fig. 4.31 T-spline mesh for a single-edge notched beam (up) and stress contour plot derived from isogeometric analysis (down). [152] 76

Chapter 5. Proposed constitutive modelling of concrete under cyclic loading conditions: State of the art and proposed algorithmic description of the model

Fig. 5.1 Cyclic loading constitutive model for concrete according to Rule and Rowlands [8]. 80

Fig. 5.2 Schematic representation of the modification of stress-strain relation of Giuffre-Menegotto-Pinto [34] steel model [20]. 81

Fig. 5.3 Schematic representation of the uniaxial stress-strain law according to Darwin and Pecknold [6]. 81

Fig. 5.4 Schematic representation of the uniaxial stress-strain law according to Balan et al. [16]. 82

Fig. 5.5 Schematic representation of the contact element proposed by Au and Bai [21]. 83

Fig. 5.6 Schematic representation of the bounding surface model: (a) bounding surface, (b) radial mapping proposed by Pagnoni et al. [159] 84

Fig. 5.7 Stress and strain components on each microplane according to Ozbolt et al. [9] (m,k: the coordinate vectors defined for each microplane, $\boldsymbol{\varepsilon}_T$: the tangential vector component of $\boldsymbol{\varepsilon}$) 84

Fig. 5.8 Schematic representation of the compression-field theory for membrane elements according to Vecchio and Collins [154]. 85

Fig. 5.9 Schematic representation of stress-strain envelope curves according to He et al. [22]. 86

Fig. 5.10 Cyclic uniaxial constitutive law of concrete according to Belletti et al. [162]. 87

Fig. 5.11 Stress-strain characteristics for cyclic strut-and-tie model elements according to To et al. [23]. 87

Fig. 5.12 Linear element and zero-length section element according to Melo et al. [24]. 88

Fig. 5.13 Decomposition of a cracked medium into hydrostatic (opening and closing) and deviatoric (frictional sliding) effects [25]. 89

Fig. 5.14 Unloading response of (a) elastic damage, (b) elastoplastic, (c) elastoplastic damage models [163]. 89

Fig. 5.15 Numerically obtained discrete crack paths for a double-edge notched specimen according to (a) Feist et al. [169] and (b) Roth et al. [170]. 90

Fig. 5.16 Schematic representation of the effect of cracking on the interface. (a) Slipped before cracking, (b) deformation of concrete element (down) due to residual forces caused by cracking (up) and the effect on bar slipping, according to Lykidis and Spiliopoulos [28] (s_{bc}=slippage before cracking, s_{ac}=slippage after cracking). 91

Fig. 5.17 Schematic representation of the coupling effect between stress deviation τ_0 and volume change $\varepsilon_{0(d)}$: (a) stress path followed, (b) resulting strains. ([3]) 92

Fig. 5.18 Schematic representation of the internal-stress concept used to account for the non-linear constitutive relations of concrete materials. ([3]) 93

Fig. 5.19 Experimental $\sigma_o - \varepsilon_{o(h)}$ relationships for various $f_{c.}$ ([3]) 94

Fig. 5.20 Variation of σ_{id} with τ_0 for various values of σ_0 for a typical concrete with f_c = 31.7 MPa. [3] 96

Fig. 5.21 Schematic representation of the approach used to evaluate σ_{id} for a given combination of σ_0 and τ_0. [3] 96

Fig. 5.22 Variation of the (a) bulk moduli (K_s, K_t) with σ_0 and (b) shear moduli (G_s, G_t) with τ_0 for a given concrete with f_c = 31.7 MPa. [3] 98

Fig. 5.23 Schematic representation of the ultimate-strength surface : (a) general view in stress space, (b) typical cross section of the strength envelope with a deviatoric plane (a plane of constant σ_0, viewed along the axis $\sigma_1 = \sigma_2 = \sigma_3$). [3] 99

Fig. 5.24 Calculation of τ_{0e} τ_{0c} which corresponds to the ultimate strength of concrete under triaxial compression and triaxial extension. [3] 100

Fig. 5.25 Three-dimensional view of the predicted ultimate-strength surface. [3] 100

Fig. 5.26 Schematic representation of the stress-strain relationship for the behavior of uncracked concrete under cyclic loading conditions. 102

Fig. 5.27 Schematic representation of two crack planes and their relative local axes at the same Gauss Point [31]. 104

Fig. 5.28 Crack patterns at a) first increments of cyclic loading (N=1) (b) when the deformation of cyclic loading reaches its maximum value (at the 10th displacement increment, N=10), (c) when the shear wall has returned to its initial state of equilibrium (at the 20th displacement increment, N=20) 106

Fig. 5.29 Strain perpendicular to the crack plane versus displacement increments at (a) a Gauss point near the base of the shear wall and (b) a Gauss point near the top of the shear wall. 107

Fig. 5.30 Schematic representation of the variables that consist the expression (5.62) in an example of a half loading cycle. Each branch is divided by 10 increments. The y-axis consists the numbers of increments. 108

Fig. 5.31 Flow chart of the proposed algorithm responsible in updating the stress-strain tensors and constitutive matrix for the case of an uncracked Gauss point. 109

Fig. 5.32 Flow chart of the proposed algorithm responsible in updating the stress-strain tensors and constitutive matrix for the case of a cracked Gauss point. 110

Fig. 5.33 Characteristics of the hysteretic steel stress-strain behavior of reinforcement steel (CEB 1996 [105])..... 112

Fig. 5.34 Menegotto-Pinto constitutive model for steel reinforcement..... 112

Chapter 6. Numerical implementation for RC members under cyclic loading conditions

Fig. 6.1 Geometry and Reinforcement details of shear walls SW31, SW32 and SW33 [177]. 115

Fig. 6.2 Load histories presented in the form of imposed displacements for a) SW31, (b) SW32 and (c) SW33. 116

Fig. 6.3 Shear walls. 3D and XY views of the FE mesh of the steel bars. 116

Fig. 6.4 Kotsovos and Lefas (Left) Shear walls. (Right) XZ and 3D views of the FE mesh, constraints and imposed displacement of the 8-noded hexahedral elements. 117

Fig. 6.5Comparison between numerical and experimental results of the force deflection curves of specimens (a) SW31, (b) SW32, (c) SW33 with NBCFB elements for the steel reinforcement of diameter 8mm and (d) SW33 with trusses 118

Fig. 6.6 Comparison between numerical and experimental results of the force deflection curve SW31 for different mesh discretizations (131, 226 hexahedrals) and for different external displacement increments (Ext10, Ext30, Ext60). 120

Fig. 6.7 Comparison between numerical and experimental results of the force deflection curve SW33 for different shear retention factors. 120

Fig. 6.8 Crack patterns during the first cycle when the imposed displacement reaches its maximum magnitude (a) horizontal displacement along the positive x axis and (b) negative x axis..... 121

Fig. 6.9 Comparison between experimental with numerical results in terms of crack patterns for a) SW31 when the horizontal load was 65 kN, b) SW32 when the horizontal load was 90 kN and c) SW31 when the horizontal load was 110 kN (prior to failure). 123

Fig. 6.10 Kotsovos and Lefas Shear walls. Required NR iteration per displacement increment from the last cycle of loading (until failure) for (a) SW31, (b) SW32 and (c) SW33 124

Fig. 6.11 Geometry and reinforcement details of shear wall W4 [13] 125

Fig. 6.12. Shear wall W4. 3D views of the (left) FE mesh of concrete elements and (right) steel reinforcement. 126

Fig. 6.13 Comparison between numerical and experimental data for specimen W4. 127

Fig. 6.14 Comparison between numerical and experimental data for specimen W4 for a) 1st cycle, b) 2nd cycle, c) 3rd cycle. 127

Fig. 6.15 Comparison between numerical and experimental results of the force deflection curve for different mesh discretizations (105, 201 and 321 hexahedrons) and different displacement increments (10 and 20 per load branch). 128

Fig. 6.16 Crack patterns during the first cycle a) when the imposed displacement is -0.65mm (directed downwards) b) when the imposed displacement is +0.65mm (directed upwards) when using 105 and 321 hexahedral elements. 128

Fig. 6.17 Shear wall W4. Comparison between experimental [7] and numerical results in terms of crack patterns near failure. 129

Fig. 6.18 Shear wall W4. Required NR iteration per displacement increment during the last cycle. 129

Fig. 6.19 Geometry and reinforcement details of beam column joint (Del Toro Rivera [178]). All lengths are in mm. 130

Fig. 6.20 Load history presented in the form of imposed displacements for the interior frame joint. 131

Fig. 6.21 Interior frame joint. 3D views of the FE mesh of concrete elements and steel reinforcement. 131

Fig. 6.22 Interior frame joint. Comparison between numerical and experimental results. Complete force-displacement history. 132

Fig. 6.23 Interior frame joint. Comparison between numerical and experimental results (a) for cycles ±26 mm and (b) for cycles ±39 mm. 133

Fig. 6.24 Interior frame joint. Comparison between numerical and experimental results for different mesh discretization (76 and 164 hexahedrons) (a) for cycles ±26 mm and (b) for cycles ±39 mm. 133

Fig. 6.25 Crack patterns during the first cycle (a) when the imposed displacement is +13mm (directed eastward) and (b) when the imposed displacement is -13mm (directed westward). Left: 76 and Right: 164 hexahedral elements. 134

Fig. 6.26 Interior frame joint. Required NR iteration per displacement increment for the last 70 displacement increments. 134

Fig. 6.27 Geometry and reinforcement details of the corner frame joint. All dimensions are given in mm. 135

Fig. 6.28 Load history presented in the form of imposed displacements for the corner frame joint. 136

Fig. 6.29 RC Corner Frame Joint. 3D views of the FE mesh of concrete elements and steel reinforcement. 136

Fig. 6.30 RC Corner Frame Joint. Comparison between the numerical and experimental results. Force-displacement history. 137

Fig. 6.31 Exterior frame joint. Required NR iteration per displacement increment..... 138

Chapter 7. The hybrid modeling approach and numerical implementation to RC structures that undergo cyclic loading

Fig. 7.1 Schematic representation of the global and local scale modeling proposed in Mata et al. [192]. 142

Fig. 7.2 Kinematic constraints imposed by the 1D structural member on the interface section Ω_i^1 143

Fig. 7.3 Schematic representation of the master and slave nodes of the interface section. ... 145

Fig. 7.4 Different reduction levels of hybrid simulation of a 3D RC frame. [37] 146

Fig. 7.5 Von Mises contours and deformed shapes of clamped beam models.[4] 146

Fig. 7.6 Bilinear model for cyclic analysis. 147

Fig. 7.7 2D and 3D views of the FE meshes of the three HYMOD models. 149

Fig. 7.8 Frame Joint. Comparison between numerical and experimental results. Complete force-displacement history. 150

Fig. 7.9 Frame Joint. Comparison between Full Hexa and HYMOD 1 numerical results. Complete force-displacement history. 150

Fig. 7.10 Frame Joint. Comparison between Full Hexa and HYMOD 2 numerical results. Complete force-displacement history. 151

Fig. 7.11 Frame Joint. Comparison between Full Hexa and HYMOD 3 numerical results. Complete force-displacement history. 151

Fig. 7.12 Frame Joint. von Mises strain contour at displacement increment 10 and 30 (1^{st} cycle of loading). Maximum x-axis displacement: ±13 mm. 153

Fig. 7.13 Frame Joint. Von Mises strain contour at displacement increments 210 and 230 (6^{th} cycle of loading). Maximum x-axis displacement: ±39 mm 154

Fig. 7.14 2D and 3D views of the FE mesh of the concrete elements used during the HYMOD mesh sensitivity analysis. 156

Fig. 7.15 Frame Joint. Comparison between experiment and Full Hexa 1. Complete force-displacement history. 157

Fig. 7.16 Frame Joint. Comparison between experiment and HYMOD 1.1. Complete force-displacement history. 157

Fig. 7.17 Frame Joint. Comparison between experiment and Full Hexa 2. Complete force-displacement history. 158

Fig. 7.18 Frame Joint. Comparison between experiment and HYMOD 1.2. Complete force-displacement history. 158

Fig. 7.19 Frame Joint. Von Mises strain contour at load step 10 and 30 (1^{st} cycle of loading) for the refined meshes. Maximum x-axis displacement: ±13 mm. 159

Fig. 7.20 South face of the SERFIN four-storey RC building. [42] 161

Fig. 7.21 One-storey frame. Geometric (cm) and reinforcement details (Ømm/cm). 161

Fig. 7.22 One-storey frame. 3D HYMOD FE mesh. 162

Fig. 7.23 One-storey frame. 3D HYMOD FE mesh of the reinforcement rebar elements. 162

Fig. 7.24 Load history presented in the form of imposed displacements for the one-storey RC frame. 163

Fig. 7.25 One-storey RC frame. Comparison between different displacement increments with a convergence tolerance 10^{-3}. Complete force-displacement history. 164

Fig. 7.26 One-storey RC frame. Comparison between different displacement increments with a convergence tolerance 10^{-4}. Complete force-displacement history. 164

Fig. 7.27 One-storey RC frame. Opening and closing of cracks during the first loading cycle for the first model (40 displacement increments per loading cycle). 165

Fig. 7.28 Two-storey RC frame. Geometric details. 166

Fig. 7.29 Two-storey RC frame. FE meshes of a. Full Hexa, b. HYMOD 1 and c. HYMOD 2 models. 166

Fig. 7.30 Two-storey RC frame. Comparison between HYMOD 1 and Full Hexa for different displacement increments with a convergence tolerance 10^{-5}. Complete force-displacement history. 168

Fig. 7.31 Two-storey RC frame. Comparison between HYMOD 2 and Full Hexa for different displacement increments with a convergence tolerance 10^{-5}. Complete force-displacement history. 168

Fig. 7.32 Two-storey RC frame. Opening and closing of cracks during the 1st loading cycle for the first model (40 displacement increments per loading cycle). 169

Chapter 8. Simplified HYMOD non-linear simulations of a full-scale multistory retrofitted RC structure that undergoes multiple cyclic excitations – An infill RC wall retrofitting study

Fig. 8.1 Three-sided CFRP jacketing. [42] 175

Fig. 8.2 Material model of the CFRP jacketing. [196] 175

Fig. 8.3 Four-storey RC specimen in the lab. [195] 176

Fig. 8.4 Reinforcement details of the RC fame. [42] 177

Fig. 8.5 Water barrel setup and actuator attachment beams. [195] 178

Fig. 8.6 Views of the SERFIN specimen showing the water barrels and the actuators. [42] 178

Fig. 8.7 Four-Storey RC specimen. Displacement histories of the specimen. 179

Fig. 8.8 Full Hexa FE mesh. (Left) Discretization of the concrete domain and (Right) Embedded rebar elements. 180

Fig. 8.9 HYMOD FE mesh. (Left) Discretization of the concrete domain and (Right) Embedded rebar elements. 181

Fig. 8.10 Retrofitted five-storey RC building. Push over analysis. (a) Initial crack pattern and (b) Crack pattern prior to failure. 182

Fig. 8.11 FE mesh of the reinforcement details of the South shear wall and its foundation (different colors represent different rebar dimeters). 182

Fig. 8.12 Discretization of the CFRP jacketing through the use of hexahedral elements. 183

Fig. 8.13 1st loading test (0.1g). Von Mises strain contour for displacement increment 375 (δ_H = -23 mm). 184

Fig. 8.14 1st loading test (0.1g). Von Mises strain contour for displacement increment 390 (δ_H = 24 mm). 185

Fig. 8.15 1st loading test (0.1g). Crack pattern of the South wall for (a) δ_H = -23 mm and (b) δ_H = 23.5 mm. Maximum computed crack width 0.15 mm. 185

Fig. 8.16 1st loading test (0.1g). Remaining von Mises strain contour after the completion of the test (displacement increment 675; δ_H = 0 mm). 186

Fig. 8.17 1st loading test (0.1g). Experimental vs numerical curves. Total base shear vs horizontal displacement of the top floor. 187

Fig. 8.18 1st loading test (0.1g). Number of internal iterations vs displacement increment.. 188

Fig. 8.19 2nd loading test (0.25g). Experimental vs numerical curves. Total base shear-horizontal displacement of the top floor. 189

Fig. 8.20 2nd loading test (0.25g). Displacement history with 2 initial preparatory cycles applied at the top floor. 189

Fig. 8.21 2nd loading test (0.25g). Von Mises strain contour for displacement increments (a) 690 (δ_H = -92 mm) and (b) 720 (δ_H = 108 mm). South frame. 190

Fig. 8.22 2nd loading test (0.25g). Von Mises strain contour for displacement increments (a) 690 (δ_H = -92 mm) and (b) 720 (δ_H = 108 mm). North frame. 191

Fig. 8.23 2nd loading test (0.25g). Numerically computed strain ε_x history at the points N1 and S1. 191

Fig. 8.24 2nd loading test (0.25g). Numerically computed strain ε_z history at the points N2 and S2. 191

Fig. 8.25 2nd loading test (0.25g). Numerically computed strain ε_z history at the points N3 and S3. 191

Fig. 8.26 2nd loading test (0.25g). Numerically computed strain ε_z history at the points N4 and S4. 192

Fig. 8.27 2nd loading test (0.25g). Remaining von Mises strain contour after the completion of the test (displacement increment 1,560; δ_H = 0 mm). Deformation magnification factor x20. 192

Fig. 8.28 2nd loading test (0.25g). Number of internal iterations vs displacement increment. 193

Fig. 8.29 3rd loading test ("funeral cycles"). Experimental vs numerical curves. Total base shear-horizontal displacement of the top floor. Undamaged model. 194

Fig. 8.30 Combo 1 displacement history applied at the top floor of the specimen. 194

Fig. 8.31 3rd loading test ("funeral cycles"). Experimental vs numerical curves. Total base shear-horizontal displacement of the top floor. Combo 1 displacement history. 195

Fig. 8.32 Combo 2 displacement history applied at the top floor of the specimen. 195

Fig. 8.33 3rd loading test ("funeral cycles"). Experimental vs numerical curves. Total base shear-horizontal displacement of the top floor. Combo 2 displacement history. 196

Fig. 8.34 3rd loading test ("funeral cycles"). Experimental vs numerical curves. Total base shear-horizontal displacement of the top floor. Model with modified material properties. Combo 2 displacement history. 197

Fig. 8.35 3rd loading test ("funeral cycles"). Number of internal iterations vs displacement increment. Undamaged model. 198

Fig. 8.36 3rd loading test ("funeral cycles"). Number of internal iterations vs displacement increment. Combo 1 displacement history. 198

Fig. 8.37 3rd loading test ("funeral cycles"). Number of internal iterations vs displacement increment. Combo 2 displacement history. 198

Fig. 8.38 3D view of the hexahedral HYMOD mesh of the bare frame. 199

Fig. 8.39 Loading test ("funeral cycles"). RC Model with bare frame vs infilled RC walls. Total base shear-horizontal displacement of the top floor..... 200

Fig. 8.40 3D mesh view of the four-storey RC building with infill RC walls at the (a) ground floor and (b) ground and first floors..... 201

Fig. 8.41 Loading test ("funeral cycles"). HYMOD Models with different retrofitting configurations. Total base shear-horizontal displacement of the top floor. 202

Fig. 8.42 One-Storey infill RC walls model. Von Mises stain contour for displacement increment 750 (δ_H = -110 mm). 204

Fig. 8.43 Two-Storey infill RC walls model. Von Mises stain contour for displacement increment 750 (δ_H = -100mm). 205

Fig. 8.44 Views of the eigenmodes of the four-storey building with different retrofitting configurations..... 207

Fig. 8.45 3D views of the 3rd eigenmode of the models with (a) a bare frame, (b) one-storey infill RC walls, (c) two-storey infill RC walls and (d) fully retrofitted frame. Embedded rebar elements deformed views..... 208

Chapter 9. Nonlinear static cyclic and dynamic analysis of RC structures considering damage factors

Fig. 9.1 Schematic representation of the values of the damage factor D_c as a function of the parameter a and f_{CC}. 216

Fig. 9.2 Flow chart of the proposed algorithm of the concrete material model..... 218

Fig. 9.3 Flow chart of the proposed algorithm for updating the stress-strain tensors and constitutive matrix for the case of an uncracked Gauss point. 219

Fig. 9.4 Flow chart of the proposed algorithm for updating the stress-strain tensors and constitutive matrix for the case of a cracked Gauss point. 220

Fig. 9.5 Menegotto-Pinto steel model that accounts for the accumulated damage due to the opening and closure of cracks. 221

Fig. 9.6 Interior frame joint. Comparison between numerical and experimental results with different values of a_n and a_s for the cases of (a) first cycle (b) second cycle, (c) third cycle and (d) forth cycle..... 223

Fig. 9.7 Geometry and reinforcement details of the beam-column joint [38]. All dimensions are in mm. 225

Fig. 9.8 Imposed displacement history of the interior frame joint. 225

Fig. 9.9 RC beam-column frame joint. (a) FE concrete mesh with imposed displacements, (b) steel reinforcement elements and applied loads. 225

Fig. 9.10 Beam-Column frame joint. Comparison between numerical and experimental results. Complete force-displacement history. 226

Fig. 9.11 RC beam-column frame joint. Comparison of experimentally and numerically obtained crack patterns..... 227

Fig. 9.12 RC beam-column frame joint. Required Newton-Raphson iteration per displacement increment..... 228

Fig. 9.13 RC Column. (a) Geometry and reinforcement details [40] (b) Hexahedral and embedded rebar meshes. 229

Fig. 9.14 Imposed displacement history at the top of the column. 229

Fig. 9.15 RC Column. Comparison between numerical and experimental results. 230

Fig. 9.16 RC Column. Required Newton-Raphson internal iteration per displacement increment..... 232

Fig. 9.17 Geometric and reinforcement details of specimens of the RC-frames. (a) L30 and (b) H30. [40] 233

Fig. 9.18 3D view of the FE mesh of 8-noded hexahedral and embedded rebar elements (a) L30 and (b) H30. 233

Fig. 9.19 Base acceleration that were subjected during the experiments [40] and the numerical analyses of specimens (a) L30 and (b) H30. Spectrum acceleration diagrams of (c) L30 and (d) H30 loading histories. 234

Fig. 9.20 L30 frame. Comparison between the numerical and experimental results of the 1st storey displacement response. 235

Fig. 9.21 L30 frame. Comparison between the numerical and experimental results of the 2nd storey displacement response. 235

Fig. 9.22 L30 frame. Comparison between the numerical and experimental results of the base shear-time history during test 1. 236

Fig. 9.23 L30 frame. Comparison between the numerical and experimental results of the base shear-time history for three different concrete damage factor formulations. 236

Fig. 9.24 H30 frame. Comparison between the numerical and experimental results of the 1st storey displacement response. 237

Fig. 9.25 H30 frame. Comparison between the numerical and experimental results of the 2nd storey displacement response. 237

Fig. 9.26 Required Newton-Raphson internal iterations per dynamic step increment of models (a) L30 and (b) H30. 238

Fig. 9.27 H30 frame. Comparison between (a) numerical and (b) experimental [40] obtained crack patterns at the end of test. 239

Fig. 9.28 H30 frame. Comparison between the numerical models that use rod and beam elements for modeling the rebars. Second storey displacement history..... 240

Fig. 9.29 H30 frame. Comparison between the numerical and experimental results of the second story displacement history of the proposed model and the modified model. 241

Fig. 9.30 3D view of the FE mesh of the L30 RC frame which consists (a) 294, (b) 318, (c) 512, (d) 576 hexahedral elements. 242

Fig. 9.31 Comparison between numerical and experimental results of the second storey's displacement response for the different mesh discretizations. 243

Fig. 9.32 W050 RC frame. Geometric details [207] and FE mesh with solid and beam finite elements. 246

Fig. 9.33 W050 RC frame. Base acceleration of the shake table. 246

Fig. 9.34 W050 RC frame. Comparison between numerical and experimental results of the displacement response..... 247

Fig. 9.35 W050 RC frame. Comparison between numerical and experimental results of the base shear response. 248

Fig. 9.36 W050 RC frame. a) Comparison between numerical and experimental base shear curve for the case of modified model and the proposed model. b) Comparison between numerical and experimental base shear curve for the case of modified model during the 15^{th} and 24^{th} seconds. 248

Fig. 9.37 W050 RC frame. Required Newton-Raphson internal iterations per dynamic step increment..... 249

Fig. 9.38 Three-storey, three-bay RC frame geometrical and reinforcement details. [208].. 250

Fig. 9.39 Three-strorey, three-bay RC frame. Acceleration history subjected during the experiment [210]. 250

Fig. 9.40 Three-strorey, three-bay RC frame. 3D view of the FE mesh of 8-noded (a) hexahedral and (b) embedded rebar elements. 251

Fig. 9.41 Three-strorey, three-bay RC frame. Comparison between the numerical and experimental results of the first storey displacement response using damping ratio equal to a) 5%, b) 7%, c) 9%. 252

Fig. 9.42 Three-strorey, three-bay RC frame. Comparison between the numerical and experimental results of base shear capacity using damping ratio equal to a) 5%, b) 7%, c) 9%. 253

Fig. 9.43 Three-strorey, three-bay RC frame. Comparison between the numerical and experimental results of base shear-fist storey drift curvesy using damping ratio equal to a) 5%, b) 7%, c) 9%. 257

Fig. 9.44 Three-strorey, three-bay RC frame. Number of internal iterations per dynamic step increment..... 257

Chapter 10. Capturing the mechanical response of RC members with pinching effects

Fig. 10.1 Schematic representation of load-deflection hysteretic loops as presented by Zeynalian et al. [211]. 261

Fig. 10.2 Load deflection curves of RC beams with (a) long shear span ration (no pinching effects), (b) with short shear span ratio (pinching effects). [215] 262

Fig. 10.3 Load displacement curves of RC joint (experimental setup –photo up and left) with (a) confined joint according to ACI 318-08 code [216], (b) Unconfined joint with no transverse reinforcement and (c) Unconfined joint and inadequate anchorage length of beam bottom bars [217]. 263

Fig. 10.4 Load displacement hysteretic curves of (a) Slender RC shear wall (b) Squat RC shear wall, taken from [219]..... 263

Fig. 10.5 Schematic representation of the stress development in steel bars in a concrete RC panel with (a) 45 steel grid orientation and (b) 0 steel grid orientation. (Mansour et al. [215])..... 264

Fig. 10.6 Cyclic bond-slip model from Eligehausen et al. [221]..... 265

Fig. 10.7 Menegotto-Pinto steel model that uses the modified formulation for parameters E´ (Eq. (9.10) for different values of the damage factor D_S. 267

Fig. 10.8 Menegotto-Pinto steel model that uses the modified formulation for parameter R´ (Eq. (10.1)) due to the opening and closure of cracks with different values of the damage factor D_R. 267

Fig. 10.9 Menegotto-Pinto steel model that uses the modified formulation for parameters E´(Eq. (9.10), R´(Eq. (10.1)) with different values of the damage factor D_R and D_S. 268

Fig. 10.10 Beam Column joints. Geometry of (a) A1 and (b) A3 specimens, and reinforcement details of the (c) beam, (d) column and (e) joint section. [38] 269

Fig. 10.11 RC beam-column frame joint. FE concrete mesh with imposed displacements for specimen a) A1 and (b) A2. Steel reinforcement mesh and applied axial loads for specimen a) A1 and (b) A2. 270

Fig. 10.12 Beam-Column frame joint. Comparison between numerical and experimental results. Complete force-displacement history for specimens A1 (up) and A3 (down). 271

Fig. 10.13 Beam-Column frame joint. Comparison between numerical results that consider for the (a) concrete damage factor and (b) concrete and steel reinforcement damage factors. 271

Fig. 10.14 Geometric and reinforcement details of Shear wall SW4 [236]. 272

Fig. 10.15 Loading history subjected to SW4 273

Fig. 10.16 Shear wall SW4. 3D views of the FE mesh of concrete and embedded steel rebar elements. 273

Fig. 10.17 Shear Wall SW4. Comparison between numerical and experimental results in terms of the force-deflection curves..... 274

Fig. 10.18 RC column U1. Comparison between numerical results considering damage factors for (a) concrete (b) considering damage factors for both concrete and steel reinforcement. 275

Fig. 10.19 Geometric and reinforcement details of the beam-column joints tested in Garcia et al. [237]. 276

Fig. 10.20 Test setup (units: mm) and instrumentation of RC joints. [237]..... 277

Fig. 10.21 Failure of JB2 specimen [237]. 277

Fig. 10.22 RC joint JB2. (Left) Hexahedral and (Right) embedded rebar finite elements.... 278

Fig. 10.23 JB2 Joint. Comparison between the numerical and experimental results. 278

Chapter 11. Conclusions and Future work

Fig. 11.1 Stress contour and deformed shape of the two RC beam models caused by posttensioning force [241]. 286

Fig. 11.2 Hymod method with soil mesh.[243] 287

Fig. 11.3 Subdomains developed by ReConAn Paarallilo 287

List of Tables

Chapter 6. Numerical Implementation for RC members under Cyclic Loading Conditions

Table 6.1 SW31.Comparison of the horizontal load of each cycle between experimental and numerical results. 119

Table 6.2 SW32.Comparison of the horizontal load of each cycle between experimental and numerical results. 119

Table 6.3 SW33.Comparison of the horizontal load of each cycle between experimental and numerical results. 119

Table 6.4 SW33.Comparison of the dissipated energy of the last two cycles between experimental and numerical results..... 120

Table 6.5 Kotsovos and Lefas Shear walls. CPU time for different tasks of the nonlinear analysis..... 125

Table 6.6 Červenka Shear Wall. Comparison of the horizontal load of each cycle between experimental and numerical results..... 127

Table 6.7 Červenka Shear Wall. Dissipated energy comparison between the experimental and numerical results. 127

Table 6.8 Shear wall W4. CPU time for different tasks of the nonlinear analysis..... 130

Table 6.9 Interior Frame Joint. Comparison of the horizontal load for each cycle (experimental and numerical results). 132

Table 6.10 Interior Frame Joint. Comparison of the dissipated energy for each cycle (experimental and numerical results). 132

Table 6.11 Interior Frame Joint. CPU time for different tasks of the nonlinear analysis..... 135

Table 6.12 Exterior Frame Joint. Comparison of the horizontal load of each cycle between experimental and numerical results..... 137

Table 6.13 Exterior Frame Joint. Comparison of the dissipated energy of each cycle between experimental and numerical results..... 138

Table 6.14 Exterior Frame Joint. CPU time for different tasks of the nonlinear analysis..... 138

Chapter 7. Hybrid Modeling approach and numerical implementation to RC structures that are submitted to Cyclic loading conditions

Table 7.1 Description of the reduction levels. (Markou and Papadrakakis [37])..... 145

Table 7.2 FE mesh details of the frame joint model..... 149

Table 7.3 Full Hexa numerical results. Comparison of the horizontal load for each cycle… 152

Table 7.4 HYMOD 1 and 2 numerical results. Comparison of the horizontal load for each cycle. 152

Table 7.5 HYMOD 3 numerical results. Comparison of the horizontal load for each cycle. 152

Table 7.6 Computational performance of the four frame joint models. 154

Table 7.7 FE mesh details of the frame joint model used for the mesh sensitivity analysis. 155

Table 7.8 Full Hexa 1 and HYMOD 1.1 numerical results. Comparison of the horizontal load for each cycle. 160

Table 7.9 Full Hexa 2 and HYMOD 1.2 numerical results. Comparison of the horizontal load for each cycle. 160

Table 7.10 One-storey frame. Material details. 161

Table 7.11 FE mesh details of the one-storey RC frame model. 163

Table 7.12 One-storey RC frame. Computational performance of the five analyses. 164

Table 7.13 FE mesh details of the 1-storey RC frame model 167

Table 7.14 Two-storey RC frame. Computational performance of the nine analyses 169

Chapter 8. Simplified HYMOD non-linear simulations of a full-scale multistory retrofitted RC structure that undergoes multiple cyclic excitations – An infill RC wall retrofitting study

Table 8.1 FE mesh details of the four-storey RC frame models. 181

Table 8.2 Material details used in the FE model. 183

Table 8.3 Computational performance of the HYMOD algorithm for the case of the 0.1g test. 187

Table 8.4 Computational performance of the algorithm for the case of the 0.25g test. 193

Table 8.5 Computational performance of the Funeral and Combo Final cycle analyses. 198

Table 8.6 Base shear comparison between the RC model with infill shear wall and without shear wall 200

Table 8.7 Dissipated energy comparison between the RC model with infill shear wall and without shear wall 200

Table 8.8 Base shear comparison between the RC model with one-storey infill shear walls vs the bare frame model 203

Table 8.9 Base shear comparison between the RC model with two-storey infill shear walls vs the bare frame model 203

Table 8.10 Base shear comparison between the RC model with one- and two-storey infill shear walls vs the bare frame model 204

Table 8.11 Computational performance of the Modal Analysis Algorithm. Computing 12 eigenmodes. 209

Chapter 9. Nonlinear Static and Dynamic Analysis of Reinforced Concrete Structures Considering Damage Factors

Table 9.1 Combinations of the values a_n and a_s that were investigated. 222

Table 9.2 Comparison of the dissipated energy between experimental results and the proposed numerical model 223

Table 9.3 Comparison of the dissipated energy between experimental results and the numerical model with $a_n = 0.5$ and $a_s = 0.5, 0.125$. 223

Table 9.4 Comparison of the dissipated energy between experimental results and the numerical model with $a_n = 0.125$ and $a_s = 0.125$. 223

Table 9.5 Comparison of the horizontal load of each cycle between experimental and numerical results of the initial model. 224

Table 9.6 Comparison of the horizontal load of each cycle between experimental and numerical results of the proposed model. 224

Table 9.7 Comparison of the dissipated energy between the experimental and numerical data. 227

Table 9.8 Comparison of the horizontal load of each cycle between experimental and numerical results of the proposed model. 227

Table 9.9 RC beam-column frame joint. CPU time for different tasks of the numerical solution. 228

Table 9.10 Comparison of the dissipated energy between experimental results and the numerical model. 230

Table 9.11 Comparison of the horizontal load of each cycle between experimental and numerical results of the proposed model. 231

Table 9.12 CPU time for different tasks of the nonlinear analysis for RC Column. 232

Table 9.13 CPU time for different tasks of the nonlinear analysis for L30 and H30. 238

Table 9.14 CPU time for the nonlinear dynamic analysis of the H30 frame by using beam and rod elements for modeling the steel reinforcement. 240

Table 9.15 Computational demand resulted through the sensitivity analysis of the L30 frame. 244

Table 9.16 Natural frequencies resulted through the sensitivity analysis of the L30 frame.. 244

Table 9.17 CPU time for different tasks of the nonlinear analysis for the W050 RC Frame. 249

Table 9.18 Three-strorey, three-bay RC frame. Comparison between the numerical and the experimental natural periods. 251

Table 9.19 Three-strorey, three-bay RC frame. Experimental results in terms of first-displacement drift and base shear capacity. 254

Table 9.20 Three-strorey, three-bay RC frame. Numerical results in terms of first-displacement drift for damping ratios 5%, 7% and 9%. 254

Table 9.21 Three-strorey, three-bay RC frame. Comparison between numerical and experimental results in terms of first-displacement drift for damping ratios 5%, 7% and 9%. 255

Table 9.22 Three-strorey, three-bay RC frame. Numerical results in terms of base shear capacity for damping ratios 5%, 7% and 9%. 255

Table 9.23 Three-strorey, three-bay RC frame. Comparison between numerical and experimental results in terms of base-shear capacity for damping ratios 5%, 7% and 9%. 256

Table 9.24 Three-strorey, three-bay RC frame. CPU time for different tasks of the nonlinear analysis. 258

Chapter 10. Modifications for capturing Shear & Flexural characteristics of RC members under Limit states of Cyclic Loading

Table 10.1 Beam-Column frame joint. Comparison of the maximum storey shear between experimental and numerical results..... 272

Table 10.2 Material properties of Shear wall SW4 272

Abbreviations

Abbreviation	Description
1D	One-Dimensional
2D	Two-Dimensional
3D	Three-Dimensional
CPU	Central Processing Unit
CFP	Compressive Force Path
DE	Discrete Element
DOF	Degree(s) Of Freedom
FE	Finite Element
FEA	Finite Element Analysis
FEM	Finite Element Method
GP	Gauss Point
Hexa8	8-noded hexahedral element
Hexa20	20-noded hexahedral element
HYMOD	HYbrid MODeling method
LFI	Local Fracture Initiation
NEAK	New Greek Seismic
NR	Newton-Raphson
OSFP	Onset of Stable Fracture Propagation
OUFP	Inset of Unstable of Fracture Propagation
RC	Reinforced Concrete
ReConAn	Reinforced Concrete Analysis
RL	Reduction Level
UTCA	Unified Total Crack Approach

Chapter 1. Introduction

1.1 General

During the last decades, many complex numerical models have been developed and proposed for the simulation of RC structures, as can be seen from the numerous contributions to conferences and scientific journals the last five decades. However, the increasing complexity of the proposed numerical material concrete models is also contributing towards the likelihood of oversights and errors, which question the objectivity of the results obtained by the numerical modeling. Additionally, the RC is a composite inhomogeneous material with a very complex nonlinear material behavior. There are many parameters such as loading conditions, construction process, geometry and reinforcement configurations that affect the behavior of RC structures. Therefore, it is very difficult to develop a constitutive model that can take into account all the crucial parameters that affect the RC structures.

Many constitutive models have been developed for the description of the complex constitutive behavior of RC structures. The state-of the-art consists many constitutive models which, are based on the plasticity theory, thermodynamic laws, fracture mechanics and their combinations of them. These sophisticated models can be the basis of design of complex structures where the design codes and analytical methods cannot be used. However, most of these models in the literature show lack of consistency in results between various structural forms. Therefore, there are models which can simulate specific structures with specific mechanical characteristics but cannot be extended to different structural members with different mechanical behavior. This lack of objectivity of the methods is caused mainly by the unrealistic material description and the various numerical instabilities that occur when the cracking phenomenon initiates.

The above constitutive modeling approaches describe the non-linear behavior of concrete by introducing material parameters that model the post-peak material characteristics such as strain softening, tension stiffening and shear retention abilities. These approaches are developed in order to model particular structural problems. Thus, there are models that can capture the mechanical behavior of columns, beams, shear walls or frames with particular characteristics. Each modeling approach depends on the values of certain material and numerical parameters in order to capture different structural member's behavior. Therefore, these models introduce a large number of parameters that require to be defined prior to the analysis, thus constitute the use of these models numerically complicated. Furthermore, in many cases these material properties are modified as such to reproduce the experimental data especially when dealing with different types of RC structural members such as beams, columns, joints and walls. These material property assumptions indicates the necessity of a 3D constitutive law without adding parameters, that are not associated with the physical behavior of concrete at a material level.

The objective and efficient simulation of concrete is a very difficult subject because of its complex mechanical behavior characteristics. RC is an inhomogeneous material with a very complex nonlinear behavior mainly caused by cracking and other nonlinear phenomena. This is also attributed to the fact that the concrete material parameters like modulus of elasticity, compressive strength and Poisson's ratio show a large scatter in comparison with other construction materials.

There are many FEM softwares like SAP2000, Abaqus, LS-DYNA, TNO DIANA, ANSYS, ATENA, ADINA, GT STRUDL, FEMAP with NXNastran, STAAD Pro, SEISMOSTRUCT, etc., that incorporate material models that require different material parameters that relate to the nonlinear constitutive behavior of concrete. It is evident that there isn't a reliable constitutive model which can be applicable to every RC member.

The mechanisms that are activated in order to transfer the applied load to the supports during the ultimate limit state loading conditions of RC structures are described by the use of truss or strut-and-tie methods and used for the development of concrete design (EC2 2004 [1]) as illustrated in Fig. 1.1 for an RC beam. It must be noted herein that, this is an oversimplification when compared with the 3D behavior of a real RC beam.

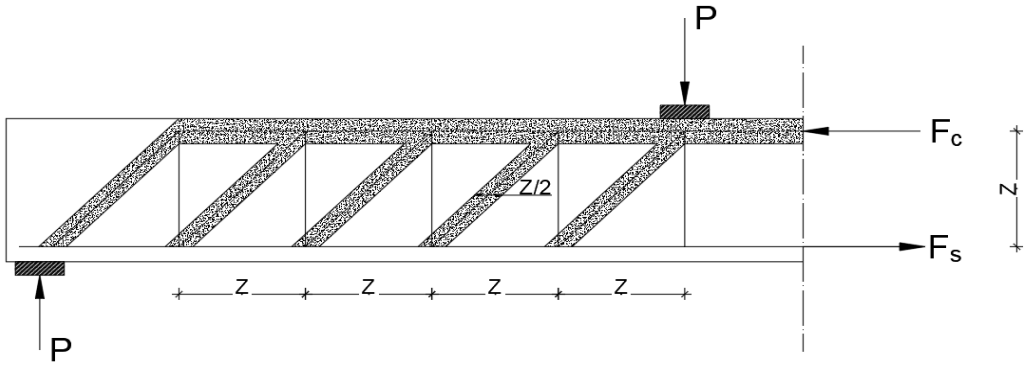

Fig. 1.1 Truss model of an RC beam.

Many mechanisms derived of this concept imply the development of post-peak characteristics of concrete. The development of inclined struts implies the development of frictional forces resisting the shearing movement of the crack faces. Furthermore, the above procedure neglects the development of transverse strains orthogonal to the axial compression. The failure of the longitudinal strut occurs when the compressive strain concrete reaches the value of ε_c=0.0035 (EC2 2004 [1]) corresponding to a post-peak stress of the order of $0.85f_c$ (where f_c is the cylindrical uniaxial compressive strength of concrete). However visible cracking appears when compressive strain reaches the value of 0.002. Therefore, the above failure criterion implies the existence of significant stiffness and strength of cracked concrete of the longitudinal strut.

Experimental evidence shows that the failure of an RC beam member (designed according to EC2 2004 [1]) is mainly brittle and it occurs before the flexure capacity has been exhausted due to severe inclined cracks within its shear span. Similarly, there are many cases when RC columns suffer from severe damage despite their earthquake resistance design as illustrated in Fig. 1.2a. Many RC columns suffered from severe inclined cracking which unexpectedly occurred at mid-height, rather than at the columns end regions as stated by the limit-state design philosophy [1]. Additionally, the beam-column joints are modelled in order to withstand the forces transferred by the adjacent beam and column members. However, many RC joints suffered from severe cracking at early load stages as shown in Fig. 1.2b, violating the assumption of the “rigid joint” behavior.

The heterogeneous nature of concrete leads to the development of out of plane actions, which cannot be ignored during monotonic or cyclic analysis. Small transverse stresses lead to significant changes in the carrying capacity of concrete specimens. Thus, the assumption of plane-stress conditions is unrealistic even in cases when in-plane loading is applied. This demonstrates the necessity of the triaxial description of the behavior of concrete which also explains the brittle failure mechanisms that dominate the RC members. A constitutive modeling method has to be based on the above experimental characteristics in order to provide realistic predictions of the behavior of a wide range of structural structures without modifications of the material parameters.

(a) (b)

Fig. 1.2 (a) Bridge collapse after the Kobe earthquake in Japan 1995, (b) Failure of beam column exterior joint joints (Sezen et al. 2000 [2]*).*

Taking the above into account, a suitable numerical model has to be developed in order to accurately describe the constitutive modeling of concrete based on realistic theoretical context. Another important issue is the integration of the developed constitutive model into a suitable type of finite element. The inappropriate choice of finite elements has major consequences in the stability and the accuracy of the numerical problem. For example the Bernoulli hypothesis usually used for beam finite elements, does not realistically describe the strain distribution of the cross-sections of cracked concrete members, hence it is hindered with a limited accuracy

Generally, beam theory formulations are not indicated for capturing the 3D behavior of concrete which is characterized by 3D shear strains, cracking, with significant effects on the out-of-plane stresses that can lead to increase (confinement) or decrease of the strength capacity of the structural member. Therefore, a detailed simulation is proposed herein that uses 3D solid elements are used for capturing the nonlinear behavior of concrete. To be able to adopt this modeling approach, a computationally efficient technique has to be implemented in order to study any RC structures without size limitations applied on the models.

The proposed model in this research work presents a numerical procedure which is based on the brittle nature of the material of concrete where, the model prevents the excessive concentrations of stresses in the cracked areas, which may lead to numerical instabilities. The combination of this numerical approach with the smeared crack method that treats cracking by redistributing the cracked stresses to the uncracked areas makes the modeling methodology numerically more stable. Additionally, the use of an innovative crack closing criterion which is crucial in cyclic loading conditions provides stability during the nonlinear analysis even when the loading is close to load carrying-capacity of the structure. Furthermore, the use of the natural beam-column flexibility based element was found to increase the numerical stability of the nonlinear iterative procedure due to its advanced formulation features. Finally, the ability to capture the 3D cyclic behavior of RC members with a small number of hexahedral elements keeps the computational demand low, a crucial factor when dealing with large-scale models. Furthermore, in order to extend the proposed method for modeling large-scale structures, the developed technology was combined with the HYMOD approach. Several structural members (RC joints and frames) were analyzed by using the HYMOD in order to investigate the corresponding level of reduction applied without decreasing the level of numerical efficiency.

Furthermore, though this work, the numerical abilities and limitations of the proposed numerical modeling method are investigated. The developed modeling method was also used to study the mechanical behavior of different specimens that use various retrofitting methods. A numerical study of different infill RC wall retrofitting configurations is also presented in detail.

Finally, the method is complemented in a manner to improve the stability and efficiency of numerical analysis when many loading cycles are applied and when the numerical model is subjected to dynamic limit state loading conditions. The introduction of two new material damage factors that are directly connected to the opening-closing procedure was also tested and found to be able to describe accurately the mechanical behavior of RC members that is characterized by strength and stiffness degradation and manage to capture the pinching effect.

1.2 Objectives of the Thesis

The cyclic analysis of RC structural members is characterized by heavy nonlinearities which is mainly caused by the cracking of the concrete material. The complex static cyclic and dynamic behavior of concrete makes the numerical procedure even more difficult to converge, thus provide with accurate results. The constitutive models that are proposed in the literature, try to describe the mechanical characteristics of RC structural members through idealized constitutive laws based on the plasticity theory, thermodynamic laws and fracture mechanics. The lack of their objectivity derives from the need of introducing many new material parameters and energy functions in order to capture the experimental behavior of concrete like all models they sometimes manage to capture the mechanical behavior of concrete and some others they fail to do so. Many of these parameters derived from the thermodynamic framework, therefore, do not have physical interpretations and their value changes significantly when different mechanical behaviors of RC structures are numerically examined. In addition, these models present many numerical instabilities that make it difficult to be used for static cyclic or dynamic analysis, where they are unable to model full scale RC structures.

Another weakness of the currently available models found in the literature, is the use of uniaxial constitutive relations. This explains the use of parameters that introduce triaxial characteristics, such as plasticity, effect of confinement, triaxial crushing and interaction between compressive and tensile stresses in the concrete members. Therefore, the constitutive model of concrete can be constructed based on the triaxial behavior of concrete, and its brittle nature.

Therefore, the main objectives of the current work are summarized as follows:

- Develop a constitutive model which can describe the triaxial behavior of concrete without adding new material parameters with no physical interpretation.
- The model has to be successfully incorporated in a 3D detailed FEM model.
- Propose a new algorithm that will be able to account for the concrete material deterioration in a realistic manner.
- Develop a robust and efficient solution algorithm for static cyclic and dynamic analysis.
- Validate the proposed model with experimental results.
- Apply the developed numerical model in simulating full-scale RC structures.
- Develop an algorithmic implementation for the modal analysis of HYMOD models.

- Use the obtained numerical results for the study and assessment of the overall mechanical behavior of RC structures.
- Develop recommendations on the retrofitting of RC buildings.

1.3 Layout of the Thesis

This Thesis consists of 11 chapters including the introduction **chapter 1**.

In **chapter 2**, the characteristics of the formulation of the NBCFB element that is used for modeling the steel reinforcement are presented.

In **chapter 3**, the type of finite elements for concrete and steel elements are shown. Additionally, the kinematic relations that describe their interaction is discussed. Furthermore, the procedure of the mesh generation for the case of allocation the embedded rebar elements inside hexahedral concrete elements is also found in this chapter. Finally the nonlinear solution techniques that are used for the nonlinear dynamic and modal analysis are presented.

In **chapter 4**, the basic characteristics of the uniaxial, biaxial and triaxial concrete behavior are discussed. The basic constitutive modeling theories that are used for the representation of concrete behavior are presented. Additionally some numerical instabilities concerning the modeling of cracking and post-cracking characteristics are discussed.

In **chapter 5**, the proposed constitutive modeling of RC structures is presented. It starts with an exhaustive literature review about the other constitutive models that have been proposed and their limitations, whereas, the proposed algorithmic procedure that was developed during this research work, is covered in detail.

In **chapter 6**, several numerical implementations of the proposed modeling method are presented. The numerical results are compared with experimental data and their comparison is discussed in detail in terms of computational efficiency and numerical accuracy. Furthermore, mesh sensitivity analyses are performed and the stress locking effects are investigated thoroughly.

In **chapter 7**, the HYMOD approach is presented. The numerical technique is combined with the proposed material models in order to model RC structure. Several numerical implementations and reduction levels are investigated in this chapter. Finally, mesh sensitivity analyses demonstrates the computational efficiency and numerical accuracy of the HYMOD approach.

In **chapter 8**, a complete numerical investigation of a full-scale nonlinear cyclic modeling of the 4-storey RC building was performed by using the proposed modeling approach. Furthermore, a numerical investigation of different retrofitting configurations is performed. Finally, a modal analysis algorithm was performed in order to further study the mechanical behavior of the HYMOD meshes.

In **chapter 9**, the new concrete and steel damage factors are presented. The proposed damage factors are used for the analysis of RC structures under static cyclic and dynamic loading conditions. The numerical accuracy of the proposed model has been demonstrated by comparing the numerical results with the corresponding experimental data. A numerical investigation concerning the proposed damage factors, the crack closing criterion and the type of embedded rebar elements is discussed. Finally, a mesh sensitivity analysis is performed and the corresponding numerical results are shown herein.

In **chapter 10**, the phenomena of pinching, strength and stiffness degradation of RC members under cyclic loading are discussed, where a literature review on experimental and numerical

information is provided. Numerical implementations are performed and their numerical results are compared with the experimental data. Modifications of the proposed damage factors are investigated in order to capture extreme damage characteristics of RC retrofitted members under cyclic loading conditions. Two numerical models are preformed and compared with their corresponding experimental results.

In **chapter 11**, the conclusions derived from this research work are presented and the proposed future research work is discussed.

Chapter 2. The natural beam-column flexibility-based elements

Contents of Chapter 2

2.1 Problems related to the numerical analysis of concrete structures 9
2.2 Natural mode approach 10
2.3 Natural modes for different finite elements 12
2.4 Beam-column elements for modeling RC structures 13
2.4.1 Lumped models 14
2.4.2 Distributed models 15
2.4.3 Displacement- and force-based elements 16
2.4.4 Beam-column model formulation incorporated in this work 19

2.1 Problems related to the numerical analysis of concrete structures

Over the last few decades, the design and analysis of any RC structure, can be completed with the help of relevant computer software. As it can be seen from the various publications, many numerical models have been developed in order to simulate the mechanical behavior of simple and complex in geometry RC structures. The accuracy of each numerical model depended on the numerical modeling techniques that are used for the discretization of the geometry of the structure and the proper constitutive modeling approach that accompanies the numerical model.

The problem in accurately simulating the behavior of RC structures is explained by the fact that there are various characteristics of the structure which significantly affect their response such as [44]:

- The material of concrete is an inhomogeneous material with complex nonlinear behavior which makes it difficult to predict the experimental behavior of different concrete members. The stiffness and strength degradation due to cracking are the most significant aspects of the nonlinear behavior, therefore, they have to be taken into account in order to accurately capture the hysteretic behavior of structures.
- The basic material parameters such as, the modulus of elasticity E_c, the concrete compressive strength f_c and the Poisson's ratio v show a large scatter in the case of concrete members. The exact construction conditions such as workmanship, weather conditions and curing affect significantly the values of these material parameters.
- The material of concrete is usually used for large scale structures where the simple assumptions of Bernoulli hypothesis of a linear strain distribution over the depth of the cross-section cannot be applied. Therefore, the standard beam and plate elements cannot be used for the simulation of concrete structures without expecting any lose in terms of accuracy.
- There are members of concrete structures such as slabs and shear walls (plane shell structures) and deep beams that present excessive cracking and nonlinear hysteretic behavior thus a design based on an elastic material behavior is not appropriate.
- The actual steel reinforcement configuration plays a very significant role for the behavior of the structure and not just for the calculation of the forces and the amount of reinforcement. Therefore, the modeling of actual steel bars with their actual location is very important for obtaining an accurate capacity prediction.
- There are many concrete members with arbitrary shapes and cross-sections.
- It is very important to take into account the construction process and the time-dependent behavior of concrete.

Considering the above characteristics, a proper FEM design of concrete structure is a very difficult and crucial matter in the field of Civil Engineering. However, a complex FE approach does not always lead to more realistic results. The results of every numerical model can only be as accurate as its underlying assumptions. Furthermore, every numerical model can always assume that there is a considerable variation in the actual boundary conditions and in the properties of the materials.

In this work, the NBCFB finite element is used so as to model beam and columns in an attempt to maximize the numerical accuracy of the adopted models. This element is also used for the modeling of embedded rebars within the concrete domain. The numerical superiority of this FE was demonstrated in [4] thus adopted herein.

2.2 Natural mode approach

The analysis of structures which present large displacements, strains and inelastic behavior led to the basic concepts of geometrical stiffness and the idea of natural modes. The natural modes are invariant fields that describe the elemental kinematics as a combination of rigid body and pure straining deformations. This approach was initiated by Argyris and Scarpf [5,6] who produced the technique of creating finite elements based on rigid body and deformation modes. This technique is used for the truss, beam, plate, shell triangular elements and tetrahedron elements in order to model large scale structures with geometrical nonlinearities. The most common elements that use natural modes, are beams and shells (Argyris and Tenek [7,8]), which are usually combined with the fiber approach in order to capture accurately the nonlinear behavior of composite structures.

In the natural mode method the deformation $\boldsymbol{u}(x,y,z)$ at any point in a finite element can be expressed as a linear combination of the nodal Cartesian displacements $\boldsymbol{r_e}$ through the following expression:

$$\underset{(3x1)}{\boldsymbol{u}(x,y,z)} = \underset{(3xn)}{\boldsymbol{C}(x,y,z)} \cdot \underset{(nx1)}{\boldsymbol{r_e}} \tag{2.1}$$

Where n represents the nodal dofs. Additionally, a finite element can deform in n different modes, therefore, the total deformation of the element can be expressed as a linear combination of the imposed n modes such as:

$$\boldsymbol{u} = \boldsymbol{u}_1 + \boldsymbol{u}_2 + \ldots + \boldsymbol{u}_n \tag{2.2}$$

If $\boldsymbol{\rho}$ is the vector containing the natural modes, Eq. (2.2) can be written as follows:

$$\boldsymbol{u} = \begin{bmatrix} \omega_u^1 & \omega_u^2 & \ldots & \omega_u^n \\ \omega_v^1 & \omega_v^2 & \ldots & \omega_v^n \\ \omega_w^1 & \omega_w^2 & \ldots & \omega_w^n \end{bmatrix} \cdot \begin{bmatrix} \rho_1 \\ \rho_2 \\ \ldots \\ \rho_n \end{bmatrix} = \underset{(3xn)}{\boldsymbol{\omega}} \times \underset{(nx1)}{\boldsymbol{\rho}} \tag{2.3}$$

Additionally the natural displacements $\boldsymbol{\rho}$ are linked to the nodal Cartesian displacements $\boldsymbol{r}$ through the following equation:

$$\underset{(nx1)}{\boldsymbol{r}} = \underset{(nxn)}{\boldsymbol{A}} \cdot \underset{(nx1)}{\boldsymbol{\rho}} \Rightarrow \boldsymbol{\rho} = \boldsymbol{A}^{-1} \cdot \boldsymbol{r} = \boldsymbol{a} \cdot \boldsymbol{r} \tag{2.4}$$

Therefore, by combining Eq. (2.3) and Eq. (2.4),

$$\boldsymbol{u} = \underset{(3xn)}{\boldsymbol{\omega}} \cdot \underset{(nx1)}{\boldsymbol{\rho}} = \underset{(3xn)}{\boldsymbol{\omega}} \cdot \underset{(nx1)}{\boldsymbol{a}} \cdot \underset{(nx1)}{\boldsymbol{r_e}} \tag{2.5}$$

Therefore, Eq. (2.1) takes the following form:

$$\boldsymbol{C} = \boldsymbol{\omega} \cdot \boldsymbol{a} \tag{2.6}$$

In regards to the elemental natural modes, it is convenient to express the elemental matrices in a natural coordinate system, which is formed by the elemental geometry. For instance, the natural coordinate of a truss or a beam element is simply a single direction a spanning the truss or beam axis. The use of a natural coordinate system helps the assignment of invariant

deformation measures, the natural nodes and the description of kinematical field of the finite element.

Furthermore, the natural modes $\boldsymbol{\rho}$ will always have two parts, the natural rigid body modes $\boldsymbol{\rho_0}$ and the natural straining modes $\boldsymbol{\rho_N}$, which describe the pure straining deformation. The main characteristic of the rigid body modes, is that they are not allowed to produce strain energy. In order to ensure this, the rigid modes are always separated from the straining modes, thus only the straining modes are used for the formation of the elastic stiffness matrix. Therefore, a nodal displacement vector $\boldsymbol{\rho'}$ which contains the rigid body $\boldsymbol{\rho_0}$ and the natural straining modes $\boldsymbol{\rho_N}$ components, must have a unique and reversible relation to a Cartesian vector $\boldsymbol{\rho}$ such as:

$$\boldsymbol{\rho}' = \begin{bmatrix} \boldsymbol{\rho}_0 \\ \boldsymbol{\rho}_{\mathrm{N}} \end{bmatrix} = \begin{bmatrix} \boldsymbol{a}_0 \\ \boldsymbol{a}_N \end{bmatrix} \cdot \boldsymbol{\rho} = \boldsymbol{a} \cdot \boldsymbol{\rho} \Rightarrow \boldsymbol{\rho}_0 = \boldsymbol{\alpha}_0 \cdot \boldsymbol{\rho}, \boldsymbol{\rho}_{\mathrm{N}} = \boldsymbol{\alpha}_{\mathrm{N}} \cdot \boldsymbol{\rho} \tag{2.7}$$

and

$$\boldsymbol{\rho} = \boldsymbol{\alpha}^{-1} \cdot \boldsymbol{\rho}' = \begin{bmatrix} \boldsymbol{A_0} & \boldsymbol{A_N} \end{bmatrix} \cdot \begin{bmatrix} \boldsymbol{\rho}_0 \\ \boldsymbol{\rho}_{\mathrm{N}} \end{bmatrix} = \boldsymbol{A} \cdot \boldsymbol{\rho}' \Rightarrow \boldsymbol{A} = \boldsymbol{\alpha}^{-1} \tag{2.8}$$

Similarly, there are corresponding load vectors $\boldsymbol{P}$, which contains natural rigid body $\boldsymbol{P_0}$ and straining generalized forces $\boldsymbol{P_N}$ so that the external work can always be obtained as a scalar product of the displacements and loads. Therefore, according to the invariance of virtual work in Cartesian and natural coordinate systems, the following equations are derived:

$$\begin{aligned} &\boldsymbol{P}^t \cdot \delta\boldsymbol{\rho} = \boldsymbol{P}'^t \cdot \delta\boldsymbol{\rho}' = \boldsymbol{P}'^t \cdot \boldsymbol{\alpha} \cdot \delta\boldsymbol{\rho} \\ &\Rightarrow \boldsymbol{P} = \boldsymbol{a}^t \cdot \boldsymbol{P}' = \boldsymbol{a}_0^t \cdot \boldsymbol{P}_0 + \boldsymbol{a}_N^t \boldsymbol{P}_N \end{aligned} \tag{2.9}$$

$$\Rightarrow \boldsymbol{P}' = \begin{bmatrix} \boldsymbol{P}_0 \\ \boldsymbol{P}_N \end{bmatrix} = \boldsymbol{A}^t \cdot \boldsymbol{P} = \begin{bmatrix} \boldsymbol{A}_0^t \\ \boldsymbol{A}_N^t \end{bmatrix} \cdot \boldsymbol{P}_t \tag{2.10}$$

From Eq. (2.10), the following expressions are derived:

$$\begin{aligned} &\boldsymbol{\rho}_N = \boldsymbol{a}_N \cdot \boldsymbol{\rho} \,,\, \boldsymbol{P}_0 = \boldsymbol{A}_0^t \cdot \boldsymbol{P} \\ &\boldsymbol{P}_N = \boldsymbol{A}_N^t \cdot \boldsymbol{P} \,,\; \boldsymbol{P} = \boldsymbol{a}_N^t \cdot \boldsymbol{P}_N \,,\; \boldsymbol{P}' = \boldsymbol{A}_N^t \cdot \boldsymbol{P} \end{aligned} \tag{2.11}$$

Thus, the connection between the natural and Cartesian displacements, and the connection between the natural and Cartesian load vectors, is accomplished by using the matrices $\boldsymbol{a}$ and $\boldsymbol{A}$. These matrices are usually functions of geometry of the element. By ignoring the presence of initial strains, the elastic strain vector $\boldsymbol{\varepsilon}$ takes the following form:

$$\boldsymbol{\varepsilon} = \boldsymbol{\alpha}_{\mathrm{N}} \cdot \boldsymbol{\rho}_{\mathrm{N}} \tag{2.12}$$

Where $\boldsymbol{\rho_N}$, is the vector of natural modes and $\boldsymbol{a_N}$ is a strain operator matrix. The principle of virtual work has the following expression:

$$\begin{aligned} &\delta\boldsymbol{U} = \delta\boldsymbol{W} \\ &\int_V \boldsymbol{\sigma}^t \cdot \delta\boldsymbol{\varepsilon} \cdot \boldsymbol{dV} = \int_S \boldsymbol{p}_S^t \cdot \delta\boldsymbol{u} \cdot \boldsymbol{dS} + \int_V \boldsymbol{p}_V^t \cdot \delta\boldsymbol{u} \cdot \boldsymbol{dV} + \boldsymbol{R}^t \cdot \delta\boldsymbol{u} + \boldsymbol{M}^t \cdot \delta\boldsymbol{\theta} \end{aligned} \tag{2.13}$$

Where $\boldsymbol{p_V}$ and $\boldsymbol{p_S}$ are the body forces and surface tractions, $\boldsymbol{R}$ is the concentrated forces vector and $\boldsymbol{M}$ the concentrated moments vector, $\delta\boldsymbol{u}$ and $\delta\boldsymbol{\theta}$ represent the virtual displacements and rotations, respectively. By inserting Eq. (2.12), the first integral of Eq. (2.13) takes the form:

$$\int_V \boldsymbol{\sigma}^t \cdot \delta\boldsymbol{\varepsilon} \cdot \boldsymbol{dV} = \int_V \boldsymbol{\varepsilon}^t \cdot \boldsymbol{\kappa} \cdot \delta\boldsymbol{\varepsilon} \cdot \boldsymbol{dV} = \boldsymbol{P''^t} \delta\boldsymbol{\rho}^t \tag{2.14}$$

Similarly, by inserting the Eq. (2.12), the above expression takes the following form:

$$\delta\boldsymbol{\rho}_N^t \cdot \left[\int_V \boldsymbol{\sigma}^t \cdot \boldsymbol{a}_N \cdot \boldsymbol{dV} \right] = \delta\boldsymbol{\rho}_N^t \cdot \left[\int_V \boldsymbol{a}_N^t \cdot \boldsymbol{\kappa} \cdot \boldsymbol{a}_N \cdot \boldsymbol{dV} \right] \cdot \rho_{\mathrm{N}} = \boldsymbol{P}_0^t \cdot \delta\boldsymbol{\rho}_0 + \boldsymbol{P}_{\mathrm{N}}^t \cdot \delta\boldsymbol{\rho}_{\mathrm{N}} \tag{2.15}$$

From the Eq. (2.15), it is found that:

$$\boldsymbol{P}_0 = 0 \tag{2.16}$$

$$\left[\int_V \boldsymbol{a}_N^t \cdot \boldsymbol{\kappa} \cdot \boldsymbol{a}_N \cdot \boldsymbol{dV} \right] \cdot \rho_{\mathrm{N}} = \int_V \boldsymbol{\sigma}^t \cdot \boldsymbol{a}_N \cdot \boldsymbol{dV} \Rightarrow \boldsymbol{k}_N \cdot \rho_{\mathrm{N}} = \boldsymbol{P}_N \tag{2.17}$$

Eq. (2.16) states that the rigid body forces acting on an element must be equal to zero. The elemental stiffness $\boldsymbol{k_N}$ can be expressed as:

$$\boldsymbol{k}_N = \int_V \boldsymbol{a}_N^t \cdot \boldsymbol{\kappa} \cdot \boldsymbol{a}_N \cdot \boldsymbol{dV} \tag{2.18}$$

and the resultant natural loads are expressed as:

$$\boldsymbol{P}_N = \int_V \left[\boldsymbol{a}_N^t \cdot \boldsymbol{\sigma} \right] \cdot \boldsymbol{dV} \tag{2.19}$$

where,

$$\boldsymbol{P}_0 = 0$$

$$\boldsymbol{k}_N \boldsymbol{\rho}_{\mathrm{N}} = \boldsymbol{P}_N \tag{2.20}$$

By using the appropriate transformation matrices, the natural stiffness matrix $\boldsymbol{k_N}$ can be transformed to the local elemental and ultimately to the global Cartesian coordinates.

2.3 Natural modes for different finite elements

The natural modes are always equal in number to the difference between the global dofs and the rigid body modes. Furthermore, the natural modes must satisfy all kinematic compatibility conditions at boundaries. The natural modes of the NBCFB finite element are presented bellow as described in Tenek and Argyris [49].

The beam element has 2 nodes and 6 Cartesian freedoms (u, v, w, θ, φ, ψ) at each node. If the local Cartesian coordinates are denoted as x′y′z′, with the axis x′ directed along the element, the beam can have 5 rigid modes. These modes contain three rigid body translations in x′, y′, z′ and three rigid body rotations with respect to x′, y′ and z′ axes, respectively. Therefore the natural mode number is equal to 6 while there are 12 global dofs and 6 rigid body modes (Fig.

2.1). Thus six strain modes have to be selected in order to describe the deformation of the beam element. The natural stiffness matrix is obviously of order (6x6).

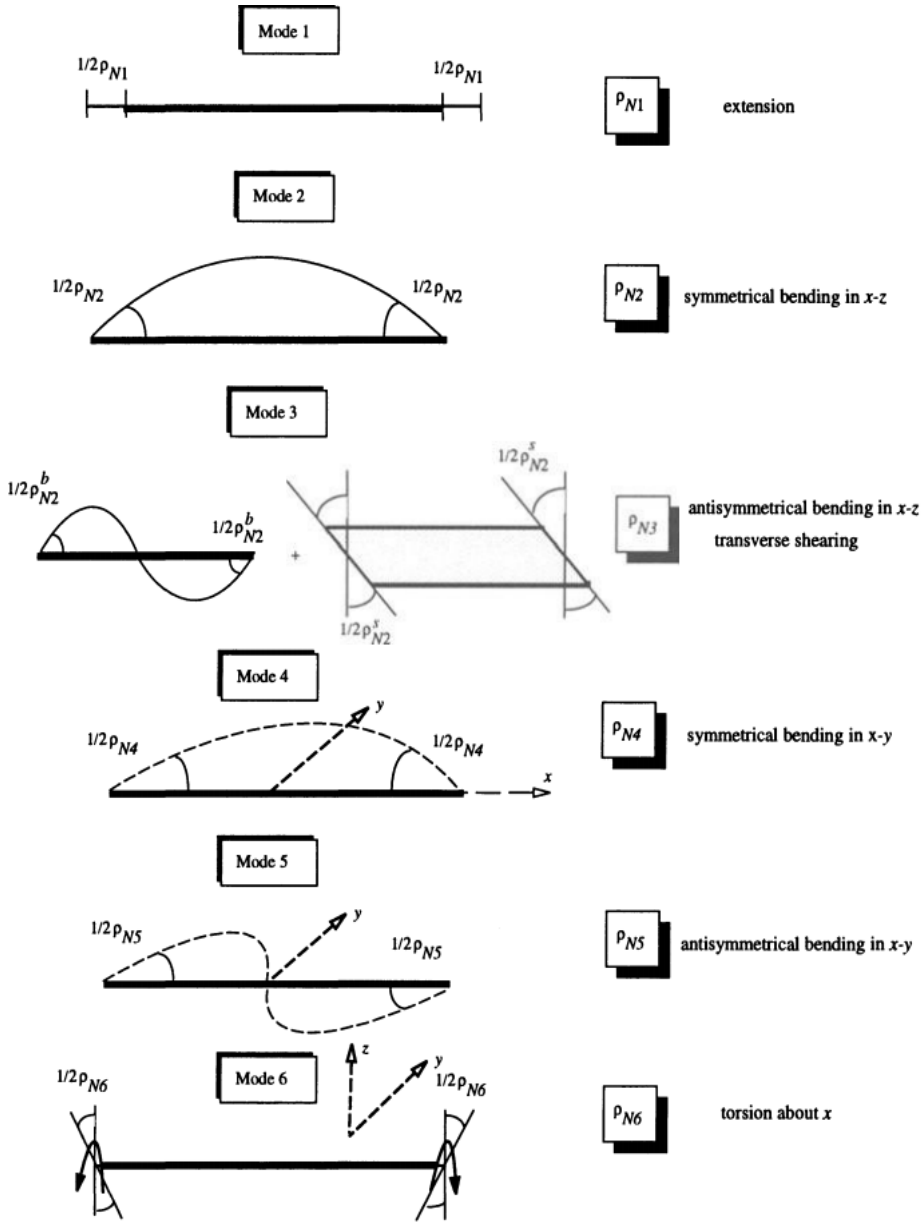

Fig. 2.1 Strain modes for a beam finite element. [49]

2.4 Beam-column elements for modeling RC structures

More than half a century, the nonlinear analysis of RC structures is performed by using beam-column finite elements. The beam-column elements introduce the material nonlinearity usually through plasticity theory. The formulation of the 1D models are based on two theories:

I. Euler-Bernoulli beam theory in which the plane sections remain plane and normal to the longitudinal axis of the beam as shown Fig. 2.2(a). Therefore, there are no shear deformations.
II. Timoshenko beam theory in which the plane sections remain plane but not normal to the longitudinal axis as shown Fig. 2.2(b). In this case, the rotation difference between the normal axis and the plane section represents the shear deformation.

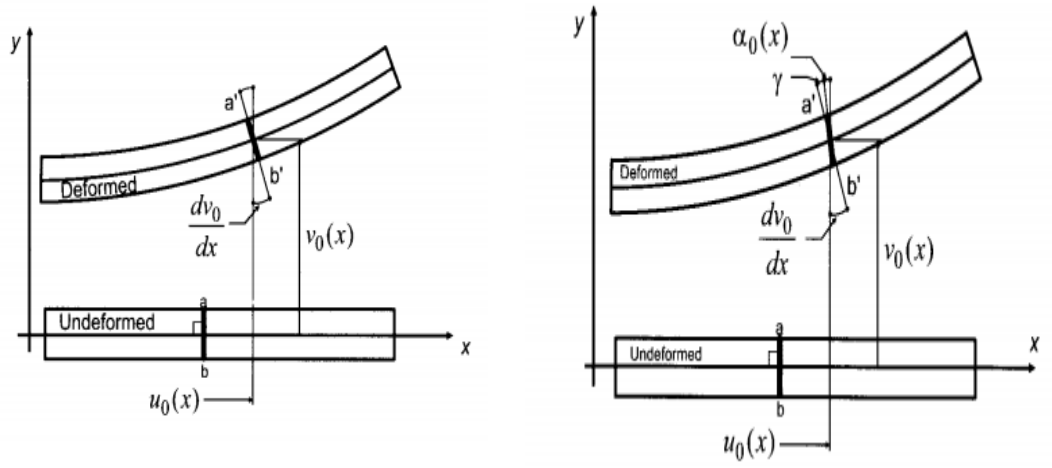

(a) (b)

Fig. 2.2 Beam element: (a) Euler Bernoulli beam theory, (b) Timoshenko beam theory. [50]

The beam-column finite elements, can be divided in two categories: the lumped models and the distributed models. These two models are presented in the following sections.

2.4.1 Lumped models

It is assumed that the inelastic behavior of concrete is concentrated in certain sections, usually the ends of girders and columns for seismic loads, and at the midspan for distributed static loads. The critical sections are modelled with nonlinear zero-length springs connected by linear elastic elements. These critical sections are forming the so called plastic hinges. These models consist of several springs, which are connected either in series or in parallel. Clough and Johnston [51], proposed a parallel component element which allowed for a bilinear moment-rotation relationship. The element consists of two parallel elements, one elastic-perfectly plastic to represent yielding and the other perfectly elastic to represent strain-hardening as illustrated in Fig. 2.3(a). Additionally, Takizawa [52] generalized the previous model by implementing multi-linear monotonic laws simulating the effect of cracking in reinforced concrete members. Furthermore, Filippou and Issa [53] used many different sub-elements to describe the inelastic behavior of concrete. Each sub-element present a different inelastic behavior such as: bending behavior, shear behavior at the interface or bond-slip behavior at the beam-column joint.

Furthermore, the series models were introduced by Giberson (1967) [54] which consist linear elastic elements with one equivalent nonlinear rotational spring located to each end. The inelastic behavior of the model depends on the selection of the appropriate moment-rotation relationship for the springs at the ends of the beam as illustrated in Fig. 2.3(b). Many phenomenological relationships have been also used for the springs in this modeling approach.

The distributed models simplify the different aspects of the inelastic behavior of reinforced concrete and due to this numerical assumption they are limited in their applicability. The parameters of the springs cause many limitations to these models, that are affected by loading patterns and the level of inelastic deformation. The problem is enhanced in this case when the axial loading of the beam members doesn't have a constant value.

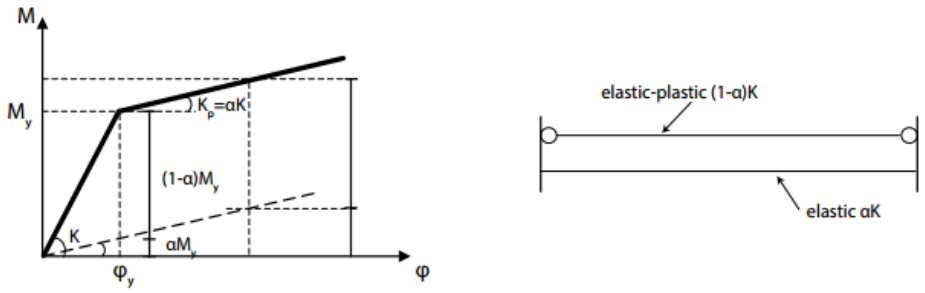

(a)

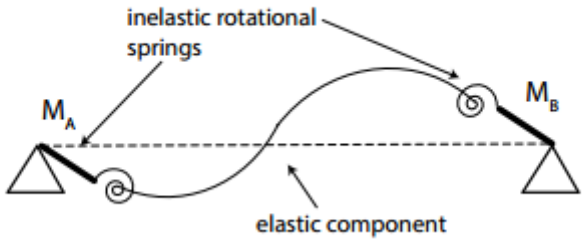

(b)

Fig. 2.3 Lumped models (a) Clough and Johnston [51], *(b) Giberson* [54]

2.4.2 Distributed models

These models distribute the material nonlinearity at any element section and the element behavior is derived by a weight integration at the section response level. Each cross-section describes the hysteretic behavior of the material according to the plasticity theory in terms of stress-strains resultants or it is derived through the fiber approach. The fiber approach assumes that each cross-section is divided into layers along both directions forming the fibers, as illustrated in Fig. 2.4. Therefore, according to the axial strain of each fiber, the uniaxial stress and tangent Young modulus are calculated from the uniaxial constitutive law of the materials of concrete and steel. Then the fiber stresses and moduli are summed up over the cross-section, where the forces and the stiffness of the cross section are calculated. Finally, the nodal internal forces and the elemental tangent stiffness matrix are computed. Given that this approach (Fig. 2.4) has the ability to capture the plastification along the height and width of the section, is adopted in this work.

There are many nonlinear distributed models that are proposed for the analysis of RC structures use the classical displacement based finite element method. The displacement-based models lead to an approximate equilibrium in the state of the element level during the nonlinear analysis (the elemental forces depend on the integral on each sectional forces located along the element). Therefore, in the cases of inelastic behavior, the members (beam and columns) have to be subdivided into multiple elements in order to obtain accurate results increasing the computational cost. Therefore, an alternative formulation has been developed to address this issue which is known as the force-based beam formulation and it is also adopted in this research work.

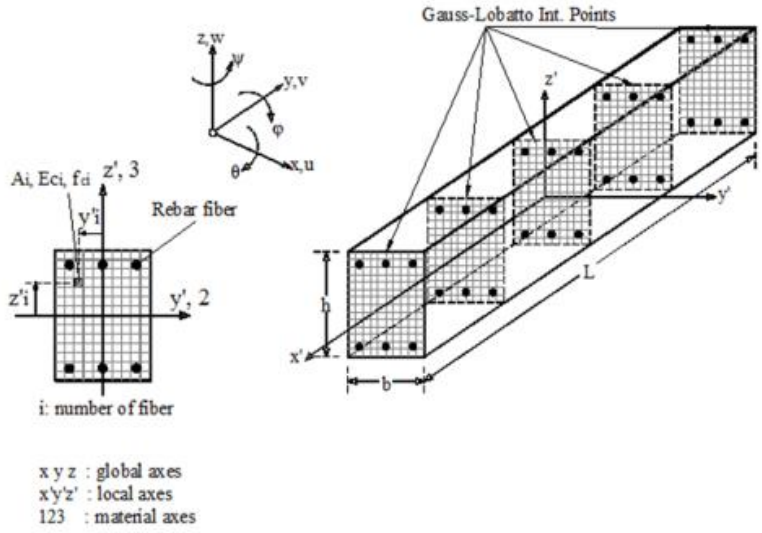

Fig. 2.4 Distributed fiber beam model. [49]

2.4.3 Displacement- and force-based elements

- Displacement-based formulation

The displacement based beam formulation starts with the assumption of a displacement field along the element that is defined in terms of nodal displacements. If ***U*** is the nodal displacement vector for a beam, which is formulated based on the Euler-Bernoulli theory, the section displacements are calculated by:

$$\boldsymbol{u}(\boldsymbol{x}) = \boldsymbol{N}_{\boldsymbol{U}}(\boldsymbol{x})\boldsymbol{U} \tag{2.21}$$

Where $\mathbf{N_U(x)}$ is the matrix that contains the shape functions that describe a linear axial displacement and a cubic transverse displacement of the beam element as illustrated in Fig. 2.5 such as:

$$\boldsymbol{N}_{\boldsymbol{U}}(\boldsymbol{x}) = \begin{bmatrix} 1-\dfrac{\boldsymbol{x}}{\boldsymbol{L}} & 0 & 0 & \dfrac{\boldsymbol{x}}{\boldsymbol{L}} & 0 & 0 \\ 0 & 1-3\left(\dfrac{\boldsymbol{x}}{\boldsymbol{L}}\right)^2+2\left(\dfrac{\boldsymbol{x}}{\boldsymbol{L}}\right) & \boldsymbol{x}\left(1-\dfrac{\boldsymbol{x}}{\boldsymbol{L}}\right)^2 & 0 & 3\left(\dfrac{\boldsymbol{x}}{\boldsymbol{L}}\right)^2-2\left(\dfrac{\boldsymbol{x}}{\boldsymbol{L}}\right)^3 & -\boldsymbol{x}\left(\dfrac{\boldsymbol{x}}{\boldsymbol{L}}\right)+\boldsymbol{x}\left(\dfrac{\boldsymbol{x}}{\boldsymbol{L}}\right)^2 \end{bmatrix} \tag{2.22}$$

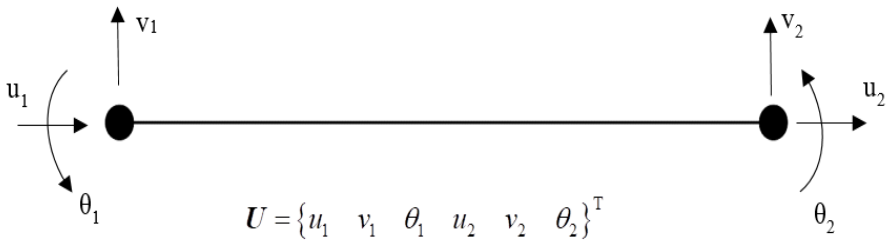

Fig. 2.5 2D Beam finite element using the displacement based formulation.

Additionally, by using the minimum potential energy, the element stiffness matrix **K** and the internal forces **F** are defined such as:

$$\boldsymbol{K} = \int_{L} \boldsymbol{B}^{t}(x)\boldsymbol{k}(x)\boldsymbol{B}(x)\boldsymbol{dx} \tag{2.23}$$

And

$$\boldsymbol{P} = \int_{L} \boldsymbol{B}^{t}(x)\boldsymbol{s}(x)\boldsymbol{dx} \tag{2.24}$$

Where **B(x)** in an array that contains the derivatives of the shape functions and **k(x)** is the cross sectional stiffness matrix. As stated before, the cross-sectional stiffness matrix depends on the behavior and the level of inelasticity of the cross section. The cross-section force vector **s(x)** is defined as follows:

$$\boldsymbol{s}(x) = \begin{Bmatrix} \boldsymbol{N}(x) & \boldsymbol{M}(x) \end{Bmatrix}^{t} \tag{2.25}$$

- Force-based formulation

The force-based beam formulation starts with the assumption of a force field instead of a displacement field along the element. Therefore, if ***P*** is the nodal vector which consists the nodal forces for a beam which is formulated based on the Euler-Bernoulli theory as shown in Fig. 2.6 and neglecting the rigid body modes, the section forces can be calculated by:

$$\boldsymbol{s}(x) = \boldsymbol{N}_{p}(x)\boldsymbol{P} \tag{2.26}$$

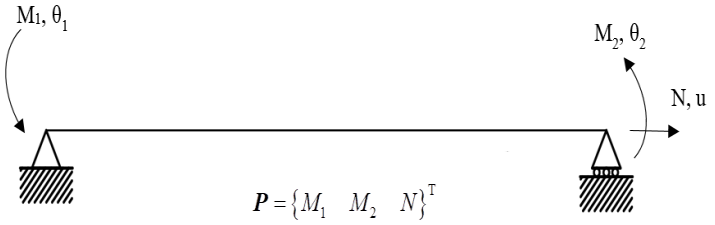

Fig. 2.6 2D Beam finite element, that uses the force-based formulation.

Where $\mathbf{N_p(x)}$ is the force interpolation functions array given by:

$$\boldsymbol{N}_{p}(x) = \begin{bmatrix} 0 & 0 & 1 \\ \dfrac{x}{L} - 1 & \dfrac{x}{L} & 0 \end{bmatrix} \tag{2.27}$$

Similarly, by assuming the principle potential energy the expressions of the element flexibility matrix and corresponding nodal deformations can be derived, such as;

$$\boldsymbol{F} = \int_{L} \boldsymbol{N}_{p}^{t}(x)\,\boldsymbol{f}(x)\boldsymbol{N}_{p}(x)\boldsymbol{dx} \tag{2.28}$$

$$\boldsymbol{U} = \int_{L} \boldsymbol{N}_{p}^{t}(x)\boldsymbol{e}(x)\boldsymbol{dx} \tag{2.29}$$

Where ***f(x)*** is the section flexibility matrix and ***e(x)*** is a vector containing the section deformations:

$$\boldsymbol{e}(\boldsymbol{x}) = \left\{ \boldsymbol{\varepsilon}_0(\boldsymbol{x}) \quad \boldsymbol{k}(\boldsymbol{x}) \right\}^t \tag{2.30}$$

The major characteristic of the force-based beam elements is the fact that equilibrium is satisfied at any point along the element irrespective of the beam cross-section and material behavior. The element stiffness matrix derives by inverting the flexibility matrix Eq. (2.28). This is the reason why the method is denoted also as flexibility-based method. The calculation of the element resisting forces is a complex problem which is based on the relation of the element resisting forces with the section resisting forces.

For both formulations (displacement- and force- based formulations), the shear deformation can also be included by assuming the Timoshenko beam theory. The corresponding expressions of the displacement and force-based formulation can be found in [50]. The Timoshenko beam element can develop shear locking, while significant energy goes into the shear deformation mode increasing the stiffness of the element. Furthermore, most beam finite elements that are based on classical finite element methods combined with classical, first order or higher order lamination theories lead to parasitic phenomena such as shear locking, rigid failure and zero-energy modes.

For the needs of this work, the force-based formulation is combined with the natural mode method. As explained in section 2.3, the total dofs of the element are separated in two components rigid body modes and strain modes. Therefore, a 3D beam elements which has 12 Cartesian dofs, produces 6 rigid body motions as illustrated in Fig. 2.7 and 6 pure deformations as shown in Fig. 2.1. Only the straining modes are used in the elemental stiffness matrix.

Many nonlinear beam finite elements have been proposed in the literature for the analysis of RC structures. Mohammad and Spacone [55] used both formulations of the displacement-based and force-based methods. They proposed a deformable interface which takes into account the bond-slip between the elemental components. Schultz and Filippou [56] proposed a spatial Timoshenko beam element with a total Lagragian formulation which was independent on the rigid body modes. Limkatany and Spacone ([17,18]) extended the work of Mohammad and Spacone [55] by using three different formulations: displacement-based, flexibility-based and the two-field mixed formulation. Papaioannou et al. [59] introduce a fiber flexibility-based beam with is combined with the natural mode method proposed by Argyris et al. [60] This element is analytically described in Markou [4] and it is adopted in this work. Mazars et al. [61] presented an enhanced multifiber beam element accounting for shear and torsion through the Timoshenko beam theory. Marini and Spacone [62] presented a flexibility-based shear-deformable beam element which was implemented with phenomenological constitutive laws in order to account the shear behavior.

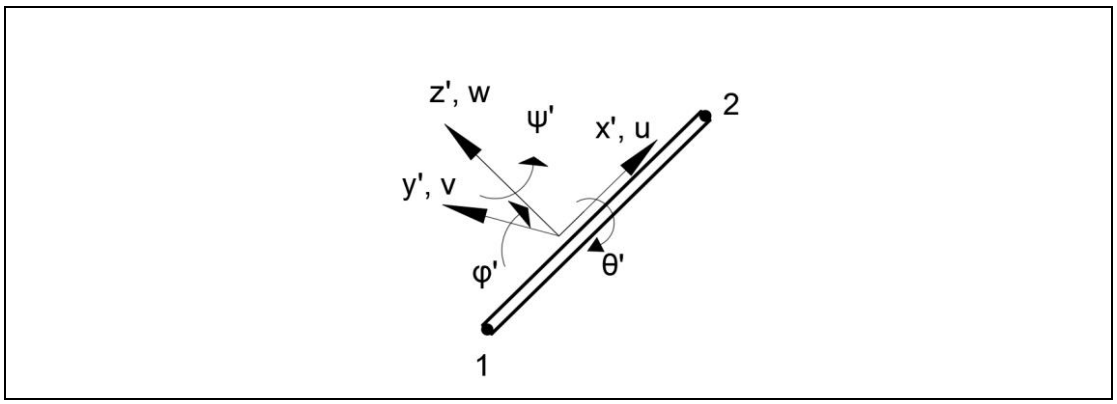

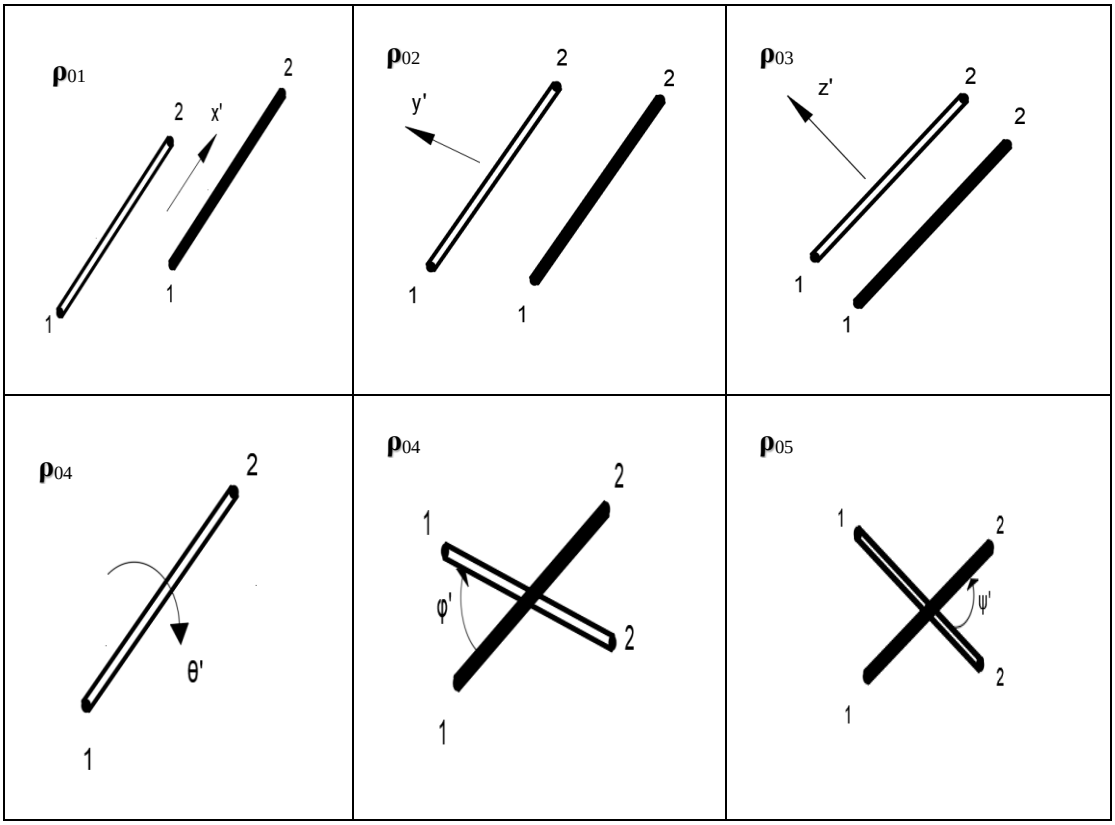

Fig. 2.7 Natural rigid body modes for a 3D beam element.

Mata et al. [63] presented a beam model by using the displacement-based formulation and a thermodynamically consistent 3D constitutive law for the description of the material behavior. Papachristidis et al. [64] extended the work of Papaioannou et al. [59] by incorporating the Klinkel and Govindjee [65] three dimensional plasticity law to capture the nonlinear behavior of shear deformable RC structures. Valipour and Foster [66] used the flexibility formulation in order to model the hysteretic behavior of RC framed structures, which were subjected to torsion. A detailed literature review of the nonlinear beam element models can be found in Markou [4].

It is obvious that the several beam-column formulations presented above attempt to include two or three dimensional material characteristics proposing models that will provide with objectivity and numerical robustness. The numerical problem herein is enhanced when shear dominated RC structures that present shear strains, cracking, warping, and confinement are modeled with the beam-column formulation. It is evident that the detailed modeling is a more realistic approach for modeling geometrically realistic RC structures but this choice increases significantly the computational cost. In the next chapters a proposed algorithmic approach for a 3D detailed modeling is presented, which provides numerical accuracy and computational efficiency whereas it is used for modeling numerous RC structures with different mechanical behaviors subjected to ultimate limit state cyclic and dynamic loading conditions.

2.4.4 Beam-column model formulation incorporated in this work

In this work, the beam model is used to simulate steel-reinforcement bars inside the hexahedral elements and RC members that are characterized by flexural dominated behavior. The beam-column model combines the natural mode concept of Argyris et al. [60] (see section 2.2) with the flexibility-based approach (see subsection 2.4.3). The detailed formulation of the beam model is presented in Markou [4].

The final form of the elemental stiffness matrix is defined by the following integral:

$$\boldsymbol{k}_N = \frac{1}{\boldsymbol{L}^2}\int_V \begin{bmatrix} \boldsymbol{E}_{xx} & \boldsymbol{z}\boldsymbol{E}_{xx} & \cdot & \boldsymbol{y}\boldsymbol{E}_{xx} & \cdot & \cdot \\ & \boldsymbol{z}^2\boldsymbol{E}_{xx} & \cdot & \boldsymbol{z}\boldsymbol{y}\boldsymbol{E}_{xx} & \cdot & \cdot \\ & & 9\boldsymbol{z}^2\boldsymbol{\zeta}\boldsymbol{E}_{xx} & \cdot & \cdot & \cdot \\ & & & \boldsymbol{y}^2\boldsymbol{E}_{xx} & \cdot & \cdot \\ & \boldsymbol{symm.} & & & 9\boldsymbol{y}^2\boldsymbol{\zeta}^2\boldsymbol{E}_{xx} & \cdot \\ & & & & & \boldsymbol{G}_{xy}(\Psi_{,y}-\boldsymbol{z})^2+\boldsymbol{G}_{xz}(\Psi_{,y}-\boldsymbol{z})^2 \end{bmatrix} \tag{2.31}$$

By considering an isotropic material the stiffness matrix has the following form:

$$\boldsymbol{k}_N = \frac{1}{\boldsymbol{L}}\begin{bmatrix} \boldsymbol{EA} & \cdot & \cdot & \cdot & \cdot & \cdot \\ & \boldsymbol{EI}_{yy} & \cdot & \cdot & \cdot & \cdot \\ & & 9\boldsymbol{z}^2\boldsymbol{\zeta}\boldsymbol{E}_{xx} & \cdot & \cdot & \cdot \\ & & & \boldsymbol{EI}_{zz} & \cdot & \cdot \\ & \boldsymbol{symm.} & & & 3\boldsymbol{EI}_{zz} & \cdot \\ & & & & & \boldsymbol{GI}_p \end{bmatrix} \tag{2.32}$$

Where E, G, A, I_{yy}, I_{zz} and J_p are the Young Modulus, the shear Modulus, the area of the section, the moment of inertia with respect to the y and z axis, and the polar moment of inertia, respectively.

For the calculation of the element resisting forces, an iterative method proposed by Spacone et al. (1966) [67] is used. The procedure is a Newton-Raphson iterative method under imposed nodal displacements that computes the element forces and section deformations until the compatibility between section deformations and imposed nodal deformations is accomplished.

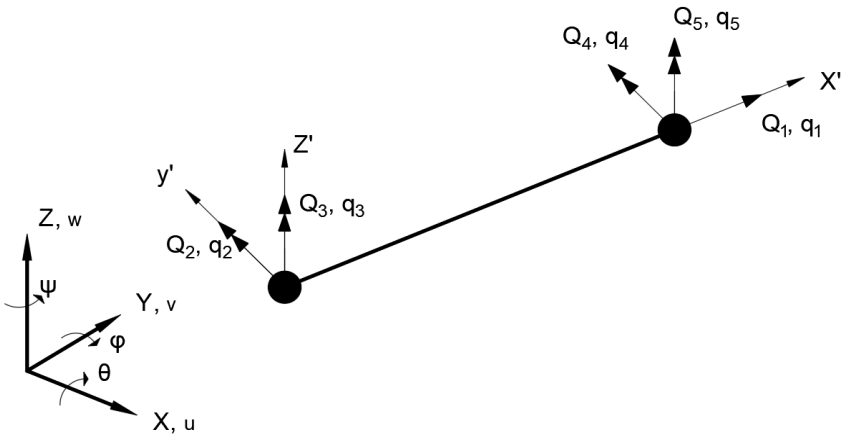

Fig. 2.8 Generalized displacement and forces of flexibility based element.

Considering a natural beam-column element that has 12 dofs as illustrated in Fig. 2.8, the force $\boldsymbol{P}$ and displacements $\boldsymbol{\rho}$ that refer to the global system are written in the following forms:

$$\boldsymbol{P} = \begin{bmatrix} \boldsymbol{P}_1 \\ \boldsymbol{P}_2 \\ \vdots \\ \vdots \\ \boldsymbol{P}_{11} \\ \boldsymbol{P}_{12} \end{bmatrix}, \quad \boldsymbol{\rho} = \begin{bmatrix} \boldsymbol{\rho}_1 \\ \boldsymbol{\rho}_2 \\ \vdots \\ \vdots \\ \boldsymbol{\rho}_{11} \\ \boldsymbol{\rho}_{12} \end{bmatrix} \tag{2.33}$$

The straining modes of the element are five, assuming that the torsion response is linear elastic and uncoupled from the other dofs. Therefore, the straining modes are: one axial extension ρ_1, two rotations relative to the cord at each node (ρ_2, ρ_3) at node 1 and (ρ_4, ρ_5) at node 2. These five deformations are called element generalized deformations and denoted as q and their corresponding generalized forces Q consist: Q_1 the axial force and (Q_2, Q_3) the bending moments at node 1 and (Q_4, Q_5) the bending moments at node 2. These two vectors take the following forms:

$$\boldsymbol{Q} = \begin{bmatrix} Q_1 \\ Q_2 \\ Q_3 \\ Q_4 \\ Q_5 \end{bmatrix}, \; \boldsymbol{q} = \begin{bmatrix} q_1 \\ q_2 \\ q_3 \\ q_4 \\ q_5 \end{bmatrix} \tag{2.34}$$

The connection between the straining modes and the total deformation is accomplished by the following expression:

$$\underset{(6x1)}{\boldsymbol{q}} = \underset{(6x12)}{\boldsymbol{a}_N} \cdot \underset{(12x12)}{\boldsymbol{T}_{04}} \cdot \underset{(12x1)}{\boldsymbol{\rho}}, \quad \boldsymbol{q}(6) = 0 \tag{2.35}$$

Where $\boldsymbol{T_{04}}$ is a matrix that contains submatrices of direction cosines such as:

$$\boldsymbol{T}_{04} = \begin{bmatrix} \boldsymbol{T}_0 & \cdot & \cdot & \cdot \\ \cdot & \boldsymbol{T}_0 & \cdot & \cdot \\ \cdot & \cdot & \boldsymbol{T}_0 & \cdot \\ \cdot & \cdot & \cdot & \boldsymbol{T}_0 \end{bmatrix}, \quad \boldsymbol{T}_0 = \begin{bmatrix} \boldsymbol{c}_{x'x} & \boldsymbol{c}_{x'y} & \boldsymbol{c}_{x'z} \\ \boldsymbol{c}_{y'x} & \boldsymbol{c}_{y'y} & \boldsymbol{c}_{y'z} \\ \boldsymbol{c}_{z'x} & \boldsymbol{c}_{z'y} & \boldsymbol{c}_{z'z} \end{bmatrix} \tag{2.36}$$

And $\mathbf{a_N}$ is the connection matrix (see Eq. (2.7)), which contains only geometrical parameters and has the following form:

$$\boldsymbol{a}_N = \begin{bmatrix} -1 & \cdot & \cdot & \cdot & \cdot & \cdot & 1 & \cdot & \cdot & \cdot & \cdot & \cdot \\ \cdot & \cdot & \cdot & \cdot & -1 & \cdot & \cdot & \cdot & \cdot & \cdot & 1 & \cdot \\ \cdot & \cdot & \dfrac{2}{\boldsymbol{L}} & \cdot & -1 & \cdot & \cdot & \cdot & -\dfrac{2}{\boldsymbol{L}} & \cdot & -1 & \cdot \\ \cdot & \cdot & \cdot & \cdot & \cdot & 1 & \cdot & \cdot & \cdot & \cdot & \cdot & -1 \\ \cdot & \dfrac{2}{\boldsymbol{L}} & \cdot & \cdot & \cdot & 1 & \cdot & -\dfrac{2}{\boldsymbol{L}} & \cdot & \cdot & \cdot & 1 \\ \cdot & \cdot & \cdot & -1 & \cdot & \cdot & \cdot & \cdot & \cdot & 1 & \cdot & \cdot \end{bmatrix} \tag{2.37}$$

The section forces and deformation vectors are given as:

$$\boldsymbol{D}(\xi) = \begin{Bmatrix} \boldsymbol{N}(\xi) \\ \boldsymbol{M}_y(\xi) \\ \boldsymbol{M}_z(\xi) \end{Bmatrix}, \; \boldsymbol{d}(\xi) = \begin{Bmatrix} \boldsymbol{\varepsilon}(\xi) \\ \boldsymbol{x}_y(\xi) \\ \boldsymbol{x}_z(\xi) \end{Bmatrix} \tag{2.38}$$

By using the fiber approach, each geometrical and material parameter for each section is stored into the fibers that subdivide each section. Therefore, the fiber strain and stress vectors are formed as:

$$\boldsymbol{e}(\xi)=\begin{Bmatrix}\varepsilon_1(\xi,y_1,z_1)\\ \vdots\\ \varepsilon_{ifiber}(\xi,y_{ifiber},z_{ifiber})\\ \vdots\\ \varepsilon_n(\xi,y_n,z_n)\end{Bmatrix},\quad \boldsymbol{E}(\xi)=\begin{Bmatrix}\sigma_1(\xi,y_1,z_1)\\ \vdots\\ \sigma_{ifiber}(\xi,y_{ifiber},z_{ifiber})\\ \vdots\\ \sigma_n(\xi,y_n,z_n)\end{Bmatrix} \tag{2.39}$$

The fiber strain vector $\boldsymbol{e(\xi)}$ and the section deformation vector $\boldsymbol{d(\xi)}$ are related through the following expression:

$$\boldsymbol{e}(\xi)=\boldsymbol{l}(\xi)\boldsymbol{d}(\xi)\ \text{ where }\ \boldsymbol{l}(\xi)=\begin{bmatrix}1 & -z_1 & y_1\\ & \vdots & \\ 1 & -z_{ifiber} & y_{ifiber}\\ & \vdots & \\ 1 & -z_n & y_n\end{bmatrix} \tag{2.40}$$

As stated before, Spacone et al. [67] proposed a deformation shape function for approximating the force and displacement fields, and simplified the two-field mixed method as follows:

$$\begin{aligned}&\Delta\boldsymbol{d}^{\boldsymbol{i}}=\boldsymbol{a}(\xi)\Delta\boldsymbol{q}\\ &\boldsymbol{D}^{\boldsymbol{i}}=\boldsymbol{b}(\xi)\boldsymbol{Q}^{\boldsymbol{i}}\ \text{ and }\ \Delta\boldsymbol{D}^{\boldsymbol{i}}=\boldsymbol{b}(\xi)\Delta\boldsymbol{Q}^{\boldsymbol{i}}\end{aligned} \tag{2.41}$$

Where Δ denotes the increment of the corresponding quantities, $\boldsymbol{a(\xi)}$ and $\boldsymbol{b(\xi)}$ are the deformation and force interpolation matrices respectively. The $\boldsymbol{a(\xi)}$ vector is calculated according to Mahasuverachai and Powell [68], while the $\boldsymbol{b(\xi)}$ is defined with the assumption that the axial force is constant and the two bending moments are linear along the element.

Finally, the section stiffness matrix is computed as follows:

$$\boldsymbol{K}^{j}(\xi)=\begin{bmatrix}\sum_{ifiber=1}^{nfibers}E^{j}_{ifiber}\cdot A_{ifiber} & -\sum_{ifiber=1}^{nfibers}E^{j}_{ifiber}\cdot A_{ifiber}\cdot z_{ifiber} & \sum_{ifiber=1}^{nfibers}E^{j}_{ifiber}\cdot A_{ifiber}\cdot y_{ifiber}\\ -\sum_{ifiber=1}^{nfibers}E^{j}_{ifiber}\cdot A_{ifiber}\cdot z_{ifiber} & \sum_{ifiber=1}^{nfibers}E^{j}_{ifiber}\cdot A_{ifiber}\cdot z^{2}_{ifiber} & -\sum_{ifiber=1}^{nfibers}E^{j}_{ifiber}\cdot A_{ifiber}\cdot z_{ifiber}\cdot y_{ifiber}\\ \sum_{ifiber=1}^{nfibers}E^{j}_{ifiber}\cdot A_{ifiber}\cdot y_{ifiber} & -\sum_{ifiber=1}^{nfibers}E^{j}_{ifiber}\cdot A_{ifiber}\cdot z_{ifiber}\cdot y_{ifiber} & \sum_{ifiber=1}^{nfibers}E^{j}_{ifiber}\cdot A_{ifiber}\cdot y^{2}_{ifiber}\end{bmatrix} \tag{2.42}$$

Where A_{ifiber} is the areas of each fiber and E_{ifiber} is the Young Modulus of each fiber. The internal resisting forces are determined by the following vector:

$$\boldsymbol{D}^{j}_{R}(\xi)=\begin{Bmatrix}\sum_{ifiber=1}^{nfibers}\sigma^{j}_{ifiber}\cdot A_{ifiber}\\ -\sum_{ifiber=1}^{nfibers}\sigma^{j}_{ifiber}\cdot A_{ifiber}\cdot z_{ifiber}\\ \sum_{ifiber=1}^{nfibers}\sigma^{j}_{ifiber}\cdot A_{ifiber}\cdot y_{ifiber}\end{Bmatrix} \tag{2.43}$$

The element's state determination that combines the forced-based method (flexibility based), the fiber approach and the natural mode method is described in detailed in Markou [4]. The method is schematically described in the two flow charts as shown in Fig. 2.9 and Fig. 2.10.

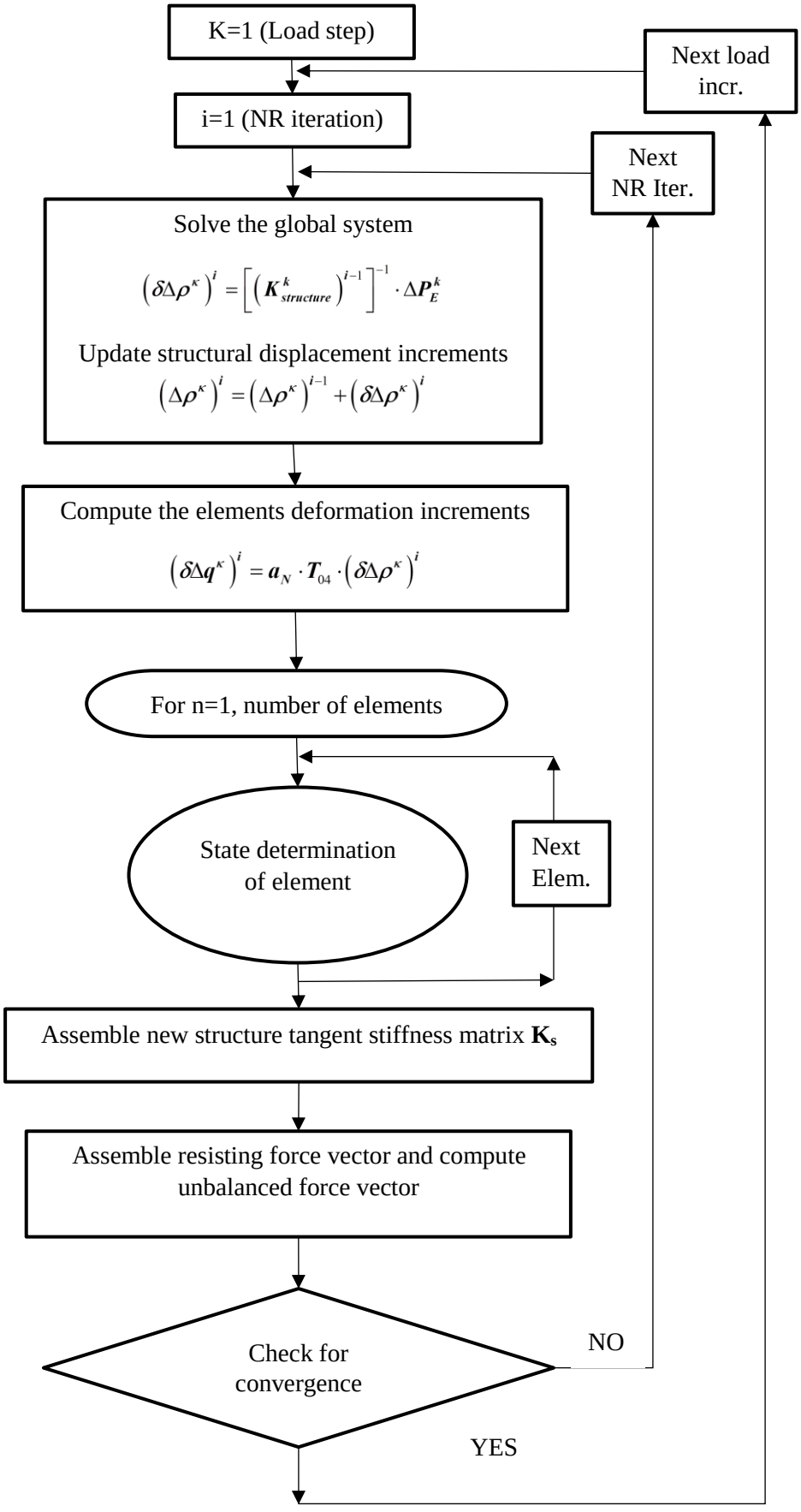

Fig. 2.9 Flow chart of the full model state determination

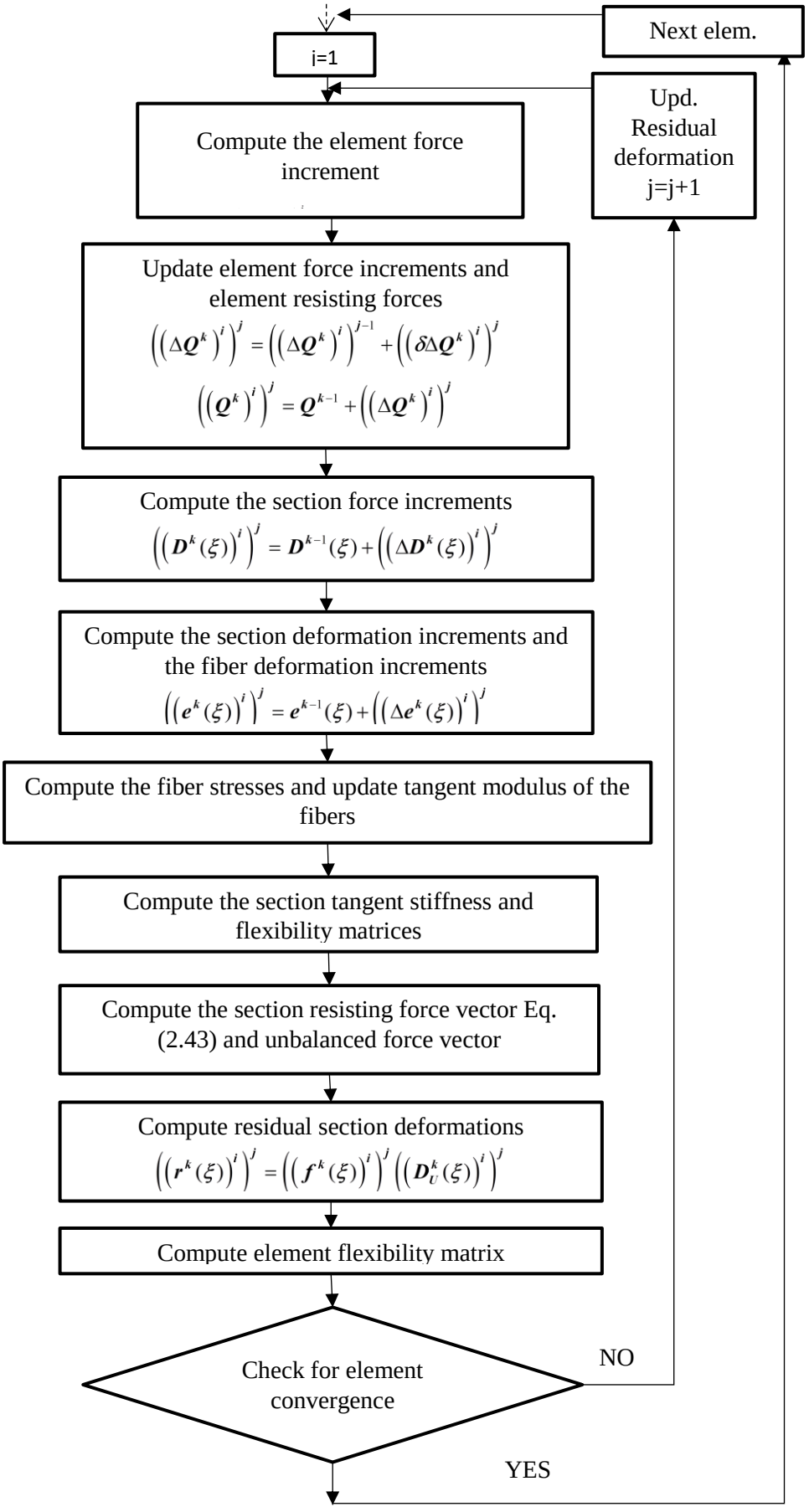

Fig. 2.10 Flow chart of the element state determination

Chapter 3. Proposed finite element modeling

Contents of Chapter 3

3.1 Concrete elements 27

3.2 Steel reinforcement 30

3.3 Modeling of embedded rebar elements 30

3.4 Generating embedded rebars 33

3.5 Solution algorithms for static nonlinear analysis 35

3.6 Solution algorithms for dynamic nonlinear analysis 40

3.7 Solution algorithms for modal analysis 42

3.1 Concrete elements

The concrete regions are discretized with the use of hexahedral (or brick-type) 8-node and 20-node three dimensional isoparametric elements as shown in Fig. 3.1. The geometry and displacement field are specified in parametric form and are interpolated using the same shape functions. The shape function are polynomials of the local coordinates ξ, η and ζ (-1≤ ξ,η,ζ ≤1).

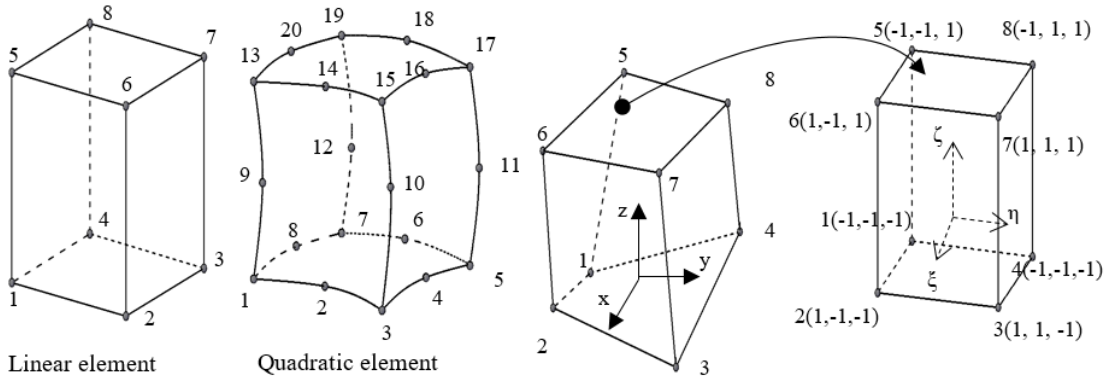

Fig. 3.1 Linear and quadratic finite elements and the representation of the 8-node hexahedral element in the natural coordinate system.

Both coordinates and displacements are interpolated with the same shape function such as:

$$\boldsymbol{u_i} = \sum_{\boldsymbol{k}=1}^{\boldsymbol{n}} \boldsymbol{N_k} \cdot \boldsymbol{u_i^k} \tag{3.1}$$

$$\boldsymbol{x_i} = \sum_{\boldsymbol{k}=1}^{\boldsymbol{n}} \boldsymbol{N_k} \cdot \boldsymbol{x_i^k} \tag{3.2}$$

Where i=1,2,3 and {**u**}={u, υ, w}, {**x**} = {x, y, z} and n is the number of nodes of the element. The shape functions of the 8-node hexahedral element are calculated through the following equation:

$$\boldsymbol{N_i} = \frac{1}{8}(1+\xi_0)(1+\eta_0)(1+\zeta_0) \tag{3.3}$$

Where $\xi_0 = \xi\xi_i, \eta_0 = \eta\eta_i, \zeta_0 = \zeta\zeta_i$. Similarly the shape functions of the 20-node hexahedral element (see Fig. 3.1) can be written as:

$$\boldsymbol{N_i} = \frac{1}{8}(1+\xi_0)(1+\eta_0)(1+\zeta_0)(\xi_0+\eta_0+\zeta_0-2),\ i = 1, 3, 5, 7, 13, 15, 17, 19 \tag{3.4a}$$

$$\boldsymbol{N_i} = \frac{1}{8}(1-\xi^2)(1+\eta_0)(1+\zeta_0),\ i = 2, 6, 14, 18 \tag{3.4a}$$

$$\boldsymbol{N_i} = \frac{1}{8}(1-\eta^2)(1+\xi_0)(1+\zeta_0),\ i = 4, 8, 16, 20 \tag{3.4a}$$

$$\boldsymbol{N_i} = \frac{1}{8}(1-\zeta^2)(1+\xi_0)(1+\eta_0)\ ,\ \ i = 9,\ 10,\ 11,\ 12 \tag{3.4a}$$

In the above shape functions the ξ_i, η_i, ζ_i are the values of natural coordinates and ξ, η, ζ are the nodal coordinates.

The strain vector $\boldsymbol{\varepsilon}$ contains the six components of the strain tensor and has the following form:

$$\{\varepsilon\} = \begin{bmatrix} \varepsilon_x & \varepsilon_y & \varepsilon_z & \gamma_{xy} & \gamma_{yz} & \gamma_{zx} \end{bmatrix}^t \tag{3.5}$$

The strain displacement matrix has the following form:

$$\boldsymbol{B} = [\boldsymbol{B}_1 \quad \boldsymbol{B}_2 \quad \cdots \quad \cdots \quad \boldsymbol{B}_{n-1} \quad \boldsymbol{B}_n] \tag{3.6}$$

Where n is the number of nodes (8 or 20) and

$$[\boldsymbol{B}_i] = \begin{bmatrix} \frac{\partial \boldsymbol{N_i}}{\partial \boldsymbol{x}} & 0 & 0 \\ 0 & \frac{\partial \boldsymbol{N_i}}{\partial \boldsymbol{y}} & 0 \\ 0 & 0 & \frac{\partial \boldsymbol{N_i}}{\partial \boldsymbol{z}} \\ \frac{\partial \boldsymbol{N_i}}{\partial \boldsymbol{y}} & \frac{\partial \boldsymbol{N_i}}{\partial \boldsymbol{x}} & 0 \\ 0 & \frac{\partial \boldsymbol{N_i}}{\partial \boldsymbol{z}} & \frac{\partial \boldsymbol{N_i}}{\partial \boldsymbol{y}} \\ \frac{\partial \boldsymbol{N_i}}{\partial \boldsymbol{z}} & 0 & \frac{\partial \boldsymbol{N_i}}{\partial \boldsymbol{x}} \end{bmatrix} \tag{3.7}$$

By using the Jacobian operator $\boldsymbol{J}$ in order to relate the cartecian coordinate derivatives to the natural coordinate derivatives, the derivatives of the shape functions in respect to the global Cartesian coordinates are obtained through the following formulation:

$$\begin{Bmatrix} \frac{\partial \boldsymbol{N_i}}{\partial \boldsymbol{x}} \\ \frac{\partial \boldsymbol{N_i}}{\partial \boldsymbol{y}} \\ \frac{\partial \boldsymbol{N_i}}{\partial \boldsymbol{z}} \end{Bmatrix} = [\boldsymbol{J}]^{-1} \begin{Bmatrix} \frac{\partial \boldsymbol{N_i}}{\partial \boldsymbol{\xi}} \\ \frac{\partial \boldsymbol{N_i}}{\partial \boldsymbol{\eta}} \\ \frac{\partial \boldsymbol{N_i}}{\partial \boldsymbol{\zeta}} \end{Bmatrix} \tag{3.8}$$

and the Jacobian matrix takes the following form:

$$[\boldsymbol{J}] = \begin{bmatrix} \frac{\partial x}{\partial \xi} & \frac{\partial y}{\partial \xi} & \frac{\partial z}{\partial \xi} \\ \frac{\partial x}{\partial \eta} & \frac{\partial y}{\partial \eta} & \frac{\partial z}{\partial \eta} \\ \frac{\partial x}{\partial \zeta} & \frac{\partial y}{\partial \zeta} & \frac{\partial z}{\partial \zeta} \end{bmatrix} \tag{3.9}$$

The partial derivatives of x, y, z in respect to the ξ, η, ζ are calculated with the use of the shape functions and nodal displacements as according to Eq. (3.10a)-(3.10a)

$$\frac{\partial \boldsymbol{x}}{\partial \boldsymbol{\xi}} = \sum \frac{\partial \mathrm{N}_i}{\partial \boldsymbol{\xi}} \boldsymbol{x}_i \,,\ \frac{\partial \boldsymbol{x}}{\partial \boldsymbol{\eta}} = \sum \frac{\partial \mathrm{N}_i}{\partial \boldsymbol{\eta}} \boldsymbol{x}_i \,,\ \frac{\partial \boldsymbol{x}}{\partial \boldsymbol{\zeta}} = \sum \frac{\partial \mathrm{N}_i}{\partial \boldsymbol{\zeta}} \boldsymbol{x}_i \tag{3.10a}$$

$$\frac{\partial \boldsymbol{y}}{\partial \boldsymbol{\xi}} = \sum \frac{\partial \mathrm{N}_i}{\partial \boldsymbol{\xi}} \boldsymbol{y}_i \,,\ \frac{\partial \boldsymbol{y}}{\partial \boldsymbol{\eta}} = \sum \frac{\partial \mathrm{N}_i}{\partial \boldsymbol{\eta}} \boldsymbol{y}_i \,,\ \frac{\partial \boldsymbol{y}}{\partial \boldsymbol{\zeta}} = \sum \frac{\partial \mathrm{N}_i}{\partial \boldsymbol{\zeta}} \boldsymbol{y}_i \tag{3.10a}$$

$$\frac{\partial \boldsymbol{z}}{\partial \boldsymbol{\xi}} = \sum \frac{\partial \mathrm{N}_i}{\partial \boldsymbol{\xi}} \boldsymbol{z}_i \,,\ \frac{\partial \boldsymbol{z}}{\partial \boldsymbol{\eta}} = \sum \frac{\partial \mathrm{N}_i}{\partial \boldsymbol{\eta}} \boldsymbol{z}_i \,,\ \frac{\partial \boldsymbol{z}}{\partial \boldsymbol{\zeta}} = \sum \frac{\partial \mathrm{N}_i}{\partial \boldsymbol{\zeta}} \boldsymbol{z}_i \tag{3.10a}$$

Therefore, the stiffness matrix takes the following form:

$$[\boldsymbol{K}] = \int_{\boldsymbol{V}} [\boldsymbol{B}]^{t} [\boldsymbol{E}][\boldsymbol{B}] \boldsymbol{dV} \tag{3.11}$$

Where $\boldsymbol{E}$ is the elasticity matrix and is expressed as:

$$[\boldsymbol{E}] = \begin{bmatrix} \lambda+2\mu & \lambda & \lambda & 0 & 0 & 0 \\ \lambda & \lambda+2\mu & \lambda & 0 & 0 & 0 \\ \lambda & \lambda & \lambda+2\mu & 0 & 0 & 0 \\ 0 & 0 & 0 & \mu & 0 & 0 \\ 0 & 0 & 0 & 0 & \mu & 0 \\ 0 & 0 & 0 & 0 & 0 & \mu \end{bmatrix} \tag{3.12}$$

Where λ and μ are elastic Lame constants that can be computed through the use of the elasticity modulus E and the Poisson ratio v according to Eq. (3.13):

$$\lambda = \frac{\nu \mathrm{E}}{(1+\nu)(1-2\nu)},\ \mu = \frac{\mathrm{E}}{2(1+\nu)} \tag{3.13}$$

The integration of the stiffness matrix in Eq. (3.11) is carried out in the natural coordinate system of the element, based on the following equation:

$$[\boldsymbol{K}] = \int_{\boldsymbol{V}} [\boldsymbol{B}]^{t} [\boldsymbol{E}][\boldsymbol{B}] \boldsymbol{dV} = \int_{-1}^{1}\int_{-1}^{1}\int_{-1}^{1} [\boldsymbol{B}(\xi,\eta,\zeta)]^{t} [\boldsymbol{E}][\boldsymbol{B}(\xi,\eta,\zeta)] |\boldsymbol{J}| \boldsymbol{d\xi d\eta d\zeta} \tag{3.14}$$

By using the Gauss quadrature rule, the above integral is calculated as:

$$\boldsymbol{I} = \int_{-1}^{1}\int_{-1}^{1}\int_{-1}^{1} \boldsymbol{f}(\xi,\eta,\zeta) \boldsymbol{d\xi d\eta d\zeta} = \sum_{i=1}^{n}\sum_{j=1}^{n}\sum_{k=1}^{n} \boldsymbol{f}(\xi_i,\eta_j,\zeta_k) \boldsymbol{w_i w_j w_k} \tag{3.15}$$

The weighting factors w_i, w_j and w_k are selected appropriately in order to calculate the integration with maximum accuracy but at the same time avoid additional cost. For linear elements the 2x2x2 integration scheme (n=2) is recommended, while for quadratic elements the integration scheme that was a 3x3x3 GPs is recommended.

3.2 Steel reinforcement

The steel reinforcement is discretized with the use of forced-base beam-column elements and truss elements. The formulation of the beam element was briefly described in Chapter 2 and for more details refer to Markou [4]. The isoparametric truss element has the classical formulation (see Fig. 3.2) in which the shape functions used are the followings:

$$\mathrm{N}_1 = \frac{1}{2}(1-\xi),\ \mathrm{N}_2 = \frac{1}{2}(1+\xi) \tag{3.16}$$

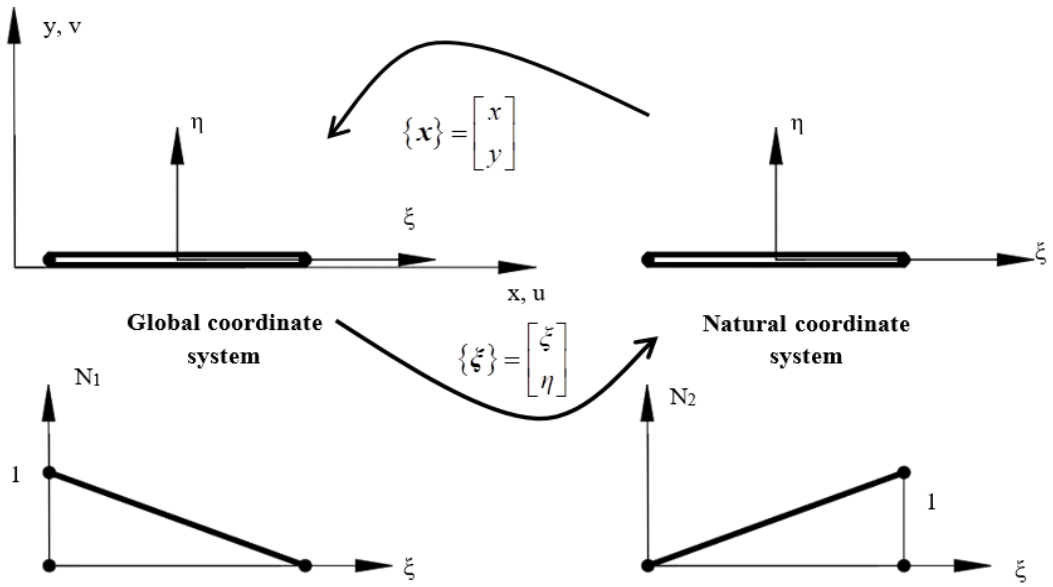

Fig. 3.2 Isoparameteric truss element in global and natural coordinate system and the shape functions in respect to the natural coordinate system.

Furthermore the stiffness matrix of the element takes the following form:

$$[\mathrm{K}] = \frac{\mathrm{EA}}{\mathrm{L}}\begin{bmatrix} 1 & -1 \\ -1 & 1 \end{bmatrix} \tag{3.17}$$

3.3 Modeling of embedded rebar elements

The use of beam elements for discretizing the embedded rebars inside hexahedral element affects significantly the kinematic connection formulation between concrete and steel elements. Although the shear and bending stiffness of steel reinforcement is considered to be insignificant, in cases when excessive cracking is occurs combined with extreme shear deformation, the stiffness of the steel reinforcement can play an important role in capturing the RC structural behavior. Furthermore, the use of the NBCFB element was found to increase the numerical stability of the NR iteration procedure due to its iterative formulation process. The interaction between hexahedral concrete elements with truss and beam-column steel bars is illustrated in Fig. 3.3.

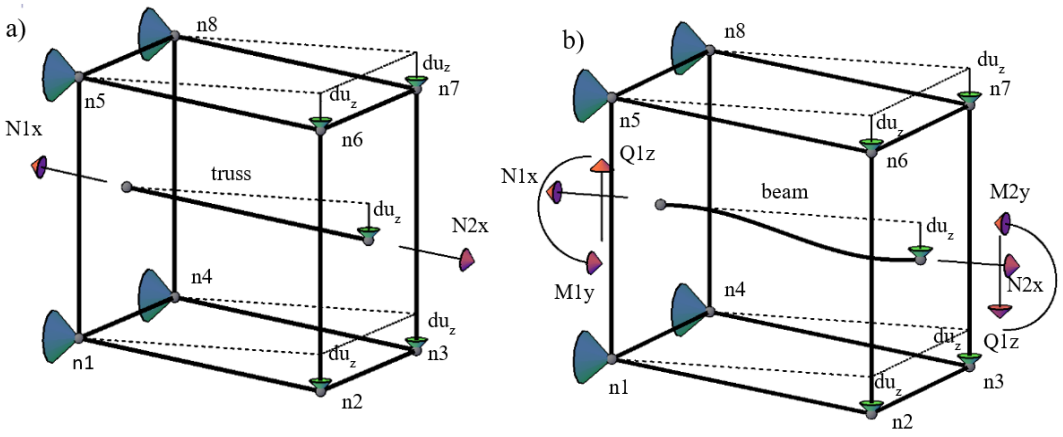

Fig. 3.3 Embedded rebar elements under transverse deformation in the case of a) truss and b) beam element.

In the case of truss embedded elements, the connection of the truss element nodes with the corresponding hexahedral are described through the translational dofs. When embedded beam-column elements are modelled, besides the translational dofs, the compatibility of the rotational dofs with the corresponding translational dofs of the hexahedron has to be enforced. Therefore, the connection between the hexahedral face rotation with the rotational dof of the beam node has to be established. In order to define the rotational face, a master triangle is assigned as shown in Fig. 3.4 by the three nearest nodes of the corresponding face containing the rebar node [4]. Additionally, it is assumed that the angle $\bar{\theta}$ between the longitudinal axis of the rebar and the normal $\bar{n}$ on the master triangle remains fixes after deformation.

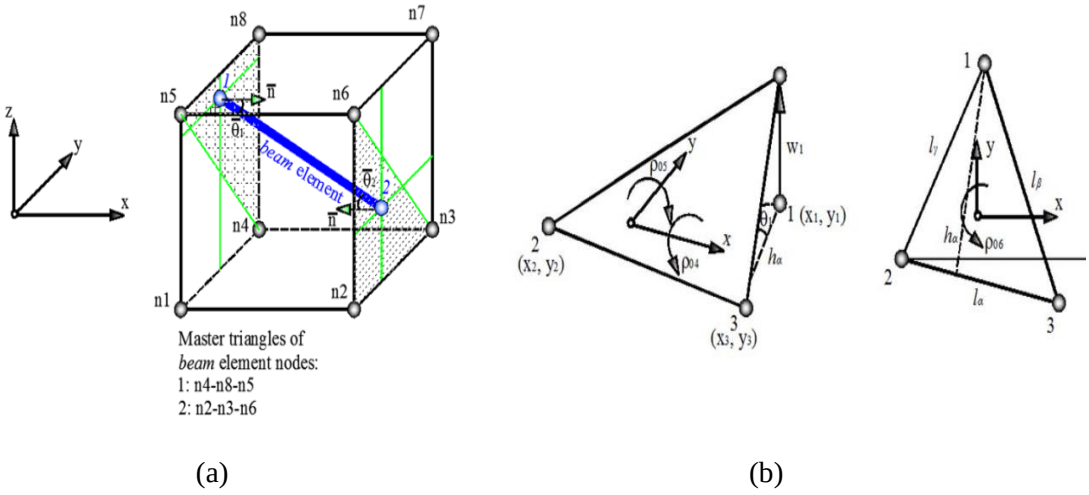

Fig. 3.4 (a) Master triangles of beam element nodes 1 and 2 (b) schematic representation of rotation $\bar{\theta}$.[4]

The kinematic relations that connect the beam nodal displacements with the nodal displacement of the hexahedral face, have the following form:

$$\underset{(12x1)}{\boldsymbol{u^B}} = \underset{(12x24)}{\boldsymbol{T}} \cdot \underset{(24x1)}{\boldsymbol{U^H}}, \quad \underset{(24x1)}{\boldsymbol{F^H}} = \underset{(24x12)}{\boldsymbol{T^t}} \cdot \underset{(12x1)}{\boldsymbol{F^B}} \tag{3.18}$$

Where $\boldsymbol{u^B}$ and $\boldsymbol{U^H}$ are the displacement vectors of the beam and hexahedral elements respectively. The vectors $\boldsymbol{F^B}$ and $\boldsymbol{F^H}$ are the vectors of the corresponding internal forces. The

transformation matrix $\boldsymbol{T}$ consists of 32 submatrices which are computed through the use of the natural nodal-coordinates. The matrix $\boldsymbol{T}$ has the following form:

$$\underset{(12x24)}{\boldsymbol{T}} = \begin{bmatrix} \boldsymbol{T}_1^1 & \boldsymbol{T}_2^1 & \boldsymbol{T}_3^1 & \boldsymbol{T}_4^1 & \boldsymbol{T}_5^1 & \boldsymbol{T}_6^1 & \boldsymbol{T}_7^1 & \boldsymbol{T}_8^1 \\ 0 & 0 & 0 & \boldsymbol{R}_4^1 & \boldsymbol{R}_5^1 & 0 & 0 & \boldsymbol{R}_8^1 \\ \boldsymbol{T}_1^2 & \boldsymbol{T}_2^2 & \boldsymbol{T}_3^2 & \boldsymbol{T}_4^2 & \boldsymbol{T}_5^2 & \boldsymbol{T}_6^2 & \boldsymbol{T}_7^2 & \boldsymbol{T}_8^2 \\ 0 & \boldsymbol{R}_2^2 & \boldsymbol{R}_3^2 & 0 & 0 & \boldsymbol{R}_6^2 & 0 & 0 \end{bmatrix} \tag{3.19}$$

The rows 1 and 3 of the matrix in Eq. (3.19) contains the submatrices that correspond to the translational displacements, while the other rows correspond to the rotational displacements of the rebars. The matrix $\boldsymbol{T}$ describes the relation between the dofs of the nodes *1* and *2* of the rebar element with the nodes n4-n5-n8 and n2-n3-n6 of the master triangles as illustrated in Fig. 3.4(a). Each submatrice is calculated by using the following equation:

$$\underset{(3x3)}{\boldsymbol{T}_i^j} = \begin{bmatrix} \boldsymbol{N}_i^j & 0 & 0 \\ 0 & \boldsymbol{N}_i^j & 0 \\ 0 & 0 & \boldsymbol{N}_i^j \end{bmatrix} \tag{3.20}$$

As stated before, the rotation of the embedded rebar nodes have to be calculated through the rotation of the master triangle which is defined by the three nearest nodes of the corresponding face of the hexahedron element [4]. The master triangle body rotations are calculated according to the natural theory of Argyris et al. [69]. Therefore the rotational submatrices of the master triangles shown in Fig. 3.4(b) take the following form:

$$\underset{(3x3)}{\bar{\boldsymbol{R}}_1^j} = \begin{bmatrix} 0 & 0 & \frac{\boldsymbol{x}_a}{2\Omega} \\ 0 & 0 & \frac{\boldsymbol{y}_a}{2\Omega} \\ -\frac{\boldsymbol{x}_a}{2\Omega} & -\frac{\boldsymbol{y}_a}{2\Omega} & 0 \end{bmatrix}, \underset{(3x3)}{\bar{\boldsymbol{R}}_2^j} = \begin{bmatrix} 0 & 0 & \frac{\boldsymbol{x}_\beta}{2\Omega} \\ 0 & 0 & \frac{\boldsymbol{y}_\beta}{2\Omega} \\ -\frac{\boldsymbol{x}_\beta}{2\Omega} & -\frac{\boldsymbol{y}_\beta}{2\Omega} & 0 \end{bmatrix}, \underset{(3x3)}{\bar{\boldsymbol{R}}_2^j} = \begin{bmatrix} 0 & 0 & \frac{\boldsymbol{x}_\gamma}{2\Omega} \\ 0 & 0 & \frac{\boldsymbol{y}_\gamma}{2\Omega} \\ -\frac{\boldsymbol{x}_\gamma}{2\Omega} & -\frac{\boldsymbol{y}_\gamma}{2\Omega} & 0 \end{bmatrix} \tag{3.21}$$

The way that the above relations are derived, is described in detailed in Markou [4]. By using the cosine matrix $\boldsymbol{T_0}$ the rotational submatrices are expressed according to the Cartesian coordinate system such as:

$$\underset{(3x3)}{\boldsymbol{R}_m^j} = \underset{(3x3)}{\boldsymbol{T}_0^t} \underset{(3x3)}{\bar{\boldsymbol{R}}_m^j} \underset{(3x3)}{\boldsymbol{T}_0} \tag{3.22}$$

Where,

$$\underset{(3x3)}{\boldsymbol{T}_0} = \begin{bmatrix} \boldsymbol{C}_{x'x} & \boldsymbol{C}_{x'y} & \boldsymbol{C}_{x'z} \\ \boldsymbol{C}_{y'x} & \boldsymbol{C}_{y'y} & \boldsymbol{C}_{y'z} \\ \boldsymbol{C}_{z'x} & \boldsymbol{C}_{z'y} & \boldsymbol{C}_{z'z} \end{bmatrix} \tag{3.23}$$

The stiffness matrix of the hexahedral element taking into account the stiffness contribution of its embedded rebars, is calculated as follows:

$$\underset{(24x24)}{\widehat{\boldsymbol{K}}_{Hexa}} = \underset{(24x24)}{\boldsymbol{K}_{Hexa}} + \sum_{i=1}^{nr} \underset{(24x12)}{(\boldsymbol{T}_i)^t} \cdot \underset{(12x12)}{\boldsymbol{K}_i^{rebar}} \cdot \underset{(12x24)}{\boldsymbol{T}_i} \tag{3.24}$$

Where $\boldsymbol{T_i}$ is the transformation matrix given in Eq. (3.19), $\boldsymbol{K_{Hexa}}$ is the stiffness matrix of the hexahedral element and *nr* is the number of the embedded rebars, found within the hexahedral.

3.4 Generating embedded rebars

The mesh generation of the structural structures is performed by using the Femap software [70]. Therefore, the initial rebar node coordinates are created through the use of the pre-processor and then the generation of embedded rebars is performed for each macro-element in order to define the natural coordinates of each embedded rebar element inside each hexahedral element. The rebars can have an arbitrary positioning inside the concrete elements and the numerical procedure that is used is described in Markou [4].

Therefore, a search procedure is performed in order to detect the embedded virtual nodes. The virtual nodes are the nodes that are found at by the intersection of the embedded macro-elements with the hexahedral faces. It is obvious that this procedure becomes cumbersome when dealing with a large number of hexahedral elements with many embedded rebars. Thus, Markou and Papadrakakis [30] proposed a geometrical constraint in order to restrict the volume of searching the nodes of the embedded elements. The geometric constraint defines a sphere with radius R_c:

$$R_c = c \times L \tag{3.25}$$

Where,

$$L = \sqrt{s_x^2 + s_y^2 + s_z^2} \tag{3.26}$$

And

$$s_x = \frac{\left(\sum_{n=1}^{8}(s_x^{cen} - s_x^n)\right)}{8},\ s_y = \frac{\left(\sum_{n=1}^{8}(s_y^{cen} - s_y^n)\right)}{8},\ s_z = \frac{\left(\sum_{n=1}^{8}(s_z^{cen} - s_z^n)\right)}{8} \tag{3.27}$$

Where s^n and s^{cen} are the coordinates of the node *n* and the centroid of the hexahedral respectively. The parameter c defines the size of the active volume of the sphere and after a parametric investigation in Markou and Papadrakakis [30], it is set to 5. If the macro-element nodes are inside the sphere, then the searching procedure is performed. This means that the following relation is satisfied:

$$d_{n1} \text{ or } d_{n2} < R_c \tag{3.28}$$

Where, $d_{n1}^i = \left|s^{cen} - s_{rebar}^{n1}\right|$, $d_{n2}^i = \left|s^{cen} - s_{rebar}^{n2}\right|$ are the distances of the macro-elements end nodes from the hexahedral centroid.

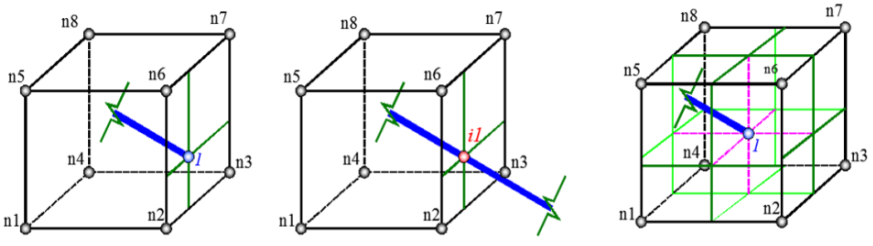

(a)

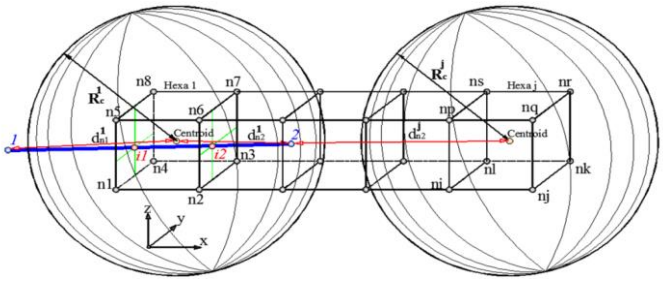

(b)

Fig. 3.5 Schematic representation of the possible locations of rebar nodes. (a) Three cases: (Left) Rebar node on hexahedral face, (middle) Rebar-hexahedral face intersection, (right) Rebar node inside hexahedral mesh. (b) Geometric constraint for the search of embedding rebars. [30]

The possible location of the embedded rebar nodes are shown in Fig. 3.5 which describes by three different cases. In case 1, the rebar node lies on the hexahedral face, where the natural coordinates of any given point P inside the hexahedral are calculated according to the following expressions:

$$\xi_p = \frac{s_x^p - s_x^{cen}}{d_X^{Hexa}},\ \eta_p = \frac{s_y^p - s_y^{cen}}{d_Y^{Hexa}},\ \zeta_p = \frac{s_z^p - s_z^{cen}}{d_Z^{Hexa}} \tag{3.29}$$

Where,

$$d_X^{Hexa} = s_x^{Hn1} - s_x^{cen},\ d_Y^{Hexa} = s_y^{Hn1} - s_y^{cen},\ d_Z^{Hexa} = s_z^{Hn1} - s_z^{cen} \tag{3.30}$$

Eq. (3.30) is used to complete the distances between the hexahedral centroid and its first node's coordinates located in the corresponding hexahedral connectivity matrix. Therefore, point *P* is constraint inside the hexahedral concrete element if its natural coordinates (Eq. (3.29)) satisfy the following criterion:

$$\left|\xi_p, \eta_p, \zeta_p\right| \le 1 \tag{3.31}$$

In case 2 (see Fig. 3.5), the line-plane intersection is shown. In this case, the natural coordinates are defined by using Eq. (3.29). Similarly with case 1, the natural coordinates of the intersection point have to satisfy Eq. (3.31). When cases 1 and 2 are not applicable, the natural coordinates of the macro-element nodes (Eq. (3.29)) are checked if they satisfy Eq. (3.32):

$$\left|\xi_p, \eta_p, \zeta_p\right| < 1 \tag{3.32}$$

If the above inequality is satisfied, then the macro-element node is located inside the concrete element (case 3 of Fig. 3.5).

In order to use Eq. (3.29), the shape of the hexahedral elements is required to be orthogonal parallepiped. In cases where irregular hexahedral shapes are found in the concrete mesh, the standard Barzegar and Maddipudi [71] method is activated in order to allocate the natural coordinates of the virtual nodes.

3.5 Solution algorithms for static nonlinear analysis

The equilibrium equation of a numerical model that is discretized through the use of the finite element method at time t_{n+1}, is reduced to the following:

$$\boldsymbol{F}_{\boldsymbol{ext}}^{\boldsymbol{n+1}} - \boldsymbol{F}_{\boldsymbol{int}}^{\boldsymbol{n+1}} = 0 \tag{3.33}$$

where, $\boldsymbol{F}_{\boldsymbol{int}}^{\boldsymbol{n+1}}$ are the nodal forces that correspond to the internal stresses of the structure and $\boldsymbol{F}_{\boldsymbol{ext}}^{\boldsymbol{n+1}}$ are the externally applied nodal forces of the structure. The well-known Newton-Raphson method is used to solve the nonlinear system equations that results from the finite element numerical model. There are many versions of the classical Newton-Raphson procedure in the literature. The basic three Newton-Raphson iteration algorithms are the (I) Force-Control, (II) Displacement-Control and III) Arc-length.

I. Force-Control.

In the Force-Control method, which is also called as the Newton's method, the external load is divided into load steps and thus the external load is applied incrementally at each time step based on the following expression:

$$\boldsymbol{F}_{\boldsymbol{ext}}^{\boldsymbol{n+1}} = \lambda_{\boldsymbol{n+1}} \cdot \bar{\boldsymbol{F}}_{\boldsymbol{ext}} \tag{3.34}$$

Where λ_{n+1} is the load factor at t_{n+1} and $\bar{\boldsymbol{F}}_{\boldsymbol{ext}}$ is computed only once at the beginning of the incremental procedure. For the case of static loads, the definition of time specifies the number of load steps (external increments).

At the typical iteration (k) of the Newton-Raphson scheme the linear equilibrium system described in Eq. (3.33), is transformed to:

$$\boldsymbol{K}_{\boldsymbol{T}} \delta \boldsymbol{u}^{(\boldsymbol{k})} = -\boldsymbol{r}^{(\boldsymbol{k}-1)} \tag{3.35}$$

Where, $\boldsymbol{r}^{(\boldsymbol{k-1})}$ is the residual force vector, which is computed as:

$$\boldsymbol{r}^{(\boldsymbol{k}-1)} = \boldsymbol{f}_{\text{int}}(\boldsymbol{u}_{\boldsymbol{n+1}}^{(\boldsymbol{k}-1)}) - \boldsymbol{f}_{\boldsymbol{ext}}^{\boldsymbol{n+1}} \tag{3.36}$$

And $\mathbf{K_T}$ is the global tangent stiffness matrix:

$$\boldsymbol{K}_{\boldsymbol{T}} = \left.\frac{\partial \boldsymbol{r}}{\partial \boldsymbol{u}_{\boldsymbol{n+1}}}\right|_{\boldsymbol{u}_{\boldsymbol{n+1}}^{(\boldsymbol{k}-1)}} \tag{3.37}$$

The global tangent stiffness matrix is defined through the use of the global displacement vector of the previous Newton-Raphson iteration $\boldsymbol{u}_{n+1}^{k-1}$. The solution of the Eq. (3.36) derives the displacement vector increment $\delta \boldsymbol{u}^{(\boldsymbol{\kappa})}$. Therefore, the global displacement vector is defined as:

$$\boldsymbol{u}_{\boldsymbol{n+1}}^{(\boldsymbol{k})} = \boldsymbol{u}_{\boldsymbol{n+1}}^{(\boldsymbol{k}-1)} + \delta \boldsymbol{u}^{(\boldsymbol{k})} \tag{3.38}$$

and can be also expressed through Eq. (3.39)

$$\begin{aligned} &\boldsymbol{u}_{\boldsymbol{n+1}}^{(\boldsymbol{k})} = \boldsymbol{u}_{\boldsymbol{n}} + \Delta \boldsymbol{u}^{(\boldsymbol{k})}, \\ &\Delta \boldsymbol{u}^{(\boldsymbol{k})} = \Delta \boldsymbol{u}^{(\boldsymbol{k}-1)} + \delta \boldsymbol{u}^{(\boldsymbol{k})} \end{aligned} \tag{3.39}$$

The Force-method is schematically represented in Fig. 3.6. The calculation of the tangent stiffness matrix, after each iteration, is necessary to be performed since the stresses that are updated within each iteration leads to material stiffness deterioration. However, the procedure of computing and decomposing the stiffness matrix in every iteration can be computationally demanding. Therefore, there are other alternative procedures which avoid the update of stiffness matrix in every NR iteration. It is assumed that the stiffness matrix is updated at the beginning of each load step and remains constant for all the internal iterations (see Fig. 3.6b). This alternative gains in computer time within each load step but it could require much more internal iterations to reach convergence when compared to the full Newton-Raphson. Therefore, many researchers update the tangential stiffness matrix only once within every loading step (Fig. 3.6b) while others use the initial stiffness method in which the update of the stiffness matrix is performed only at the beginning of each first loading step.

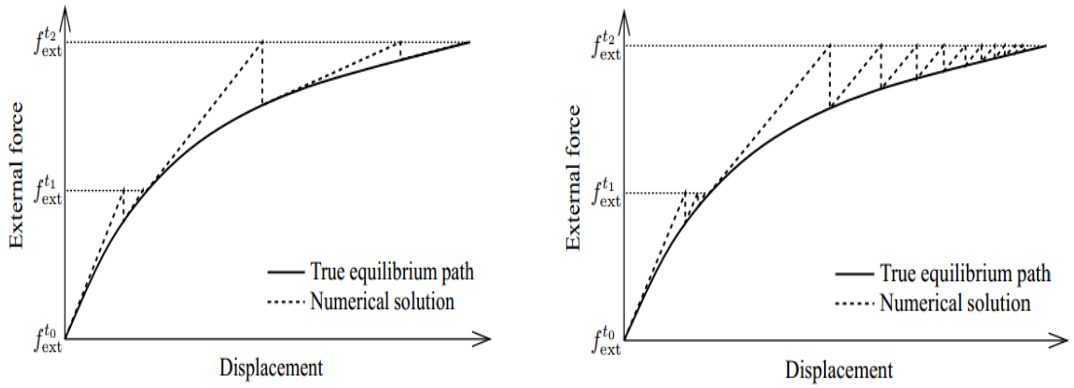

Fig. 3.6 (a) Full Newton-Raphson incremental-iterative solution procedure (b) Modified Newton-Raphson iterative scheme [72]

II. Displacement-Control.

The force-control method is very efficient for solving non-linear system of equations up to the limit point of the model. In cases where cohesive elements are modelled that present descending stress-strain behavior, the load-control is unable to predict any equilibrium points after the ultimate capacity limit. Therefore, the snap-through behavior occurs in this case as illustrated in Fig. 3.7. The displacement control is used in order to avoid this numerical phenomenon to predict the behavior accurately before and after this limit point. In the displacement-control Newton-Raphson procedure, displacement increments are applied instead of load steps. This procedure causes stress development in the under study numerical model that result nodal forces at the nodes where the displacements are implemented. The total summation of these forces gives the total reaction forces which have to be equal to the equivalent external load that would be caused by the implemented displacements.

The displacement vector is decomposed into a displacement vector that contains only free dofs ($\Delta \boldsymbol{u}_f$) and displacements that are imposed $\Delta \boldsymbol{u}_i$:

$$\Delta \boldsymbol{u} = \begin{bmatrix} \Delta \boldsymbol{u}_f \\ \Delta \boldsymbol{u}_i \end{bmatrix} \tag{3.40}$$

Similarly the stiffness matrix is rearranged to the following matrix:

$$\boldsymbol{K} = \begin{bmatrix} \boldsymbol{K}_{ff} & \boldsymbol{K}_{fi} \\ \boldsymbol{K}_{if} & \boldsymbol{K}_{ii} \end{bmatrix} \tag{3.41}$$

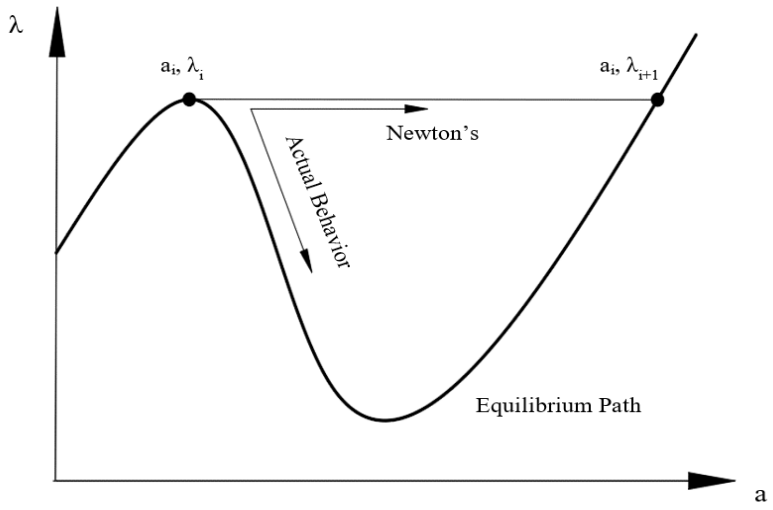

Fig. 3.7 The snap-through behavior when force-control is performed.

Therefore, at the first iteration (1) of the Newton-Raphson scheme the linear equilibrium system is described as follows:

$$\begin{bmatrix} \boldsymbol{K}_{ff} & \boldsymbol{K}_{fi} \\ \boldsymbol{K}_{if} & \boldsymbol{K}_{ii} \end{bmatrix} \begin{bmatrix} \Delta \boldsymbol{u}_f \\ \Delta \boldsymbol{u}_i \end{bmatrix} = - \begin{bmatrix} \boldsymbol{f}_{int,f}^{(0)} \\ \boldsymbol{f}_{int,i}^{(0)} \end{bmatrix} \tag{3.42}$$

and,

$$\Delta \boldsymbol{u}_f^{(1)} = -\boldsymbol{K}_{ff}^{-1} \left(\boldsymbol{K}_{fi} \cdot \Delta \boldsymbol{u}_i + \boldsymbol{f}_{int,f}^{(0)} \right) \tag{3.43}$$

At the (k) iteration of the Newton-Raphson scheme the linear equilibrium system can be described as:

$$\Delta \boldsymbol{u}_f^{(k)} = -\boldsymbol{K}_{ff}^{-1} \left(\boldsymbol{f}_{int,f}^{(k-1)} \right) \tag{3.44}$$

The above description shows that the vector $\boldsymbol{K_{fi} \cdot \Delta u_i}$ can play the role of the equivalent external force vector $\boldsymbol{F_{int}^{n+1}}$. It has to be noted that, for the displacement-control is required to inverse a reduced matrix $\boldsymbol{K_{ff}}$, while the load-control the inversion (in practice the LDU decomposition) is performed on the total matrix ***K.***

It must be noted that the nonlinear solution strategy used in this work, is the Newton-Raphson displacement control algorithm combined with a work-based convergence criterion given by Eq. (3.47). Generally the usual convergence criteria that are used for the nonlinear analysis are:

$$e_{err} = \frac{\left\| \Delta \boldsymbol{u}^{j} \right\|}{\left\| \boldsymbol{u}^{t+\Delta t} \right\|} \leq e_{D} \tag{3.45}$$

$$e_{err} = \frac{\left\| \boldsymbol{F}_{ext}^{t+\Delta t} - \boldsymbol{F}_{int}^{t+\Delta t} \right\|}{\left\| \boldsymbol{F}_{ext}^{t+\Delta t} - \boldsymbol{F}_{int}^{t} \right\|} \leq e_{F} \tag{3.46}$$

$$e_{err} = \frac{\Delta \boldsymbol{u}^{j} \left\| \boldsymbol{F}_{ext}^{t+\Delta t} - \boldsymbol{F}_{int}^{t+\Delta t} \right\|}{\Delta \boldsymbol{u}^{1} \left\| \boldsymbol{F}_{ext}^{t+\Delta t} - \boldsymbol{F}_{int}^{t} \right\|} \leq e_{E} \tag{3.47}$$

$$\boldsymbol{r}^{j} = \boldsymbol{F}_{ext}^{t+\Delta t} - \boldsymbol{F}_{int}^{t+\Delta t} \tag{3.48}$$

Where j corresponds to the internal iteration, e_d is the displacement, e_F is the force and e_E is the energy convergence tolerance criteria, respectively. The general convergence tolerance that was used for all the numerical nonlinear analyses performed in this research work was $e_E=10^{-4}$ in order to achieve high accuracy and induce additional stability during the cyclic nonlinear analysis.

III. Arc-length.

The Arc-length (Riks [73]) method is a very efficient solution procedure when the problem presents many critical points. As illustrated in Fig. 3.8, the use of the displacement control avoids the problem of snap-through instability caused by the use of the load-control method. However the use of the displacement-control exhibits snap-back behaviors. This kind of behavior can be captured by the arc-length method.

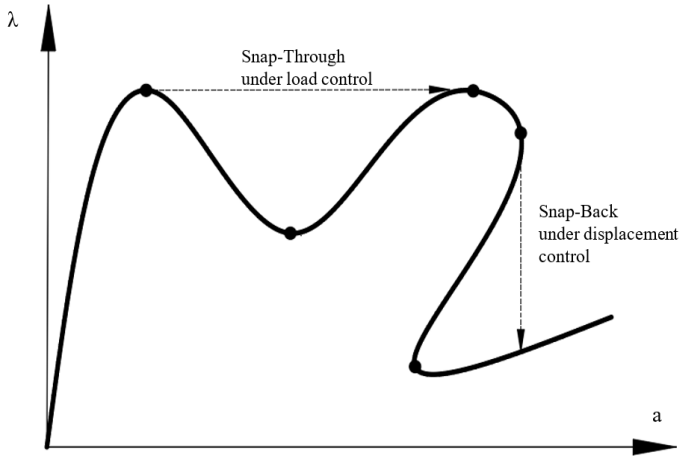

Fig. 3.8 A system that presents snap-through and snap-back instabilities when load and displacement control are used respectively.

The difference of the previous Newton-Raphson methods is that the arc-length method assumes a simultaneous variation in both the displacements $\Delta\mathbf{u}$ and the load vector coefficient $\Delta\lambda$ which are unknowns in the equilibrium system. Therefore, the equilibrium equation for a point $(u_0+\Delta u, \lambda_0+\Delta\lambda)$ can be written as:

$$\boldsymbol{F}_{\text{int}}(\boldsymbol{u}_{\mathbf{0}} + \Delta\boldsymbol{u}) - (\lambda_{\mathbf{0}} + \Delta\lambda)\boldsymbol{q} = 0 \tag{3.49}$$

If the above equation is not satisfied, then the necessary corrections (δu, δλ) have to be introduced. Hence,

$$\boldsymbol{F}_{\text{int}}(\boldsymbol{u_0}+\Delta\boldsymbol{u}+\delta\boldsymbol{u})-(\lambda_0+\Delta\lambda+\delta\lambda)\boldsymbol{q}=0 \tag{3.50}$$

therefore,

$$\boldsymbol{F}_{\text{int}}(\boldsymbol{u_0}+\Delta\boldsymbol{u})+\left[\frac{\partial \boldsymbol{F}^{\text{int}}(\boldsymbol{u})}{\partial \boldsymbol{u}}\right]_{\boldsymbol{u_0}+\Delta\boldsymbol{u}}\cdot\delta\boldsymbol{u}-(\lambda_0+\Delta\lambda+\delta\lambda)\boldsymbol{q}=0 \tag{3.51}$$

The above equation can be written as:

$$\left[\boldsymbol{K}_T\right]_{\boldsymbol{u_0}+\Delta\boldsymbol{u}}\cdot\delta\boldsymbol{u}-\delta\lambda\boldsymbol{q}=-[\boldsymbol{F}_{\text{int}}(\boldsymbol{u_0}+\Delta\boldsymbol{u})-(\lambda_0+\Delta\lambda)\boldsymbol{q}] \tag{3.52}$$

where $[\boldsymbol{K_T}]=\frac{\partial \boldsymbol{F}_{int}}{\partial u}$.

In order to define δ$\boldsymbol{u}$ and δλ, a supplementary equation is required. The following equation is called the Arc length equation and has the following form:

$$(\Delta\boldsymbol{u}+\delta\boldsymbol{u})^T\cdot(\Delta\boldsymbol{u}+\delta\boldsymbol{u})+\psi^2(\Delta\lambda+\delta\lambda)^2\left(\boldsymbol{q}^T\cdot\boldsymbol{q}\right)=\Delta\boldsymbol{l}^2 \tag{3.53}$$

Where ψ and Δl are user defined parameters. The system of equations can be written with the following form:

$$\begin{bmatrix}\left[\boldsymbol{K}_T\right] & -\boldsymbol{q}\\ 2\Delta\boldsymbol{u}^T & 2\psi^2\Delta\lambda\left(\boldsymbol{q}^T\boldsymbol{q}\right)\end{bmatrix}\begin{bmatrix}\delta\boldsymbol{u}\\ \delta\lambda\end{bmatrix}=-\begin{bmatrix}\boldsymbol{R}\\ \boldsymbol{A}\end{bmatrix}, \tag{3.54a}$$

$$\boldsymbol{R}=\boldsymbol{F}_{\text{int}}(\boldsymbol{u_0}+\Delta\boldsymbol{u})-(\lambda_0+\Delta\lambda)\boldsymbol{q} \tag{3.54a}$$

$$\boldsymbol{A}=-\left(\Delta\boldsymbol{u}^T\cdot\Delta\boldsymbol{u}+\psi^2\Delta\lambda^2\left(\boldsymbol{q}^T\cdot\boldsymbol{q}\right)-\Delta\boldsymbol{l}^2\right) \tag{3.54a}$$

From the system, δ$\boldsymbol{u}$ and δλ are derived and update the previous $\Delta\boldsymbol{u}$ and $\Delta\lambda$ respectively until convergence is achieved. When ψ=1, the Eq. (3.53) describes that the points $\Delta\boldsymbol{u}+\delta\boldsymbol{u}$ and $\Delta\lambda+\delta\lambda$ belong to a circle with radius Δl and the method is called Spherical Arc-Length Method. A schematic representation of the iterative procedure is illustrated in Fig. 3.9

Crisfield [74], proposed a different formulation of the above equations. The Eq. (3.52) can be rewritten as:

$$\delta\boldsymbol{u}=\delta\bar{\boldsymbol{u}}-\delta\lambda\delta\boldsymbol{u}_t\,, \tag{3.55a}$$

$$\delta\bar{\boldsymbol{u}}=-\left[\boldsymbol{K}_T\right]^{-1}_{\boldsymbol{u_0}+\Delta\boldsymbol{u}}[\boldsymbol{F}_{\text{int}}(\boldsymbol{u_0}+\Delta\boldsymbol{u})-(\lambda_0+\Delta\lambda)\boldsymbol{q}] \text{ and} \tag{3.55a}$$

$$\delta\boldsymbol{u}_t=\left(\left[\boldsymbol{K}_T\right]^{-1}_{\boldsymbol{u_0}+\Delta\boldsymbol{u}}\cdot\boldsymbol{q}\right) \tag{3.55a}$$

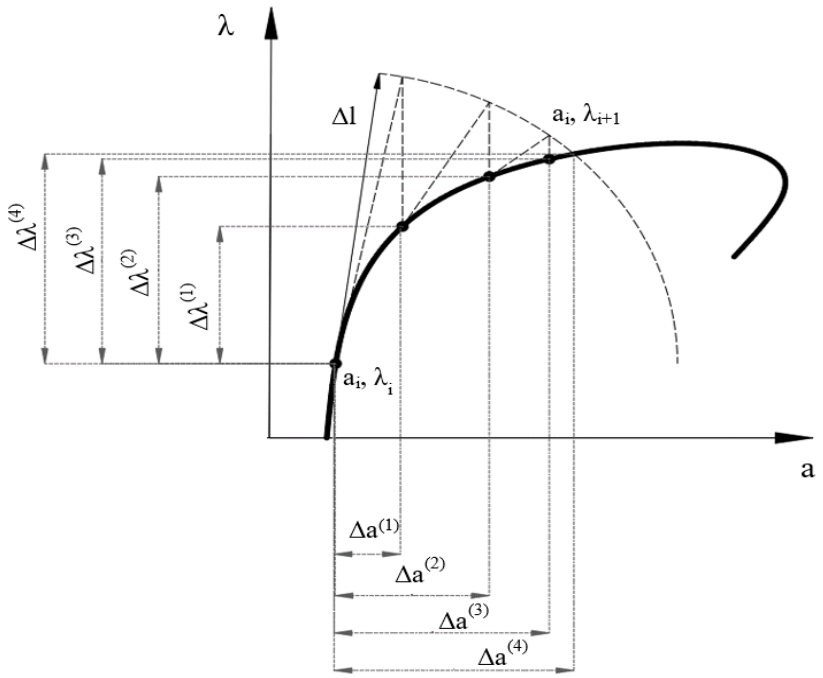

Fig. 3.9 Schematic representation of the Arc-Length method iterations.

The Eq. (3.55a) can be substituted in the arc-length Eq. (3.52). Hence:

$$a_1\delta\lambda^2 + a_2\delta\lambda + \alpha_3 = 0\,, \tag{3.56a}$$

$$\alpha_2 = \delta\boldsymbol{u}^{\boldsymbol{T}} \cdot \delta\boldsymbol{u} + \psi^2\left(\boldsymbol{q}^{\boldsymbol{T}} \cdot \boldsymbol{q}\right) \text{ and} \tag{3.56a}$$

$$\alpha_3 = (\Delta\boldsymbol{u} + \delta\bar{\boldsymbol{u}})^{\boldsymbol{T}} \cdot (\Delta\boldsymbol{u} + \delta\bar{\boldsymbol{u}}) + \psi^2\Delta\lambda^2\left(\boldsymbol{q}^{\boldsymbol{T}} \cdot \boldsymbol{q}\right) - \Delta\boldsymbol{l}^2 \tag{3.56a}$$

The Eq. (3.56a), describes a simple quadratic equation for δλ which can easily be solved. Then the δλ can be substituted to Eq. (3.55a) in order to update the displacement variation and complete the iteration. It must be noted herein that, all three nonlinear solution methods are available within ReConAn FEA.

3.6 Solution algorithms for dynamic nonlinear analysis

The literature review shows that the Newmark method is most commonly used for the numerical solution of the equation of motion in dynamic analysis of RC structures. This implicit integration method is indicated in earthquake analysis, because it is characterized with unconditionally numerical stability. Thus, the time step does not have to be very small, which could increase the computational cost of the analysis.

The equilibrium of the system at time t+Δt is expressed with the following equation:

$$M\,{}^{t+\Delta t}\ddot{u}^{(k)} + C\,{}^{t+\Delta t}\dot{u}^{(k)} + {}^{t}K\Delta u^{(k)} = {}^{t+\Delta t}R - {}^{t+\Delta t}F^{(k-1)} \tag{3.57}$$

and

$${}^{t+\Delta t}u^{(k)} = {}^{t+\Delta t}u^{(k-1)} + \Delta u^{(k)} \tag{3.58}$$

Where k is the number of the internal iteration during the Newton-Raphson iteration method. Using the trapezoidal rule of time integration method, which provides accuracy to the numerical solution, the following equations can be assumed:

$$^{t+\Delta t}u = {}^{t}u + \frac{\Delta t}{2}\left({}^{t}\dot{u} + {}^{t+\Delta t}\dot{u}\right) \tag{3.59}$$

$$^{t+\Delta t}\dot{u} = {}^{t}\dot{u} + \frac{\Delta t}{2}\left({}^{t}\ddot{u} + {}^{t+\Delta t}\ddot{u}\right) \tag{3.60}$$

Combining the Eqs. (3.60) and (3.58), the following expression derives:

$$^{t+\Delta t}\ddot{u}^{(k)} = \frac{4}{\Delta t^2}\left({}^{t+\Delta t}u^{(k-1)} - {}^{t}u + \Delta u^{(k)}\right) - \frac{4}{\Delta t}{}^{t}\dot{u} - {}^{t}\ddot{u} \tag{3.61}$$

Substituting Eq. (3.61) to (3.57), the equation bellow occurs:

$$^{t}\hat{K}\Delta u^{(k)} = {}^{t+\Delta t}R - {}^{t+\Delta t}F^{(k-1)} - M\left(\frac{4}{\Delta t^2}\left({}^{t+\Delta t}u^{(k-1)} - {}^{t}u\right) - \frac{4}{\Delta t}{}^{t}\dot{u} - {}^{t}\ddot{u}\right) - C\left(\frac{2}{\Delta t}\left({}^{t+\Delta t}u^{(k-1)} - {}^{t}u\right) - {}^{t}\dot{u}\right) \tag{3.62}$$

Where:

$$^{t}\hat{K} = {}^{t}\mathrm{K} + \frac{4}{\Delta t^2}M + \frac{2}{\Delta t}C \tag{3.63}$$

For the needs of this research work, the Newmark method was integrated within ReConAn FEA to perform nonlinear dynamic analysis.

Rayleigh damping matrix

By using the assumption of the linear viscous damping in structures, the Rayleigh damping known as proportional damping or classical damping model is used in this work. This model expresses damping as a linear combination of the mass and the stiffness matrix:

$$\boldsymbol{C} = a_K \cdot \boldsymbol{K} + a_M \cdot \boldsymbol{M} \tag{3.64}$$

Where,

$$a_K = \frac{2 \cdot \xi}{\omega_1 + \omega_2},\ a_M = \frac{2 \cdot \xi \cdot \omega_1 \cdot \omega_2}{\omega_1 + \omega_2} \tag{3.65}$$

The symbol, ξ represents the damping ratio and the ω_1, ω_2 parameters are the first (minimum) angular frequencies of the system. This model is very popular because it requires only the computation of the two coefficients α_K and α_M. These coefficients are defined after performing a modal analysis by which the first and second modes of free vibration are calculated. The damping matrix is calculated at the beginning of the analysis and then remains constant, which leads to a procedure with low computational cost.

However, during the nonlinear dynamic analysis, the stiffness matrix is significantly changed, mainly due to the cracking of the concrete domain. Therefore, the angular frequencies have to be changed due to this nonlinearity and generally the damping and dissipating properties of the structure cannot remain constant. The hysteretic loops defined from the stress-strain relation due to material deterioration are obviously the main parameter that describes the dissipative

capabilities of the structure. Nevertheless, there are structure that remain elastic and exhibit a damped response that cannot be assumed as negligible. Many authors claim that the use of the classical damping model can create unrealistic damping forces. This scenario implies increasing fractions of critical damping (the damping ratio ξ) as the stiffness of the structure reduces with the inelastic response which is unrealistic (Carr [75]).

Different approaches have been tested in the literature, considering changes of the parameters a_K and a_M by calculating the new angular frequencies for each external iteration. This procedure, requires the solution of an eigenvalue problem for each external iteration which increases significantly the computational cost. Others suggest that the elimination of the mass proportional damping contribution and bound the stiffness-proportional damping can provide the analysis with reasonable damping forces (Hall [76]).

In addition to the above, researchers suggest that the use of tangent stiffness matrix should be engaged in this procedure. In this case the damping is being reduced when the structure behaves inelastic (by reducing the stiffness matrix) a behavior that is assumed unrealistic. However, this reduction can be partially compensated for the excessive higher mode damping associated with the Rayleigh damping model. There are cases when this assumption can give realistic and unrealistic results, (Jehel et al. [77]). Puthanpurayil et al. [78] suggest an elemental damping formulation that can lead to smaller and more realistic damping moments in plastic hinges. For more information about the relative problems when using the Rayleigh damping model can be found in Charney [79], Lin and Zhu [80], Zareian and Medina [81] and Zhang et al. [82].

It is the author's belief that hysteretic damping models have to be introduced related to the material deterioration characteristics of the RC structure (such as the opening of cracking or the development of friction as an extra dissipative mechanism) during the dynamic analysis in order to accurately capture the hysteretic responses. The formulation of accurate damping strategies which ensures reasonable damping forces is an area that needs further research. In this work, the use of low damping ratios (max damping ratio used was 2%) ensures that the Rayleigh damping contribution plays a small role on the overall structure's response.

3.7 Solution algorithms for modal analysis

The solution of eigenvalues and eigenvectors of the finite element model is carried out by using the subspace iteration procedure. This procedure that was also integrated in ReConAn FEA for the need of this work, allows to calculate eigenvalues and eigenvectors of large finite element systems. The method was developed by Bathe [83] and can be described by three steps:

1. Set q starting iteration vectors and p which is the number of eigenvalues and eigenvectors to be calculated so that q>p.
2. Use simultaneous inverse iteration on the q vectors and Ritz analysis to extract the best approximations on the eigenvalue and eigenvector values from the q iterations.
3. After the convergence of the procedure, a Sturm sequence is used in order to verify that the required eigenvalues and eigenvectors have been calculated.

The method is relatively easy and provides robust results. The Subspace iteration procedure is described in detail in Bathe [84].

Chapter 4. 3D Constitutive behavior of concrete material

Contents of Chapter 4

4.1 General 45
4.2 Concrete under uniaxial compression 45
4.3 Concrete under biaxial compression 49
4.4 Concrete under triaxial compression 50
4.5 Concrete under uniaxial tension 55
4.6 Concrete subjected to shear 56
4.7 Time dependent properties 57
4.7.1 Shrinkage 57
4.7.2 Creep 59
4.7.3 Rate of loading 60
4.8 3D Constitutive Modelling of Concrete Material 60
4.8.1 Elasticity-based models 61
4.8.1.1 Isotropic linear-elastic models 61
4.8.1.2 Cauchy elastic-models 61
4.8.1.3 Hyperelastic (Green-elastic) model 62
4.8.1.4 Hypoelastic model (incremental type) 62
4.8.1.5 Variable moduli model 62
4.8.2 Plasticity-based models 62
4.8.2.1 Classical 62
4.8.2.2 Elastoplastic fracture models 63
4.8.2.3 Endochronic models 64
4.8.3 Damage mechanic models 64
4.8.4 Microplane models 65
4.8.5 Crack models 65
4.8.5.1 Discrete crack models 66
4.8.5.2 Smeared crack models 67
4.8.5.2.1. Standard fixed smeared crack models 68
4.8.5.2.2. Multidirectional fixed smeared crack models 69
4.8.5.2.3. Rotated smeared crack models 69
4.8.5.2.4. Stress locking effects and mesh sensitivity 70
4.8.5.3 Discrete Modelling 73
4.8.5.4 Meshless Modelling 74
4.8.5.5 Isogeometric Modelling 75

4.1 General

The complex behavior of RC under biaxial or triaxial cyclically varying stresses necessitates fundamental investigations into the behavior of such structures. In addition, analytical or numerical models allow the extrapolation of experimental results to cover the many parameter variations which cannot be experimentally investigated because of the high cost. Models are usually quite successful in providing failure load estimates for monotonic loading conditions. Cyclic material properties of concrete are not well established yet, so that no generally acceptable constitutive model exists. Many models are dependent on the values of many numerical parameters that formulate the constitutive relations and determine the mechanical behavior of the under study structural member. These models can describe only aspects of concrete's behavior and their implementation is limited to examples of small practical interest. It is important to formulate a constitutive model which represents accurately the actual mechanical behavior of concrete structures. The model has to be validated experimentally for predicting the behavior of cyclically loaded RC structures.

Most numerical approaches place emphasis on the description of the post-peak material characteristics that constitute the behavior of a discontinuous material although the modeling is based on continuum mechanics theories. Therefore, constitutive models based on theories such as endochronic, damage, plasticity, fracture, viscoplasticity and combinations of them, are usually used to describe the phenomenological features of the behavior of concrete under multiaxial state of stress. The purpose of these theories is the formation of analytical expressions which are calibrated through the use of experimental data.

The basic characteristics of RC that describe its complex nonlinear behavior are summarized below:

1. Nonlinear stress-strain behavior under multiaxial state of stress.
2. Strain-softening behavior in compression and anisotropic elastic degradation.
3. Progressive cracking induced by tensile stress or strain.
4. Post cracking behavior such as bond-slip between steel and concrete, aggregate interlock, dowel action of reinforcing steel and tension-stiffening characteristics.
5. Time-dependent behavior such as creep and shrinkage.

The three-dimensional modeling of concrete under general loading conditions has been an open subject over the last 30 years mainly motivated by the practical need of a simple constitutive model that can be used for the analysis of RC structures with numerical accuracy and computational efficiency. It is necessary to examine the behavior of concrete under compression and under tension separately to conclude the basic features that control its mechanical response.

4.2 Concrete under uniaxial compression

Concrete specimens can be subjected to uniaxial, biaxial or triaxial stresses. However, the assumption of uniaxial or plane-stress conditions is unrealistic in order to simulate the behavior of a concrete structure. The anisotropic behavior of concrete which is combined with a low tensile strength results to a nonuniform distribution of the internal stresses that leads to the development of out-of plane stresses, affecting significantly the strength of concrete. In cases when compressive strengths are developed in one of the three principal stress directions the

compressive strength in the orthogonal direction is increased. On the contrary, the compressive strength and stiffness of concrete decrease significantly with the increase of tensile stress in the transverse direction. This phenomenon also explains the necessity of the triaxial approach when dealing with the constitutive behavior of concrete.

Typical stress-strain curves for concrete under cyclic uniaxial compression can be depicted in Fig. 4.1. It shows that the unloading and reloading curves do not coincide and are not parallel to the initial loading curve. The experimental data show the stiffness degradation described by the stress-strain curve which occurs at the early stages of stress. Additionally, it is noted that the stiffness degradation is reflected from the decrease of the slopes of the reloading curves. The reloading curves of the first cycles are linear up to a level where the intersection of the reloading curve with the unloading one is found. After that point, the reloading curve becomes significantly non-linear resulting a softening response. Furthermore, the dissipated areas (the areas enclosed by the unloading-reloading hysteresis loops), become larger as the unloading strain increases. Finally, the envelope of the reloading strain is always larger in comparison to the envelope formed by the unloading strain, regardless if there is a partial or full unloading. [85]

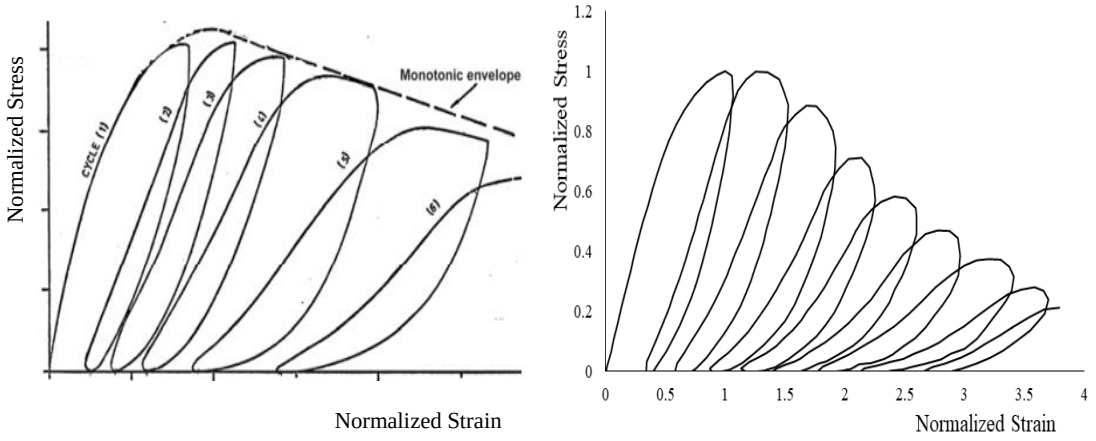

(a) (b)

Fig. 4.1 Behavior of concrete under cyclic uniaxial compression adapted from a) Karsan and Jirsa [86] *and b) Sinha et al.* [87].

The constitutive modeling of concrete has to be able to describe a realistic behavior of concrete under generalized 3D state of stress. Therefore, it has to take into account the effect of the out-of-plane small stresses that are usually ignored by the simplistic 1D and 2D approach. The strain-softening stress-strain descending branch, which appears at every uniaxial constitutive model in compression is attributed to the interaction between the specimen and the loading platens [88,89].

The uniaxial compression test is usually held by loading concrete specimens in the shape of cylinders or cubes at a constant rate of displacement through a testing machine that could be a loading system able to release almost instantaneously any load over the strength of the specimen (Ahmad and Shah [90]) or through a rigid steel system which transfers the load from the steel to concrete (Wang et al. [91]). The size of the tested specimen, is also important issue because of the effect of the loading device-concrete specimen interaction that creates triaxial stress state phenomena. If the specimen has a small size, the concrete zones that experience a triaxial state

of stress are caused by the frictional restraint from the device-specimen interaction and affect significantly the ultimate strength. This also explains why the cube specimens present larger ultimate strength than the cylinder ones. However, the central zone of the specimen, is subjected to a near-uniform uniaxial compressive stress and its behavior is unaffected by triaxial phenomena. Newman and Lachance [92] showed that the uniaxial- compressions strength of the cylinders with a height-to-diameter ratio of 2.5 is significantly unaffected of the frictional restraint conditions across the loaded surface. The schematic representations of the regions of the triaxial and uniaxial stress-fields and their stress paths are illustrated in Fig. 4.2.

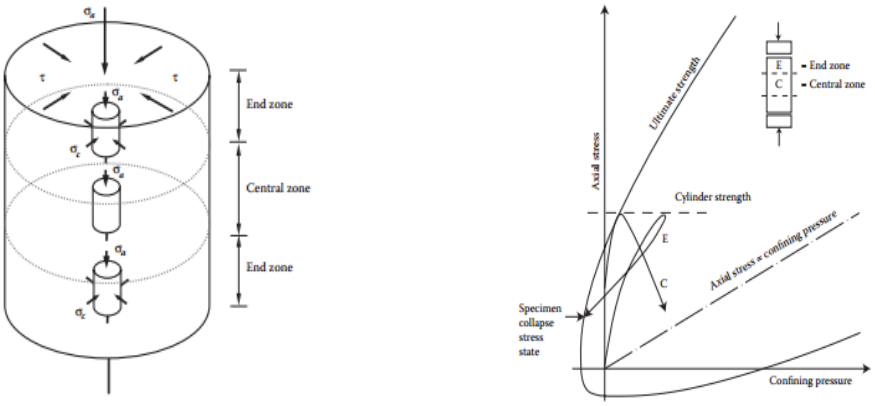

(a) (b)

Fig. 4.2 Cylindrical concrete specimen. a) Boundary conditions effect under uniaxial compression and b) Stress paths for the central and the end zones cylinders under increasing uniaxial compression. [3].

In order to examine the brittle nature of concrete, different types of loading systems were tested in order to diminish the friction effects of the specimen-loading device interaction. Therefore, dry steel plates, lubricated steel plates, brush bearing plates, fluid cushion, flexible membrane, flexible platens and standard triaxial test equipment are loading systems, are used as illustrated in Fig. 4.3 and presented by Gerstle et al. [93].

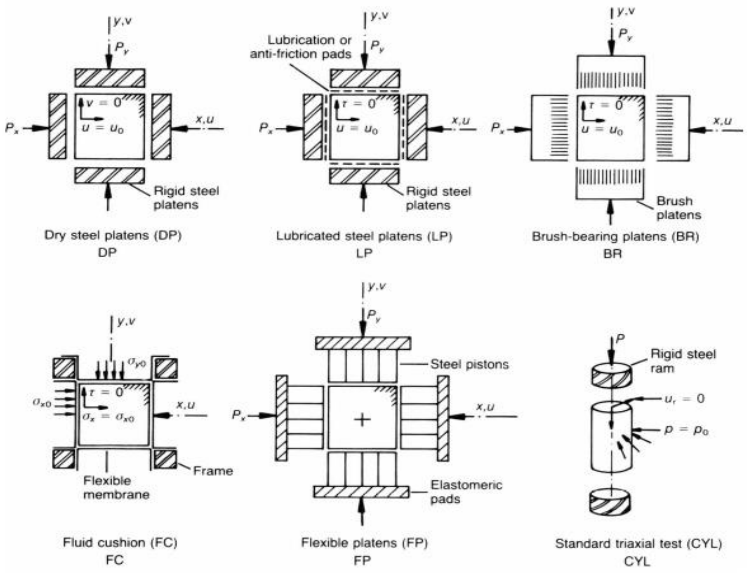

Fig. 4.3 Different types of loading systems (Gerstle et al. [93])

Fig. 4.4 describes the load-displacement relationships for concrete specimens under uniaxial compression that are derived based on the experimental method used to apply the load in an attempt to eliminate the frictional effects.

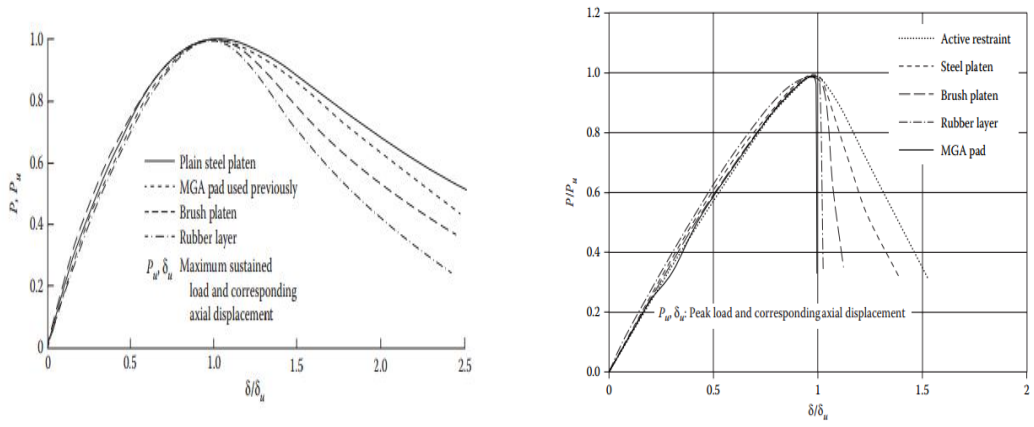

(a) (b)

Fig. 4.4 Load-displacement curves for the cylinder specimens subjected to different test methods with uniaxial compressive strength a) $f_c = 29MPa$, b) $f_c = 50MPa$ ([3]*)*

It is evident that, the inclination of the post-ultimate curve is referred to the lower-concrete strength cylinder is less steep than the one obtained by the higher concrete-strength cylinder. This discrepancy appeared due to the different sizes of the central zones (see Fig. 4.2) of the specimens. It is observed that the central zone of the higher concrete-strength specimens are substantially larger than the one of the lower concrete-strength specimen, a finding that indicates differences on the crack propagation of the specimens. The cracks of the lower concrete-strength specimens present a slow extension (usually in one direction), a pattern that leads to a maintenance of at least one of the end zones. In the contrary, the behavior of the higher concrete-strength specimens seems to eliminate the triaxial phenomena by reducing the end zones as illustrated schematically in Fig. 4.5. ([3])

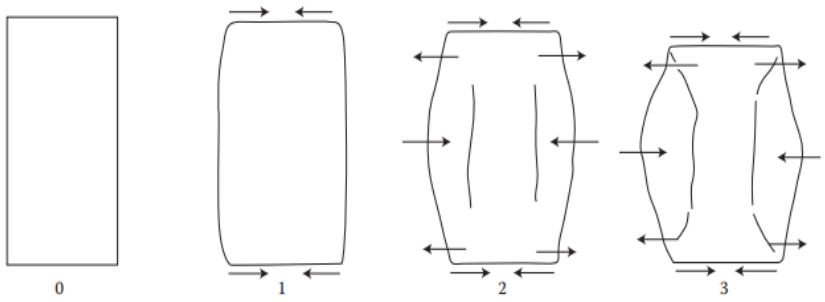

Fig. 4.5 Schematic representation of crack-extension behavior of concrete cylinders under uniaxial compression. [3]

It appears from the above, that the post-ultimate stress-strain relationship is eliminated as the friction effects are increasingly reduced. Generally, these friction effects appear under triaxial loading conditions, enhancing the assumption that concrete behaves as a brittle material. Therefore, neglecting the post ultimate stress-strain relation is found to be more realistic for

describing the concrete behavior at a material level. The post-ultimate deformation branch can be attributed to the interaction between specimen and loading platens (Shah and Sankar [94]).

4.3 Concrete under biaxial compression

Many researchers, have studied the behavior of concrete subjected to biaxial or triaxial loading conditions. A schematic representation of the experimental setup of a biaxial loading is illustrated in Fig. 4.6.

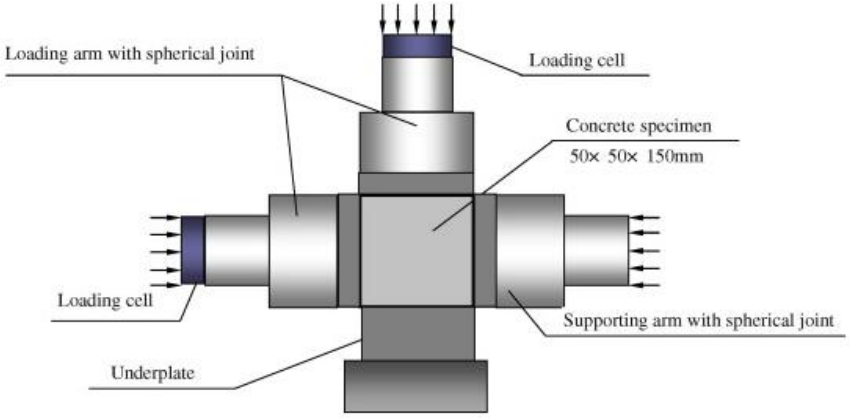

Fig. 4.6 Schematic representation of the experimental setup of a biaxial loading. (Li and Ren [95]*)*

Usually, researchers investigate the strength of concrete under two-dimensional loading and they try to create a failure/yield surface which can be used for different stress-strain histories under multiaxial loading. The most common failure surfaces obtained from experimental data are illustrated in Fig. 4.7. Kupfer et al. [96] and Yin et al. [97] conduct similar tests and conclude to similar surfaces with some discrepancies. They both set to zero the third principle stress (σ_3), which was out of the in-plane loading (σ_1- σ_2). Their discrepancies in the failure surface are shown in Fig. 4.7(a) and are attributed to the differences of the type of coarse aggregate used in the two studies and the fact that in Kupfer et al. [96] a slower rate of loading was used.

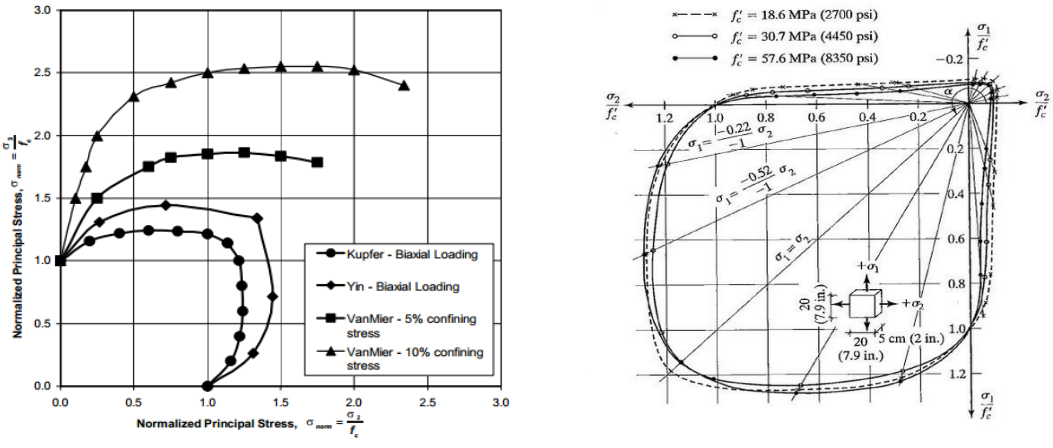

(a) (b)

Fig. 4.7 Biaxial compressive yield Surface for concrete for different (a) confining pressure (Kupfer et al. [96]*, Yin et al.* [97] *and Van Mier* [98]*), (b) compressive strength (Kupfer et al.* [96]*)*

Van Mier [98] extended the failure surfaces of Kupfer et al. [96] and Yin et al. [97] by adding a low level of confining pressure in the third dimension. The confining pressure tested was 5% or 10% of one of the in-plane stresses. The results of this study show that even a small confining pressure can lead to significant increase of the compressive strength of concrete in the plane of primary loading.

4.4 Concrete under triaxial compression

As explained before, the development of frictional (chapter 1.1) or confining (chapter 1.2) stresses can significantly increase the compressive strength of concrete. On the contrary the out-of-plane tensile stresses can drastically lead to the development of cracking which significantly decrease the strength of concrete. The heterogeneous material of concrete is characterized by anisotropic behavior and can easily lead to the development of out-of-plane stresses that cause the triaxial response of concrete. This explains the necessity of conducting triaxial experimental tests to obtain the three-dimensional stress-strain behavior of concrete under general loading conditions. A schematic representation of the experimental setup of a triaxial loading is illustrated in Fig. 4.8.

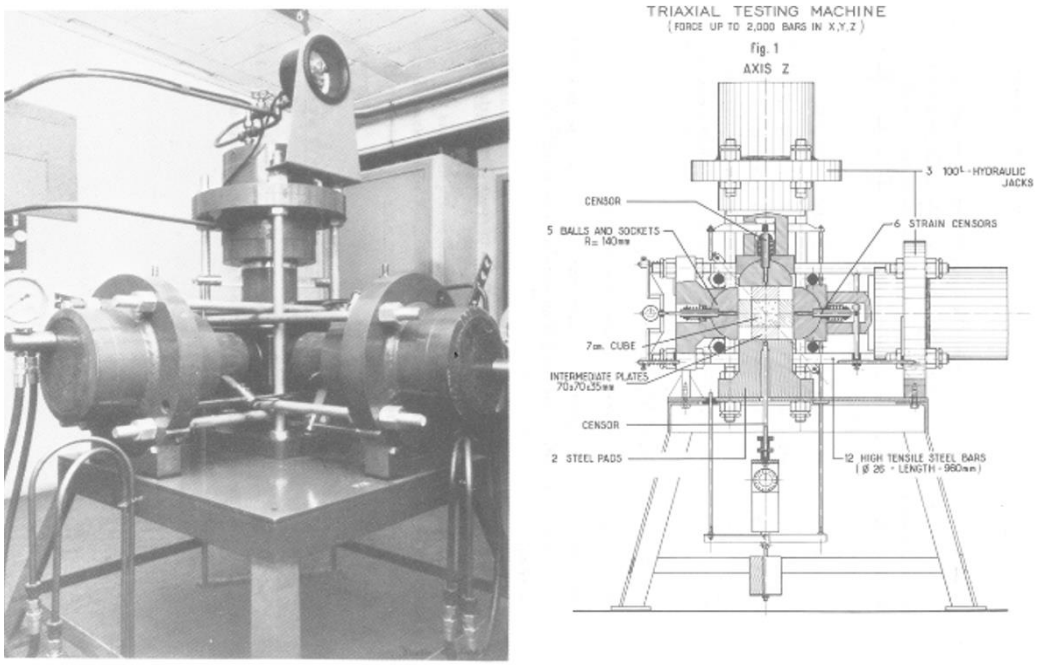

Fig. 4.8 Schematic representation of the experimental setup of a triaxial testing machine. (Launay and Gachon [99]*)*

A research project in the late 1970s (Gerstle et al. [93]) in which triaxial tests are conducted by seven laboratories and consisted of a hydrostatic pre-loading at levels ranging from 75-200% of the uniaxial strength, followed by different types of deviatoric paths up to the specimen failure, reported the following findings:

- The measured strains of concrete that is subjected to multiaxial stresses, present a considerable scatter no matter what test method is used.
- The behavior of concrete can be represented conveniently in terms of the first stress and strain invariants (octahedral values). This representation implies the assumption of isotropy for the behavior of concrete. The assumption of isotropy is considered valid at a macroscopic level, until the stress states reaches failure.

- The relationships between volumetric and deviatoric stresses with strains can be expressed by the evolution of two independent moduli K and G.
- A coupling effect between octahedral shear stress and volumetric strain is observed and can be described by introducing a coupling modulus H.

Basically, the non-linear behavior of concrete is presented due to the fracture processes that occur even under low levels of stress. The main cause of fracture and failure of concrete is the existence of micro-cracks before the application of the load. These micro-cracks are attributed to various reasons such as:

- Discontinuities in the cement paste matrix resulting from its complex morphology.
- Voids caused by shrinkage or thermal movements due to incompatibility between the properties of the various phases present in concrete.
- Discontinuities at the boundary between the aggregate particles and the paste or mortar matrix caused by segregation.
- Voids present in concrete as a result of incomplete compaction.

These micro-cracks is the main reason for the nonlinear behavior of concrete from the early stage. In small regions near the micro-crack tips, high tensile stresses and strains are concentrated at low loading levels. These concentrations cause gradually the crack extension and initiation of branches. As the load is increasing, the braches are starting to propagate. Gradually the crack propagation is becoming unstable (macro-cracking) and that leads to the ultimate failure of the specimen. It is found that the crack extension occurs in the direction of the maximum principal compressive stress applied to the boundaries of a specimen (Brace and Bombolakis [100], Hoek and Bieniawski [101]). Any increment of the applied load leads to an excessive stain energy concentration, which is eventually released by the extension of cracking. The above processes present two contradictory phenomena. The reduction of the stresses and strains that are excessively concentrated near the crack tips, causing a contraction of the material in the direction normal to the crack-extension path, while void formation tends to cause an extension.

The fracture process of concrete can be categorized as follows:

A. The fracture process follows a unique orientation since the propagation path coincides with the direction of the applied maximum principal compressive stress. This process may occur under any type of non-hydrostatic state of stress but it is unlikely to take place under pure hydrostatic stress.

B. The crack propagation follows a random orientation. This process may occur under any stress state but it is considered to be reduced to a minimum under a pure deviatoric stress.

It is assumed that under deviatoric state of stress, the principal directions of both local and applied state of stress coincide. Under increasing deviatoric stress the fracture process follows four stages that define the initiation and the propagation of cracks [3]:

Stage 1. The formation of micro-cracks takes place, additional to those pre-existing in the material at isolated points where the tensile stress concentrations due to the incompatible deformations of the aggregate and cement-paste phases are highest at early loading stages. The micro-cracks do not propagate but remain stable.

Stage 2. This stage describes the concentration of the high tensile strains and stresses near the crack tips as the load is increased. This process leads to the initiation of branches in the direction of the maximum principal compressive stress. The branching process causes the release of the strain energy concentration and that leads to a strain redistribution inside the concrete body. The main characteristic of this stage is that the crack configuration remain stable during further increases of the applied load. In this stage, the contraction of the concrete material predominates over the extension due to void formation. This process causes the rate of increase of the tensile strain in the direction at right angles to that of branching to be reduced with respect to the rate of increase of the strain in the direction of branching. The start of such deformational behavior has been termed as **local fracture initiation (LFI)** and is considered to mark the start of the branching-initiation process.

Stage 3. This stage describes the beginning of crack propagation. The cracks are extended in a relatively stable manner as the process ceases when the load remains constant. In this stage the void formation is such that it causes the rate of increase of the strain at right angles to the direction of branching to increase with respect to the rate of increase of the strain in the direction of branching. The above behavior is considered to mark the start of stable crack-propagation process and has been termed **onset of stable fracture propagation (OSFP)**.

Stage 4. As the load is increased, the cracking is increasing excessively. The fracture process becomes unstable and failure occurs even if the load remains constant. The start of this stage has been termed **onset of unstable fracture propagation (OUFP)**. This level is easily defined since it coincides with the level at which the overall volume of the material becomes a minimum. On the contrary, under tensile stress states concrete member's volume seems to rapidly increase.

The crack stages that describe the fracture process which is developed in the material of concrete are illustrated in Fig. 4.9.

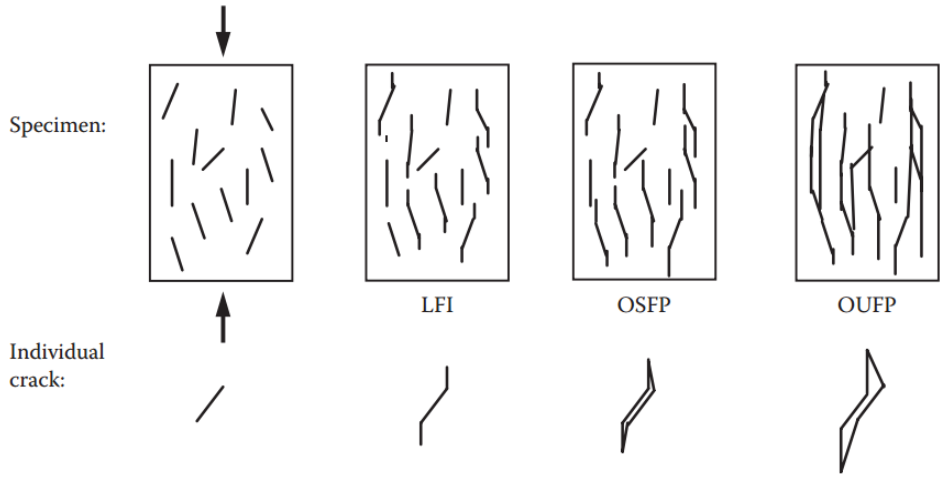

Fig. 4.9 Schematic representation of the stages of the fracture process for concrete under compressive stress. [3]

The first three stages define the non-linear behavior of concrete at the material level and therefore they compose its constitutive relations. These stages can be denoted by the term of micro-cracking. The propagation of cracking is described as a static process as the fracture ceases when the load remains constant. The fourth stage which is considered as macro-cracking defines the failure of the localized regions and affects concrete at the structure level. Macro-

cracking presents a dynamic phenomenon where the crack extension continues even if the load is maintained constant.

Under a hydrostatic stress the fracture process can be described by the 3 stages similar to those described under deviatoric stress. The characteristic feature of this process is that the cracks are extended randomly in the concrete body. Therefore, it is very likely that a crack will be situated in the path along which a potential crack may propagate. Consequently the former crack will act as a crack-propagation 'inhibitor' that will tend to increase the energy required to start the crack-propagation process. For practical purposes, it is assumed that the stress strain relation and the formation of the ultimate state envelope are effectively independent of the stress path.

In conclusion, the non-linear characteristics of concrete are based on triaxial material behavior. Small secondary stresses that develop within the structural member have a major effect on the load-carrying capacity of the member. A small confining pressure of the uniaxial cylinder compressive strength is sufficient to increase the load-carrying capacity considerably while tensile stresses could abruptly have the opposite effect. Generally the failure occurs invariably in tension before the ultimate state of concrete in compression is exceeded. It is considered that concrete under compression never fails by 'crushing' in the regions where the compressive stresses are largest. Instead it fails by 'splitting' in adjacent regions where the compressive stresses may be small due to the development of the secondary tensile stresses.

The constitutive model of concrete is constructed by defining the key characteristics that cause the non-linear behavior. The fracture process indicates two opposing phenomena that are occurred during the propagation of cracking.

A. The strain energy which is localized in regions near the crack tips is released and that causes a reduction of the predominately tensile stress concentrations. This reduction of the tensile stresses can be assumed to be equivalent to the application of a compressive stress that tends to reduce the volume of concrete.

B. The excessive cracking produces voids and causes an increase in the volume of concrete.

The fracture process can be described by four stages. For practical reasons only three stages are used as presented below.

I. In the first stage, the cracking is localized and the formation of voids is not significant in the structure. Therefore, the effect A is greater than the effect B and the volume of the material decreases.

II. In the second stage, both effects A and B are significant but the phenomenon of contraction predominates over the extension of the material. Therefore, the effect A is greater than the effect B. The beginning of this stage defines the OSFP level, at which the rate of increase of strain $\varepsilon 2$ begins to exceed the rate of increase of strain $\varepsilon 1$ even though $\varepsilon 1$ still exceeds $\varepsilon 2$ (see Fig. 4.10).

III. The final stage describes the formation of voids, which cause the increase of volume of the material. Therefore, both effects occur but the effect B predominates. The beginning of this stage defines the OUFP level and corresponds to the level at which the volume of the material becomes a minimum.

The above stages compose the non-linear behavior of concrete structure that consist of the following three components (as illustrated in the Fig. 4.10):

1. A linear component which is unaffected by the above fracture processes.

2. A non-linear component that takes into account the effect of the internal stresses, which develop during the fracture process.
3. A non-linear component which describes the effect of the void formation.

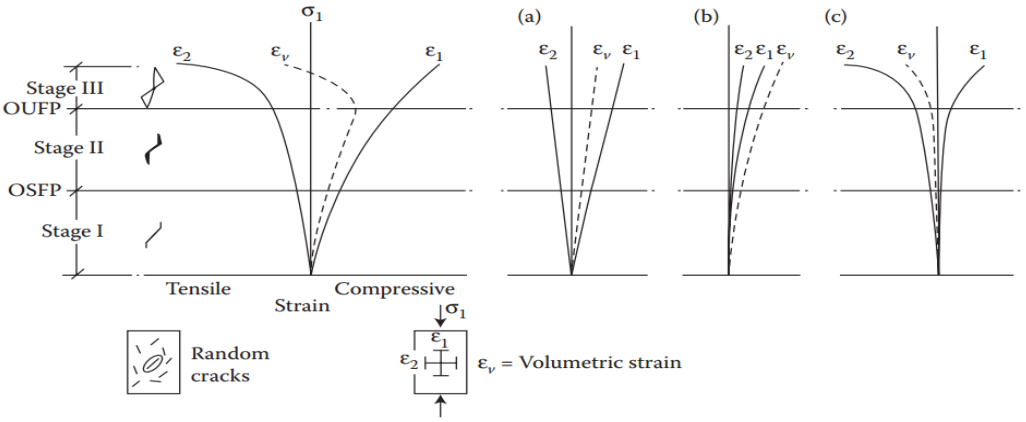

Fig. 4.10 Stress-strain characteristics during the stages of fracture processing. (a) Linear material properties, (b) Internal stresses effect, (c) Void formation effect. [3]

The stress-strain relationships are expressed most conveniently by decomposing each state of strain and stress into hydrostatic and deviatoric components. Thus the normal and shear octahedral stresses (σ_0, τ_0) and strains (ε_0, γ_0) are used. It is evident that the application of hydrostatic stresses σ_0 cause the variation of the volumetric strain $\varepsilon_{0(h)}$ while the application of deviatoric stresses τ_0 cause both volumetric and deviatoric strains. Experimental investigation shows that all the stress-strain relationships are independent on the different loading paths [3].

Typical stress-strain behaviors under uniaxial and triaxial experimental cyclic loading tests [3] are shown in Fig. 4.11. The hysteretic loop exhibited in the first cycle is negligible. Therefore, a linear stress-strain relationship can be used to describe the concrete behavior in case of unloading and subsequent reloading up to the maximum stress level experienced previously by the material This is explained by the fact that during unloading, the fracture process ceases and as a result the concrete behaves elastically. Obviously, when the maximum stress level previously experienced by the material is exceeded, the fracture process continues.

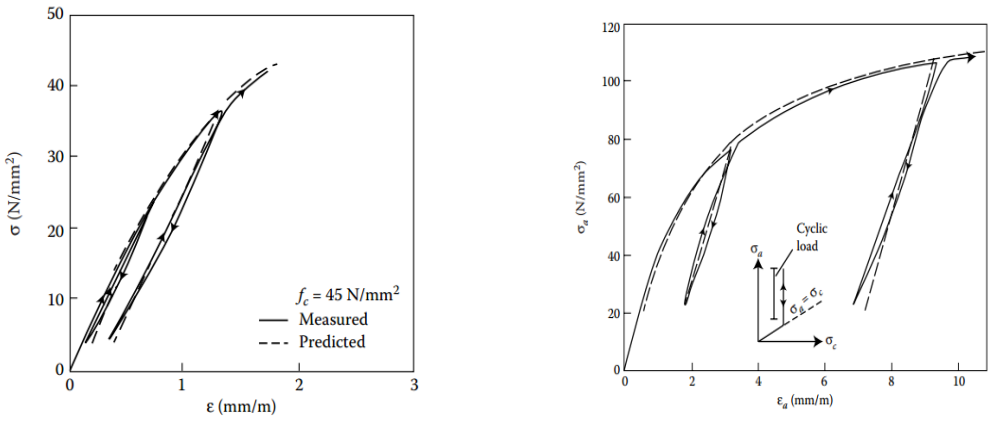

(a) (b)

Fig. 4.11 Stress-strain relationships (measured and predicted) for a typical concrete (with f_c=45 MPa) under (a) uniaxial and (b) triaxial compression. [3]

4.5 Concrete under uniaxial tension

The nonlinear behavior of concrete basically results from its tensile failure which occurs in the early stages of stress, while the tensile capacity of concrete is really low and it is about 5-10% of its compressive strength. The tensile capacity of concrete is often neglected after tensile failure occurs for design purposes. However, experimental evidence show that concrete presents a small tensile strength after failure, developing a softening regime.

Duda [102], shows that before the specimen reach its tensile strength, additional microcracks accumulate in a weak region forming a microcrack band of width *h* as illustrated in Fig. 4.12.

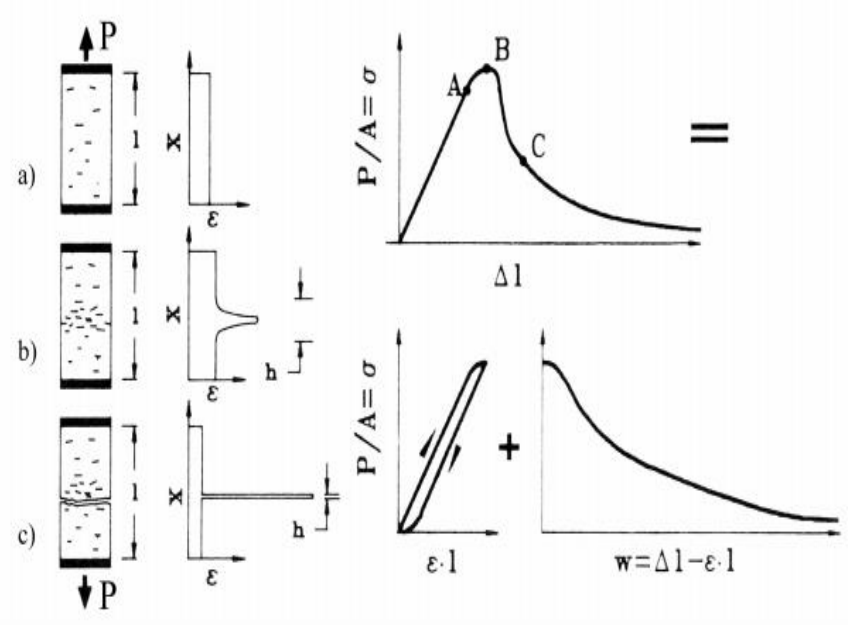

Fig. 4.12 Behavior of concrete under tensile stresses. [102]

Typical stress-deformation responses of concrete subjected to uniaxial tensile deformation under cyclic loading and reversed cyclic loading are illustrated in Fig. 4.13. The basic characteristics of the behavior of tensile concrete are summarized by Lowes [103]:

1. The behavior of concrete is basically linear elastic until the stresses reach the tensile strength. At this stage, small number of stable microcracks are opened.
2. After the tensile strength has been reached, any further loading results in loss of load capacity. This behavior leads to the development of continuous cracks.
3. The unloading-reloading cycles that initiate after the tensile strength, present a significantly low material stiffness due to the remaining cracks that are opened under the peak tensile stress.

However, according to Kotsovos and Pavlovic [67] the descending branches in tension do not have a reliable experimental basis. Furthermore, they show that the strain-softening branches may lead to numerical instabilities as concerned the modeling of cracked concrete. Cracked concrete can contribute to the overall stiffness and strength of the structure by activating the mechanisms of “aggregate interlock” and “tension stiffening”. The former is referred to the remaining stiffness due to aggregate interlocking along the crack’s surface, while the latter is correlated to the fact that the concrete in between cracks (where the stresses are below the tensile strength) contributes to the overall stiffness of the system, as the tensile stresses are

transferred from steel to concrete. The "tension stiffening" is usually modelled with the use of a post-peak descending branch as a gradually descending strength in the cracked concrete region. It is concluded by the study presented in [67] that these mechanisms play a negligible role in the load carrying capacity of a member highlighting the brittle nature of concrete.

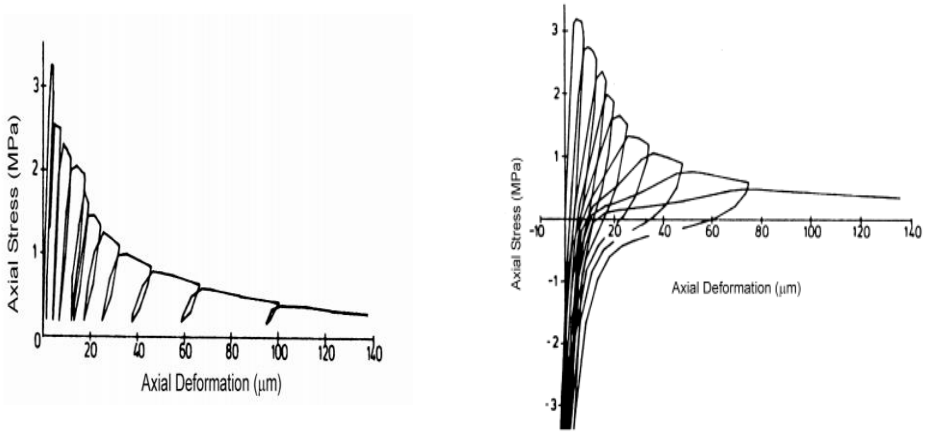

(a) (b)

Fig. 4.13 Stress-deformation response for concrete subjected to (a) cyclic tensile loading, (b) reversed cyclic loading. [104]

4.6 Concrete subjected to shear

Shear stresses that subject to concrete areas cause the development of cracking perpendicular to the orientation of the principle stress. Therefore, the material behavior of concrete is similar to the concrete response under tensile loading. The concrete response under shear loading can be modeled as a material behavior that combines compression and tension stress states. However, the cracked concrete can also develop mechanisms in order to withstand shear loading.

Shear transfer across the crack's surfaces has been the subject of many experimental investigations. Experimental studies, usually use pre-cracked specimens and then subject to shear loading across the established crack surface. In this way, for relatively small crack widths load transfer across the crack plane takes place through the "aggregate interlock" (as mentioned in the previous subsection). This mechanism is referring to the development of bearing forces between pieces of aggregate (see Fig. 4.14). It is obvious that the capacity of the system is determined by the width of the crack opening.

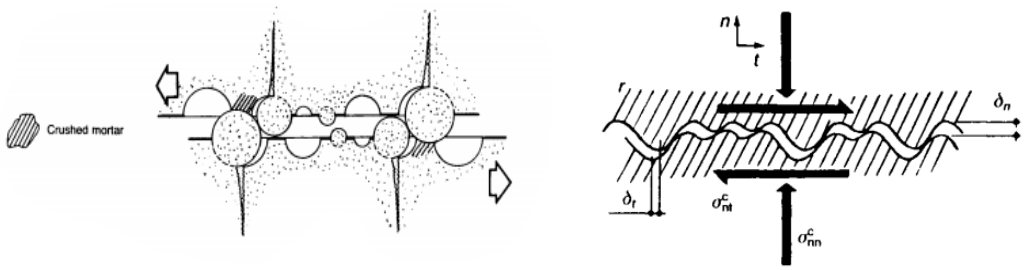

(a) (b)

Fig. 4.14 Schematic representation of the mechanism "aggregate interlock" (a) crack morphology, (b) stresses that caused by the slip of the crack surfaces. (CEB [105]*)*

In the case when reinforcement is crossing the crack plane, allows the steel reinforcement to contribute to the shear capacity and stiffness of the structure. This mechanism is called “dowel action” because the steel bars which connect the two crack faces act as “dowels” as illustrated in Fig. 4.15 (a). Both mechanisms (“aggregate interlock” and “dowel action”) are very sensitive to the cyclic loading conditions and of the associated slip along the crack. The cyclic loading can lead to smoother crack surfaces that reduce the effectiveness of aggregate interlock. Furthermore, the “dowel action” can cause concrete crushing locally and reduce significantly the bond connection between concrete and steel bars. Subsequently the effectiveness of the mechanism is severely decreased. The dowel action-slip curves under cyclic loading condition are depicted in Fig. 4.15 (b) as described in Vitzileou and Tassios [106].

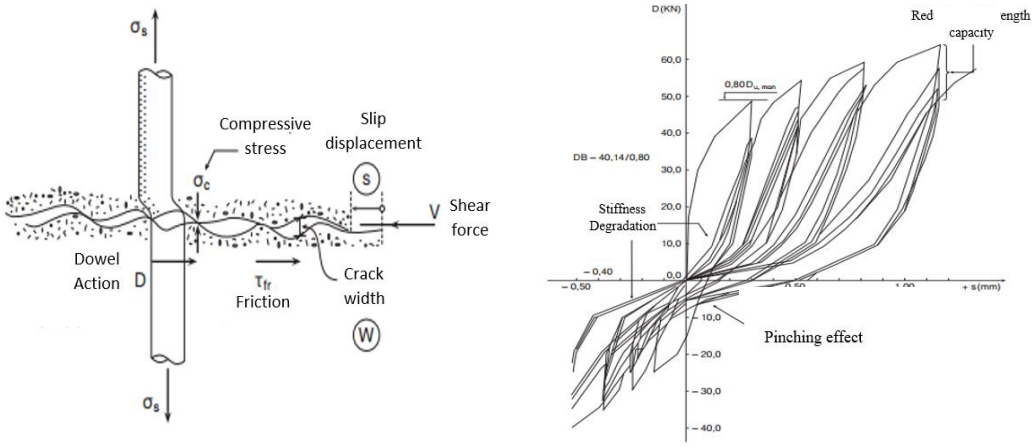

Fig. 4.15 Schematic representation of the mechanism “Dowell action” (a) crack morphology, (b) Dowel action-slip curves under cyclic loading conditions. [106]

The basic characteristics of the behavior of cracked concrete under shear loading are summarized in Lowes [103]:

1. The shear capacity and the stiffness of a crack plane are increasing with the increase of the concrete strength and they are decreasing with the increase of the crack width.
2. The size and shape of the concrete aggregates have relatively little effect on shear strength and stiffness.
3. Generally, the shear resistance reaches a maximum strength of $0.20f_c$ to $0.30f_c$ and then begins to decrease when concrete is subjected to monotonically increasing slip across the crack plane.

4.7 Time dependent properties

4.7.1 Shrinkage

Shrinkage of concrete material is the time-dependent phenomenon where the volume change of concrete occurs without any external loading. The water moves out of the concrete medium in stages when concrete is not fully rigid and that movement leads to contraction. The total shrinkage deformation can be separated into four different components:

a. Plastic Shrinkage or capillary shrinkage, occurs when water is lost by evaporation from the surface of the concrete, while it is still in the plastic state. If the amount of water lost per unit area exceeds the amount of water brought to the surface by bleeding, surface crack can occur known as plastic shrinkage cracking.

b. Autogenous shrinkage or self-desiccation shrinkage or chemical shrinkage is correlated with volume changes after setting has taken place. The continued hydration can lead to shrinkage phenomenon when no moisture movement to or from the cement paste is permitted. Autogenous shrinkage tends to increase at higher temperatures, with a higher cement content and possibly with finer cements. Member size and the moisture content in the surrounding environment do not affect autogenous shrinkage. For normal strength concrete, autogenous shrinkage is relatively small compared to drying shrinkage.

c. Drying shrinkage is caused by the water reduction in concrete to the level of moisture that the surrounding air contains. As the water content increases, the hardened paste expands and drying produces shrinkage. A portion of this volume change is irreversible as illustrated in Fig. 4.16.

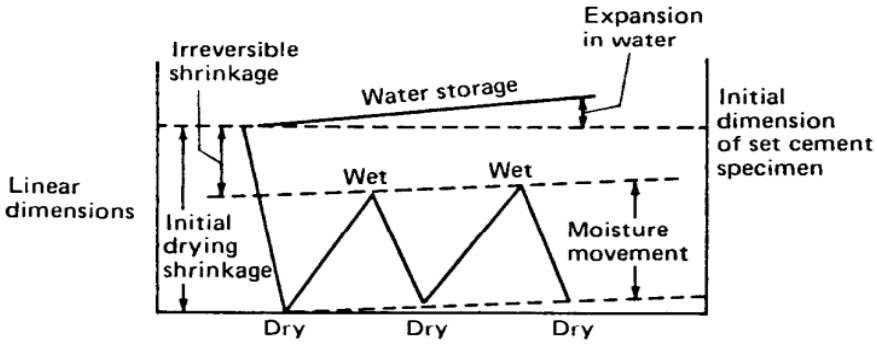

Fig. 4.16 Schematic representation of changes in dimensions of cement pastes, mortars and concretes with moisture conditions. [107]

The movement of moisture depends upon the following factors:

1. Range of relative humidity
2. Composition of the concrete
3. Degree of hydration at the time of initial drying.

The ratio of autogenous and drying shrinkage in total shrinkage is schematically illustrated in Fig. 4.17

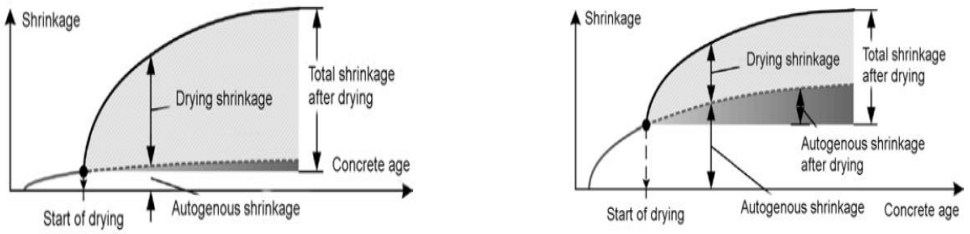

Fig. 4.17 Shrinkage strain components in (a) normal and (b) high-strength concrete [108].

d. Carbonation shrinkage which is caused by the reactions of carbon dioxide CO_2 present in the atmosphere with the hydrated cement minerals in the presence of

moisture. The action of CO_2 takes place even in small concentrations such as present in rural air, where the content of CO_2 is about 0.03% by volume. The contribution of carbonation shrinkage is limited to the outer zones and is negligible in most cases.

4.7.2 Creep

Creep is the physical phenomenon for the time-dependent increase of strain at constant stress and it is considered to be directly related to the stress state and temperature of concrete. The phenomenon of creep is occurred due to the re-arrangement of water particles in consequence of internal stresses and deviations. Therefore, the creep behavior is mainly governed by the consistency of cement paste. Creep will increase if the ratio of cement paste is high compared to the aggregates or if the aggregate stiffness is small. Furthermore, large creep strains can be caused by large water cement ratio.

For the analytical description of the value of creep, it is convenient to split the creep into several components. It was observed that creep has not only irreversible but also reversible components. Furthermore, the reversible strains are appeared with some delay. The development in time of the delayed strain component varies considerably among various materials. Consequently, the reversible component is referred to as delayed elastic strain ε_{cd} and the irreversible is flow ε_{cf} as shown schematically in Fig. 4.18.

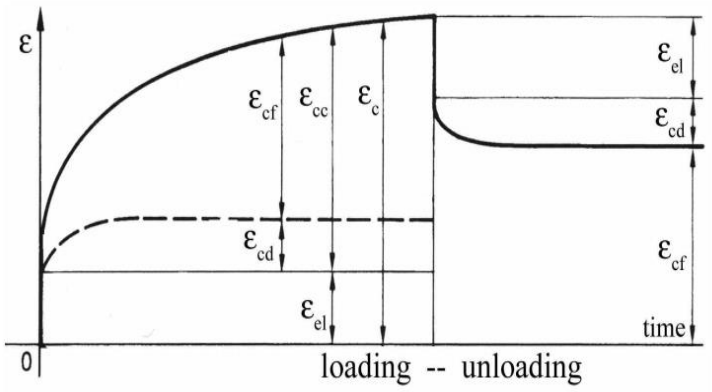

Fig. 4.18 Schematic representation of creep strain components. [108]

Fig. 4.18 shows that for a constant internal stress state and temperature around a concrete specimen, the rate of strains attributed to creep, decreases geometrically converging to a steady state which is constant (Ross et al. [109], England [110], Browne [111], Lykidis [112] and Grübl [108]).

Creep can also be assumed that is separated by two other components: basic creep and drying creep. Basic creep occurs under a condition of no moisture to or from the environment whereas drying creep is the additional creep that occurs during drying of concrete. Finally, another way to differentiate creep comes from the observation that a considerable portion of flow occurs on the first day after the sustained load is applied. Therefore, creep can be divided to short-time creep and long-time creep. Short time creep is caused by stress-induced redistribution of water while long time creep is caused by displacement of particles in the hardened cement paste (Wittmann [113]).

4.7.3 Rate of loading

Many researchers have investigated the effect of load rate on concrete material response. Since the purpose of this study is the analysis of reinforced concrete members and structures subjected to static cyclic and earthquake loading conditions, it is considered that the response of concrete is subjected to rapid load rates. Researchers associate load rate for materials with applied strain rate. Mahin et al [114] show that the maximum strain rate in RC structures subjected to severe earthquake ground motion is between 0.001 per second and 0.25 per second. In order to examine the load rate effect on the response of the concrete structure, it is necessary to study the variation in material properties that cause compressive, tensile strength and material stiffness to change.

Ross et al. [115],[116] have proposed a relationship that derives from the basis of fracture mechanics and calibrated to fit experimental data, while the relationship of Yon [117] fits empirical data. Additionally, Hughes and Watson [118] showed experimental data which are derived from impact tests on concrete cubes for the effect on compression strength of concrete. The data are illustrated in Fig. 4.19, where it can be seen shows that the increased strength in not significant for the strain strength of interest.

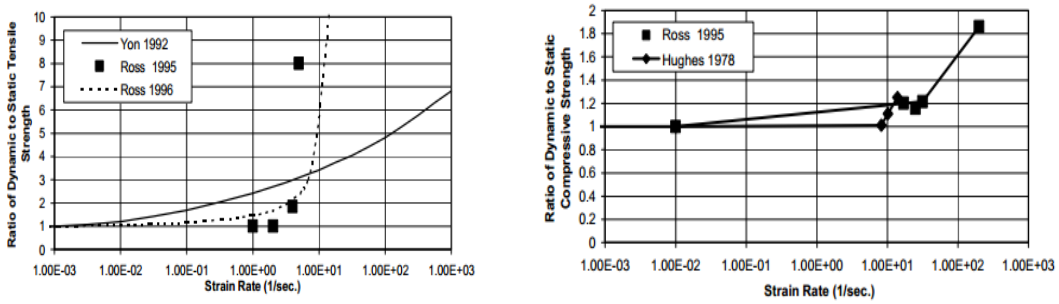

(a) (b)

Fig. 4.19 Effect of strain rate on concrete (a) tensile, (b) compressive strength. [103]

4.8 3D Constitutive Modeling of Concrete Material

The heterogeneous composite material of concrete (a composite of aggregates and cement paste) is usually modelled as homogeneous, isotropic up to a stress level with material properties, which introduce triaxial and nonlinear characteristics of concrete. RC members, behavior is controlled by the two constituents (concrete and steel reinforcement) and therefore, is different than the behavior that characteristizes the two materials. Therefore, the two materials are usually modelled separately (discrete reinforcing bars) and it is assumed that the numerical models of the two materials (concrete and steel) describe reliably the behavior of this composite reinforced material.

The appropriate finite element modeling for simulating RC structures has to combine the proper constitutive modeling of materials, a complicated numerical problem that was the main research study of many researcher projects the last few decades. A microlevel approach which can describe the behavior of the aggregates, their connection with the cement paste and their interaction with the steel bars is a difficult task with prohibitively large requirements in experimental data and in computer time and memory. The experimental evidence obtained by specimens and structural members that describe the general characteristics of the materials of concrete and steel under different loading conditions, fits ideally with the macroscopic approach of modeling RC structures.

The constitutive models of concrete usually consisted by relations that are based on theories of elasticity, plasticity, thermodynamic laws, fracture, damage mechanics and the combinations of the above. These relations express the stress-strain relationships that describe the experimental behavior of concrete under compression and tension. These stress-strain relationships are enriched with material properties which are obtained usually from experimental evidence in order to correct the theoretical approach and make the relationships fit experimental data. Additionally, researchers use different approaches to describe the compression and the tension behavior of concrete. Usually the stress-strain curve under tension is elastic up to the tensile strength of concrete. Furthermore, they use different modeling-approaches to describe pre-cracking and post-cracking behavior under tension and compression.

The post-cracking modeling characteristics of concrete behavior is the main cause of nonlinear behavior of concrete. Many researchers emphasize on the post-cracking regions in order to realistically capture the mechanical behavior of RC structures. Modeling of cracking is treated with the smeared or discrete crack approaches. The most reliable modeling technique for numerically capturing the cracking phenomenon, is depended by the numerical simulation and the algorithmic approach of each model foreseeing numerical accuracy and computational efficiency. Although the discrete crack methods are more realistic, they increase the computational effort significantly making it prohibitive for modeling RC structures under cyclic loading conditions. Therefore, various models treat cracking through adopting different variants of the smeared crack technique.

The corresponding constitutive models treat RC as a non-homogeneous continuum with smeared properties. The material properties, the effect of cracking and the discrete steel reinforcement are locally averaged within the volume of an integration point of this type of element. In the next subsection, the most common constitutive models of RC structures will be presented that are used for cyclic loading conditions.

4.8.1 Elasticity-based models

4.8.1.1 Isotropic linear-elastic models

These models have the following form:

$$\sigma_{ij} = \frac{E}{1+\nu} \cdot \varepsilon_{ij} + \frac{\nu \cdot \mathrm{E}}{1+\nu} \cdot \varepsilon_{kk} \cdot \delta_{ij} \tag{4.1}$$

These type of models require only two material parameters: the Young's modulus of elasticity E and the Poisson's ratio ν. All the constitutive models use a linear elastic relation of this form in order to describe the tensile behavior of concrete until tensile strength and the compressive behavior of concrete up to a stress level lower than 50%of compressive strength.

4.8.1.2 Cauchy elastic-models

These models, generally are described by uniaxial stress-strain relations through the following form:

$$\sigma = f(\varepsilon) \tag{4.2}$$

These relations are obtained by fitting the numerical curves with the experimental data of the behavior of concrete under compression and tension. These type of models are characterized with simplicity, therefore, they are commonly used for RC members. The constitutive relations

of these models are not formed based on the thermodynamic standards. Many researchers believe that this kind of models may violate the laws of thermodynamic. Unless care is given, these models may generate energy under certain loading-unloading cycles. Such behavior is physically inadmissible since it violates the laws of thermodynamics.

4.8.1.3 Hyperelastic (Green-elastic) model

This kind of models is based on the assumption of the existence of a strain energy-density function W (or a complementary energy-density function Ω),

$$\sigma_{ij} = \frac{\partial W}{\partial \varepsilon_{ij}}, \ \varepsilon_{ij} = \frac{\partial \Omega}{\partial \sigma_{ij}} \tag{4.3}$$

The thermodynamic laws are always satisfied with the use of the above constitutive relations. However, the material constants of this class of materials do not have physical interpretation in general, so that it is not easy to quantify the values of those constants experimentally.

4.8.1.4 Hypoelastic model (incremental type)

This type of models describe the material behavior in terms of the increments of stress $(d\sigma_{ij})$ and strain $(d\varepsilon_{ij})$. The stress-strain relations are then expressed by using the tangent stiffness $\boldsymbol{D}^{t}_{ijkl}$ matrix which varies with the current stress state and have the following form:

$$d\sigma_{\boldsymbol{ij}} = \boldsymbol{D}^{\boldsymbol{t}}_{\boldsymbol{ijkl}}\left(\sigma_{\boldsymbol{ij}}, \varepsilon_{\boldsymbol{kl}}\right) \cdot d\varepsilon_{kl} \tag{4.4}$$

These models are dependent on the deformation history. Furthermore, the behavior is becoming anisotropic at load levels near the strength of concrete and that leads to complicated formulation of the stiffness matrix.

4.8.1.5 Variable moduli model

These models have different forms for the material-response functions in case of loading, unloading and reloading. The models are generally irreversible even for incremental loading. The models, aimed at describing pre-peak concrete behavior in the combined states of tension-tension, tension-compression and compression-compression with a low hydrostatic pressure. Generally these models are reasonably good at describing moderate nonlinear concrete behavior but they become complicated for practical use when multiple loading conditions are under study. Additionally, they are not based on solid mechanical foundations.

4.8.2 Plasticity-based models

4.8.2.1 Classical

The model is based on the idea that the total strain is separated into an elastic and a plastic component such as:

$$d\varepsilon_{ij} = d\varepsilon^{e}_{ij} + d\varepsilon^{p}_{ij} \tag{4.5}$$

These models contain three basic characteristics:

a) Yield surface (von Mises, Mohr-Coulomb, Drucker-Prager, Tresca-Guest, Huber-Mises-Hecky, Mroz multi-surface plasticity) that defines the stress level where the plastic deformation begins.

b) Hardening rule, which regulates the evolution of the subsequent loading surfaces during the course of plastic flow. Three different hardening mechanisms are used:

    1. Isotropic hardening where the surface undergoes an isomorphic expansion depending on a parameter usually related to the total plastic deformation.

    2. Kinematic hardening where the loading surface does not change shape but it is transformed depending on the plastic strain increment or on the current stress level.

    3. Mixed mechanism that is a combination of the above.

c) Flow rule which defines an incremental plastic stress-strain relationship by using a plastic potential function. Therefore:

$$d\varepsilon_{ij}^{p} = d\lambda \cdot \frac{\partial Q}{\partial \sigma_{ij}} \tag{4.6}$$

Where, $d\lambda$ is a proportionality constant (plastic multiplier) and Q is the plastic function. If the plastic function Q coincides with the failure surface, then the flow rule is associated. If the plastic potential is different to the failure function, the flow rule is referred to as non-associated flow rule.

4.8.2.2 Elastoplastic fracture models

This type of model exhibits an elastic behavior during the state of unloading from a given stress state on the yield surface and reloading to the same state on the yield surface. The following equation describes the elastic material behavior:

$$\dot{\sigma} = C \cdot \left(\dot{\varepsilon} - \dot{\varepsilon}_{pl} \right) \tag{4.7}$$

In cases of cyclic loading conditions, excessive cracking will appear in concrete regions which leading to the decrease of the elastic modulus. The degradation of the elastic material moduli depends on the increase of the deformation and it is mathematically expressed as follows:

$$\dot{\sigma} = C \cdot \dot{\varepsilon}_{el} + \dot{C} \cdot \varepsilon_{el} \tag{4.8}$$

Where, $\dot{\varepsilon} = \dot{\varepsilon} - \dot{\varepsilon}_{pl}$ and $\dot{C}$ denote the rate of the elastic material moduli.

These models can describe better the nonlinear behavior of concrete than the classical plasticity models. However, many material parameters are introduced associated with the fracturing theory that have to be defined in an attempt to provide accuracy and numerical stability during the solution process. These models become more complex when they are used to simulate 3D constitutive behavior. Especially in cases of cyclic loading conditions, there are many numerical problems, which are associated with the fact that one element can experience both fracture and plasticity strains in different directions simultaneously. It is evident that few numerical approaches with 3D elastoplastic fracture models have succeeded to be used for the simulation of RC members under cyclic loading conditions.

4.8.2.3 Endochronic models

These models acquire their formulation through the concept of intrinsic time (or endochronic time) which can be defined in terms of strain or stress used to measure the extent of change or damage of the structure subjected to deformation. This type of models contain an extensive set of functions that fit experimentally observed effects like inelasticity, inelastic dilatancy, strain softening and hardening, hysteretic behavior, degradation of elastic moduli, aging and rate dependency. They are characterized by the dependence of the viscosity of the strain rate in addition to its dependence on stress and strain.

The plasticity-based models can be viewed as a discontinuous material model that are separating the material responses into several stages. Loading, unloading and reloading processes can then be considered as different steps in the structural analysis and design, thus have considerably simplified analytical procedures. However, real material behavior is usually continuous and includes many complicated cross effects.

4.8.3 Damage mechanic models

The continuum damage mechanic models are based on thermodynamic laws and are usually used by many researchers to describe the nonlinear behavior of concrete caused by cracking. These models simulate the effect of void growth on material behavior by introducing an internal damage variable in the constitutive relation. The damage variable of a surface area *S*, has the following form:

$$D = \frac{S - \tilde{S}}{S} = \frac{S_D}{S} \tag{4.9}$$

Where, *S* is the overall section area, $\tilde{S}$ is the effective resisting area (due to the damage caused by microcracks). Therefore, S_D represents the surface of microcracks. This scalar variable D depends upon the point and the direction considered and is bounded by 0 and 1 such as:

- $D = 0$, this means that the material is undamaged.
- $D = 1$, this means that the material is fully broken in two parts.

The stiffness degradation can be expressed by the material damage. Therefore, the elasticity modulus of the damaged material is defined by the following expression:

$$\tilde{E} = E \cdot (1 - D) \tag{4.10}$$

The scalar damage variable is used for isotropic damage behavior, which is useful especially under conditions of proportional loading when the principal directions of the stresses remain constant. In the case of anisotropic damage, a tensorial representation of damage is used in order to cove the non-proportional load cases. In order to describe the behavior in three dimensions by using a one dimension variable D, which represents damage, it has to be assumed that the existence of energy potential can be derived from the state of laws and the kinetic constitutive equation. According to thermodynamic theory, two potentials are introduced and identified within the framework of the "State Kinetic Coupling theory" (Lemaitre and Marquis[119]). These models are usually combined with other elastoplastic models.

4.8.4 Microplane models

In this type of models, the constitutive properties of concrete are defined separately on planes of various orientations. As explained in Z. P. Bazant and P.C. Pratt [120], the constitutive law is characterized as a relation between normal (volumetric and deviatoric) and shear stresses and strains on these planes, called the microplanes. Therefore, the stress-strain relation is expressed independently on various planes in the material assuming that either the stresses on these planes are the components of the macroscopic stress tensor (static constrains) or the strain components on these planes are the components of the macroscopic strain tensor (kinematic constraint). The microplanes represent the weak planes that are formed in the concrete area as illustrated in Fig. 4.20

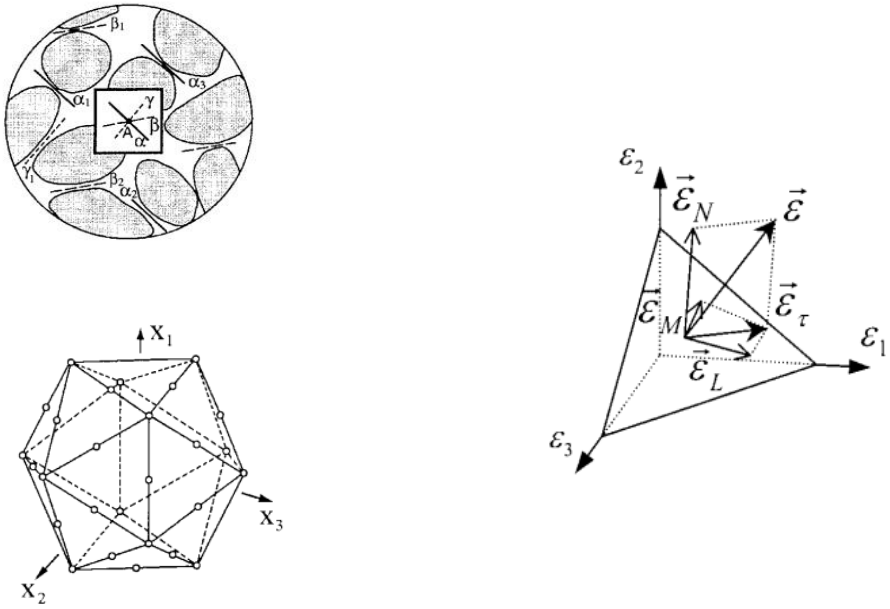

Fig. 4.20 Schematic representation of the microstructure with the microplanes on which stress and strain components are developed. [121]

According to CEB [105], these models are capable to model realistically the behavior of plain concrete under different various loading conditions. Additionally, the rate effect can be taken into account using these models, by combining damage with Maxwell's rheological model. Nevertheless, these models were not found to be suitable for full-scale RC structures modeling due to their large computational demands.

4.8.5 Crack models

The nonlinear behavior of concrete is characterized by microcracking that progressively leads to macrocracking and failure of the material. The simulation of the cracking effect on the concrete behavior is the most important feature of the constitutive modeling of concrete. The previous types of constitutive models usually are combined with a crack model in order to model the post-cracking behavior. When a tensile stress reaches the tensile strength of concrete, a crack is considered to occur. There are two categories of modeling cracking, thus, can be categorized into discrete and smeared crack methods.

Furthermore, there are other methods of representing the crack opening and the crack propagation. During the last decades, the Discrete element methods (Particle Hydrodynamics),

Meshless or Meshfree methods, and Isogeometric methods are used for fracture analysis illustrating good characteristics but currently with many numerical and computational problems to be solved. In the next subchapters, a brief representation of the crack models is presented emphasizing in the smeared crack approach which was the method adopted in this research work.

4.8.5.1 Discrete crack models

The discrete and the smeared crack approaches can be distinguished by the fact that the former models a crack as a geometrical discontinuity, whereas the latter assumes that the cracked concrete remains as a continuum region whereas a corresponding numerical modification of the constitutive material matrix is performed.

When the discrete crack model was first introduced, a geometrical discontinuity was developed when a crack formed at a predefined crack locations. It is obvious that this assumption introduced a bias in the solution process and consequently a different method was proposed in which cracks were represented by separation between the finite element edges (Ngo and Scordelis [122], Nilson [123]) as illustrated in Fig. 4.21. However, this approach implies a continuous change in the nodal connectivity, that does not fit the nature of the finite element displacement method. In this crack location finite element mesh depended because it is constrained to follow the element edges. As a consequence, the response obtained by this method is stiffer than the experimental one (CEB [105]).

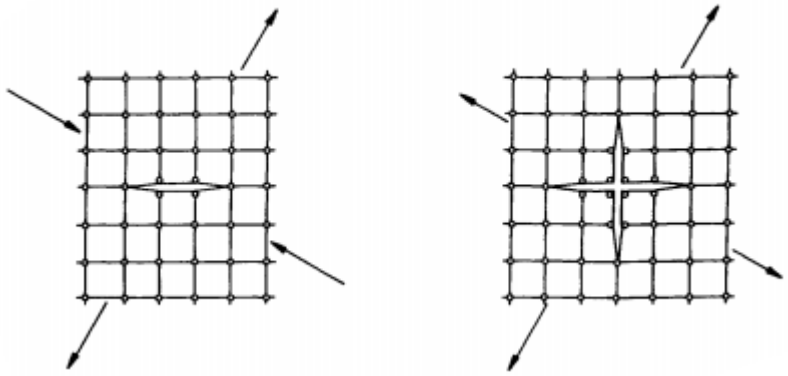

Fig. 4.21 Schematic representation of discrete crack modeling by nodal separation on adjacent elements. (CEB [105]*)*

Therefore, different methods for crack initiation and propagation have been proposed in order to overcome the drawbacks of the previous discrete crack approaches. Cracks are considered to be located inside the elements intersecting the sides of the element based on the work of Miguel [124], Gupta and Maestrini [125]. This introduces the need of re-meshing the existing finite element topology through different methods. As illustrated in Fig. 4.22, the intersecting crack points can become the nodes of the finite element mesh to which a neighboring existing node is moved. Another way of representing cracking, is to add new nodes at the intersecting points and create interelement boundaries which can separate the elements. In this case, the new nodes define the new interelement boundaries have to be provided from the beginning of the analysis, where cracks may potentially develop. These nodes are usually combined with linkage or contact elements and connect the two faces of the crack through normal stress-crack width and shear stress-shear slip-crack width relations. Additionally different types of these interface

elements can be used. Lumped interface elements (Ngo and Scordelis [122]) evaluate the tractions and displacement at isolated mode-set and continuous interface elements (Goodman et al. [126]) can smooth the behavior along an interpolated field.

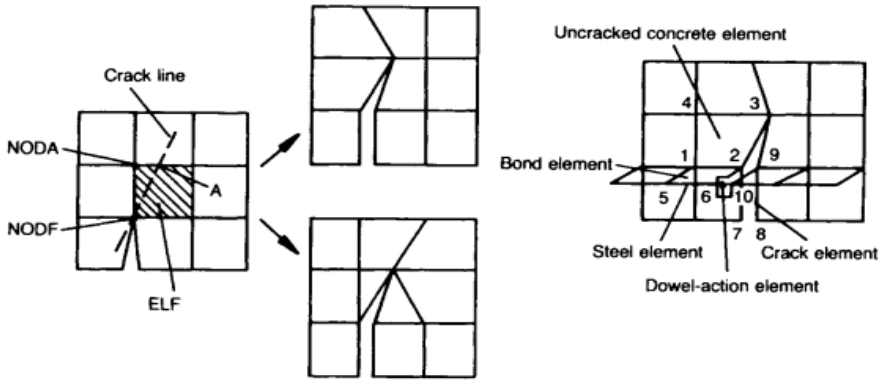

Fig. 4.22 Schematic representation of remeshing methods for discrete crack approach proposed byMiguel [124].

Although, discrete crack models are close to the physical concept of fracture, by introducing discontinuities to represent cracking, the method is restricted to the analysis of simple concrete members. These members usually present initial local discontinuities and are subjected to monotonic loading conditions such that the orientation of the crack propagation can be predicted. The need of remeshing or introducing new interpolation fields in the predefined crack locations, increase significantly the computational cost constituting this modeling technique unable to be used for the analysis of RC structures with multiple loading conditions and thereafter full-scale RC structures. This explains the fact that when the overall behavior of a concrete structure that presents distributed fracture phenomena, the smeared crack approach has gained much wider acceptance from the international scientific community.

4.8.5.2 Smeared crack models

As previously stated based on the smeared crack approach, the cracked solid is assumed to continue to behave as a continuum when cracking occurs. The basic idea of the smeared crack approach, is to take into account the cracking effects by modifying the stiffness properties at the corresponding integration points where the criterion of tensile failure is satisfied. The main advantage of this approach is the fact that it models cracking without the need of remeshing or any kinds of change of the existing mesh typology like the discrete crack approach as explained in the previous subsection. Usually, the common RC structure is characterized with distributed fracture especially at concrete members such as beam-column joints and shear walls, which have densely distributed reinforcement and present diffused cracking subjected to monotonic or cyclic loading conditions (see Fig. 4.23).

Therefore, the smeared crack approach fits the experimental evidence in regards to the study of the macroscopic behavior of RC members and full-scale structures subjected to multiple loading conditions. When cracking appears, the material behavior change from isotropic stress-strain law to orthotropic law, with the axes of orthotropy being determined according to a condition of crack initiation. The smeared crack concepts can be categorized into the standard (orthogonal) fixed, multi-directional (non-orthogonal) fixed and rotating smeared crack concepts. In the next subsections, a brief description of these concepts will be presented.

(a) (b)

Fig. 4.23 Schematic representation of crack patterns in (a) RC shear wall [127] *and (b) beam-column RC joint* [3].

4.8.5.2.1. Standard fixed smeared crack models

When the principle tensile stress developed at an integration point, exceeds the tensile strength of concrete, then a crack is opened and the material matrix should be formed accordingly in order to introduce the anisotropic post-cracking behavior. The uncracked behavior is usually treated as an isotropic material behavior. When cracking occurs, the material behavior is changed to an orthotropic law, which is expressed with reference to the fixed principle axes of orthotropy (*n, s, t)*, where *n* refers to the direction normal to the crack (mode I) and (*s,t)* refer to the directions tangential to the crack (mode II and mode III). This is expressed as follows:

$$\begin{bmatrix} \sigma_{nn} \\ \sigma_{ss} \\ \sigma_{tt} \\ \sigma_{ns} \\ \sigma_{st} \\ \sigma_{tn} \end{bmatrix} = \begin{bmatrix} E_{nn} & E_{ns} & E_{nt} & 0 & 0 & 0 \\ E_{ns} & E_{ss} & E_{st} & 0 & 0 & 0 \\ E_{nt} & E_{st} & E_{tt} & 0 & 0 & 0 \\ 0 & 0 & 0 & G_{ns} & 0 & 0 \\ 0 & 0 & 0 & 0 & G_{st} & 0 \\ 0 & 0 & 0 & 0 & 0 & G_{nt} \end{bmatrix} \cdot \begin{bmatrix} \varepsilon_{nn} \\ \varepsilon_{ss} \\ \varepsilon_{tt} \\ \gamma_{ns} \\ \gamma_{st} \\ \gamma_{tn} \end{bmatrix} \tag{4.11}$$

The direction of cracking which is defined by the principle tensile stress that causes cracking (or it is predefined by predicting the direction of cracking), remains fixed until the end of the analysis. According to Rashid [128], Červenka [5] and Valliapan and Doolan [129], the E_{nn}, E_{ns}, $E_{nt,}$ $G_{ns,}$ G_{nt} have to be set equal to zero. This leads to the crack normal stress σ_{nn} and shear stresses σ_{ns} and σ_{tn} being abruptly set to zero when cracking occurs. It is believed that this assumption may be crude and it could introduce some numerical instabilities to the analysis (Rots and Blaauwendraad [130]). Therefore, many researchers use the isotropic expression for the material matrix with the initial elastic properties adding some reduction factors for the normal and the shear modulus (Bazant and Oh [14], Leibengood et al. [14] and Rots et al.

[131]). This modeling approach, implies that the second crack is forced to be orthogonal to the first one. This method has been observed to result much stiffer mechanical response than the actual one (Rots and Blaauwendraad [130], Crisfield and Wills [132] and Barzegar [133]). Therefore, the multidirectional (non-orthogonal) fixed smeared crack approach was thereafter introduced.

4.8.5.2.2. Multidirectional fixed smeared crack models

This approach allows the second crack to be formed in its actual direction (normal to the principle tensile stress) only if the angle of the first crack direction with the second one exceeds a certain threshold value which is empirically chosen. Obviously, the angle of the third crack direction with both the first one and the second one have to exceed the threshold value.
Another approach according to Barzegar [133], was the use of multidirectional non-orthogonal cracking combining with the concept of strain decomposition in cracked concrete. According to this concept, the strain increment tensor is decomposed into one component for the intact concrete between the cracks and as many additional components as the number of multidirectional cracks at a point. The strain and stress increment tensors that are associated with each one of the multidirectional cracks, are obtained by appropriate rotation transformations from the local coordinate system of each crack to the global system.

It is worth mentioning that, after cracking the zero shear modulus can lead to significant numerical instabilities. Therefore, a shear retention factor is included in cases of fixed smeared crack approaches in order to avoid these instabilities. This shear factor is usually a constant value less than 1.0 (Wang et al. [134]) or it is progressively decreased as the strain component normal to the crack plane is increased (Bathe et al. [135] and Hibbitt et al. [136]). In the case of the orthogonal smeared crack approach, the shear retention factor value can lead to stiffer responses and introduce some stress locking phenomena. The use of a law value of shear retention factor to a non-orthogonal approach has negligible effect to the response as it will be shown Chapter 6. This factor can be connected with the mechanism of the aggregate interlock in allowing the development of bearing forces between pieces of aggregate. The multidirectional smeared crack approach is used in this study and it is analytically presented in Chapter 5.

4.8.5.2.3. Rotated smeared crack models

This approach has been proposed by Gupta and Akbar [137] and forces the direction of orthotropy to coincide with the instantaneous principle directions of smeared strain. This means that the axes of material orthotropy co-rotate with the axes of principle strain. Therefore, the crack loses its physical meaning and follows the most predominant crack direction at a point, without retaining any memory of the previous history of cracking directions. The stress and strain vectors in the global coordinates are defined by the transformation of rotation from the local coordinates which coincide with the principle coordinate system. The value of the effective shear modulus is less important than it is in the case of the fixed crack approach, given that the shear strains are equal to zero, while the local coordinates are coincident with the principle strain coordinates. However, according to Bazant [138], the assumption of material orthotropy generally implies the rotation of principle stress to deviate from the rotation of principle strain. Therefore, the shear modulus has to be defined accordingly, in order to enforce coaxiality between principal stress and strain. For instance, the tangential shear modulus G_{12}, referred to the principal axes 1 and 2 takes the following form:

$$G_{12} = \frac{(\sigma_{11} - \sigma_{22})}{2(\varepsilon_{11} - \varepsilon_{22})} \tag{4.12}$$

The linearized tangential stress-strain law for a consistent rotating crack concept has the following form (Rots and Blaauwendraad [130]):

$$\begin{bmatrix} \Delta\sigma_{11} \\ \Delta\sigma_{22} \\ \Delta\sigma_{33} \\ \Delta\sigma_{12} \\ \Delta\sigma_{23} \\ \Delta\sigma_{31} \end{bmatrix} = \begin{bmatrix} \frac{\partial\sigma_{11}}{\partial\varepsilon_{11}} & \frac{\partial\sigma_{11}}{\partial\varepsilon_{22}} & \frac{\partial\sigma_{11}}{\partial\varepsilon_{33}} & 0 & 0 & 0 \\ \frac{\partial\sigma_{22}}{\partial\varepsilon_{11}} & \frac{\partial\sigma_{22}}{\partial\varepsilon_{22}} & \frac{\partial\sigma_{22}}{\partial\varepsilon_{33}} & 0 & 0 & 0 \\ \frac{\partial\sigma_{33}}{\partial\varepsilon_{11}} & \frac{\partial\sigma_{33}}{\partial\varepsilon_{22}} & \frac{\partial\sigma_{33}}{\partial\varepsilon_{33}} & 0 & 0 & 0 \\ 0 & 0 & 0 & \frac{\sigma_{11} - \sigma_{22}}{2(\varepsilon_{11} - \varepsilon_{22})} & 0 & 0 \\ 0 & 0 & 0 & 0 & \frac{\sigma_{22} - \sigma_{33}}{2(\varepsilon_{22} - \varepsilon_{33})} & 0 \\ 0 & 0 & 0 & 0 & 0 & \frac{\sigma_{33} - \sigma_{11}}{2(\varepsilon_{33} - \varepsilon_{11})} \end{bmatrix} \cdot \begin{bmatrix} \Delta\varepsilon_{11} \\ \Delta\varepsilon_{22} \\ \Delta\varepsilon_{33} \\ \Delta\varepsilon_{12} \\ \Delta\varepsilon_{23} \\ \Delta\varepsilon_{31} \end{bmatrix} \tag{4.13}$$

Finally, it has been shown (Rots and Blaauwendraad [130]) that the multidirectional smeared crack model is reduced to the rotating crack model if:

- The shear modulus ensures coaxility and is expressed as shown in the Eq. (4.12)-(4.13).
- The threshold value is set to zero.
- The previous cracks become inactive and erased from the memory (assumed elastic unloading)

4.8.5.2.4. Stress locking effects and mesh sensitivity

Generally, smeared crack models seem to suffer from the numerical phenomenon known as stress-locking effect. This effect lead the model to develop excessive stiffness where numerical instabilities occur. The problem of stress locking is attributed to the imposed displacement continuity between softening cracked elements and neighboring uncracked ones. The problem is discussed in detail in Rots and Blaauwendraad [130] and it is illustrated in Fig. 4.24.

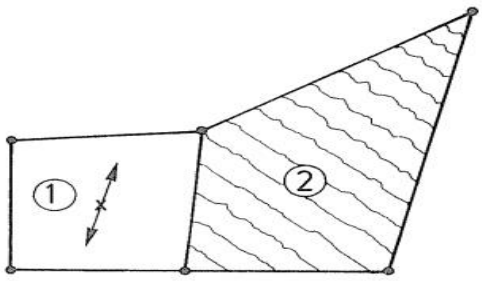

Fig. 4.24 Schematic representation of the interaction of a cracked element (2) with the uncracked neighboring element (1) when the smeared crack approach is used [130].

Element (2) in Fig. 4.24 is cracked as such that it causes an inclined displacement in element (1) that lead to the development of tensile stresses. Therefore, the stresses at element (1) which is in the elastic regime will increase. Consequently, the tensile stresses of element (1) will either exceed the tensile strength and start softening or it will not. This means that either the increase of the tensile stress will cause cracking leading to spurious cracking and discourages localization, or it will not cause cracking and the stress will be locked-in (spurious stiffening). The discrete crack approach realistically separate the elements when cracking occurs and there isn't displacement compatibility between cracked elements and neighboring uncracked ones. Therefore, the stresses at the crack become zero, which is a condition that agrees with the physical phenomenon. It has to be noted here that, the stress-locking does not disappear on mesh refinement since mesh refinement does not remove the fundamental assumption of displacement compatibility. Furthermore, the stress-locking effects are occurred whenever a smeared softening approach (also softening plasticity) is used to simulate localization (Rots and Blaauwendraad [130]). The problem becomes less serious when the rotating crack approach is used, or the fixed crack with a zero shear retention factor ($\beta = 0$) is adopted. However, the problem still remains present.

The problem of mesh objectivity is also attributed to the fact that the cracked softening elements interact with the uncracked neighboring elements. From the mathematical point of view, the mesh sensitivity problem is caused by the local loss of elipticity or equivalently loss of hyperbolicity for dynamic loadings (Rene de Borst et al. [72]). In Rene de Borst et al. [72], a simple one dimensional example is presented in order to indicate the instability problem which derives from the softening behavior of the elements. The problem is a bar subjected to tensile stress and it is discretized by *m* elements as shown in Fig. 4.25(a). It is assumed that one element has a tensile strength that is less than the others (*m-1)* elements. In this case, as shown in [72], the response of the bar is described by the following equation:

$$\bar{\varepsilon} = \frac{\sigma}{\mathrm{E}} + \frac{\mathrm{E} - h}{\mathrm{E} \cdot h} \cdot \frac{\sigma - f_t}{m} \tag{4.14}$$

Where $\bar{\varepsilon}$ the average strain of the bar, E is the Young modulus of elasticity, h is the softening material modulus, σ is the stress within the bar, f_t is the tensile strength and m is the number of elements that discretize the bar. The response described by Eq. (4.14) is illustrated in Fig. 4.25(b).

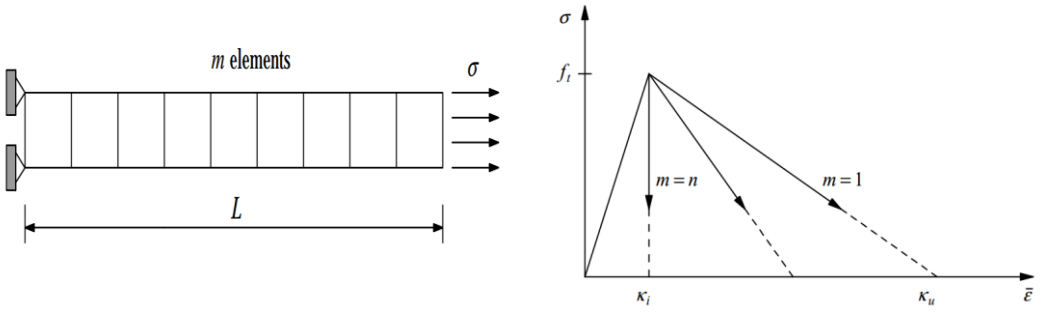

(a) (b)

Fig. 4.25 (a) Bar length L with an axial tensile stress σ, (b) Stress-strain response of the bar with one finite element exceeding its tensile strength. [72]

It is evident herein that as the number of elements increases, the post-peak curve becomes more brittle. Generally, it seems that the number of finite elements define or alter the response of the structural member. Therefore, when a mesh is refined, a more brittle behavior is obtained and the solution becomes very unstable. This numerical phenomenon is explained by the fact that, the solution process has many possible equilibrium states that depend on the mesh refinement (Eq. (4.14), Fig. 4.25b). The problem can be addressed when the assumption of the existence of the cohesive-zone models in front of the crack tip takes place (as shown in Fig. 4.26). For this scenario, at the front of the crack tip, a small-scale yielding or ductility occurs. The use of cohesive-zone model for quasi-brittle materials was first introduced by Hillerbog et al. [139] where they called it fictitious crack model and they widely used it in fracture modeling problems.

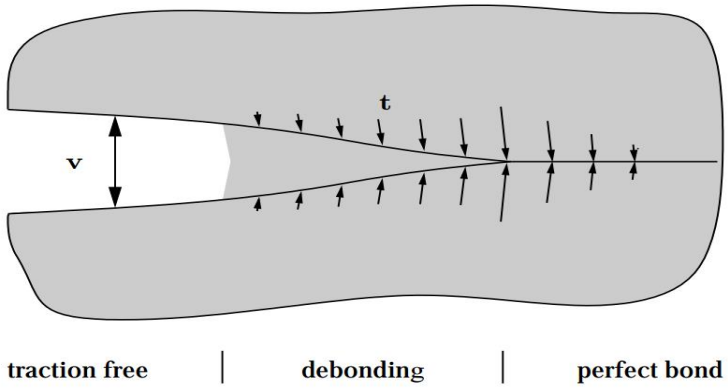

Fig. 4.26 Schematic representation of cohesive zone in front of the crack tip [72].

These models define the slope and the size of the softening curves in tension for quasi-brittle materials. These models use two material parameters, the tensile strength f_t and the fracture energy G_c that is the work needed to create a unit area of fully developed crack (corresponds to the area under the softening curve), and it is measured in J/m^2 (see Eq. (4.15)).

$$G_c = \int_{v_n=0}^{\infty} t_n dv_n \tag{4.15}$$

Where, t_n and v_n are the normal traction and the normal relative displacement across the fracture process zone respectively. The most commonly used decohesion relations are illustrated in Fig. 4.27 as they were presented in [72]. The fracture energy introduces an internal length scale into the model since the fraction G_c/E has the dimension of length.

The cohesive-zone can be used into a continuum formulation by distributing the fracture energy into the volume w in which the crack localizes (Bazant and Oh [14]). The length scale w is usually equal or proportional to the element size. Therefore, if a cohesive-zone model is used for the bar shown in Fig. 4.26, assuming a linear softening relation as illustrated in Fig. 4.27 (a) and defined as $w=L/m$ (with L the length of the bar and m the number of elements), the response of the bar is expressed by Eq. (4.14) that is transformed to:

$$\bar{\varepsilon} = \frac{\sigma}{\mathrm{E}} + \frac{2 \cdot G_c \cdot (\sigma - f_t)}{L \cdot f_t^2} \tag{4.16}$$

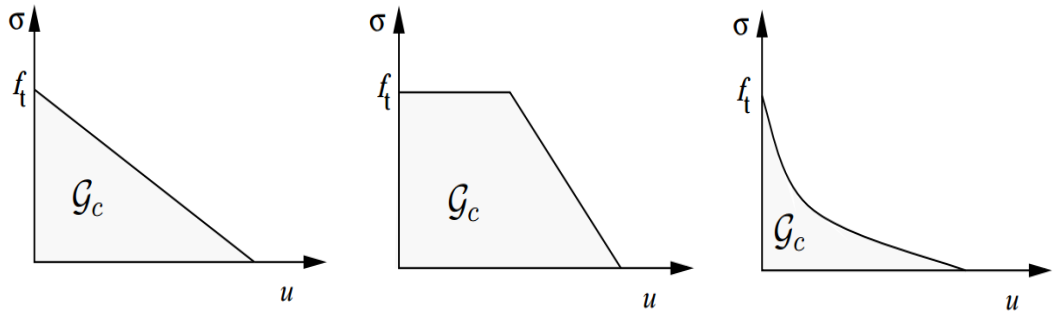

(a) (b) (c)

Fig. 4.27 Stress-displacement curves for (a) linear decohesion, (b) ductile solid and (c) a quasi-brittle solid [72].

As it can be observed, the number of elements *m* is disappears from Eq. (4.16). Therefore, the introduction of the fracture energy as a material parameter has made the relation stress-average and strain independent from the mesh refinement. However, Eq. (4.14) is defined by the value of *w* implying the connection of the model with the size of the elements. Many expressions have been proposed for defining parameter *w*. It is here noted, that the number of the equilibrium states is not reduced, but the numerical procedure is more stable because of the change of the softening branches given the introduction of the fracture energy, which produce more ductility for finer meshes.

4.8.5.3 Discrete Modeling

The Discrete Element Method (DEM) is a numerical method which assumes that the material is consisted of millions of particles. Therefore, it is used to model the bulk behavior of granular materials and many geomaterials such as coal, ores, soil, rocks, aggregates, pellets, tablets and powders. The particle discrete element method assumes particle elements that are rigid spheroid or disc shaped, and can overlap or detach. The contact forces between two particles are determined from the overlap and relative movements of the particle pair according to a specified force–displacement law. The method is usually coupled with other computational methods such as smooth-particle hydrodynamics (SPH) for problems involving fluid-structure interaction and computational fluid dynamics (CFD) for problems involving flow in porous material. Generally, the basic idea is to discretize the continuum media with relatively small discrete elements (tetrahedral, hexahedral, spheres) are connected to each other through special boundary conditions. Therefore, the discrete element method is a reliable approach for the simulation of granular material such as concrete. However, this approach is computationally expensive due to the large number of elements required when very small sizes during discretization are implemented and also is highly affected by the particle sizes that are used to discretize the concrete domain.

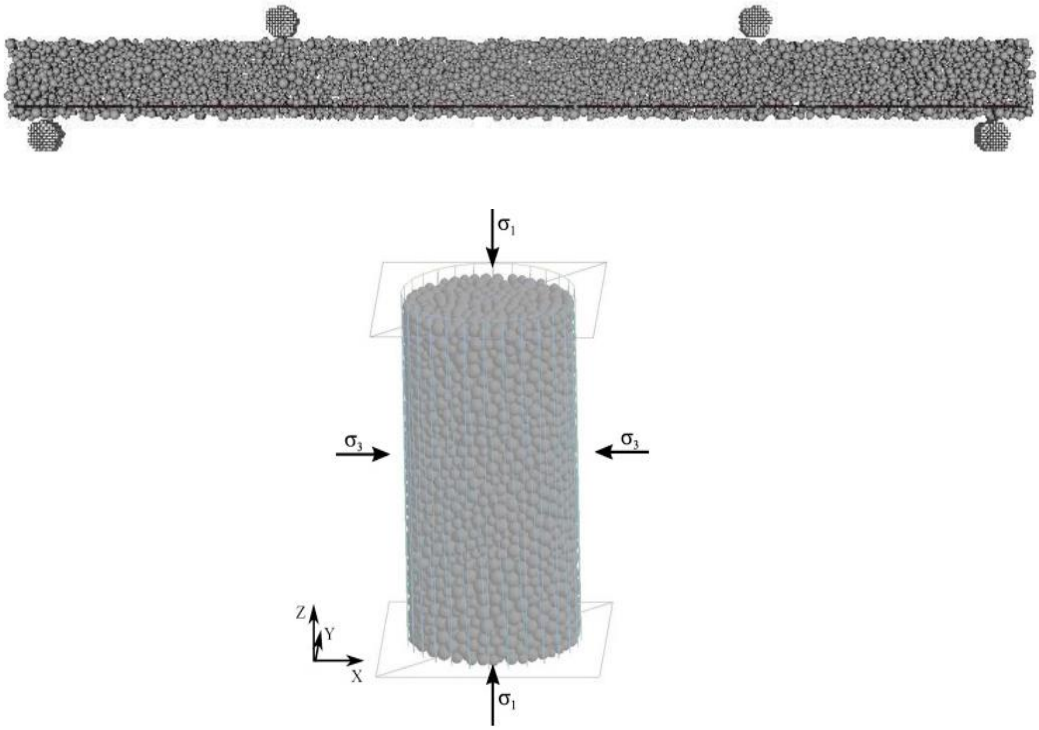

Fig. 4.28 Examples of discrete modeling of a RC beam and cylindrical concrete specimen ([140,141]*).*

Hentz et al. [140] defined an interaction range as a criterion to establish inter-particle bonds between neighboring particles. Azevedo et al. [142] used a multi-phase model by making a distinction between the particles that represent aggregates and those that represent the cement paste (see Fig. 4.28). Generally, this method is restricted to simulate single structural element problems due to its excessive computational cost. More details and literature about discrete methods can be found in Rousseau et al. [141], Hentz et al. [140], Onate et al. [143] and Sinaie et al. [144].

4.8.5.4 Meshless Modeling

While the finite element method is most frequently used numerical method for stress analysis, it suffers from some drawbacks. One is its, low accuracy when steep stress gradients have to be computed. This phenomenon affects the accuracy of linear elastic fracture mechanics since the elasticity solution presents singularities at the edges within the domain at the tip of cracks. Therefore, the crack initiation cannot be well predicted by using standard finite elements. Furthermore, the crack propagation necessitates remeshing around the crack tips because the geometry of the body has changed.

Meshless or meshfree methods do not require an explicitly defined connectivity between nodes for the definition of the shape functions. Each node has a domain of influence that does not depend on the arrangement of the nodes. Many approaches have been proposed for meshless modeling such as the element-free Galerkin method [145] and the partition-of-unity method [146]. The latter method can model the extension of a crack during the analysis being unbiased to the original discretization. This feature gives an advantage over the use of predefined

interface elements (discrete modeling). The meshfree methods can be used to model the crack propagation, crack branching (see Fig. 4.29) and even extreme cracking caused by explosive loading (see Fig. 4.30).

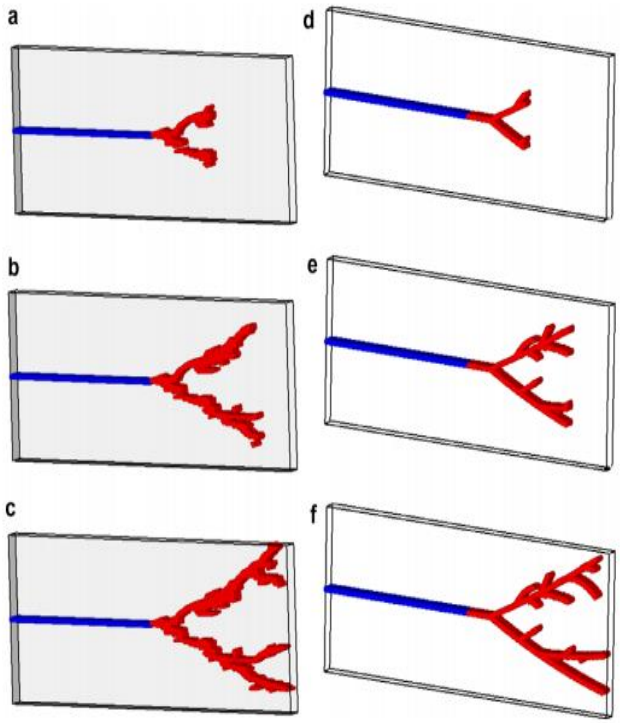

Fig. 4.29 Three-dimensional crack branching at different time steps for the cases of non-adaptive (a-c) and adaptive methods (d-f). [147]

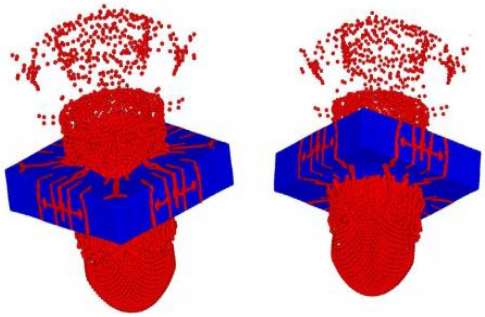

Fig. 4.30 Concrete slab under explosive loading using approximately 265,000 particles. [147]

As stated in Radczuk and Belytschko [147], the cracks can be arbitrarily oriented and their growth is represented discretely by activating of crack surfaces at individual particles providing a method which is less complex than the extended finite element method (Camacho and Ortiz [148], Ortiz and Pandolfi [149], Zhou and Molinari [150] and Belytschko and Gracie [151]).

4.8.5.5 Isogeometric Modeling

The basic idea of isogeometric analysis is to directly use the design for analysis purposes without the need of meshing operations. For engineering design purposes B-splines, NURNS and T-splines are the dominant tools for isogeometric analysis. For the analysis in non-linear solid mechanics, splines are indicated for the flexible insertion of discontinuities, providing a useful tool for fracture modeling including cohesive zone approaches. The ability to accurately

represent complex geometries is of particular interest in cohesive zone models. Additionally, higher-order continuity conditions can be achieved with the use of isogeometric finite elements. This is crucial in cohesive zone models since cracks can be modelled by smooth surfaces [152]. In Fig. 4.31, an example of a single-edge notched bean which is modelled with T-spline mesh and the corresponding contour plot derived from the analysis, are shown.

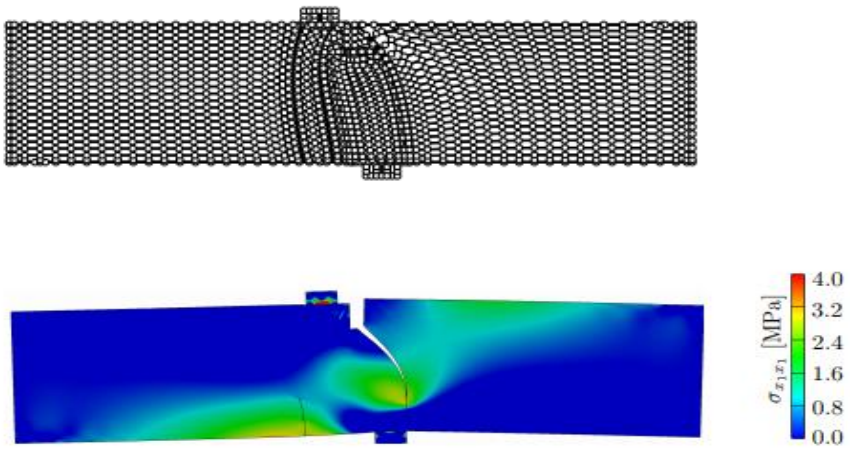

Fig. 4.31 T-spline mesh for a single-edge notched beam (up) and stress contour plot derived from isogeometric analysis (down). [152]

In general, the isogeometric method has not been excessively studied thus used for RC structure modeling, by accounting extreme material nonlinearities. Therefore, there is a need of future investigation towards this direction.

Chapter 5. Proposed constitutive modeling of concrete under cyclic loading conditions: State of the art and proposed algorithmic description of the model

Contents of Chapter 5

5.1 State-of-the-art in modelling of RC structures under cyclic loading conditions 79

5.1.1 Elasticity based and Elastoplastic uniaxial constitutive laws 79

5.1.2 Equivalent uniaxial strain concept 81

5.1.3 Bounding surface models 83

5.1.4 Microplane models 84

5.1.5 Models based on the compression field theory 85

5.1.6 Elasticity based and Elastoplastic models combined with fracture energy based smeared crack approaches 86

5.1.7 Hybrid modelling with different constitutive laws in different regions 87

5.1.8 Damage models and coupling between plasticity and damage modeling 88

5.1.9 Discrete approaches 89

5.1.10 3D elasticity based constitutive laws based on CFP theory combined with smeared crack approach 90

5.2 Mathematical description of non-linear stress-strain concrete behavior based on Kotsovos and Pavlovic material model 91

5.2.1 Three-moduli approach 91

5.2.2 Internal-stress approach 92

5.2.3 Combined approach 97

5.3 Strength envelope for concrete 99

5.4 Proposed algorithmic approach of constitutive modelling of concrete under cyclic loading conditions 100

5.4.1 Constitutive model of Concrete 100

5.4.2 Behavior of uncracked concrete under cyclic conditions 101

5.4.3 Behavior of cracked concrete under cyclic conditions 103

5.4.4 Compressive failure of concrete 111

5.4.5 Constitutive model of steel reinforcement 111

5.1 State-of-the-art in modeling of RC structures under cyclic loading conditions

The complex behavior of RC under biaxial or triaxial cyclically varying stresses necessitates fundamental investigations into the behavior of such structures. In addition, analytical or numerical models allow the extrapolation of experimental results to cover the many parameter variations that cannot be experimentally investigated because of the excessive number of required laboratory tests. Models are usually quite successful in providing failure load estimates for monotonic loading. It is obvious that a simple but reliable constitutive model is required to be developed and validated experimentally for predicting the behavior of cyclically loaded RC structures. This derives from the fact that the cyclic material properties of concrete are not well established yet, so there are no generally acceptable constitutive models yet.

Most of the models can describe only certain aspects of concrete behavior and their implementation is limited to examples of small practical interest. It is important to formulate a constitutive model by representing accurately the actual mechanical behavior of concrete structures. A literature review of the constitutive models used for the description of the cyclic loading behavior is described below. The models are categorized by their corresponding adopted constitutive modeling approach as it was presented in the previous chapter.

5.1.1 Elasticity based and Elastoplastic uniaxial constitutive laws

Most researchers use elastoplastic uniaxial constitutive laws in order to describe the mechanical behavior of concrete. The uncracked concrete is assumed to behave as an isotropic material, while after cracking an orthotropic constitutive law normal to the crack direction is used. Červenka [5] proposed an inelastic behavior of RC planar triangular elements subjected to in plane forces. The model used a uniaxial constitutive law of concrete which behaves as elastic-perfectly-plastic in compression and elastically in tension. For cracking the smeared crack approach is used. The proposed model was used for the analysis of shear walls under monotonic and cyclic loading conditions. This model succeeded to simulate the bending mechanism which is characterized by formation of plastic regions in the reinforcement and the behavior of concrete under compression. It failed though to capture the shear type failure mechanism which is characterized by opening of large diagonal crack. This study indicates the necessity of accurate simulation of bond-slip and multiple cracking during cyclic loading. Agrawal et al. [7] proposed an elastoplastic behavior for both concrete and steel reinforcement in order to simulate planar RC members under cyclic loads. This study predicts the setting of two open cracks in a concrete element and its major role for the cyclic behavior of concrete. The smeared crack approach is used to simulate cracking. In addition, a crack closure criterion was presented, where a set of cracks close when the strains arising out of the Poisson's ratio effect of stresses acting parallel to the cracks exceed the strains acting normal to them.

Rule and Rowlands [8], developed a nonlinear model with the use of constant-strain triangular elements in order to predict the ultimate capacity of RC structures under cyclic plane stress conditions. The study suggests that RC behaves like a strain-induced orthotropic material and steel reinforcement would provide some shear stiffness to the RC structure by introducing a nonzero shear modulus. Parabolic stress-strain relationships are used to simulate compressive and tensile behavior as illustrated in Fig. 5.1. The tangent modulus of elasticity would be calculated by differentiating the parabolic stress-strain relationship with respect to the strain. The model was validated by simulating the biaxial response of a cyclically loaded deep beam structural member.

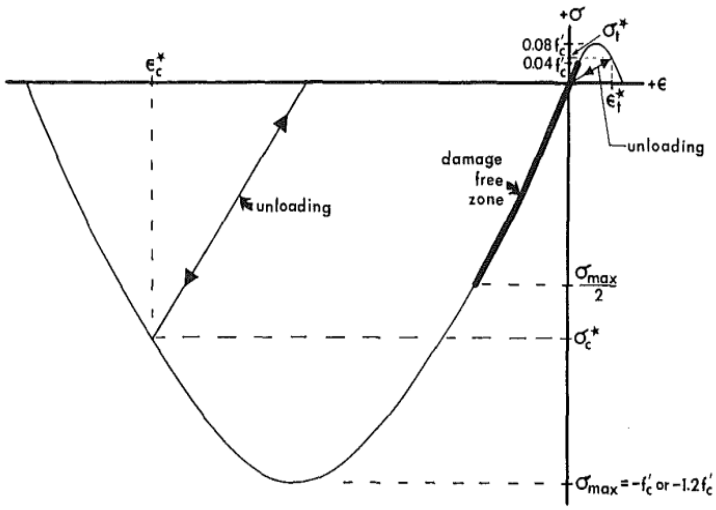

Fig. 5.1 Cyclic loading constitutive model for concrete according to Rule and Rowlands [8].

Kwan and Billington [15], implemented 8-noded plane-stress finite elements for investigating the influence of the material model and the method of simulating the postcracking characteristics of the hysteretic behavior of RC structures. The authors reported that the proposed model was able to describe efficiently the flexure-dominated behavior of the structures. The concluded remarks show that the selection of the crack model and the method of simulating the resisting shear stiffness of crack faces, have a great influence in the hysteretic behavior of concrete. Particularly, the fixed crack model with the constant shear retention factor, lead to an overestimation of the stiffness of the structure. The strain-softening response of concrete which is influenced by the confinement is necessary to be investigated extensively. Furthermore, based on the findings of this research work, it was concluded that the choice of an elastic or secant loading/reloading response of concrete does not have an important influence during the cyclic analysis. However the Bauschinger effect of steel material model has to be included in order to simulate the concrete's mechanical response accurately. Additionally the analysis has to model the buckling of steel reinforcement in order to capture realistic behavior on many structural components, in particular those with high axial compression loads.

Kwak and Kim [20], proposed a numerical orthotropic strain induced constitutive model for 2D analysis of RC shear walls subjected to cyclic loading conditions. The concrete domain is discretized by 4-noded quadrilateral elements. The stress-strain relationships of concrete are based on the Hognestad [153] curves. In order to include the biaxial behavior of concrete, a compressive strength reduction coefficient β introduced by Vecchio and Collins [154], is proposed. The unloading/reloading braches follow a hysteretic curve introduced by Pinto [34]. The Pinto [34] model is used until unloading and reloading curve reaches the monotonic envelope curve. Additionally, at the beginning of the second cycle, after the closure of the cracks, the stress-strain curve is assumed to be linear up to the maximum compressive strain experienced at the previous loading step. Their numerical model proposed a modification of the stress-strain law of steel reinforcement in order to simulate the pinching effects on the response of shear walls under cyclic loading as illustrated in Fig. 5.2.

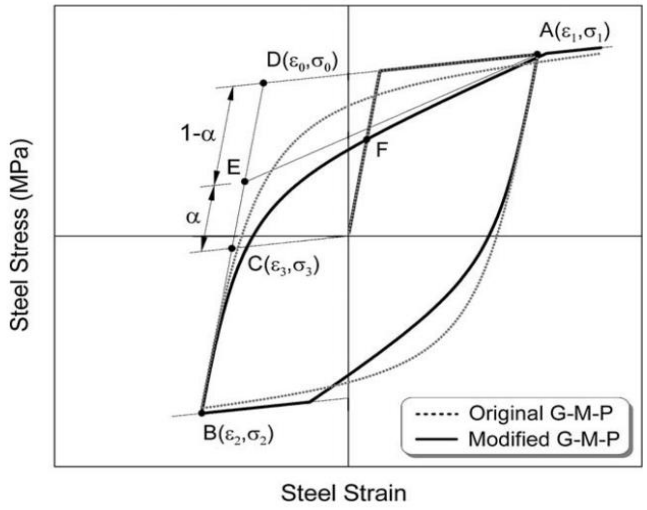

Fig. 5.2 Schematic representation of the modification of stress-strain relation of Giuffre-Menegotto-Pinto [34] *steel model* [20].

5.1.2 Equivalent uniaxial strain concept

Many researchers used the "equivalent uniaxial strain" concept introduced by Darwin and Pecknold [6] in order to associate the biaxial or triaxial response of RC structures through the use of orthotropic uniaxial constitutive laws. Darwin and Pecknold [6] developed a nonlinear stress-strain law for plain concrete under biaxial stresses and was incorporated into four-noded isoparametric quadrilateral finite elements. It was assumed that concrete behaves like an orthotropic material (strain induced orthotropy). The constitutive matrix of the concrete was generated with respect to the principle strain directions and the principle strain directions in the concrete are coincide with the principle material directions. They proposed an association between biaxial and uniaxial response of RC structures though the use of an "equivalent uniaxial strain". A 1D constitutive law was used which was suggested by Saenz [155] for the equivalent uniaxial stress-strain relationship in compression and a linear elastic brittle response in tension as shown in Fig. 5.3. The analysis showed reasonable agreement with experimental results as stated by the authors. The main restriction of their proposed modeling method [6] is that the analysis problems that can be solved are limited to 2D.

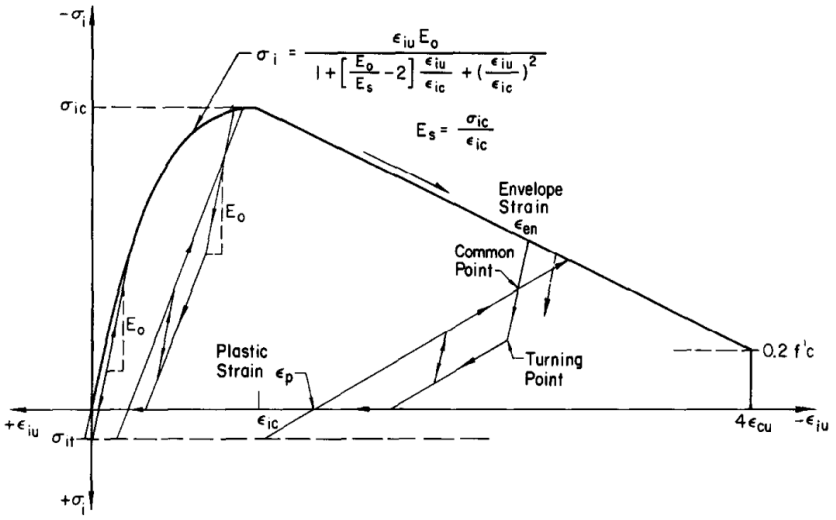

Fig. 5.3 Schematic representation of the uniaxial stress-strain law according to Darwin and Pecknold [6].

Balan et al. [16] proposed a 3D constitutive hypoplastic orthotropic model by using the equivalent uniaxial concept, introduced by Darwin and Pecnold [6]. The uniaxial stress-strain relationship of Saenz [155] was used in order to describe the equivalent stress strain relationship of the model. It was also assumed that the material axes coincide with the principle stress, where the tensile cracking, the compression crushing and strain softening are considered. The model was implemented in a single 8-noded 3D concrete element in order to capture the triaxial cyclic response of a concrete specimen. Later, Balan et al. [16] improve this model by considering the effect of the post peak behavior of concrete due to lateral confinement. It is assumed that the uncracked concrete behaves initially as an isotropic material with stress- induced anisotropy and the constitutive matrix is formed according to the principal stress matrix. Principal stress and strains are not considered coaxial in this model. Each principle direction follows an equivalent uniaxial stress-strain relationship. For this cause a combination of Popovics [156] and Saenz [155] curve was proposed for both axial compression and axial tension behavior, as illustrated in the figure Fig. 5.4.

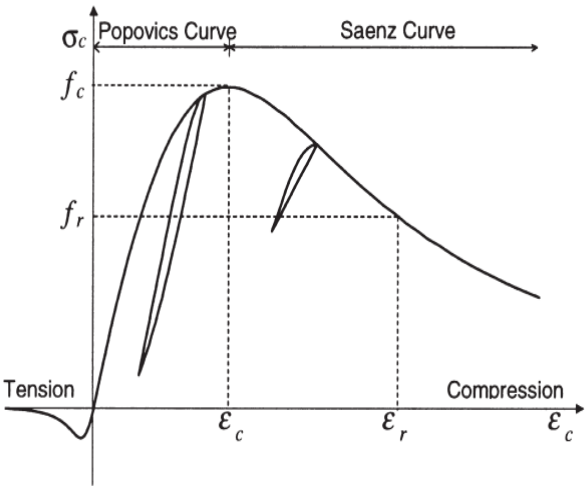

Fig. 5.4 Schematic representation of the uniaxial stress-strain law according to Balan et al. [16].

The model is also used efficiently by Kwon and Spacone [17] adding the coupling between the deviatoric and the volumetric stresses following the definition of the coupling modulus proposed by Gerstle [157]. The model is used for the analysis of the 3D response of concrete specimens under cyclic loading and RC column under monotonic loading conditions.

Girard and Bastien [19], developed a 3D hypoelastic constitutive numerical model, based on the equivalent strains proposed by Darwin and Pecknold [6], in order to investigate the cyclic response of columns taking into account the bond-slip effect. This study used 20-noded hexahedral finite elements in order to analyze a RC column. The bond slip effect is modeled by introducing an additional dof at each node of every reinforcement bar. The study indicates the essence of a realistic modeling of bond-slip effects on structural behavior. Finally, Au and Bai [21] presented an orthotropic strain induced constitutive model based on a secant modulus approach by using the uniaxial strain concept with 4-node rectangular linear displacement finite elements for 2D analysis of RC beams under monotonic and non-reversed cyclic loading. It is assumed that the constitutive matrix is orthotropic with respect to the principle strains. In each iteration, the equivalent strains were calculated in order to determine the secant modulus of elasticity. The stress-strain relation was based on the Attard and Setunge [21] curves, including the reduction coefficient β of compressive strength introduced by Vecchio and Collins [154], due to biaxial conditions. In addition, linear rules for unloading and reloading are described for

cyclic loading as illustrated bellow. Particularly, the transition between crack opening and crack closing, follows the Menegotto and Pinto [34] curve. In addition to that, the bond-slip effect was modeled by adopting contact elements as shown in Fig. 5.5. They stated that the numerical results showed good agreement with the experimental data. Nevertheless, the 2D limitation is still present.

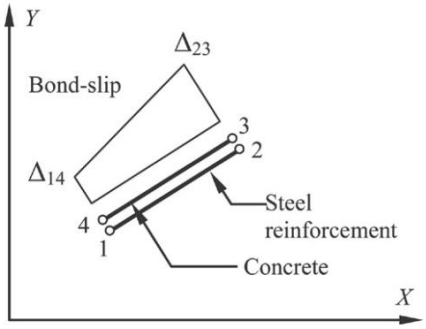

Fig. 5.5 Schematic representation of the contact element proposed by Au and Bai [21].

5.1.3 Bounding surface models

Other researchers try to construct constitutive models based on the principles of plasticity using biaxial or triaxial failure surfaces. Sfakianakis and Fardis [158] proposed a finite element formulation based on the distributed inelasticity discrete model for the flexural response of slender RC columns under cyclic loading. The tangent flexibility matrix is constructed according to the bounding surface of each cross section along the member length. In each iteration, the tangent flexibility matrix of each section is constructed, which relates the set of increments of the three normal stress resultants, (N, M_y, M_z) to the corresponding section deformations $(\varepsilon_0, \varphi_y, \varphi_z)$. The element tangent flexibility matrix is constructed by integrating the tangent flexibility matrix of each section. The relation between the normal stress components to the corresponding deformations is based on the bounding surface concept. The bounding surface includes all the possible values of (N, M_y, M_z) and generates an ultimate strength envelope. According to this approach, the model takes into account the distributed nonlinearity across the member and the effect of a non-zero and varying axial load, on the flexural response. Pagnoni et al. [159], suggested a 3D RC bounding surface model combined with the smeared crack approach with the use of the isoparametric 8-noded finite elements. The model is based on the bounding surface model, which is a locus that encloses all the possible stress points defined by a level of damage in the structure as shown in Fig. 5.6. Therefore the bounding surface is a function of the maximum value of damage ever experienced and the current stress state. Additionally, the tension stiffening effect is taken into account by modeling a linear descending branch in the cracked concrete This study indicates the necessity of the accurate prediction of concrete under triaxial state of stress.

Cela [11], described an elastic-viscoplastic law based on the Drucker-Prager model for simulating the RC behavior subjected to dynamic plain-stress loading conditions. This paper, proposed an elastic-viscoplastic law based on the Drucker-Prager model for simulating the RC behavior subjected to dynamic loads. The constitutive law of concrete is based on a Drucker-Prager yield criterion with softening or hardening post yielding curves. The classical radial return algorithm is used in order to return the stress to the yield surface. A special algorithm is developed in order to return the stresses that lie close to the apex of the Drucker-Prager cone (singular zone). Two methods are suggested in order to define the concrete material data for the

implementation of the above yield criterion. The first one proposes the expansion of the Drucker-Prager yield surface to determine the hardening or softening regime without varying the angle, while the second one proposes only the variation of the angle. More realistic plastic strain distributions are derived by the second method, as reported in [11].

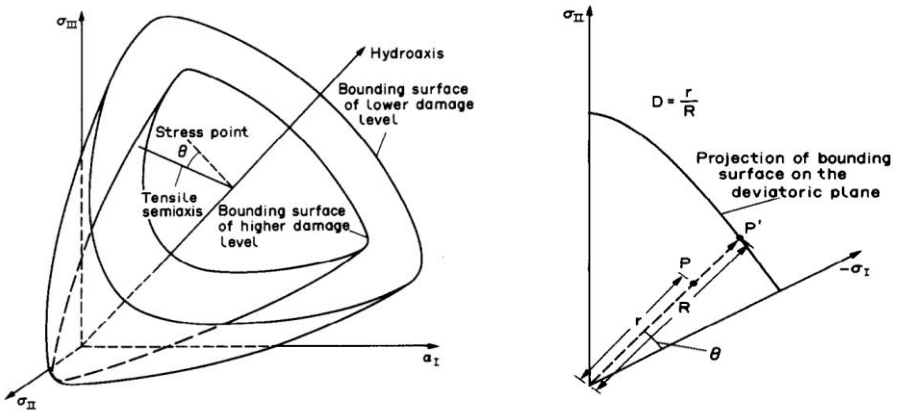

(a) (b)

Fig. 5.6 Schematic representation of the bounding surface model: (a) bounding surface, (b) radial mapping proposed by Pagnoni et al. [159].

5.1.4 Microplane models

Ozbolt et al. [9] proposed a 3D microplane model by introducing many material parameters that are defined for every microplane (see Fig. 5.7). For each microplane a constitutive model is proposed describing both volumetric and deviatoric stress-strain relationships. In addition, the rate effect is considered through the use Maxwell rheologic model. In general when the rate is increasing, the concrete strength is also increasing and the postpeak descending branch is becoming steeper. The model is implemented within a 4-noded isoparametric plane-stress finite element in order to describe the biaxial response and examine the rate effect of concrete specimens under cyclic loading conditions.

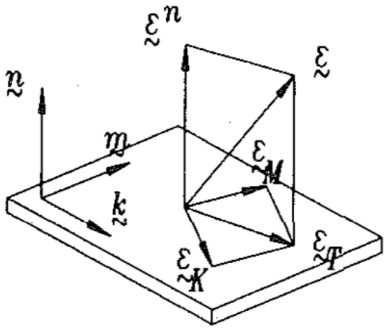

Fig. 5.7 Stress and strain components on each microplane according to Ozbolt et al. [9] *(m,k: the coordinate vectors defined for each microplane, ε_T: the tangential vector component of ε).*

Eligehausen et al. [10], studied a numerical simulation of beam-column RC joints for 3D nonlinear analyses under cyclic loading, based on Ozbolt's [9] microplane model. The bond-slip effect was taken into account by assuming a 1D nonlinear spring with a bond-slip relationship. The simulation was capable to model the general behavior of the specimens, as stated by the authors.

5.1.5 Models based on the compression field theory

Many researchers used the compression field theory to treat the behavior of cracked RC elements subjected to shear. Inoue et al. [10], presented a nonlinear finite element method for dynamic analysis of shear walls, where the hysteretic characteristics of concrete and reinforcement were proposed by using uniaxial constitutive models. It was assumed that uncracked concrete behaves as an isotropic material. The stress-strain relationship is formed in the principle co-ordinates. After cracking, the material is considered to be orthotropic with respect to the crack direction. The FEM analysis is implemented by assembling isoparametric plane-stress elements with four nodes for RC wall panels and 8-noded solid elements for slabs that were supported on wall panels.

Vecchio [12], modeled the RC members through the use of a 4-noded plane-stress finite element. A secant stiffness-based finite element algorithm was presented for the analysis of concrete structures under general loading conditions, including cyclic loads. The total strain is considered to consist of an elastic and a plastic strain, the elastic strain was used to define the effective secant stiffness. The plastic components were incorporated into the analysis through the use of prestrain forces. Constitutive relationships were formed in order to link the average stress to the average strains. For compression the Hognestad [153] and Popovics [156] monotonic curves are used to represent the backbone curve and were also modified to account for compression softening effects according to the modified compression field theory (MCFT). Palermo and Vecchio [18], predicted the load-deformation of shear walls based on a modified compression field theory by using 4-noded plane and hexahedral elements in order to evaluate 2D and 3D problems, respectively, under cyclic loading conditions. The total strain is considered to consist of an elastic and a plastic strain (or plastic offset) component. The plastic offsets were calculated for both concrete and reinforcement, and they were used to determine the prestrain forces. The elastic strains were used to define the secant stiffness, while a Mohr's circle technique was employed in order to determine plastic offset in different directions. Furthermore, the rotating smeared crack approach was used. The compression field theory is described schematically in Fig. 5.8.

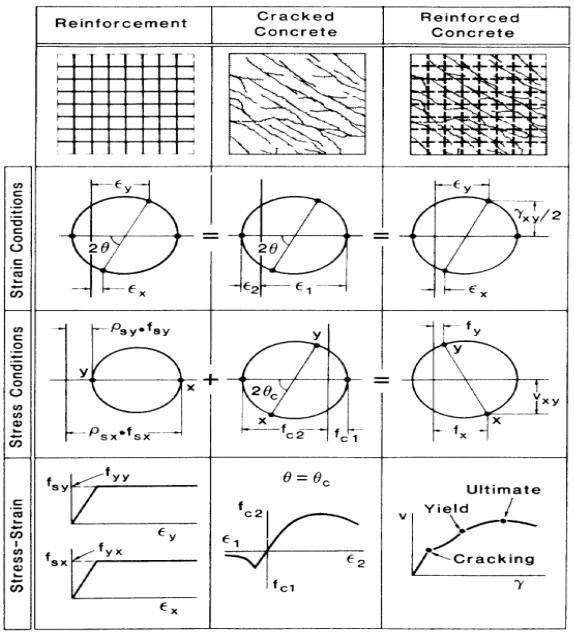

Fig. 5.8 Schematic representation of the compression-field theory for membrane elements according to Vecchio and Collins [154].

They stated that their proposed model provides satisfactory results although improvements to the hysteretic behavior were also required.

5.1.6 Elasticity based and Elastoplastic models combined with fracture energy based smeared crack approaches

Other models found in the international literature, combine the elastoplastic isotropic uncracked behavior of concrete with fracture energy based on smeared crack approaches for the cracked concrete domain. Ile and Reynouard [13], proposed a constitutive model for predicting the cyclic biaxial response of RC shear walls assuming that concrete is dominated by a plane state of stress through the use of 4-noded isoparametric finite elements. An isotropic behavior of the uncracked RC structure is assumed. A uniaxial law is described for the behavior of the point initially under tension or compression. For the cracked concrete, it is assumed that the total strain consists a continuum strain component and a cracking strain component. The cracking strain component which defines the crack opening strain is calculated by using fracture mechanics concepts (Bazant and Oh [14]). However the continuum strain component follows a linear elastic law after cracking. Generally the cracked concrete behavior is considered as an orthotropic law whose orthotropy directions are normal and parallel to the crack. The smeared crack approach is adopted with orthogonal fixed cracks. The authors reported that the numerical results showed a good correlation with the experimental data.

Furthermore, He et al. [22], proposed an energy based model incorporated in a 4-noded plane-stress quadrilateral finite element for 2D analysis under cyclic loading conditions. For compression, the ascending branch is consisted by a lineal and a parabolic function. In addition, a linear descending branch was proposed. For tension, a linear ascending branch and a descending exponential function are used to represent stress-strain relationships. The stress-strain relationships are illustrated in Fig. 5.9. The model uses the fracture energy relation, according to the crack band theory [14] in order to determine the damage of the concrete members and minimize the mesh sensitivity.

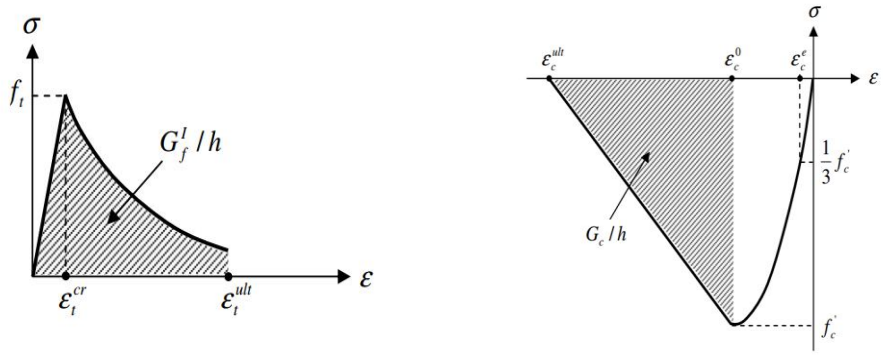

(a) (b)

Fig. 5.9 Schematic representation of stress-strain envelope curves according to He et al. [22].

The method uses the uniaxial stress-strain relationships in order to calculate the secant modulus of elasticity. The model implies the coaxiality between the principle strain and stress directions. The cracking is simulated by the smeared rotating crack approach.

Furthermore, Moharrami and Koutromanos [160] proposed a 3D constitutive model, which combines the elastoplastic and smeared crack approaches in order to describe the cyclic and dynamic behavior of concrete. The model place emphasis on the accurate modeling of inelastic buckling and fracture of reinforcing steel under cyclic loading and the effect of these

phenomena on the ductility of RC structural members. Belletti et al. ([161], [162]) proposed a unified approach based on the total strain fixed crack approach for RC membrane elements indicating the essence of taking into account the shear resistance mechanisms that are developed along cracks. The uniaxial constitutive law of concrete is shown in Fig. 5.10.

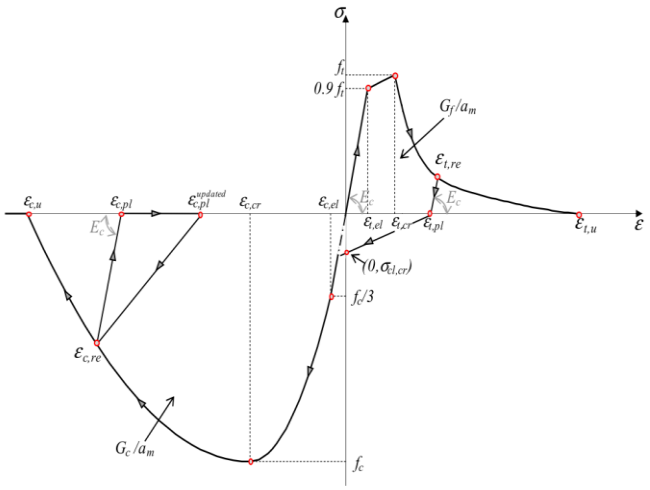

Fig. 5.10 Cyclic uniaxial constitutive law of concrete according to Belletti et al. [162].

5.1.7 Hybrid modeling with different constitutive laws in different regions

Another group of models proposes the use of different uniaxial constitutive laws in different regions inside the concrete members. To et al. [23], proposed a strut and tie nonlinear model of RC frames by using five different element types for cyclic loading conditions as illustrated in Fig. 5.11.

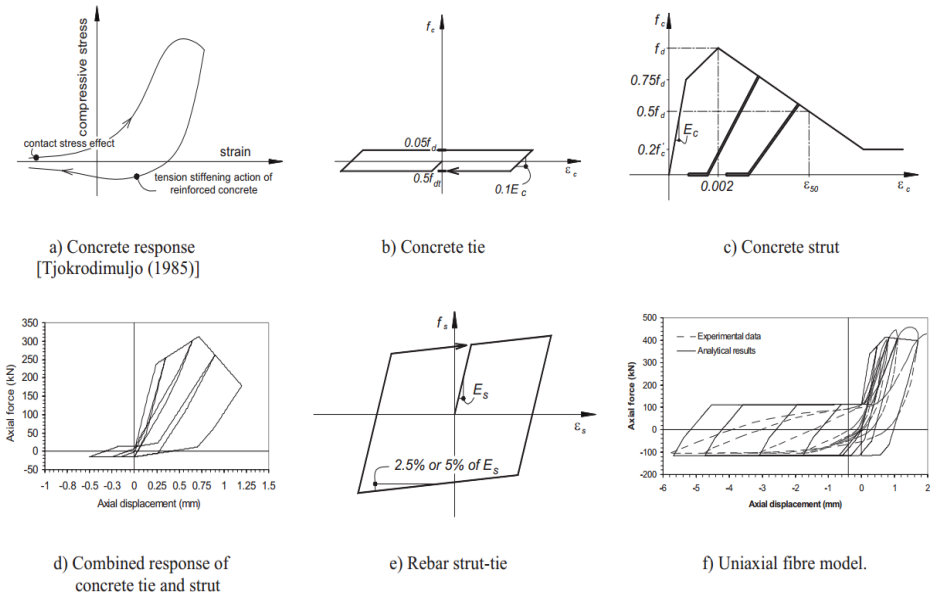

a) Concrete response [Tjokrodimuljo (1985)]
b) Concrete tie
c) Concrete strut
d) Combined response of concrete tie and strut
e) Rebar strut-tie
f) Uniaxial fibre model.

Fig. 5.11 Stress-strain characteristics for cyclic strut-and-tie model elements according to To et al. [23].

The concrete members are divided into the beam (or B-) regions and the distributed (or D-) regions. The stresses and the strains are supposed to distribute regularly in the B regions and therefore can be determined by methods based on solid mechanics accurately. However in D regions the structural behavior is characterized by irregularity and the stress-strain relations cannot be easily modeled. The model uses the B-regions to provide the nonlinear behavior until the first yield limit states of the structure. The ultimate limit-stage of the structure is determined by load-carrying capacity of the D-regions.

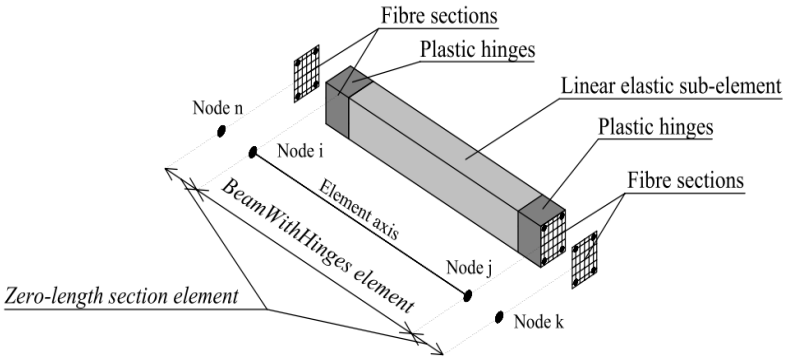

Fig. 5.12 Linear element and zero-length section element according to Melo et al. [24].

Melo et al. [24], used fiber beam elements in order to model the nonlinear analysis of a two-span RC beam during cyclic loading. Each element was divided into three partitions: two hinges at the ends and a linear-elastic region in the middle. Furthermore, two zero-length section elements are placed at the end of the beam as illustrated in Fig. 5.12.

Lu and Panagiotou [24] proposed a 3D nonlinear cyclic model for nonplanar RC walls. The model uses nonlinear Euler-Bernoulli fiber section beam elements in order to simulate the steel and concrete in vertical direction and nonlinear trusses to simulate steel and concrete in the horizontal direction, and the concrete along the diagonal directions. The model has the advantage against the fiber-section beam element models that does not impose the assumption of "plane-section-remain plain".

5.1.8 Damage models and coupling between plasticity and damage modeling

Some models based on damage mechanics are suggested for concrete behavior under cyclic loading. Richard et al. [25], presented a set of constitutive equations describing micro-cracking, sliding influence and partial stiffness recovery in order to compose a 3D constitutive model for concrete structures based on isotropic damage mechanics. The closing and opening of cracks are determined through the hydrostatic strain part of the model. The frictional sliding is modeled by the deviatoric part of the strain and stress tensors. A schematic representations of these assumption is illustrated in Fig. 5.13. The authors claimed that the proposed model could be used for large scale structures.

Additionally, Jason et al. [163] combined an elastoplastic law with isotropic damage modeling in order to describe the hardening and softening behavior of concrete under cyclic compression. The model introduced many material parameters and illustrated the improvements achieved compared to a simple damage model but it was noted that the simulated responses were mesh-dependent. A schematic representation of the coupling of elastoplastic and damage modeling during the unloading response is shown in Fig. 5.14.

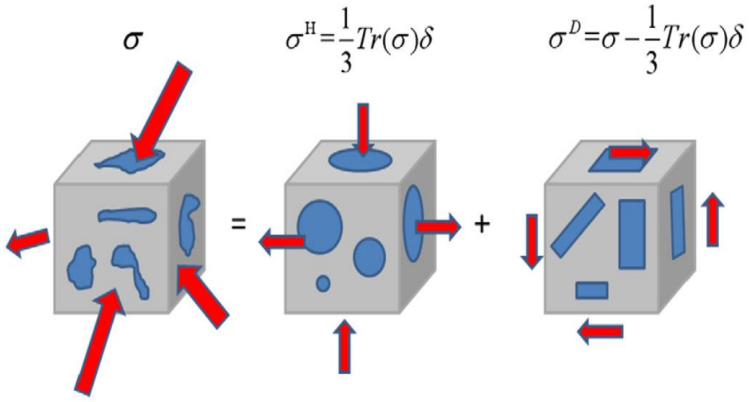

Fig. 5.13 Decomposition of a cracked medium into hydrostatic (opening and closing) and deviatoric (frictional sliding) effects [25].

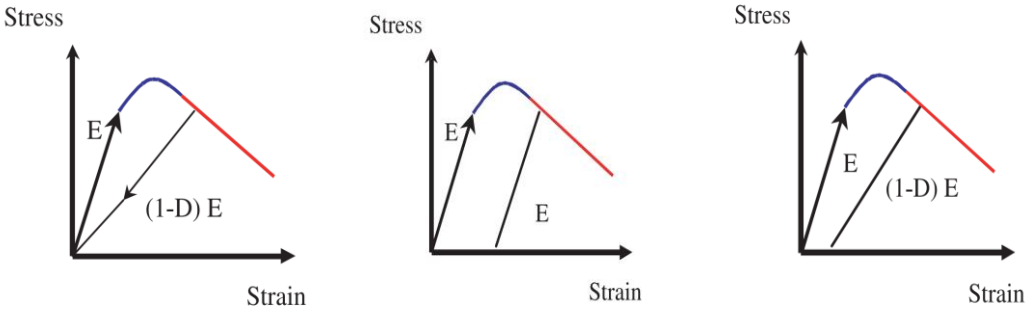

(a) (b) (c)

Fig. 5.14 Unloading response of (a) elastic damage, (b) elastoplastic, (c) elastoplastic damage models [163].

Yuchuan et al. [26], developed an energy based anisotropic damage model for analyzing the cyclic behavior of concrete structures. The model proposed nonlinear unloading branches in order to model the hysteretic behavior in tension and compression. An 8-noded hexahedral element was used to model the behavior of a concrete specimen. The authors stated that the numerical results showed reasonable agreement with the experimental ones.

Richard and Ragueneau [164], proposed the coupling between plasticity and damage modeling. Plasticity is used for the description of concrete in compression, whereas isotropic damage is used for tension. As stated in their work [164], the pathology of mesh-dependency issues was reduced by adopting a nonlocal approach proposed in [165]. Additionally, Vassaux et al. [166] used a discrete model to define and calibrate quantities such as i) proportion of closed cracks and ii) specific dissipated energy related to friction. These quantities were introduced to the previous model in order to describe the hysteretic behavior of concrete structures with crack closure and friction.

Gkimousis [167] combined plasticity and damage modeling, and incorporated this scheme into a fiber finite element model which is formulated on the basis of the two-field Hellinger-Reissner [168] energy principle. The model place emphasis on the modeling of buckling of steel reinforcement and its effect on the flexural behavior of RC structures.

5.1.9 Discrete approaches

Furthermore, recent studies try to describe the fracture mechanisms of concrete introducing discontinuities within the finite elements. Feist et al. [169] proposed a numerical model based

on the strong discontinuity approach (SDA), where elements with embedded discontinuities were used to simulate the fracture processes in plain concrete. Roth et al. [170] combined a damage mechanics model with the extended finite element method (XFEM). In this method, the kinematic enrichment was done by introducing additional dofs at the nodes of the finite elements. Additionally, in order to capture the mechanisms of heterogeneous and quasi-brittle materials, multiscale models have been proposed by defining the size of the representative volume element (RVE) which contains homogenized properties ([171], [172]) and represents the microstructure of the material. Both of these methods are indicated for describing local phenomena, while they are difficult to be extended for the simulation of large scale structures, due to the increased computational demands (see Fig. 5.15).

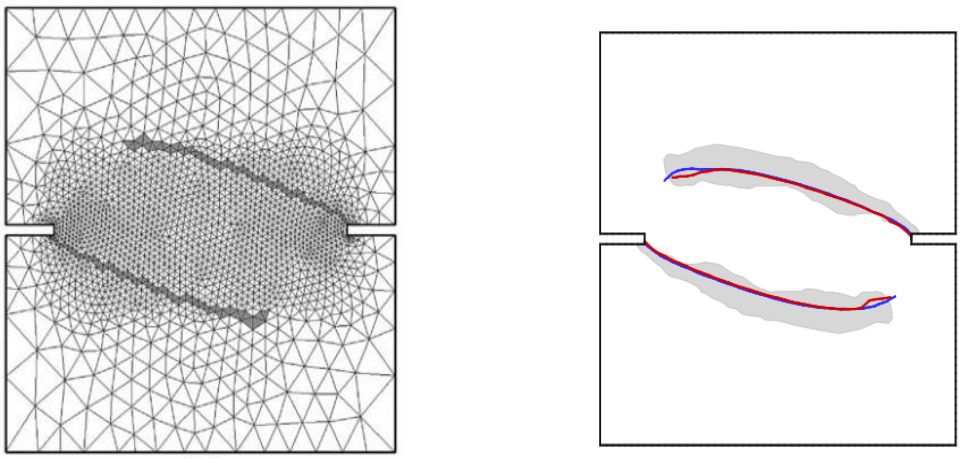

(a) (b)

Fig. 5.15 Numerically obtained discrete crack paths for a double-edge notched specimen according to (a) Feist et al. [169] *and (b) Roth et al.* [170].

Furthermore, Sinaie et al. [144] proposed a micro-mechanical damage model for concrete under cyclic loading conditions for intel-particle bonds. The model uses a multi-phase implementation simulating aggregates and the mortar matrix with different types of particles. The model was validated by comparing experimental and numerical results of concrete specimens.

5.1.10 3D elasticity based constitutive laws based on CFP theory combined with smeared crack approach

Finally, Lykidis and Spiliopoulos [27,28], presented a 3D numerical method integrated in 27-noded hexahedral elements by using the triaxial constitutive law of Kotsovos and Pavlovic [29]. The procedure was reported to be efficient and indicated the necessity of modeling the bond-slip properties that were accounted during their analyses (see Fig. 5.16).

Kotsovos [3], proposed a material model which was based on Kotsovos & Pavlovic [29] by using the 27-noded Lagragian finite element and tested their model under monotonic, cyclic and dynamic loading conditions. The proposed procedure includes some restrictions about the number of cracks that are formed in every incremental iteration, which hinders the objectivity of the method.

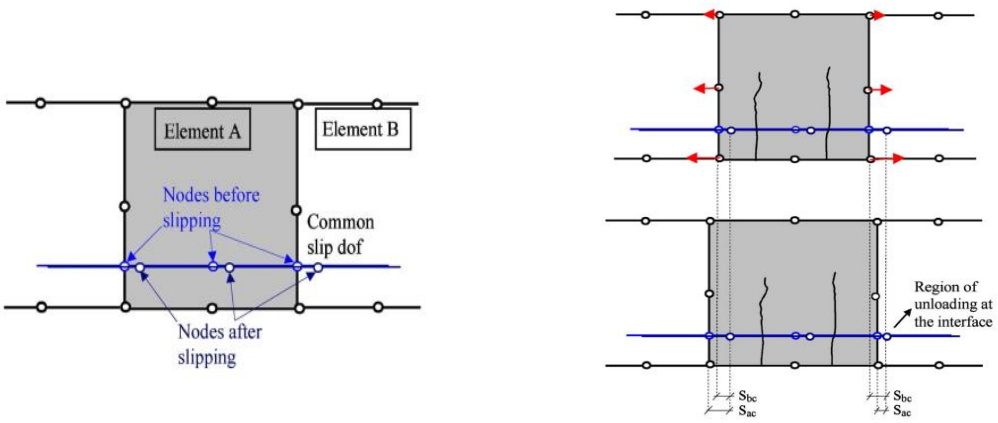

(a) (b)

Fig. 5.16 Schematic representation of the effect of cracking on the interface. (a) Slipped before cracking, (b) deformation of concrete element (down) due to residual forces caused by cracking (up) and the effect on bar slipping, according to Lykidis and Spiliopoulos [28] *(s_{bc}=slippage before cracking, s_{ac}=slippage after cracking).*

5.2 Mathematical description of non-linear stress-strain concrete behavior based on Kotsovos and Pavlovic material model

The aim of this section is to describe the mathematical stress-strain relations that derived from the experimental data presented in subsection 4.4 in a suitable form in order to be incorporated into the finite elements that are used for the analysis of concrete structures. Three possible approaches are presented bellow for the mathematical description of the constitutive modeling.

5.2.1 Three-moduli approach

The most common way to describe the behavior of an isotropic material, is to express the constitutive material relationship as a function of two constants by the use of Young's modulus *E* and Poisson's ratio *v* or by the means of Lame's expressions. In this study, the octahedral stresses and strains are adopted, thus, it is more convenient to use the bulk modulus K and the shear modulus G in order to describe the volume and the distortional changes in the material as described in Eq. (5.30) , (5.31).

$$K = \sigma_0 / (3\varepsilon_0) = \mathrm{E} / [3 \cdot (1 - 2\nu)] \tag{5.30}$$

$$G = \tau_0 / (2\gamma_0) = \mathrm{E} / [2 \cdot (1 + \nu)] \tag{5.31}$$

Due to the non-linear behavior of concrete, the K and G are functions of the stress and strain levels of the material. For example the secant bulk and shear moduli can be expressed as:

$$K_s = \sigma_0(\varepsilon_0) / (3\varepsilon_0) \tag{5.32}$$

$$G_s = \tau_0(\gamma_0) / (2\gamma_0) \tag{5.33}$$

The deviatoric stresses cause both volumetric and deviatoric strains. Therefore, the model has to include the coupling between stress deviation and volume change in order to compose accurately the ascending branch of stress-strain relation up to the OUFP (onset of stable fracture propagation) level. A third material modulus *H* (Gerstle et al. [93]) is proposed to serve this purpose (see Eq. (5.34)):

$$H_s = \tau_0 / \varepsilon_{0(d)} \tag{5.34}$$

Generally, the total octahedral strains resulting from the application of an external stress state (σ_0, τ_0) may take the following form:

$$\varepsilon_0 = \varepsilon_{0(h)} + \varepsilon_{0(d)} = \sigma_0 / (3 \cdot \mathrm{K_s}) + \tau_0 / \mathrm{H_s} \tag{5.35}$$

$$\gamma_0 = \gamma_{0(d)} = \tau_0 / 2G_s \tag{5.36}$$

Although the material is assumed to be isotropic, the introduction of the coupling effect by the use of a third modulus leads to a quasi-isotropic behavior as illustrated in Fig. 5.17. Finally, it is evident that the coupling effect is negligible at low values of σ_0.

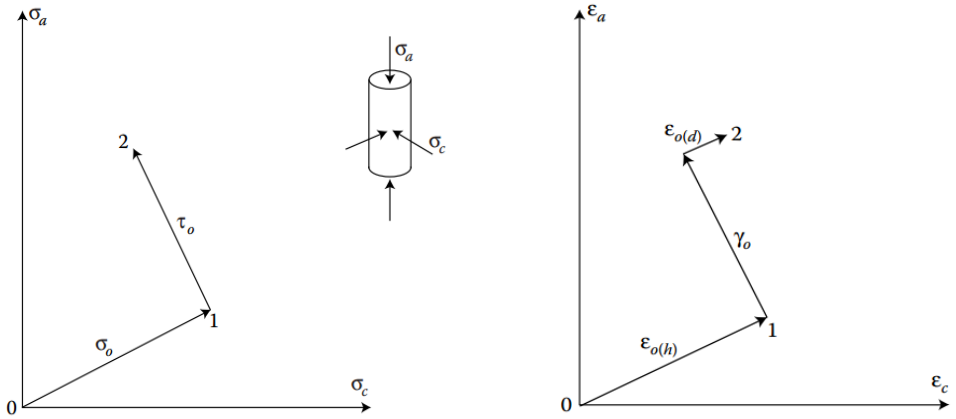

(a) (b)

Fig. 5.17 Schematic representation of the coupling effect between stress deviation τ_0 and volume change $\varepsilon_{0(d)}$: (a) stress path followed, (b) resulting strains. ([3]*)*

5.2.2 Internal-stress approach

This approach is described in Fig. 5.18. The micro-cracking in this case is the main cause of the nonlinear behavior of concrete. It is calculated as an equivalent internal compressive state of stress which tends to reduce the tensile stresses localized near the crack tips. Consequently the nonlinear constitutive relation of concrete can be determined, if the linear stress strain relation is corrected by the introduction of the internal stresses developed during the fracture process.

The generalized form of Hooke's law may be written as:

$$\varepsilon_{ij} = -\frac{\nu_e}{E_e}\sigma_{kk}\delta_{ij} + \frac{1+\nu_e}{E_e}\sigma_{ij} \tag{5.37}$$

Or, equivalently

$$\varepsilon_{ij} = -\frac{3K_e - 2G_e}{18K_eG_e}\sigma_{kk}\delta_{ij} + \frac{1}{2G_e}\sigma_{ij} \tag{5.38}$$

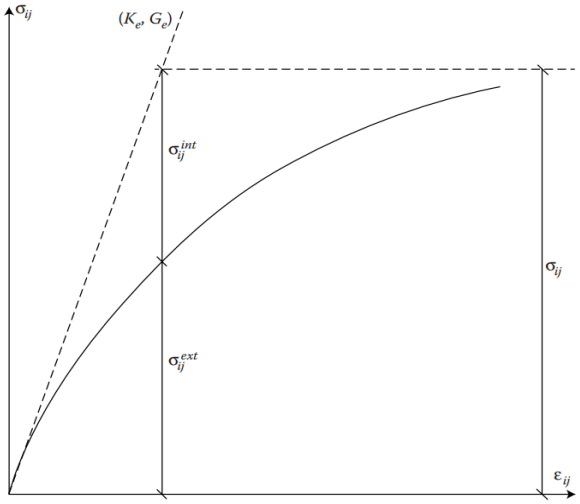

Fig. 5.18 Schematic representation of the internal-stress concept used to account for the non-linear constitutive relations of concrete materials. ([3]*)*

By introducing both the hydrostatic $\varepsilon_0 = \frac{\varepsilon_{kk}}{3}$ and $\sigma_0 = \frac{\sigma_{kk}}{3}$ and the deviatoric components $e_{ij} = \varepsilon_{ij} - \varepsilon_0 \delta_{ij}$ and $s_{ij} = \sigma_{ij} - \sigma_0 \delta_{ij}$ simple alternative expression for Hooke's law in its generalized form is obtained:

$$\varepsilon_{ij} = \varepsilon_0 \delta_{ij} + e_{ij} = \frac{\sigma_0}{3K_e} \delta_{ij} + \frac{s_{ij}}{2G_e} \tag{5.39}$$

This approach is based in the following equation:

$$\sigma_{ij} = \sigma_{ij}^{ext} + \sigma_{ij}^{\text{int}} \tag{5.40}$$

Where the *ext* and *int* refer to the external (applied) and the internal (microcracking) stress states, respectively. The strain component due to σ_{ij}^{ext} is recoverable during unloading while the strain which is caused by σ_{ij}^{int} is permanent and equivalent to the strain state caused by the maximum level of σ_{ij}^{int} previously experienced by the material. The elastic moduli K_e and G_e may be expressed as follows ([173]):

$$K_e = 1000 + 3.2 f_c^2 \tag{5.41}$$

$$G_e = 9224 + 136 f_c + 3296 \times 10^{-15} f_c^{8.273} \tag{5.42}$$

Where the uniaxial cylinder compressive strength f_c is expressed in MPa. By decomposing each state of stress and strain into a hydrostatic and a deviatoric component, the internal stress state may be quantified by using experimental data. A regression analysis of $\sigma_o - \varepsilon_{o(h)}$ data (see Fig. 5.19) has led to the following analytical expression for the relationship between external stress and resulting strain (Kotsovos [173]):

$$\varepsilon_{0(h)} = (\sigma_0 + 3\alpha K_e \sigma_0^b)/(3K_e) \quad \text{for } \sigma_0 / f_c \le 2 \tag{5.43}$$

$$\varepsilon_{0(h)} = [\sigma_0 + 3\alpha b K_e (2f_c)^{b-1}\sigma_0 + 3\alpha(1-b)K_e(2f_c)^b]/(3K_e) \quad \text{for } \sigma_0 / f_c > 2 \tag{5.44}$$

where *a* and *b* are parameters that depend on the material properties and can be evaluated by regression analysis. The parameter *b* is calculated by the following expression:

$$b = 2.0 + 1.81 \times 10^{-8} f_c^{4.461} \tag{5.45}$$

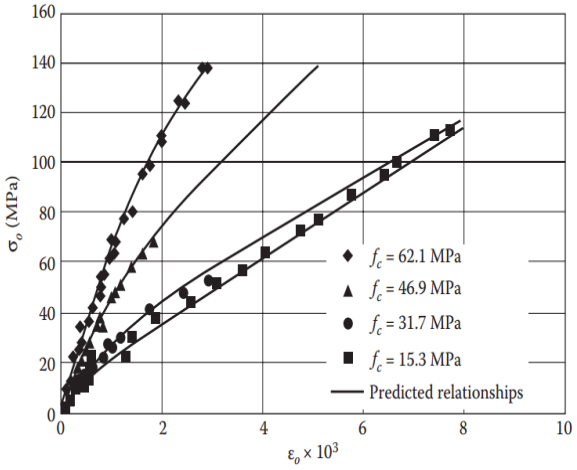

Fig. 5.19 Experimental $\sigma_o - \varepsilon_{o(h)}$ relationships for various f_c. ([3])

Under hydrostatic state of stress, the micro-cracks are distributed randomly in the material of concrete. Therefore, it is very likely that the micro-cracks are situated in the path along a potential crack propagation. This phenomenon leads the new cracks to increase their energy to start the fracture process. Thus, the micro-cracks act as crack inhibitors. It is evident that this phenomenon tends to ceases as the applied stresses are increasing. These assumptions are supported also experimentally and show that the σ_0-τ_0 relationship becomes linear when the hydrostatic stress is higher than $2f_c$. The hydrostatic component of the internal state of stress $\sigma_{0(h)}^{\text{int}} = \sigma_{ih}$ (Eqs. (5.43) and (5.44)) resulting from the external hydrostatic stress $\sigma_0^{ext} = \sigma_0$ (first term of the right-hand side of equation Eq. (5.39)) must be:

$$\sigma_{ih} / f_c = A(\sigma_0 / f_c)^b \quad \text{for } \sigma_0 / f_c \le 2 \tag{5.46}$$

$$\sigma_{ih} / f_c = 2^{b-1} Ab(\sigma_0 / f_c) + 2^b A(1-b) \quad \text{for } \sigma_0 / f_c > 2 \tag{5.47}$$

Where,

$$A = 3aK_e f_c^{b-1} \tag{5.48}$$

With a regression analysis of experimental data, yielding the following expressions for A (which now incorporates and defines a)

$$A = 0.516 \text{ for } f_c \le 31.7 \tag{5.49}$$

$$A = 0.516 / [1 + 0.0027(f_c - 31.7)^{2.397}] \text{ for } f_c > 31.7 \tag{5.50}$$

The hydrostatic stresses cause volumetric strains in the material of concrete. On the contrary, the deviatoric stresses cause both hydrostatic and deviatoric strain components. The analytical description of τ_0-γ_0 data may take the form:

$$\gamma_0 = (\tau_0 + 2cG_e\tau_0^d) / (2G_e) \tag{5.51}$$

Where G_e is given by Eq. (5.42). The material parameter d is given by the following expression:

$$d = 2.12 + 0.0183 f_c \quad \text{for} \quad f_c \le 31.7 \tag{5.52}$$

$$d = 2.7 \text{ for } f_c > 31.7 \tag{5.53}$$

The Eq. (5.51) has to be compatible with the second term of the right-hand side of the Eq. (5.39) and, therefore, the deviatoric component $\tau_{0(d)}^{\text{int}} = \tau_{id}$ must be:

$$\tau_{id} / f_c = C(\tau_0 / f_c) \tag{5.54}$$

Where

$$C = 2cG_e f_c^{d-1} \tag{5.55}$$

The material parameter c is defined by the parameter C. Experimental data for the τ_0 relation reveals the following expressions:

$$C = 3.573 \text{ for } f_c \le 31.7 \tag{5.56}$$

$$C = 3.573 / [1 + 0.0134(f_c - 31.7)^{1.414}] \quad \text{for} \quad f_c > 31.7 \tag{5.57}$$

Finally the hydrostatic component $\sigma_{0(d)}^{\text{int}} = \sigma_{id}$ of the internal stress state resulting from an external deviatoric stress has to be determined. A value for σ_{id} can be obtained from the relationship of σ_0-$\varepsilon_{0(h)}$. In this way, represented values of $\varepsilon_{0(d)}$ and σ_{id} are determined. Therefore, the σ_{id} -τ_0 relationship can be derived from the τ_0-$\varepsilon_{0(d)}$ relation as shown in the Fig. 5.20. This procedure is illustrated schematically in Fig. 5.21.

A regression analysis of the experimental data lead to the following analytical expressions:

$$\sigma_{id} / f_c = M(\tau_0 / f_c)^n \tag{5.58}$$

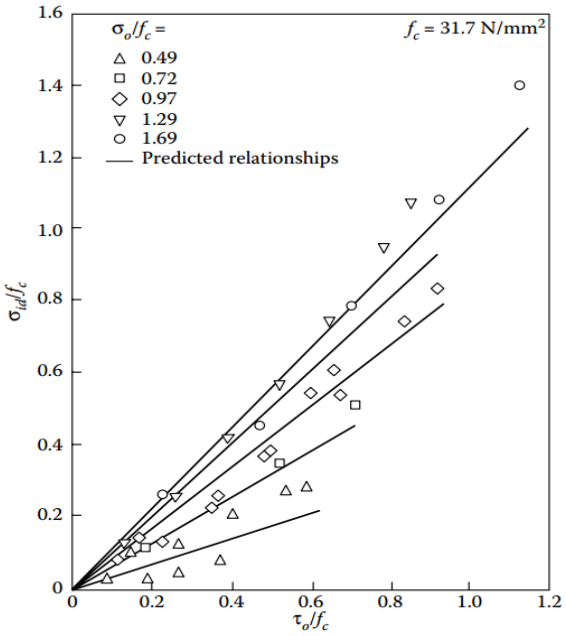

Fig. 5.20 Variation of σ_{id} with τ_0 for various values of σ_0 for a typical concrete with f_c = 31.7 MPa. [3]

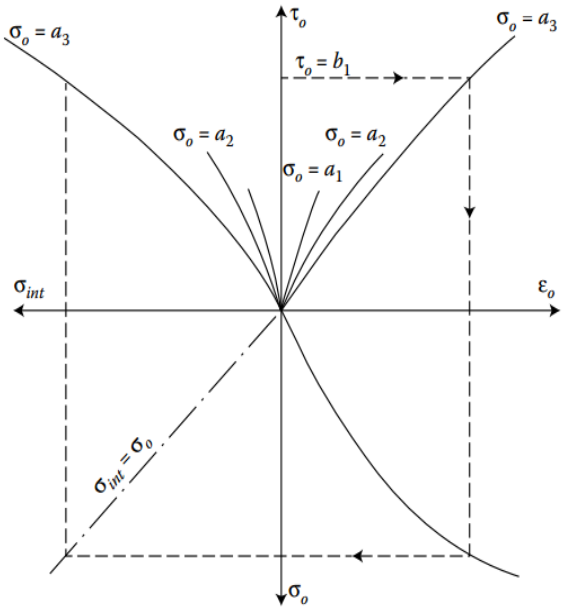

Fig. 5.21 Schematic representation of the approach used to evaluate σ_{id} for a given combination of σ_0 and τ_0. [3]

$$M = k / [1 + l(\sigma_0 / f_c)^m] \tag{5.59}$$

$$k = 4 / [1 + 1.087(f_c - 15)^{0.23}] \tag{5.60}$$

$$l = 0.222 + 0.01086 f_c - 0.000122 f_c^2 \tag{5.61}$$

$$m = -2.415 \text{ for } f_c \le 31.7 \tag{5.62}$$

$$m = -3.531 + 0.0352 f_c \text{ for } f_c > 31.7 \tag{5.63}$$

$$n = 1 \text{ for } f_c > 31.7 \tag{5.64}$$

$$n = 0.3124 + 0.0217 f_c \text{ for } f_c > 31.7 \tag{5.65}$$

In this approach, the coupling effect between the deviatoric stress and volumetric variation is taken into account by the calculation of the σ_{id}. The σ_{id} is an equivalent external stress required to produce the actual $\varepsilon_{0(d)}$.

The loading/unloading criterion can de expressed using the internal stress concept, as follows:

a. Hydrostatic loading. This occurs when the current external σ_o exceeds any previous external σ_o, thus resulting in an increase of σ_{id}.

b. Deviatoric loading. This occurs when the current external τ_o exceeds any previous external τ_o, thus resulting in an increase of σ_{id}.

c. Combined loading. This occurs when the current combination of external σ_o and τ_o results in a σ_{id} larger than any previous σ_{id}. This loading may occur when at least one of (a) and (b) is true.

5.2.3 Combined approach

The combined approach is based on the use of the bulk modulus K and the shear modulus G which describe the non-linear σ_0-$\varepsilon_{0(h)}$ and τ_0-$\gamma_{0(d)}$ behavior combined with the use of σ_{id} in order to take into account the coupling effect τ_0-$\varepsilon_{0(d)}$. The σ_{id} is an equivalent external stress that can be added to the externally applied hydrostatic stress. The constitutive relations take the following form:

$$\varepsilon_0 = \varepsilon_{0(h)} + \varepsilon_{0(d)} = (\sigma_0 + \sigma_{id}) / (3K_s) \tag{5.66}$$

$$\gamma_0 = \gamma_{0(d)} = \tau_0 / (2G_s) \tag{5.36}$$

In this approach, the third modulus H_s (Eq. (5.34)) is replaced by the use of an equivalent stress σ_{id} which is based on the internal-stress concept.

It is considered that the bulk modulus and the shear modulus describe the nonlinear behavior of the material and they are calculated by using Eqs. (5.32) and (5.33) based on the secant approach. Therefore, their analytical expressions can be derived by using Eqs. (5.43), (5.44) and (5.51):

$$K_s / K_e = 1/[1 + A(\sigma_0 / f_c)^{b-1}] \text{ for } \sigma_0 / f_c \le 2 \tag{5.67}$$

$$K_s / K_e = 1/[1 + 2^{b-1}Ab - 2^b(b-1)A(\sigma_0 / f_c)^{-1}] \text{ for } \sigma_0 / f_c > 2 \tag{5.68}$$

$$G_s / G_e = 1/[1 + C(\tau_0 / f_c)^{d-1}] \tag{5.69}$$

By differentiating Eqs. (5.43), (5.44) and (5.51), analytical expression of the tangent forms of bulk ($K_t = (1/3)d\sigma_0/d\varepsilon_0$) and shear ($G_t = (1/2)d\tau_0/d\gamma_0$) modulus can be obtained.

$$K_t / K_e = 1/[1 + Ab(\sigma_0 / f_c)^{b-1}] \quad \text{for } \sigma_0 / f_c \le 2 \tag{5.70}$$

$$K_t / K_e = 1/[1 + 2^{b-1} Ab] \text{ for } \sigma_0 / f_c > 2 \tag{5.71}$$

$$G_t / G_e = 1/[1 + dC(\tau_0 / f_c)^{d-1}] \tag{5.72}$$

The above expressions of the secant and tangent moduli are illustrated in Fig. 5.22.

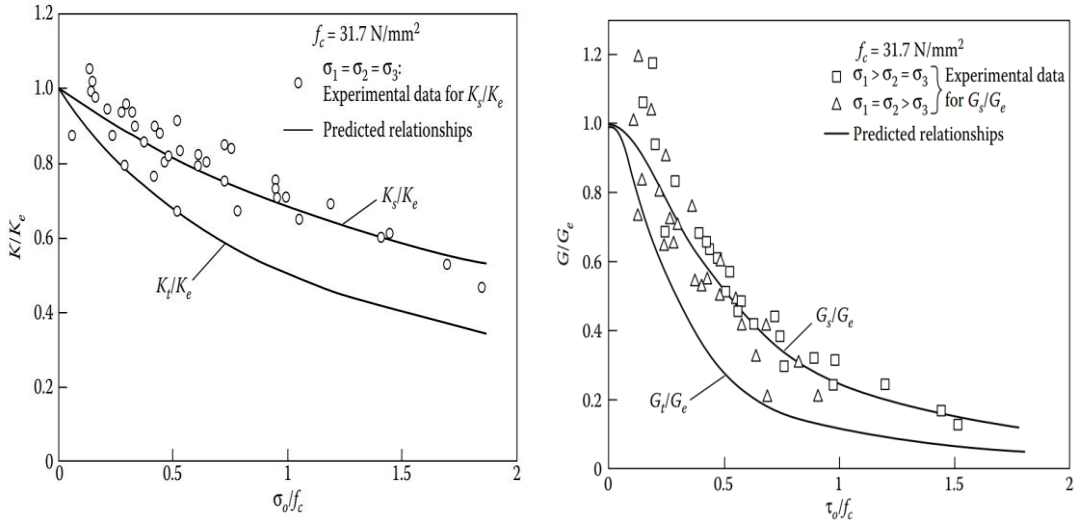

(a) (b)

Fig. 5.22 Variation of the (a) bulk moduli (K_s, K_t) with σ_0 and (b) shear moduli (G_s, G_t) with τ_0 for a given concrete with f_c = 31.7 MPa. [3]

The following expression is derived by combining Eqs. (5.66) and (5.39), which is used to determine the strains along the global coordinate directions:

$$\varepsilon_{ij} = (\sigma_{ij} + \sigma_{id}\delta_{ij}) / (2G_s) - (3\nu_s / E_s)(\sigma_0 + \sigma_{id})\delta_{ij} \tag{5.73}$$

Where $E_s(\sigma_o, \tau_o, f_c)$ and $\nu_s(\sigma_o, \tau_o, f_c)$ are the secant Young's modulus and Poisson's ratio, respectively, derived from K_s and G_s by the following standard formulae of linear elasticity:

$$E = (9KG) / (3K + G) \tag{5.74}$$

$$\nu = (3K - 2G) / (6K + 2G) \tag{5.75}$$

Generally, the global stresses and strains are calculated following the above procedure:

- The octahedral stresses (σ_o, τ_o) are calculated either from the principal stresses (σ_1, σ_2, σ_3) or directly from the first and second stress invariants expressed in terms of the global stresses $\sigma_{ij}(\sigma_x, \sigma_y, \sigma_z, \tau_{xy}, \tau_{xz}, \tau_{yz})$.
- The secant modulus K_s, G_s and E_S, ν_s are calculated.
- The hydrostatic correction σ_{id} is calculated.
- Global strains ε_{ij} are calculated.

During the nonlinear procedure which is divided into many increments, the stress and strain increments are calculated using the tangent expressions of modulus K_t, G_t and E_t, ν_t.

5.3 Strength envelope for concrete

It is convenient to formulate a strength envelope of concrete governed by combinations of maximum stresses in terms of hydrostatic and deviatoric components acting on the octahedral plane. Therefore, the orthogonal coordinate system ($\sigma_1,\sigma_2,\sigma_3$) is transformed into the cylindrical coordinate system. Axis z is related to the hydrostatic stress that coincides with the space diagonal $\sigma_1 = \sigma_2 = \sigma_3$, while the radius r is similarly related to the magnitude of the deviatoric stress component. The rotational variable θ defines the deviatoric stress orientation on the octahedral plane.

The strength envelope has the characteristics of convex failure surfaces that is open in compression since concrete can sustain larger deviatoric stresses as σ_0 increases and the cross-section of the strength envelope is getting wider. According to Fig. 5.23, only the on sixth of the surface has to be defined due to the symmetry of the surface about the space diagonal $\sigma_1 = \sigma_2 = \sigma_3$. Therefore experimental data are obtained in order to calculate τ_{0e} and τ_{0c} (see Fig. 5.24). The τ_{0e} $(\theta=0°)$ corresponds to the state of $\sigma_1=\sigma_2>\sigma_3$ (triaxial extension) while τ_{0c} $(\theta=60°)$ correspond to the state of $\sigma_1>\sigma_2=\sigma_3$ (triaxial compression). The value of ultimate deviatoric stress value for every intermediate θ between 0° and 60° may be interpolated by the τ_{0e} and τ_{0c} stresses by using the Willam and Warnke [33] expression:

$$\tau_{0u} = \frac{2\tau_{0c}(\tau_{0c}^2 - \tau_{0e}^2)\cos\theta + \tau_{0c}(2\tau_{0e} - \tau_{0c})\sqrt{4(\tau_{0c}^2 - \tau_{0e}^2)\cos^2\theta + 5\tau_{0e}^2 - 4\tau_{0c}\tau_{0e}}}{4(\tau_{0c}^2 - \tau_{0e}^2)\cos^2\theta + (2\tau_{0e} - \tau_{0c})^2} \qquad (5.76)$$

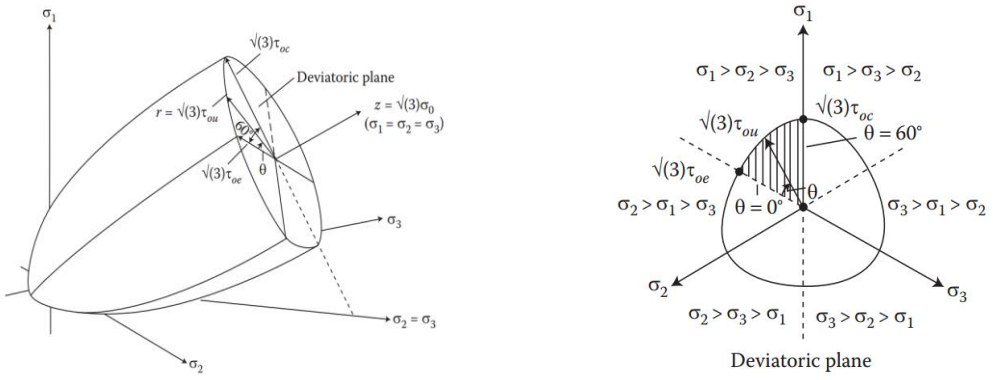

(a) (b)

Fig. 5.23 Schematic representation of the ultimate-strength surface : (a) general view in stress space, (b) typical cross section of the strength envelope with a deviatoric plane (a plane of constant σ_0, viewed along the axis $\sigma_1 = \sigma_2 = \sigma_3$). [3]

As illustrated in figure Fig. 5.24, the expressions of τ_{0e} and τ_{0c} are derived through an experimental investigation and are expressed as:

$$\tau_{0c} / f_c = 0.944(\sigma_0 / f_c + 0.05)^{0.724} \qquad (5.77)$$

$$\tau_{0e} / f_c = 0.633(\sigma_0 / f_c + 0.05)^{0.857} \qquad (5.78)$$

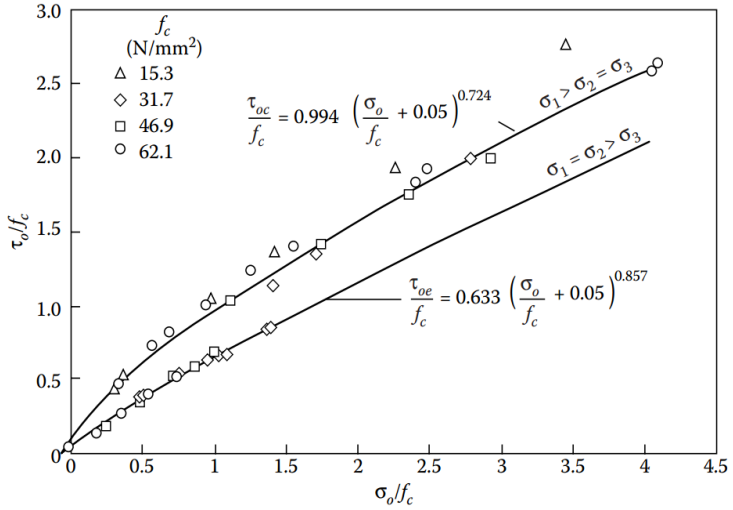

Fig. 5.24 Calculation of τ_{0e} τ_{0c} which corresponds to the ultimate strength of concrete under triaxial compression and triaxial extension. [3]

Finally the three-dimensional view of the predicted ultimate-strength surface is illustrated in Fig. 5.25.

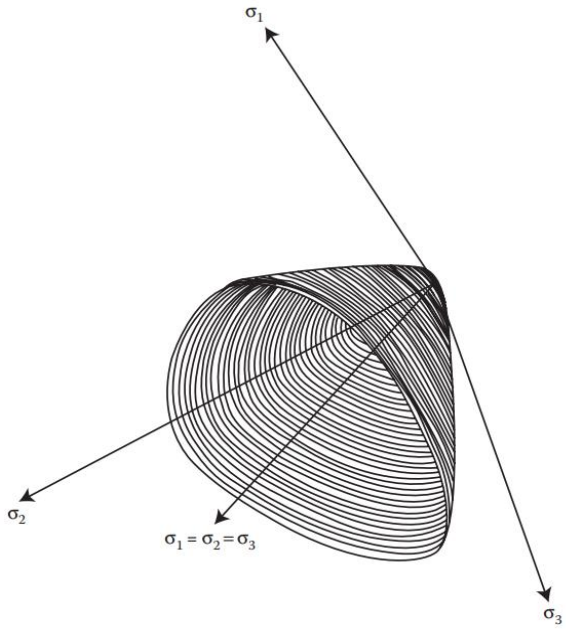

Fig. 5.25 Three-dimensional view of the predicted ultimate-strength surface. [3]

5.4 Proposed algorithmic approach of constitutive modeling of concrete under cyclic loading conditions

5.4.1 Constitutive model of Concrete

The constitutive modeling of concrete has to describe a realistic behavior of concrete under generalized three-dimensional states of stress. Therefore, it has to take into account the effect of out of plane stresses that are usually ignored when 1D and 2D material models are adopted. According to the adopted model, it is assumed that the uncracked concrete behaves as an

isotropic material. The strain-softening stress-strain descending branch which appears at most uniaxial constitutive models in compression, is attributed to the interaction between the concrete specimen and the loading platens [29], therefore, it is not accounted for in this study.

The stress-strain relationships are expressed most conveniently by decomposing each state of strain and stress into hydrostatic and deviatoric components as explained before. Therefore, the normal and shear octahedral stresses (σ_0, τ_0) and strains $(\varepsilon_0, \gamma_0)$ are used. It is evident that hydrostatic stresses σ_0 induce the variation of the volumetric strain $\varepsilon_{0(h)}$, while the application of deviatoric stresses τ_0 cause both volumetric and deviatoric strains. The combined approach presented by Kotsovos and Pavlovic [29] and described in 5.2.3 is used herein. This approach is based on the use of the bulk modulus *K* and the shear modulus *G*, which describe the non-linear σ_0-$\varepsilon_{0(h)}$ and τ_0-$\gamma_{0(d)}$ behavior combined with the use of σ_{id} in order to take into account the coupling effect of τ_0-$\varepsilon_{0(d)}$ (*h* and *d* stand for hydrostatic and deviatoric component respectively). The σ_{id} is an equivalent external stress added to the externally applied hydrostatic stress. The constitutive relations take the following form:

$$\varepsilon_0 = \varepsilon_{0(h)} + \varepsilon_{0(d)} = (\sigma_0 + \sigma_{id}) / (3K_s) \tag{5.66}$$

$$\gamma_0 = \gamma_{0(d)} = \tau_0 / (2G_s) \tag{5.36}$$

Where K_s *and* G_s is the secant forms of bulk and shear moduli respectively. An extensive experimental investigation in [29] led to the analytical expressions of the σ_{id} and the secant and tangent forms of bulk and shear modulus as functions of current state of stress (σ_0, τ_0, f_c) (see Fig. 5.6 and Eq. (5.67)-(5.72)).

The strains in global coordinates are determined by the use of the Eq. (5.66) and takes the following equivalent form:

$$\varepsilon_{ij} = \frac{\sigma_{ij} + \sigma_{id}\delta_{ij}}{2G_s} - \left(\frac{3v_s}{E_s}\right)(\sigma_0 + \sigma_{id})\delta_{ij} \tag{5.73}$$

Where E_s (σ_o, τ_o, f_c) and v_s (σ_o, τ_o, f_c) are the secant Young's modulus and Poisson's ratio, respectively, derived from *Ks* and *Gs* through the following standard formulae of linear elasticity:

$$E_s = (9K_sG_s)/(3K_s + G_s), \tag{5.79a}$$

$$v_s = (3K_s - 2G_s)/(6K_s + 2G_s) \tag{5.79a}$$

During the nonlinear procedure the stress and strain increments are calculated by using the tangent expressions of modulus K_t, G_t, E_t *and* v_t. Eq. (5.73) is used in order to correct the stresses and strains taking into account the σ_{id} which represents the coupling effect of τ_0-$\varepsilon_{0(d)}$.

5.4.2 Behavior of uncracked concrete under cyclic conditions

According to the nonlinear solution that algorithm was developed herein, in each Newton-Raphson iteration the strains at the Gauss points are calculated from the nodal displacements. Then the stresses are defined by using the constitutive matrix of the material computed during the previous Newton-Raphson iteration. The terms of "cracked" and "uncracked" Gauss points, are used to declare material points at the integration points of the hexahedral elements, which represent cracked and uncracked concrete areas in the structure.

It is also assumed that the uncracked concrete behaves elastically at low stress levels. Particularly, when the deviatoric stress of an uncracked Gauss point of a concrete element, is less than 50% of the corresponding ultimate strength, then the elastic constitutive matrix is used

[31]. Otherwise, the constitutive material matrix is updated by using the tangent expressions of bulk and shear moduli. The elastic/uncracked constitutive matrix takes the form:

$$D=\begin{bmatrix} 2G_t+\mu & \mu & \mu & 0 & 0 & 0 \\ \mu & 2G_t+\mu & \mu & 0 & 0 & 0 \\ \mu & \mu & 2G_t+\mu & 0 & 0 & 0 \\ 0 & 0 & 0 & G_t & 0 & 0 \\ 0 & 0 & 0 & 0 & G_t & 0 \\ 0 & 0 & 0 & 0 & 0 & G_t \end{bmatrix} \tag{5.80}$$

where $\mu = K_t\text{-}2G_t/3$ *and* $K_t=K_t(\sigma_0,\tau_0,f_c)$, $G_t=G_t(\sigma_0,\tau_0,f_c)$.

Furthermore, the strains are recalculated by taking into account the coupling effect $\tau_0\text{-}\varepsilon_{0(d)}$ through the use of the expression in Eq. (5.66) where the stresses are updated.

Unloading occurs when the current deviatoric stress τ_0 is less than any previous external τ_0, otherwise it is considered to be in the state of loading [32]:

$$\text{Loading: } \tau_0^{current} \geq \tau_0^{previous} \tag{5.81a}$$

$$\text{Unloading: } \tau_0^{current} < \tau_0^{previous} \tag{5.81a}$$

It is assumed that the unloading branch is elastic and therefore the elastic constitutive matrix of the material is used ($D_{elastic}$). During reloading, the stress-strain relation follows an elastic branch until the deviatoric stress of the corresponding Gauss point reaches 50% of its ultimate strength. When this limit is exceeded, the constitutive matrix is updated according to Eq. (5.80) and the stress-strain relation accounts for nonlinearities due to microcracking.

The criterion that determines the state of loading or unloading at a Gauss point is carried out during the Newton-Raphson internal iteration. Thus, it is possible that a Gauss point will be in different loading states within a single loading increment. A schematic representation of the stress-strain relationship of uncracked concrete is illustrated in Fig. 5.26.

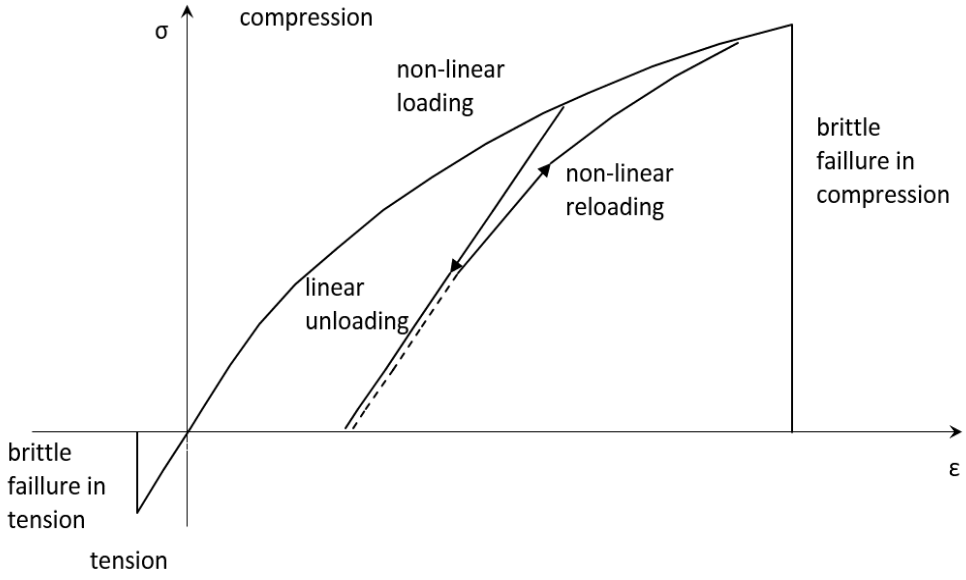

Fig. 5.26 Schematic representation of the stress-strain relationship for the behavior of uncracked concrete under cyclic loading conditions.

5.4.3 Behavior of cracked concrete under cyclic conditions

When the failure criterion is satisfied, then a crack plane is assumed to form in the direction orthogonal to the maximum principle tensile stress. Cracking is modeled through the smeared-crack approach where the stiffness corresponding to the direction of the maximum principle tensile stress is set to zero by transforming the constitutive matrix of the material. Assuming that the crack is perpendicular to *z'* axis (Fig. 5.27), the constitutive matrix takes the following form:

$$\boldsymbol{D} = \begin{bmatrix} 2G_t + \mu & \mu & \mathbf{0} & 0 & 0 & 0 \\ \mu & 2G_t + \mu & \mathbf{0} & 0 & 0 & 0 \\ \mathbf{0} & \mathbf{0} & \mathbf{0} & 0 & 0 & 0 \\ 0 & 0 & 0 & G_t & 0 & 0 \\ 0 & 0 & 0 & 0 & \boldsymbol{\beta} G_t & 0 \\ 0 & 0 & 0 & 0 & 0 & \boldsymbol{\beta} G_t \end{bmatrix} \tag{5.82}$$

This expression of the constitutive matrix describes the anisotropic behavior of concrete at the local axis. Therefore, the constitutive matrix has to be transformed to global axes by using the standard coordinate system transformation laws as follows:

$$\boldsymbol{D_{gl}} = \boldsymbol{T}^T \boldsymbol{D} \boldsymbol{T} \tag{5.83}$$

Where **T** is the transformation matrix from the local Cartesian system *(x', y', z')* to a global *(x, y, z)* with the direction cosines given by (l_i, m_i, n_i) which define the relative orientation of i-axis of system *(x', y', z')* to *x, y, z* respectively. The transformation matrix is given by the following expression:

$$\boldsymbol{T} = \begin{bmatrix} l_1^2 & m_1^2 & n_1^2 & l_1 m_1 & m_1 n_1 & n_1 l_1 \\ l_2^2 & m_2^2 & n_2^2 & l_2 m_2 & m_2 n_2 & n_2 l_2 \\ l_3^2 & m_3^2 & n_3^2 & l_3 m_3 & m_3 n_3 & n_3 l_3 \\ 2l_1 l_2 & 2m_1 m_2 & 2n_1 n_2 & l_1 m_2 + l_2 m_1 & m_1 n_2 + m_2 n_1 & n_1 l_2 + n_2 l_1 \\ 2l_3 l_1 & 2m_3 m_1 & 2n_3 n_1 & l_3 m_1 + l_1 m_3 & m_3 n_1 + m_1 n_3 & n_3 l_1 + n_1 l_3 \\ 2l_2 l_3 & 2m_2 m_3 & 2n_2 n_3 & l_2 m_3 + l_3 m_2 & m_2 n_3 + m_3 n_2 & n_2 l_3 + n_3 l_2 \end{bmatrix} \tag{5.84}$$

Additionally, a constant residual shear stiffness is considered along the crack in order to improve the numerical stability. Therefore, a parameter β is introduced when using the smeared crack approach given that one or more cracks open. The parameter is related to the remaining stiffness due to aggregate interlocking along the crack surface. The parameter β is very important for the numerical stability of the smeared crack approach. As indicated by Vidosa et al. [174], a zero retention factor can lead to ill-conditioning effects. However, a non-zero retention factor combined with the smeared crack approach, could lead to stress locking effects. It is evident that high values of the shear retention factor, result in an overestimation of the stiffness in the cracked areas that can cause further cracking and create instabilities during the analysis. Consequently, an appropriate value of the parameter has to be chosen in order to avoid numerical instabilities and simultaneously avoid stress-locking effects. Vidosa et al. [175] suggested the value of β in the approximate range $0.1 \leq \beta \leq 0.5$ implying that a shear retention factor less than 10% can produce numerical instabilities to their models. Furthermore, Vidosa et al. [175] conducted a numerical investigation in which they found that the aggregate interlock

in cracked concrete has a physically negligible contribution to the stiffness of the structural members.

In this study, it is assumed that the value of this parameter is β=0.05, which implies that 5% of the initial shear strength is remaining after the opening of a crack, fitting perfectly with the negligible contribution of aggregate interlock and provide numerical stability as shown through the numerical applications presented in the Chapter 6.

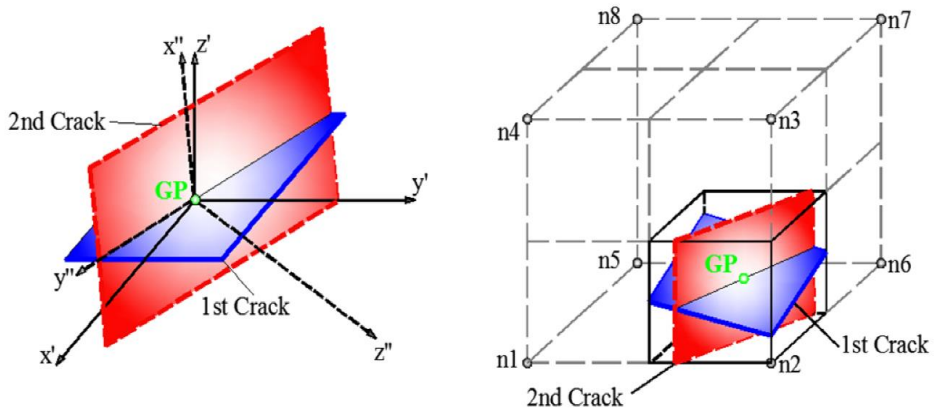

Fig. 5.27 Schematic representation of two crack planes and their relative local axes at the same Gauss Point [31].

Similarly, the second crack plane is also perpendicular to the direction of the new maximum principal tensile stress which together with the first crack plane leaves only stiffness along the intersection of the two planes. As shown in Fig. 5.27 the intersection of the two crack planes is a line which coincides with the local axis y''. Consequently, the constitutive matrix takes the form:

$$\boldsymbol{D} = \begin{bmatrix} \mathbf{0} & \mathbf{0} & \mathbf{0} & 0 & 0 & 0 \\ \mathbf{0} & 2G_t + \mu & 0 & 0 & 0 & 0 \\ \mathbf{0} & 0 & 0 & 0 & 0 & 0 \\ 0 & 0 & 0 & \boldsymbol{\beta} G_t & 0 & 0 \\ 0 & 0 & 0 & 0 & \beta G_t & 0 \\ 0 & 0 & 0 & 0 & 0 & \beta G_t \end{bmatrix} \tag{5.85}$$

Finally, the third tensile crack leads to a constitutive matrix with only residual shear stiffness components. In this case the constitutive matrix takes the following form:

$$\boldsymbol{D} = \begin{bmatrix} 0 & 0 & 0 & 0 & 0 & 0 \\ 0 & \mathbf{0} & 0 & 0 & 0 & 0 \\ 0 & 0 & 0 & 0 & 0 & 0 \\ 0 & 0 & 0 & \beta G_t & 0 & 0 \\ 0 & 0 & 0 & 0 & \beta G_t & 0 \\ 0 & 0 & 0 & 0 & 0 & \beta G_t \end{bmatrix} \tag{5.86}$$

The constitutive matrix is transformed from the local to the global coordinate system when one or two cracks open, introducing the anisotropic behavior of concrete as described in Eqs. (5.82) and (5.85). At each iteration, the crack planes are formed normal to the maximum principle tensile stresses, which can rotate during the analysis causing the crack planes to have an

orientation based on their direction. After a crack opens, its direction remains constant until it closes due to unloading.

Furthermore, the tensile stresses that inflict the failure of concrete, is set to zero and transformed into equivalent unbalanced forces distributed to the surrounding concrete volume. When a crack is formed normal to the direction of the maximum principal tensile stress $\sigma_{I,}$ that stress σ_I is set to zero. Thus, the stresses are calculated through the following expression:

$$\boldsymbol{\sigma}_{\boldsymbol{Cr}} = \boldsymbol{T}^{-1} \begin{bmatrix} \sigma_1 = 0 \\ \sigma_2 \\ \sigma_3 \\ 0 \\ 0 \\ 0 \end{bmatrix} \tag{5.87}$$

where $\boldsymbol{T}^{-1}$ is the inverse transformation matrix (Eq. (5.84)) that is used to transform the principal stress axes to the initial *x*, *y* and *z* axes.

The closure of crack plays a major role in the mechanical behavior of the structure (this was also verified through this study after an excessive numerical investigation). The closure of cracks in the first half of a cycle loading defines the residual stiffness of the structure in the second half (a half cycle includes loading and unloading in one direction). The comparison between the numerical results with the experimental data shows that the strains which are directed normal to the crack plane could reach a small value by which it is assumed that they cause the crack closure. Furthermore, it is known that the smeared crack approach leads to significant stress-strain concentrations inside the uncracked areas. These stress-locking effects are caused by the fact that geometrical discontinuity (cracking) is simulated by the assumption of displacement continuity. The phenomenon is enhanced when the fixed crack approach is used in combination with a descending branch of constitutive models that describe the mechanical behavior of cracked concrete (Rots and Blaauwendraad [130]). The assumption of the brittle behavior of concrete (abrupt loss of strength capacity) and the rotating smeared crack approach (as presented above) prevent the major stress concentration that can lead to local failure within the concrete domain. The strain concentration becomes an issue especially in cyclic loading conditions because it prevents the closure of the cracks.

An analytical investigation performed in this research work showed that during unloading, the strains which are directed orthogonal to the crack plane are getting much smaller (not necessarily negative) than the value of strains that cause the crack formation. Fig. 5.28 shows the crack pattern of a shear wall in three deformational states:

a) cracking at first increments of cyclic loading (first equilibrium point of the incremental procedure),

b) cracking when the deformation of cyclic loading reaches its maximum value (at 10th increment),

c) cracking when the shear wall has returned to its initial state of equilibrium (at 20th increment).

It is noted that the cracks that opened at the initial step (see Fig. 5.28a) were closed when the shear wall was unloaded (see Fig. 5.28c). On the contrary the new cracks that opened near the top rigid beam illustrated in Fig. 5.28b, did not close (see Fig. 5.28c). The graph in Fig. 5.29, illustrates the opening of two cracks in terms of strains at two different Gauss points located at a) near the base and b) near the top of the shear wall. The first crack opens at the first displacement increment, while the second at the 10th displacement step. The red dashed line in the graph represents the value of the strain at which the cracks opened at the corresponding

Gauss point, while the cracks' strain is assumed to be zero prior to the crack opening. The graph in Fig. 5.29b shows that the strain related to the crack that opened at the loading step N=10 (crack initiated close to the rigid beam), starts to close thus at N=20 (last displacement step) has a strain value found to be smaller than the value that caused the actual crack formation. Given that the algorithm assumes that the crack is still under a tensile strain state, the crack remains open. This remaining stain is the main cause preventing the algorithm from closing the crack and subsequently the abrupt loss of capacity of the structure during the cyclic loading at an overall level (given that other cracks are also found to be under the same strain state).

Therefore, a criterion is proposed in order to determine the tolerance limits of strains that define the closure of these cracks. The criterion takes the following form:

$$\varepsilon_i \leq a\varepsilon_{cr} \tag{5.88}$$

Where ε_i is the current strain in the i-direction normal to the crack plane and ε_{cr} is the strain that causes the cracking formation. The parameter α is a reduction factor, whereas a numerical procedure is applied in order to calculate this parameter.

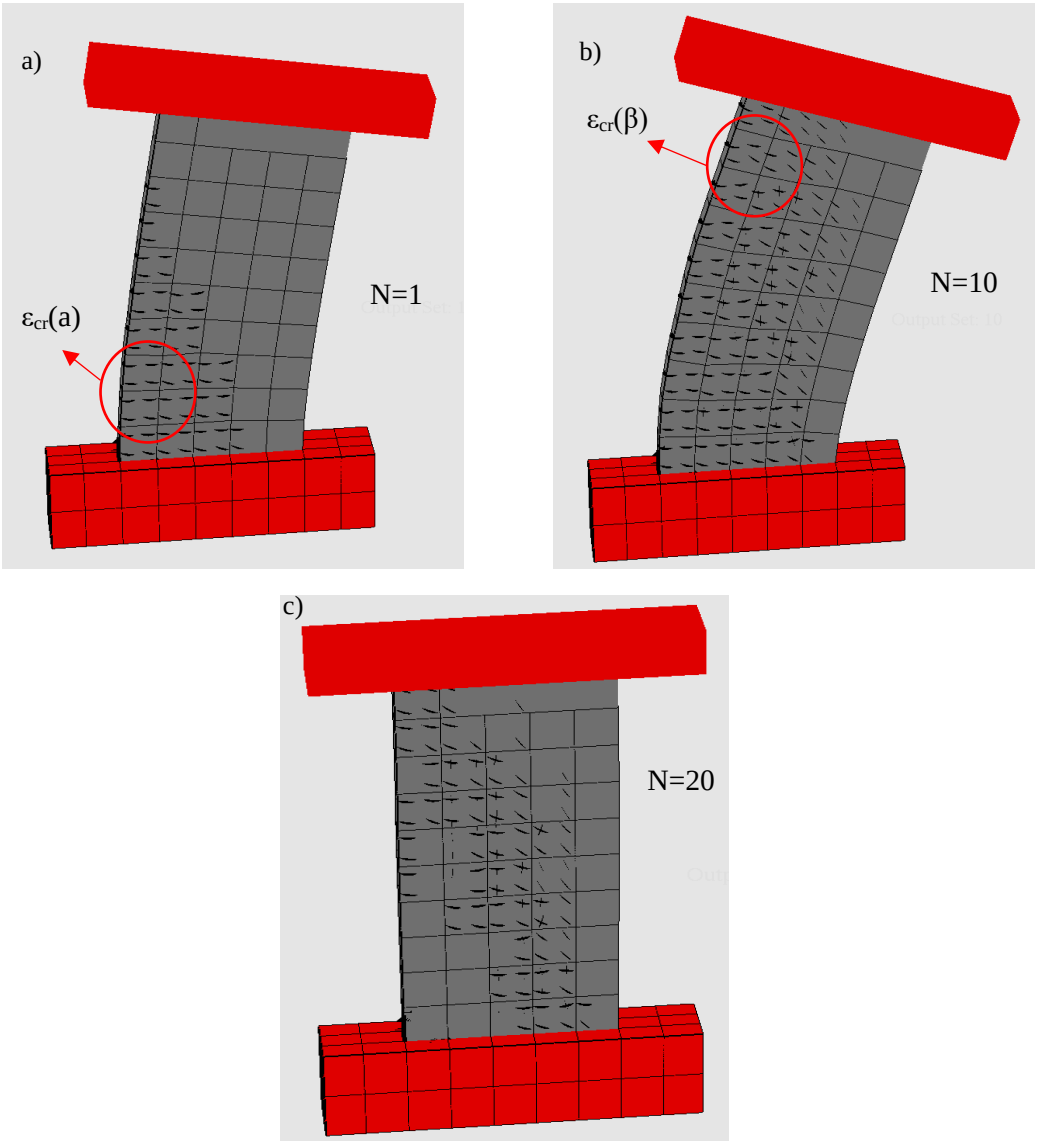

Fig. 5.28 Crack patterns at a) first increments of cyclic loading (N=1) (b) when the deformation of cyclic loading reaches its maximum value (at the 10th displacement increment, N=10), (c) when the shear wall has returned to its initial state of equilibrium (at the 20th displacement increment, N=20)

Following a numerical investigation, it appears that when the crack of a Gauss point is formed at the first increment of the imposed displacement branch, then $\varepsilon_i \cong \varepsilon_{cr}$ when the structure is back to the initial state of equilibrium. In addition, when the crack of a Gauss point is formed at the last increment of the imposed displacement branch, then $\varepsilon_i \cong 0$ when the structure is back to the initial state of equilibrium (Fig. 5.29). According to the above observations parameter α was computed according to the following expression:

$$a = 1 - \frac{\varepsilon_{cr}}{\varepsilon_{\max}} \tag{5.89}$$

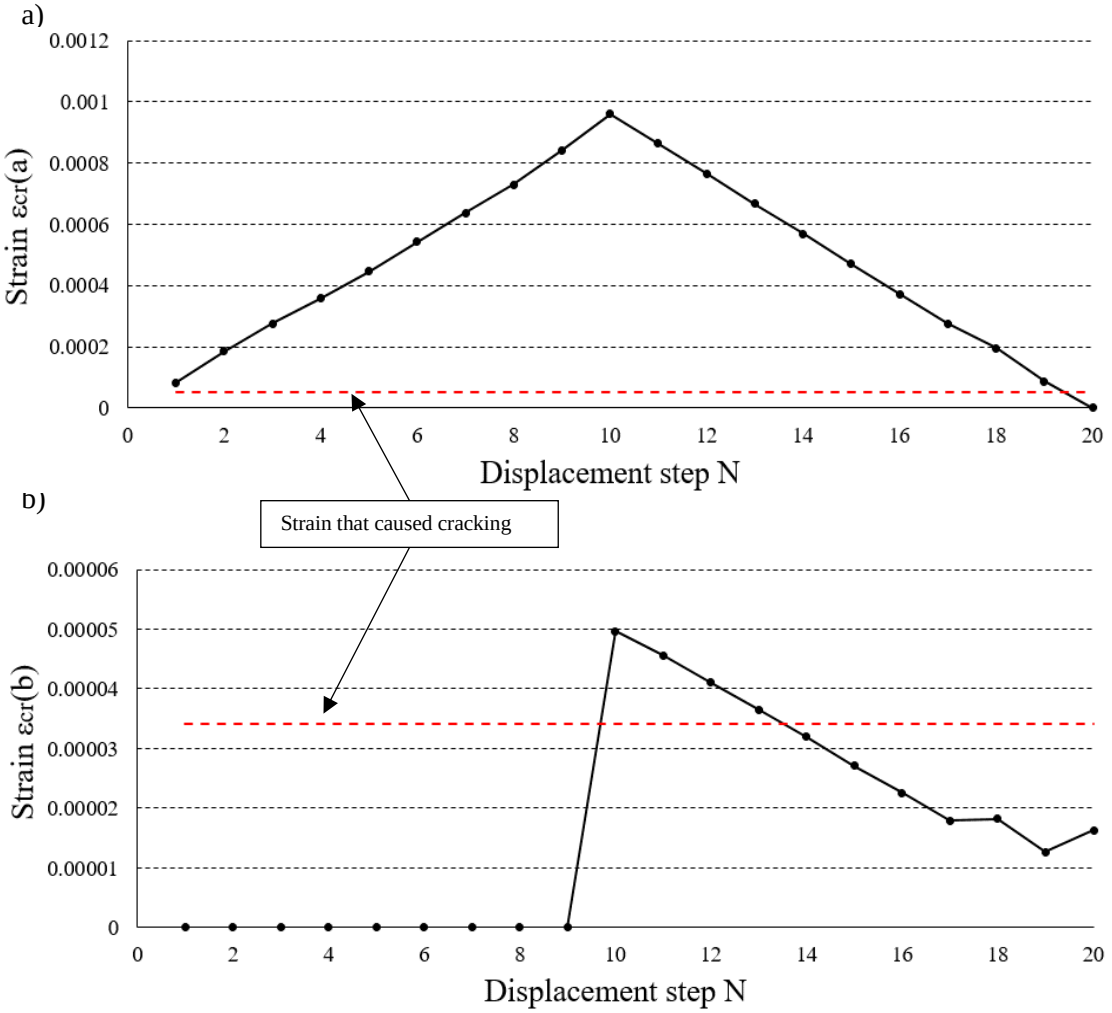

Fig. 5.29 Strain perpendicular to the crack plane versus displacement increments at (a) a Gauss point near the base of the shear wall and (b) a Gauss point near the top of the shear wall.

The ε_{max} is the maximum value of strain that is concentrated in the direction orthogonal to the crack plane. It is considered that $\varepsilon_{cr} \approx n_{cr}\varepsilon$ and $\varepsilon_{max} \approx n_{tot}\varepsilon$ ("≈" is due to the stress σ_{id} incorporated in Eq. (5.66)), where n_{cr} and n_{tot} correspond to the respective number of increment, that the crack is formed and the total number of increments that an imposed displacement branch is divided into, respectively. Furthermore, ε is the strain that corresponds to each iteration increment. Therefore, the expression of Eq. (5.89) takes the following form:

$$a = b - \frac{n_{cr}}{n_{tot}} \tag{5.90}$$

Where *b* is the number of the imposed displacement branch. Finally, in order to increase the tolerance of limits of strains that define the closure of the cracks, the fracture $1/n_{tot}$ is added to Eq. (5.90) and the parameter takes the final form as shown below:

$$a = b - \frac{n_{cr} - 1}{n_{tot}} \tag{5.91}$$

A schematic representation of the variables that are shown in Eq. (5.91), is illustrated through Fig. 5.30 which is an example of a half loading cycle. Each branch is divided by 10 increments. The *y*-axis consists the number of increments (the d^{incr} is the imposed displacement of each incremental iteration) and the x-axis represents the number of loading cycles.

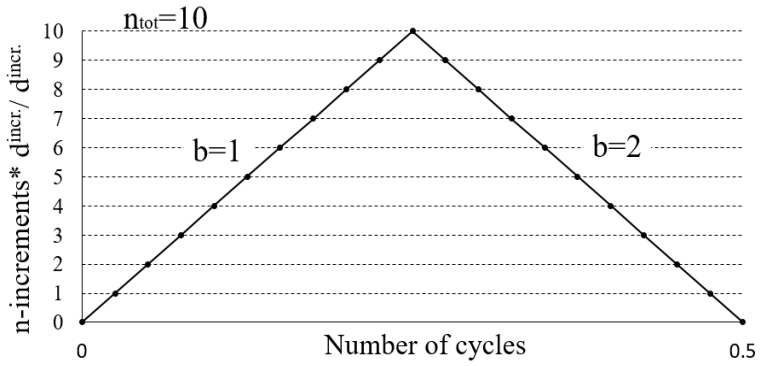

Fig. 5.30 Schematic representation of the variables that consist the expression (5.91) in an example of a half loading cycle. Each branch is divided by 10 increments. The y-axis consists the numbers of increments.

When a crack is closed, the elastic constitutive matrix is used in order to calculate the stresses of the previously cracked Gauss point during the next iteration. Therefore, the total stresses of the *i*-Newton-Raphson iteration are calculated by Eq. (5.92).

$$\boldsymbol{\sigma}^{i} = \boldsymbol{\sigma}^{i-1} + \mathbf{D}_{\mathbf{el}} \Delta \boldsymbol{\varepsilon}^{i} \tag{5.92}$$

Where the $\boldsymbol{D}_{el}$ has the form of the expression in Eq. (5.80) with $K=K_{el}(f_c)$ and $G=G_{el}(f_c)$ as presented in [29]. $\Delta\varepsilon^{i}$ are the current strains of the *i*-iteration and $\boldsymbol{\sigma}^{i-1}$ are the total stresses of the *(i-1)*-iteration when the GP developed the crack.

Finally, in the present work the unified total crack approach (UTCA) proposed by Spiliopoulos and Lykidis [176] is adopted. This means that the state of crack formation or closure is treated in a unified way within every Newton-Raphson internal iteration. The proposed behavior of both cracked and uncracked GPs are described in the flow charts presented in Fig. 5.31 and Fig. 5.32, respectively.

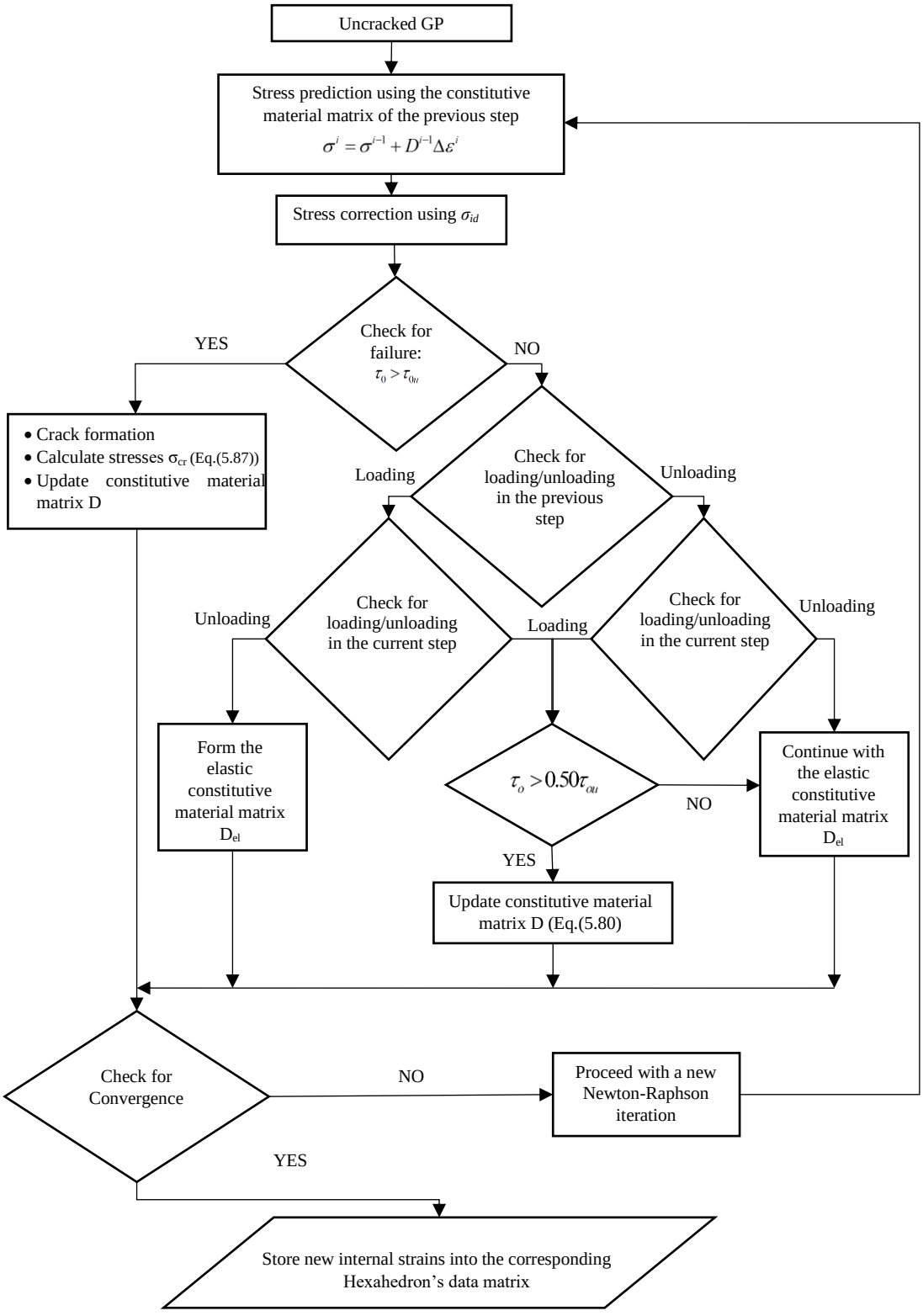

Fig. 5.31 Flow chart of the proposed algorithm responsible in updating the stress-strain tensors and constitutive matrix for the case of an uncracked Gauss point.

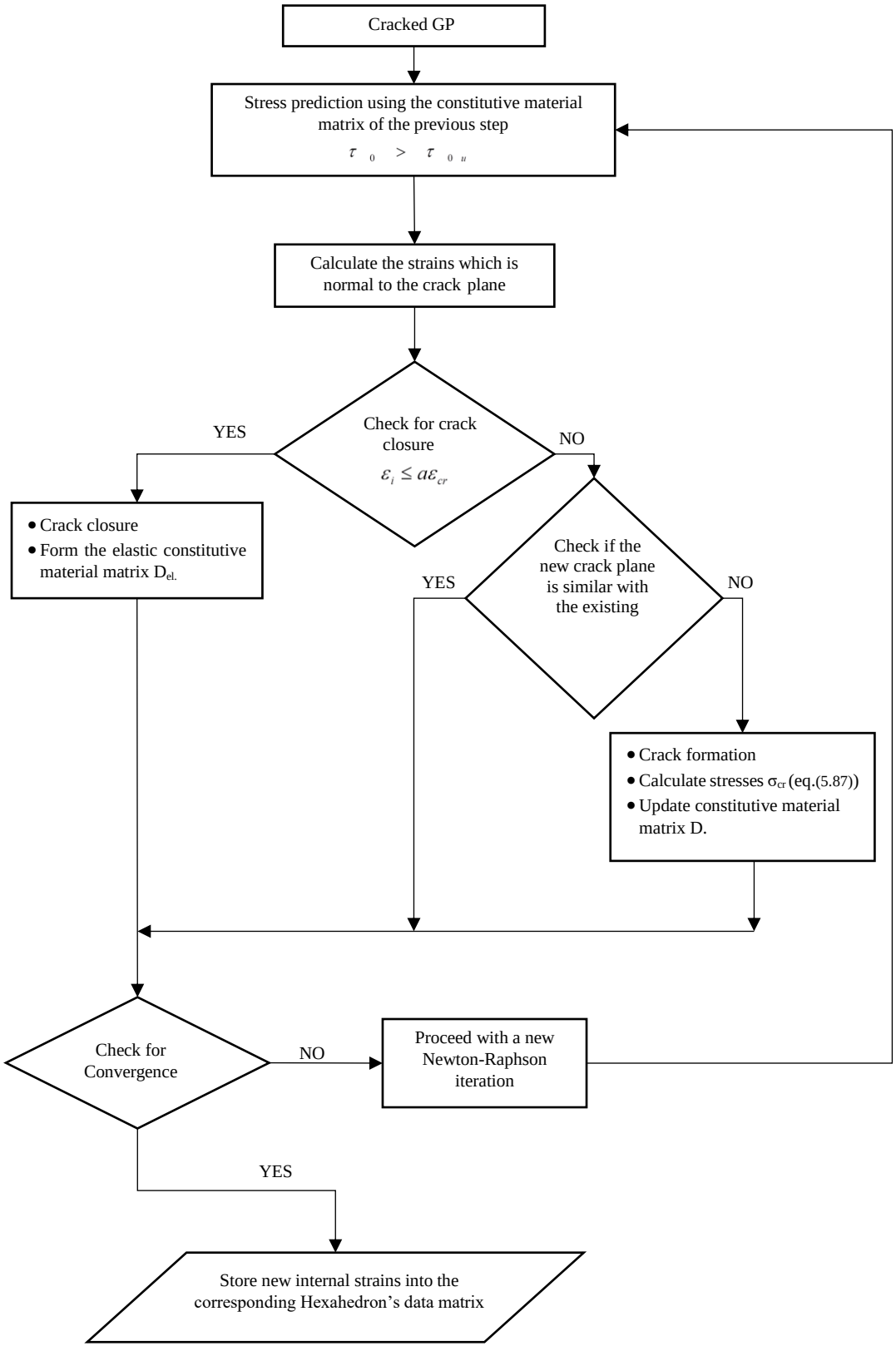

Fig. 5.32 Flow chart of the proposed algorithm responsible in updating the stress-strain tensors and constitutive matrix for the case of a cracked Gauss point.

5.4.4 Compressive failure of concrete

It is convenient to formulate a strength envelope of concrete which is governed by the combination of maximum stresses in terms of hydrostatic and deviatoric components acting on the octahedral plane. Therefore, the orthogonal coordinate system (σ_1, σ_2, σ_3) is transformed into the cylindrical coordinate system. The axis z is related to the hydrostatic stress that coincides with the space diagonal $\sigma_1 = \sigma_2 = \sigma_3$, while the radius r is similarly related to the magnitude of the deviatoric stress component. The rotational variable θ defines the deviatoric stress orientation on the octahedral plane and the graph has the characteristics of convex failure surfaces as shown in Fig. 5.23. As it was mentioned in the previous section, it is open in compression since concrete can sustain larger deviatoric stresses as σ_0 increases. Experimental data were obtained in order to calculate the deviatoric stresses τ_{0e} $(\theta=0°)$ and τ_{0c} $(\theta=60°)$, which correspond to the state of $\sigma_1=\sigma_2>\sigma_3$ (triaxial extension) and $\sigma_1>\sigma_2=\sigma_3$ (triaxial compression), respectively (Kotsovos & Pavlovic [29]). The value of ultimate deviatoric stress can be interpolated by using the τ_{0e} and τ_{0c} stresses through the expressions of Willam and Warnke [33] based on Eqs. (5.76), (5.77) and (5.78).

It is also known that concrete's strength under tension is unaffected by triaxial phenomena. Therefore, it is considered that concrete fails in tension when a tensile stress σ_{ij} exceeds the tensile strength of concrete f_{ct}.

Finally, most researchers combine the failure surface with the softening constitutive laws in order to describe the cracked behavior of concrete. Consequently, the smeared crack approach introduces stress-strain localizations causing numerical instabilities throughout the nonlinear analysis. These models are mesh-dependent as locale failures in finer meshes could lead to smaller limit loads. For this reason, most of these studies introduce crack band models [14] to eliminate this numerical issue. The 3D brittle constitutive law adopted herein is presented as a more realistic approach that discharges the cracked areas from excessive stress concentrations by releasing them to the surrounding uncracked areas as described in Eq. (5.87). This way, the numerical problems which are appeared due to softening behaviors are prevented. The numerical problems that might occur in this case, are mesh-independent as shown in the numerical applications discussed in the next section.

5.4.5 Constitutive model of steel reinforcement

The steel-reinforcement has to be modelled as a reinforcing steel material in particular rather than as a general structural steel behavior. During cyclic loading conditions, the compressive strains that are developed in reinforcing bars are not as large as tensile strains. When the crack previously opened, is closed and the concrete cover has not spalled, the compressive forces are largely carried by concrete. In cases when the cracks are open, the bonding deterioration between crack and steel rebars, prevents the development of large strains in steel reinforcement. Therefore, the steel bars hardly ever yield in compression before the spalling of concrete cover (CEB 1996 [105]).

The modeling of steel reinforcement has to be characterized by computational efficiency and accuracy. The behavior of steel reinforcement plays a significant role to the overall behavior of RC members particularly when excessive cracking has been developed and in regions when cracks are not closed after unloading and reloading of the member. The basic features of the hysteretic behavior of steel reinforcement are:

- Onset of strain hardening.
- Bauschinger effect.
- Isotropic strain hardening under plastic strain reversals.

These characteristics are illustrated schematically in Fig. 5.33.

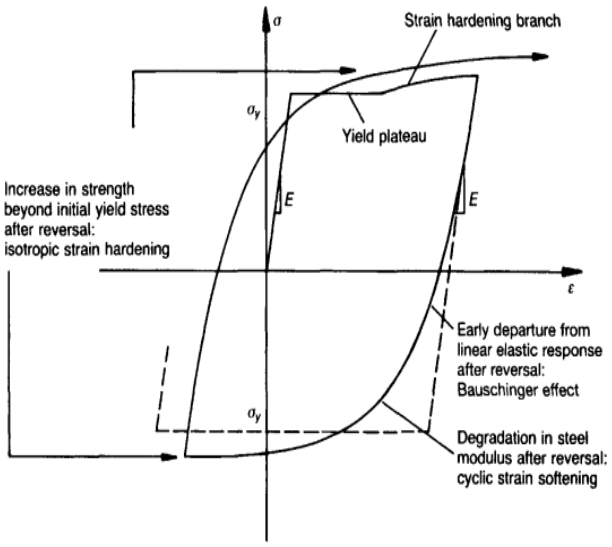

Fig. 5.33 Characteristics of the hysteretic steel stress-strain behavior of reinforcement steel (CEB 1996 [105]*).*

Several nonlinear hysteretic models have been proposed during the last decades. The most successful one is the Menegotto-Pinto [34] model. Therefore, the material of steel-reinforcement is modeled through the use of the Menegotto-Pinto [34] model that takes into account the Bauschinger effect. The stress-strain relation takes the form:

$$\sigma^* = b \cdot \varepsilon^* + \frac{(1-b)\cdot \varepsilon^*}{\left(1+\varepsilon^{*R}\right)^{\frac{1}{R}}} \tag{5.93}$$

where, $\varepsilon^* = (\varepsilon - \varepsilon_r)/(\varepsilon_0 - \varepsilon_r)$, $\sigma^* = (\sigma - \sigma_r)/(\sigma_0 - \sigma_r)$ and

$$R = R_0 - \frac{a_1 \xi}{\alpha_2 + \xi} \tag{5.94}$$

which is the stress-strain relation of the steel reinforcement as illustrated in Fig. 5.34

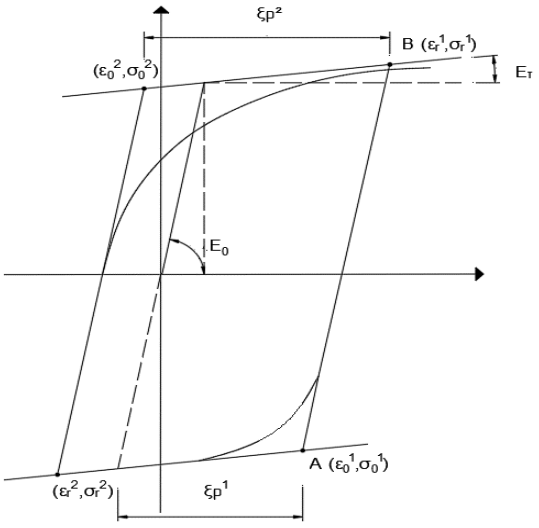

Fig. 5.34 Menegotto-Pinto constitutive model for steel reinforcement

The parameter b is the strain hardening ratio between E_0 and E_t, ε_0 and σ_0 are the coordinates of the point where the asymptotes of the branch intersect, ε_r and σ_r are the coordinates of the point where the last strain reversal with stress increment of equal sign takes place. The parameter R is a decreasing function of ξ, which is the strain difference between the current asymptote intersection point and the previous load reversal point with maximum or minimum strain, depending on whether the corresponding steel stress at reversal is positive or negative. R_0, a_1 and a_2 are experimentally determined parameters and assumed to be 20, 18.5 and 0.15, respectively, in this study.

Chapter 6. Numerical implementation for RC members under cyclic loading conditions

Contents of Chapter 6

6.1 Introduction 115

6.1.1 Lefas and Kotsovos Shear Walls 115

6.1.2 Červenka Shear Wall W4 125

6.1.3 RC Frame Joints 130

6.1.3.1 Del Toro Rivera Frame Joint 130

6.1.3.2 Beam-Column Corner Joint 135

6.2 Conclusions 138

6.1 Introduction

A numerical verification of the accuracy and efficiency of the proposed numerical method (as described in 5.4) will be presented in this chapter. In order to achieve this objective, four RC shear walls and two RC frame joints have been modeled under cyclic loading. The models are analyzed by using the displacement-control Newton-Raphson iterative method that foresees the use of an energy convergence tolerance criterion with a convergence tolerance equal to 10^{-4}.

6.1.1 Lefas and Kotsovos Shear Walls

Three identical shear wall specimens were investigated experimentally in Lefas and Kotsovos [177] are denoted as walls SW31, SW32 and SW33. The geometric details of the shear walls are given in Fig. 6.1. All walls were 650 mm wide, 1.300 mm high and 70 mm thick. The uniaxial compressive strength (f_c) of SW31, SW32 and SW33 is 35.2, 53.6 and 49.2 MPa, respectively. The yielding stresses (f_y) of the steel reinforcement were 420, 520 and 470 MPa for the 4, 6 and 8 mm diameter bars used, respectively. All walls were monolithically connected to a rigid RC beam at both top and bottom. Each shear wall was subjected to different cyclic loading conditions, while the loading histories are presented in the form of imposed displacements in Fig. 6.2.

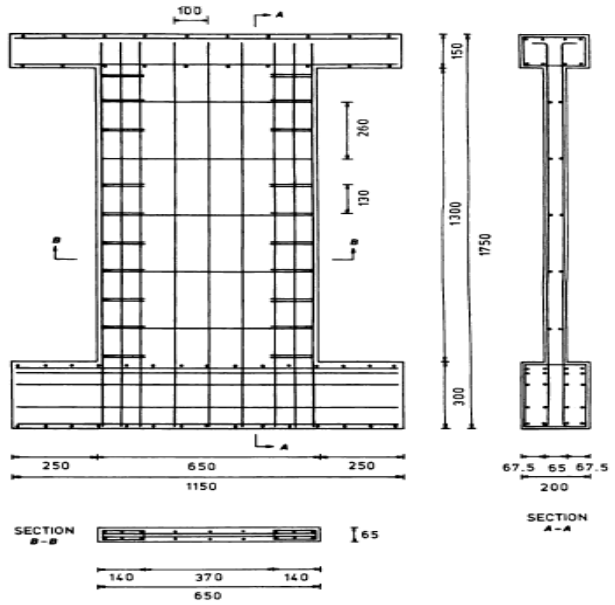

Fig. 6.1 Geometry and Reinforcement details of shear walls SW31, SW32 and SW33 [177].

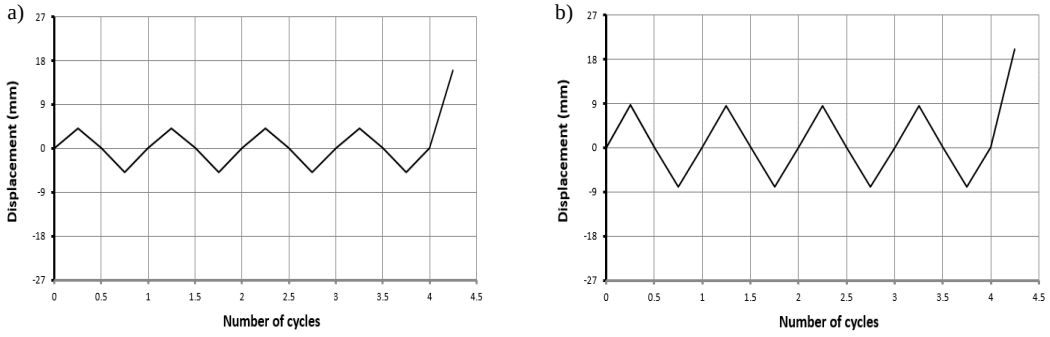

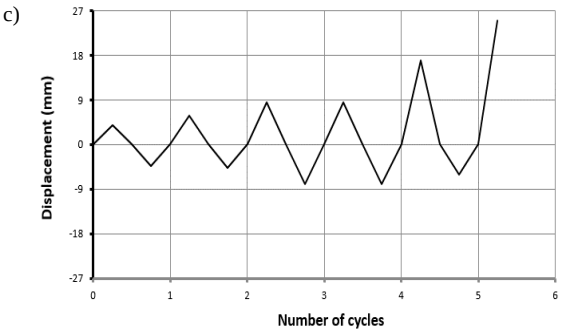

Fig. 6.2 Load histories presented in the form of imposed displacements for a) SW31, (b) SW32 and (c) SW33.

The concrete domains are modeled with 8-noded hexahedral finite elements and the steel reinforcement is modeled by using truss finite elements. For the SW33 specimen, the transverse steel elements are also modeled by using NBCFB elements in order to investigate their effect on the dissipation energy of the structural member. As illustrated in Fig. 6.3 the embedded steel elements (transverse and longitudinal) have the exact location and direction of the actual reinforcement. At the top and the bottom of the shear wall, 81 rigid 8-noded hexahedral elements are used to discretize the rigid RC beams, while 50 concrete finite elements (13cm X 13cm X 6.5cm) and 318 steel elements are used to model the rebars as illustrated in Fig. 6.3, Fig. 6.4.

It must be noted at this point that, for the need of the cyclic analysis it was assumed that 10 external displacement increments for each displacement branch (quarter of the loading cycle) of the loading history shown in Fig. 6.2 are used for SW31 and SW32. For the specimen SW33, 30 displacement increments are used for the displacement branches that reach a displacement equal to 15cm (the first half of the 5^{th} loading cycle) and 10 displacement increments are used for the other displacement branches. Based on this assumption, the total number of displacement steps used to analyze SW31, SW32 and SW33 were 200, 210 and 290, respectively.

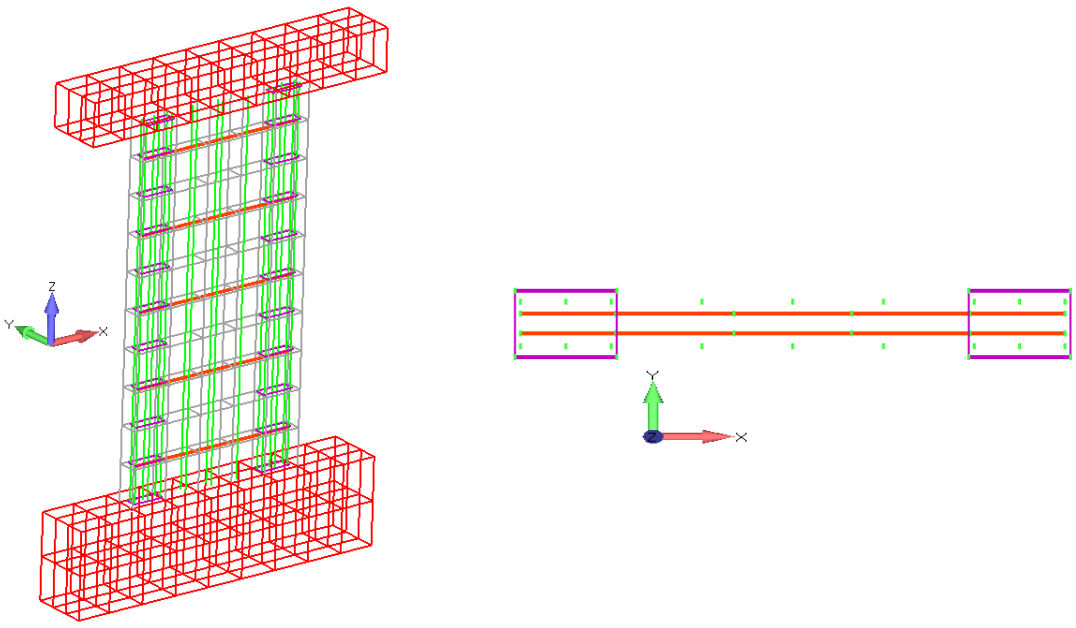

Fig. 6.3 Shear walls. 3D and XY views of the FE mesh of the steel bars.

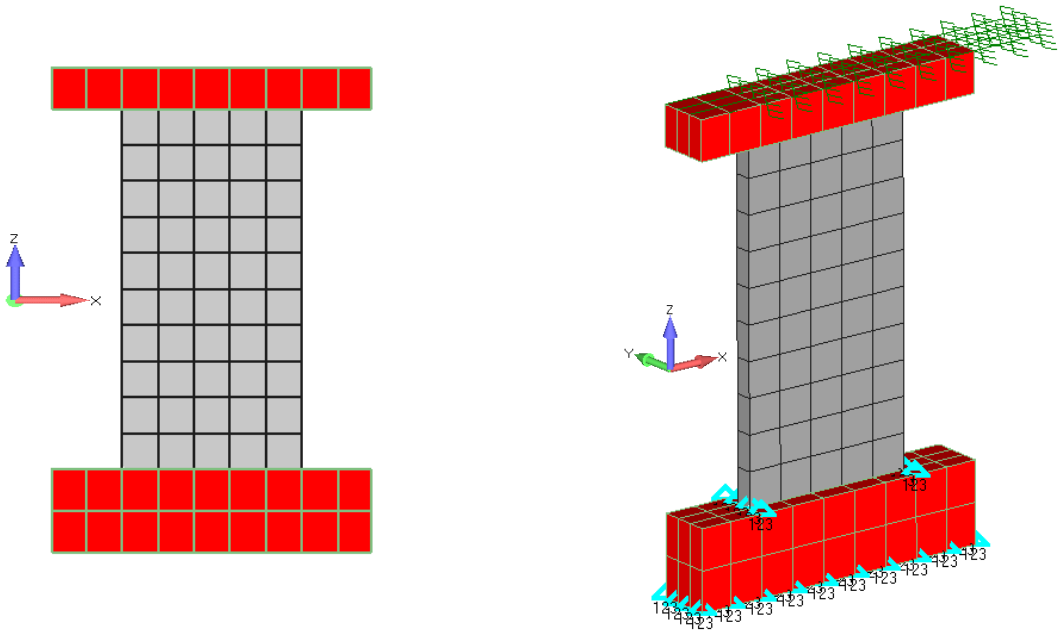

Fig. 6.4 Kotsovos and Lefas (Left) Shear walls. (Right) XZ and 3D views of the FE mesh, constraints and imposed displacement of the 8-noded hexahedral elements.

The numerical results are compared with the corresponding experimental curves in Fig. 6.5. As it can be seen, the numerical results match very well with the experimental curves in terms of stiffness and strength. The experimental results show that specimens SW31, SW32 and SW33 had a load-carrying capacity of 119 kN, 112 kN and 112 kN, respectively, whereas the numerically predicted load-carrying capacities were 120 kN, 113.5 kN and 106 kN, respectively. The comparisons between the experimental and the numerical results for each imposed loading cycle for the three shear walls, are given in Table 6.1, Table 6.2 and Table 6.3. The experimental curves show that the width of the hysteretic loop appears to be greater than the numerically predicted. This discrepancy is negligible in the first two specimens SW31 and SW32. The experimental curve of SW33, in the last cycle presents large plastic displacements (Fig. 6.5c) greater than the numerical ones.

According to Lefas and Kotsovos [177] the energy dissipation causes the increase of the ductility level of the cyclic loading. This implies that the energy dissipation is influenced mainly by the yielding of the tensile bars rather than concrete cracking. Table 6.4, shows the comparison between the experimental and the numerical energy dissipation for the last two cycles. It is evident that the use of truss elements underestimates the dissipation energy of the specimen SW33, mainly in the last two loading cycles. However, the model that adopts the NBCFB element model manages to simulate more realistically the plastic deformations of the structure, which are mainly caused by the yielding of the tensile bars. Additionally, the comparison shows a satisfying agreement between the numerical and experimental results. It should be noted that, the NBCFB elements were also tested for the other shear wall models and was found that the numerical results demonstrated a negligible effect mainly because the dissipation energy appeared to be considerably small.

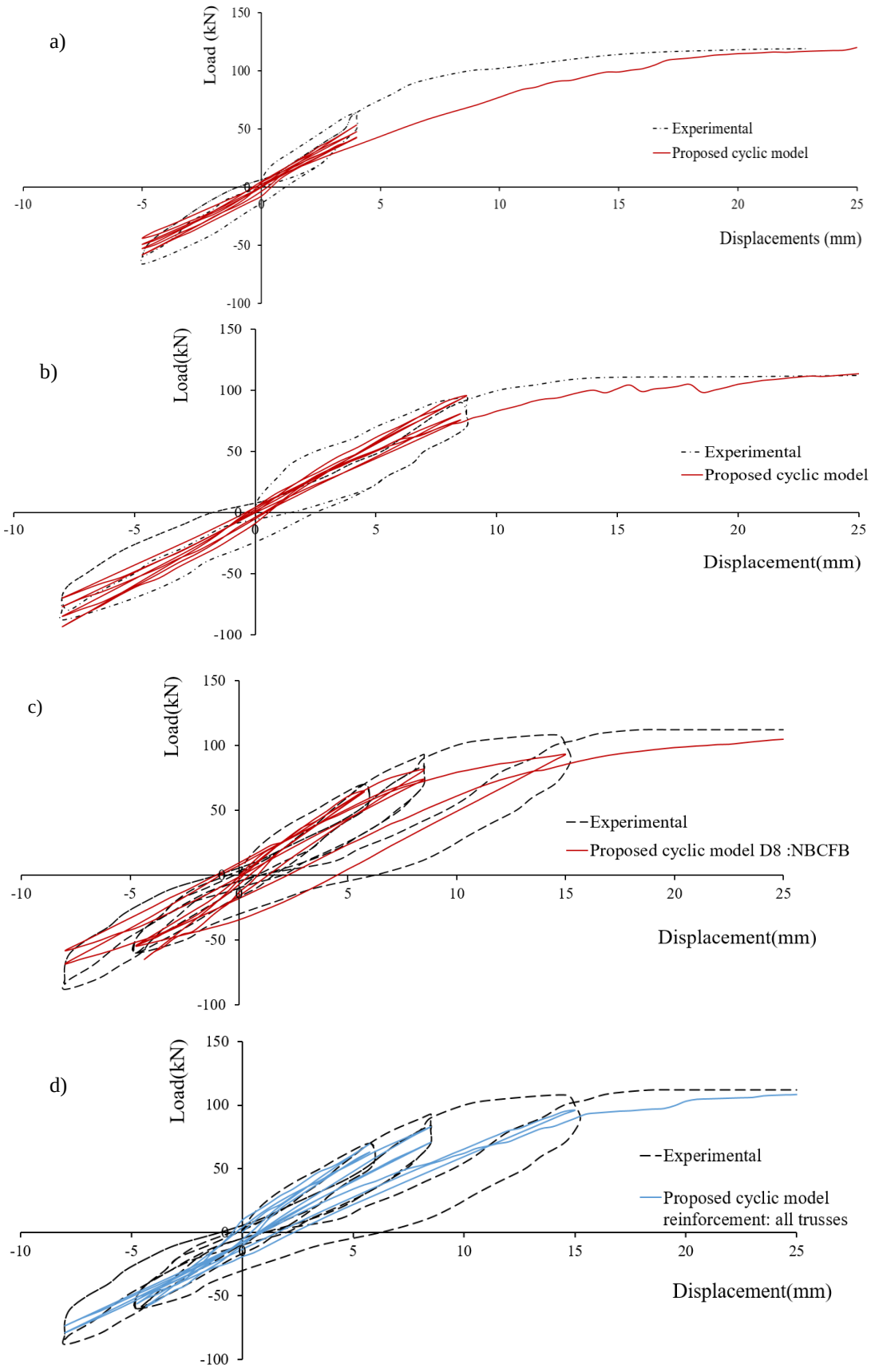

Fig. 6.5Comparison between numerical and experimental results of the force deflection curves of specimens (a) SW31, (b) SW32, (c) SW33 with NBCFB elements for the steel reinforcement of diameter 8mm and (d) SW33 with trusses

Fig. 6.6 shows the force deflection curves for two different discretizations (131 and 226 hexahedral elements) for the case of the SW31 specimen. In addition to that, different external displacement increments are used for the analysis so as to study the displacement-increment-size sensitivity. As it resulted from the sensitivity analysis, both the size of the displacement increment and the mesh discretization size, have negligible effects on the overall nonlinear mechanical response of the models. Moreover, Fig. 6.7 shows the force deflection curves of the analysis of the SW33 when using different values of the shear retention factor β. When the factor has values $0.05 \leq \beta \leq 0.1$, the deflection curves are almost identical .The maximum divergence was obtained when β was set to 0.3 and 0.5, where the shear retention factors had very high values (they overestimate the remaining stiffness significantly).

Table 6.1 SW31.Comparison of the horizontal load of each cycle between experimental and numerical results.

Loading Cycle	Horizontal Load Experimental (kN)		Horizontal Load Predicted (kN)	
	Positive	Negative	Positive	Negative
1st	64	-66	48	-58
2nd	64	-60	53	-54
3rd	64	-60	48	-50
4th	64	-60	43	-44
Failure	119		120	

Table 6.2 SW32.Comparison of the horizontal load of each cycle between experimental and numerical results.

Loading Cycle	Horizontal Load Experimental (kN)		Horizontal Load Predicted (kN)	
	Positive	Negative	Positive	Negative
1st	94	-88	95	-93
2nd	94	-88	93	-85
3rd	90	-70	80	-77
4th	90	-70	76	-70
Failure	112		113.5	

Table 6.3 SW33.Comparison of the horizontal load of each cycle between experimental and numerical results.

Loading Cycle	Horizontal Load Experimental (kN)		Horizontal Load Predicted (kN)	
	Positive	Negative	Positive	Negative
1st	70	-60	65	-65
2nd	70	-60	66	-55
3rd	93	-88	82	-69
4th	84	-84	75	-59
5th	108	-60	94	-55
Failure	112		106	

Table 6.4 SW33.Comparison of the dissipated energy of the last two cycles between experimental and numerical results.

Loading Cycle	Dissipated Energy Experimental (kN mm)	Dissipated Energy Predicted (NBCFB as embedded rebars) (kN mm)	Dissipated Energy Predicted (trusses as embedded rebars) (kN mm)
4th	292.25	127.53	13.56
5th	927.70	521.96	141.97

Based on the numerical findings of this investigation, it is concluded that the proposed modeling approach does not face any stress locking effects and the proposed value $\beta = 0.05$ fits ideally with the theory stating that there is a negligible contribution of aggregate interlock ($\beta \leq 0.1$). The comparison also shows that the proposed model can accurately predict the non-linear hysteretic behavior of the under study RC structural members that undergone limit-state cyclic loading conditions.

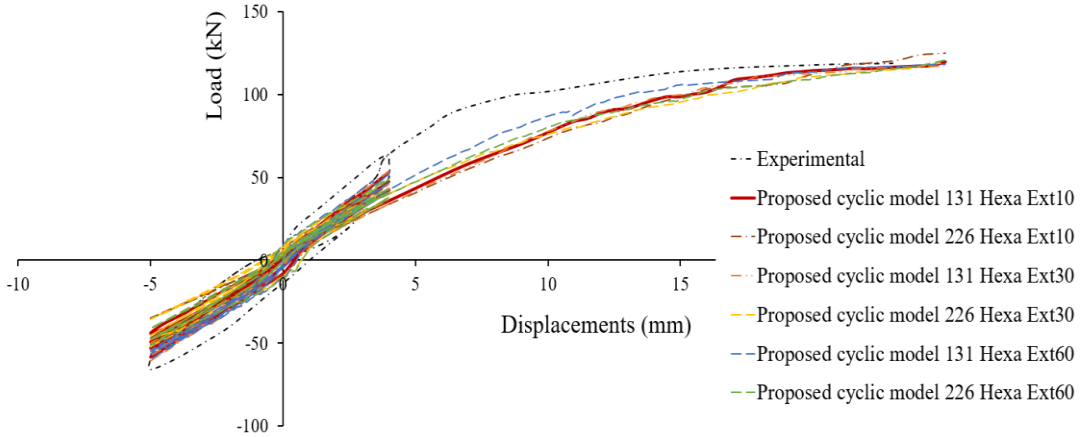

Fig. 6.6 Comparison between numerical and experimental results of the force deflection curve SW31 for different mesh discretizations (131, 226 hexahedrals) and for different external displacement increments (Ext10, Ext30, Ext60).

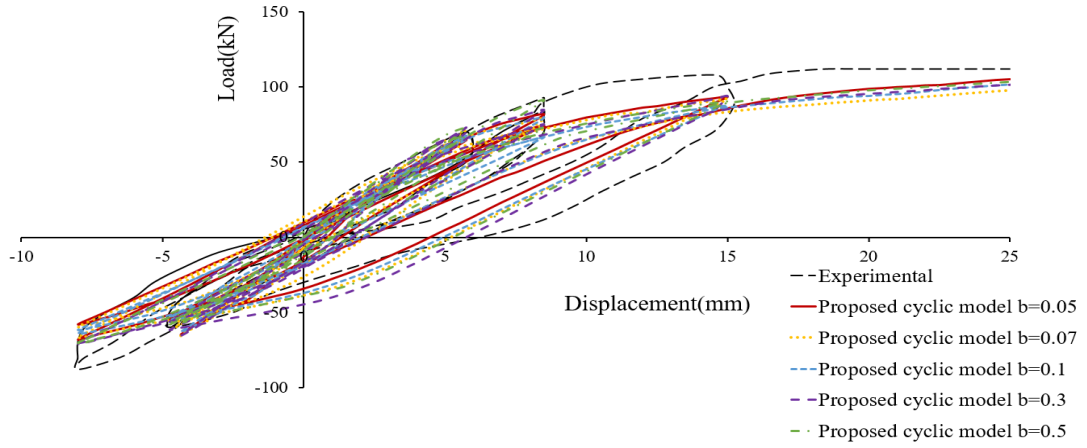

Fig. 6.7 Comparison between numerical and experimental results of the force deflection curve SW33 for different shear retention factors.

Furthermore, Fig. 6.8 shows the crack patterns that are formed when the structure reach the maximum imposed displacements at both opposite directions during the first cycle. When the maximum imposed displacement is reached, the cracks are formed within the areas of the

section that are under tension due to the bending moment, while this was the reason why the cracks appear to be mainly horizontal. As the cracks form closer to the compressive zone of the section, they develop a relative inclination due to the shear deformation of the web. Additionally, the figures show a great concentration of cracks in the center of the shear wall which is dominated by a more complex state of stress due to triaxial phenomena.

SW31

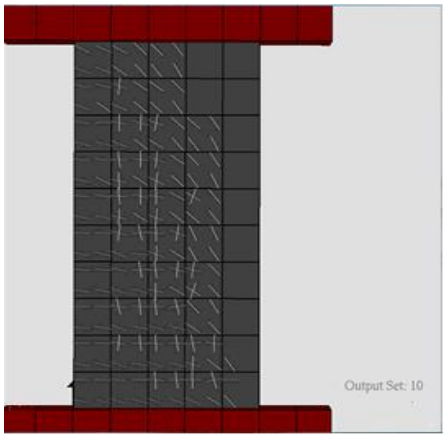

(a)

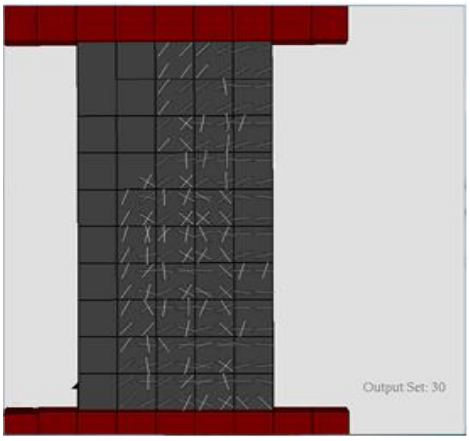

(b)

SW32

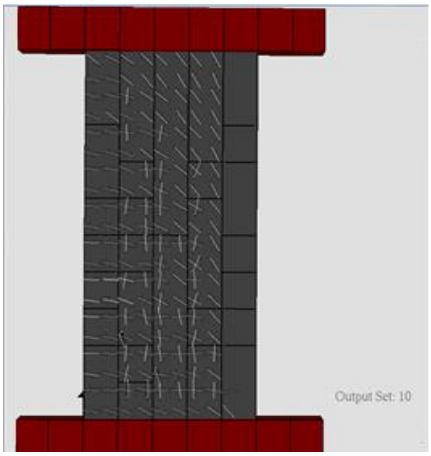

(a)

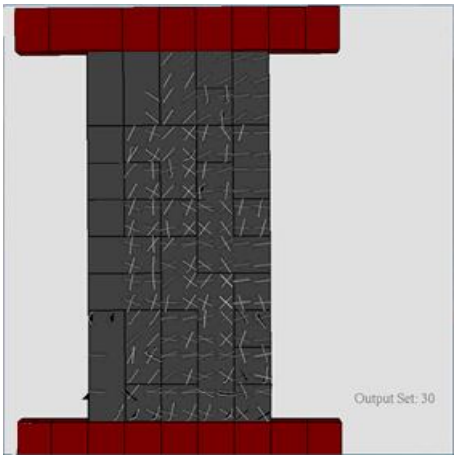

(b)

SW33

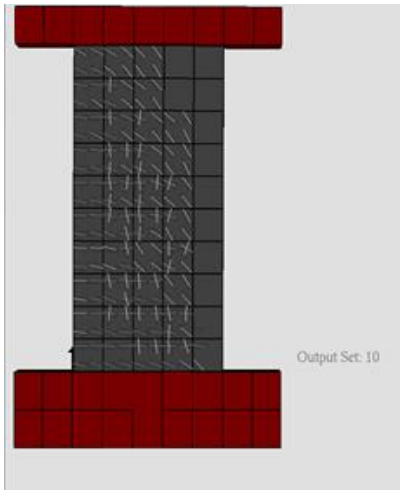

(a)

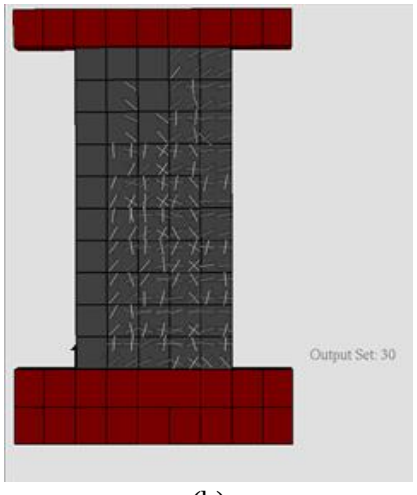

(b)

Fig. 6.8 Crack patterns during the first cycle when the imposed displacement reaches its maximum magnitude (a) horizontal displacement along the positive x axis and (b) negative x axis.

The crack patterns near the failure mode are depicted in Fig. 6.9. The cracks are initiated at the bottom area of the tensile zone of the walls (fixed base). These cracks, which are located at the base of the walls, were found to be the largest ones when the specimen reached the failure mode. As the horizontal displacement was increased, excessive inclined cracks were developed at the middle of the walls, which tend to extend near the compressive zones. Finally, the cracks formed orthogonally crisscrossing crack patterns, which are verified by the numerical crack patterns shown in Fig. 6.9. It is obvious that the numerical crack patterns appear to be denser than the experimental ones, a numerical phenomenon attributed to the smeared crack approach. However, it is evident that there is a good agreement on the distribution, the location and the direction of the predicted cracks.

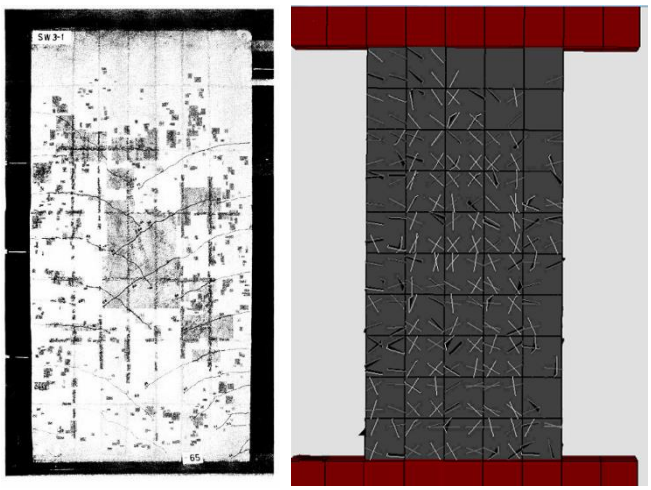

(a)

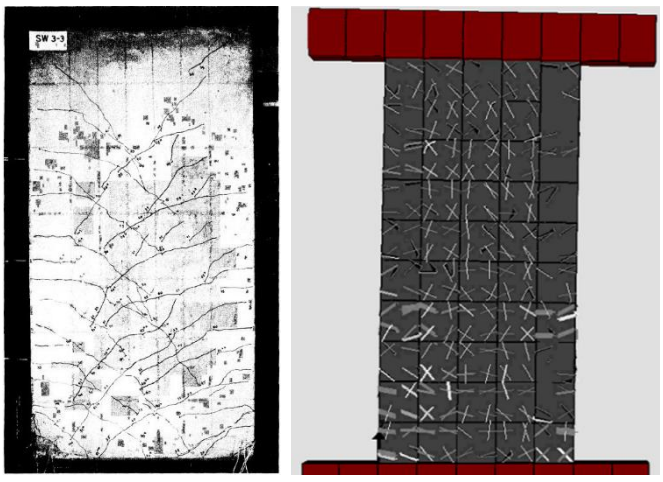

(b)

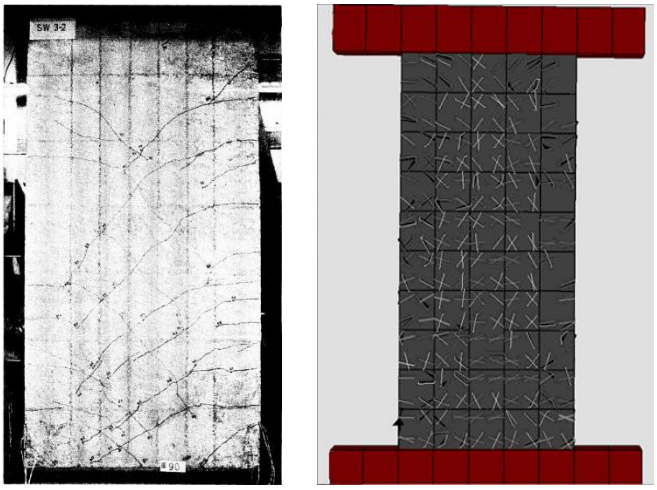

(c)

Fig. 6.9 Comparison between experimental with numerical results in terms of crack patterns for a) SW31 when the horizontal load was 65 kN, b) SW32 when the horizontal load was 90 kN and c) SW31 when the horizontal load was 110 kN (prior to failure).

The required NR iterations during the solution procedure of these shear wall models are depicted in the graphs of Fig. 6.10 where the values are given for the last loading cycles until complete failure (80, 90 and 130 displacement increments for SW31, SW32 and SW33, respectively). For the SW31 and SW32, 40 displacement increments were solved at the last loading cycle, while 80 displacement increments were solved for the analysis of the last cycle of SW33. The maximum number of NR iterations occurred when the imposed displacement reached a maximum value where the structural member was close to failure due to excessive cracking. The required computational time for the nonlinear solution procedure for each model is given in Table 6.5, and each corresponds to a total of 200, 210 and 290 displacement increments that were solved for SW31, SW32 and SW33 models, respectively. Both Fig. 6.10 and Table 6.5 show the computational efficiency and robustness of the proposed nonlinear procedure that manages to solve on average numerical problem in 5 seconds. The use of the NBCFB element seems to increase the total computational cost as far as the time of the nonlinear incremental-iterative solution. This occurs due to the fact that the complex flexibility-based formulation of the NBCFB element, implements an iterative algorithm in order to calculate the internal forces during the element state determination. Furthermore, given that the number of concrete element is smaller than that of the embedded rebars, the use of the NBCFB elements were found to increase the computational demand of the nonlinear procedure. Finally, as it can be observed from Fig. 6.10, the number of required internal iterations for all models is limited to an average of 3 to 4, underlining the numerical stability of the proposed method. Especially for SW33, the internal iterations have an average value equal to 4 when using the NBCFB element for modeling the longitudinal steel rebars, while the corresponding specimen that uses the truss elements has an average of 3 internal iterations per displacement increment.

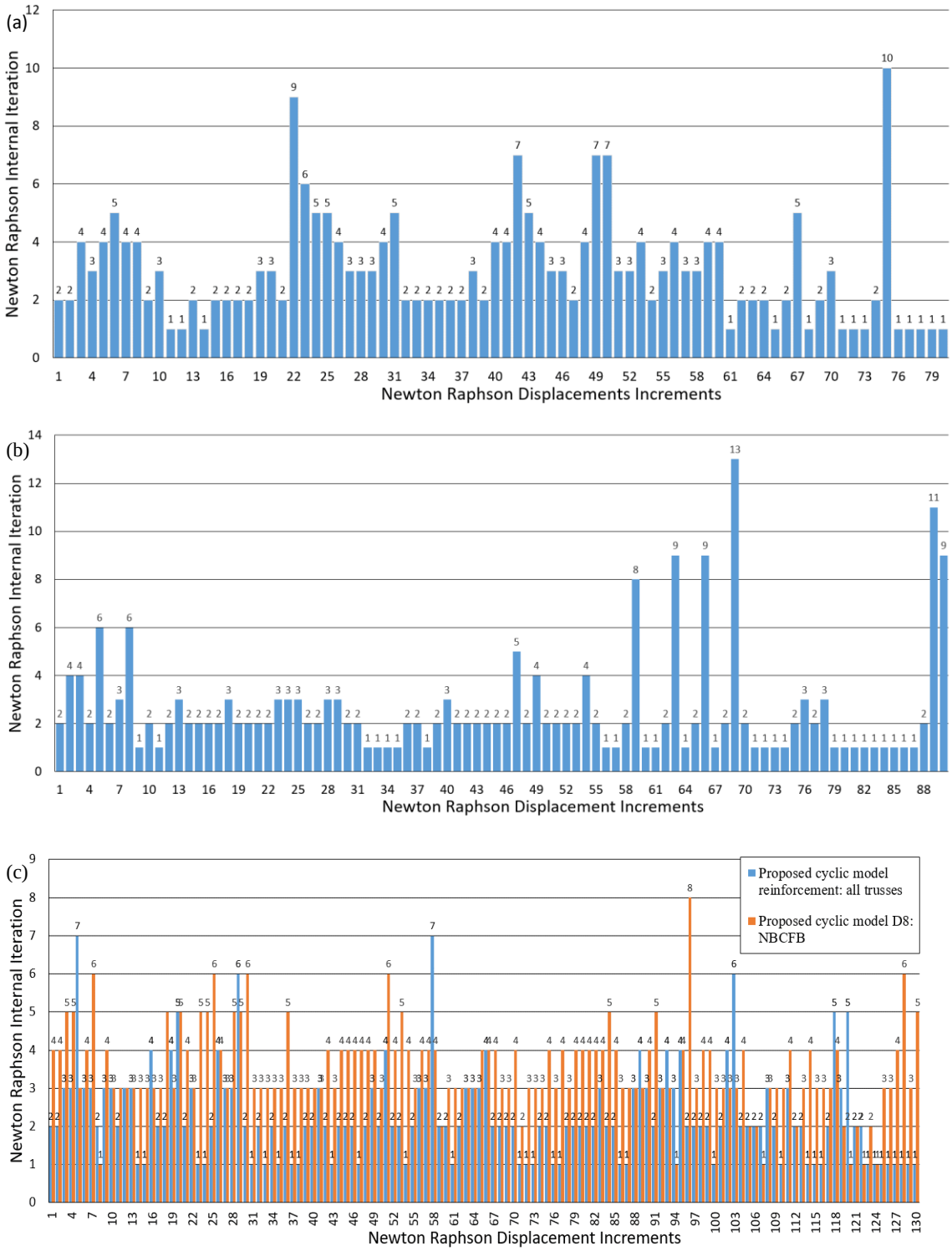

Fig. 6.10 Kotsovos and Lefas Shear walls. Required NR iteration per displacement increment from the last cycle of loading (until failure) for (a) SW31, (b) SW32 and (c) SW33

Table 6.5 Kotsovos and Lefas Shear walls. CPU time for different tasks of the nonlinear analysis.

Task	CPU Time (s)			
	SW31	SW32	SW33 (NBCFB as embedded rebars)	SW33 (trusses as embedded rebars)
Embedded rebar element mesh generation	0.032	0.035	0.033	0.026
Nonlinear incremental-iterative solution	4.85	4.46	15.79	5.68
Total Time	4.882	4.495	15.823	5.713

6.1.2 Červenka Shear Wall W4.

The shear wall W4 tested by Červenka [5] has been analyzed by many researchers in the past (Darwin and Pecknold [6], Ile and Reynouard [13], Kwak and Kim [20], Spiliopoulos and Lykidis [28]). The wall W4 was subjected to 5 load cycles, where the first 2 cycles are performed in the elastic range of steel. In the other three cycles, the magnitude of loading is close to the monotonic load-carrying capacity. The wall W4 has 76.20 cm height and a 7.62 cm thickness as shown in Fig. 6.11. The horizontal and vertical reinforcement ratio were both equal to 1.22%. The cylindrical uniaxial compressive strength of concrete was f_c=26.5 MPa, the tensile strength f_t=1.60 MPa and the Young modulus of elasticity was E=20.4 GPa. The yielding strength of steel was reported to be equal to f_y=360 MPa and the Young modulus of elasticity was E_s=192 GPa.

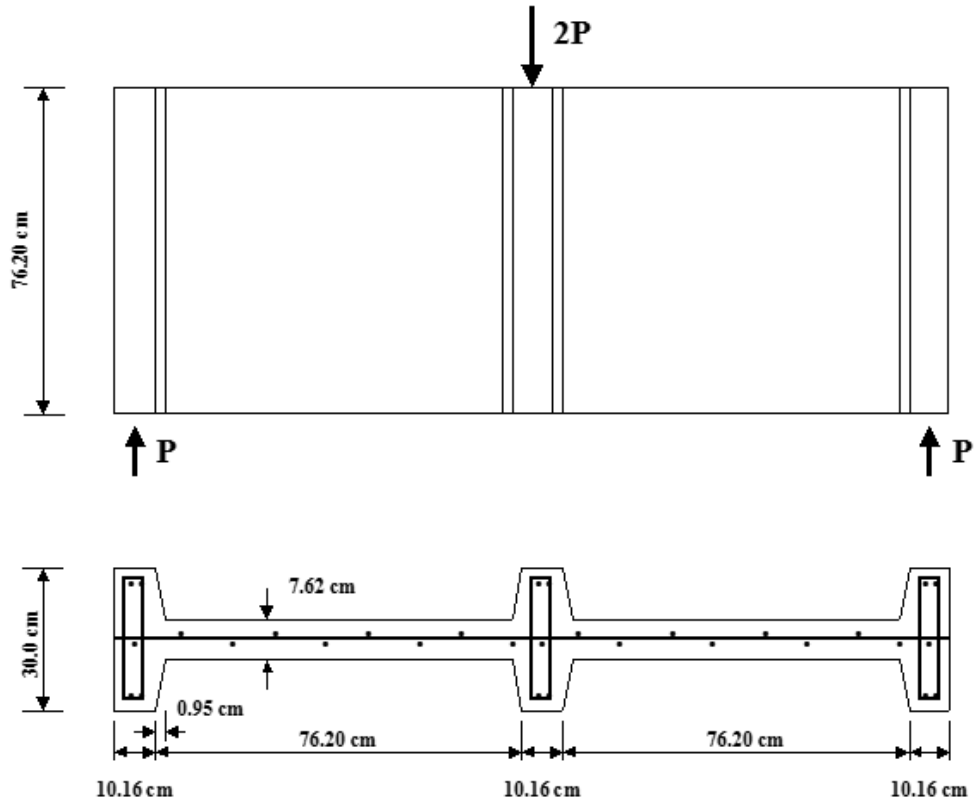

Fig. 6.11 Geometry and reinforcement details of shear wall W4 [13]

The concrete domain was modeled by using the 8-noded hexahedral finite element and the vertical and longitudinal steel reinforcement were modeled through the use of NBCFB finite element, while the stirrups were modeled with the truss element. 96 solid concrete finite elements (10.16cm x 7.62cm x 19cm) and 368 rebar elements (272 beam and 96 truss elements) were used in total to develop the final finite element mesh, that is shown in Fig. 22.

The numerical model foresees that the shear wall is simply supported as shown in Fig. 6.11. In addition to that, 8-noded hexahedral finite elements are used at the support and at the top center where the displacements are imposed so as to simulate the metallic plates, which are placed in order to avoid local failure (see Fig. 6.12). The displacements are imposed at the center of the wall as it was reported within the loading history from the experimental data presented by Ile and Reynouard [13], which are also used here to compare the derived force-displacement numerical response of the proposed model.

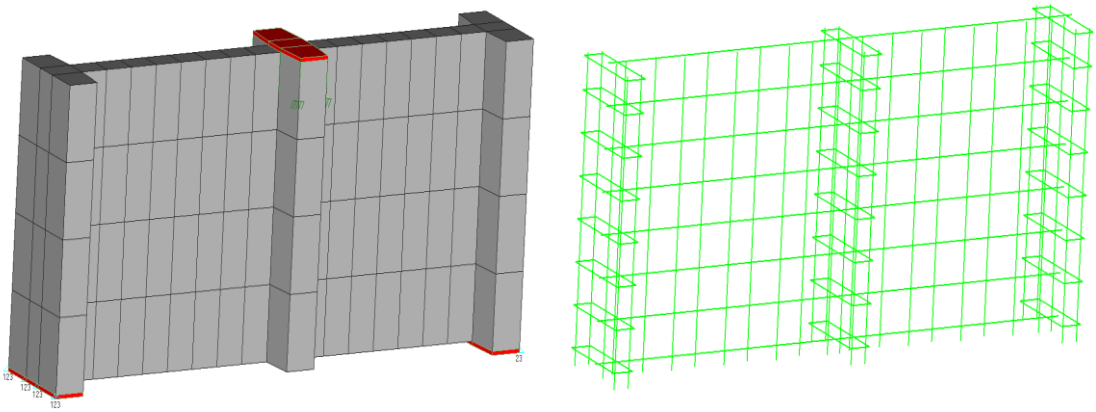

Fig. 6.12. Shear wall W4. 3D views of the (left) FE mesh of concrete elements and (right) steel reinforcement.

The numerical curves are compared with the corresponding experimental curves in Fig. 6.13, where it can be seen that the numerically obtained results match very well the experimental curves in terms of stiffness, strength and energy dissipation. The comparison between the experimental and the numerical values for each cycle for the Červenka shear wall, can be depicted in Table 6.6. Additionally, Table 6.7, shows the comparison between the experimental and the numerical energy dissipation areas for each cycle. In the first two loading cycles, plastic displacements are presented although the cycling loading is carried in the elastic range of steel (see Fig. 6.14a, 6.14b). This nonlinear behavior is caused by the excessive concrete damage which prevents the closure of the cracks. So as to further assess the numerically predicted curves, Fig. 6.14 was developed. As it can be seen in Fig. 6.14, each numerically predicted hysteretic loop is compared to its corresponding experimental, where it is easy to observe a good agreement between the curves.

Furthermore, two denser meshes, containing 201 and 321 concrete elements were created in order to investigate the mesh sensitivity of the proposed model. Fig. 6.15 illustrates the numerical accuracy and robustness of the proposed method. As it can be seen, the variation of the predicted curves for different meshes and for different displacement increments is insignificant.

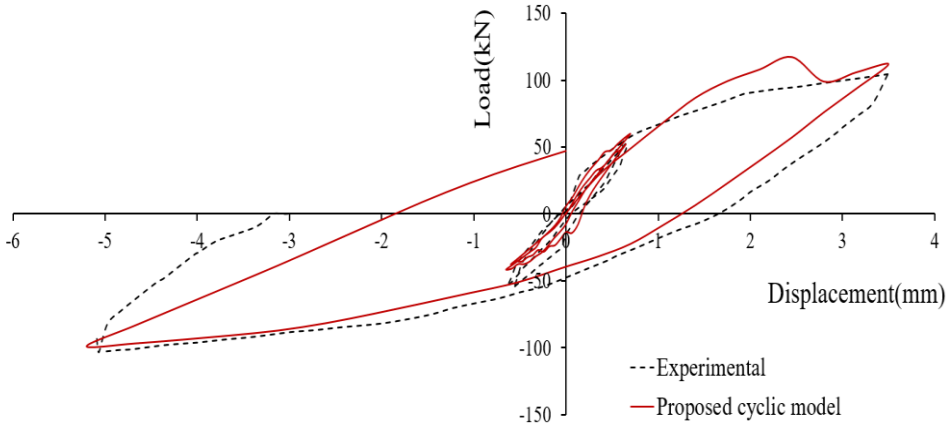

Fig. 6.13 Comparison between numerical and experimental data for specimen W4.

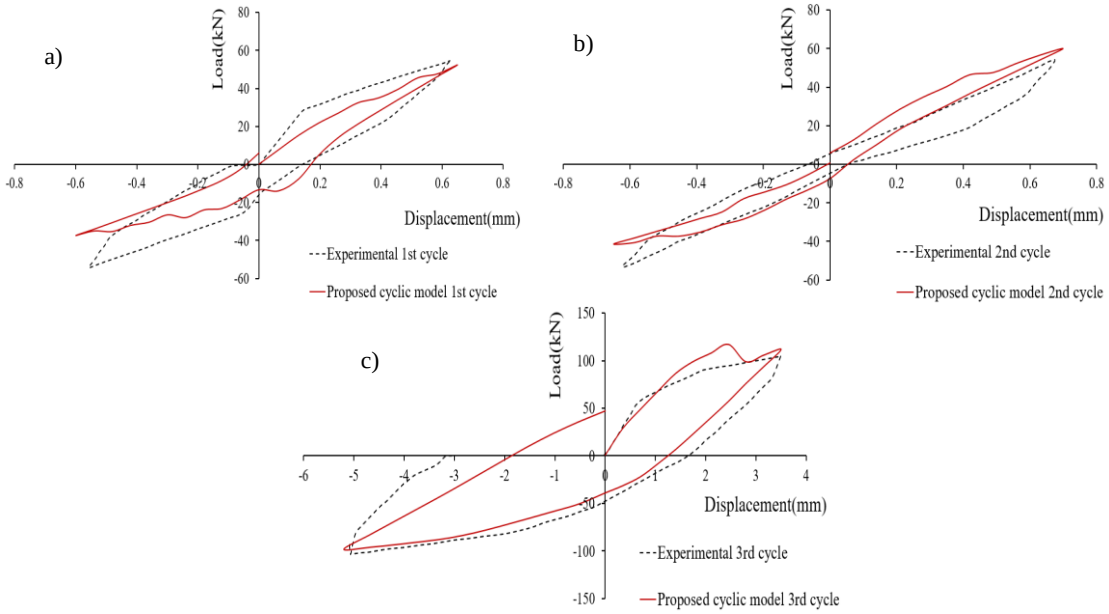

Fig. 6.14 Comparison between numerical and experimental data for specimen W4 for a) 1st cycle, b) 2nd cycle, c) 3rd cycle.

Table 6.6 Červenka Shear Wall. Comparison of the horizontal load of each cycle between experimental and numerical results.

Loading Cycle	Horizontal Load Experimental (kN)		Horizontal Load Predicted (kN)	
1st	55	-55	53	-38
2nd	55	-54	60	-42
3rd	104	-104	112	-99

Table 6.7 Červenka Shear Wall. Dissipated energy comparison between the experimental and numerical results.

Loading Cycle	Dissipated Energy Experimental (kN mm)	Dissipated Energy Predicted (kN mm)
1st	11.40	11.66
2nd	14.37	9.7
3rd	485.54	478.22

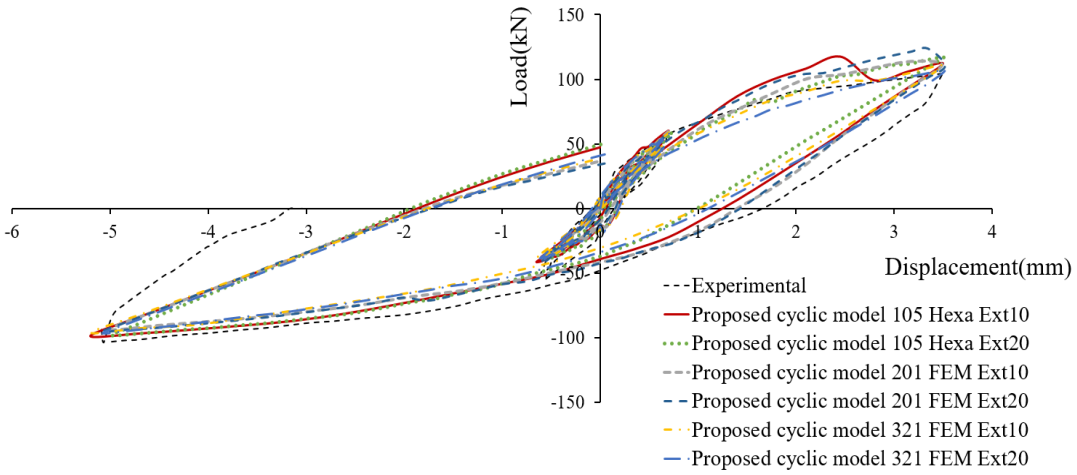

Fig. 6.15 Comparison between numerical and experimental results of the force deflection curve for different mesh discretizations (105, 201 and 321 hexahedrons) and different displacement increments (10 and 20 per load branch).

Fig. 6.16 shows the crack patterns that are formed when the structure reach the maximum imposed displacements at both opposite directions during the first cycle. The cracks are formed in the tension regions for both positive and negative imposed deflections. The crack patterns show that the cracks opened and closed in a realistic manner (when concrete is under compression or tension due to unloading load reversal), according to imposed displacements.

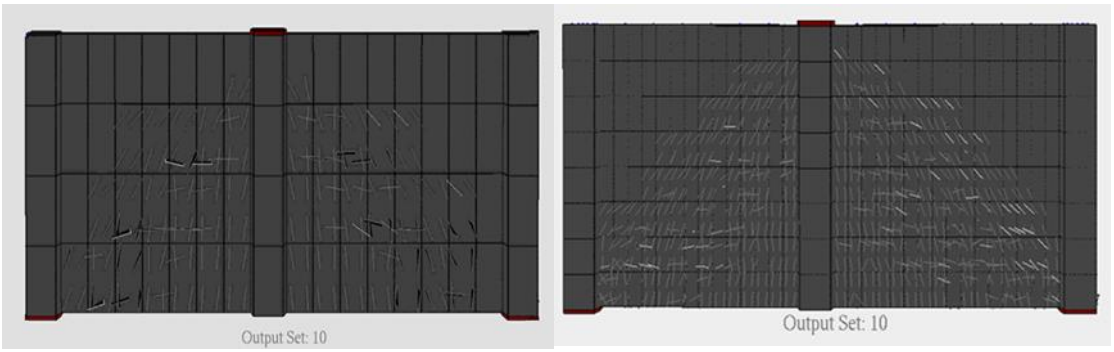

(a)

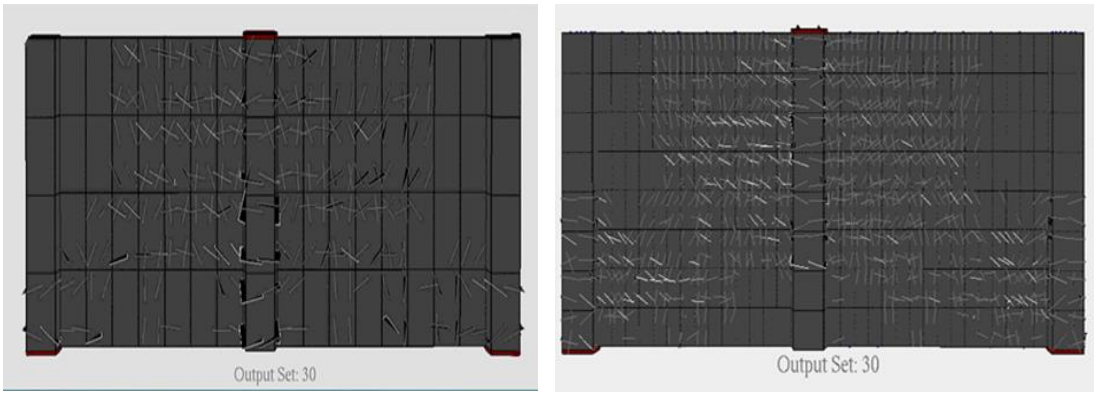

(b)

Fig. 6.16 Crack patterns during the first cycle a) when the imposed displacement is -0.65mm (directed downwards) b) when the imposed displacement is +0.65mm (directed upwards) when using 105 and 321 hexahedral elements.

Fig. 6.17 compares the numerical with the experimentally derived crack patterns (found in [7]) near the failure mode. The numerically computed cracks show once more a denser pattern due to the smeared crack approach. In Fig. 6.17, the continuous lines represent the cracking which is formed when the imposed displacement is directed downwards, while the dashed lines represent the cracks which are formed when the imposed displacement is directed upwards. It is easy to observe that, the direction and the location of the numerically obtained cracks match well with the experimental cracks.

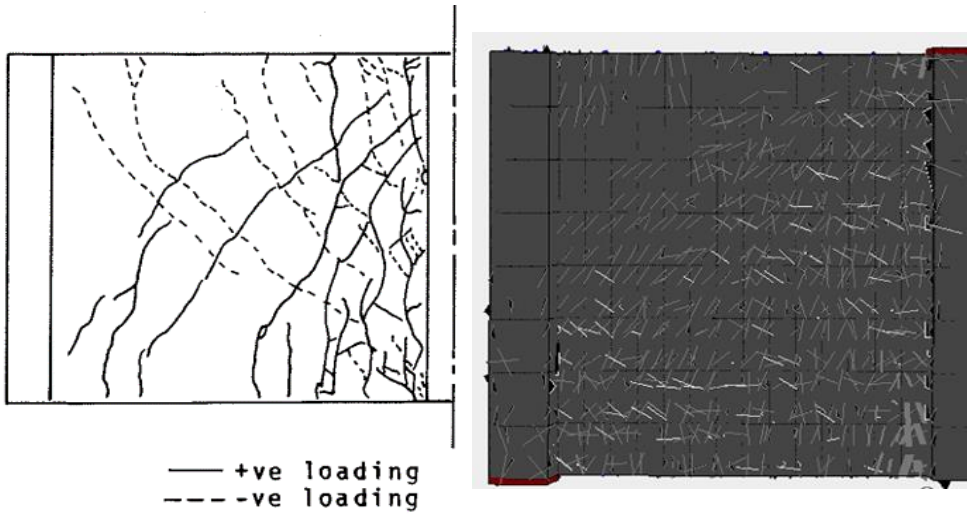

Fig. 6.17 Shear wall W4. Comparison between experimental [7] *and numerical results in terms of crack patterns near failure.*

The required NR iterations for shear wall W4 model are shown in Fig. 6.18 at the initiation of the last cycle of loading until failure. According to the findings, the maximum number of NR iterations occurs when the imposed displacement reaches its maximum value. As it can be seen, even in the case where significant nonlinearities occur, where the concrete is excessively cracked (at the last loading cycle), the nonlinear procedure appears to be numerically efficient and robust (low number of required internal iterations). The computational time for the nonlinear solution procedure is given in Table 6.8 and refers to the total displacement increments used to solve complete displacement history. According to the numerical investigation, the solution of the numerical problem was performed in just 9.5 seconds.

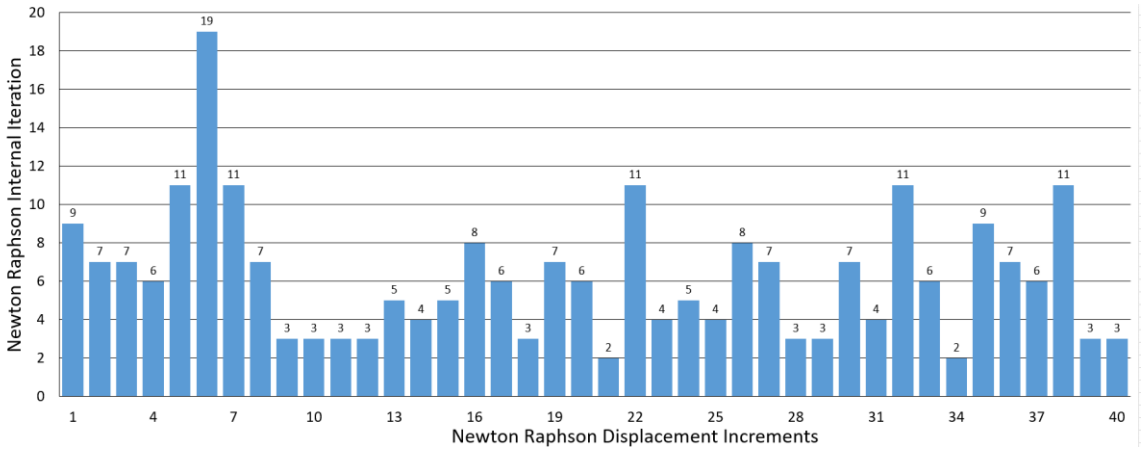

Fig. 6.18 Shear wall W4. Required NR iteration per displacement increment during the last cycle.

Table 6.8 Shear wall W4. CPU time for different tasks of the nonlinear analysis

Task	CPU Time (s)
Embedded rebar element mesh generation	0.03
Nonlinear incremental-iterative solution	9.27
Total Time	9.30

6.1.3 RC Frame Joints

During an earthquake excitation, the frame joints develop excessive strains and stresses concentrations (plastic hinges) in order to absorb the energy which is caused during the cyclic deformation. Therefore, it is significant for any proposed finite element model to be able to capture the nonlinear mechanical behavior of these structural members and to simulate accurately their complex nonlinear response. In order to demonstrate the ability of the proposed model to capture the mechanical response of frame joints under cycling loading, two different experimental setups were studied and presented in this section.

6.1.3.1 Del Toro Rivera Frame Joint

A schematic representation of the under study RC frame joint is shown in Fig. 6.19. The beam-column joint was tested by Del Toro Rivera [178] and analyzed by Fleury et al. [179]. The uniaxial compressive concrete strength was f_c=40 MPa and the yielding stress of the steel reinforcement were 570, 490, 440 and 554 MPa for the 10, 12, 14 and 20 mm diameter bars, respectively. The Young modulus of elasticity of steel was E_S= 200 GPa.

This interior frame joint was subjected to different cyclic loading conditions according to the experimental setup. The loading history is presented in the form of imposed displacements in Fig. 6.20.

For the development of the numerical model, the concrete domain was discretized with 8-noded hexahedral finite elements and the steel reinforcement was discretized with the NBCFB finite elements and truss elements. The steel bars that had 12, 14 and 20 mm diameter were modeled through the use of the beam element and the steel bars that had 10 mm diameter were modeled through the use of truss finite elements. A total number of 76 concrete (20cm x 20cm x 16cm) and 446 steel finite elements were used so as to discretize the frame joint, as illustrated in Fig. 6.21.

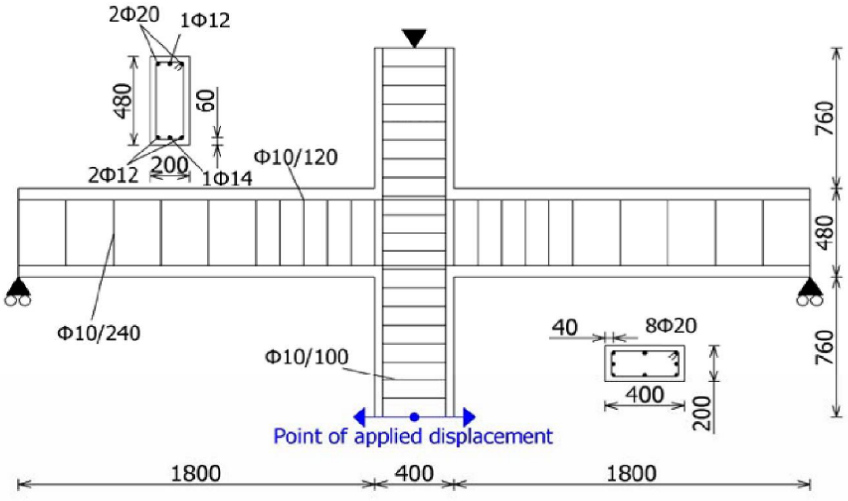

Fig. 6.19 Geometry and reinforcement details of beam column joint (Del Toro Rivera [178]*). All lengths are in mm.*

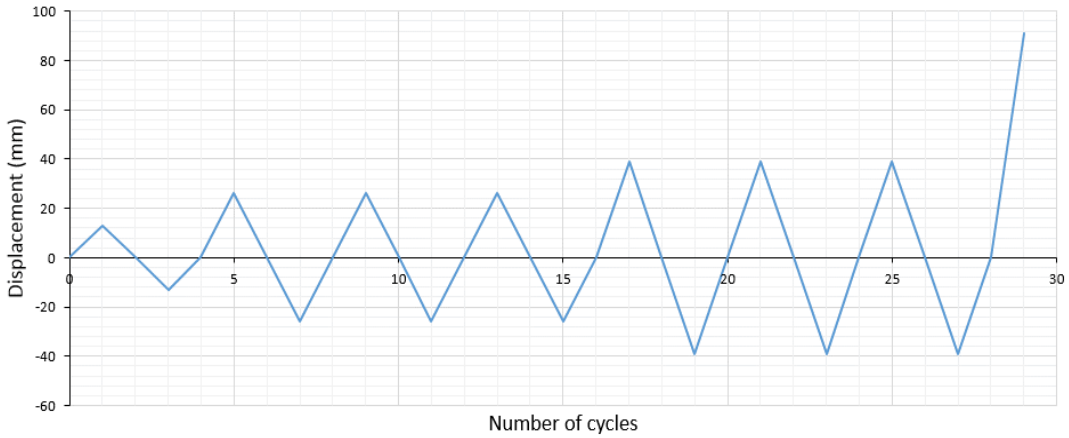

Fig. 6.20 Load history presented in the form of imposed displacements for the interior frame joint.

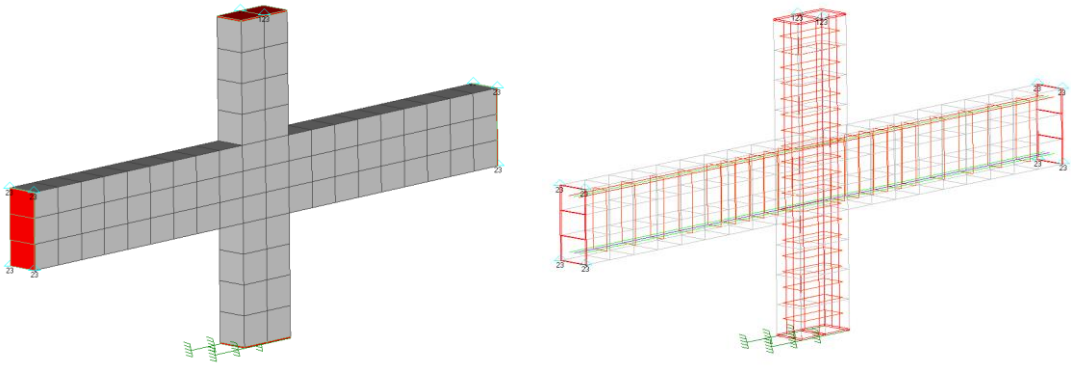

Fig. 6.21 Interior frame joint. 3D views of the FE mesh of concrete elements and steel reinforcement.

The interior frame joint is supported according to the experimental configuration shown in Fig. 6.19, where the boundary conditions implemented within the developed model are shown in Fig. 6.21. As it can be seen in Fig. 6.19 the displacements were imposed at the bottom face of the column, while a 200 kN compressive force was also applied on the top face of the column in order to simulate the vertical loads of the upper floors (according to the experimental setup [178]).

The numerically derived force-displacement curves are compared with the corresponding experimental data in Fig. 6.22 and Fig. 6.23. As it can be seen, the numerical results match very well with the experimental ones. From this numerical investigation, it was found that for the case of cycles up to 26 mm (Fig. 6.23a), the stiffness and the resulted load-carrying capacity of the specimen were predicted in an accurate manner. Even for the case of cycles up to 39 mm (Fig. 6.23b), the nonlinear behavior of the developed model was similar to the experimental curves. The comparison between the experimental and the numerical values for each cycle is given in Table 6.9. In addition to that, Table 6.10, shows the comparison between the experimental and the numerical energy dissipation values for each cycle. As it can be seen in the two tables, there is a good agreement between the numerically predicted and the experimentally derived results, with some exceptions mainly found in the energy dissipation table. This is attributed to the experimentally obtained pinching effect which appeared mostly in the large in magnitude loading cycles (Fig. 6.23b). This numerical finding is attributed to the slippage of the reinforcement steel bars that is not accounted in the proposed numerical model. Nonetheless, the proposed model managed to capture the cyclic mechanical behavior for all imposed displacement cycles with an acceptable accuracy and numerical efficiency. Moreover,

Fig. 6.24 shows the comparison between the force-deflection curves that derived by using 76 and 164 concrete elements for discretizing the RC frame joint. As it can be seen, the two meshes resulted two curves deriving the same mechanical behavior, demonstrating the ability of the proposed method to reproduce the experimental data through the use of different mesh sizes.

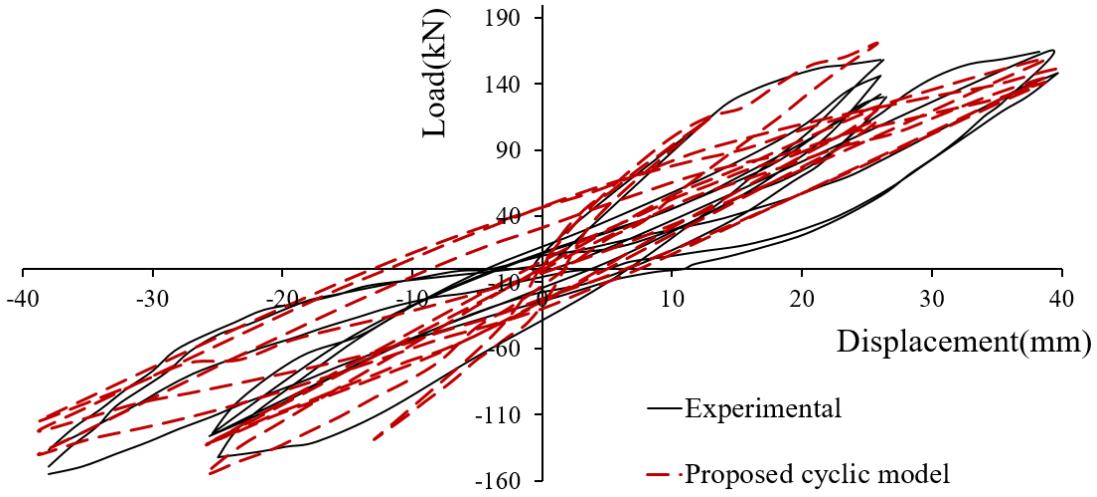

Fig. 6.22 Interior frame joint. Comparison between numerical and experimental results. Complete force-displacement history.

Table 6.9 Interior Frame Joint. Comparison of the horizontal load for each cycle (experimental and numerical results).

Loading Cycle	Horizontal Load Experimental (kN)		Horizontal Load Predicted (kN)	
	Positive	Negative	Positive	Negative
1st	158	-142	166	-152
2nd	146	-126	123	-136
3rd	130	-124	95	-136
4th	164	-154	138	-150
5th	164	-154	130	-134
6th	149	-137	144	-106

Table 6.10 Interior Frame Joint. Comparison of the dissipated energy for each cycle (experimental and numerical results).

Loading Cycle	Dissipated Energy Experimental (kN mm)	Dissipated Energy Predicted (kN mm)
1st	2596.34	1165.14
2nd	1264.12	669.37
3rd	1212.48	942.64
4th	3287.87	1953.10
5th	3287.87	2728.33
6th	1446.43	2602.47

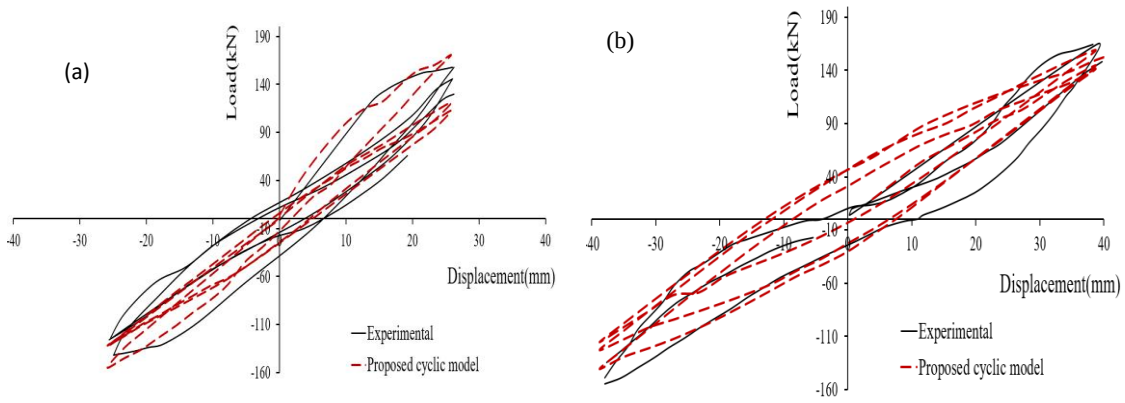

Fig. 6.23 Interior frame joint. Comparison between numerical and experimental results (a) for cycles ±26 mm and (b) for cycles ±39 mm.

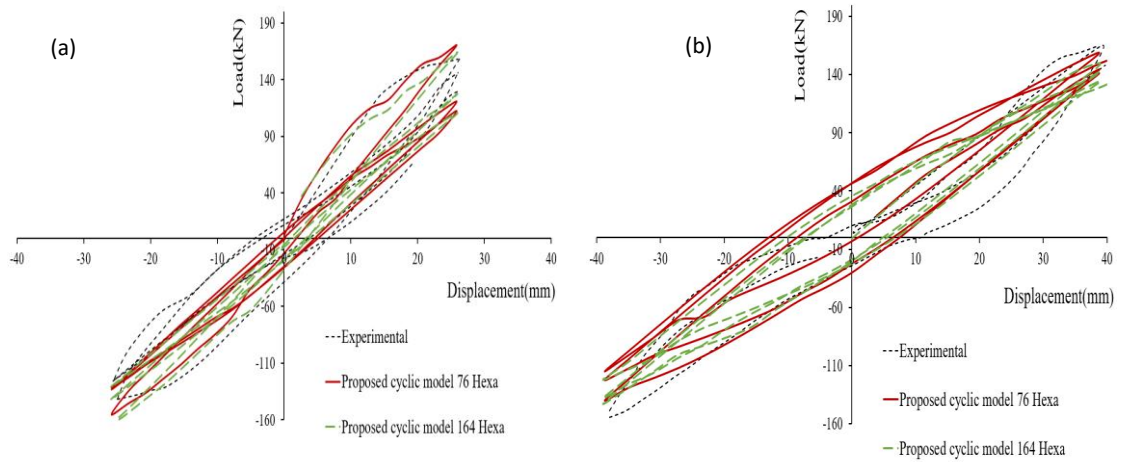

Fig. 6.24 Interior frame joint. Comparison between numerical and experimental results for different mesh discretization (76 and 164 hexahedrons) (a) for cycles ±26 mm and (b) for cycles ±39 mm.

Fig. 6.25 shows the crack patterns that are formed when the structure reaches the maximum imposed displacements at both directions during the first cycle of loading. According to Fig. 6.25a, cracks are formed at the bottom fiber of the left beam and at the top sectional fiber of the right beam (both crack formations resulted due to the tensile stresses of the corresponding bending moments). Moreover, the cracks are reversed as the imposed displacement changes direction as illustrated in Fig. 6.25b (tensile cracks close and opening of new cracks due to the inversed bending moments). The cracks of the joint present an intense inclination indicating the characteristic shear diagonal cracking. Generally, the crack pattern shows that the crack formation and the crack closure are numerically captured in a realistic manner.

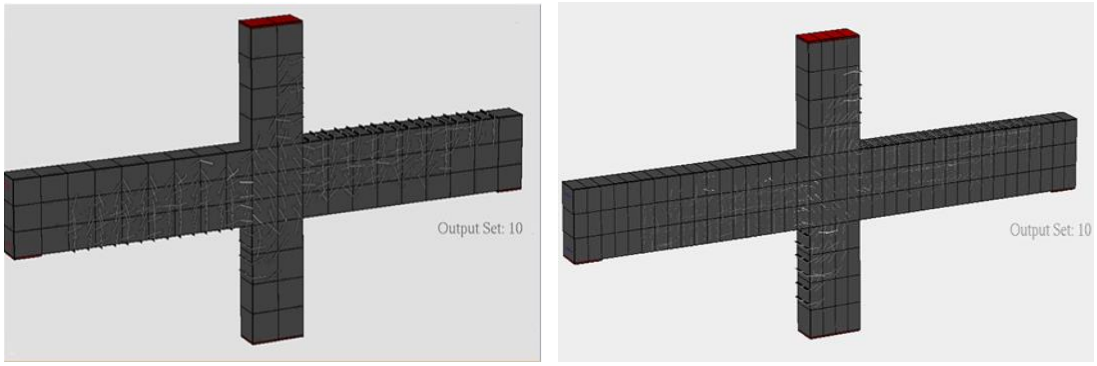

(a)

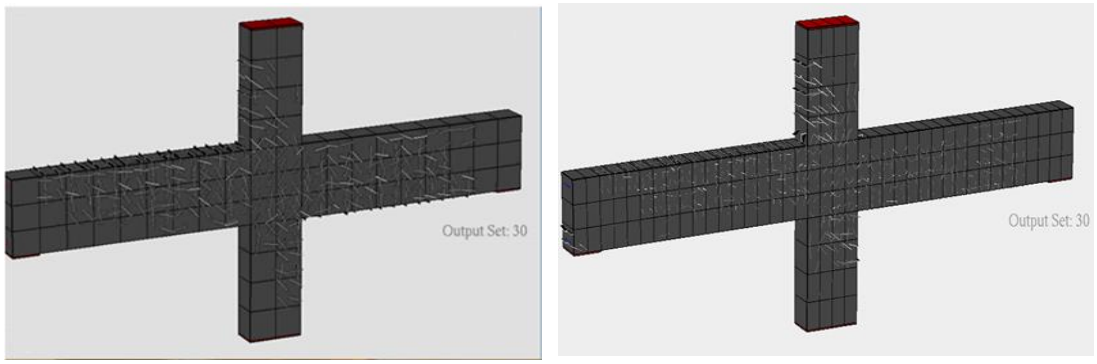

(b)

Fig. 6.25 Crack patterns during the first cycle (a) when the imposed displacement is +13mm (directed eastward) and (b) when the imposed displacement is -13mm (directed westward). Left: 76 and Right: 164 hexahedral elements.

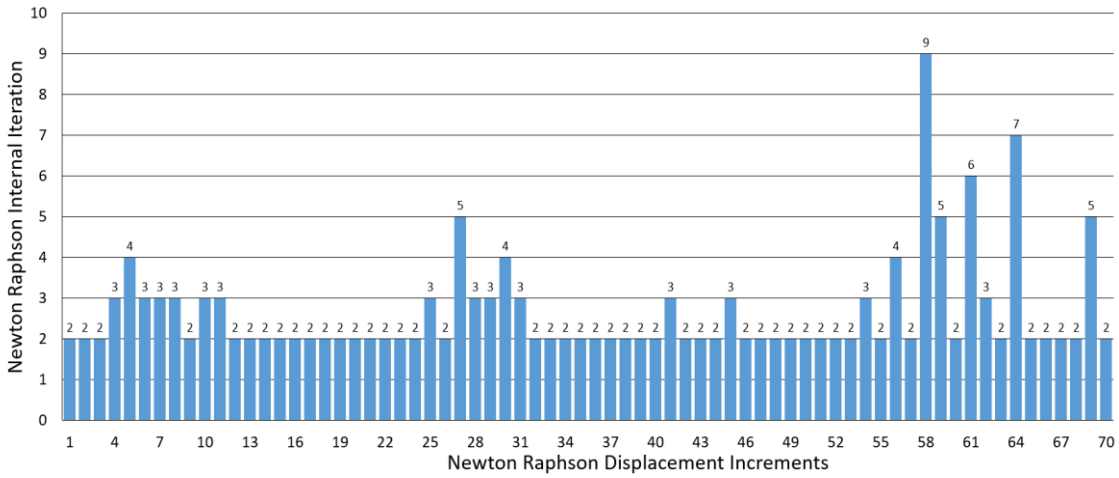

Fig. 6.26 Interior frame joint. Required NR iteration per displacement increment for the last 70 displacement increments.

The required NR iterations for the last loading cycle which foresees the loading of the structure until complete failure are shown in Fig. 6.26 . As it resulted for the analysis, all the displacement increments required reasonable number of iterations to reach convergence regardless the intense nonlinear behavior of the structure. The computational time for the nonlinear solution procedure is given in Table 6.11 where it can be easily depicted that a total of 9.5 seconds is required so as to solve 310 displacement increments. This illustrates the numerical superiority

of the proposed algorithm (due to the closing of cracks criterion) demonstrating the overall stability of the nonlinear solution procedure. It is important to note here that, the usual number of required internal iterations per load increment until convergence, when dealing with this type of numerical models, is not less than 30 or some times more than 40, forcing researchers to use larger convergence criteria so as to allow their solutions to proceed. Most of the times, this type of analysis cannot be performed due to numerical instabilities.

Table 6.11 Interior Frame Joint. CPU time for different tasks of the nonlinear analysis.

Task	CPU Time (s)
Embedded rebar element mesh generation	0.023
Nonlinear incremental-iterative solution	9.29
Total Time	9.31

6.1.3.2 Beam-Column Corner Joint

The last FE model which was numerically investigated by using the proposed model, was a beam-column corner joint. This joint was experimentally investigated by Luiki [180] and analyzed by Hartl [181] and at a later stage by Lykidis and Spiliopoulos [27] for monotonic and cyclic loading. The uniaxial compressive concrete strength was reported to be equal to f_c = 35 MPa, where the yielding stress of steel reinforcement was 430 MPa for the 20 mm diameter bars and 550 MPa for all the other bar diameters. The Young modulus of elasticity of steel was E_S = 206 GPa, which was also the value used within the numerical model. The cyclic loading in this experiment, was applied on the RC joint through the use of a steel beam. A schematic representation of the RC frame joint is shown in Fig. 6.27.

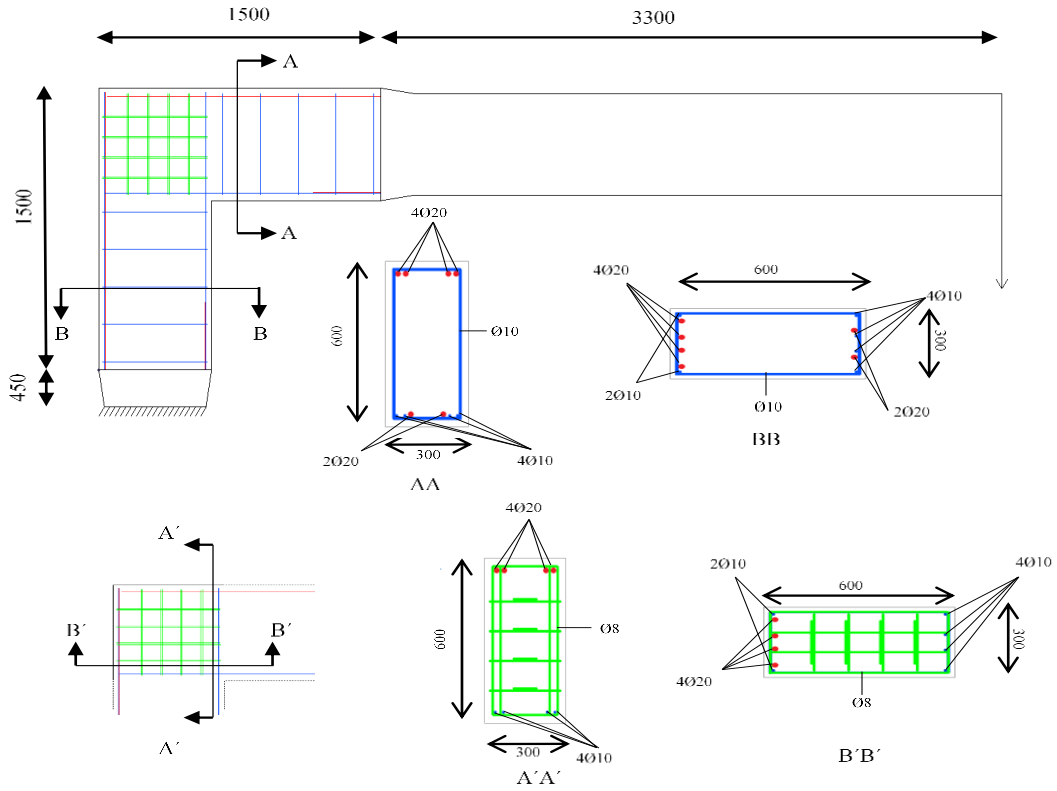

Fig. 6.27 Geometry and reinforcement details of the corner frame joint. All dimensions are given in mm.

It is evident from the experimental data [180] that the bond between the steel bars and the surrounding concrete area of the RC joint becomes crucial during the cyclic loading, which was also the main objective of this experimental test. In order to illustrate the abilities and the limitations of the proposed numerical model, without the damage factors, the simulation of this specimen is presented herein. The frame joint is subjected to different cyclic loading conditions. The displacement history is given in the form of imposed displacements in Fig. 6.28, where it can be seen that the joint is cyclically loaded until complete failure.

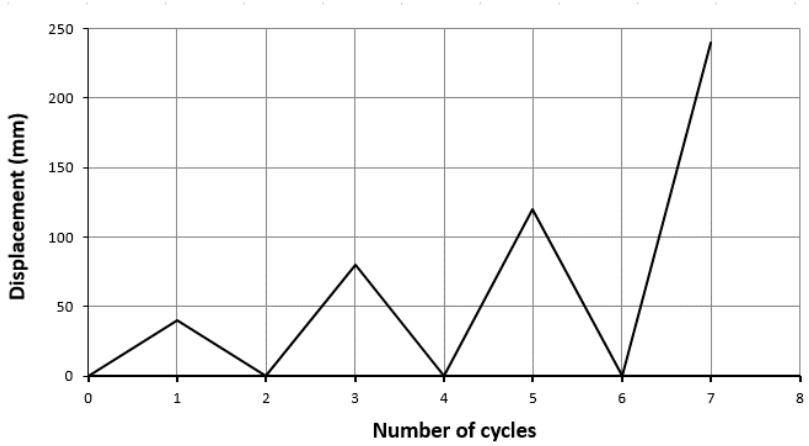

Fig. 6.28 Load history presented in the form of imposed displacements for the corner frame joint.

Two numerical models were developed so as to simulate this RC corner frame joint. In the first model, the concrete was modeled by using the 8-noded hexahedral finite element, while in the second the concrete domain was discretized by using the 20-noded hexahedral element. The steel reinforcement was modeled by using the embedded beam and truss finite elements. In the case of the first model (that foresaw the use of 8-noded hexahedral concrete elements), the steel bars which had a 20 mm diameter, were modeled through the use of the beam finite element while the remaining steel bars were modeled with truss elements. For the case of the second model, all embedded rebar elements were discretized by using truss elements. A total number of 78 hexahedral concrete finite elements (15cm x 20cm x 18cm), 72 hexahedral metallic elements and 256 rebar elements were used in both models, as illustrated in Fig. 6.29.

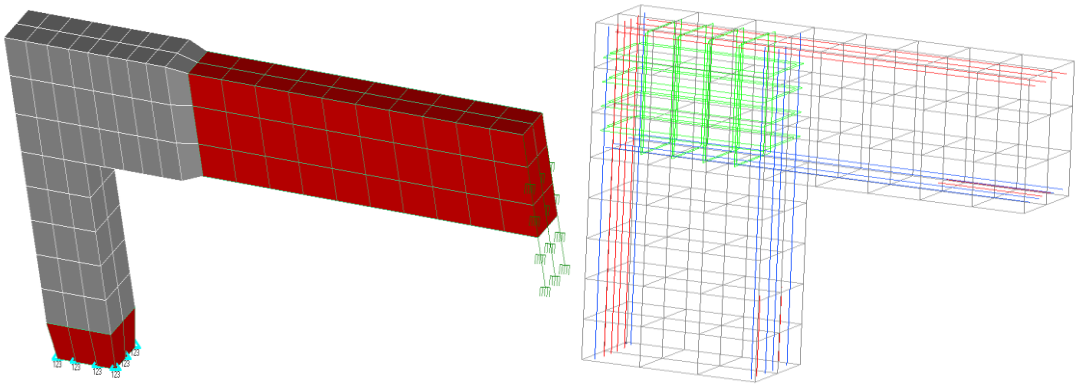

Fig. 6.29 RC Corner Frame Joint. 3D views of the FE mesh of concrete elements and steel reinforcement.

The beam-column corner frame joint was fixed at the base as shown in Fig. 6.27. The displacements were imposed at the edge of the metallic beam (see red elements), which was the method through which the joint was loaded during the experimental test.

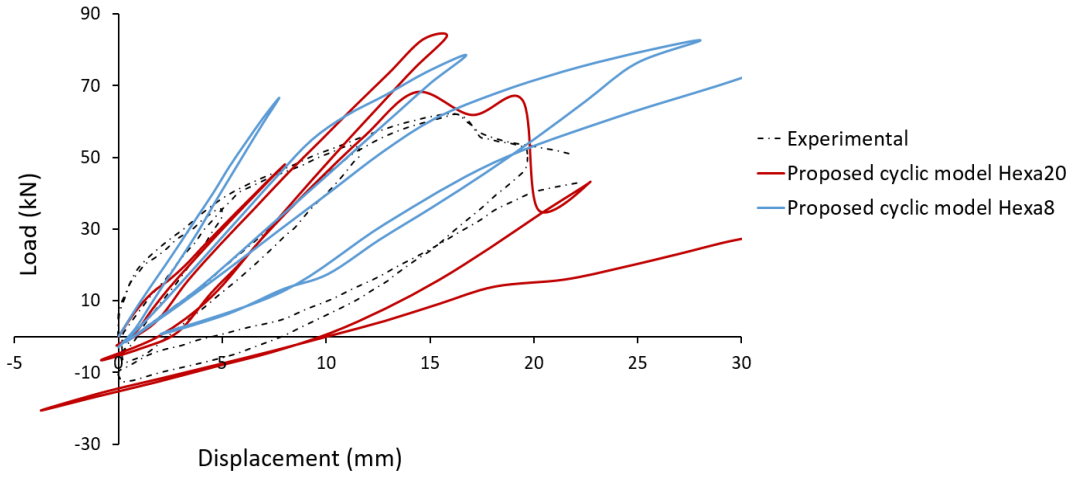

Fig. 6.30 RC Corner Frame Joint. Comparison between the numerical and experimental results. Force-displacement history.

The numerical curves results compared with the corresponding experimental data (see Fig. 6.30), where it can be seen that the numerically predicted response overestimates the capacity of the specimen in the case where 8-noded hexahedral elements are used, while the second model derives a more flexible numerical behavior due to the quadratic isoparametric solid finite elements, used to discretize the concrete domain. Even though the effect of slippage is significant, the proposed model manages to capture the overall cyclic behavior, where the predicted ultimate load from the first model was 52% larger in comparison to the experimental ultimate load, while the second model overestimated it by 19%. This highlights the need of introducing numerical methodologies through which the slippage will be accounted for. The comparison between the experimental and the numerical values for each loading cycle, is given in Table 6.12. Furthermore, Table 6.13, shows the comparison between the experimental and the numerical energy dissipation values for each loading cycle that was analyzed. The deviation of the results is mainly attributed to the fact that the bond-slip is not accounted for in the proposed model, while the experimental setup was designed to be significantly affected by this phenomenon. Nonetheless, this numerical investigation shows that the proposed model which uses 20-noded hexahedral elements manages to capture the overall mechanical behavior of the specimen (see Fig. 6.30). Furthermore, the bond-slip problem is discussed in chapter Chapter 90 where the integration of the proposed damage factor is presented.

Table 6.12 Exterior Frame Joint. Comparison of the horizontal load of each cycle between experimental and numerical results.

Loading Cycle	Horizontal Load Experimental (kN)		Horizontal Load Hexa20 Predicted (kN)		Horizontal Load Hexa8 Predicted (kN)	
1st	34	-7	48	-38	66	-3
2nd	53	-7	83	-8	78	-1.6
3rd	62	-13	68	-20	82	0

Table 6.13 Exterior Frame Joint. Comparison of the dissipated energy of each cycle between experimental and numerical results.

Loading Cycle	Dissipated Energy Experimental (kN mm)	Dissipated Energy Hexa20 Predicted (kN mm)	Dissipated Energy Hexa8 Predicted (kN mm)
1st	58.33	14.71	27.72
2nd	188.77	118.36	125.62
3rd	546.77	729.53	387.47

The required NR iterations for the exterior frame joint are depicted in Fig. 6.31 for the last 67 displacement increments (last loading cycle until failure). An average of 6 to 7 internal iterations are required so as to reach convergence, a numerical response that highlights the numerical efficiency of the developed algorithm. Furthermore, the 20-noded model required more internal iterations in comparison to the 8-noded model. This is attributed to the larger number of Gauss points used within each 20-noded finite element resulting a larger number of cracks therefore larger unbalanced forces when cracking occurs. The computational time for the nonlinear solution procedure is depicted in Table 6.14 that refers to the analysis of the 8-noded model. It is obvious that the 20-noded model increase the computational cost significantly in relation to the 8-noded finite element mesh due to the increase of the dofs and the additional internal iterations that were performed at each displacement increment until convergence.

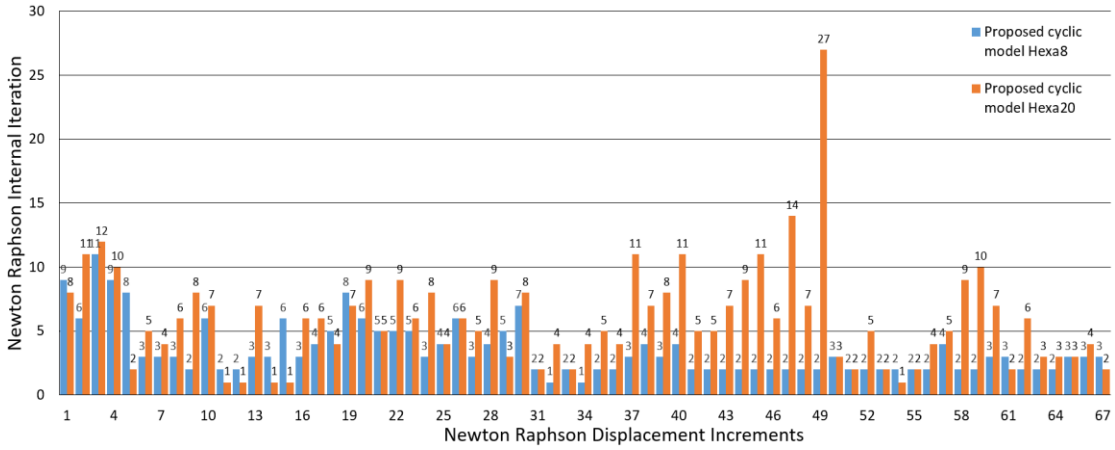

Fig. 6.31 Exterior frame joint. Required NR iteration per displacement increment.

Table 6.14 Exterior Frame Joint. CPU time for different tasks of the nonlinear analysis.

Task	CPU Time(s)	
	Hexa8	Hexa20
Embedded rebar element mesh generation	0.028	0.062
Nonlinear incremental-iterative solution	3.2	130.4
Total Time	3.23	130.46

6.2 Conclusions

In order to validate the objectivity and numerical robustness of the proposed numerical model, six experimental tests were numerically investigated through the proposed model (four RC shear walls and two RC joints). The comparison between the numerical and the experimental results showed that the proposed nonlinear procedure is capable in capturing accurately and efficiently the hysteretic behaviors of RC specimens for different loading levels. Although the

proposed numerical model foresees a brittle material behavior for concrete, the proposed method manages to obtain hysteretic cycles and an overall behavior which is characterized by ductile components. Furthermore, a mesh sensitivity analysis was performed which revealed that the variation between the numerical results which occurred through the use of different meshes was insignificant.

In addition to that, the computational efficiency of the developed algorithm was illustrated by discussing the required computational time in order to solve each numerical model. As it was illustrated, the developed modeling method was able to result a complete analysis for all the under studied problems in less than two minutes by using a standard computer system with a 2,50 GHz CPU. The overall computational efficiency is attributed to the proposed concrete material model algorithm for cyclic loading and the optimum algorithmic implementation that uses the latest Fortran programming language and compiler.

Finally, the numerical investigation showed that the consideration of slippage of the reinforcement is essential in order to analyze the behavior of RC joints that do not follow the modern design trends (sufficient anchorage length), thus the incorporation of a bond-slip model is required.

Chapter 7. The hybrid modeling approach and numerical implementation to RC structures that undergo cyclic loading

Contents of Chapter 7

7.1 Introduction 141

7.2 Hybrid modeling formulation – kinematical coupling of 1D and 3D finite elements. 142

7.3 Reduction Levels of HYMOD meshes 145

7.4 Numerical Results and Discussion 147

7.4.1 Del Toro Rivera RC Frame Joint 147

7.4.2 One-Storey RC Frame with a Shear Wall 160

7.4.3 Two-storey RC Frame with Shear Wall 165

7.5 Conclusions 170

7.1 Introduction

The cyclic simulation of different structural components of RC buildings like beams, columns, monolithic connections, shear walls, slabs and foundation footings, has two main challenges; numerical accuracy and computational efficiency. Many simplified models have been developed for the simulation of RC structural members under ultimate limit state cyclic loading conditions with moderate success. The accuracy limitations of these numerical models is well documented thus researchers turned towards more detailed 3D approaches (Kotsovos and Pavlovic [29]; Hartl [181]; Lykidis and Spiliopoulos, [28]; Červenka and Papanikolaou [182]; Papanikolaou and Kappos [183]; Markou and Papadrakakis [37]) in an attempt to develop accurate and robust modeling methods that will be able to predict the mechanical response of any RC structural member or structure. These research studies adopt the use of hexahedral elements that treat cracks through the use of the smeared crack approach and model rebars as embedded rod or beam finite elements.

As it was concluded by Markou and Papadrakakis [37], the computational complexity of such detailed models makes their use impractical for simulation of real-scale RC structures under cyclic loads. Additionally, the use of numerically unstable material models, such as the smeared crack approach in concrete (Markou and Papadrakakis [31]), increases the numerical sensitivity to various user-defined parameters. Therefore, there is a need of developing a more robust and numerically efficient finite element modeling approach that will alleviate the abovementioned numerical limitations for simulating full-scale RC structures under ultimate limit state monotonic and cyclic conditions, with accuracy and computational efficiency. A suggested method in overcoming this numerical problem was the HYMOD approach [37] that foresees the combination of different in dimensionality FEs to decrease the computational demand. Bellow, a summary is provided of the research work found in the international literature that deal with HYMOD.

A mixed element formulation was reported in Formaggia et al. [184]; Urquiza et al. [185] and Blanco et al. [186] in an attempt to deal with the connection of plates and 3D solid elements. This method was extended to the connection of shells and solid elements by Huang [187]. Nazarov [188], [189] and Kozlov & Maz'ya [190] presented an asymptotic analysis for the coupling between a 3D elastic body and a dimensionally reduced structure. Blanco et al. [191] presented a generalized approach on the kinematic coupling of incompatible elements, whereas Mata et al. [192] used two different FE models (3D solid and 1D beam elements), where the structure was initially discretized with beam elements and when predefined regions entered the nonlinear state, they were assumed prismatic and were discretized with 3D solid elements. In this way, a two-scale, global and local analysis was performed as illustrated in Fig. 7.1. The dimensional-coupling between scales was developed through surface-interfaces imposing the kinematic hypothesis assumed for the beam model.

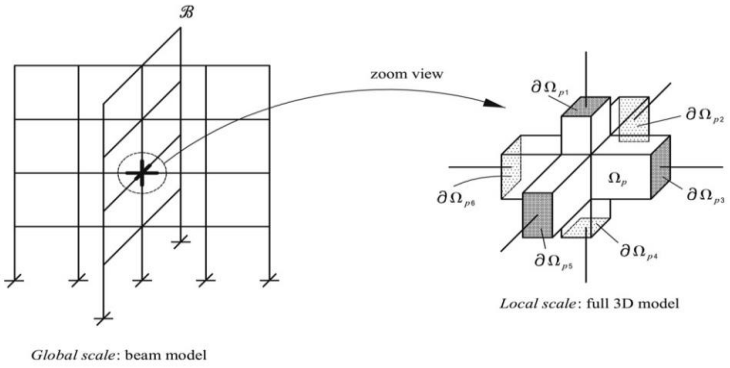

Fig. 7.1 Schematic representation of the global and local scale modeling proposed in Mata et al. [192].

Bournival et al. [193], [194] used mixed-dimensional FEA models for the simulation of steel structures, combining beam, shell and 3D solid finite elements. According to their research work, it was reported that they managed to reduce the computational effort at the expense of losing the accuracy across the interface of the incompatible finite elements.

When dealing with the cyclic loading of RC structural members, the computational demand increases significantly, while there were no research publications in the international literature that attempt to implement any type of hybrid modeling concepts for the prediction of the cyclic response of RC structures.

The proposed HYMOD approach for modeling RC structures under ultimate limit cyclic loading is based on the work presented in [37] and requires minimal transformations for the coupling demands of line and 3D elements. Therefore, it maximizes the computational efficiency during the analysis, while maintaining adequate accuracy in calculating the internal forces at the critical regions of the structure. In addition to that, the adopted concrete material model (presented in Chapter 5) requires the definition of a minimum number of material parameters so as to describe and simulate the nonlinear mechanical behavior of concrete under cyclic loading conditions, which significantly simplifies the procedure of material model definition.

7.2 Hybrid modeling formulation – kinematical coupling of 1D and 3D finite elements

According to the proposed HYMOD approach that was presented by Markou and Papadrakakis [37], the method combines hexahedral and beam-column finite elements, where the coupling between them is achieved through kinematic constraints. The coupling between the two types of elements (natural beam-column flexibility-based "NBCFB" and hexahedral "HEXA" finite elements) is performed with kinematic constraints that are enforced at each hexahedral node, located at the interface between the beam and the solid elements. The kinematic connection is performed as follows:

$$\underset{(3x1)}{\boldsymbol{u}_i^{HEXA}} = \underset{(3x6)}{\boldsymbol{T}_{im}} \cdot \underset{(6x1)}{\boldsymbol{u}_m^{NBCFB}} \quad , \tag{7.1}$$

with

$$\underset{(3x6)}{\boldsymbol{T}_{im}} = \begin{bmatrix} 1 & 0 & 0 & 0 & z_i - z_m & y_m - y_i \\ 0 & 1 & 0 & z_m - z_i & 0 & x_i - x_m \\ 0 & 0 & 1 & y_i - y_m & x_m - x_i & 0 \end{bmatrix} \tag{7.2}$$

Therefore, Eq. (7.1) takes the following form;

$$\begin{bmatrix} u_i \\ v_i \\ w_i \end{bmatrix} = \begin{bmatrix} 1 & 0 & 0 & 0 & z_i - z_m & y_m - y_i \\ 0 & 1 & 0 & z_m - z_i & 0 & x_i - x_m \\ 0 & 0 & 1 & y_i - y_m & x_m - x_i & 0 \end{bmatrix} \begin{bmatrix} u_1^{NBCFB} \\ v_1^{NBCFB} \\ w_1^{NBCFB} \\ \theta_1^{NBCFB} \\ \varphi_1^{NBCFB} \\ \psi_1^{NBCFB} \end{bmatrix} \tag{7.3}$$

where $\boldsymbol{u}_m^{NBCFB}$ and $\boldsymbol{u}_i^{HEXA}$ are the displacement vectors of the NBCFB node corresponding to 6 dofs and the hexahedral nodes (3 dofs per node) at the interface, respectively. The subscript i of the global coordinates x, y, z refers to the hexahedral node ID located at the interface section $\boldsymbol{\Omega_i^1}$, while subscript m refers to the NBCFB elemental node ID that controls the displacements (master node) of the interface section $\boldsymbol{\Omega_i^1}$ (Fig. 7.2). The connection matrix $\boldsymbol{T}_{im}$ is computed from the compatibility conditions of NBCFB and hexahedral nodal coordinates.

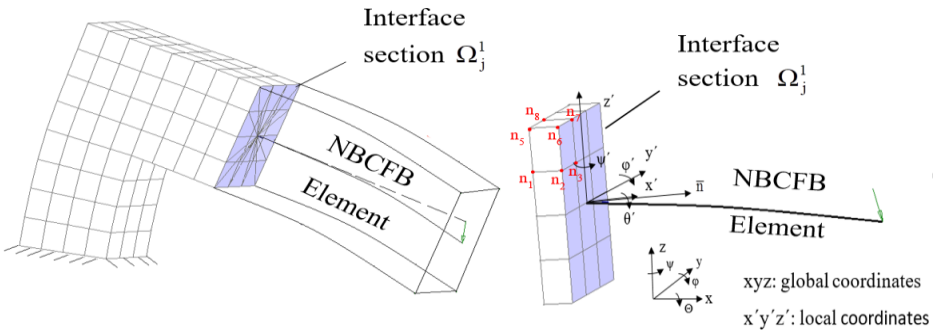

Fig. 7.2 Kinematic constraints imposed by the 1D structural member on the interface section $\boldsymbol{\Omega_i^1}$.

If we assume that a hexahedral node is located at the interface of a NBCFB and hexahedral elements, it should follow the body movements of section $\boldsymbol{\Omega_i^1}$, which are enforced by the NBCFB element nodal translational and rotational displacements (Fig. 7.2). Therefore, the computation of the new position for any point on the interface section $\boldsymbol{\Omega_i^1}$ is obtained through a linear transformation expressed by Eq. (7.4):

$$\underset{(24x1)}{\boldsymbol{U}^{\mathrm{HEXA}}} = \underset{(24x18)}{\boldsymbol{T}_H} \cdot \underset{(18x1)}{\boldsymbol{U}^{hybrid}} \tag{7.4}$$

where,

$$\begin{Bmatrix} u_1 \\ v_1 \\ w_1 \\ u_2 \\ v_2 \\ w_2 \\ u_3 \\ v_3 \\ w_3 \\ u_4 \\ v_4 \\ w_4 \\ u_5 \\ v_5 \\ w_5 \\ u_6 \\ v_6 \\ w_6 \\ u_7 \\ v_7 \\ w_7 \\ u_8 \\ v_8 \\ w_8 \end{Bmatrix} = \begin{bmatrix} 1 & . & . & . & . & . & . & . & . & . & . & . & . & . & . & . & . & . & . & . & . & . & . & . \\ . & 1 & . & . & . & . & . & . & . & . & . & . & . & . & . & . & . & . & . & . & . & . & . & . \\ . & . & 1 & . & . & . & . & . & . & . & . & . & . & . & . & . & . & . & . & . & . & . & . & . \\ . & . & . & . & . & . & . & . & . & . & . & . & 1 & . & . & . & z_2 - z_{m1} & y_{m1} - y_2 \\ . & . & . & . & . & . & . & . & . & . & . & . & . & 1 & . & z_{m1} - z_2 & . & x_2 - x_{m1} \\ . & . & . & . & . & . & . & . & . & . & . & . & . & . & 1 & y_2 - y_{m1} & x_{m1} - x_2 & . \\ . & . & . & . & . & . & . & . & . & . & . & . & 1 & . & . & . & z_3 - z_{m1} & y_{m1} - y_3 \\ . & . & . & . & . & . & . & . & . & . & . & . & . & 1 & . & z_{m1} - z_3 & . & x_3 - x_{m1} \\ . & . & . & . & . & . & . & . & . & . & . & . & . & . & 1 & y_3 - y_{m1} & x_{m1} - x_3 & . \\ . & . & . & 1 & . & . & . & . & . & . & . & . & . & . & . & . & . & . \\ . & . & . & . & 1 & . & . & . & . & . & . & . & . & . & . & . & . & . \\ . & . & . & . & . & 1 & . & . & . & . & . & . & . & . & . & . & . & . \\ . & . & . & . & . & . & 1 & . & . & . & . & . & . & . & . & . & . & . \\ . & . & . & . & . & . & . & 1 & . & . & . & . & . & . & . & . & . & . \\ . & . & . & . & . & . & . & . & 1 & . & . & . & . & . & . & . & . & . \\ . & . & . & . & . & . & . & . & . & . & . & . & 1 & . & . & . & z_6 - z_{m1} & y_{m1} - y_6 \\ . & . & . & . & . & . & . & . & . & . & . & . & . & 1 & . & z_{m1} - z_6 & . & x_6 - x_{m1} \\ . & . & . & . & . & . & . & . & . & . & . & . & . & . & 1 & y_6 - y_{m1} & x_{m1} - x_6 & . \\ . & . & . & . & . & . & . & . & . & . & . & . & 1 & . & . & . & z_7 - z_{m1} & y_{m1} - y_7 \\ . & . & . & . & . & . & . & . & . & . & . & . & . & 1 & . & z_{m1} - z_7 & . & x_7 - x_{m1} \\ . & . & . & . & . & . & . & . & . & . & . & . & . & . & 1 & y_7 - y_{m1} & x_{m1} - x_7 & . \\ . & . & . & . & . & . & . & . & . & 1 & . & . & . & . & . & . & . & . \\ . & . & . & . & . & . & . & . & . & . & 1 & . & . & . & . & . & . & . \\ . & . & . & . & . & . & . & . & . & . & . & 1 & . & . & . & . & . & . \end{bmatrix} \cdot \begin{Bmatrix} u_1 \\ v_1 \\ w_1 \\ u_4 \\ v_4 \\ w_4 \\ u_5 \\ v_5 \\ w_5 \\ u_8 \\ v_8 \\ w_8 \\ u_1^{NBCFB} \\ v_1^{NBCFB} \\ w_1^{NBCFB} \\ \theta_1^{NBCFB} \\ \varphi_1^{NBCFB} \\ \psi_1^{NBCFB} \end{Bmatrix} \tag{7.5}$$

For computing the transformation matrix $\boldsymbol{T}_H$, the coordinates of the slave nodes that are controlled by the kinematic constraints and the x_m, y_m, z_m coordinates of the corresponding master node are required. The transformation matrix $\boldsymbol{T}_H$ is used for the purpose of obtaining the 18x18 transformed stiffness matrix of any hybrid hexahedron, according to Eq. (7.6), while the nodal displacements of the slave nodes are computed according to Eq. (7.4).

$$\underset{(18x18)}{\boldsymbol{K}_H^{\text{HEXA}}} = \underset{(18x24)}{\boldsymbol{T}_H^T} \cdot \underset{(24x24)}{\boldsymbol{K}^{\text{HEXA}}} \underset{(24x18)}{\boldsymbol{T}_H} \tag{7.6}$$

The calculation of the internal forces of the transformed hexahedral elements is performed as follows:

$$\underset{(18x1)}{\boldsymbol{F}_H} = \underset{(18x24)}{\boldsymbol{T}_H^T} \cdot \underset{(24x1)}{\boldsymbol{F}^{\text{HEXA}}} \tag{7.7}$$

where $\boldsymbol{F}_H$ is the internal force vector of the transformed hexahedral element. The above kinematic constraint expresses the assumption that the interface section remains undeformed throughout the solution process since its deformation is controlled by the deformations of the

master node of the NBCFB element. This local constraint has insignificant influence on the overall mechanical behavior of the structure as shown in Markou and Papadrakakis [37]. Furthermore, the numerical implementations performed in this research work confirmed the numerical findings at [37], thus show that the reduced models that derived from this hybrid approach produce accurate results not affected by the assumed kinematic constraints.

The procedure is based on the definition of the rigid connection between the master node of the NBCFB element and the slave nodes of the hexahedral nodes of the interface section. The model generation is performed with Femap pre-processing software in which rigid elements are constructed in order to connect the master node with its corresponding slave nodes of the interface section as shown in Fig. 7.3.

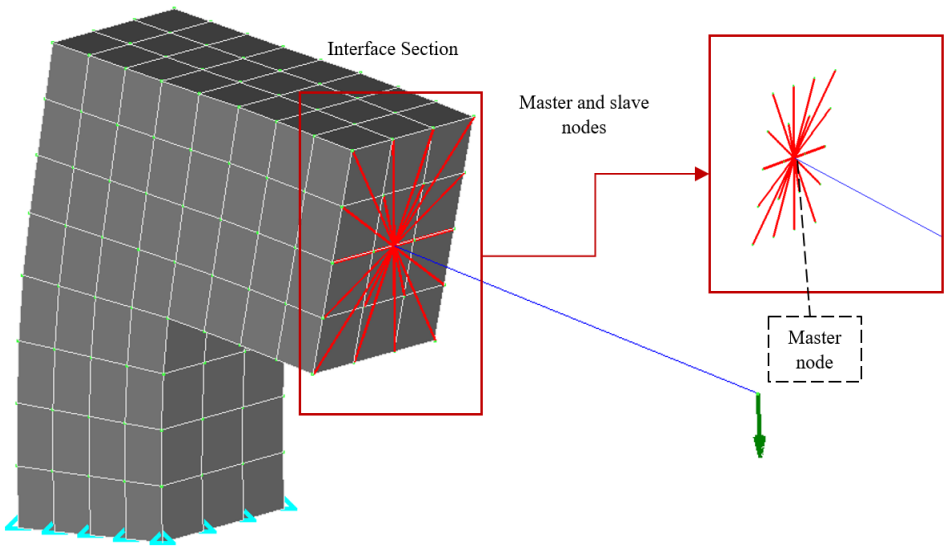

Fig. 7.3 Schematic representation of the master and slave nodes of the interface section.

More details on the kinematic constraints can be found in Markou and Papadrakakis [37].

7.3 Reduction Levels of HYMOD meshes

A numerical investigation has been performed by Markou and Papadrakakis [37] in order to reduce the dofs of the unreduced model without affecting its numerical accuracy. In Fig. 7.4, different reduction levels (RL) are illustrated for the hybrid simulation of 3D RC frame structures. The description of the different discretization schemes depicted in Fig. 7.4 is presented in Table 7.1.

Table 7.1 Description of the reduction levels. (Markou and Papadrakakis [37]*)*

Reduction Level of the Model	Description
0	The whole structure is discretized with 3D solid elements
1	Shear dominated structural members (shear walls, junctions etc.) are discretized with solid elements and the remaining part of the structure with beam elements.
2	Shear walls are discretized with solid elements and the rest of the structure with beam elements.
3	The whole structure is discretized with beam elements.

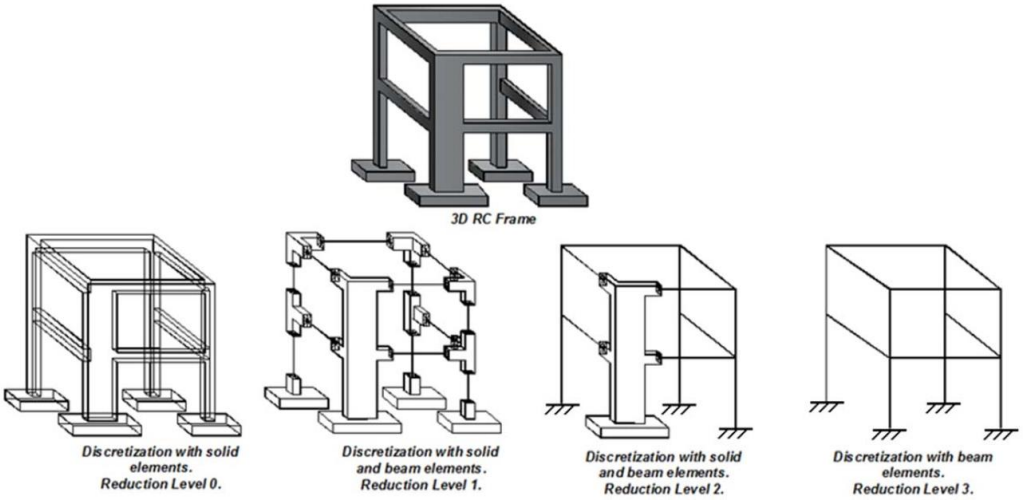

Fig. 7.4 Different reduction levels of hybrid simulation of a 3D RC frame. [37]

The key geometrical parameter of the above approach for the reduction of the mesh by using hybrid modeling techniques, is the length L_i of the solid part (plastic hinge length) which has to be defined for each frame joints at the edges of beams and columns (see RL1 and RL2 in Fig. 7.4). The selection of the plastic hinge length is crucial for the overall accuracy of the nonlinear analysis. These areas of the structure experience excessive stresses and strains during an earthquake, which lead to severe cracking and therefore it is assumed that plastic hinges will develop in these regions. The numerical investigation conducted in [37], shows that the length of the potential plastic hinge at the ends of the structural members should be equal to the height of the members' section h, or *2h* for the case of a potential symmetric plastic hinge in the middle of the member as illustrated in Fig. 7.5 for the case of a clamped beam model.

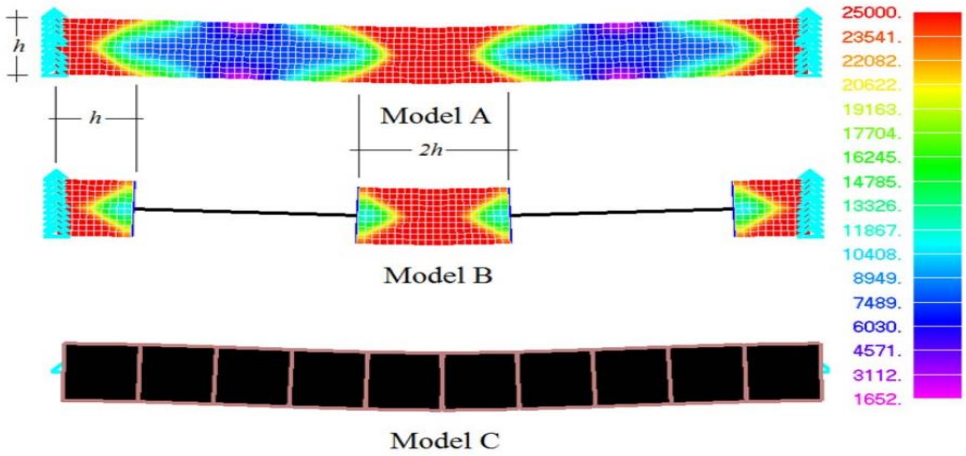

Fig. 7.5 Von Mises contours and deformed shapes of clamped beam models.[4]

In order to test the accuracy of the HYMOD approach and the adopted length L_i, several numerical implementations have been performed for RC structures under monotonic loading conditions as presented in Markou and Papadrakakis [37]. In the numerical investigations performed in this work, the proposed plastic hinge lengths are adopted, whereas the numerical investigations will be limited to the study of the proposed model's accuracy.

7.4 Numerical Results and Discussion

Given that the HYMOD approach [37] considers two different types of FE simulations that their formulation is based on one- and three-dimensional models, two different material models are adopted herein for the cycling analysis of RC structures. For the case of the 1D NBCFB finite element, the model foresees the discretization of each beam-column section through the use of fibers that have the ability to account for nonlinearities through the use of the bilinear model (see Fig. 7.6), while for all analyses performed in this research work the hardening modulus was set to zero.

The numerical analysis results will be presented in this sections for the case of three models that were selected for the purpose of this research work. The first is the Del Toro Rivera [178] frame joint that is used herein to demonstrate the ability of the proposed HYMOD algorithm to capture accurately experimental results. The other two models (1- and 2-storey RC frames) are used to demonstrate the computational efficiency of the proposed modeling approach in solving numerically demanding problems with significant shear nonlinearities and excessive cracking. It must be noted at this point that the nonlinear solution strategy used to perform the analyses presented in this section, was the Newton-Raphson displacement-control algorithm in combination with a work-based convergence criterion (see Eq. (3.46)). The general convergence tolerance that was used for all the numerical nonlinear analyses (where it is not stated) was 10^{-4} in order to achieve a high accuracy and induce additional stability during the cyclic nonlinear analysis. The CPU used to perform all the analyses presented in this section had a 3.7 GHz computing power.

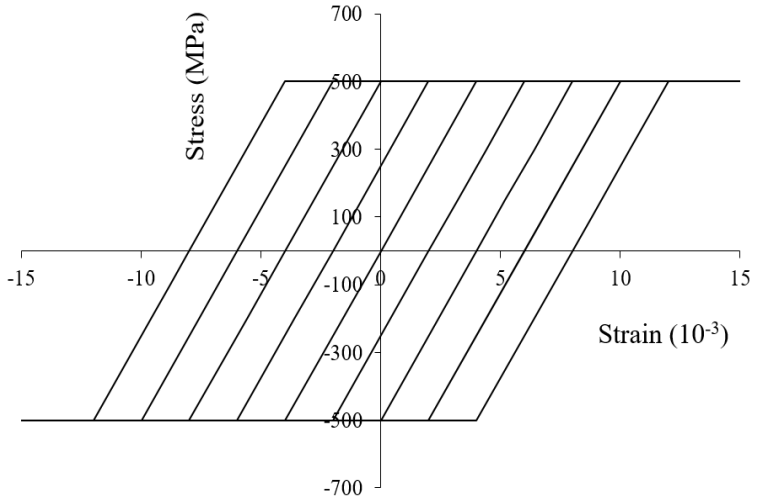

Fig. 7.6 Bilinear model for cyclic analysis.

7.4.1 Del Toro Rivera RC Frame Joint

Fig. 6.19 illustrates the schematic representation of the under study RC frame joint that was tested by Del Toro Rivera [178]. As it was presented in Chapter 6, the uniaxial compressive concrete strength of the joint was f_c = 40 MPa and the corresponding yielding stresses of the steel reinforcement were 570, 490, 440 and 554 MPa for the 10, 12, 14 and 20 mm diameter bars, respectively. The Young modulus of elasticity of the reinforcement steel was E_S = 200 GPa, which was also the material parameter used in this numerical investigation. The strength under tension was set to be equal to 5% of the uniaxial compressive strength, while the shear retaining factor β was set equal to 0.05 in all numerical models.

The under study interior frame joint was subjected to different cyclic loading conditions according to the experimental setup (Del Toro Rivera [178]). The loading history is presented in the form of imposed displacements in Fig. 6.20. It is important to note here that the joint was also loaded with a vertical load of 200 kN at the point of the applied displacement (see Fig. 6.19) so as to simulate the effect of the superstructure's loads. This load configuration generated 3D stress states, thus it was one of the reasons why this experimental setup was selected in order to demonstrate the numerical and computational capabilities of the proposed HYMOD algorithm in capturing experimental results under extreme cyclic loading conditions. The numerical model shown in 6.1.3.1 was used to develop the HYMOD meshes. For the unreduced numerical model, the steel bars that had 14 mm diameter were modeled through the use of beam elements while in 6.1.3.1, the steel bars that had 14 mm were modeled with truss elements. This minor change proves to provide more accurate numerical results closer to the experimental response.

As it can be seen in Fig. 7.7, the HYMOD 1 mesh corresponds to the modeling of two thirds of the horizontal beams of the joint with the NBCFB element and the remaining joint is discretized with HEXA elements (one NBCFB element was used for each structural beam member). The model was additionally reduced in HYMOD 2 mesh so as to further study the performance and numerical stability of the proposed algorithm, in which half of the upper column is modeled by hexahedral elements and the other half by one NBCFB element. In the last model (HYMOD 3), the same discretization concept that was implemented in HYMOD 2 was considered, where both vertical structural members of the specimen were reduced, therefore, one NBCFB element was used to model half of each column (upper and lower) as can be seen in Fig. 7.7. Table 7.2 shows the FE mesh details as they resulted from the reduction of the initial hexahedral model.

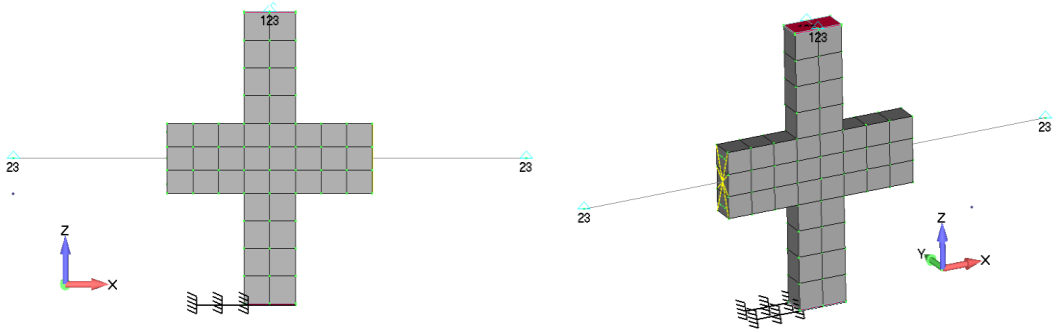

HYMOD 1.

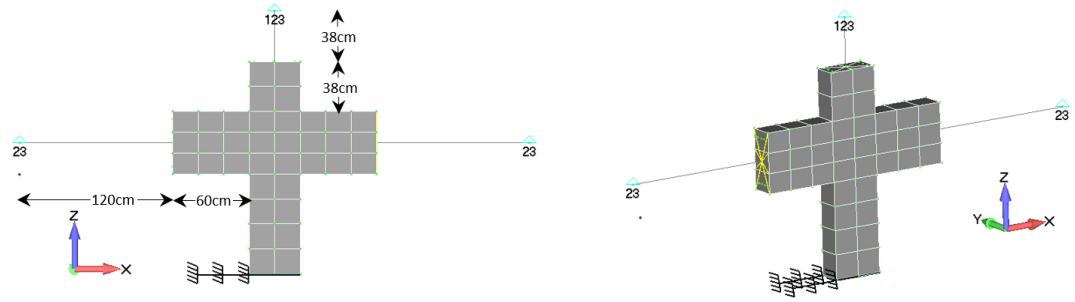

HYMOD 2.

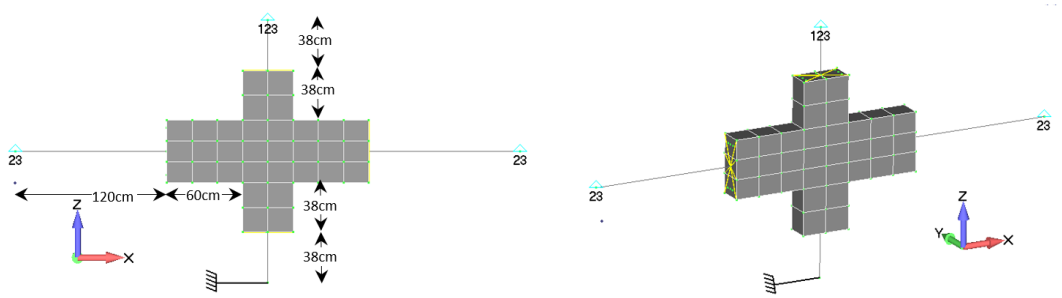

HYMOD 3.

Fig. 7.7 2D and 3D views of the FE meshes of the three HYMOD models.

As it was mentioned before, according to the parametric investigation performed in [37], a length between *h-2h*, was found to be adequate in order to determine the optimum plastic hinge length that has to be modeled with the hexahedral finite element. This rule was also applied herein for the case of the mesh of HYMOD 1, while for the other two meshes this rule was not followed, given that the two vertical structural elements foresaw a plastic hinge length of 38 cm, which is equal to a 0.95*h*. Even though the minimum hinge length is not satisfied the models were not modified in an attempt to further test the computational robustness and the numerical accuracy of the proposed algorithm.

Table 7.2 FE mesh details of the frame joint model.

a/a	Model	Hexahedral Elements	Embedded Rebar Elements	RC NBCFB Elements	Total Number of Dof	Dof Reduction (%)
1	Full Hexa	76	446	-	686	-
2	HYMOD 1	40	330	2	362	47
3	HYMOD 2	36	296	3	305	56
4	HYMOD 3	32	262	4	245	64

Fig. 7.8 illustrates the comparison between the experimental and numerical results for the case of the Full Hexa model. The diagram shows the complete force-displacement history as it is computed from the nonlinear solution of 310 displacement increments. As it can be seen in Fig. 7.8 and Table 7.3, the numerical results match very well with the experimental ones, while the average value of the divergence between the numerical and experimental load data per cycle was found to be equal to 11%, for both negative and positive maximum displacements. Given that the derived curves are rather complicated and difficult to graphically compare, the numerically predicted curve (Full Hexa) will be used herein as the base of comparison with the corresponding HYMOD numerical results in order to graphically present the numerical performance of the proposed algorithm.

Fig. 7.9-Fig. 7.11, depict the complete force-displacement history of the three hybrid models where the numerical results are compared with the response predicted by the Full Hexa model. As it can be seen from the three diagrams, the HYMOD models manage to capture the cyclic response with an adequate accuracy with regard to the full model. HYMOD 2 was found to be the model that had the closest numerical response with almost similar hysteretic loops with the ones obtained from the full model (see Fig. 7.10), while HYMOD 3 managed to attain the closest maximum load (169.9 kN) to the one obtained from the Full Hexa model (177.75 kN). According to Table 7.4 and Table 7.5, the horizontal load of each cycle of the numerical model HYMOD 2 was found to derive almost identical with the one that was obtained from the Full Hexa model (Table 7.3).

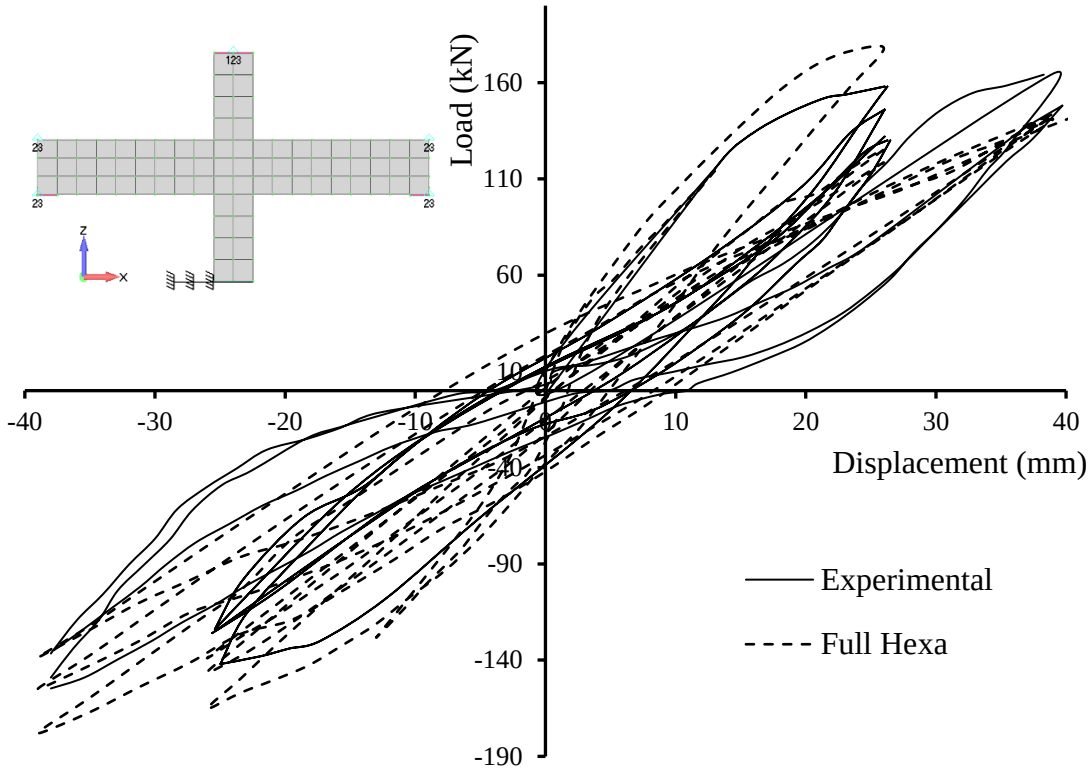

Fig. 7.8 Frame Joint. Comparison between numerical and experimental results. Complete force-displacement history.

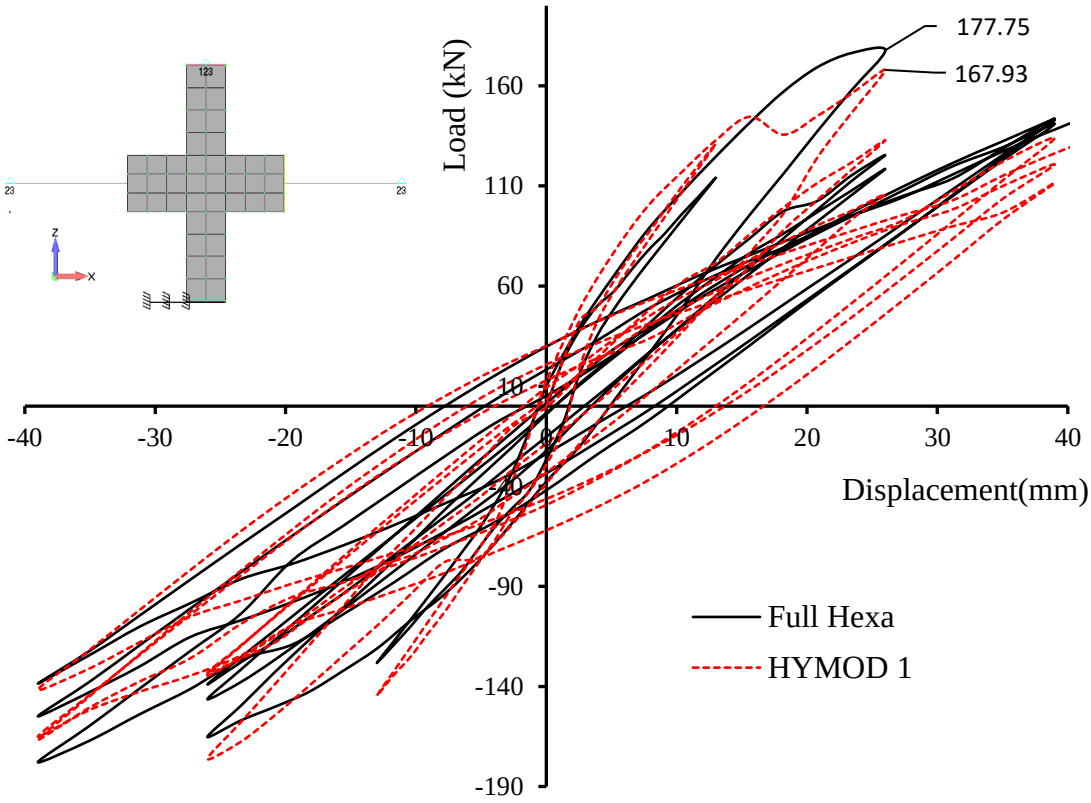

Fig. 7.9 Frame Joint. Comparison between Full Hexa and HYMOD 1 numerical results. Complete force-displacement history.

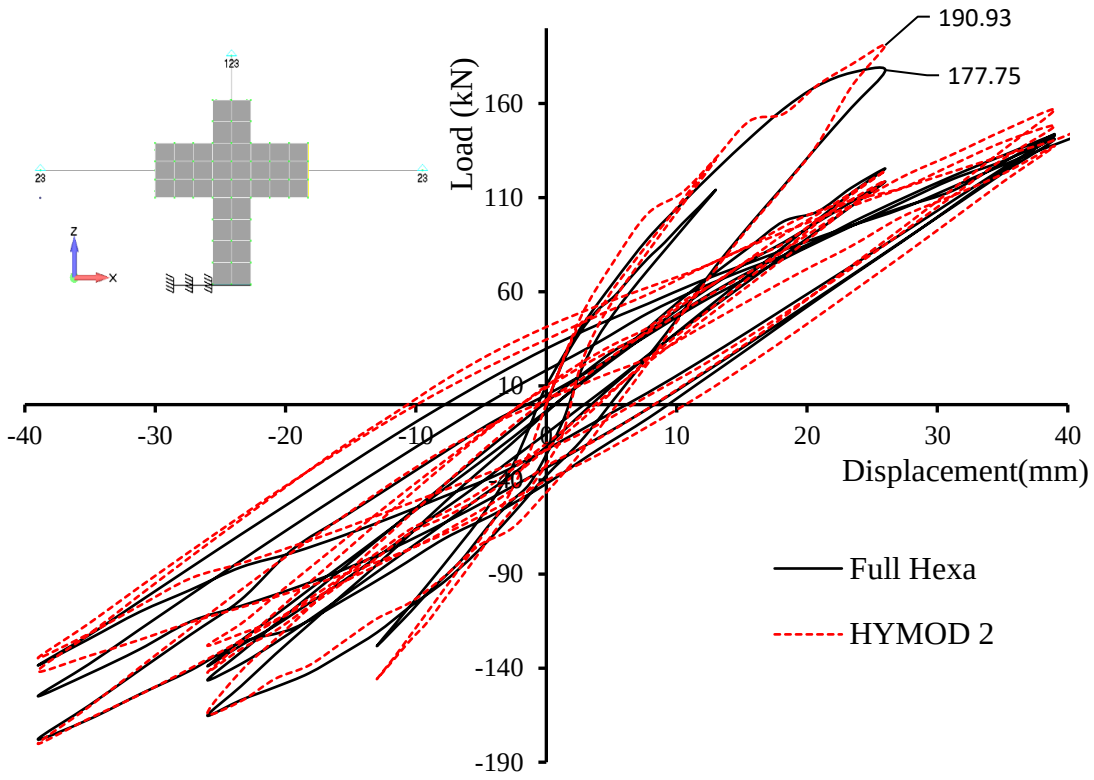

Fig. 7.10 Frame Joint. Comparison between Full Hexa and HYMOD 2 numerical results. Complete force-displacement history.

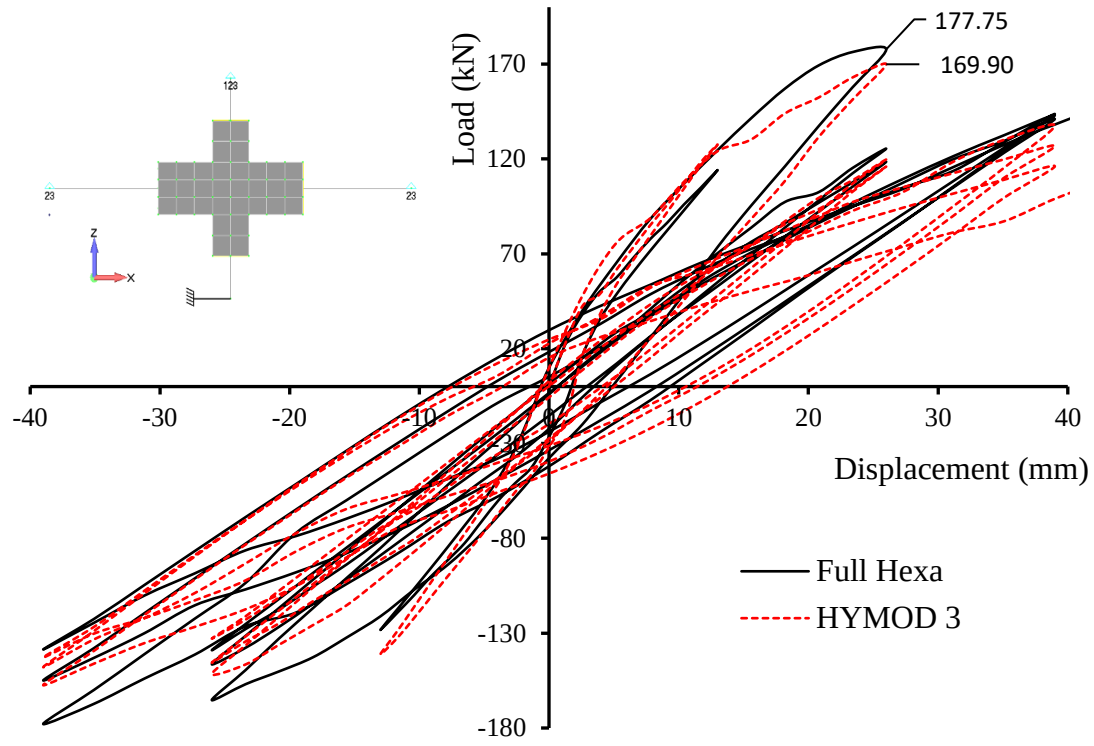

Fig. 7.11 Frame Joint. Comparison between Full Hexa and HYMOD 3 numerical results. Complete force-displacement history.

Table 7.3 Full Hexa numerical results. Comparison of the horizontal load for each cycle.

Loading Cycle	Horizontal Load Experimental (kN)		Horizontal Load Predicted Full Hexa (kN)		Divergence from experimental Full Hexa	
	Positive	Negative	Positive	Negative	Positive (%)	Negative (%)
1st	158	-142	177	-165	12.03	16.20
2nd	146	-126	125	-146	14.38	15.87
3rd	130	-124	118	-139	9.23	12.10
4th	164	-154	144	-178	12.20	15.58
5th	164	-154	141	-155	14.02	0.65
6th	149	-137	143	-139	4.03	1.46
				Average	10.98	10.31

Table 7.4 HYMOD 1 and 2 numerical results. Comparison of the horizontal load for each cycle.

Loading Cycle	Horizontal Load HYMOD 1 (kN)		Horizontal Load HYMOD 2 (kN)		Divergence from Full Hexa-HYMOD 1		Divergence from Full Hexa-HYMOD 2	
	Positive	Negative	Positive	Negative	Positive (%)	Negative (%)	Positive (%)	Negative (%)
1st	167.93	-171.22	190.93	-164.09	5.12	3.77	7.87	0.55
2nd	132.85	-134.55	124.30	-142.39	6.28	7.84	0.56	2.47
3rd	105.82	-133.46	119.00	-128.00	10.32	3.98	0.85	7.91
4th	134.00	-166.69	156.82	-180.18	6.94	6.36	8.90	1.23
5th	111.50	-165.08	137.46	-141.65	20.92	6.51	2.51	8.61
6th	120.73	-141.71	148.11	-134.69	15.58	1.95	3.57	3.10
				Average	10.86	5.07	4.05	3.98

Table 7.5 HYMOD 3 numerical results. Comparison of the horizontal load for each cycle.

Loading Cycle	Horizontal Load Predicted HYMOD 3 (kN)		Divergence from Full Hexa-HYMOD 3	
	Positive	Negative	Positive (%)	Negative (%)
1st	169.90	-152.62	4.01	7.50
2nd	119.71	-132.87	4.23	9.00
3rd	115.94	-145.57	1.75	4.72
4th	137.63	-147.94	4.42	16.89
5th	126.84	-142.82	10.04	7.86
6th	116.15	-157.40	18.78	13.24
		Average	7.21	9.87

In order to further compare the numerically obtained results, Fig. 7.12 and Fig. 7.13 depict the von Mises strain contours for the displacement increment in the first and sixth cycle of loadings, respectively. Fig. 7.12 illustrates the von Mises strain contours for the case of load increments 10 and 30. It must be stated here that each displacement cycle was divided into 10 displacement increments, therefore, for each imposed loading cycle the algorithm had to solve 40 displacement increments. The imposed maximum displacements at the tip of the column for the 1st cycle were +13 mm and -13 mm, respectively, along the x-axis. The von Mises contours illustrate the ability of the three HYMODs to capture the strain state within the solid joint without any numerical problems. It is also notable that the HYMODs developed a higher strain concentration within the hexahedral domain when compared to the contour obtained from the full model. As explained by Markou and Papadrakakis [37], this numerical phenomenon is attributed to the stiffness difference between the NBCFB and hexahedral elements, where the

beam FE is stiffer in this case forcing the more flexible domain that is discretized with hexahedrons, to develop higher strains. Nevertheless, the proposed algorithm manages to capture the overall behavior in a robust and accurate manner. In addition to that, the three HYMODs gave almost identical von Mises strain contours.

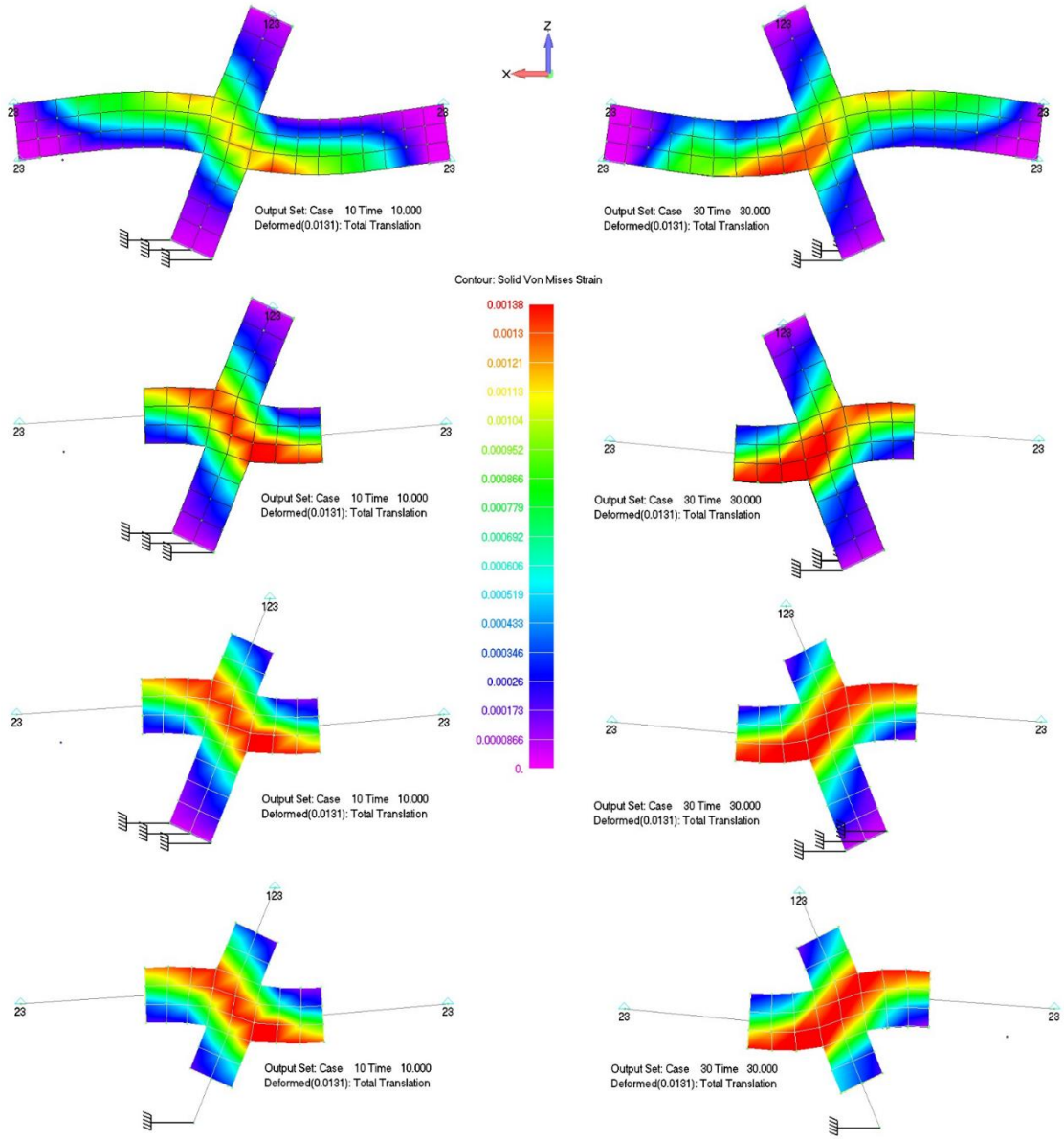

Fig. 7.12 Frame Joint. von Mises strain contour at displacement increment 10 and 30 (1st cycle of loading). Maximum x-axis displacement: ±13 mm.

Fig. 7.13 illustrates also von Mises strain contours that were obtained from the four models, for the displacement increments 210 and 230. In this case, it is easy to observe that the deformation shape of the four models is the same, while the von Mises strain contours are more disturbed when it comes to this extreme deformation stage. At this point, the specimen has undergone 6 complete cycles where it already developed significant cracking. Therefore, the nonlinear analysis has updated the stiffness matrix several times while the crack opening and closing was performed hundreds of times within the joint area at the GPs located within this domain. The differences in the results derived from the HYMODs is mainly attributed to the use of the NBCFB element within the HYMOD mesh that induces additional stiffness to the HYMODs numerical model.

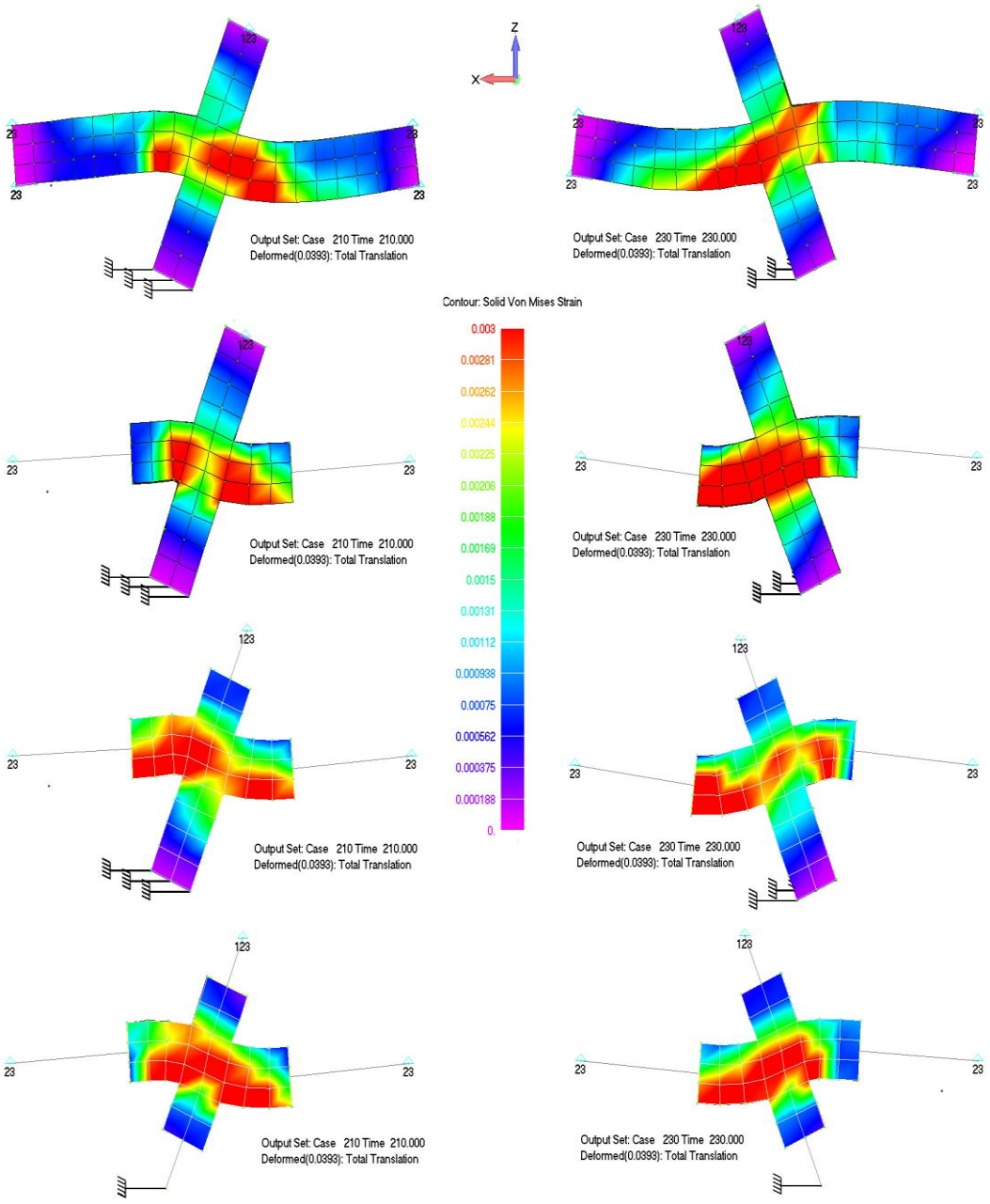

Fig. 7.13 Frame Joint. Von Mises strain contour at displacement increments 210 and 230 (6th cycle of loading). Maximum x-axis displacement: ±39 mm

Table 7.6 Computational performance of the four frame joint models.

a/a	Model	Num. of Displ. Incr.	Total Internal Iter.	Average Numerical Error	CPU Time Nonlinear Solution (sec)	Reduction in CPU Nonlinear Solution (%)	Reduction of Overall CPU Time (%)
1	Full Hexa	310	1052	1.94×10^{-5}	11.5	-	-
2	HYMOD 1	310	856	6.77×10^{-6}	5.9	48.7	35.22
3	HYMOD 2	310	827	8.00×10^{-6}	5.3	53.91	41.09
4	HYMOD 3	310	787	7.51×10^{-6}	5.2	54.78	48.67

Table 7.6 shows the CPU times required to solve the nonlinear numerical problems of the four numerical models. It is evident that the HYMODs exhibit a numerical stability that decreases

the required internal iterations per displacement increment. HYMOD 3 required a total of 787 internal iterations to achieve convergence during the 310 displacement increments, while the Full Hexa model required 1,052 internal iterations. The HYMODs 1 and 2 required 856 and 827 internal iterations, respectively. The reduction regarding the CPU time required to solve the nonlinear problem was found to be proportional to the reduction of the dofs in each model. This underlines the numerical advantage in terms of computational stability, when the HYMOD is deployed, even in the case of extreme cyclic loading conditions where the stress-strain fields are highly complex thus derive increased numerical stability demands.

In order to investigate the mesh sensitivity of the proposed algorithm, two denser meshes were used for the discretization of the frame joint. Fig. 7.14 shows the meshes that were constructed and their corresponding HYMODs that were used so as to study the numerical response in terms of mesh sensitivity of the HYMOD approach. As it can be seen in this figure, only the first level of reduction (HYMOD 1) was performed in order to reduce the required number of analyses that will be presented herein without losing the objectivity of the performed parametric investigation. Table 7.7 shows the FE mesh details of the four refined models that were constructed for the mesh sensitivity analysis. As it can be seen, the overall dof reduction that derived after the level 1 reduction scheme was implemented, was approximately 48% in both refined models.

Table 7.7 FE mesh details of the frame joint model used for the mesh sensitivity analysis.

a/a	Model	Hexahedral Elements	Embedded Rebar Elements	RC NBCFB Elements	Total Number of Dof	Dof Reduction (%)
1	Full Hexa 1	152	710	-	1,298	-
2	HYMOD 1.1	80	454	2	674	48.07
3	Full Hexa 2	304	910	-	1,955	-
4	HYMOD 2.1	160	598	2	1,001	48.80

Fig. 7.15-Fig. 7.18 show the comparison between the experimental results of the four refined models presented in Fig. 7.14. It can be seen that all models managed to capture the experimental results thus the accuracy of the proposed algorithm is not affected by the mesh refinement in this case. Table 7.8 and Table 7.9 show that the Full Hexa1, Full Hexa2 and HYMOD 1.2 managed to obtain almost similar highest response in terms of the horizontal load deriving a very good agreement with the experimental ones (<10% divergence from the experimental values). The horizontal loads derived from HYMOD 1.1 present the biggest discrepancy of all the models (20%) compared to the experimental results. The numerical curves in Fig. 7.16, show that during the cycles 4, 5 and 6 (in which the imposed displacement has the highest value during the experiment) the structural member of HYMOD 1.1 derives a more flexible response than the experimental one, where the derived prediction was in favor of safety. Furthermore, this discrepancy is not noted when using a denser mesh (see HYMOD 1.2), where the proposed algorithm manages to maintain its ability in predicting the overall mechanical behavior of the understudy experiment. From the above overall results, it is evident that the proposed modeling approach manages to capture the experimental results through the use of 8 different meshes, while dealing with a highly nonlinear cyclic loading problem. This numerical finding demonstrates the numerical robustness of the proposed modeling approach.

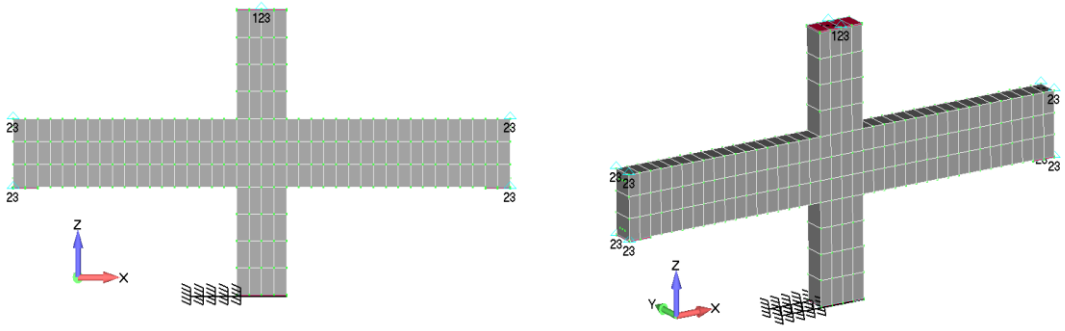

Full Hexa 1.

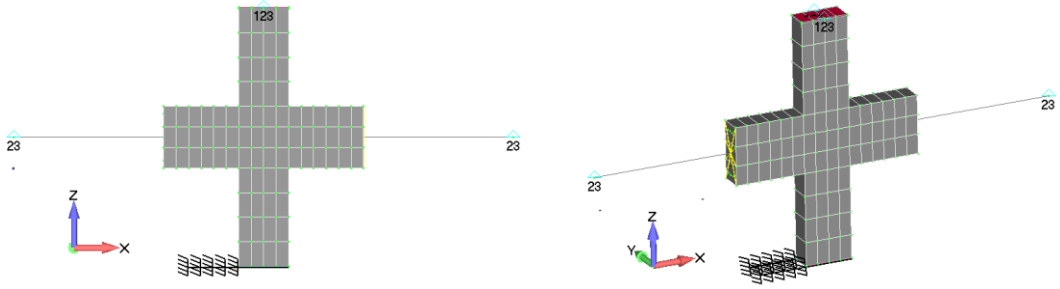

HYMOD 1.1.

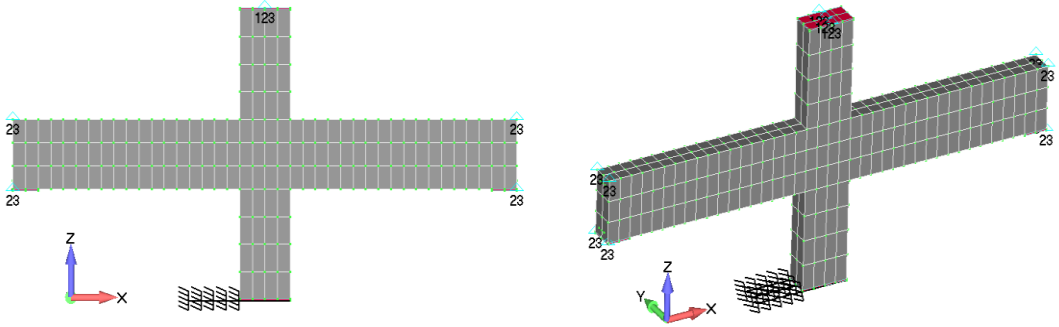

Full Hexa 2.

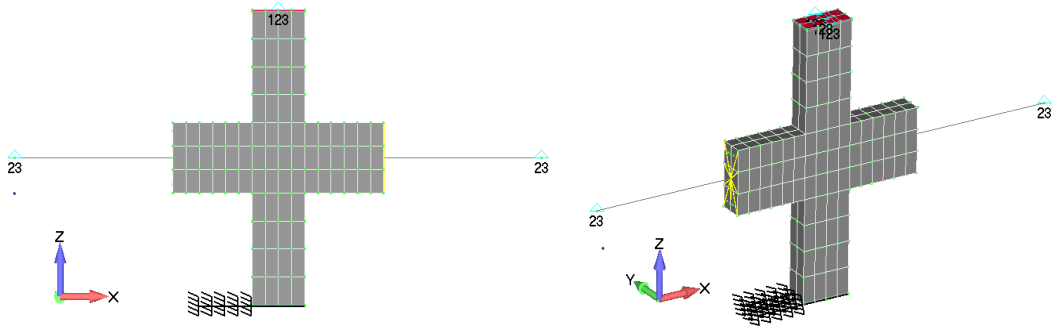

HYMOD 1.2.

Fig. 7.14 2D and 3D views of the FE mesh of the concrete elements used during the HYMOD mesh sensitivity analysis.

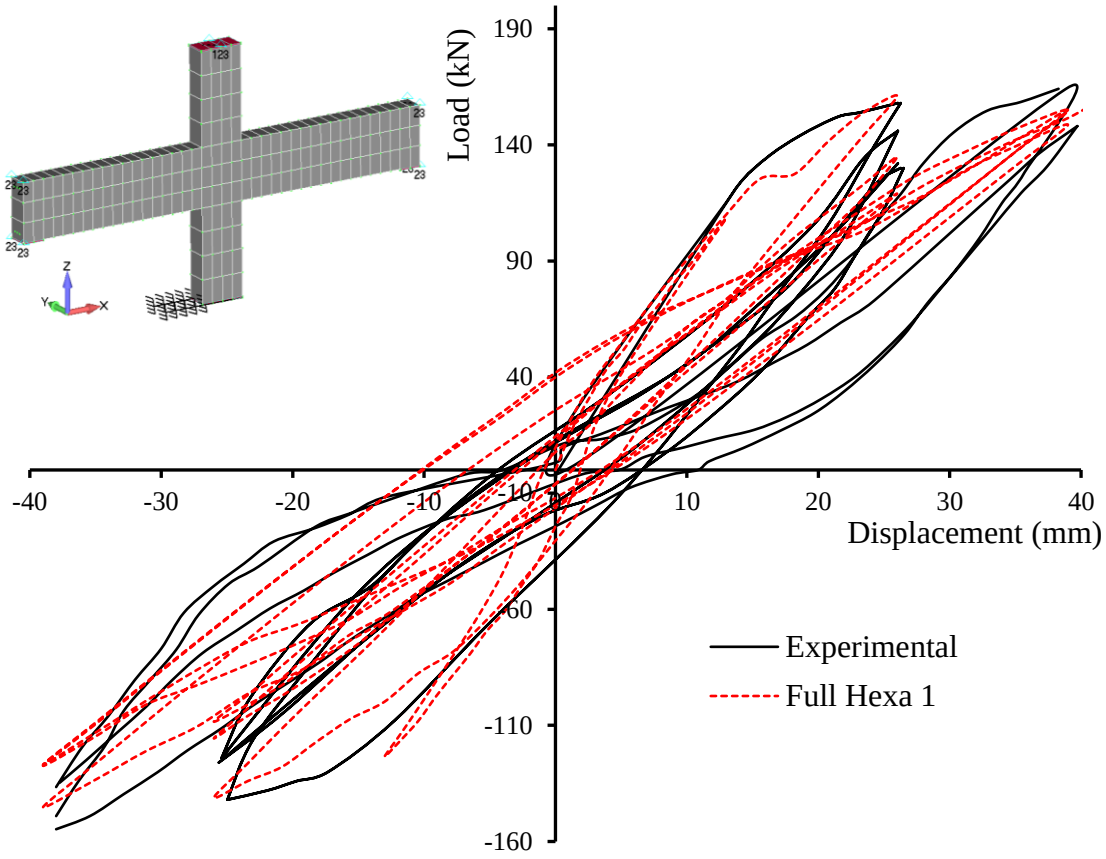

Fig. 7.15 Frame Joint. Comparison between experiment and Full Hexa 1. Complete force-displacement history.

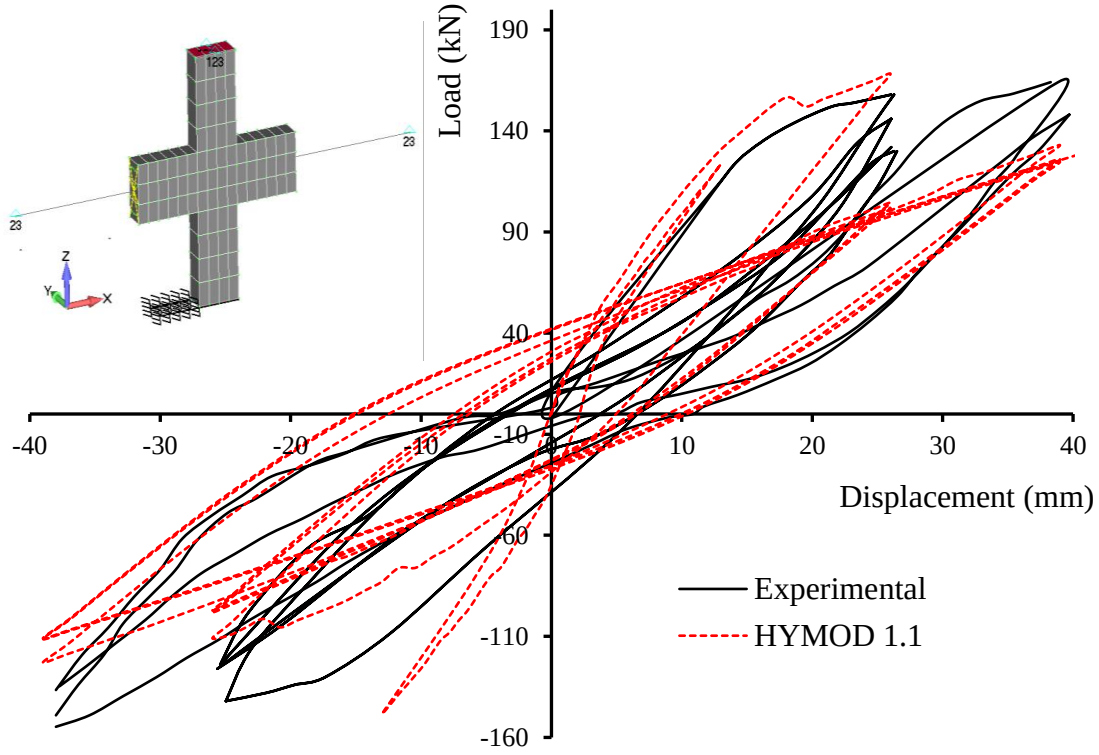

Fig. 7.16 Frame Joint. Comparison between experiment and HYMOD 1.1. Complete force-displacement history.

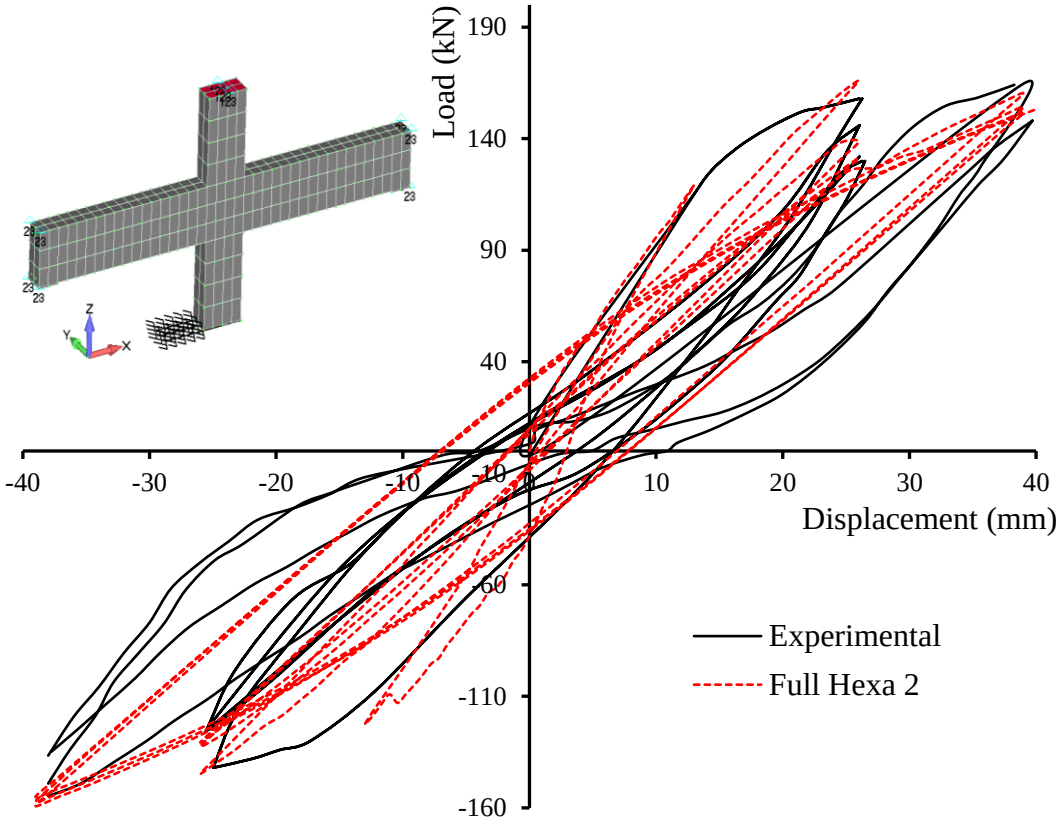

Fig. 7.17 Frame Joint. Comparison between experiment and Full Hexa 2. Complete force-displacement history.

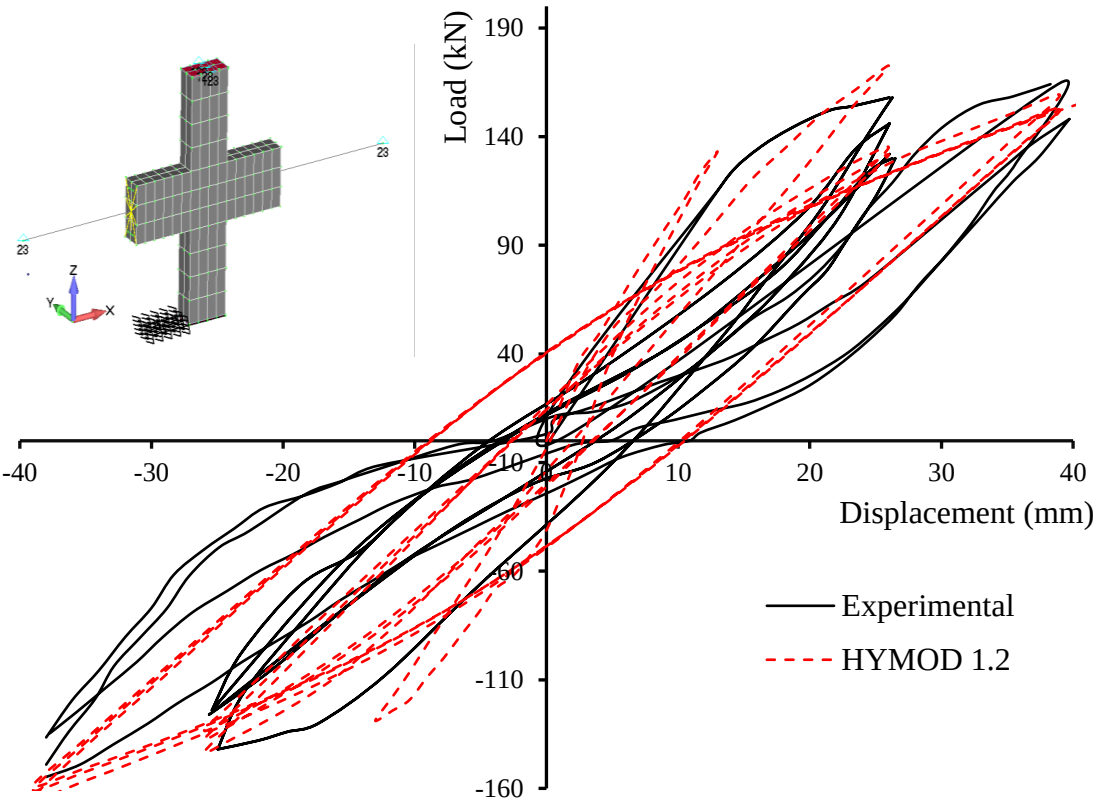

Fig. 7.18 Frame Joint. Comparison between experiment and HYMOD 1.2. Complete force-displacement history.

For the case of the von Mises strain contours, Fig. 7.19 illustrates the numerically obtained results for the case of the first cycle. As it can be observed, the same pattern as before has been computed thus the numerically predicted strains are not significantly affected by the mesh refinement. The displacement increment used for the solution of the two first models was 40 per loading cycle, while for the case of the models 3 and 4 an 80 displacement increments per cycle was implemented so as to avoid any numerical instabilities due to the finer meshes and the increased number of cracks within the joint domain. It must be noted at this point that by using very small in size elements will lead to very dense meshes that will require larger computational times, making this modeling approach unsuitable for full scale RC building simulations.

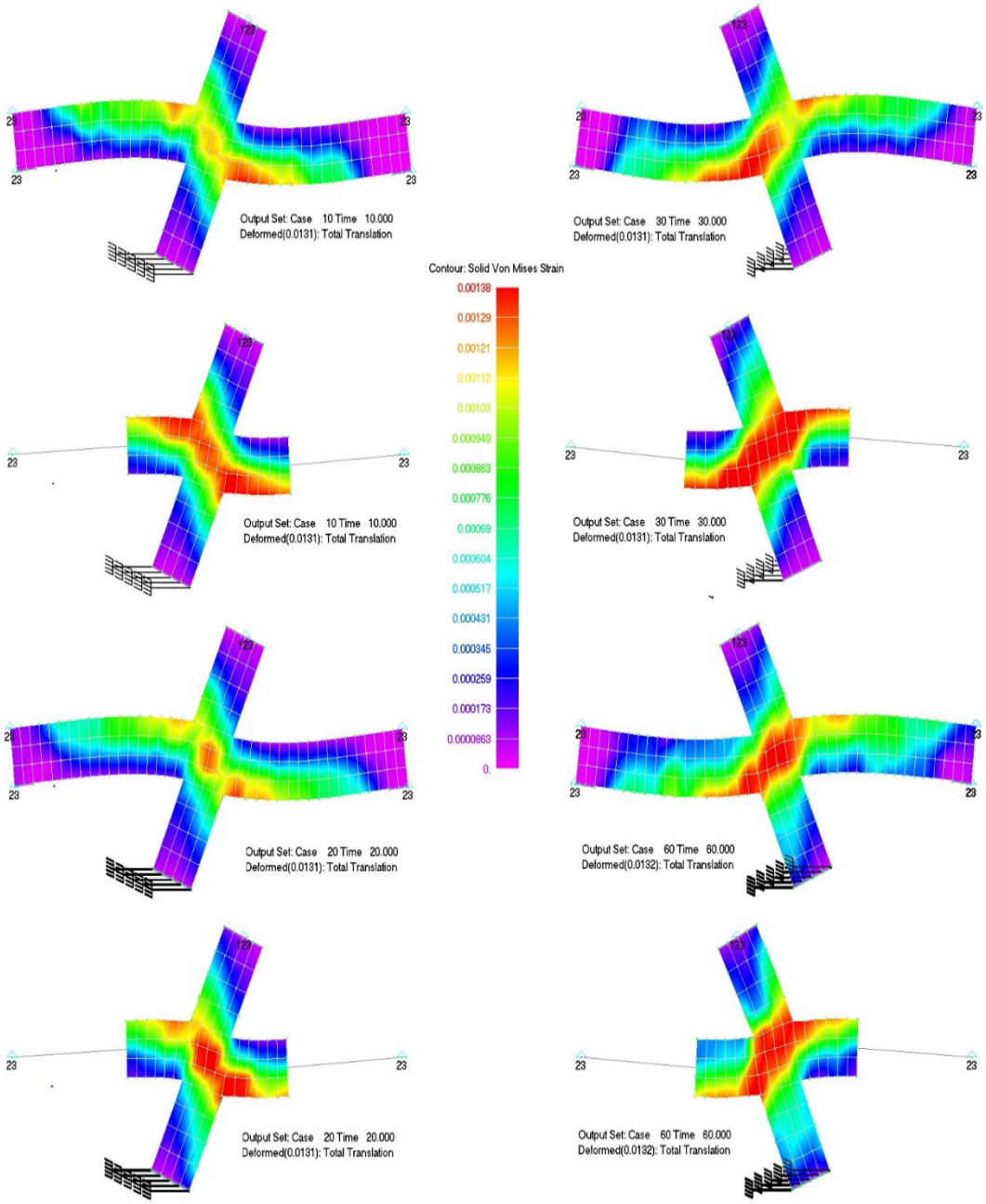

Fig. 7.19 Frame Joint. Von Mises strain contour at load step 10 and 30 (1st cycle of loading) for the refined meshes. Maximum x-axis displacement: ±13 mm.

Table 7.8 Full Hexa 1 and HYMOD 1.1 numerical results. Comparison of the horizontal load for each cycle.

Loading Cycle	Horizontal Load Full Hexa1 (kN)		Horizontal Load HYMOD 1.1 (kN)		Divergence from experimental-Full Hexa 1		Divergence from experimental-HYMOD 1.1	
	Pos.(+)	Neg.(-)	Pos.(+)	Neg.(-)	Pos.(+) (%)	Neg.(-) (%)	Pos.(+) (%)	Neg.(-) (%)
1st	161.04	-141.20	168.24	-110.95	1.93	0.56	6.48	21.87
2nd	134.86	-115.62	104.43	-97.18	7.63	8.24	28.47	22.88
3rd	119.01	-108.37	101.88	-98.12	8.45	12.61	21.63	20.87
4th	155.09	-145.31	132.94	-122.95	5.43	5.64	18.94	20.16
5th	154.88	-127.37	124.70	-111.39	5.56	17.29	23.97	27.67
6th	148.66	-126.97	125.91	-111.02	0.23	7.32	15.50	18.96
				Average	4.87	8.61	19.16	22.07

Table 7.9 Full Hexa 2 and HYMOD 1.2 numerical results. Comparison of the horizontal load for each cycle.

Loading Cycle	Horizontal Load Full Hexa 2 (kN)		Horizontal Load HYMOD 1.2 (kN)		Divergence from experimental-Full Hexa 2		Divergence from experimental-HYMOD 1.2	
	Pos.(+)	Neg.(-)	Pos.(+)	Neg.(-)	Pos.(+) (%)	Neg.(-) (%)	Pos.(+) (%)	Neg.(-) (%)
1st	166.04	-144.75	172.62	-143.48	5.09	1.94	9.25	1.04
2nd	138.76	-132.54	135.11	-137.54	4.96	5.19	7.46	9.16
3rd	131.36	-130.68	131.76	-133.42	1.04	5.38	1.35	7.60
4th	160.39	-159.12	159.07	-165.03	2.20	3.33	3.00	7.16
5th	154.20	-157.33	152.84	-160.80	5.98	2.16	6.80	4.41
6th	151.70	-155.10	152.19	-158.91	1.81	13.21	2.14	15.99
				Average	3.51	5.20	5.00	7.56

7.4.2 One-Storey RC Frame with a Shear Wall

In this section, the numerical results of a parametric investigation related to the numerical efficiency of the proposed simulation will be presented for a one-storey RC frame based on the experimental setup of the SERFIN project (Poljanšek et al. [42]). This project deals with the construction of a full-scale four-storey RC building with 25x40cm columns and the retrofit of the middle openings through the use of infill shear walls. Fig. 7.20 shows the south face of the four-storey's RC building that was tested for cyclic loading during the SERFIN project, while the part of the structure that was used to be modeled herein is shown within the framed region of Fig. 7.20 (see rectangle with dashed line).

The main objective in this section is to study the numerical behavior of the proposed modeling approach, whereas the full cyclic modeling of the building will be presented in Chapter 8. Therefore, the material properties that are shown in Table 7.10, are based on the properties reported in Poljanšek et al., [42], while the geometry of the RC frame shown in Fig. 7.21 is according to the specimen's geometrical details found in the project's report. The reinforcement details of the sections used to construct the model in Fig. 7.22, are shown in Fig. 7.21. The foundation of the frame was reinforced with 16 mm in diameter bars every 25 cm (bottom and top of the foundation in both directions), while 12 mm stirrups were used to further increase the strength of the foundation. A 3D representation of the reinforcement grid of the foundation and the rest of the structural members used in the considered model can be seen in Fig. 7.23. In regards to the concrete cover, all structural members foresaw the use of 20 mm nominal concrete cover.

Table 7.10 One-storey frame. Material details.

Material	Young Modulus (GPa)	Hardening Modulus (GPa)	Yielding Stress (MPa)	Compressive Strength (MPa)	Poisson Ratio
Concrete	30	-	-	20	0.2
Steel	200	2.0	400	-	0.3

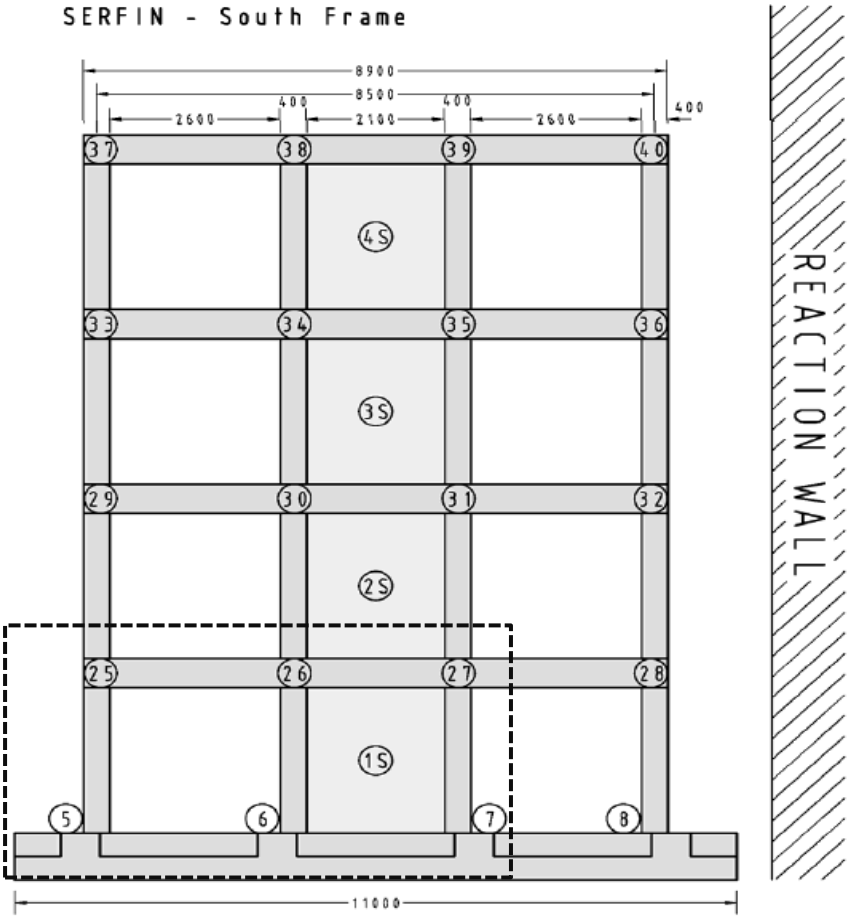

Fig. 7.20 South face of the SERFIN four-storey RC building. [42]

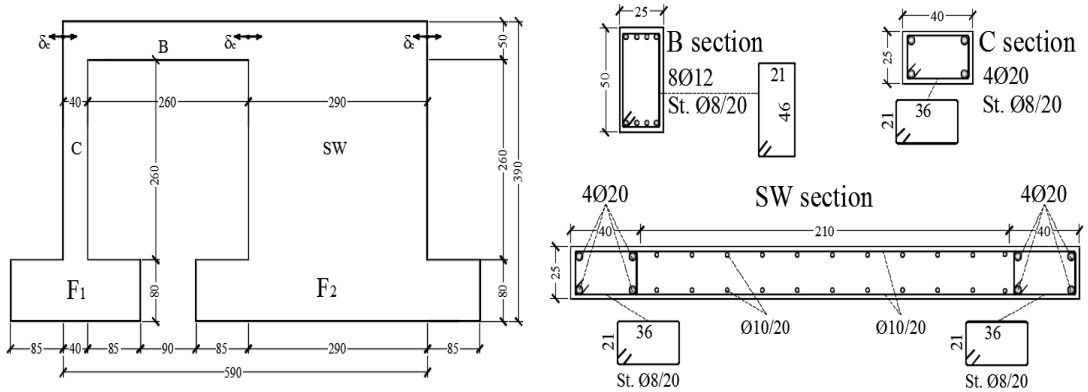

Fig. 7.21 One-storey frame. Geometric (cm) and reinforcement details (Ømm/cm).

Fig. 7.22 and Fig. 7.23 show the FE mesh that was developed for the needs of this numerical investigation. The HYMOD mesh consists of a detailed mesh (hexahedral elements) for the shear dominated structural members (shear wall and structural joints), while the flexural dominated structural members (beams and columns) are discretized with beam elements (reduction level 1, see section 7.3). The hinge lengths that were used in this model foresaw a length of 50 and 60 cm for the column and beam, respectively. As it can be seen in Fig. 7.21-Fig. 7.23, three points were selected along the beam as the points through which the displacement history was imposed simultaneously, in order to simulate the cyclic loading conditions. The embedded rebar elements were all modeled as beam elements so as to incorporate maximum computational demand. Table 7.11 shows the details of the developed HYMOD model.

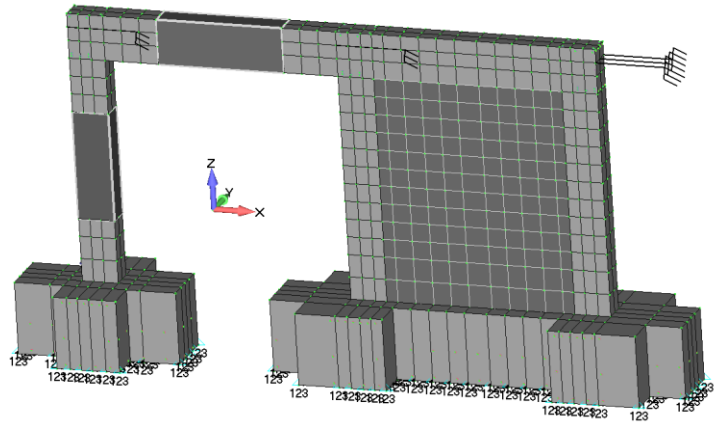

Fig. 7.22 One-storey frame. 3D HYMOD FE mesh.

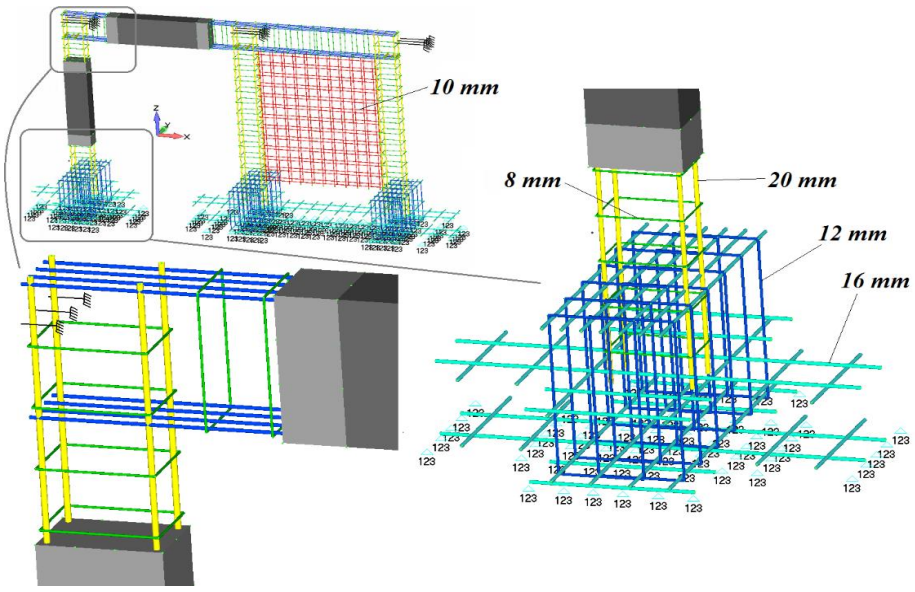

Fig. 7.23 One-storey frame. 3D HYMOD FE mesh of the reinforcement rebar elements.

The displacement history that was selected for the needs of this numerical investigation is presented in Fig. 7.24, where it can be noted that the cyclic displacement history foresees 7 complete cycles, while at the end of the analysis the frame is pushed until a total horizontal displacement of 100 mm. The displacement history diagram in Fig. 7.24, was developed by

using 120 displacement increments per cycle. The displacement increment is also going to be investigated numerically and the findings will be presented in this section.

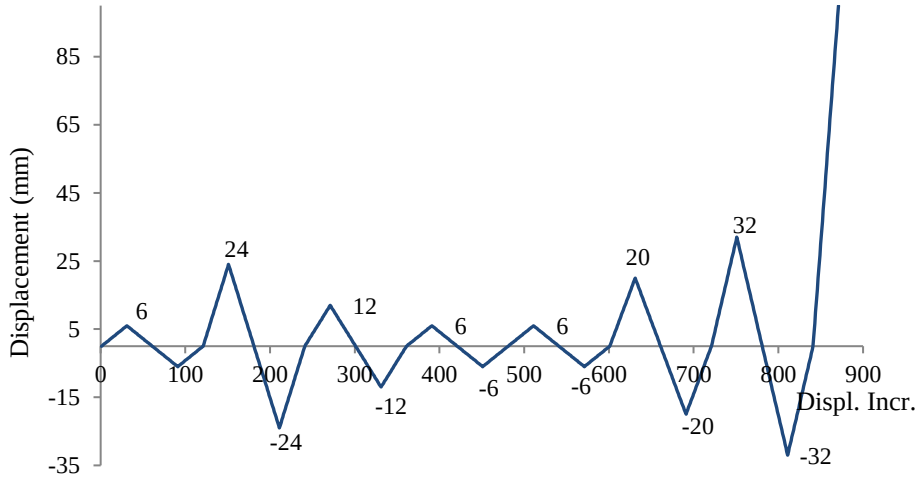

Fig. 7.24 Load history presented in the form of imposed displacements for the one-storey RC frame.

Table 7.11 FE mesh details of the one-storey RC frame model.

a/a	Model	Hexahedral Elements	Embedded Rebar Elements	RC NBCFB Elements	Total Number of Dofs
1	HYMOD	750	2,594	2	3,474

For the first set of analysis the number of displacement increments per loading cycle were set to 40, 80 and 120. As it derived, the two first models with 40 and 80 displacement increments per cycle did not manage to capture the complete displacement history thus failed to converge near the maximum positive displacement magnitude of 24 mm. This is attributed to the loose convergence tolerance at each nonlinear iteration which is not sufficient to achieve a stable solution and the nonlinear analysis Fig. 7.25 reaches to a point where it diverges. On the other hand, when a smaller displacement increment is used, the algorithm manages with the same convergence tolerance, to converge for all 870 displacement increments, as it is shown in Fig. 7.25. A stricter convergence tolerance of 10^{-4} led to an improved performance of the 80 displacement increments model but not of the 40 increments one, as, it is shown in Fig. 7.26.

Fig. 7.27 illustrates the crack patterns for different displacement increments, where the opening and closing of cracks can be seen. It can be observed that the shear wall develops tensile cracks due to the bending moment at the base (output set 1), while diagonal cracks appear at output set 10 (δ = 6 mm) due to shear deformations at the middle of the shear wall. Thereafter, the frame is forced to return to its initial position (output set 20), while cracks start to close from output sets 18 and 19. When the frame is forced to deform along the positive x-axis, cracks develop due to the inverse bending moment and shear deformation that force the structure in developing horizontal and diagonal cracking in a mirrored pattern (see output set 27 in Fig. 7.27). It must be noted here that the tensile rebars of the beam and shear wall yield when the horizontal displacement during the 2nd loading cycle is larger than 10 mm, a deformation stage where excessive material nonlinearities occur. This numerical response causes the frame to develop large hysteretic loops for the remaining loading cycles, as depicted in Fig. 7.25 and Fig. 7.26.

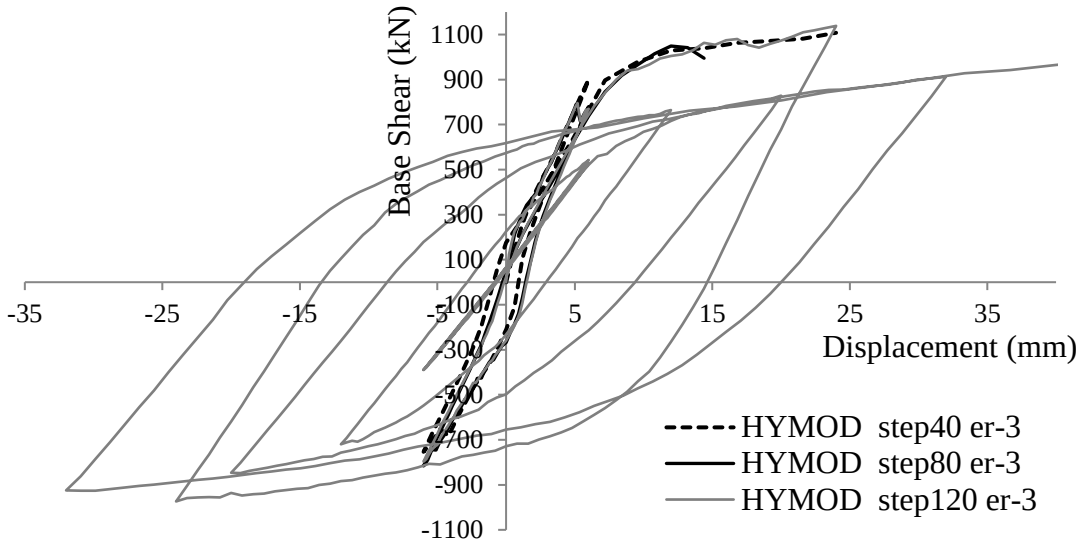

Fig. 7.25 One-storey RC frame. Comparison between different displacement increments with a convergence tolerance 10^{-3}. Complete force-displacement history.

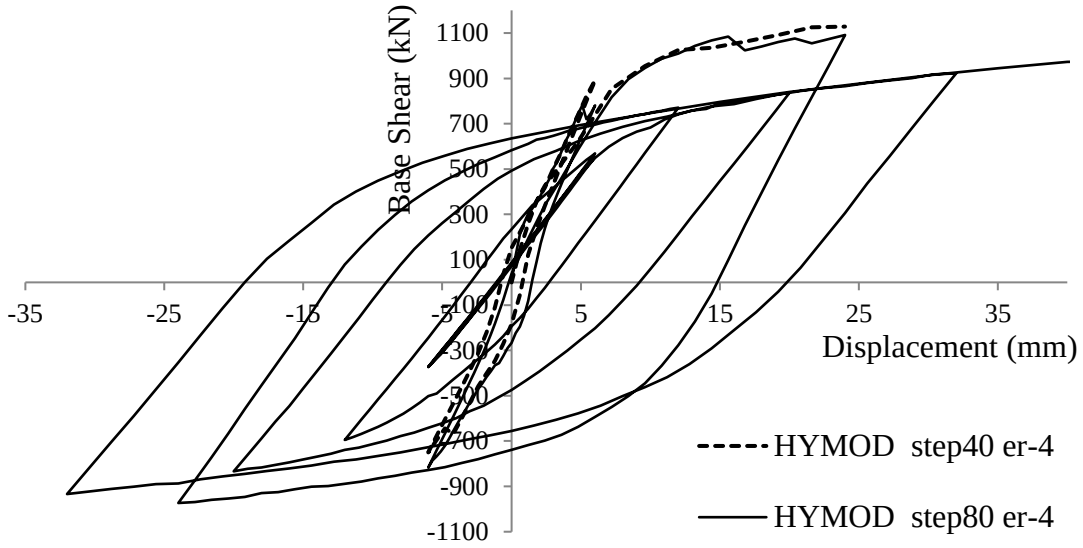

Fig. 7.26 One-storey RC frame. Comparison between different displacement increments with a convergence tolerance 10^{-4}. Complete force-displacement history.

Table 7.12 One-storey RC frame. Computational performance of the five analyses.

a/a	Model	Num. of Displ. Incr. per cycle	Conv. Toler.	Total Displ Incr. Solved	Total Internal Iter.	Average Numerical Error	CPU Time Nonlinear Solution (sec)
1	HYMOD	40	10^{-3}	50	283	$9.46x10^{-4}$	33
2	HYMOD	80	10^{-3}	92	489	$1.04x10^{-3}$	58
3	HYMOD	120	10^{-3}	870	2,160	$5.31x10^{-4}$	259
4	HYMOD	40	10^{-4}	50	414	$2.00 x10^{-4}$	46
5	HYMOD	80	10^{-4}	575	2,285	$7.05x10^{-5}$	271

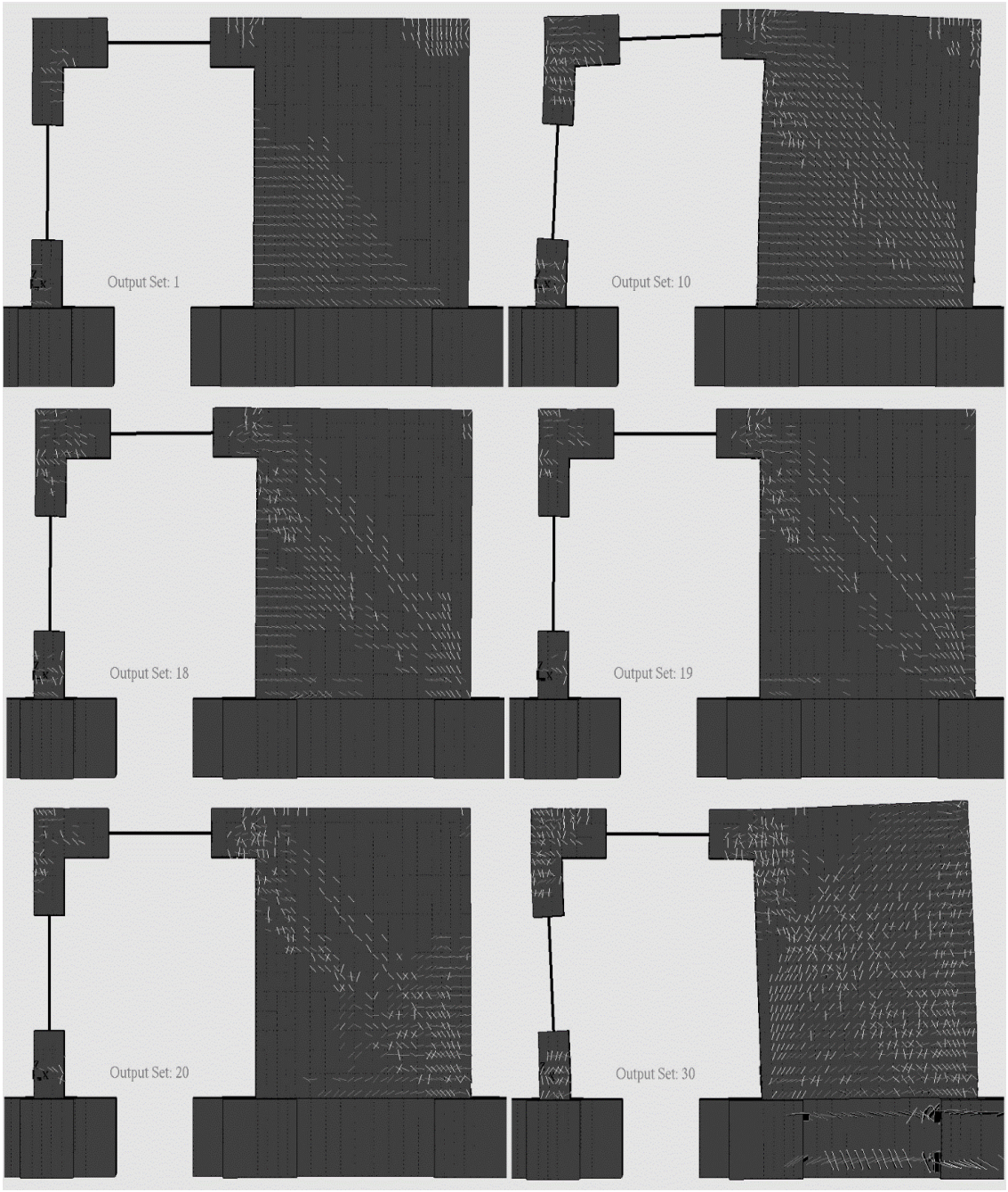

Fig. 7.27 One-storey RC frame. Opening and closing of cracks during the first loading cycle for the first model (40 displacement increments per loading cycle).

Table 7.12 shows the computational time as it resulted from each analysis, where it can be seen that even in the case of analysis 5, for which a total of 2,285 internal iterations are performed, the total nonlinear analysis time was just 271 seconds with an average error of 7.05×10^{-5}.

7.4.3 Two-storey RC Frame with Shear Wall

The third model, which is shown in Fig. 7.28, is a two-storey RC frame that was constructed by adding an extra floor on the model presented in the previous section. The reinforcement details were kept the same for all structural members, as well as the displacement history that was applied to the top beam (Fig. 7.28 and Fig. 7.29). The main goal of this numerical investigation is to illustrate the ability of the algorithm to solve larger nonlinear numerical

problems with the same efficiency and numerical robustness. Furthermore, the HYMOD's limitations in terms of maintaining its accuracy are also investigated.

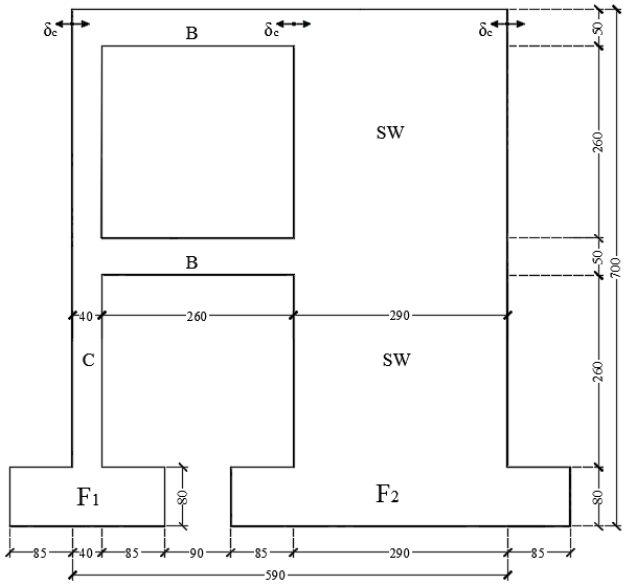

Fig. 7.28 Two-storey RC frame. Geometric details.

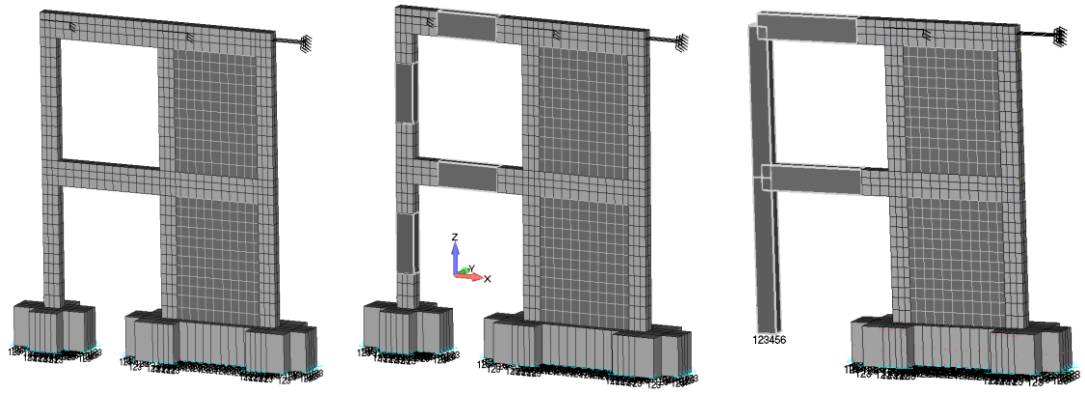

a. b. c.

Fig. 7.29 Two-storey RC frame. FE meshes of a. Full Hexa, b. HYMOD 1 and c. HYMOD 2 models.

Table 7.13 shows the FE mesh details of the new models constructed so as to study the proposed numerical model through the simulation of the two-storey RC frame (Fig. 7.29). The three models investigated were: Full Hexa FE mesh with 1,506 hexahedral elements, HYMOD 1 with 1,350 hexahedral elements and the HYMOD 2, with 1,160 hexahedral elements, while the corresponding number of the embedded rebar elements that were used to model the reinforcement were 4,544, 5,134 and 3,348 for the Full Hexa, HYMOD 1 and HYMOD 2 models, respectively (see Table 7.13). The reduction of the total number of dofs for HYMOD 1 and 2 were 13.96% and 26.54%, respectively. In order to intensify the computational demand of this numerical problem, the convergence tolerance was set to 10^{-5}, where nine analyses were performed for the needs of this numerical investigation.

Table 7.13 FE mesh details of the 1-storey RC frame model.

a/a	Model	Hexahedral Elements	Embedded Rebar Elements	RC NBCFB Elements	Total Number of Dofs	Dof Reduction (%)
1	Full Hexa	1,506	4,544	-	7,392	-
2	HYMOD 1	1,350	4,134	4	6,360	13.96
3	HYMOD 2	1,160	3,348	4	5,430	26.54

Fig. 7.30 shows the force-displacement history as it resulted from the six analyses (Full Hexa and HYMOD 1 meshes) that were performed by using a constant convergence tolerance of 10^{-5} and three different displacement increments (40, 80 and 120 displacement increments per loading cycle). It is interesting to note here that for the case of the two-storey RC frame, all three models (contrary to the obtained results in the one-storey test example), managed to provide with the complete solution. This is attributed to the fact that the structure in the case of the two-storey RC frame is taller, therefore, the shear deformation is smaller, while at the same time the crack openings that were computed were less (given that the same displacement history was applied in both models, one- and two-storey RC frames; therefore, the shortest structure is expected to develop the largest shear deformation and higher crack openings). With regard to the comparison between the resulted force-displacement hysteretic loops of HYMOD 1 and the Full Hexa model, it is easy to observe that they are almost identical (Fig. 7.30), illustrating once more the robustness of the proposed modeling approach.

An additional finding that can be depicted in Fig. 7.30, is the drop of the overall strength that the full Hexa model exhibited after all the displacement cycles were applied in the case of the 40 displacement increments per loading cycle was used. When using a larger displacement increment (40 displacement increments per loading cycle), the decreased strength that the Hexa model exhibited, is observed as a result of the premature deterioration of the concrete material that can lead to the decrease of the overall strength (Fig. 7.30), after all the displacement cycles have been applied (see the dotted line P-δ curve). It can also be seen that the HYMOD 1 mesh provides the required numerical accuracy and robustness so as to overcome this numerical phenomenon, whereas all three HYMOD 1 analyses presented in Fig. 7.30 are almost identical to the Full Hexa model that uses the two displacement increments (80 and 120 displacement increments per loading cycle).

Fig. 7.31 depicts the force-displacement curves that resulted from the Full Hexa and the HYMOD 2 models. It is evident that the HYMOD 2 mesh derives a stiffer behavior at the initial cycles of the loading obtaining a maximum base shear of 761 KN, which is 19% larger than the corresponding value that was computed by the Full Hexa model. This numerical finding is attributed to the stiffer NBCFB FE that does not take into account the full magnitude of nonlinearities that occur at the beam-column joint and at the base of the column. After the first 4 loading cycles are solved (where the HYMOD 2 demonstrates a stiffer behavior) the curve manages to capture the Full Hexa curve with a 9.7% accuracy highlighting the ability of the method to maintain an acceptable accuracy, even in the case of high mesh reduction levels.

Furthermore, for the case of this numerical investigation, it was found that the crack opening and closing algorithm managed once more to capture this numerically demanding and unstable process successfully providing the additional numerical stability that is required to solve this highly nonlinear numerical problem. Fig. 7.32 shows the opening and closing of cracks for the 1st loading cycle of the two-storey RC frame as it resulted from the analysis. It is evident that in the case of the two-storey RC frame the number of crack openings is significantly lower than the one-storey RC frame HYMOD 1, especially in the case of displacement increment 1. This justifies the previous conclusion in regards to the main reason why HYMOD 1 for the one-

storey RC frame did not manage to attain the complete displacement history when the displacement increments per loading cycle was set to 40.

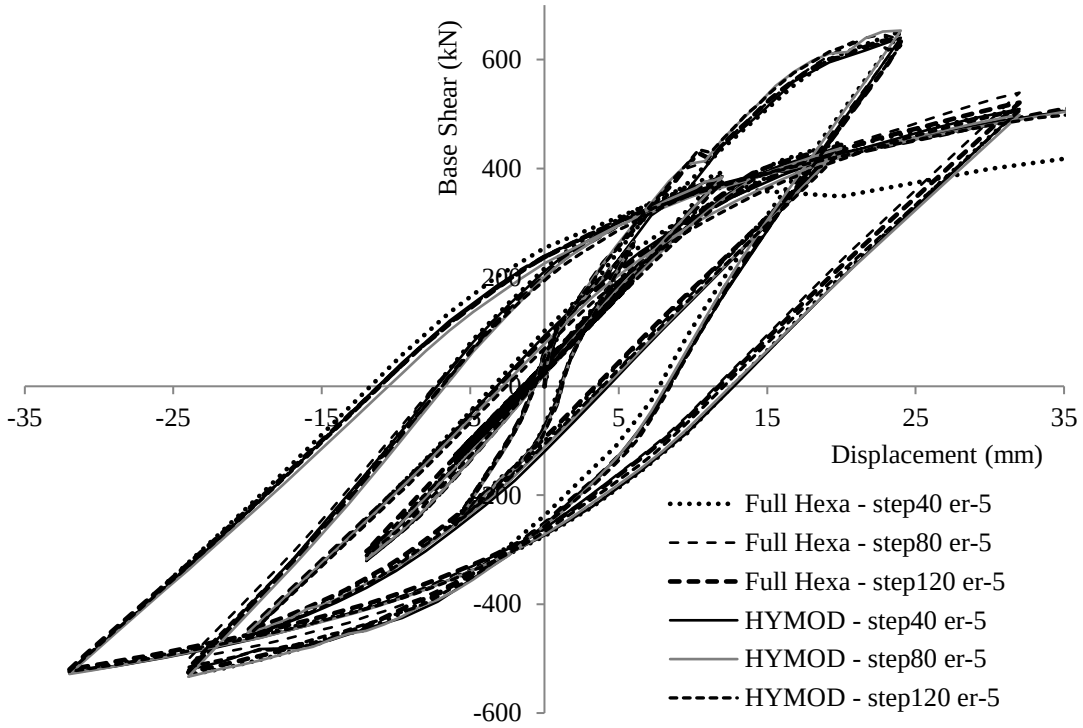

Fig. 7.30 Two-storey RC frame. Comparison between HYMOD 1 and Full Hexa for different displacement increments with a convergence tolerance 10^{-5}. Complete force-displacement history.

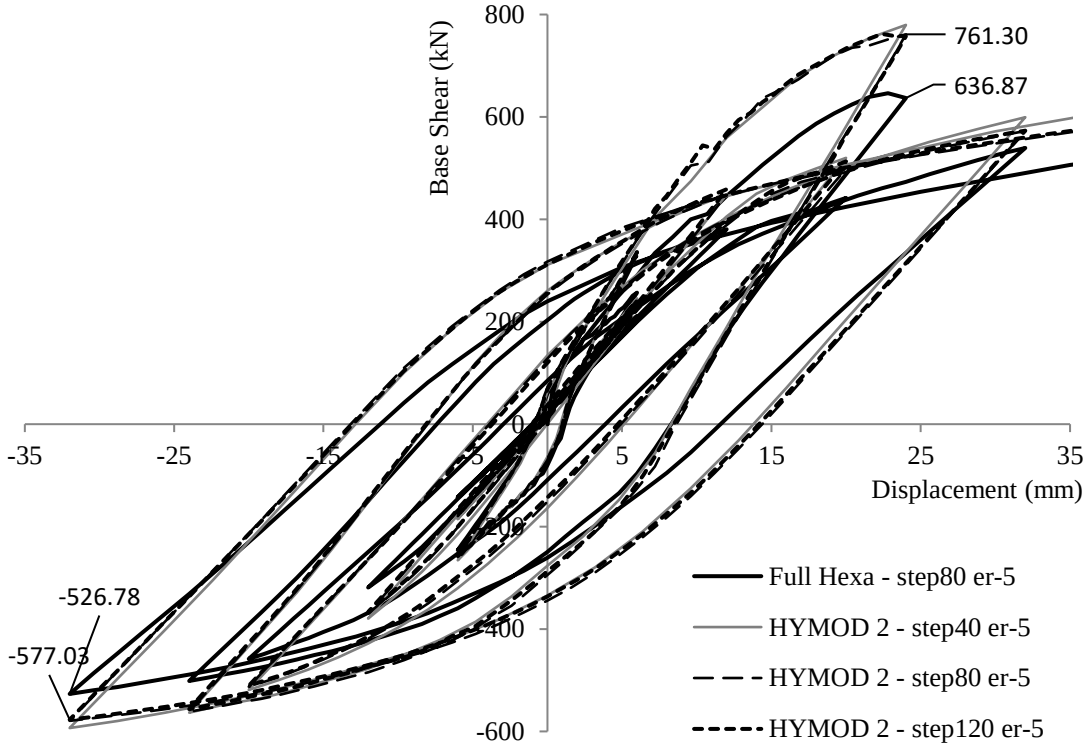

Fig. 7.31 Two-storey RC frame. Comparison between HYMOD 2 and Full Hexa for different displacement increments with a convergence tolerance 10^{-5}. Complete force-displacement history.

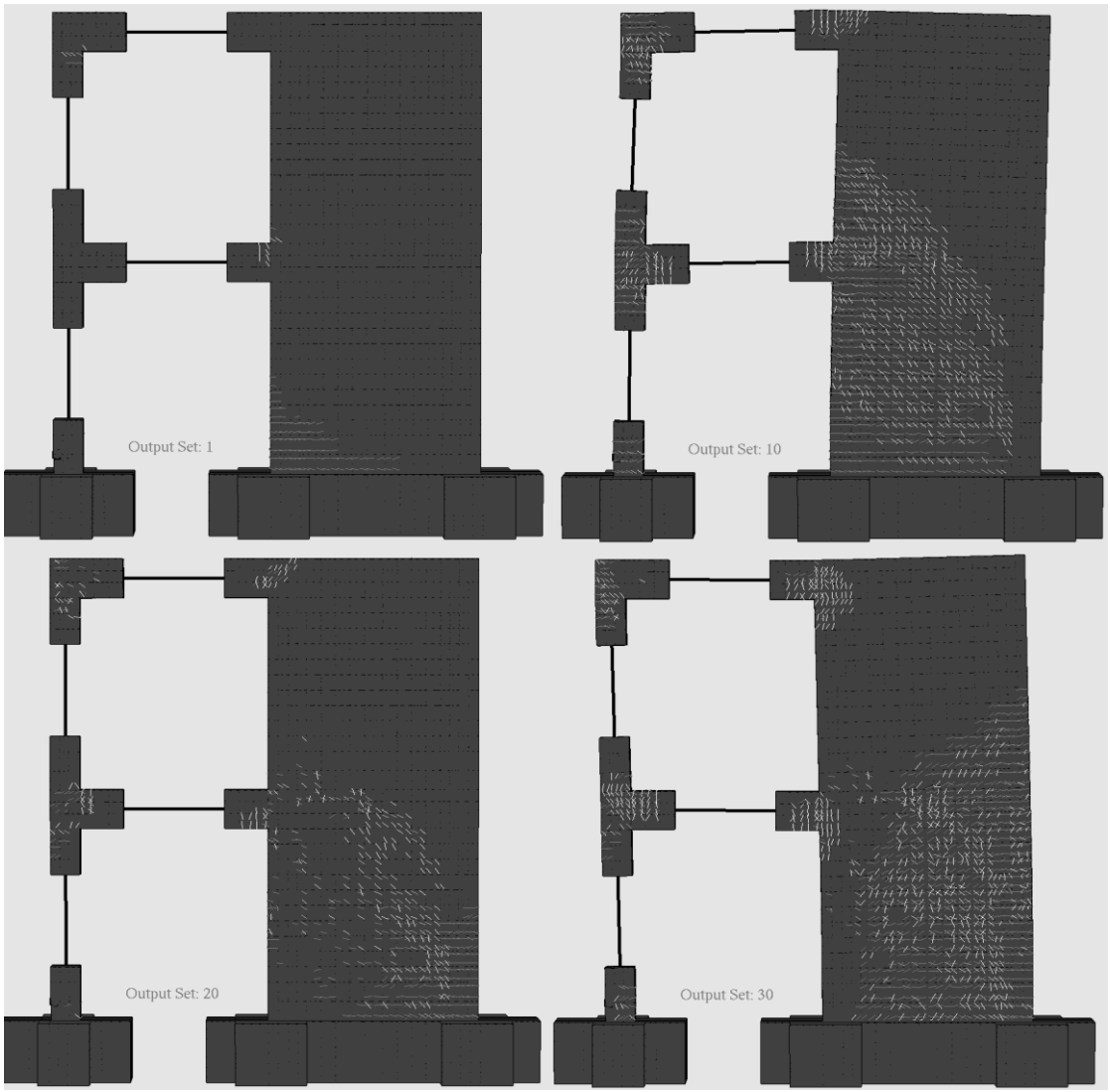

Fig. 7.32 Two-storey RC frame. Opening and closing of cracks during the 1st loading cycle for the first model (40 displacement increments per loading cycle).

Table 7.14 Two-storey RC frame. Computational performance of the nine analyses.

a/a	Model	Num. of Displ. Incr. per cycle	Total Displ Incr. Solved	Total Internal Iter.	Average Num. Error	CPU Time Nonlinear Solution (minutes)	Reduction in CPU Nonlinear Solution (%)
1	Full Hexa	40	290	2,313	$2.07x10^{-5}$	9.6	-
2	Full Hexa	80	580	3,975	$1.11x10^{-5}$	16.1	-
3	Full Hexa	120	870	5,451	$9.45x10^{-6}$	22.75	-
4	HYMOD 1	40	286	2,118	$1.546x10^{-5}$	7.3	23.63
5	HYMOD 1	80	580	3,821	$9.39x10^{-6}$	14.3	11.18
6	HYMOD 1	120	870	5,136	$7.31x10^{-6}$	19.5	14.29
7	HYMOD 2	40	290	2,092	$1.32\ x10^{-5}$	5.47	43.03
8	HYMOD 2	80	580	3,733	$9.51\ x10^{-6}$	9.6	40.37
9	HYMOD 2	120	870	4,990	$7.98x10^{-6}$	13.1	42.42

Table 7.14 shows the computational performance data obtained from the nine analyses. The average numerical error per internal iteration, for the case of the Full Hexa model, was lower than $2.1x10^{-5}$, while the HYMOD 1 managed to result an average numerical error per iteration that was less than $1.6x10^{-5}$. The same trend was found for the case of HYMOD 2, which was the most computationally efficient model. This is also evident from the computed average

number of internal iterations per displacement increment, which was always smaller in the case of the HYMOD 1 and 2. The proposed model managed to maintain a low internal iteration per displacement increment (average: 7.4, 6.6 and 5.9 for HYMOD 1 mesh with 40, 80 and 120 displacement increments, respectively), while the maximum required computational time for HYMOD 1 was 19.5 minutes for the solution of 5,136 internal iterations. The corresponding performance for the case of HYMOD 2 were 7.2, 6.4 and 5.7 average internal iterations per displacement increment and a 0.156 seconds overall average required computational time per internal iteration. The overall average for the case of the HYMOD 1 model was 0.223 seconds per internal iteration. On the other hand, the Full Hexa models had an average internal iteration per displacement increment equal to 7.96, 6.85 and 6.27 for the case of 40, 80 and 120 displacement increments per loading cycle, respectively. The corresponding average computational time per internal iteration was 0.248 seconds, which is 10% slower compared to the HYMOD 1 and 37.1% slower than the HYMOD 2.

The above numerical finding is attributed to the decreased number of hexahedral elements, the decrease of the required internal iterations per displacement increment and the lower number of embedded rebars, when the proposed HYMOD approach is implemented. In general, the overall decrease in the computational time is equal or larger than the decrease of the dof achieved according to the reduction of the full hexahedral mesh. Furthermore, the numerical model HYMOD 2 manages to reduce the nonlinear solution time by 42% by just applying a corresponding dof decrease of a mere 26.54%. This demonstrates the computational efficiency boost that the nonlinear cyclic solution procedure can develop when the HYMOD approach is applied.

7.5 Conclusions

The HYMOD approach presented in this work for the nonlinear simulation of RC structures under cyclic loading conditions, is a compromise between a detailed finite element model and the simplified beam-type model. In order to decrease the computational demand during a cyclic nonlinear analysis of a RC structure, without decreasing the level of numerical accuracy, the use of detailed models with hexahedral elements for the concrete and rebar elements for the reinforcement, is used to discretize the parts of the structure which undergo shear dominated deformation, while the rest of the structural members are discretized through the use of beam-column finite elements.

The numerical investigation performed in a number of FE models revealed the ability of the proposed HYMOD approach to accurately predict the nonlinear response of RC structural members under cyclic loading conditions, with a reduced computational effort. The proposed formulation was found to be computationally robust since it does not require any special algorithmic procedure for its implementation. The integration of the HYMOD algorithm with the cyclic concrete material model further fortified the numerical method with additional numerical stability deemed essential when the cracks begin to open and close. The numerical results revealed that the proposed simulation manages to retain a low ratio of internal iterations per displacement increment thus further reducing the computational demand.

By accounting the numerical findings obtained in section 7.4 of this research work, it is safe to conclude that the proposed numerical simulation method can provide with the ability to study the cyclic nonlinear simulation of full-scale RC structures, thus this cumbersome numerical modeling problem is now feasible. Therefore, this simulation task can be achieved at an affordable computational effort without the need of powerful computational resources, while maintaining at the same time the desired accuracy during the cyclic analysis.

Chapter 8. Simplified HYMOD non-linear simulations of a full-scale multistory retrofitted RC structure that undergoes multiple cyclic excitations – An infill RC wall retrofitting study

Contents of Chapter 8

8.1 Introduction 173

8.2 Material Modeling 174

8.3 Experimental Data 176

8.4 Numerical Model, Results and Discussion 179

8.4.1 Finite Element Mesh 180

8.4.2 Analysis Results for the 0.1g Test 183

8.4.3 Analysis Results for the 0.25g Test 188

8.4.4 Analysis Results for the Final Loading Test 193

8.5 Numerical Investigation of Different Infill RC Wall Retrofitting Configurations 199

8.6 Conclusions 209

8.1 Introduction

Based on the discussion presented in the previous chapter, when dealing with the modeling of (RC structures under extreme cyclic loading conditions, many numerical challenges arise given the complexity of the mechanical behavior of the concrete material. Many researchers attempted to develop numerous simplified numerical models that would provide with the ability to simulate the nonlinear mechanical behavior of concrete structures in an accurate and computationally efficient manner. Nonetheless, engaging 1D and 2D numerical models has a main challenge that relates to the accuracy limitations of these type of models. Therefore, researchers try to use detailed 3D approaches, in order to develop accurate numerical models that will be able to provide them with the necessary tools for predicting the mechanical response of any RC structural member in an objective manner.

One of the main numerical limitations when dealing with 3D detailed modeling through the use of solid elements, is the high computational demand that arises during nonlinear analysis that limited this research work (Hartl [181], Lykidis and Spiliopoulos [27], Červenka and Papanikolaou [182], Papanikolaou and Kappos [183], Markou and Papadrakakis [37]), to study single RC structural members or relatively small structural configurations (i.e. 1-span RC frames). When using the 3D detailed numerical approach, scientists are forced to study single structural members or joints in order to get results in an acceptable computational time. This modeling constraint is always accompanied by the problem that is known as "numerical instabilities", which immerses due to the numerically complicated nature of the cyclic mechanical response of concrete (mainly due to the opening and closing of cracks and the material's deterioration due to multiple loading cycles).

In order to overcome these computational limitations, several scientists proposed the use of hybrid models that foresee the combination of different in dimensionality finite elements that are used to discretize the frame of any structure. As it was presented in Chapter 7, mixed element formulations and other hybrid techniques were proposed in several publications where only one of them was actually dealing with the cyclic analysis of RC frames (Mata et al. [192]). In this chapter the proposed HYMOD approach is used so as to develop the full-scale model of the four-storey RC specimen that was experimentally studied in Poljanšek et al. [42]. The physical experiment [42] foresaw three different cyclic loading tests that the RC specimen undergone in a serial manner. This is considered to be the most recent research work that uses the HYMOD approach after the method was presented in [37]. Based on the research findings presented in the previous chapter, the proposed algorithm has set the foundations for full-scale RC structure simulations by presenting an integrated algorithm that uses 8-noded hexahedral finite elements that treat cracking through the smeared crack approach and model the reinforcement through the use of embedded rebar finite elements (rod or beam).

The proposed HYMOD algorithm is used in this work so as to model all three loading history tests imposed on the four-storey RC building that was experimentally tested by Poljanšek et al. [42], in an attempt to demonstrate the HYMOD's numerical advantages when dealing with large-scale models and excessive nonlinearities that result into significant material degradations. It must be noted at this point that an attempt to simulate the four-storey RC building was performed by Kyriakides et al. [195], where 1D and 2D finite elements were used to develop the finite element models and analyze the specimen for the case of the 2nd loading test. Based on their numerical models [195], the CFRP jacketing was not included during the analyses, whereas the damage that occurred during the 1st loading test was also not accounted for during the analysis of the 2nd loading test. Furthermore, the actual uniaxial compressive strength of concrete reported in Poljanšek et al. [42] was 20 MPa (C20/25) for a cylindrical specimen, while the uniaxial compressive strength used during the analysis by Kyriakides et al.

[195] was 33.8 MPa and had a 3.6 MPa (10.65% *fc*) tensile strength, which deviates by 69% from the reported value. The Young modulus of elasticity for concrete was set to 20 GPa, as it was experimentally obtained in Kyriakides et al. [195], which was also not equal to the 30 GPa reported value found in [42]. The 2D developed model presented in [195], was used to simulate approximately a 70% of the 2nd loading test, deriving numerical results that underestimated the maximum experimentally obtained capacity of the base-shear by more than 25%. A more accurate prediction in terms of base shear capacity was obtained when a SAP2000 model was used, but in this case the hysteretic behavior of the numerically computed curve was not able to match the experimental data, while the CFRP jacketing was once again not accounted for nor the damage that occurred during the 1st loading test.

This highlights the need of a more accurate and numerically robust modeling method, in order to be able to assess retrofitted structures by using full-scale numerical models that will account for the full spectrum of loading conditions and account for material degradation due to previous loading excitations. This is also of great importance when assessing existing RC buildings that have undergone an earthquake thus have previously developed damages at different parts of their framing system.

One of the main objectives herein, is to demonstrate that the proposed modeling scheme is able to satisfy the above requirements without making simplification assumptions or significantly altering the material properties in comparison to the experimentally reported values. The adopted material constitutive models and the HYMOD approach that were used in this work were presented in Chapter 7, while the retrofitting types that were applied on the RC building (and numerically modeled in this research work) are presented in section 8.3. The computational efficiency, robustness and accuracy of the proposed algorithm are investigated and discussed in section 8.4. Furthermore, the ability in capturing the mechanical behavior of retrofitted RC structures is presented in this section as well, while the numerical ability of the developed algorithm in capturing the stiffness and capacity degradation of the building due to the concrete damage during the three loading tests is also demonstrated through an additional parametric investigation that will be presented in section 8.4.4.

Finally, a modal analysis algorithm that is able to compute the eigenmodes and eigenfrequencies of HYMOD models is developed and applied herein in an attempt to further investigate different retrofitting configurations that are presented in section 8.5. This numerical investigation aims in the detail study of the retrofitting method that foresees the use of infill RC walls and it's qualitative and quantitate effects in terms of shear capacity and energy dissipation enhancement. The numerical results of this numerical investigation are discussed in section 8.5.

8.2 Material Modeling

Two concrete material constitutive models have to be considered in order to simulate any structure by using HYMOD meshes. When the NBCFB is used, the discretization foresees the division of each beam-column section into fibers that have the ability to account for nonlinearities through the bilinear model (as presented in Chapter 7). The 3D concrete material model, which is incorporated into the 8-noded hexahedral element, is based on the proposed algorithm presented in Chapter 5, where the cyclic mechanical behavior of RC members is numerically investigated. The model is based on the concrete material model that was integrated with a new crack closure criterion, which induces numerical stability during the cyclic analysis (Chapter 5).

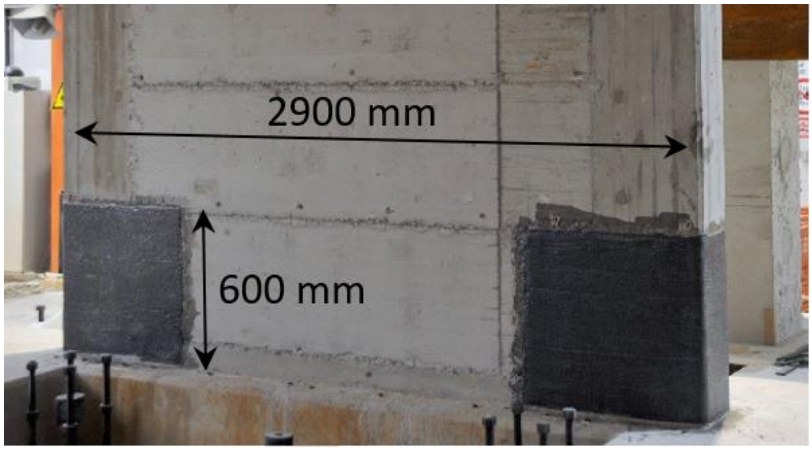

Fig. 8.1 Three-sided CFRP jacketing. [42]

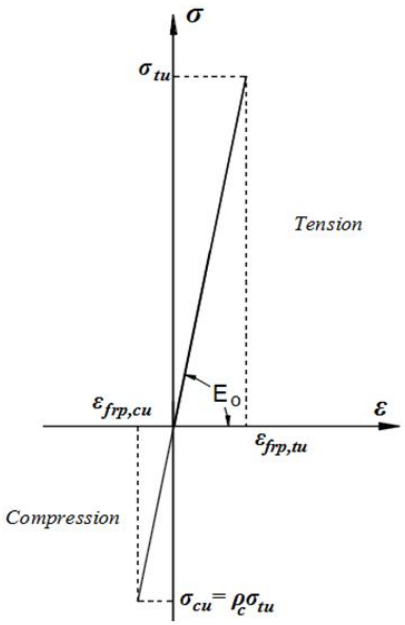

Fig. 8.2 Material model of the CFRP jacketing. [196]

The under study multi-storey RC structure was retrofitted through the use of a three-sided Carbon Fiber Reinforced Polymer (CFRP) jacket so as to confine the edges of the two walls at the ground floor level. This was done in an attempt to avoid a premature termination of the experiment due to a potential high concrete deterioration (Poljanšek et al. [42]) at the wall edges. Fig. 8.1 shows the CFRP jacket (600 mm in height) that was used to reinforce the wall edges according to the design of the experimental setup found in [42].

In this research work, the CFRP jacketing was also discretized in detail (see section 8.4.1) by using hexahedral elements, where the material model used in simulating the stress-strain relationship for the CFRP jacketing, foresaw a linear behavior until complete failure for both tension and compression states, as illustrated in Fig. 8.2. When the ultimate stress level is reached within the CFRP material, the model foresees a complete loss of its capacity. The experimental results reported that the CFRP jackets did not exhibit any damages or failure at the material level. Therefore, the ultimate tensile strength was set to 1,000 MPa and the Young Modulus of elasticity was set equal to 100 GPa. In addition to that, it was also assumed that the

CFRP jacketing had full bonding with the concrete, which also complies with the experimental findings reported in Poljanšek et al. [42] (no CFRP-concrete detachment was reported).

8.3 Experimental Data

A full-scale four-storey RC building was studied in the SERFIN project [42], which was the first experimental attempt that studied a full-scale building specimen that was constructed to investigate the retrofitting of buildings through the use of RC infill walls and CFRP jacketing. As it was reported in Poljanšek et al. [42], the four-storey RC building was tested with the pseudo-dynamic method (PSD) and had two four-storey parallel frames connected through a continues slab of 15 cm thickness and four out-of-plane central beams that connected the two frames (Fig. 8.3). Each frame consisted of 3 bays with an 8.9 m of total span, with the central bay infilled with a RC wall (2.1 m net span). The structure had a total height of 12 m and the perpendicular distance between the South and North frames was 6.25 m. It must be noted here that the building's frame was designed based on the old Cyprus code used in the 1970's, which is now replaced by Eurocode (2003) [41], whereas designers use KANEPE (2012) [43] that was developed in Greece and it is currently considered to be the most comprehensive code in retrofitting design. Fig. 7.20 shows the geometrical details of the south frame and in Fig. 8.3 the four-storey RC specimen can be seen prior to testing. The reinforcement details of the different structural members can be depicted in Fig. 8.4, as they were reported in Poljanšek et al. [42].

Fig. 8.3 Four-storey RC specimen in the lab. [195]

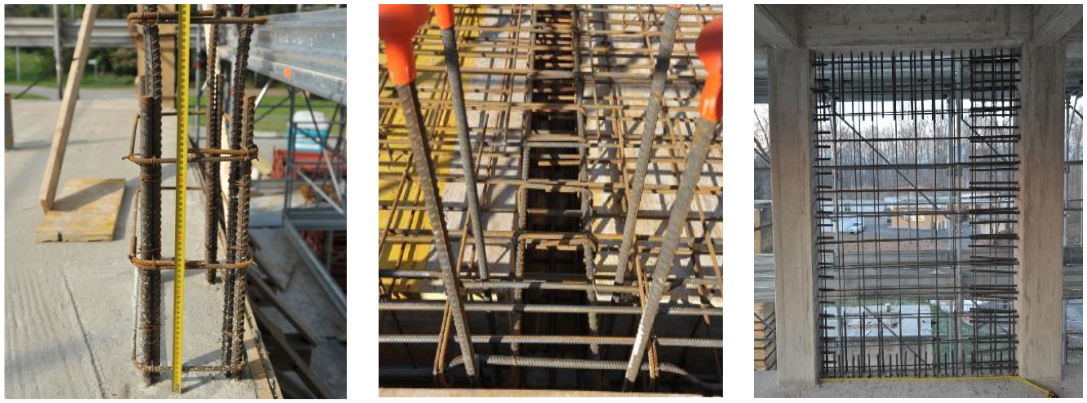

(a) Column reinforcement (b) Central beam and slab reinforcement (c) Infill shear wall reinforcement

Fig. 8.4 Reinforcement details of the RC fame. [42]

According to the experimental setup [42], the concrete material used for the construction of the RC frame was a C20/25 for all structural members. The uniaxial compressive strength was f_c = 20 MPa with a Young Modulus of elasticity equal to E_c = 30 GPa and a unit weight of 25 kN/m^3. These were also the values used in the numerical investigation presented in section 8.4 of this chapter. The steel rebar material properties that were used to perform the numerical investigation, also complied with the ones found within the technical report [42], which foresaw the use of 400 and 450 MPa of yielding stress bars. The 400 MPa steel material was used to reinforce the RC frame without the infill walls, while the 450 MPa steel material was used for the rebars that were placed within the infill RC walls. The Young Modulus of elasticity was not reported in [42] for either steel bars thus a E_s = 190 GPa was adopted herein for the needs of the numerical analysis.

The loads that were applied on the specimen assumed that each floor was loaded with a 3 kN/m^2 (dead load) and a 0.45 kN/m^2 live load (this represented the 30% of the characteristic live load and complied with the Eurocode provisions). Therefore, the same load magnitudes were applied on the FE model including the self-weight of the frame. It must be noted here that the vertically imposed loads were applied on the RC specimen through the use of water barrels located between the actuator attachment beams that were used to apply the horizontal displacements during the experiment. The actuator beams were positioned at a distance of 1.4 m from the two frames, respectively, while the distance between the actuator attachment beams was 3.45 m. (see Fig. 8.5 and Fig. 8.6).

In regards to the loading histories that were chosen to be applied on the structure, the experiment foresaw three different loading sets that corresponded to three independent earthquake intensity levels. The first loading history derived the displacements shown in Fig. 8.7a and was scaled in order to represent a low seismic acceleration of 0.1g. For the case of the second loading test, the applied loads resulted by using a high acceleration equal to 0.25g, where the slab displacements that were recorded at each storey can be depicted in Fig. 8.7b. The final set of displacements were obtained based on the last set of loading cycles applied on the building that intended to reach the specimen's maximum capacity. The corresponding displacements that derived from the 3rd and last loading set ("funeral cycles") can be seen in Fig. 8.7c. Based on this diagram, it is easy to observe that the horizontal displacements at the top floor were equal to 92, - 92, 89, -125, 37 and 0 mm. During the "funeral cycles", the structure was pushed and at the same time the base shear of the building was measured in order to observe for any sudden capacity drops (as it was reported by Kyriakides et al. [195]). During the test, the building

demonstrated a sudden drop when the horizontal displacement at the roof slab reached 125 mm (negative horizontal deformation), where it was assumed that the frame reached its ultimate resistance.

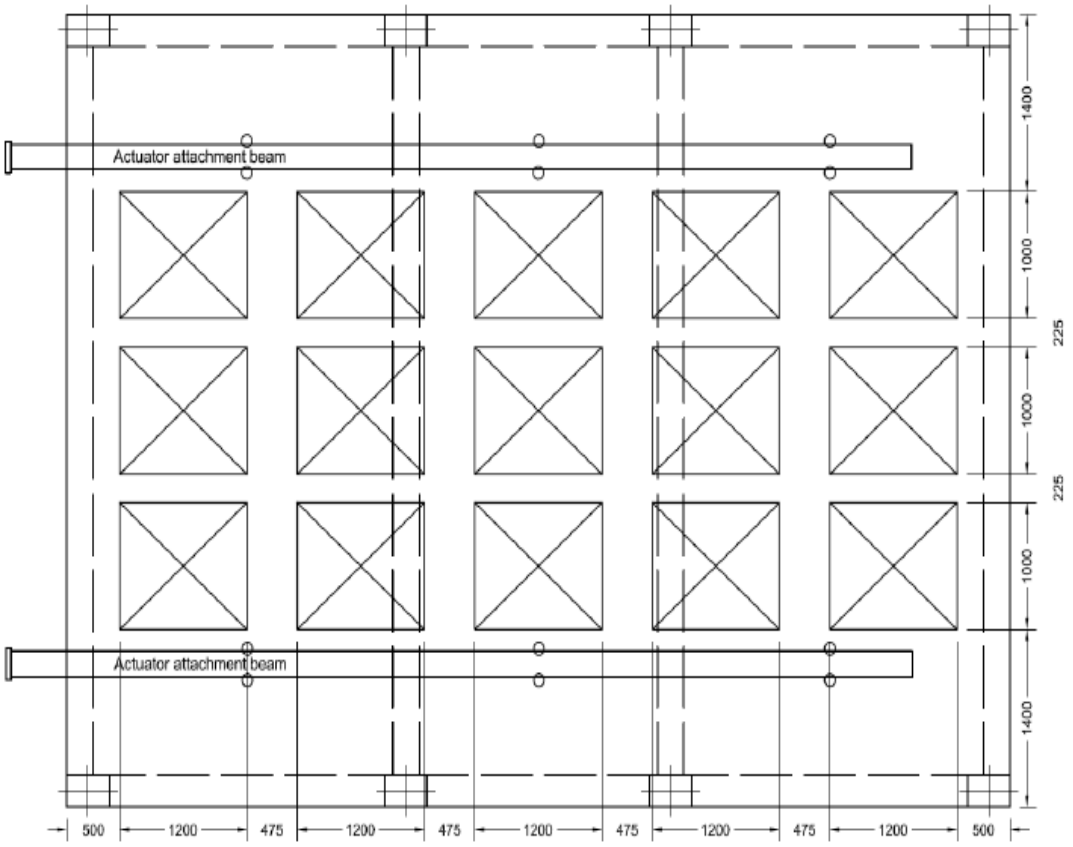

Fig. 8.5 Water barrel setup and actuator attachment beams. [195]

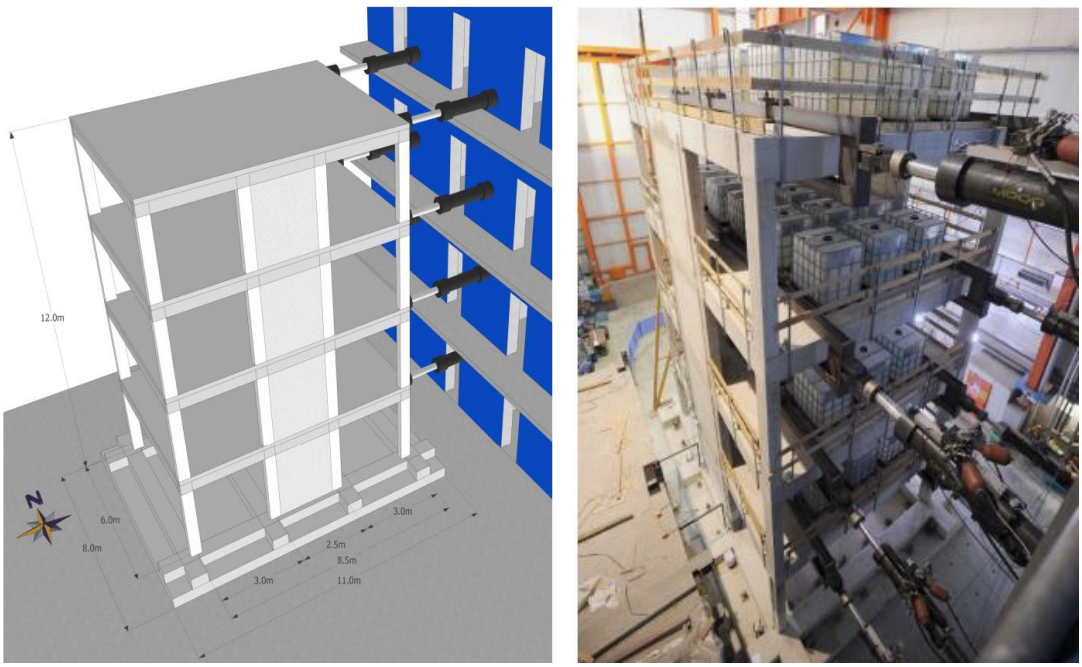

Fig. 8.6 Views of the SERFIN specimen showing the water barrels and the actuators. [42]

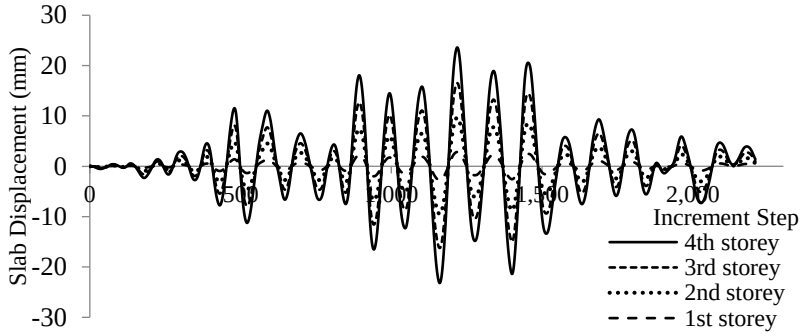

(c) 0.1g test

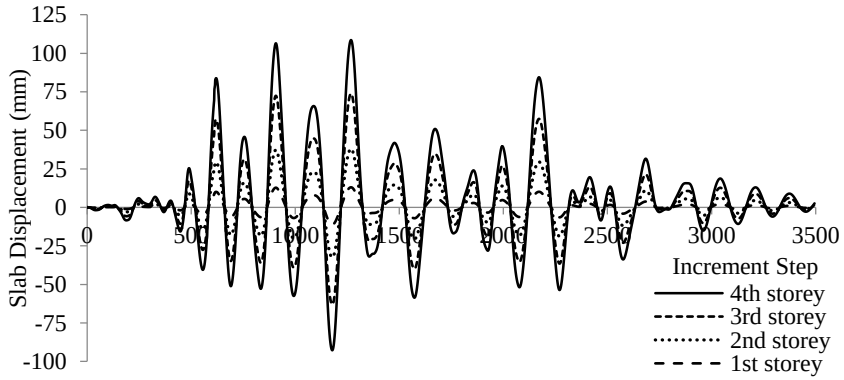

(d) 0.25g test

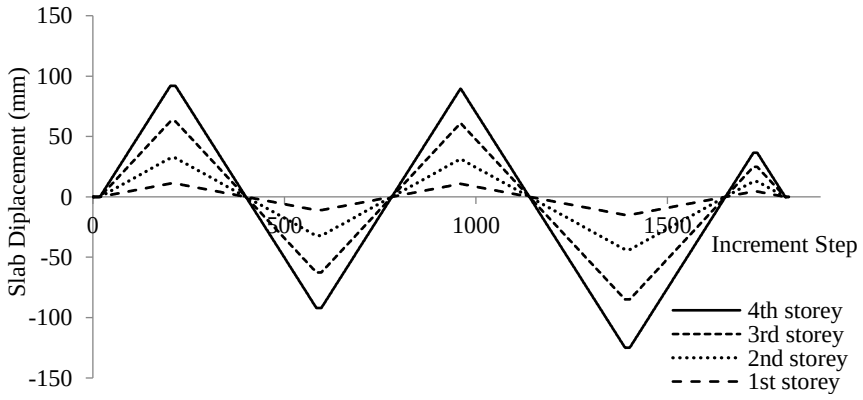

(e) Final cyclic test ("Funeral")

Fig. 8.7 Four-Storey RC specimen. Displacement histories of the specimen.

8.4 Numerical Model, Results and Discussion

The numerical model and the analysis results will be presented in this sections, for all three loading histories, in an attempt to reveal the modeling capabilities (in terms of accuracy and computational efficiency) of the proposed HYMOD approach. It must be noted here that, an energy convergence criterion was used for all the numerical nonlinear simulations as expressed in Eq. (3.46). According to the numerical findings presented in Chapter 7, the optimum convergence energy tolerance that will reassure both accuracy and numerical stability is 10^{-5},

which is the value that was adopted in this work. In addition to that, the CPU used to perform all the analyses presented in this section, had a 4.2 GHz computing power.

8.4.1 Finite Element Mesh

In this section, a brief presentation of the HYMOD FE mesh that was developed for the analyses needs, will take place. As it can be seen in Fig. 8.8, the 3D detailed full hexahedral FE mesh is shown, which consists of 16,662 hexahedrons according to Table 1 (excluding the CFRP jacketing elements) and 31,246 embedded rebar elements. This model discretized the exact geometry of the four-storey RC specimen, while the embedded rebar elements were modeled based on the exact steel reinforcement geometry (Fig. 8.8) reported in Poljanšek et al. [42]. The Full Hexa model was found to have a very high computational demand that made it practically prohibitive to be used for any type of nonlinear analysis. Thus the construction of the HYMOD mesh was performed by applying a reduction level 1 (for additional details regarding reduction levels see Markou and Papadrakakis [31]) that foresaw the deletion of all hexahedral elements found at beam and column structural members, as illustrated in Fig. 8.9. The resulted HYMOD mesh presented in Fig. 8.9, where the concrete and reinforcement FE meshes can be seen, managed to decrease the initial number of elements by 39% and the initial dofs by 48% (see Table 8.1).

As it was shown in Chapter 6, using the full model is an option when it comes to push over analyses given that the number of increments is relatively small. Using 10 or 20 load increments during the analysis can be computationally feasible even in the case of a five-storey building that is discretized through the use of 20-noded hexahedral finite elements (see Fig. 8.10). Nevertheless, the computational demand was found to be excessive in this case, given that the nonlinear solution procedure required days to complete due to the large number of elements. When it comes to the numerical solution of nonlinear cyclic analysis of full-scale structures under realistic laboratory conditions (hundreds of load increments), this approach is no longer a feasible option due to the increased computational demand during the nonlinear solution procedure.

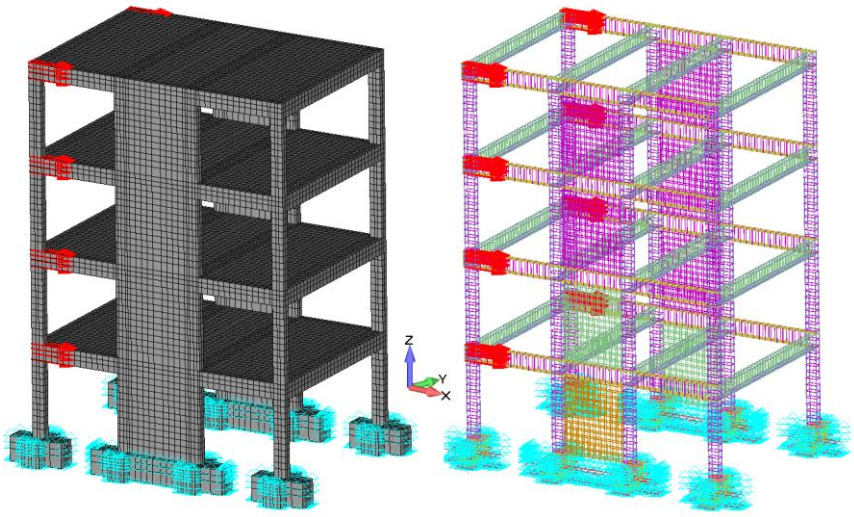

Fig. 8.8 Full Hexa FE mesh. (Left) Discretization of the concrete domain and (Right) Embedded rebar elements.

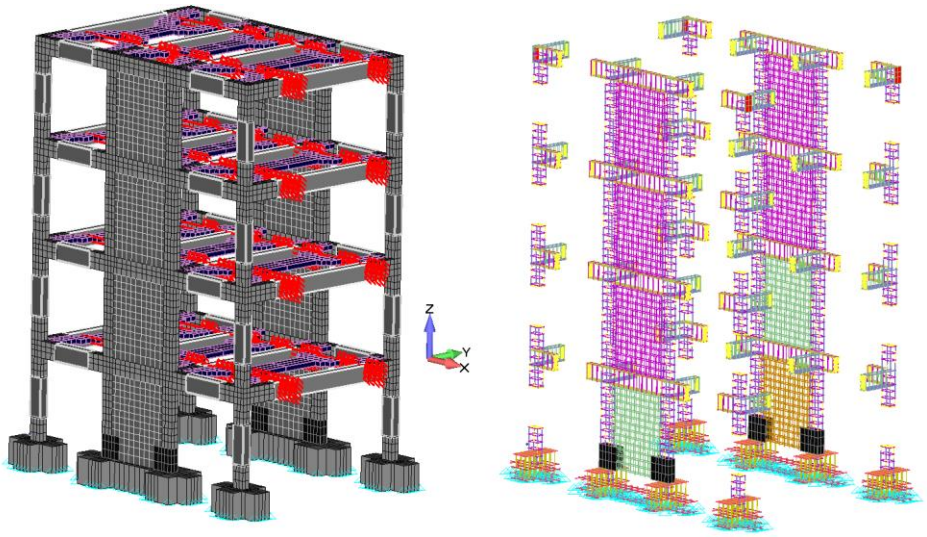

Fig. 8.9 HYMOD FE mesh. (Left) Discretization of the concrete domain and (Right) Embedded rebar elements.

Table 8.1 FE mesh details of the four-storey RC frame models.

a/a	Model	Hexahedral Elements	Embedded Rebar Elements	RC NBCFB Elements	Hexa FE Reduction (%)	Embedded Rebar FE Reduction (%)	Overall FE Reduction (%)
1	Full Hexa	16,662	31,246	-	-	-	-
2	HYMOD	8,356	20,646	48	49.85	33.92	39.46

a/a	Model	Stiffness Matrix Size (Mb)	Reduction in Stiffness Matrix Size (%)	Dofs	Dofs Reduction (%)
1	Full Hexa	1,000	-	85,191	-
2	HYMOD	335	66.5	43,896	48.47

The HYMOD mesh presented in Fig. 8.9 foresaw the discretization of all shear dominated areas of the framing system through the use of the 3D detailed approach, while the rest of the structure was modeled through the use of the NBCFB FE (beam and column structural members). In order to take into account a realistic plastic hinge length when performing the mesh reduction, the recommended hinge length was used as proposed in Markou and Papadrakakis [37] (*h-2h*, where *h* is the height of the beam or column section). Therefore, the beams within the South and North frames' plane were assigned a 60 cm hinge length, while the out-of-plane beams had a hinge length of 100 cm. The columns of the frame were discretized by using the same concept, where the plastic hinge length was set to 70 cm. The hexahedral element sizes that were used so as to discretize the RC frame, varied between 10 to 20 cm along all global directions (x, y and z). The only exception to this rule, were the hexahedral elements that were used to discretize the diaphragmatic behavior of the slabs (see Fig. 8.9). The longer elements that can be seen in this figure were constructed in an attempt to further decrease the slab's mesh without losing the corresponding numerical accuracy.

The imposed displacement histories were applied through kinematic constraints at the nodes of the four slabs that were located at the points of the actuator attachment beams-slab connections as can be seen in Fig. 8.9. The displacement histories that were applied on each slab where based on the displacements published in Poljanšek et al. [42]. Furthermore, as it was stated in the technical report Poljanšek et al. [42], the load that was applied through the two actuator attachment beams at each slab, was controlled and monitored so as to avoid any torsion development in the building. This also complies with the numerical method that was used to

implement the imposed displacements as shown in Fig. 8.9 (applying the same displacement functions along two parallel lines along each slab).

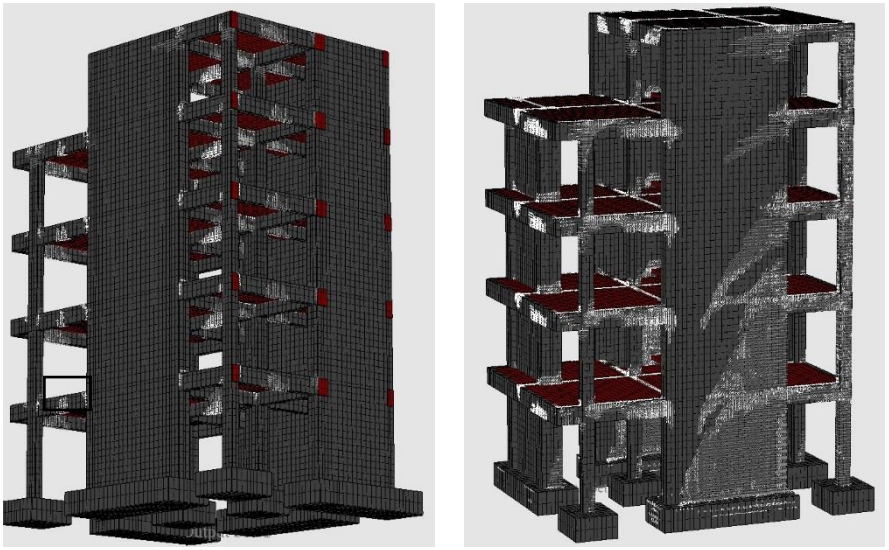

a. b.

Fig. 8.10 Retrofitted five-storey RC building. Push over analysis. (a) Initial crack pattern and (b) Crack pattern prior to failure.

The reinforcement details that refer to the shear walls, the in plane beams and columns of the two RC frames, are shown in Fig. 7.21. It must be also noted here that, the infill wall reinforcement varies and it is not identical for the North and South frames. This was intentionally done according to the experiment's design, while it was also accounted for in the developed model depicted in Fig. 8.9. Furthermore, the constitutive model for the case of bond slippage that was used during the cyclic analysis, foresaw the use of a full bond assumption that complied with the experimental findings. Fig. 8.11 shows the embedded rebar details of the shear wall's boundary columns and the infill area. As it can be observed in this figure, the full bond assumption gave also the ability to avoid the modeling of the dowel rebars that were used to achieve a solid connection between the old and new concrete material. Furthermore, this helps to simplify the modeling of the structure's rebars, while further decreases the computational cost of the model during the nonlinear cyclic analysis. The foundation reinforcement located under the retrofitted structural member can also be seen in the same figure.

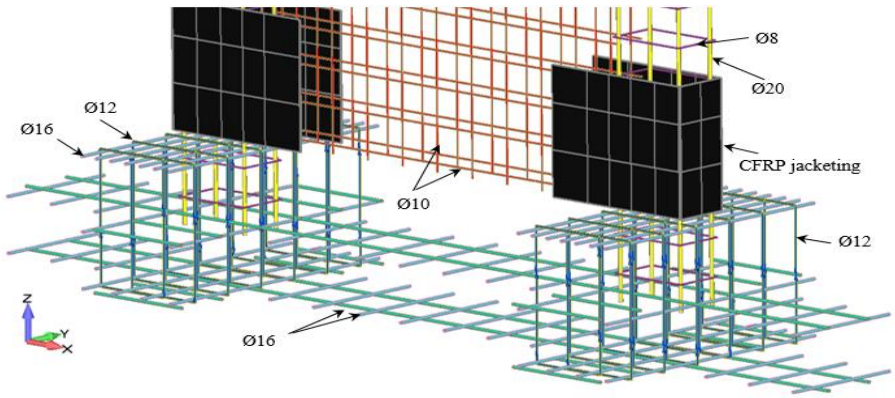

Fig. 8.11 FE mesh of the reinforcement details of the South shear wall and its foundation (different colors represent different rebar dimeters).

As it was mentioned above, the CFRP jacketing was discretized through the use of 8-noded hexahedral elements (Fig. 8.11 and Fig. 8.12). The CFRP jacketing was included in the final HYMOD mesh given that it played a significant role in the overall execution of the experiment as reported in Kyriakides et al. [195] . Therefore, this additional retrofitting method was also discretized and modeled herein. The embedded rebar elements were modeled through the use of the beam element, while the material properties that were used during all analyses are summarized and presented in Table 8.2. All the values for each property that were defined in the FE model were taken from the SERFIN project's report [42], except from the CFRP jacketing material properties that were not provided.

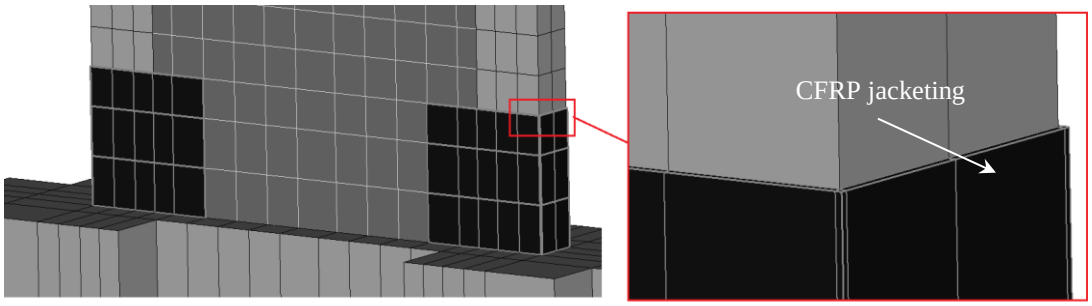

Fig. 8.12 Discretization of the CFRP jacketing through the use of hexahedral elements.

Table 8.2 Material details used in the FE model.

Material	Young Modulus (GPa)	Hardening Modulus (GPa)	Yielding Stress / Tensile Strength* (MPa)	Compressive Strength (MPa)	Shear remaining strength β	Poisson Ratio	Ultimate Strain ε
Concrete	30	-	2*	20	0.2	0.2	-
Steel inside the Frame	190	2.1	400	-	-	0.3	15%
Steel inside the Infill Walls	190	2.1	450	-	-	0.3	15%
CFRP	100	-	1,000*	1,000	-	0.3	1%

The analyses that were performed in this research work, were static cyclic displacement control analyses that used the Newton-Raphson nonlinear solution algorithm. The displacement increment was defined according to the number of displacement increments per loading cycle so as to avoid large displacement steps that would lead to large numbers of internal iterations and potential numerical instabilities. The displacement increment was selected based on the numerical findings presented in Chapter 7 and a general rule that derived from this work that requires the use of a step that will not allow the development of numerical instabilities when a large displacement increment is used. In this case, a displacement increment that was equal or less than 2 mm was adopted throughout the analyses.

8.4.2 Analysis Results for the 0.1g Test

The first set of imposed cyclic loading was performed according to the displacement histories that derived from a loading set, which represented a low intensity earthquake excitation of a 0.1g maximum acceleration. Each slab was displaced and the corresponding base shear was computed by using the HYMOD mesh shown in Fig. 8.9. As it was reported by Kyriakides at al. [195], the structure developed hairline cracks that appeared on the surface of the wall that were eventually closed down when the first cyclic loading history was finished. This implies

that the structure entered the nonlinear state from the very first set of loading cycles, which implies that concrete had developed cracks that should be accounted for during the second stage of loading test. It must be noted here that, the maximum horizontal displacement at the top floor, according to the experimentally obtained displacement history, was 23.5 mm along the positive x-axis and 23 mm along the negative.

Fig. 8.13 illustrates the von Mises strain contour for the case of the maximum negative horizontal displacement of the top floor (δ_H = -23 mm). It is easy to observe that the South frame develops larger strains at the area of the wall in comparison to the North wall, given that the foreseen reinforcement ratio was lower in the case of the South infill RC wall. The main strain concentrations were found to be located at the walls and joints of the structure, where the bending moments and shear forces were larger. In addition to that, the joints where the beams are connected with the walls are also illustrating strain concentrations (Fig. 8.13), where the contour indicates diagonal cracking in the middle of the wall. The cracks that were computed were small (0.15mm crack thickness at the first floor beam-column joints and 0.1 mm at the shear wall's web).

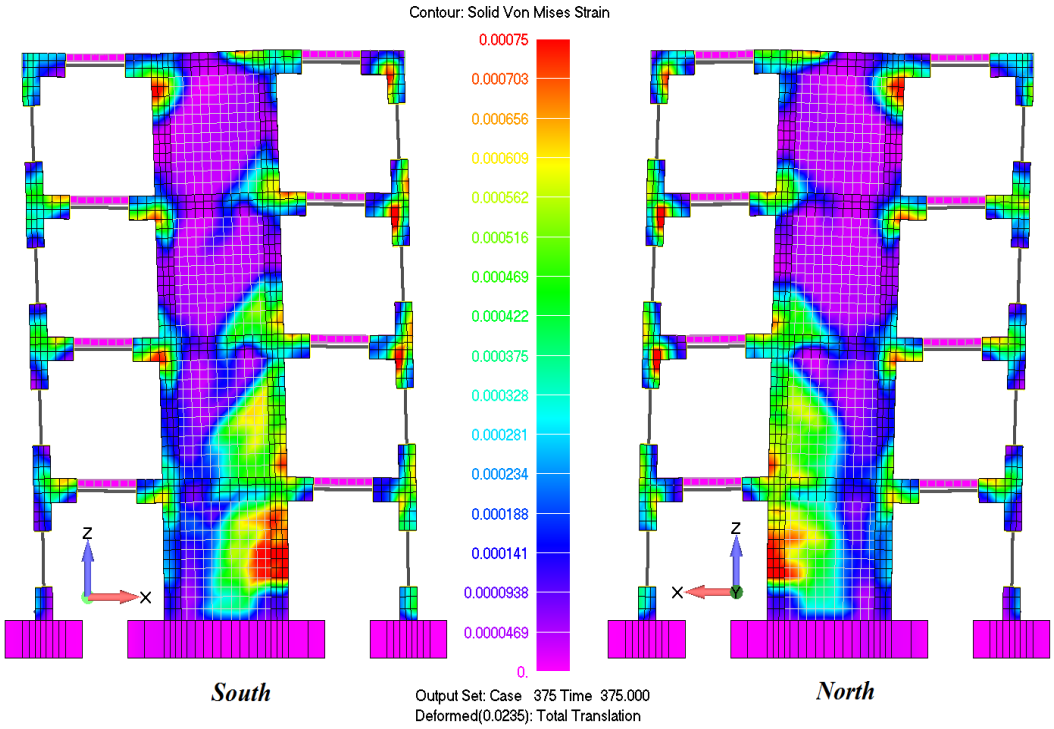

Fig. 8.13 1st loading test (0.1g). Von Mises strain contour for displacement increment 375 (δ_H = -23 mm).

Fig. 8.14 shows the corresponding von Mises strain contour for the case of δ_H = 23.5 mm, where the maximum positive horizontal displacement was applied. As it can be easily observed, the South wall derived higher strains due to the pre-mentioned reason (weaker wall due to a lower reinforcement ratio).

Poljanšek et al. [42] reported that the walls developed diagonal cracks that closed after the load test was completed, which complies with the numerically computed crack pattern. For the case of the two maximum horizontal displacements (negative and positive), Fig. 8.15a and Fig. 8.15b show the numerically derived crack patterns and their maximum width. In addition to that, the opening and closing of cracks can be easily observed from these two figures, highlighting the numerical ability of the proposed opening-closing criterion that was presented in Chapter 5 to handle this complex numerical phenomenon. It must be noted here that, the crack width was

calculated by multiplying the computed principal strain, which was developed perpendicularly to the crack plane, with the corresponding size of the hexahedral finite element along the normal direction.

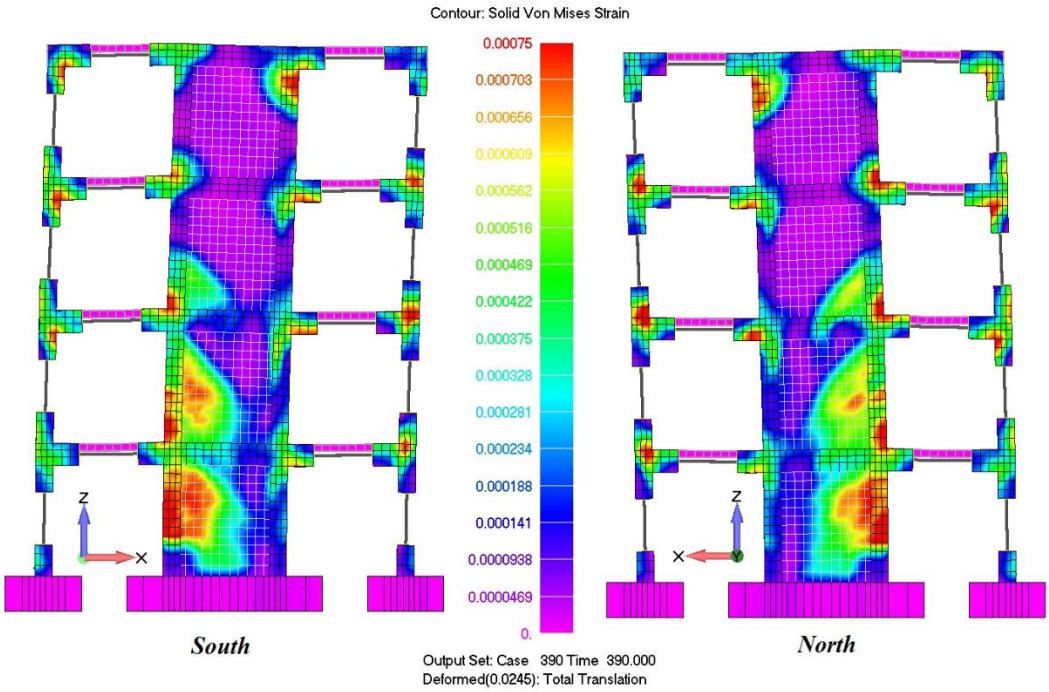

Fig. 8.14 1st loading test (0.1g). Von Mises strain contour for displacement increment 390 (δ_H = 24 mm).

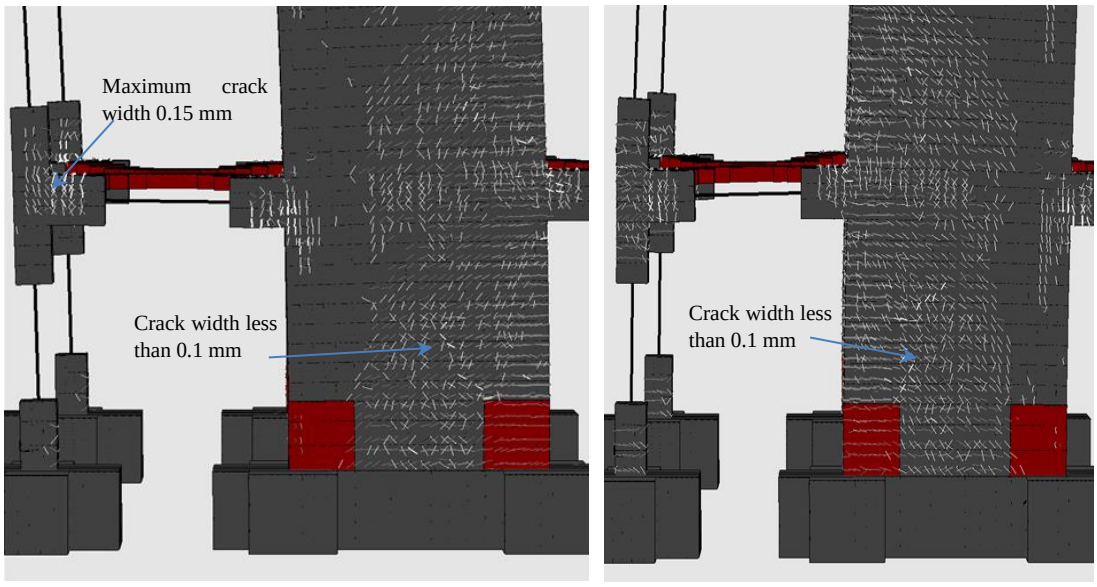

a. b.

Fig. 8.15 1st loading test (0.1g). Crack pattern of the South wall for (a) δ_H = -23 mm and (b) δ_H = 23.5 mm. Maximum computed crack width 0.15 mm.

The remaining strain contour that derived after the 1st load test analysis was completed, can be seen in Fig. 8.16, where it is easy to observe that the remaining strains are very small, while the walls and joints are the areas of the structure that developed the highest deformations (concrete was damaged but the steel still behaved in an elastic manner). The cyclic analysis revealed that

the South wall developed higher values, in terms of strain, compared to the North wall (due to the difference in the reinforcement ratio). The areas where the CFRP jacketing was applied managed to maintain a low stress-strain state due to the locally induced confinement. It is important to state here that in Fig. 8.13-Fig. 8.14 and Fig. 8.16, the CFRP jacketing FE are not shown so as to represent the strain contour behind the carbon material (only the strain contour of concrete is shown). The confinement and the overall effect of the CFRP jacketing can be easily seen in these figures (decreased stress levels at the base of the two walls), thus accounting the effect of the concrete confinement due to this retrofitting technique was found to be numerically important.

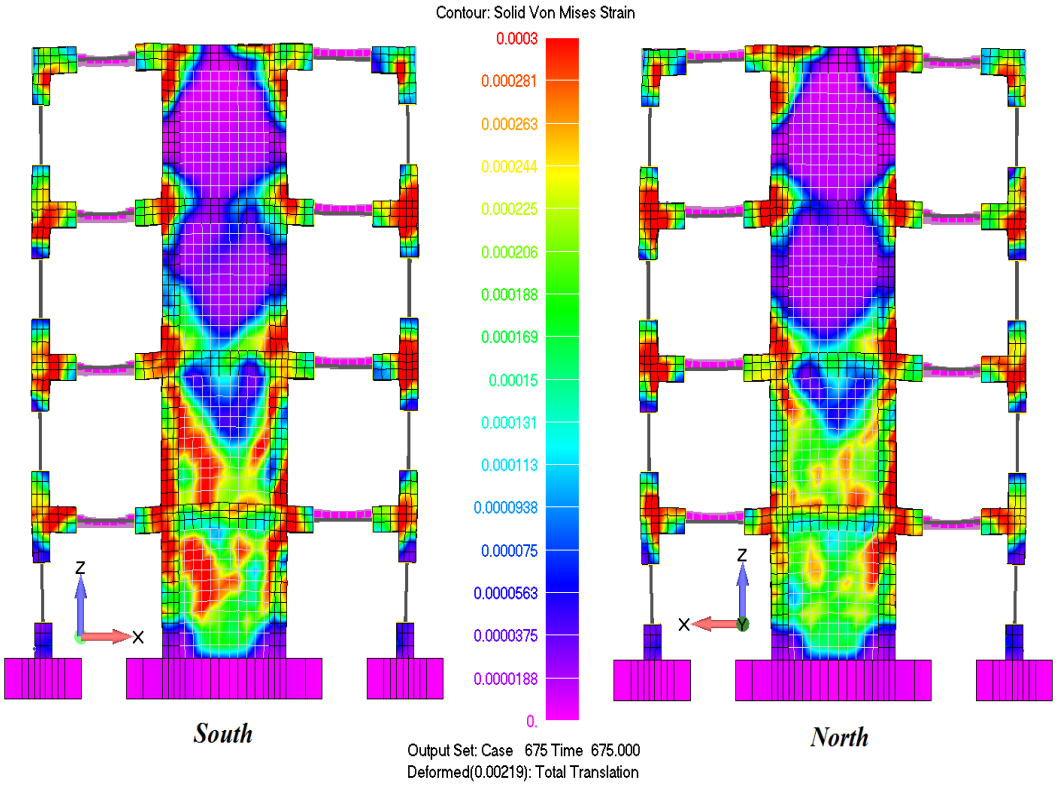

Fig. 8.16 1st loading test (0.1g). Remaining von Mises strain contour after the completion of the test (displacement increment 675; δ_H = 0 mm).

Fig. 8.17 shows the comparison between the numerical and experimental base shear-horizontal displacement curves, where it can be seen that the HYMOD managed to capture the maximum experimental base shear with high accuracy for this first loading test. The hysteretic loops of the experimental curve are larger than the corresponding numerical. This is attributed to the fact that the numerical model does not take into account the effect that time (duration of each applied displacement) has on the RC frame mechanical response. As it was resulted from the experimental data, the corresponding hysteretic loops of the curve illustrate vertical parts at the two ends of each loop, where the displacement reaches its maximum value and the RC frame is at a re-loading or un-loading state. The actual duration that the structure was pushed with a positive 24 mm or a negative 23 mm horizontal displacement is important and can increase the damage induced in the concrete material. As it is going to be presented in the next section, this numerical phenomenon is not as significant when dealing with larger deformations that induce high damage ratios to the numerical model. The maximum positive and negative numerically predicted total base shears are in favor of safety, while predict the experimental values in a satisfactory way (see Fig. 8.17). For the positive maximum cycle, the numerical results

predicted a 1,160 kN where the corresponding experimental value was 1,152 kN (0.7% difference). For the case of the maximum negative deformation the difference was 3% in favor of safety. It is evident, the HYMOD managed to capture the maximum experimental base shear with an acceptable accuracy for the first test.

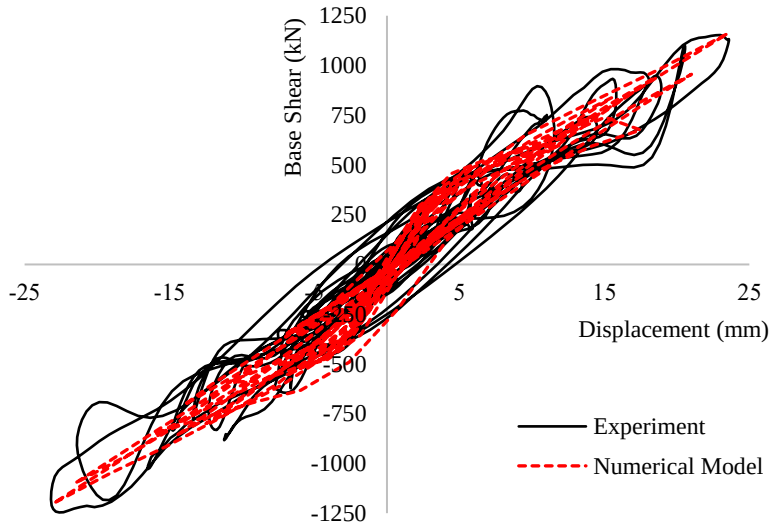

Fig. 8.17 1st loading test (0.1g). Experimental vs numerical curves. Total base shear vs horizontal displacement of the top floor.

Table 8.3 shows the computational time that was required for the solution of this problem that foresaw a total of 450 displacement increments and a total of 2833 internal iterations. The solution of these internal iterations required a total of 15 hours and 30 minutes, which corresponds to a 19.7 seconds per internal iteration. The average internal iterations per displacement increment was 6.3, while the average numerical error was found to be equal to 1.01×10^{-5}. The total required disk space in order to save the output file was 20.7 Gb, which underlines the significance of the HYMOD approach and the ability to solve such a problem thousands of times. As it was mentioned in Chapter 6, the proposed cyclic material model illustrates stability thus the number of the required iterations is relatively small, minimizing the computational demands during the nonlinear analysis. This was also verified herein, as it can be seen in Fig. 8.18 that shows the number of internal iterations per displacement increment graph. According to the statistical analysis performed on this graph, it was found that 47.11% (212) of the displacement increments require less than 5 internal iterations to reach convergence, while 77.33% (348) require less than 10. Finally, only 1.55% (7) of the displacement increments required more than 20 internal iterations so as to achieve convergence, which demonstrates the robustness and numerical stability of the developed algorithm. It must be noted here, that the algorithm used a convergence tolerance strategy that foresaw a relaxation of the convergence tolerance when the internal iterations were larger than 10. In this case a 10^{-4} convergence tolerance was assumed in order to avoid having displacement increments that will require large numbers of iterations without significant numerical benefits.

Table 8.3 Computational performance of the HYMOD algorithm for the case of the 0.1g test.

Number of Displ. Incr. per loading cycle	Total Displ Incr. Solved	Total Internal Iter.	Average Num. Error	CPU Time Nonlinear Solution (hours)	Size of the Output File (Gb)
20	450	2,833	1.01×10^{-5}	15.5	20.7

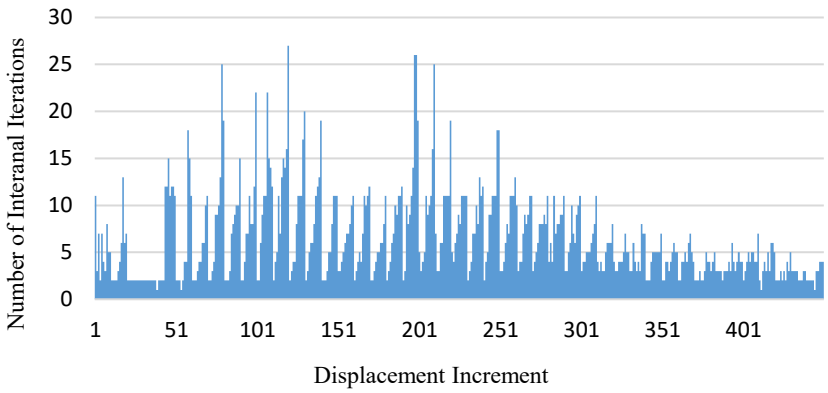

Fig. 8.18 1st loading test (0.1g). Number of internal iterations vs displacement increment.

An analysis was also performed through the use of the Full Hexa mesh (Fig. 8.8) for a single load increment in order to compare the computational demand with that of the HYMOD. The Full Hexa model required a total of 39.83 minutes so as to solve 8 internal iterations, which corresponds to a 298.75 seconds per internal iteration. This constitutes that the HYMOD is 15 times faster than the corresponding Full Hexa model, while in order to solve the 2833 internal iterations that were presented in Table 8.3, the Full Hexa would require a total of 9.8 days given that the installed RAM was sufficient. This highlights the importance of the implemented HYMOD approach when it comes to large-scale models.

8.4.3 Analysis Results for the 0.25g Test

A more numerically rigorous problem had to be solved in order to simulate the mechanical behavior of the RC structure due to the 0.25g test, according to the experimental loading campaign. As it was shown in Fig. 8.7b, the 2nd displacement history obtained from this test, foresaw the application of 24 loading cycles with a resulted positive maximum displacement equal to 108 mm and a corresponding negative of 92 mm. A total of 1,440 displacement increments were solved for the needs of this nonlinear problem, where the convergence tolerance that was used during the nonlinear analysis was set again to 10^{-5}. The initial undamaged numerical model developed in section 8.4.1 was also used to solve this 2nd loading test, without any modifications to the mesh or the material properties. The reasons why the entire loading history of the experiment (3 load tests; 0.1g, 0.25g and "funeral") was not applied through a single run, were purely computational and hardware related. Only for the output file, it was estimated that more than a 200 Gb of hard drive space and a 70 Gb of RAM for solving the entire numerical problem would have been required. Therefore, this would have exceeded the available installed RAM in the PC, which was used to perform the numerical investigation.

The numerically computed base shear vs horizontal displacement curve (dashed line) is compared with the corresponding experimental one in Fig. 8.19. It is easy to notice that the numerical model, which used the undamaged concrete material properties, exhibited a stiffer behavior than the experimental curve (for the case of positive displacements). This numerical finding is attributed to the fact that the concrete damage developed during the first loading test was not numerically accounted for during the second numerical experiment. In order to remedy this problem, a second displacement history set was developed and applied on each slab based on the diagram shown in Fig. 8.20. As it can be seen, the new loading cycles foresee two preparatory cycles that have an absolute maximum magnitude of 20 and 23 mm horizontal displacements at the top floor, respectively. This two cycles were developed based on the maximum horizontal displacements derived during the first loading test (Fig. 8.7a), where the

choice of only two preparatory cycles (in addition to the 2nd loading test history) was made to avoid the significant increase in terms of computational demand. The new total number of displacement increments solved during the new analysis was 1,560, whereas the new obtained curve is also shown in Fig. 8.19.

Based on the second numerical experiment (see Fig. 8.19), the HYMOD managed to capture the experimental data with high accuracy, given that the maximum predicted base shear capacity of the building along the positive and negative x-axis were found to be within a 10% margin and always in favor of safety. In addition to that, the ability of the HYMOD to capture the hysteretic loops is also evident, while the material model used for the concrete simulation demonstrates its ability to numerically account for the concrete strength degradation due to the multiple loading cycles.

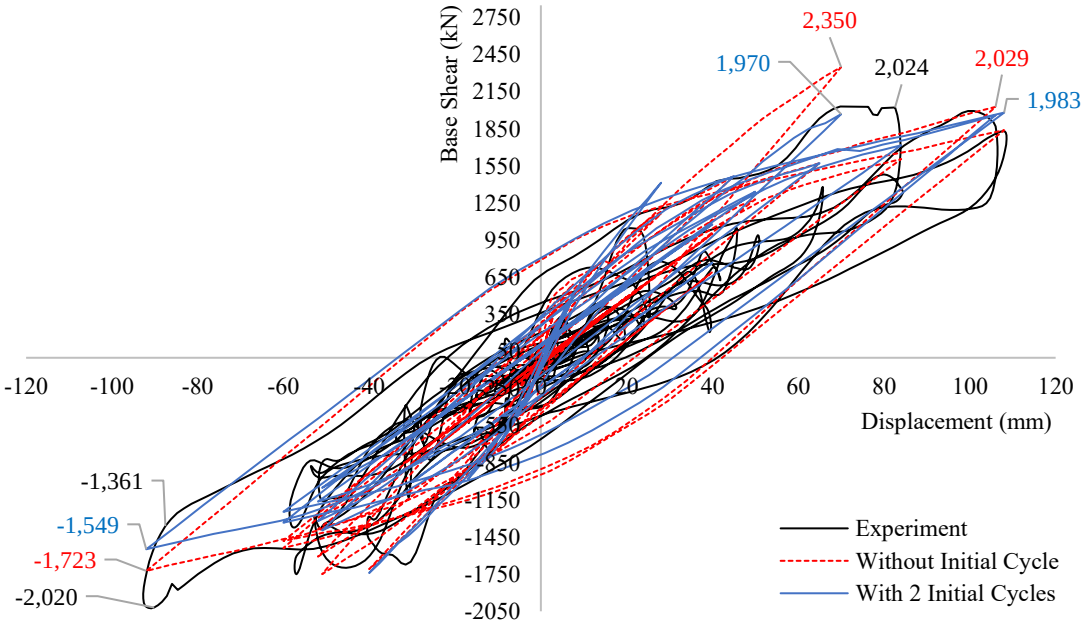

Fig. 8.19 2nd loading test (0.25g). Experimental vs numerical curves. Total base shear-horizontal displacement of the top floor.

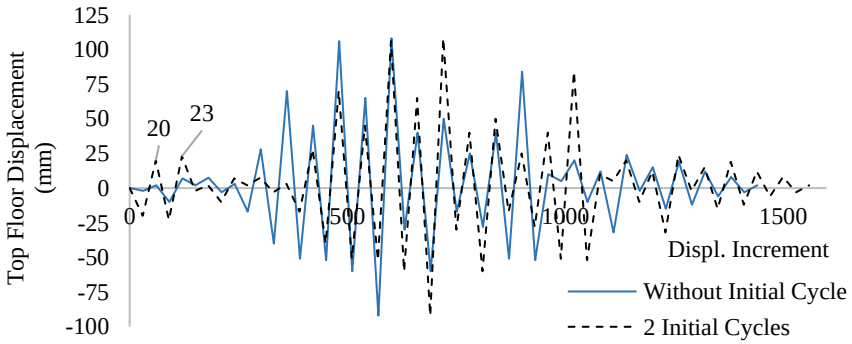

Fig. 8.20 2nd loading test (0.25g). Displacement history with 2 initial preparatory cycles applied at the top floor.

Fig. 8.21 and Fig. 8.22 show the von Mises strain contours that were numerically computed at the two frames, South and North, respectively, for the two maximum (positive and negative) horizontal roof displacements. As it can be seen, the South frame was found to be the one that developed more damages given that the reinforcement ratio used (based on the design of its RC infill wall) was lower compared to that of the North frame. In order to further investigate the deformation history at different areas of the structural frame, 4 strain history diagrams were

developed at 8 different locations labeled as (S1, S2, S3, S4) and (N1, N2, N3, N4), which can be seen in Fig. 8.21 and Fig. 8.22, respectively. The selected points were chosen to be located at areas where the strain concentration was found to be high, while the N4 and S4 locations were chosen so as to study the numerically predicted concrete confinement effect due to the CFRP jacketing. It is important to state here that, for the locations N1 and S1, the strain along the global x-axis (direction of the horizontal displacement) was studied given that they are located at the bottom fiber of the beams' sections (ground floor slab), while for the rest of the locations that are located at vertical structural members (columns and walls), the z-axis strain was chosen to be graphically visualized.

The numerically derived strain history diagrams can be seen in Fig. 8.23-Fig. 8.26, where it is evident that for all cases the locations that were chosen to be on the South frame exhibit a higher deformation at a local level. It is also characteristic that the strain at point S2 (Fig. 8.24) for the displacement increment 690 (δ_H = -92 mm), a larger deformation value equal to 0.68% resulted, which is much higher than the one obtained at the North frame (N2). This is attributed to the longitudinal rebars yielding within the column of the South frame, which was found to exhibit a more flexible mechanical behavior thus resulted higher damages at the local level. This numerical finding also complies with the experimental observations reported in Poljanšek et al. [42]. Additionally, this mechanical phenomenon, which also was captured through the analysis performed herein, is attributed to the lower reinforcement ratio that was used to reinforce the RC infill walls located at the South RC frame.

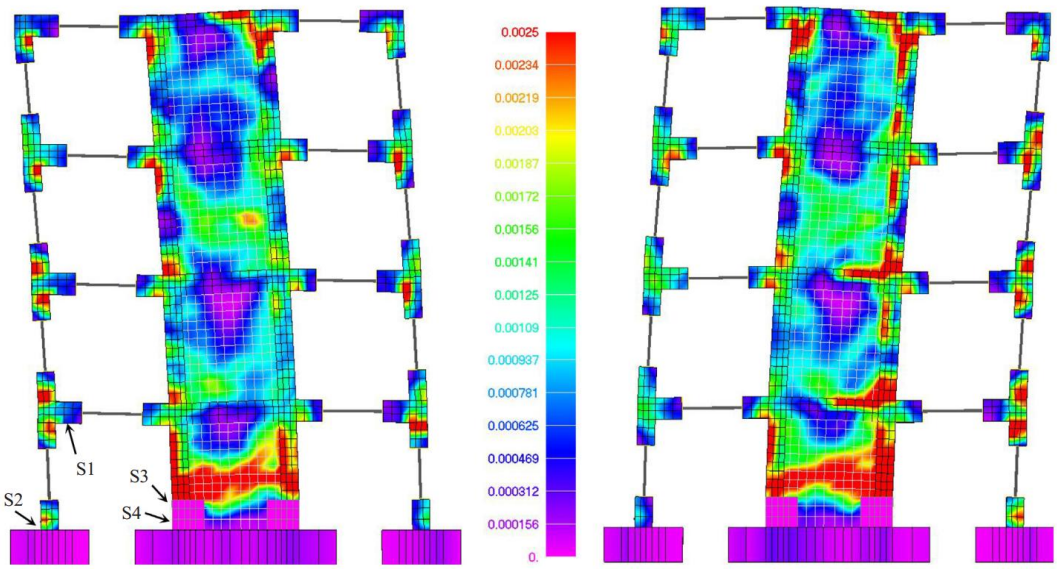

(a) (b)

Fig. 8.21 2nd loading test (0.25g). Von Mises strain contour for displacement increments (a) 690 (δ_H = -92 mm) and (b) 720 (δ_H = 108 mm). South frame.

Fig. 8.25 and Fig. 8.26, illustrate the strains at the S3-N3 and S4-N4 locations, as they resulted for the numerical analysis of the model. The numerical findings indicate that the RC domains that are located outside the CFRP confined region had a more flexible response developing larger deformations in comparison to the RC locations (S4-N4) that were confined. Based on the two graphs, it is easy to conclude that the unconfined locations developed large deformation that lead to significant cracking (due to the shifting of the plastic hinge). The maximum computed ε_{zz} strain deformation at S4 was 857×10^{-6}, which was 15% higher that the

corresponding magnitude computed at N4. Furthermore, the corresponding deformations at S3 and N3, where found to be significantly higher due to the rebar yielding that occurred within these locations.

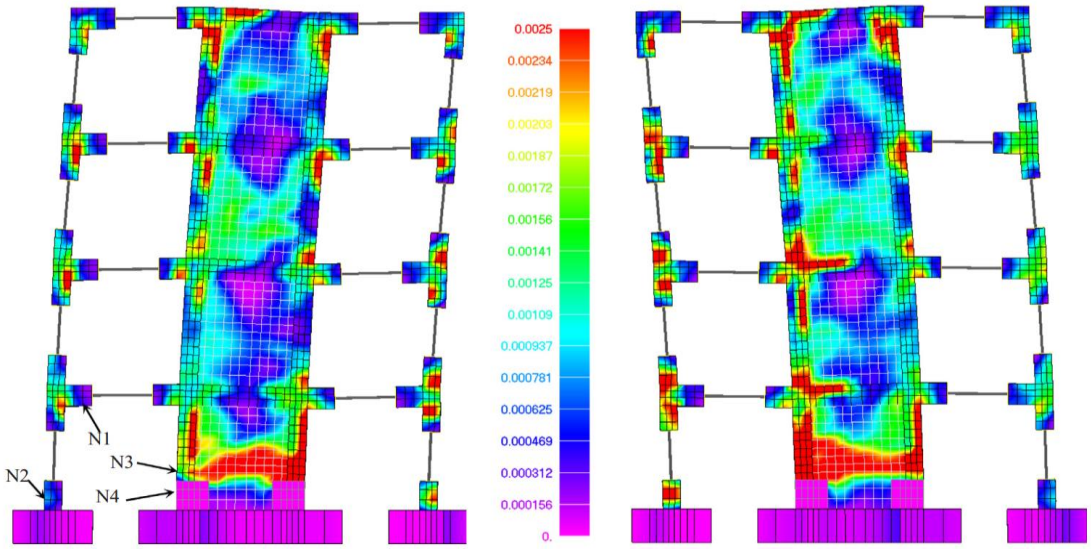

(a) (b)

Fig. 8.22 2nd loading test (0.25g). Von Mises strain contour for displacement increments (a) 690 (δ_H = -92 mm) and (b) 720 (δ_H = 108 mm). North frame.

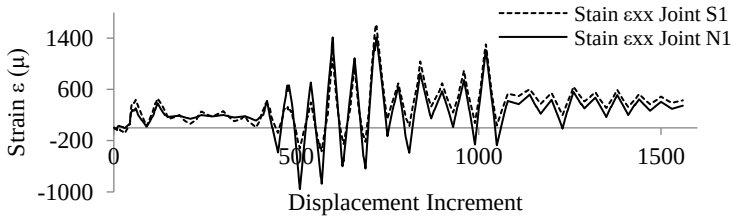

Fig. 8.23 2nd loading test (0.25g). Numerically computed strain ε_x history at the points N1 and S1.

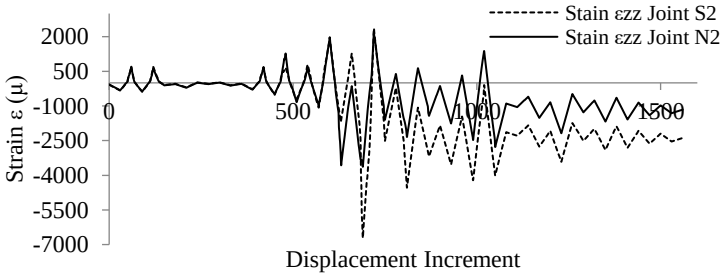

Fig. 8.24 2nd loading test (0.25g). Numerically computed strain ε_z history at the points N2 and S2.

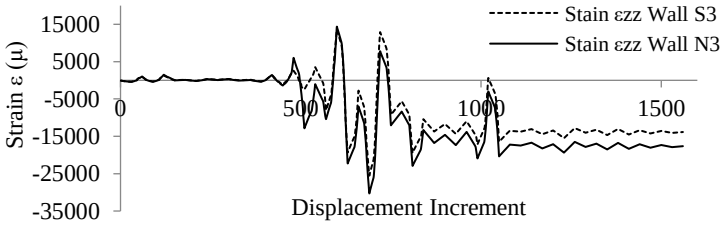

Fig. 8.25 2nd loading test (0.25g). Numerically computed strain ε_z history at the points N3 and S3.

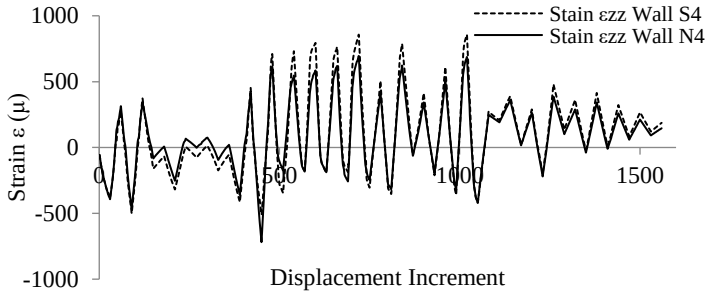

Fig. 8.26 2nd loading test (0.25g). Numerically computed strain ε_z history at the points N4 and S4.

Furthermore, after the completion of the 2nd loading test, the deformed shapes and the von Mises strain contours were visualized and illustrated in Fig. 8.27. It is evident that the remaining strains are larger compared to those obtained from the 0.1g test, given that the imposed horizontal deformations were almost 5 times larger during the 2nd test. The numerically predicted areas that derived higher damages were found to be at the column-beam joints and the RC walls, where the shear deformation was found to be excessive. This also complies with the experimental findings.

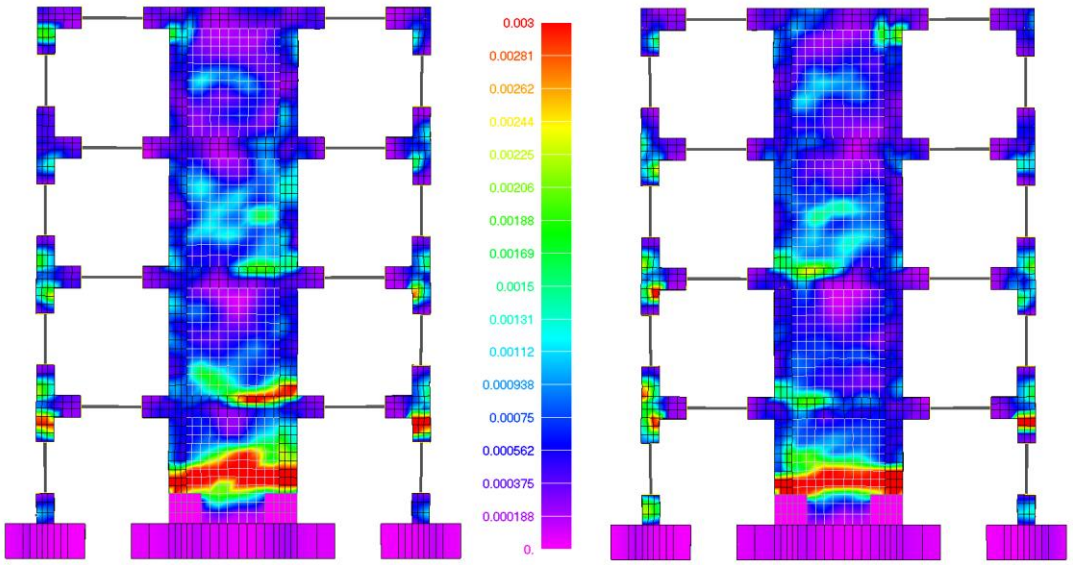

a. South Frame b. North Frame

Fig. 8.27 2nd loading test (0.25g). Remaining von Mises strain contour after the completion of the test (displacement increment 1,560; δ_H = 0 mm). Deformation magnification factor x20.

In regards to the computational details related to the 2nd numerical analysis, Table 8.4 shows the required time for the solution of 1,560 displacement increments and 7,504 internal iterations. The total computational time for the nonlinear analysis was 29 hours and 28 minutes, which corresponds to a 14.14 seconds per internal iteration. The average internal iteration per displacement increment was found to be equal to 4.81 and the average numerical error was equal to 8.92 x 10^{-6}. According to these numerical results, it is easy to conclude that this numerical problem resulted a smaller average internal iterations per displacement increment and a higher accuracy in terms of the derived error when compared with the obtained results from the 0.1g test. This numerical finding is attributed to the smaller displacement increment that was used during the nonlinear analysis procedure, even though the numerical nonlinearities that were developed during the analysis were significantly higher (cracking and rebar yielding).

This is also an additional evidence of the numerical robustness of the HYMOD algorithm in handling extreme nonlinearities.

Table 8.4 Computational performance of the algorithm for the case of the 0.25g test.

Total Displ Incr. Solved	Total Internal Iter.	Average Numerical Error	CPU Time Nonlinear Solution (hours)	Other CPU Time (hours)	Size of the Output File (Gb)
1,560	7,504	8.92×10^{-6}	29.46	2.7	70.8

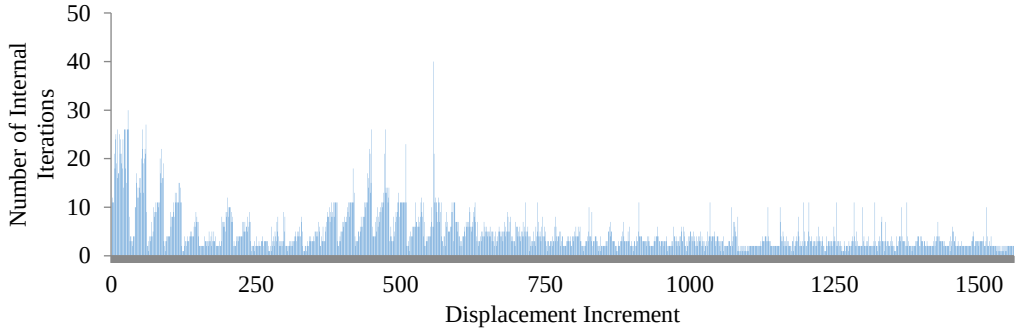

Fig. 8.28 2nd loading test (0.25g). Number of internal iterations vs displacement increment.

The total required hard disk space in order to save the output file for this run was 70.8 Gb, which once more highlights the significance of engaging the HYMOD approach and the ability to solve this type of problems through the use of commercial PC systems. Fig. 8.28 shows the graph that contains the corresponding number of internal iterations per displacement increment. According to this graph, it was found that 68.5% (1,069) of the displacement increments required less than 5 internal iterations to reach convergence, 88.2% (1,376) required less than 10 and only a mere 1.9% (30) of the displacement increments required more than 20 internal iterations so as to achieve convergence. This is a numerical response that further demonstrates the robustness and the numerical stability of the developed algorithm.

8.4.4 Analysis Results for the Final Loading Test

The final displacement test ("funeral cycles" [42]), foresaw the application of 2.5 displacement cycles (Fig. 8.7c) in an attempt to push the RC frame to reach its maximum capacity. As it was stated before, the frame was pushed and at the same time the corresponding base shear was measured [195] waiting to notice a sudden drop in terms of resistance. According to the experimental measurements, the frame was then considered to have reached its maximum capacity. For the needs of this final analysis, the undamaged model was used once more so as to simulate the mechanical behavior of the RC frame when it undergoes the "funeral cycles" displacement history test.

Fig. 8.29 shows the comparison between the numerical and the experimental results, where it is evident that the computed initial stiffness from the numerical model is significantly higher than the one measured during the experiment [42], given that the HYMOD foresaw the use of the undamaged model at the beginning of the analysis. Both positive and negative maximum base shear capacities were overestimated herein, a numerical finding that was expected, given that this modeling strategy is not realistic as it was discussed and explained in section 8.4.3. In order to establish a more realistic modeling strategy, a second analysis was performed by assuming a displacement history combination (Combo 1) that foresaw the use of a preparatory displacement history that consisted of 4 loading cycles (see Fig. 8.30), where at the end of this displacement history the "funeral cycles" were imposed based on the experimental data. The

preparatory cycles were developed by using the maximum positive and negative horizontal displacements that were developed in the two previous loading tests (0.1g and 0.25g).

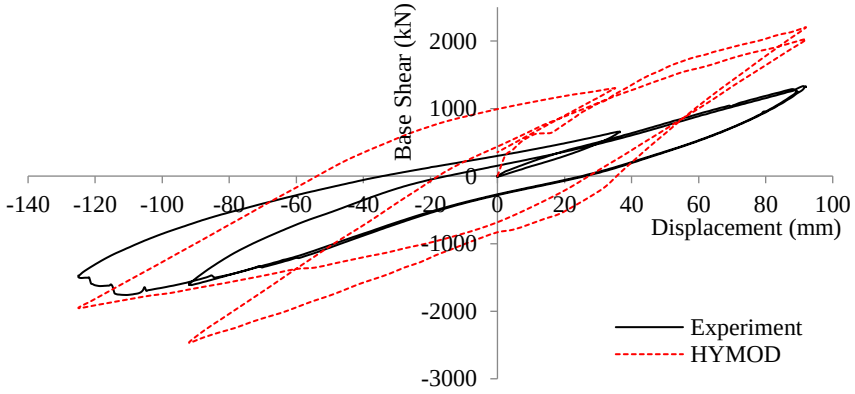

Fig. 8.29 3rd loading test ("funeral cycles"). Experimental vs numerical curves. Total base shear-horizontal displacement of the top floor. Undamaged model.

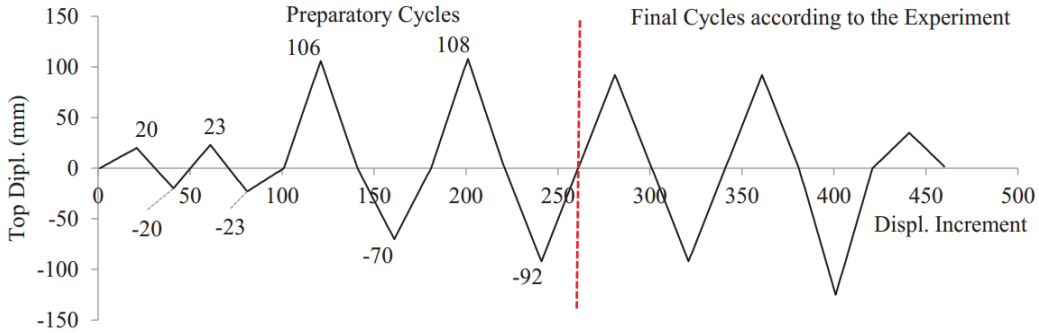

Fig. 8.30 Combo 1 displacement history applied at the top floor of the specimen.

Fig. 8.31 shows the corresponding comparison of the numerical and experimental curves for the case of the Combo 1 displacement history (Fig. 8.30). As it can be seen, the base shear drop for the numerically predicted capacity of both negative and positive maxima imposed displacements is evident, thus demonstrates the numerical ability of the algorithm in capturing the structure's deterioration due to the multiple cyclic deformations. The newly computed total base shear was found to decrease to 1,701 kN (negative displacement 92 mm), which was 3.5% larger than the experimental value (1,670 kN). Furthermore, the base shear for the case of the maximum negative displacement (125 mm) was computed to be equal to 1,882 KN, while the corresponding experimentally obtained value was 1,753 kN. Based on these new resistance values, the numerical prediction is 7.4% higher than the experimental one, a numerical phenomenon that can be also observed for the shear base values that were computed for the positive deformations (the two positive horizontal displacements of 92 mm). Based on the new numerical findings, it was concluded that there was the need of performing an additional analysis by using a refined preparatory displacement history so as to further take into account the damages occurred during tests 1 and 2, in a more realistic manner.

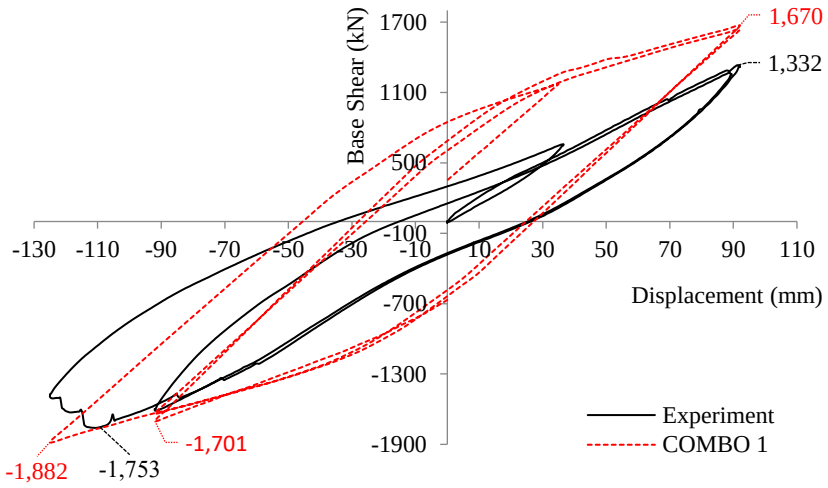

Fig. 8.31 3rd loading test ("funeral cycles"). Experimental vs numerical curves. Total base shear-horizontal displacement of the top floor. Combo 1 displacement history.

In order to improve the numerical prediction thus capture the experimental curve through a more realistic displacement history, a 3rd displacement history (Combo 2) was developed herein that foresaw the use of 7 preparatory displacement cycles. As it can be seen in Fig. 8.32, the cycles foresaw the application of horizontal displacements that varied between 108 and -92 mm. A total of 825 displacement increments were used in order to analyze this highly nonlinear numerical problem.

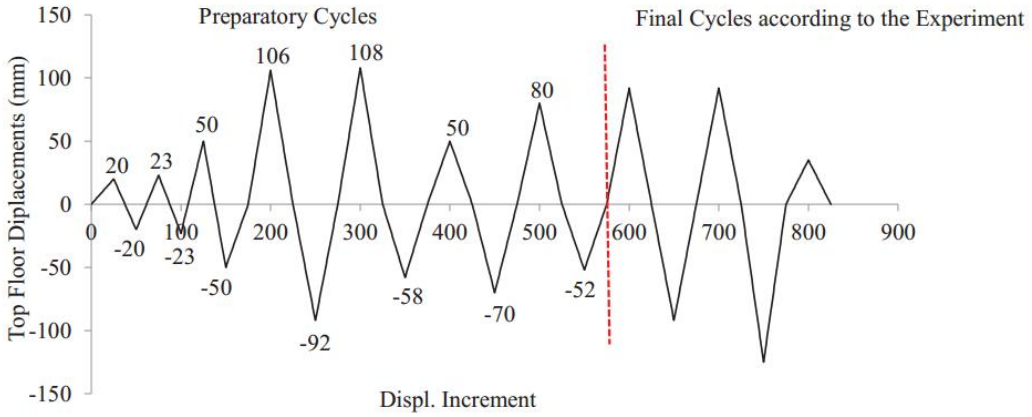

Fig. 8.32 Combo 2 displacement history applied at the top floor of the specimen.

Fig. 8.33 shows the comparison between the experimentally and numerically derived curves for the case of the Combo 2 displacement history, where it can be easily observed that the numerical trend described above, related to the capacity decrease, is confirmed through this additional simulation. Therefore, the larger the number of the preparatory cycles is, the higher the decrease of the maximum predicted base shear gets due to the concrete material deterioration (more cracks open and fail to close during the analysis). The difference between the predicted maximum negative base shear is less than 2% in the cases of -92 and -125 mm horizontal displacements, as depicted in Fig. 8.33. The maximum base shear for the case of the positive horizontal displacements are still higher than the experimental ones due to the numerical phenomenon that relates to the damage that accumulates in both concrete and steel materials.

In addition to that, it is also easy to observe that the numerically predicted hysteretic loops are larger in comparison to the experimentally obtained ones, which is a phenomenon that can be attributed to the small number of preparatory displacement cycles that were solved prior to the last set of displacement history test (Fig. 8.33) and the lack of a damage factor that will further decrease the material strength due to the multiple opening and closing of cracks. The use of damage factors in this case could help in capturing the degradation of concrete in a more realistic manner thus fortify the model in capturing more complicated phenomena such as the pintching effect. For this reason, the concrete and steel material formulations were integrated with two new damage factors that are able to account for this phenomenon based on how many times a crack has opened and closed. This will be presented in Chapter 9.

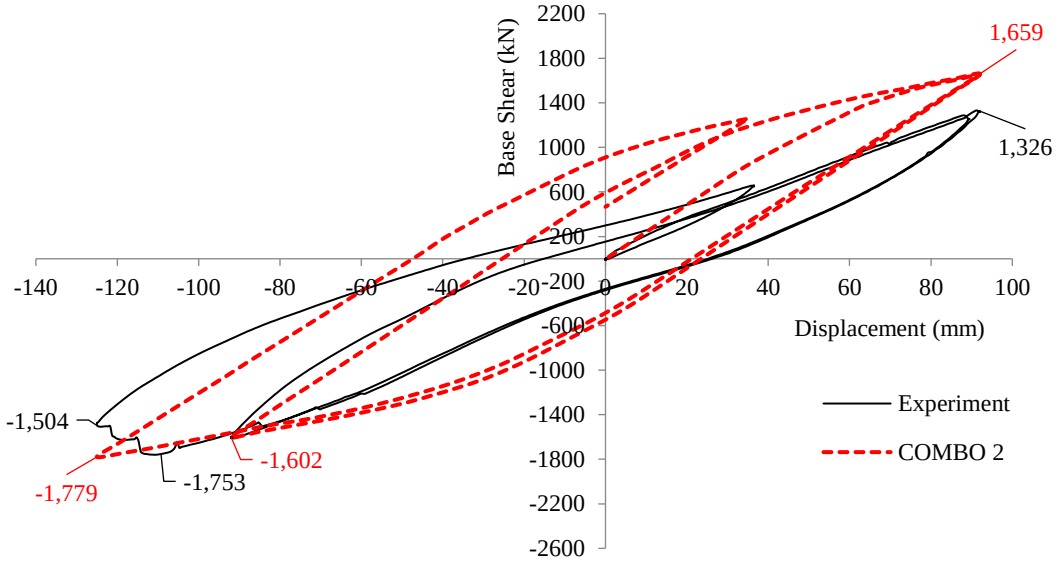

Fig. 8.33 3rd loading test ("funeral cycles"). Experimental vs numerical curves. Total base shear-horizontal displacement of the top floor. Combo 2 displacement history.

To further elaborate on the higher computed capacity for the case of the positive horizontal displacements, it must be reminded at this point that the actual experiment foresaw the cyclic loading of the building according to the loading history tests of 0.1g and 0.25g. The damage that had accumulated at the concrete and steel materials within the two frames is a factor that cannot be ignored when attempting to model the funeral cycles. This should also be the case when modeling the RC building, but for the computational-related reasons that were explained above this was not feasible. Nevertheless, a final analysis was performed so as to show the ability of the model to capture the experimental data, by modifying the material properties of concrete and steel. This is a numerical approach that is broadly acceptable and extensively used (in order to account for the existing damage). Nonetheless, this is not considered by the authors to be numerically objective given that the assumptions that are made in defining the new material values do not follow a specific set of rules but are based on the experience of the user. Therefore, in the case of the RC retrofitted building, the steel material hardening modulus was set to 20 MPa for all embedded rebar properties except for that of the 20 mm rebar element that was set to 0. The reasoning behind this approach, of applying a maximum decrease on the hardening modulus of the 20 mm rebars, was the fact that these reinforcement are located at the areas that sustained significant damages during the two first test. Especially at the columns and the boundary elements of the RC shear walls located at the ground floor, structural members that were reinforced with 20 mm in diameter rebars. The concrete material model was also modified by decreasing its tensile strength from 5% to 3%, while the same displacement history was used in performing the cyclic analysis (see Fig. 8.32).

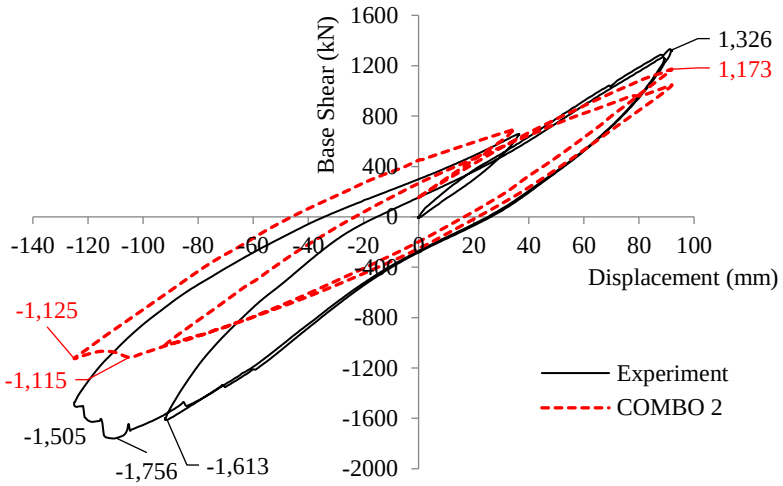

Fig. 8.34 3rd loading test ("funeral cycles"). Experimental vs numerical curves. Total base shear-horizontal displacement of the top floor. Model with modified material properties. Combo 2 displacement history.

Fig. 8.34 shows the comparison between the experimental and numerical results, where it can be easily observed that the numerically derived capacity has decreased significantly due to the material modifications. The maximum computed resistance of the building for the positive horizontal displacement was 1,173 KN, which corresponds to an 11.5% accuracy in favor of safety. On the other hand, the decrease of the numerically predicted maximum negative capacity was higher due to the rebar failures that occurred when the model was pushed to reach the -125 mm horizontal displacement. This numerical response is attributed to the low hardening modulus that was used, which resulted into larger local deformations at the rebars located in the columns and shear walls of the ground floor. Based on the parametric investigation performed herein, it was concluded that the drop in-terms of strength and energy dissipation was attributed to the hardening modulus decrease given that during the third and final displacement history test the embedded rebars located at the beam-column joints and the boundary elements of the shear walls were plastified thus the hardening modulus was controlling their mechanical behavior.

An additional conclusion that derives from this final analysis is that, when trying to predict the carrying capacity of any specimen or real structure, the greatest modeling challenge is the selection of the material property values for both steel and concrete. In the case where these values are available from material tests, then the ability of the numerical model used in predicting the structural capacity by using the exact material property values, is of great significance given that this numerical ability will eventually minimize the need of additional assumptions during the construction of the model and especially during the definition of the material parameters. This numerical finding also demonstrates the inability of the simplified numerical models (Kyriakides et al. [195]) to be considered as adequate in the case where the assessment of an existing damaged RC building is required, in an attempt to predict its current capacity.

Table 8.5 shows the computational performance data for the solution of the 3 analyses performed so as to simulate the funeral cycles. For the three analyses, the average error was calculated and found to be equal to 2.29, 1.07 and 1.28 x 10^{-5}, respectively. Fig. 8.35-Fig. 8.37 show the graphs of the corresponding internal iterations per displacement increment, as they resulted from the three analyses. It is evident that the low ratio of internal iterations per displacement increment trend is present, therefore, this numerical finding further supports the previous statement in regards to the HYMOD's algorithmic robustness and numerical stability.

The average ratios of internal iterations per displacement increment for the case of these three analyses were 8.28, 6.84 and 5.67, respectively.

Table 8.5 Computational performance of the Funeral and Combo Final cycle analyses.

a/a	Displ. Function	Total Displacement Increments Solved	Total Internal Iterations	Average Numerical Error	CPU Time Nonlinear Solution (hours)
1	Funeral cycles	240	1,988	2.29×10^{-5}	7.81
2	Combo 1	460	3,146	1.07×10^{-5}	12.37
3	Combo 2	825	4,676	1.28×10^{-5}	18.39

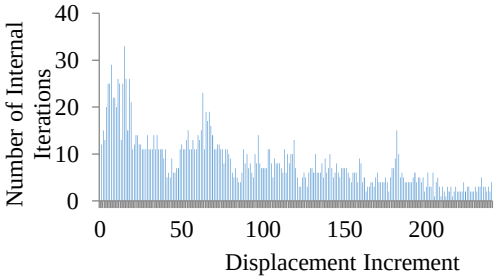

Fig. 8.35 3rd loading test ("funeral cycles"). Number of internal iterations vs displacement increment. Undamaged model.

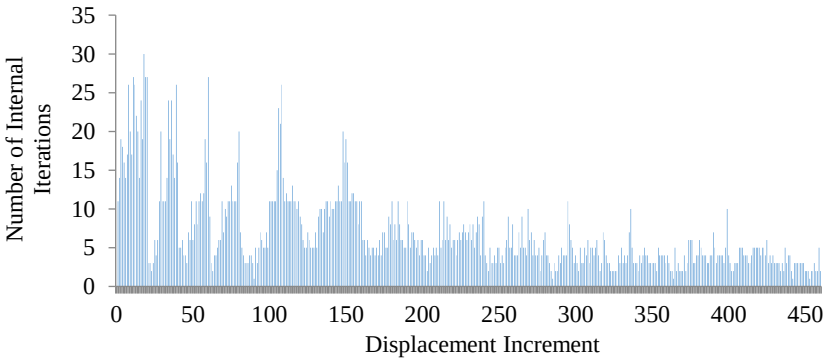

Fig. 8.36 3rd loading test ("funeral cycles"). Number of internal iterations vs displacement increment. Combo 1 displacement history.

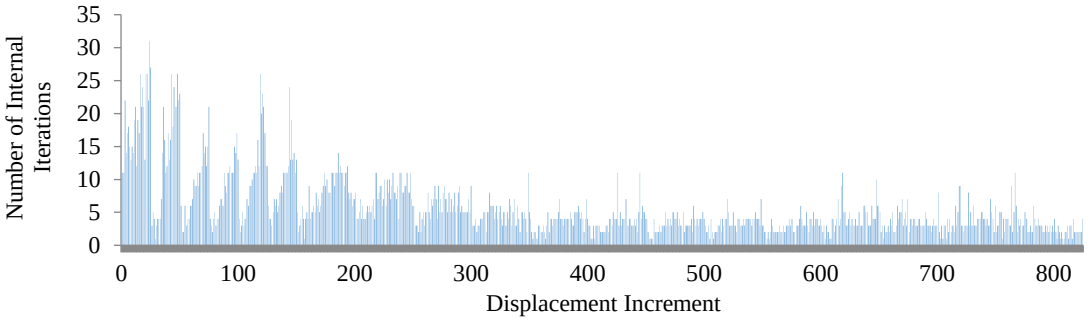

Fig. 8.37 3rd loading test ("funeral cycles"). Number of internal iterations vs displacement increment. Combo 2 displacement history.

8.5 Numerical Investigation of Different Infill RC Wall Retrofitting Configurations

The introduction of new infill RC walls within an existing framing system increase significantly the stiffness and the carrying capacity of any multistory RC building, but it can also affect its overall mechanical response that can lead to local failures during an earthquake excitation, a mechanical response that might not be anticipated by the designers. In order to further examine the effect on the mechanical behavior of RC structures when a frame is retrofitted with infill RC walls, the four-storey building without infill walls is initially examined in this section through the use of the model illustrated in Fig. 8.38. The displacement history depicted in Fig. 8.32 was applied in this case in order to compare the numerically predicted capacity of the bare frame and compute the actual strength enhancement induced to the framing system due to the introduction of the infill RC walls, as it was studied and presented above.

In Fig. 8.39, the force-displacement curves for the "funeral cycles" (last loading cycles of the graph given in Fig. 8.32) are compared for the case of the fully retrofitted and the bare frames. As it derives from the numerical investigation, the infill RC walls significantly increase the stiffness of the building's frame, while the capacity of the building increases accordingly as well. Therefore, the shear capacity of the building is significantly larger as it can be observed in Fig. 8.39, where the hysteretic cycles of the retrofitted frame are notably larger. Based on the obtained numerical results that are given in Table 8.6, the structure with the infilled RC walls presents a 155.6%, 159.5% and 223.3% larger shear capacity for the positive maximum deformations and, a 209.6% and 194.9% larger shear capacity for the respective maximum negative deformations of the imposed displacement history. This numerical finding demonstrates that the design of the infill RC walls manages to increase the shear capacity more than two times in both loading directions.

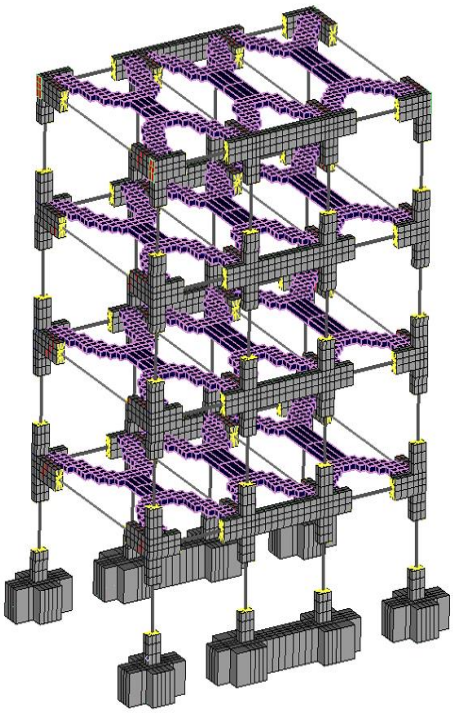

Fig. 8.38 3D view of the hexahedral HYMOD mesh of the bare frame.

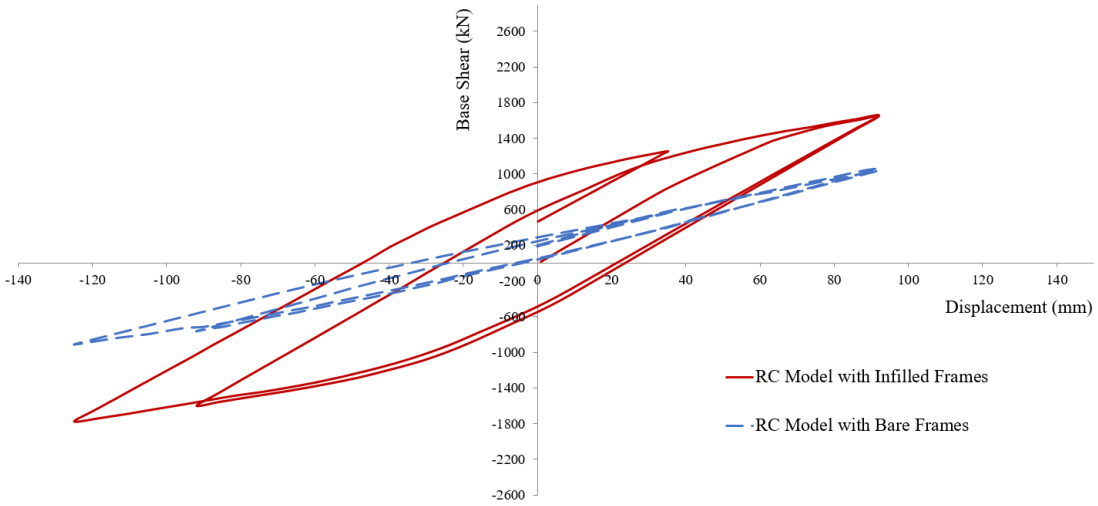

Fig. 8.39 Loading test ("funeral cycles"). RC Model with bare frame vs infilled RC walls. Total base shear-horizontal displacement of the top floor.

Table 8.6 Base shear comparison between the RC model with infill shear wall and without shear wall

Displacements (mm)		Max Base Shear of RC Model with Bare Frames-BF (kN)		Max Base Shear of RC Model with Infilled RC Walls-IF (kN)		$\frac{\mathbf{IF}}{\mathbf{BF}}$ (%)	
Positive	Negative	Positive	Negative	Positive	Negative	Positive	Negative
92	-92	1062.10	-764.68	1652.25	-1602.49	155.6	209.6
92	-125	1040.15	-912.80	1659.45	-1779.49	159.5	194.9
35	0	562.83	-	1257.00	466.66	223.3	-

Furthermore, the ability of the building to absorb energy during an earthquake excitation is significantly affected due to the infill RC walls. As illustrated in Fig. 8.39, the hysteretic loops of the model with the infill walls are found to be 5 times larger than the corresponding hysteretic loops of the areas of the model with the bare frame. Table 8.7 shows the numerically computed values of the dissipated areas for the two final loading cycles for the two numerical models, where it can be depicted that the model with the infilled RC walls exhibits a dissipated area which is 439% larger than that obtained through the model with the bare frame (for the case of the 2nd loading cycle). Therefore, the infill RC walls are found to induce a significant increase of the energy dissipation level of the structure as compared to the corresponding mechanical response derived from the bare frame. Based on the numerical study performed herein, it was concluded that as the excessive strains and stresses are developed within the RC shear walls, their presence ensures a sufficient and reliable mechanical system that is capable to dissipate energy, which is caused by extreme cyclic loading conditions. This finding further demonstrates the overall contribution of the infill RC walls in terms of earthquake resistance from a qualitative and quantitative perspective.

Table 8.7 Dissipated energy comparison between the RC model with infill shear wall and without shear wall

Dissipated Energy	RC Model with Bare Frames -BF (kN mm)	RC Model with Infilled Frames-IF (kN mm)	$\frac{\mathbf{IF}}{\mathbf{BF}}$ (%)
1st Cycle	23,758.14	104,391.98	439.4
2nd Cycle	35,018.48	175,570.06	501.4

In order to further investigate the efficiency of the infill RC wall intervention method, two new retrofitting configurations were examined and presented in this section. The two additional models that were developed by using the fully retrofitted HYMOD model shown in Fig. 8.9, foresee the use of infill RC walls at the ground floor (Fig. 8.40a) and, at the ground and first floors (Fig. 8.40b), respectively. The finite element meshes of the two additional models developed for the needs of this numerical investigation can be seen in Fig. 8.40. As a first stage of this numerical experiment, the displacement history shown in Fig. 8.32 was applied to numerically obtain the maximum carrying capacity and study the overall mechanical response of the two new retrofitted frames. Both frames did not manage to deform beyond a certain displacement limit (due to tensile rebar failures that led to the termination of the nonlinear analyses) thus the displacement history had to be modified accordingly so as to achieve a complete analysis solution for both models. According to the initial run, the first retrofitting model (Fig. 8.40a) derived a failure prior to reaching the maximum negative horizontal displacement (125 mm) thus the corresponding magnitude was decrease to 110 mm, hence manage performing the complete analysis without reaching a premature failure. For the case of the second retrofitting model (Fig. 8.40b), it was found that a failure during the first maximum positive displacement of the funeral cycles (92 mm) occurred, thus both positive and negative maximum displacement magnitudes of the funeral cycles were decreased to 80 and 100 mm, respectively.

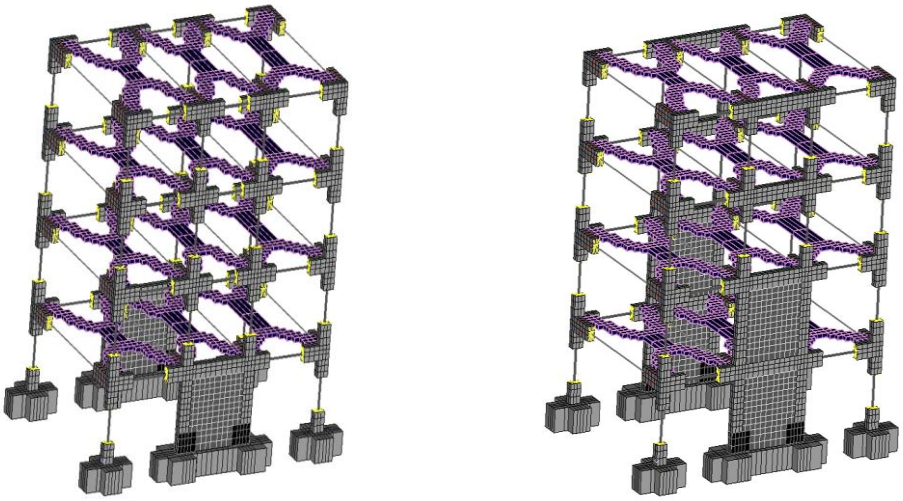

(a) (b)

Fig. 8.40 3D mesh view of the four-storey RC building with infill RC walls at the (a) ground floor and (b) ground and first floors.

Fig. 8.41 shows the comparison of the numerically predicted curves between the two different retrofitting models (see Fig. 8.40). One of the main objectives of this parametric investigation was to examine the overall effect of the different intervention geometries in terms of base shear and energy dissipation enhancement. The obtained numerical results that are shown in Fig. 8.41, show that the two new models derived an overall base shear capacity that lies between the fully retrofitted and the bare frame models. Therefore, a first finding of this study is that the fully retrofitted frame was found to be the intervention design that derives the largest capacity and energy dissipation enhancement. Nonetheless, it is also the design solution that requires the highest cost so as to be implemented.

The first retrofitting model (Fig. 8.40a) was found to be the most flexible out of the three retrofitted models examined in this work, given that it foresaw the use of infill RC walls only

at the ground floor. It is interesting to note here that the base-shear capacity of the model with the infill RC walls at the ground and first floors (Fig. 8.40b) derived a similar shear capacity with that obtained by the first retrofitted model (Fig. 8.40a). This is attributed to the local failures that were developed in the case of the second retrofitted model, which forced the use of smaller maximum positive and negative horizontal displacements during the funeral cycles (as explained above). Therefore, the shear capacity and energy dissipation enhancement achieved by the two new retrofitting designs (see Fig. 8.40) are found to be affected not only by the geometry of the infill RC walls, but also by the accumulated local damage concentrations that were developed at the non-retrofitted structural members of the RC frame. This accumulated damage development (recorded mainly at the columns that were found at the floors that were not retrofitted) was significantly affected by the stiffness irregularities along the height of the building, which were induced due to the introduction of the infill RC walls at the lower floors of the structure (Fig. 8.40). This numerical finding further highlights the complexity of the at hand problem when accumulated damage is accounted for during the seismic assessment of retrofitted RC framing systems.

It must be noted at this stage that the above numerical findings resulted through the study of a relatively simple in geometry frame configuration, where the cyclic displacement history and the corresponding deformation profile applied herein were also rather simplistic (compared to the expected deformation shape of a real structure that undergoes an actual seismic excitation). The complexity of this problem increases exponentially when a structure with an irregular geometry is under study thus is designed by a professional civil engineer to be retrofitted through the use of infill RC walls and CFRP jacketing. This highlights the importance of developing, at a first stage, computationally efficient and robust numerical tools, such as the proposed HYMOD approach, in order to provide researchers with the ability to further investigate retrofitting designs and propose rules and recommendations based on accurate numerical studies and not based on semi-empirical knowhow. Thereafter, the next step will be to further evolve this technology and eventually be able to make these numerical tools available to professional civil engineers.

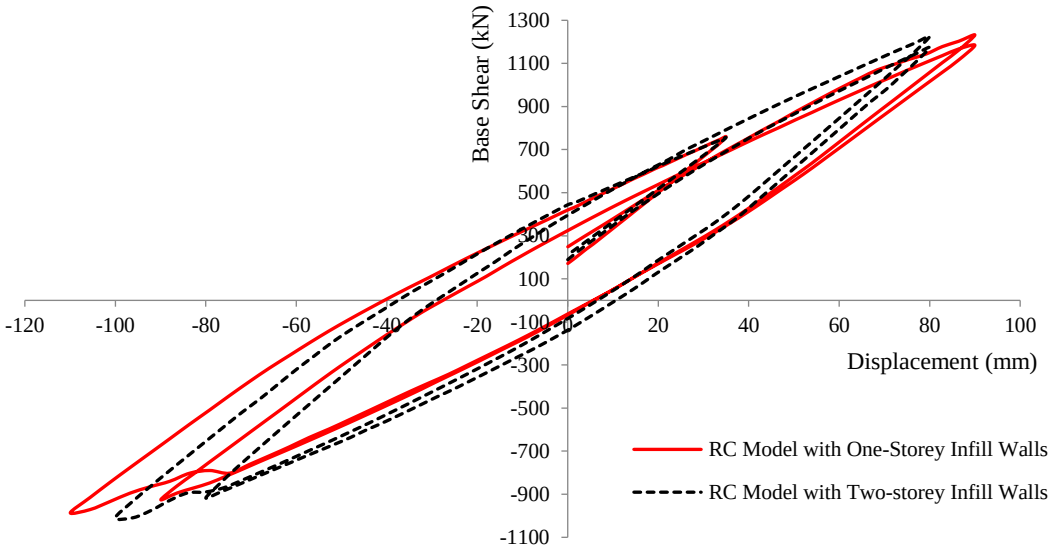

Fig. 8.41 Loading test ("funeral cycles"). HYMOD Models with different retrofitting configurations. Total base shear-horizontal displacement of the top floor.

In continuation to the above discussion, Table 8.8 shows the resulted maximum positive and negative base shear capacities of the retrofitted frame as they resulted by analyzing the model in Fig. 8.40a. The numerically obtained capacities are compared with those resulted by the bare

frame model, where it can be seen that the corresponding retrofitted frame (Fig. 8.40a) manages to increase the base shear capacity for all cycles with the maximum increase being equal to 18.4% that corresponded to the second funeral cycle's positive maximum horizontal displacement. The computed base shear capacity increase was not as significant as the increase noticed in terms of energy dissipation for the two loading cycles, which was computed to be equal to 2.3 and 2 times larger, respectively, compared to those computed by the bare frame model (see Table 8.9). Equivalent results can be seen in Table 8.8, where the numerically obtained base shear capacities of the second retrofitted (Fig. 8.40b) and the bare frames are compared. The comparison in this case shows that the shear capacity of the retrofitted model is increased by 20% for the case of the first negative maximum horizontal displacement of the 1st loading cycle, whereas the corresponding shear capacity increase is 17.9% for the second positive maximum positive horizontal displacement.

Based on the computed energy dissipation for the 1st and 2nd loading cycles, the second retrofitted model (Fig. 8.40b) also managed to increase the frame's energy dissipation capacity by 2.3 and 2 times, respectively (see Table 8.10). It is noteworthy to state at this point that the ability of the second retrofitted model (Fig. 8.40b) to deform was limited due to the local accumulated damages developed at the columns of the 3rd floor, thus the maximum horizontal imposed displacements during the funeral cycles were decreased so as for the analysis to complete successfully without any local failures occurring during the last stages of the numerical experiment. This caused the resulted maximum base shear capacities of the second retrofitted frame to remain at a lower than the expected levels (along both the positive and negative x-axis directions).

Additionally, by comparing the maximum resulted base shear capacity obtained from the three retrofitting models, it derives that the two new retrofitting models (Fig. 8.40) exhibit a 25% decreased shear capacity compared to the fully retrofitted model, while the corresponding decrease of their energy dissipation in comparison to the fully retrofitted model, is approximately equal to 2.4 times. This highlights the significant increase in terms of energy dissipation when the infill RC walls are placed throughout the height of the building.

Table 8.8 Base shear comparison between the RC model with one-storey infill shear walls vs the bare frame model

Displacements (mm)		Base Shear of RC Model with Bare Frames-BF (kN)		Base Shear of RC Model with 1-storey Infilled Frames-IF1 (kN)		$\frac{\textbf{IF1}}{\textbf{BF}}$ (%)	
Positive	Negative	Positive	Negative	Positive	Negative	Positive	Negative
92	-92	1062.10	-764.68	1184.19	-925.63	111.5	121.0
92	-110	1040.15	-912.80*	1232.01	-986.40	118.4	108.1
35	0	562.83	-	760.33	-	135.1	-

*Value corresponds to a total of -125 mm horizontal displacement.

Table 8.9 Base shear comparison between the RC model with two-storey infill shear walls vs the bare frame model

Displacements (mm)		Base Shear of RC Model with Bare Frames-BF (kN)		Base Shear of RC Model with 2-storey Infilled Frames-IF2 (kN)		$\frac{\textbf{IF2}}{\textbf{BF}}$ (%)	
Positive	Negative	Positive	Negative	Positive	Negative	Positive	Negative
80	-80	1062.10**	-764.68***	1173.92	-917.34	110.5	120.0
80	-100	1040.15**	-912.80*	1225.85	-1010.29	117.9	110.7
35	0	562.83	-	756.19	-	134.4	-

*Value corresponds to a total of -125 mm horizontal displacement.

**Value corresponds to a total of 92 mm horizontal displacement.

***Value corresponds to a total of -92 mm horizontal displacement.

Table 8.10 Dissipated energy comparison between the RC model with one- and two-storey infill shear walls vs the bare frame model

Dissipated Energy	RC Model with 1-Storey Infill Frames -IF1 (kN mm)	$\frac{\textbf{IF1}}{\textbf{BF}}$ (%)	RC Model with 2-Storey Infill Frames -IF2 (kN mm)	$\frac{\textbf{IF2}}{\textbf{BF}}$ (%)
1st Cycle	55,125.10	232.0	55,462.42	233.4
2nd Cycle	73,358.95	209.5	72,575.26	207.2

The deformation shape and the von Mises strain contours are visualized and shown in Fig. 8.42 and Fig. 8.43, for the models with the two different retrofitting configurations (Fig. 8.40). It is easy to observe that the main damages were found to develop at the RC joints and the shear walls of the four frames. It is obvious that the model with infill RC walls placed at the ground floor (Fig. 8.42) presents larger strain development within the shear walls in comparison to the model with the two-storey shear walls. This is attributed to its ability to deform beyond the limit of 100 mm horizontal displacement that was the maximum achieved negative x-axis displacement derived by the second retrofitting model (Fig. 8.43). Furthermore, it can be easily observed that for both models, the South frame seems to suffer from more damages than the North frame, a mechanical behavior attributed to the fact that a lower reinforcement ratio was used based on the design of the South and North infill walls. It must be noted here that, for comparative purposes the von Mises strain contours shown in Fig. 8.42 and Fig. 8.43, were set to have a maximum strain of 1%. Based on the numerical findings, the maximum predicted von Mises strain was equal to 5% and 4% for the first (Fig. 8.42) and second (Fig. 8.43) retrofitting model, respectively, whereas the maximum damages were located at the critical areas of the shear walls that are located at the ground floor level in both models and the beam-column joints at the 1st level. In addition to that, the applied deformation profile (which was based on the corresponding experimental data) was found to cause the models to develop significant damages at the 3rd level's columns, attributed to the relative imposed horizontal deformations.

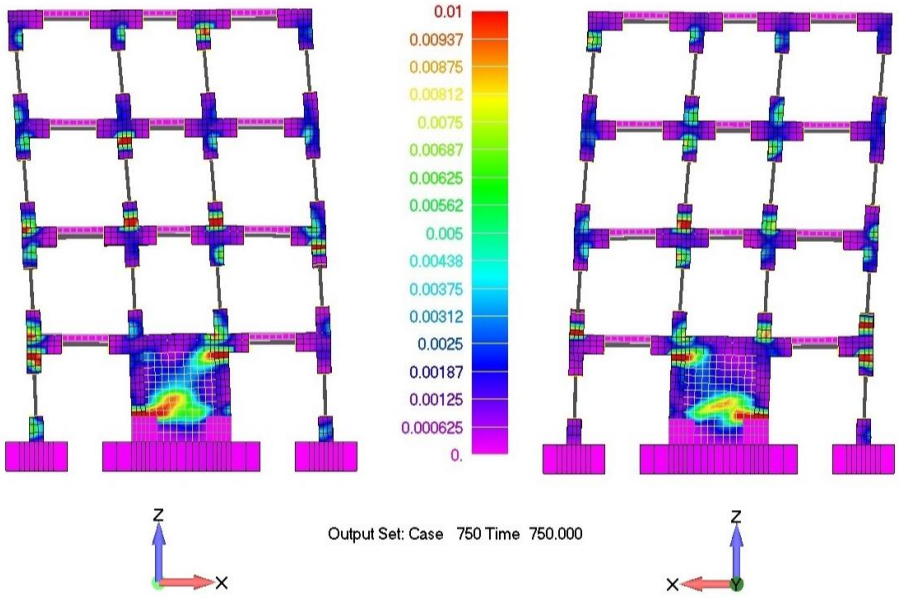

(South) (North)

Fig. 8.42 One-Storey infill RC walls model. Von Mises stain contour for displacement increment 750 (δ_H = -110 mm).

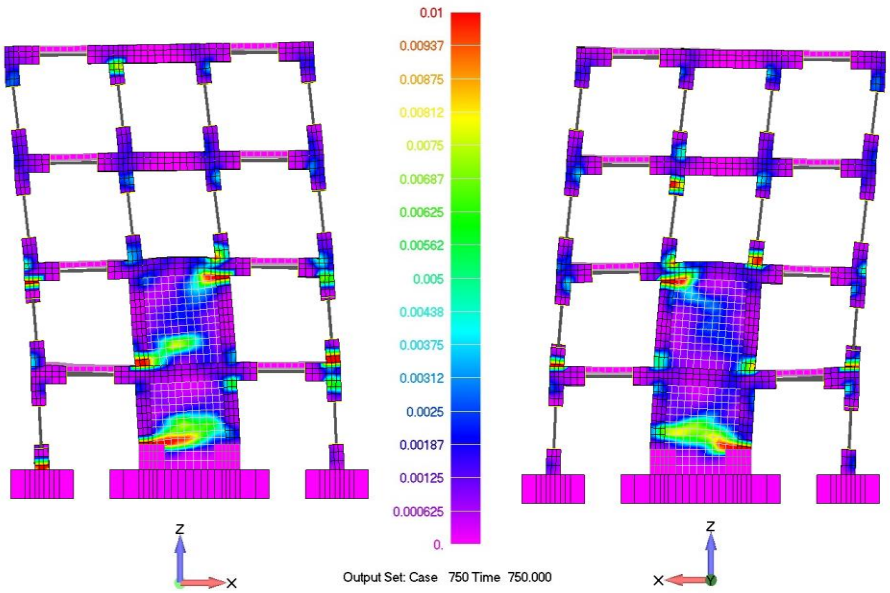

(South) (North)

Fig. 8.43 Two-Storey infill RC walls model. Von Mises stain contour for displacement increment 750 (δ_H = -100mm).

In order to further study the mechanical response of the four HYMOD models, a modal analysis algorithm was developed and applied herein for the first time in the international literature (modal analysis of HYMOD meshes) aiming to compute the fundamental periods and frequencies of the under study finite element models. The algorithmic implementation uses the Bathe [83] approach, which is known as the Subspace Iteration Method. The modal analysis presented herein, was conducted in order to investigate in-depth the effect of the different retrofitting configurations presented above and establish a better understanding of the overall mechanical behavior of each retrofitted frame (compared to the behavior of the bare frame).

In order to check the obtained values of the newly developed algorithm, the New Greek Seismic Code (NEAK 2000) [197] formula for computing the fundamental period along a certain direction was used, given that it takes into account a more realistic approach compared to both Eurocode 8 (2003) [41] and ACI-318 (2014) [198] codes. Additionally, this choice was made given that the New Greek Seismic Code formula, shown in Eq. (8.1), accounts for the presence of shear walls and the dimensions of the structure.

$$T_{1,NEAK} = 0.09 \cdot \frac{H}{\sqrt{L}} \sqrt{\frac{H}{H + \rho L}} \tag{8.1}$$

where H is the total height of the building, L is the dimension of the building along the direction that the period is computed for, and ρ is the percentage of the summation of the shear wall section areas positioned along the direction of the computed oscillation over the total section area of the vertical structural members. Based on the NEAK 2000 [197] formula the fundamental period of the bare frame along the x-axis is equal to 0.362 seconds (ρ = 0), while the corresponding fundamental period of the fully retrofitted frame (infill RC walls throughout the building's height; ρ = 0.7838) is equal to 0.288 seconds (also along the x-axis direction).

Fig. 8.44 shows the first three eigenshapes and their corresponding eigenmode values as they resulted from the four numerical models that were examined in this research work. As it can be

seen, the first mode corresponds always to an out-of-plane translational deformation, which is explained by the fact that the stiffness of the structure in the out-of-plane direction (y-axis) is always smaller than the one computed along the in-plane direction (x-axis). Additionally, the values of all the computed 1st fundamental periods are between 0.39-0.44 seconds, a numerical phenomenon attributed to the similar out-of-plane stiffness of all four models (the infill RC walls are placed along the x-axis thus the stiffness along the y-axis direction is not affected considerably from the interventions). It is also important to note at this point that, the NEAK 2000 [197] formula derives a fundamental period equal to 0.441 seconds for the y-axis direction (H = 12 m, L = 6 m, ρ = 0), which constitutes a 0.22% accuracy of the numerical analysis (see Fig. 8.44a).

The corresponding 2nd fundamental period of the bare frame was an in-plane oscillation along the x-axis and the corresponding computed value was found to be 0.37 seconds that is 2.2% larger than the corresponding value predicted by NEAK 2000. It is also easy to observe that, the 2nd fundamental period decreases as the infill RC walls increase in height within the different retrofitting configurations (see Fig. 8.44b, Fig. 8.44c and Fig. 8.44d). This mechanical response was expected in this case given that the taller the infill RC walls get within the South and North frames, the stiffer the building's overall mechanical behavior becomes, thus the corresponding 2nd fundamental period decreases accordingly. Furthermore, it is important to note that the 2nd eigenmode for the one- and two-storey infill RC walls, and the fully retrofitted models derived an overall period duration decrease of 15%, 34% and 48%, respectively, compared to the bare frame. In addition to that, it is also easy to observe the significant difference in terms of horizontal deformations between the bare and the retrofitted floors (see Fig. 8.44b and Fig. 8.44c) for the case of the 2nd eigenmode. It is evident that the floors without retrofitting within these models (Fig. 8.44b and Fig. 8.44c) exhibit larger deformations in comparison to the retrofitted floors. This mechanical behavior is attributed to the significant increase of floor stiffness that converts the framing system into an irregular one, which as a consequence affects the dynamic response of the framing system.

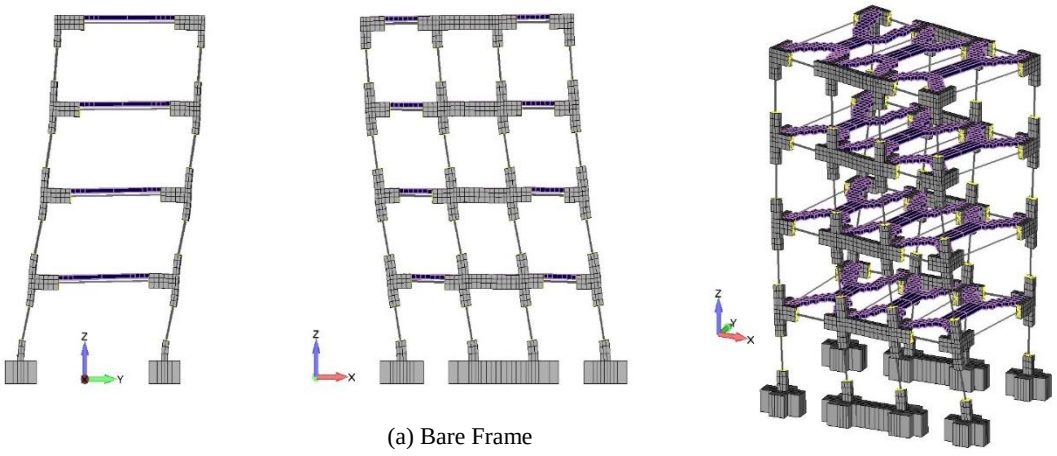

(a) Bare Frame

f_1 = 2.28 Hz, T_1 = 0.44 s f_2 = 2.74 Hz, T_2 = 0.37 s f_3 = 6.30 Hz, T_3 = 0.16 s

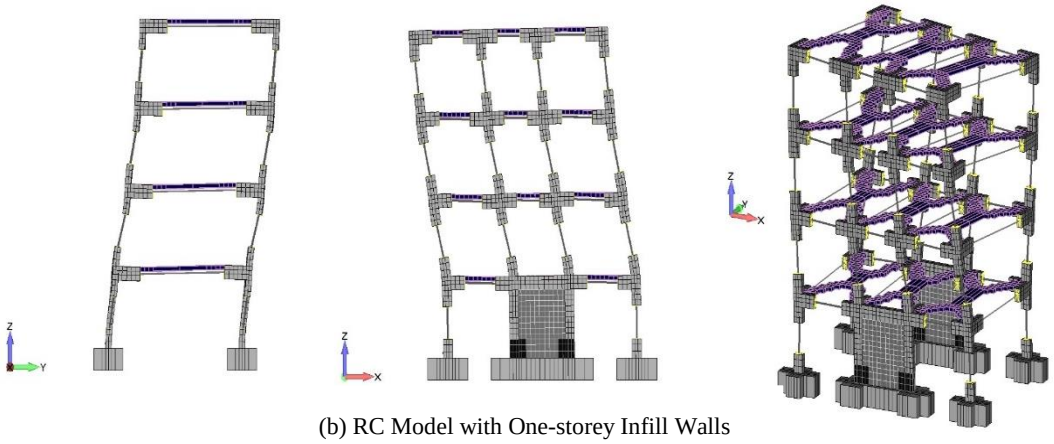

(b) RC Model with One-storey Infill Walls

f_1 = 2.38 Hz, T_1 = 0.42 s f_2 = 3.23 Hz, T_2 = 0.31 s f_3 = 6.36 Hz, T_3 = 0.16 s

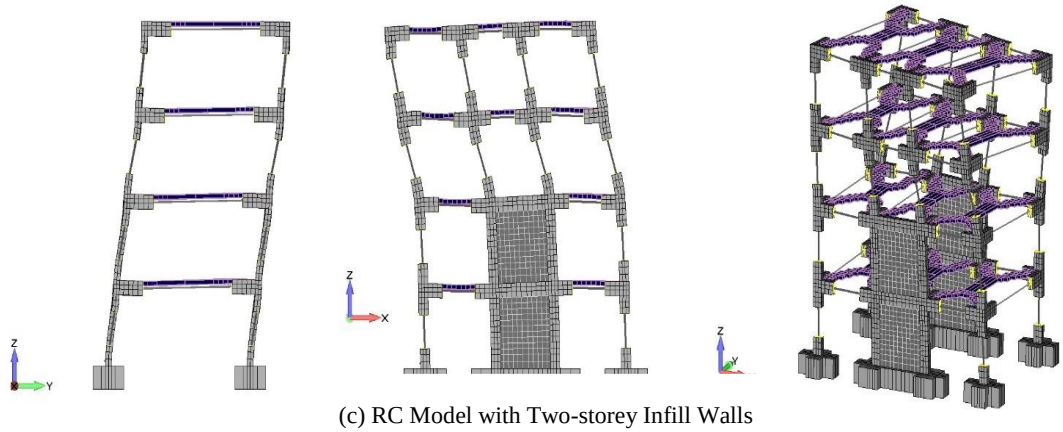

(c) RC Model with Two-storey Infill Walls

f_1 = 2.54 Hz, T_1 = 0.39 s f_2 = 4.16 Hz, T_2 = 0.24 s f_3 = 6.50 Hz, T_3 = 0.15 s

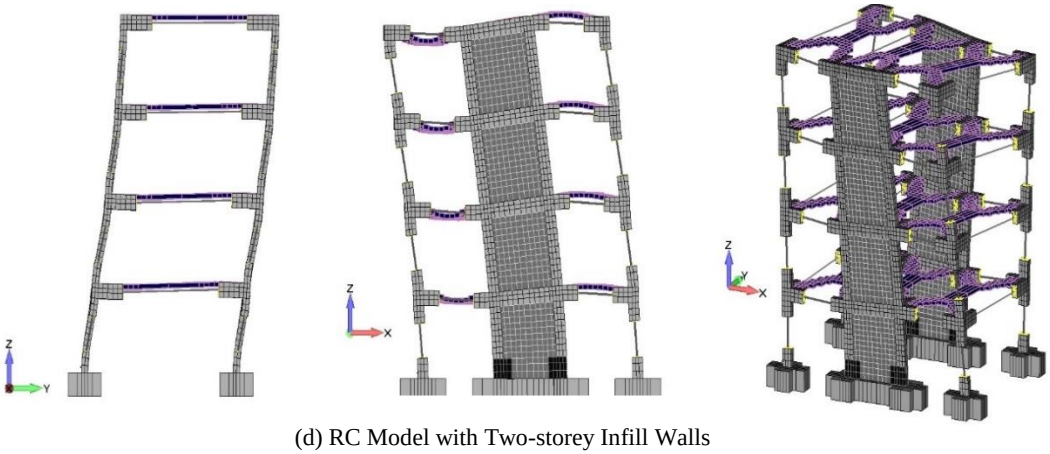

(d) RC Model with Two-storey Infill Walls

f_1 = 2.59 Hz, T_1 = 0.39 s f_2 = 5.28 Hz, T_2 = 0.19 s f_3 = 7.37 Hz, T_3 = 0.14 s

Fig. 8.44 Views of the eigenmodes of the four-storey building with different retrofitting configurations.

Finally, the 3rd eigenmode that derived though the use of all numerical models was found to be a rotational deformation about the z-axis with the last model (fully retrofitted frame shown in Fig. 8.44d) exhibiting the stiffest response with a 12.5% increase in terms of rotational stiffness compared to the bare frame. This numerical finding is connected to the placement of the infill

RC walls at all four levels of the frame, which affected the corresponding overall rotational stiffness of the building.

It is evident that, the modal analysis performed and discussed in this section illustrates the importance of selecting not only the proper retrofitting method when strengthening RC structures, but also investigate the effects that the selected geometry of the applied intervention can have on the overall mechanical behavior of the retrofitted framing system. Hence, according to the parametric investigation performed herein, it is strongly advisable to apply infill RC walls throughout the height of the structure (whenever this is architecturally feasible), while always perform full-scale analyses in allocating the weak areas of the retrofitted structure in the case where the designer foresees the use of infill RC walls at specific floors of the frame and not throughout its height.

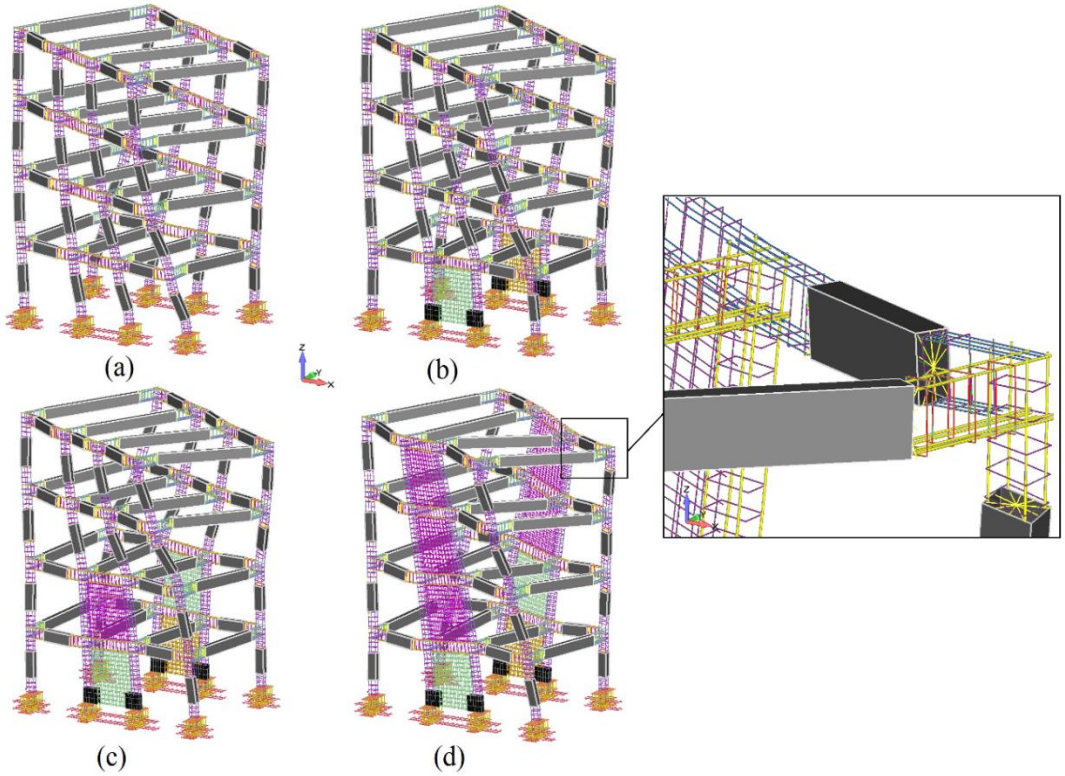

Fig. 8.45 3D views of the 3rd eigenmode of the models with (a) a bare frame, (b) one-storey infill RC walls, (c) two-storey infill RC walls and (d) fully retrofitted frame. Embedded rebar elements deformed views.

In order to further verify the developed algorithm that was used to perform the modal analysis, the deformed shape of the embedded rebar elements was visualized for all the derived eigenmodes. Fig. 8.45 shows the deformed shapes of the 3rd eigenshape for each model as they resulted from the modal analyses. In the illustrated views of Fig. 8.45, the slabs and all concrete hexahedral elements were deactivated from the model's view so as to reveal the deformed shape of the embedded rebar elements that were found in all cases to follow the deformed shape of the concrete domain. Finally, Table 8.11 shows the computational time for the solution stage of the modal analysis that were performed by using the four under study finite element HYMOD models (the requested number of modes was set to 12). As it can be seen, the required computational time to solve the modal analysis problem was between 30-37 seconds, which demonstrates the computational efficiency of the developed algorithm. The total required computational time, when computing and writing the results of the 12 first eigenmodes, including output file writing, was not more than 3 minutes for all numerical models.

To further investigate the algorithmic performance of the modal analysis implementation, two additional runs were performed through the use of the bare and fully retrofitted frame models in an attempt to compute the first 200 eigenmodes of the two framing systems. As it can be seen in Table 8.11, the corresponding modal analysis solution time was 170 and 233 seconds, respectively, which approximately corresponds to an overall average of 1 second per eigenmode. It must be noted here that, the writing procedure foresees the writing of the computed displacements for each node and the stresses and strains of each finite element's Gauss point. This makes the writing procedure of the output file time consuming, where more than 80% of the total computational time is dedicated to I/O processes (this applies for the case when the requested number of eigenmodes was set to 200). By deactivating the writing of stresses and strains, the I/O time can be decreased significantly (approximately by 90%), thus make this process more computationally efficient.

Table 8.11 Computational performance of the Modal Analysis Algorithm. Computing 12 eigenmodes.

a/a	Model	Number of Hexa Elements	Number of Embedded Rebar Elements	Total Number of Dofs	Modal Analysis Solution Time (s)	Total Comp. Time (m)
1	Bare Frame	5,500	14,546	32,028	30	1.82
2	Retrofitted 1	6,136	15,462	34,416	30	1.92
3	Retrofitted 2	6,868	17,162	37,764	31	2.13
4	Fully Retrofitted	8,356	20,646	43,896	37	2.68
5	Bare Frame	5,500	14,546	32,028	170*	19.08*
6	Fully Retrofitted	8,356	20,646	43,896	233*	27.65*

*Computing 200 eigenmodes.

8.6 Conclusions

A complete numerical investigation was performed and presented in this research work, which dealt with the full-scale nonlinear cyclic modeling of a four-storey RC building that was retrofitted with RC infill walls and CFRP jacketing. The experimental setup that foresaw the application of three consecutive loading histories was modeled and analyzed through the use of the HYMOD approach, which foresees the use of a 3D detailed FE mesh discretization of the shear-dominated parts of the structure, where the rest of the structural members are modeled through the computationally efficient NBCFB element.

Based on the numerical investigation that was presented herein, the developed proposed modeling approach managed to overcome the computational limitations when dealing with this type of problems, simulating the entire four-storey RC building for all loading tests based on the experimental data (3 cyclic loading history tests) without any numerical problems. It has to be noted that the proposed modeling approach did not foresee for any simplification assumptions, thus the geometry and the material properties fully complied with the experimental report.

Furthermore, the CFRP jacketing significantly plays an important role in terms of structural behavior, while the confined concrete regions developed smaller deformations that the unconfined locations due to the shifting of the plastic hinge. It must be further stressed out here that, the material properties used for the simulation of all cyclic loading tests presented in this research work, were the same throughout the numerical analyses, while all the material property values were equal to the material properties reported in Poljanšek et al. [42]. This numerical advantage minimized the required number of models used during the numerical investigation to just a single mesh that was adopted in performing all analyses. Furthermore, a final analysis

was performed and presented in section 8.4.4 for the case of a model that was developed by modifying the material property magnitudes of both steel and concrete materials (hardening modulus and tensile strength, respectively). This was done in order to investigate the numerical performance of the adopted modeling approach when indirectly accounting for the accumulated material damage due to consecutive cyclic loading excitations. The numerically obtained results showed that the hardening modulus of steel was the parameter that controlled the overall resistance of the framing system due to the high nonlinearities that were developed during the 3rd and final loading test. This numerical phenomenon highlights the importance of the material property magnitudes that have to be defined during the development of a FE model that is intended to be used for the assessment of a damaged or retrofitted RC building. For this reason, the need of objective numerical models that require the minimum number of material and modeling assumptions is imperative, especially when dealing with full-scale RC structural seismic assessment analyses.

Additionally, a numerical investigation has been performed for the four-strorey building with different RC wall retrofitting configurations. The numerical results show that the dissipating energy of the numerical model with the infill RC wall, was 500% larger than the bare frame model. Furthermore, the analysis shows that placing RC walls only in the 1st storey or in the first two-storeys can lead to local damage and premature failure of the structure. Finally, modal analysis was conducted and concluded that the models which were not retrofitted by using infill RC walls throughout the height of the structure present irregular stiffness distribution that causes the irregular deformation between the retrofitted and bare floors, and eventually leads to local damages of concrete.

The overall numerical response of the developed algorithm, in terms of its ability to capture the cyclic behavior of RC structures that have undergone consecutive cyclic excitations, was found to be satisfactory. Therefore, modeling and analyzing full-scale structures with 3D detailed models is now feasible, thus the proposed modeling method provides with the required tools to perform additional numerical investigations for the study of different retrofitting techniques in developing optimum retrofitting design recommendations.

Chapter 9. Nonlinear static cyclic and dynamic analysis of RC structures considering damage factors

Contents of Chapter 9

9.1 Introduction 213

9.2 Concrete and steel material constitutive models 214

9.3 Damage factor Dc for concrete 215

9.4 Damage factor Ds for steel reinforcement 217

9.5 Parametric investigation for defining constants a_n and a_s 221

9.6 Numerical Validation of the Proposed Model for Static Cyclic Analysis 224

9.6.1 RC Beam-Column Joint 224

9.6.2 RC Column 228

9.7 Numerical Validation of the Proposed Model for Dynamic Analysis 232

9.7.1 Two-Storey RC frames 232

9.7.1.1 Parametric investigation on the type of embedded element 239

9.7.1.2 Investigation of a modified crack closure criterion 241

9.7.1.3 Mesh-sensitivity Analysis 242

9.7.2 RC frame 245

9.7.3 Three-storey, three-bay RC frame subjected to High Intensity Ground Motions 249

9.8 Conclusions 258

9.1 Introduction

The accurate numerical simulation of (RC) structures under cyclic loading conditions has been a critical issue among many researchers over the last decades. Most constitutive material models are based on uniaxial laws with strain softening and tension stiffening characteristics. These models require many material parameters in order to capture the complex mechanical characteristics of concrete such as: micro-cracking, confinement, ductility, opening/closure of cracks and crushing. These studies indicate the necessity of a realistic constitutive law with parameters that have a direct physical meaning.

The complex behavior of RC structures under cyclic loading conditions makes the numerical procedure unstable, thus, it is more difficult to reach convergence when excessive cracking, rebar yielding and rebar rapture take place during the analysis. Therefore, a realistic 3D approach, which is characterized by simplicity and computational efficiency, is necessary in order to ensure accurate numerical simulations when trying to predict the carrying capacity of RC structures. A detailed literature review on the modeling of the behavior of RC structures under cyclic loading conditions was presented in Chapter 5 and Chapter 6, where a limited number of numerical approaches can be found implementing three-dimensional finite elements for the purposes of cyclic analysis.

In addition to that, very few of these numerical approaches managed to extend their static cyclic models to be implemented for solving dynamic problems. Inoue et al. [199] used the compression field theory for the dynamic analysis of RC shear walls implementing in plain stress elements for wall panels and 8-noded solid elements for slabs supported on wall panels. Cela [11] proposed an elastic-viscoplastic law, based on Drucker-Prager model, subjected to dynamic plain-stress loading conditions, while Kwan and Billington [15] suggested an elasticity-based model in order to analyze post-tensioned concrete piers by using 8-noded plane stress elements.

Ile and Reynouard [13] combined an elastoplastic isotropic uncracked behavior of concrete energy-based fracture with a smeared crack approach, for modeling the cracked concrete with the two-dimensional plane element. Han et al. [200] also proposed a fracture energy-based rotating crack model by using 2D plane elements to analyze a three-storey frame building under a seismic excitation. Mirzabozorg and Ghaemian [201] used a three-dimensional smeared crack approach with 20-noded isoparametric hexahedral elements, to study concrete gravity dams. In their work, the investigators placed emphasis on the simplicity of the model by using a small number of material parameters.

Other researchers used constitutive models which are based on the principles of continuum damage mechanics. Mazars et al. [202] proposed a lattice model to investigate shear walls under dynamic loads. Faria et al. [203] used 20-noded solid elements and 8-noded plane stress elements to analyze the seismic behavior of an arc dam and a RC wall. Richard and Ragueneau [164], proposed the coupling between plasticity and damage modeling. Plasticity is used for the description of concrete in compression, whereas isotropic damage is used for tension. As stated in their work [164], the pathology of mesh-dependency issues was reduced by adopting a nonlocal approach proposed in [165]. Additionally, Vassaux et al. [166] used a discrete model to define and calibrate quantities such as i) proportional of closed cracks and ii) specific dissipated energy related to friction. These quantities were introduced to the previous model in order to describe the hysteretic behavior of concrete structures obtained by crack closure and friction.

Finally, few researchers conducted 3D dynamic analysis by using 3D constitutive models. Spiliopoulos and Lykidis [176], and Cotsovos [204] used the triaxial constitutive model,

introduced by Kotsovos & Pavlovic [29], integrated in 27-noded hexahedral elements. The latter introduce some restrictions with regard to the number of cracks that are allowed to open in each iteration, in an attempt to obtain convergence during the analysis. Moharrami and Koutromanos [160] proposed a 3D constitutive model, which combines the elastoplastic and smeared crack approaches in order to describe the cyclic and dynamic behavior of concrete. It is noteworthy to say here that, none of these researchers investigated the computational efficiency of their proposed models, which is deemed crucial when dealing with full-scale dynamic nonlinear analyses of RC structures.

Most of the studies found in the literature are restricted to 2D analysis in order to capture the biaxial behavior of concrete structures, thus do not provide the numerical tools to study the realistic 3D mechanical behavior of RC structures. In some cases, material models use many numerical restrictions to accomplish stability of their analysis, while other models use complex mathematical procedures in order to describe the nonlinear characteristics of concrete. These customized models are consisted by many material parameters and thus are found to be unable to demonstrate objectivity and numerical robustness for different types of mechanical behaviors and structural geometries. Furthermore, it is evident that a numerical tool, which places emphasis on the simplicity of its formulation and provides numerical robustness and efficiency for the nonlinear cyclic static and dynamic analysis, has to be developed.

The proposed model in this work, describes the triaxial behavior of concrete without the need of introducing a large number of concrete material parameters. The accuracy, numerical simplicity and the computational efficiency are the most important features in order to show the practical use of any model in predicting the nonlinear static and dynamic behavior of RC structures. The proposed model adopts the numerical approach, proposed in Chapter 5 (for cyclic loading conditions), thus it is further integrated herein for simulating the dynamic response of RC structures. A new concrete damage factor is presented, which derives from the number of opening/closure cracks, while a second damage factor for steel is also introduced in this work. A thorough numerical investigation has been conducted in order to study the computational efficiency and accuracy of the proposed procedure and presented in sections 9.6 and 9.7. The use of rod and beam embedded rebar elements for the simulation of the steel reinforcement was also examined and presented in section 9.7, where a mesh sensitivity investigation discusses the objectivity of the proposed modeling method.

9.2 Concrete and steel material constitutive models

A realistic 3D behavior of concrete can be achieved by taking into account in the constitutive material model the out of plane stresses, associated with the triaxial stress-strain phenomena that affect the overall mechanical behavior of the material. As it was shown in Chapter 5, in the adopted material model, each state of stress-strain is mathematically described by hydrostatic and deviatoric components, using two moduli of elasticity (bulk K and shear G) and an equivalent external stress (σ_{id}) in order to describe the constitutive relations. The criterion, presented in Chapter 5, uses the strains associated with the initial formation of the cracks in order to determine whether a closing crack will be eventually closed during the numerical procedure. The criterion of closing crack is described through the Eqs. (5.88) and (5.89).

For the Eq. (5.89), the maximum strain ε_{max} is determined through the nonlinear Newton-Raphson procedure, whereas, in every internal Newton-Raphson iteration, the strains are calculated along the norm of the crack planes. Therefore, during an internal iteration, when a crack is formed at a Gauss point, it is assumed that $\varepsilon_{max} = \varepsilon_{cr}$. Then, for every Newton-Raphson *i* iteration the strains ε_i normal to the crack planes are checked if they are larger than the previously calculated ε_{max}. If this is the case, then ε_{max} is set equal to ε_i. More details regarding

the closing crack criterion can be found in Chapter 5 and Chapter 6, where it is assumed that the elastic constitutive matrix is used to calculate the stresses of the previously cracked Gauss point. In this chapter, an improvement is proposed concerning the formulation of the constitutive matrix of the previously cracked Gauss point, by introducing a damage factor for the concrete material. For the case of the steel material model, a damage factor is also adopted in conjunction with the Menegotto-Pinto material model, which will be discussed in section 9.4.

9.3 Damage factor Dc for concrete

During strong earthquake motions, RC structures develop excessive nonlinear behavior that is caused mainly by the intense cracking of concrete, where the steel reinforcement can also yield or rapture. The number of cracks that open is an indication of the magnitude of damage that has occurred at each RC member. Generally, the material deterioration caused by the opening and closing of cracks can determine the hysteretic behavior of the structure.

Many researchers tried to simulate the hysteretic behavior of RC structures by using damping mechanisms. The damping behavior of RC structures is still an open subject of research. Most of the studies assume a constant viscous damping with high values of damping ratios throughout the nonlinear analysis, by using the Rayleigh or a proportional damping model. In this case, the hysteretic curves, which are obtained from the numerical analysis, are characterized as constant ellipses, where the mechanical behavior of the structure is attributed to the viscosity mechanisms that are activated during the nonlinear dynamic response.

However, the experimentally derived hysteretic loops are usually characterized by more abrupt changes in terms of stiffness, while the corresponding P-δ curves present significant pinching effects. A numerical simulation of damping effect based on the hysteretic behavior of the structure could result in a more rigorous formulation in capturing the dynamic response and the complicated physical phenomena that occur due to the opening and closing of cracks. In this article, the concrete material deterioration is integrated with a new damage factor that is directly connected to the phenomenon of opening and closing of cracks in order to better describe the hysteretic behavior of RC structures and capture the pitching effect.

The material deterioration factor has to take into account the level of cracking (damage), the number of times that a crack has been closed and generally, to be associated with the dissipated energy that occurs due to the nonlinear structural behavior. The parameter *a* in Eq. (5.89), which is used in the crack closing criterion (Chapter 5), is an expression of the strains that were developed at a cracked GP after the crack opening. It is, therefore, a quantity that expresses the level of energy that is consumed at a cracked GP. When parameter *a* increases, the consumed energy increases and the damage of the structural member becomes more pronounced due to the material deterioration. Moreover, the expression -(1-*a*) is proportional to the damage that occurs at a cracked GP (this expression is suitable when used within an exponential function that outputs values lower than 1, considering that $0 \le a \le 1$). When a crack opens and closes, material damage is accumulated because of the developed irreversible strains at that specific area. It is obvious that the more times the cracks are closing and opening at a certain area, this area loses the ability to retrieve the uncracked stiffness. Based on this mechanism, the expression of the damage factor that is proposed in this work takes the following form:

$$D_c = e^{-(1-a)/f_{cc}} = e^{-\left(1-\left(1-\frac{\varepsilon_{cr}}{\varepsilon_{\max}}\right)\right)/f_{cc}} = e^{-\left(\frac{\varepsilon_{cr}}{\varepsilon_{\max}}\right)/f_{cc}} \tag{9.1}$$

where f_{cc} is the number of times that a crack has closed, which is updated at every Newton-Raphson iteration for each GP. A schematic representation of Eq. (9.1) can be seen in the Fig. 9.1.

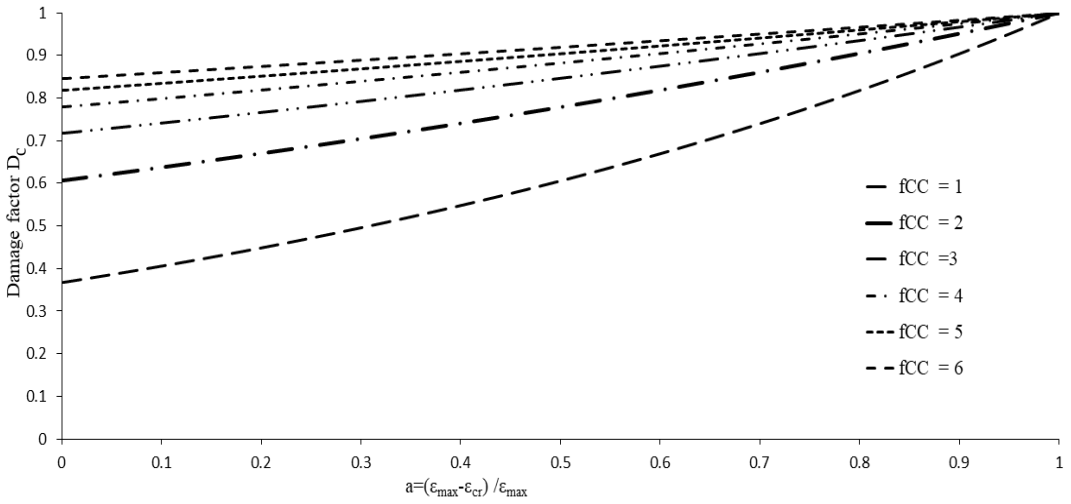

Fig. 9.1 Schematic representation of the values of the damage factor D_c as a function of the parameter a and f_{CC}.

When the criterion of crack-closure (Eq. (5.88)) at a GP is satisfied, (assuming that this GP had prior to that only one crack formation), a part of the stiffness is lost (according to Fig. 9.1) along the previous crack plane, which was assumed to form in an orthogonal direction to the maximum principle tensile stress. Therefore, the stiffness degradation is directly connected to the number of times a crack has opened and closed, thus accumulating the energy loss due to this phenomenon. By assuming that the crack is formed perpendicular to the x' axis and by using Eq. (5.80), the constitutive matrix takes the following form:

$$\boldsymbol{C}_l^{'}=\begin{bmatrix} a_n\cdot(1-D_c)\cdot(2G_t+\mu) & a_n\cdot(1-D_c)\cdot\mu & a_n\cdot(1-D_c)\cdot\mu & 0 & 0 & 0 \\ a_n\cdot(1-D_c)\cdot\mu & 2G_t+\mu & \mu & 0 & 0 & 0 \\ a_n\cdot(1-D_c)\cdot\mu & \mu & 2G_t+\mu & 0 & 0 & 0 \\ 0 & 0 & 0 & a_s\cdot(1-D_c)\cdot\beta\cdot G_t & 0 & 0 \\ 0 & 0 & 0 & 0 & a_s\cdot(1-D_c)\cdot\beta\cdot G_t & 0 \\ 0 & 0 & 0 & 0 & 0 & a_s\cdot(1-D_c)\cdot\beta\cdot G_t \end{bmatrix} \quad (9.2)$$

where β is a shear retention factor and, a_n and a_s are constants with recommended values of 0.25 and 0.125, respectively. The parameters a_n and a_s were defined following a parametric investigation conducted through the use of a number of RC structural members subjected to cyclic loading conditions, which will be presented in section 9.5. Similarly, in the case when two cracks are closing and assuming that the cracks were perpendicular to the x' and y' axes the constitutive matrix takes the following form:

$$\boldsymbol{C}_l^{'}=\begin{bmatrix} a_n\cdot(1-D_c)\cdot(2G_t+\mu) & a_n\cdot(1-D_c)\cdot\mu & a_n\cdot(1-D_c)\cdot\mu & 0 & 0 & 0 \\ a_n\cdot(1-D_c)\cdot\mu & a_n\cdot(1-D_c)\cdot(2G_t+\mu) & a_n\cdot(1-D_c)\cdot\mu & 0 & 0 & 0 \\ a_n\cdot(1-D_c)\cdot\mu & a_n\cdot(1-D_c)\cdot\mu & 2G_t+\mu & 0 & 0 & 0 \\ 0 & 0 & 0 & a_s\cdot(1-D_c)\cdot\beta\cdot G_t & 0 & 0 \\ 0 & 0 & 0 & 0 & a_s\cdot(1-D_c)\cdot\beta\cdot G_t & 0 \\ 0 & 0 & 0 & 0 & 0 & a_s\cdot(1-D_c)\cdot\beta\cdot G_t \end{bmatrix} \quad (9.3)$$

The proposed expressions of the constitutive matrix (Eqs. (9.2) and (9.3)) describes the anisotropic behavior of concrete at the local coordinate system, therefore, it has to be transformed to the global system by using the standard coordinate system transformation laws as follows:

$$\boldsymbol{C}_g = \boldsymbol{T}^T \boldsymbol{C}_l \boldsymbol{T} \tag{9.4}$$

where T is the transformation matrix given in Eq. (9.5) with the direction cosines given by (l_i, m_i, n_i), which define the relative orientation of the i-axis of the system (x′, y′, z′) to (x, y, z), respectively.

$$\boldsymbol{T} = \begin{bmatrix} l_1^2 & m_1^2 & n_1^2 & l_1 m_1 & m_1 n_1 & n_1 l_1 \\ l_2^2 & m_2^2 & n_2^2 & l_2 m_2 & m_2 n_2 & n_2 l_2 \\ l_3^2 & m_3^2 & n_3^2 & l_3 m_3 & m_3 n_3 & n_3 l_3 \\ 2l_1 l_2 & 2m_1 m_2 & 2n_1 n_2 & l_1 m_2 + l_2 m_1 & m_1 n_2 + m_2 n_1 & n_1 l_2 + n_2 l_1 \\ 2l_3 l_1 & 2m_3 m_1 & 2n_3 n_1 & l_3 m_1 + l_1 m_3 & m_3 n_1 + m_1 n_3 & n_3 l_1 + n_1 l_3 \\ 2l_2 l_3 & 2m_2 m_3 & 2n_2 n_3 & l_2 m_3 + l_3 m_2 & m_2 n_3 + m_3 n_2 & n_2 l_3 + n_3 l_2 \end{bmatrix} \tag{9.5}$$

It must be noted here that, the constitutive matrix correspond to the cases when a crack is closed at a GP, which had previously one, two or three cracks. After the crack closure, the stresses are corrected by using the following expression:

$$\boldsymbol{\sigma}^i = \boldsymbol{\sigma}^{i-1} + \boldsymbol{C}_g \cdot \boldsymbol{\Delta\varepsilon}^i \tag{9.6}$$

Finally, when all cracks at a GP have been closed (uncracked Gauss point) and the reduction factor of one of the previous cracks is larger than 0.5, then the constitutive matrix takes the following form:

$$\boldsymbol{C}_g{}' = (1 - D_c) \cdot \boldsymbol{C}_g \tag{9.7}$$

It was found via a numerical investigation that when the reduction factor of one of the previous cracks is larger than 0.5, then the accumulated damage is severe and Eq. (9.7) has to be implemented in order to take this phenomenon into account when the GP is considered uncracked. The proposed algorithms for treating cracked and uncracked Gauss points are described in the flow charts presented in Figs. Fig. 9.2, Fig. 9.3 and Fig. 9.4. The flow charts present the algorithm that is used in order to update the stresses of the previous (i-1) Newton-Raphson internal iteration to the current one (i).

9.4 Damage factor Ds for steel reinforcement

The steel reinforcement is modelled through the use of the Menegotto-Pinto [34] model that takes into account the Bauschinger effect. In shear dominated areas of a RC structure, the severe inclined cracking leads to significant strength deterioration of steel reinforcement thus affecting hysteretic loops of the entire RC member. Experimental results show that RC structures with significant shear deformations develop severe pinching characteristics around zero load. In these shear dominated areas, the steel reinforcement also develops shear deformations and debonding effects from concrete. The re-opening and re-closing of cracks at low level of shear forces enhance the slipping phenomena and leads to significant stiffness and strength

deterioration of the structure. The influence of opening and closing cracks to the pinching phenomenon is described experimentally in [35,36]. The influence of the pinching effect may be modelled by a modification of the steel stress-strain relation as described in [20]. Thus, the pinching phenomenon can indirectly be taken into account by using a reduced stiffness contribution of the steel reinforcement, thus defining the accumulated damage due to the crack opening/closure effect. This reduction can also be characterized as the loss of bonding between steel reinforcement with the surrounding damaged concrete.

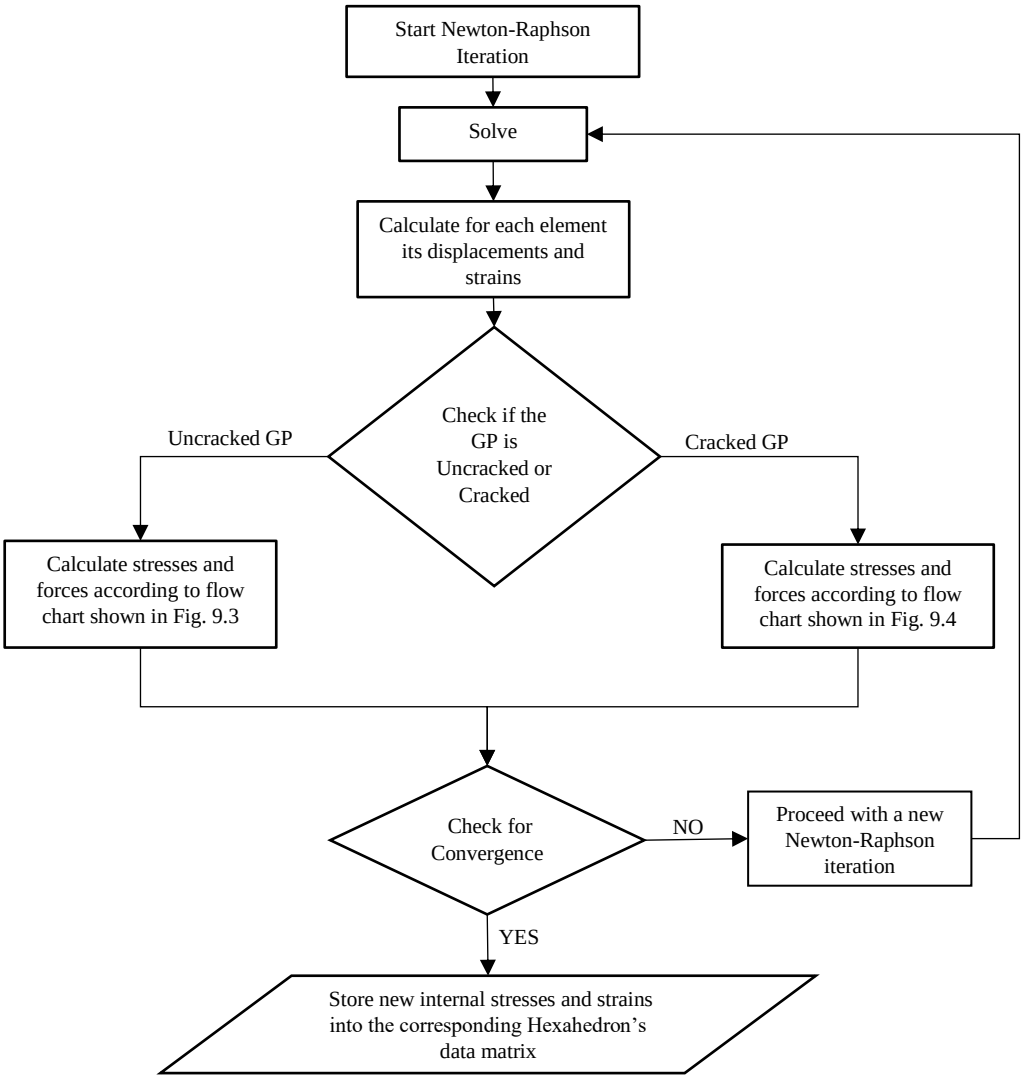

Fig. 9.2 Flow chart of the proposed algorithm of the concrete material model.

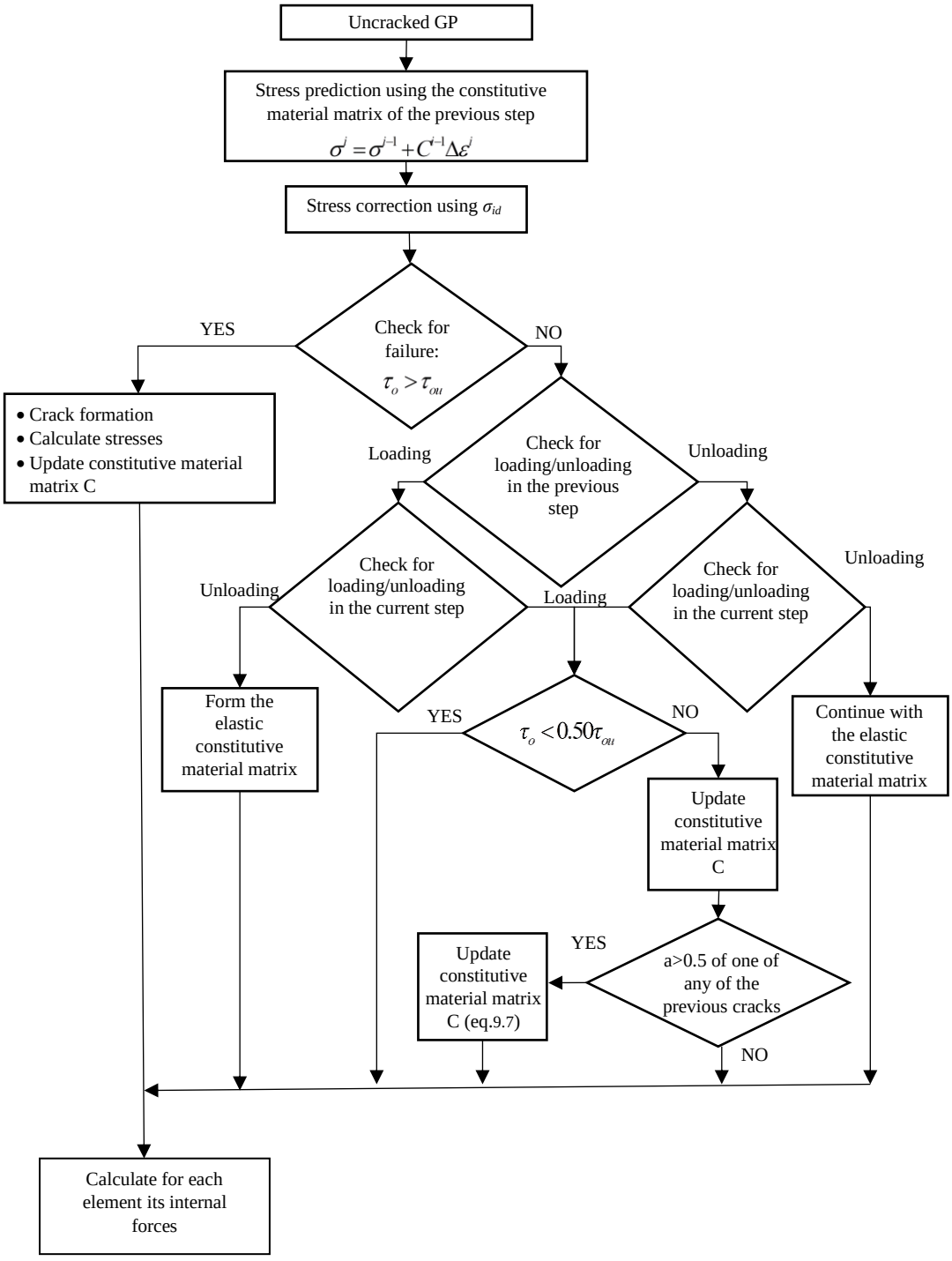

Fig. 9.3 Flow chart of the proposed algorithm for updating the stress-strain tensors and constitutive matrix for the case of an uncracked Gauss point.

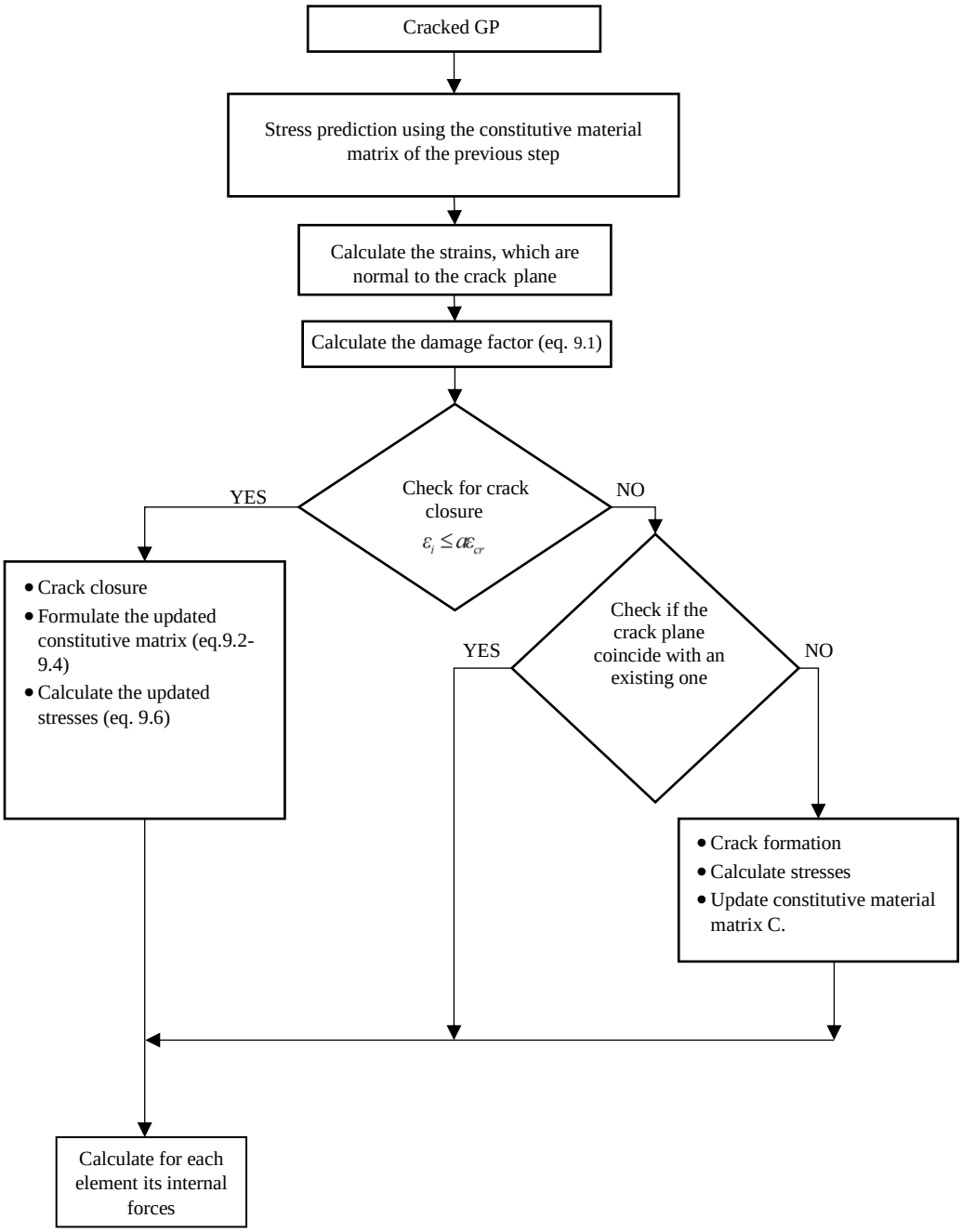

Fig. 9.4 Flow chart of the proposed algorithm for updating the stress-strain tensors and constitutive matrix for the case of a cracked Gauss point.

The level of damage that occurs due to the opening of cracks can be expressed by Eq. (5.89), Eqs (9.1)-(9.3). The average value of all parameters *a* (Eq. (5.89)), at the 8 Gauss points within a single hexahedral finite element, can determine the level of damage within the volume of the hexahedral element which can be expressed by the following expression:

$$D_s = \left[1 - a_{Element}\right] \tag{9.8}$$

where,

$$a_{Element} = \frac{\sum_{1}^{ncr} a_i}{ncr} \text{ and } ncr \text{ is the number of cracked Gauss points} \quad (9.9)$$

In the case of unloading, when the structure reaches zero deformation, a material deterioration of the steel reinforcement is estimated according to the following expression:

$$E_s^{'} = (1 - D_s) E_s \quad (9.10)$$

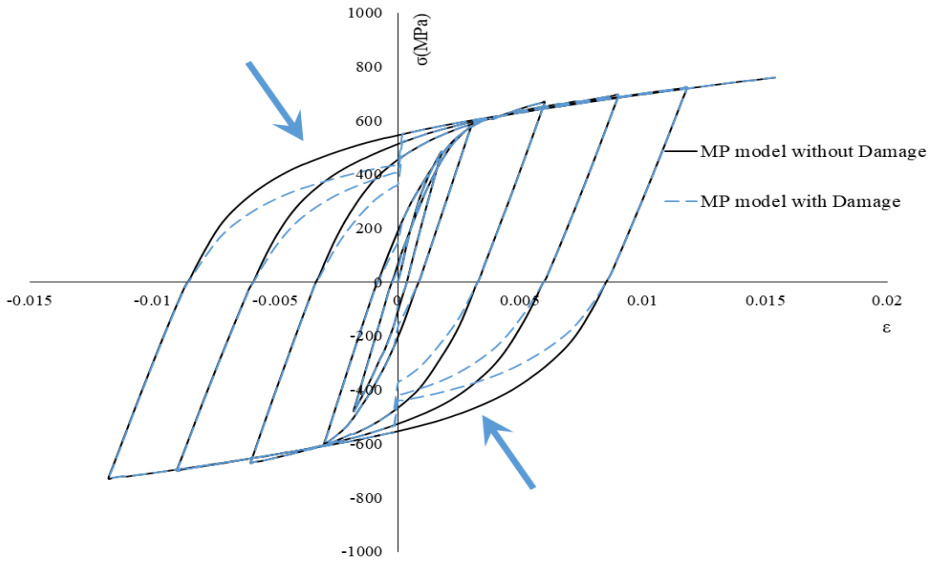

Fig. 9.5 Menegotto-Pinto steel model that accounts for the accumulated damage due to the opening and closure of cracks.

The material deterioration is applied when $\sigma_s \cdot \varepsilon_s < 0$, which describes the situations when crack closures and re-openings occur and the pinching phenomena are excessive. The σ-ε curves of the Menegotto-Pinto material model that uses the proposed steel damage factor is shown in Fig. 9.5.

According to ([162], [205]), the pinching phenomenon, which leads to the reduction of the energy dissipation capacity, is eliminated by the proper orientation of steel grid that is aligned to the direction of the applied principal stresses. Therefore, it is difficult to always explain the causes of the appearance of these pinching characteristics. The proposed modification of the steel Menegotto-Pinto model is a direct way to capture this phenomenon by taking into account the level of cracking that occurred in the surrounding area of the steel rebar, which in this case is the hexahedral element that hosts the embedded rebar. The proposed damage factors D_c and D_s are investigated in section 9.6, while the parametric investigation for defining the values of the parameters a_n and a_s is presented in the following section.

9.5 Parametric investigation for defining constants a_n and a_s

The Del Toro Rivera [178] interior frame joint of Fig. 6.19, which was analyzed in Chapter 6, is used to investigate and define the optimum values of the constant parameters a_n and a_s. The numerical results obtained for this model in Chapter 6 are defined herein as the results obtained by the "initial model" that does not use the proposed damage factors. The structural member

was subjected to different cyclic loading conditions according to the experimental test. The geometry and reinforcement details can be seen in Fig. 6.19. The concrete domain was discretized with 8-noded hexahedral finite elements and the steel reinforcement was discretized with beam elements. In order to avoid inducing parasitic stiffness within the numerical model when the cracking will occur, the values of the parameters a_n and a_s have to be lower than 1 to account for the stiffness reduction due to the material deterioration. Numerous combinations of the values of a_n and a_s have been tested, where the results of the five combinations that were found to better capture the experimental data are shown in Table 9.1.

Table 9.1 Combinations of the values a_n and a_s that were investigated.

Combination	a_n	a_s
1	0.25	0.125
2	0.5	0.5
3	0.5	0.125
4	1	1
5	0.125	0.125

The computed curves are given in Fig. 9.6, where it can be seen that the numerically obtained results match very well the experimental data. It was also found that the values of a_n and a_s have influenced the dissipated energy that derived from the hysteretic curves. Table 9.2, Table 9.3 and Table 9.4, show the values of the dissipated energy (as the area of every hysteretic curve) that were obtained by using different set of parameter values (a_n, a_s). It can be seen that the numerical curves with the smallest divergence were obtained when using the set of values of a_n = 0.25 and a_s = 0.125.

Furthermore, the load carrying capacity of the specimen was accurately predicted by all the numerical curves (divergences ≤ 15%). Table 9.5 and Table 9.6, show the comparison of the initial model and the proposed model with the experimental data in terms of maximum horizontal load for each loading cycle.

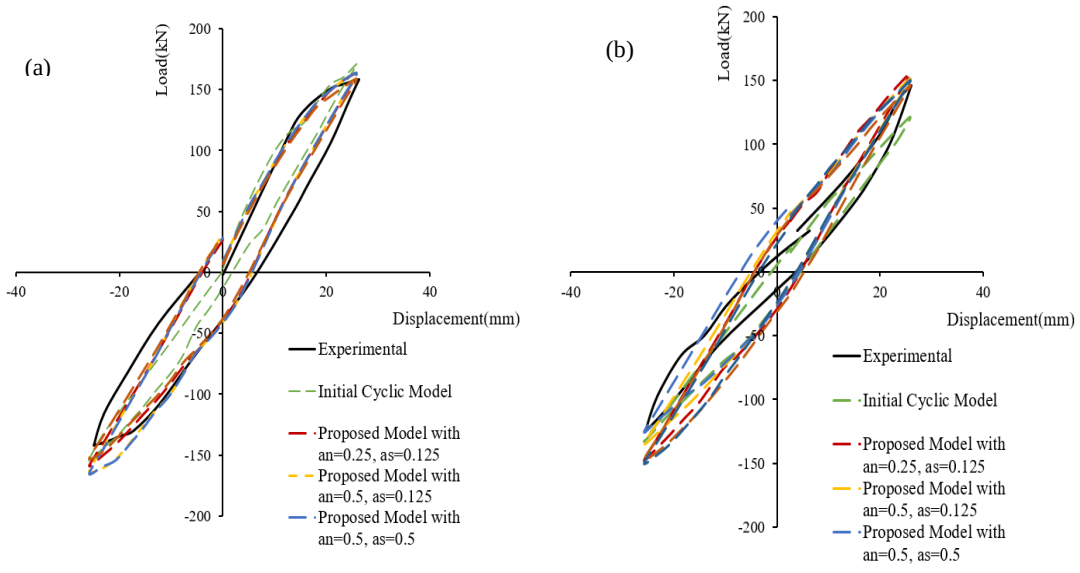

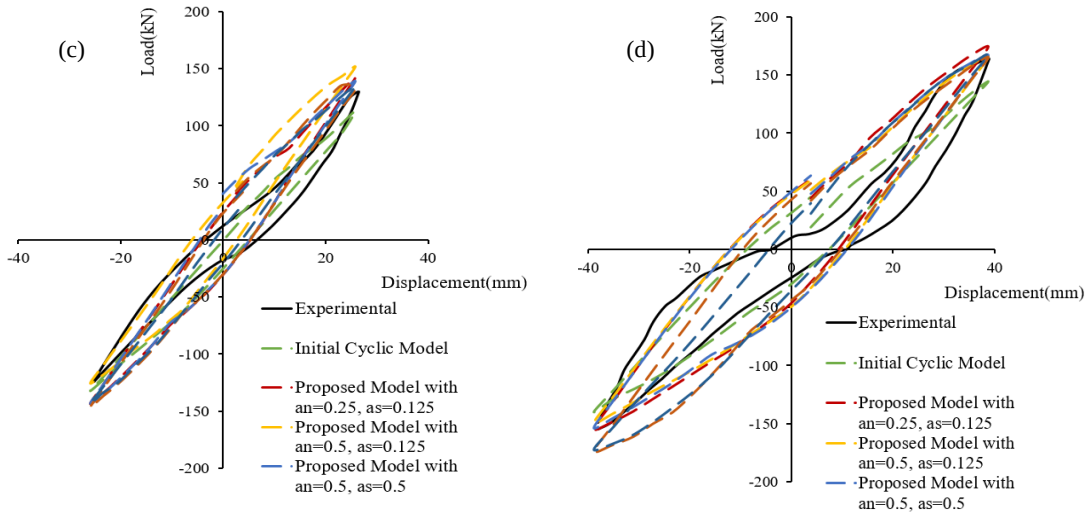

Fig. 9.6 Interior frame joint. Comparison between numerical and experimental results with different values of a_n and a_s for the cases of (a) first cycle (b) second cycle, (c) third cycle and (d) forth cycle.

Table 9.2 Comparison of the dissipated energy between experimental results and the proposed numerical model.

Loading Cycle	Dissipated Energy Experimental (kN mm)	Dissipated Energy Initial Model (kN mm)	Divergence from experimental (%)	Dissipated Energy Proposed Model a_n=0.25,a_s=0.125 (kN mm)	Divergence from experimental (%)
1st	2596.34	1165.14	55.12	1933.84	25.52
2nd	1264.12	669.37	47.05	1560.56	23.45
3rd	1212.48	942.65	22.25	1570.65	29.54
4th	3287.87	1953.10	40.60	4335.26	31.86
		Average	41.26	Average	27.59

Table 9.3 Comparison of the dissipated energy between experimental results and the numerical model with a_n = 0.5 and a_s = 0.5, 0.125.

Loading Cycle	Dissipated Energy Experimental (kN mm)	Dissipated Energy Proposed Model a_n=0.5, a_s=0.5 (kN mm)	Divergence from experimental (%)	Dissipated Energy Proposed Model a_n=0.5, a_s=0.125 (kN mm)	Divergence from experimental (%)
1st	2596.34	2150.51	17.17	2187.91	15.73
2nd	1264.12	1843.40	45.82	1598.99	26.49
3rd	1212.48	1727.10	42.44	1727.10	42.44
4th	3287.87	4450.10	35.35	4365.63	32.78
		Average	35.20	Average	29.36

Table 9.4 Comparison of the dissipated energy between experimental results and the numerical model with a_n = 0.125 and a_s = 0.125.

Loading Cycle	Dissipated Energy Experimental (kN mm)	Dissipated Energy Predicted Proposed a_n=1, a_s=1 (kN mm)	Divergence from experimental (%)	Dissipated Energy Predicted Proposed a_n=0.125, a_s=0.125 (kN mm)	Divergence from experimental (%)
1st	2596.34	2168.55	16.48	1928.35	25.73
2nd	1264.12	1771.44	40.13	1793.78	41.90
3rd	1212.48	1820.81	50.17	1721.63	41.99
4th	3287.87	4197.97	27.68	4039.17	22.85
		Average	33.62	Average	33.12

Table 9.5 Comparison of the horizontal load of each cycle between experimental and numerical results of the initial model.

Loading Cycle	Horizontal Load Experimental (kN)		Horizontal load Predicted Initial (kN)		Divergence from Experimental	
	Positive	Negative	Positive	Negative	Positive (%)	Negative (%)
1st	158	-142	177	-165	12.03	16.20
2nd	146	-126	125	-146	14.38	15.87
3rd	130	-124	118	-139	9.23	12.10
4th	164	-154	144	-178	12.20	15.58
				Avg.	11.96	14.94

Table 9.6 Comparison of the horizontal load of each cycle between experimental and numerical results of the proposed model.

Loading Cycle	Horizontal Load Experimental (kN)		Horizontal load Predicted Proposed (kN)		Divergence from Experimental	
	Positive	Negative	Positive	Negative	Positive (%)	Negative (%)
1st	158	-142	162	-159	2.58	11.83
2nd	146	-126	156	-148	6.66	17.63
3rd	130	-124	142	-144	9.49	15.82
4th	164	-154	175	-155	6.59	0.65
				Avg.	6.33	11.48

9.6 Numerical Validation of the Proposed Model for Static Cyclic Analysis

In this section, the numerical validation of the proposed model will be presented for the case of static cyclic analysis under ultimate loading conditions. It must be noted at this point that all the numerical tests presented in this research work have been performed by using a computer with a processing power of 2.50 GHz.

9.6.1 RC Beam-Column Joint

The beam-column joint shown in Fig. 9.7, was tested by Shiohara and Kusuhara [38] under static cyclic loading. The uniaxial compressive concrete strength was reported to be equal to f_c = 28.3 MPa and the yielding stress of the steel reinforcement was 456 MPa for the 13 mm diameter bars in the beam section, while the yielding stress of the bars, placed within the column section, was 357 MPa. The Young modulus of elasticity for the longitudinal bar reinforcement was reported to be equal to E_S = 176 GPa. For the stirrup reinforcement, 6 mm in diameter rebars were used with a yielding stress of 326 MPa and a Young modulus of elasticity equal to 151 GPa.

The frame joint was subjected to different cyclic loading sets according to the experiment. The loading history that was numerically applied in this work, is presented in the form of 15 cycles of imposed displacements in Fig. 9.8. The concrete domain was discretized with 8-noded hexahedral finite elements and the steel reinforcement was discretized with beam elements. A total number of 128 concrete (23cm x 15cm x 15cm) and 888 steel elements were used to discretize the entire frame joint, as illustrated in Fig. 9.9.

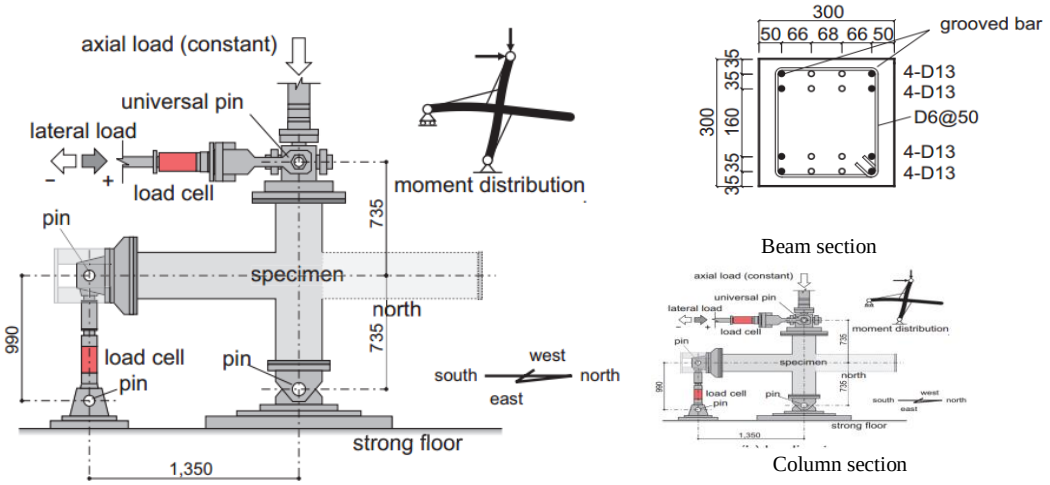

Fig. 9.7 Geometry and reinforcement details of the beam-column joint [38]. *All dimensions are in mm.*

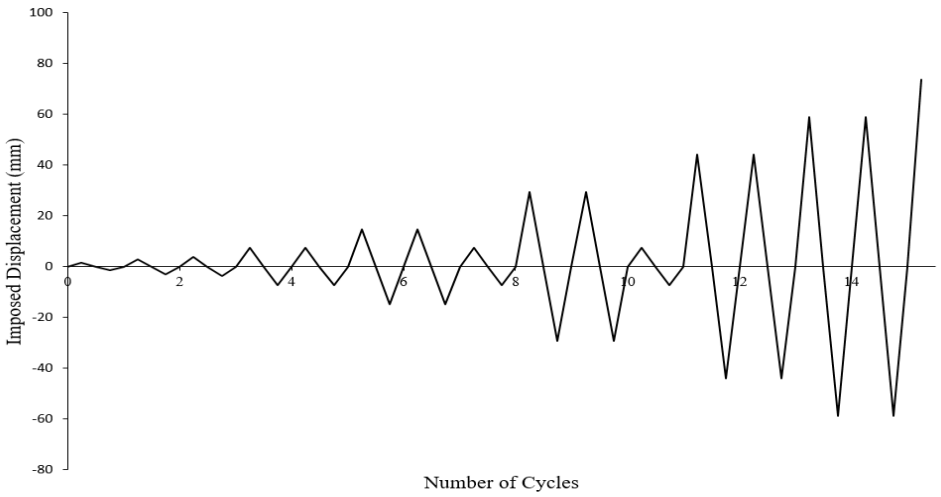

Fig. 9.8 Imposed displacement history of the interior frame joint.

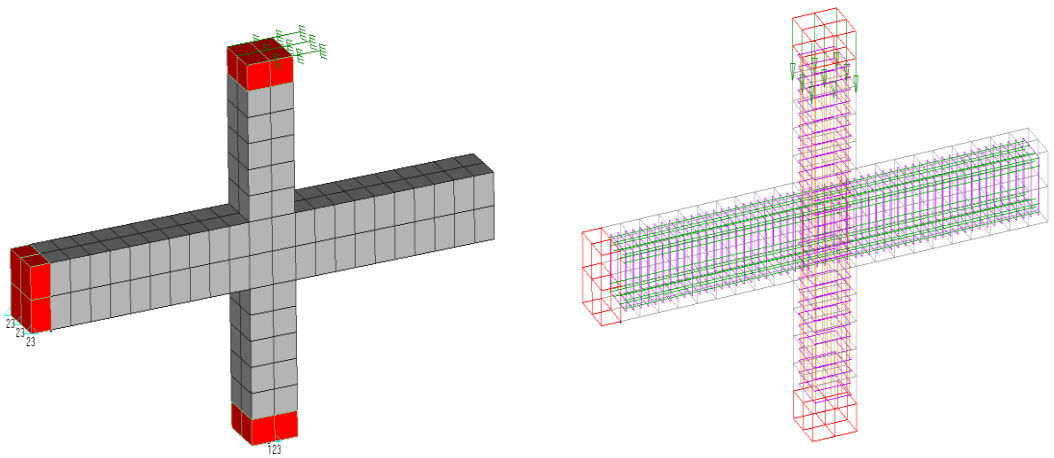

(a) (b)

Fig. 9.9 RC beam-column frame joint. (a) FE concrete mesh with imposed displacements, (b) steel reinforcement elements and applied loads.

The boundary conditions of the numerical model can be seen in Fig. 9.9, where the displacements were imposed at the top section of the column, while a 216 KN compressive force was also applied at the same section. Additionally, 8-noded hexahedral finite elements were used at the support and at the top sections of the column (red color, where the displacements are imposed) in order to simulate the metallic plates, which were placed in order to avoid local failure.

The computed force-displacement curves are compared with the corresponding experimental data in Fig. 9.10. As can be seen, the numerical results match very well with the experimental data, where the stiffness and the resulted load-carrying capacity of the specimen were predicted in an accurate manner. Furthermore, the numerical energy dissipation values are very close to the experimental ones. Fig. 9.10 also shows the force-displacement curve when the proposed modification for the Menegotto-Pinto model is not applied (the D_S damage factor is set to 0). Furthermore, the numerical results show that the proposed modification manages to capture the pinching effect in the case where both proposed damage factors were activated. During the analysis, the steel rebars did not develop severe yielding but a bond degradation has occurred due to the opening of diagonal cracks inside the joint, according to the experimental results reported in [38]. This observation indicates the importance of accounting the damage within the concrete domain and numerically transferring it to the steel rebars through the proposed damage factor D_S

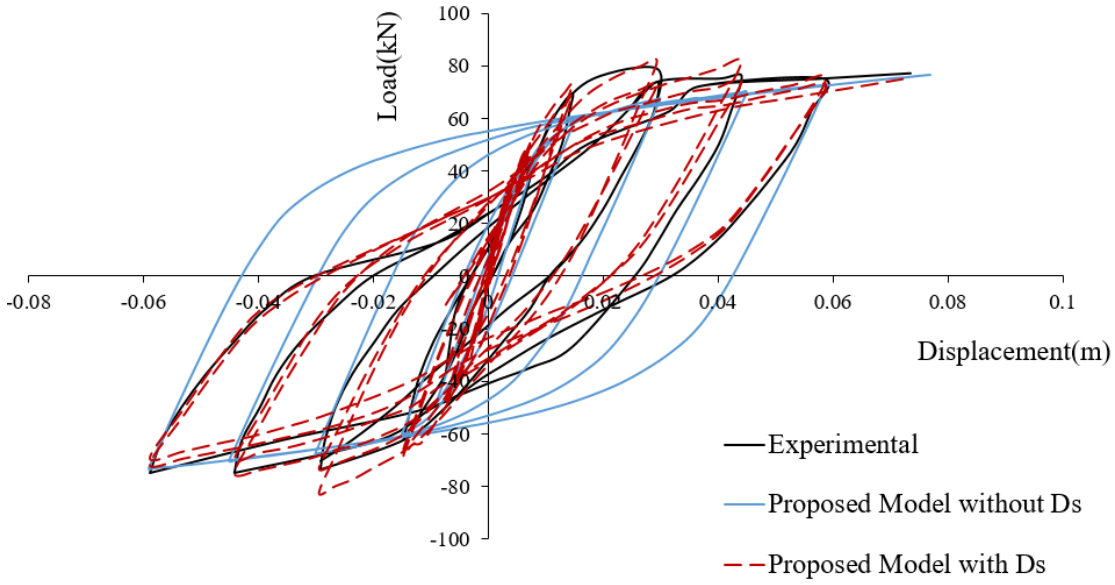

Fig. 9.10 Beam-Column frame joint. Comparison between numerical and experimental results. Complete force-displacement history.

Additionally, Table 9.7 and Table 9.8 show the comparison of the numerical and experimental results in terms of dissipating energy and load carrying capacity for cycles 5, 7, 9, 10, 13 and 15, which correspond to the last cycle of each imposed displacement (see Fig. 9.8) . The experimental data show that in the first three cycles the structural member is in the elastic region and show negligible dissipating energy, which comply with the numerical findings. Table 9.7, shows that the numerical curves capture the corresponding experimental ones in terms of dissipating energy by an average value of 20%. Furthermore, Table 9.8 shows that the load carrying capacity of the structural member was accurately predicted deriving an average error value lower than 10%. Finally, according to [38], the first rebar yielding within the beam was observed when the shear of the structure was 63.3 kN. The first yielding of beam rebars during

the numerical model analysis occurred when the shear of the structure was 65.91 kN (which represents a 4% deviation from the experimentally observed magnitude).

Table 9.7 Comparison of the dissipated energy between the experimental and numerical data.

RC Joint	Dissipated Energy Experimental (kN mm)	Dissipated Energy Predicted (kN mm)	Divergence from Experimental (%)
5th Cycle	195.23	105.46	45.98
7th Cycle	460.85	564.24	22.43
9th Cycle	2662.45	2540.25	4.59
10th Cycle	1791.00	2310.61	29.01
13st Cycle	4719.40	4275.83	9.40
15th Cycle	6174.95	5372.14	13.00
		Average	20.74

Table 9.8 Comparison of the horizontal load of each cycle between experimental and numerical results of the proposed model.

RC Joint	Horizontal load Experimental (kN)		Horizontal load Predicted Proposed (kN)		Divergence from Experimental	
	Positive	Negative	Positive	Negative	Positive (%)	Negative (%)
5th Cycle	43.75	-37.5	50.45	-47.22	15.31	-25.93
7th Cycle	69.38	-62.5	68.78	-65.91	0.86	-5.45
9th Cycle	78.75	-73.75	81.62	-82.49	3.64	-11.85
10th Cycle	73.75	-70.454545	72.85	-73.17	1.23	-3.85
13st Cycle	76.14	-75	74.05	-69.84	2.74	-6.89
15th Cycle	75.00	-75	72.15	-69.19	3.80	-7.75
				Average	4.60	-10.29

Overall, the proposed modeling approach managed to capture the cyclic mechanical behavior for all imposed displacement cycles with an acceptable accuracy.

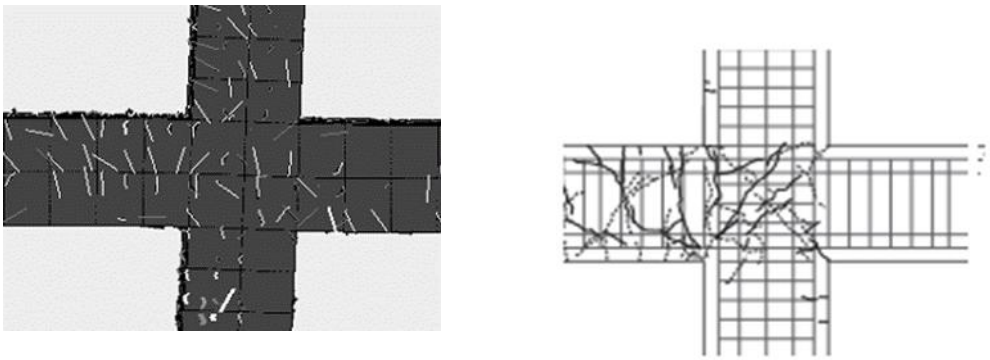

Fig. 9.11 RC beam-column frame joint. Comparison of experimentally and numerically obtained crack patterns

The crack patterns near the failure mode is depicted in Fig. 9.11, where it can be observed that the cracks within the joint indicate a characteristic shear diagonal cracking pattern. The numerical model appears to be more heavily cracked than the experimental one, which is attributed to the assumption of the smeared crack approach. Nonetheless, the crack pattern

shows that the crack formation is numerically captured in a realistic manner in-terms of location and direction.

The required Newton-Raphson internal iterations per displacement increment are shown in Fig. 9.12, where an energy convergence tolerance criterion with the acceptable numerical error of 10^{-4} is adopted. It can be seen that, all displacement increments in Fig. 9.12 required a reasonable number of internal iterations to reach convergence regardless the intense nonlinear behavior of the structure. Thus, 77% of the displacement increments require less than 5 internal iterations to converge, while 95% of the displacement increments require less than 10 internal iterations. The computational time for the nonlinear solution procedure, as given in Table 9.9, is 173 seconds to perform 610 displacement increments, which illustrates the overall stability of the proposed nonlinear solution procedure that allows for a complete analysis in less than 3 minutes.

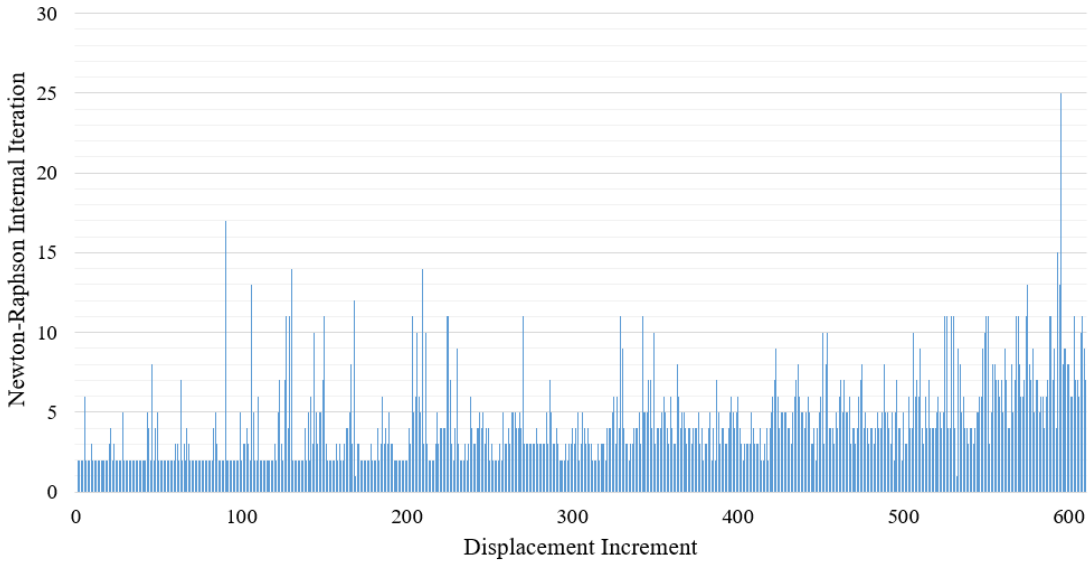

Fig. 9.12 RC beam-column frame joint. Required Newton-Raphson iteration per displacement increment.

Table 9.9 RC beam-column frame joint. CPU time for different tasks of the numerical solution.

Task	CPU Time (s)
Embedded rebar element mesh generation	0.1
Nonlinear incremental-iterative solution	173
Total Time	173.1

9.6.2 RC Column

The second structural member, which was numerically investigated with the proposed model, is a RC column that was subjected to ultimate limit state cyclic loading conditions. This column was experimentally investigated by Saatcioglou and Ozcebe [39] denoted as U4. The uniaxial compressive concrete strength was reported to be equal to f_c = 32 MPa and the yielding stress of the steel reinforcement was 438 MPa for the 25 mm rebars, while the yielding stress for the 10 mm rebars was 470 MPa. The geometry, reinforcement details and the mesh of the finite element model are illustrated in Fig. 9.13.

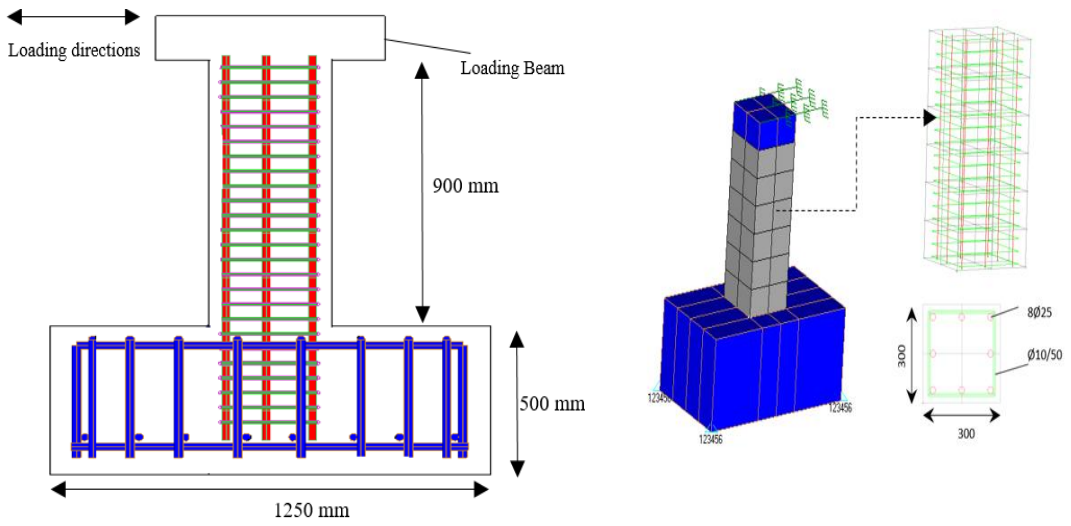

(a) (b)

Fig. 9.13 RC Column. (a) Geometry and reinforcement details [40] (b) Hexahedral and embedded rebar meshes.

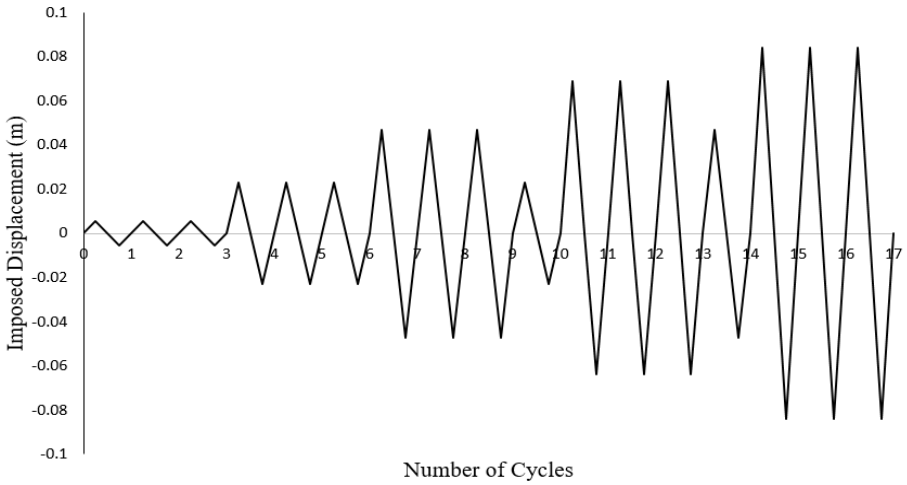

Fig. 9.14 Imposed displacement history at the top of the column.

The RC column was subjected to different cyclic loading conditions according to the experimental test. A compressive force of 600 kN was applied at the top section, where the loading history imposed, is presented in Fig. 9.14 in the form of imposed displacements (17 cycles). The concrete domain was discretized with 8-noded hexahedral finite elements and the steel reinforcement was discretized with the beam finite element. A total number of 24 concrete hexahedral (17.5cm x 17.5cm x 15cm) and 120 steel elements were used so as to discretize the RC column, as illustrated in Fig. 9.13b. In addition to that, 8-noded hexahedral finite elements (blue color) were used at the support and at the top of the column so as to simulate the boundary conditions of the specimen and to avoid any local failure.

The computed force-displacement curves are compared with the corresponding experimental data in Fig. 9.15. As it can be seen, the numerical results match very well with the experimental ones. The hysteretic curves were predicted with a satisfying accuracy, in terms of loading capacity, stiffness and energy dissipation.

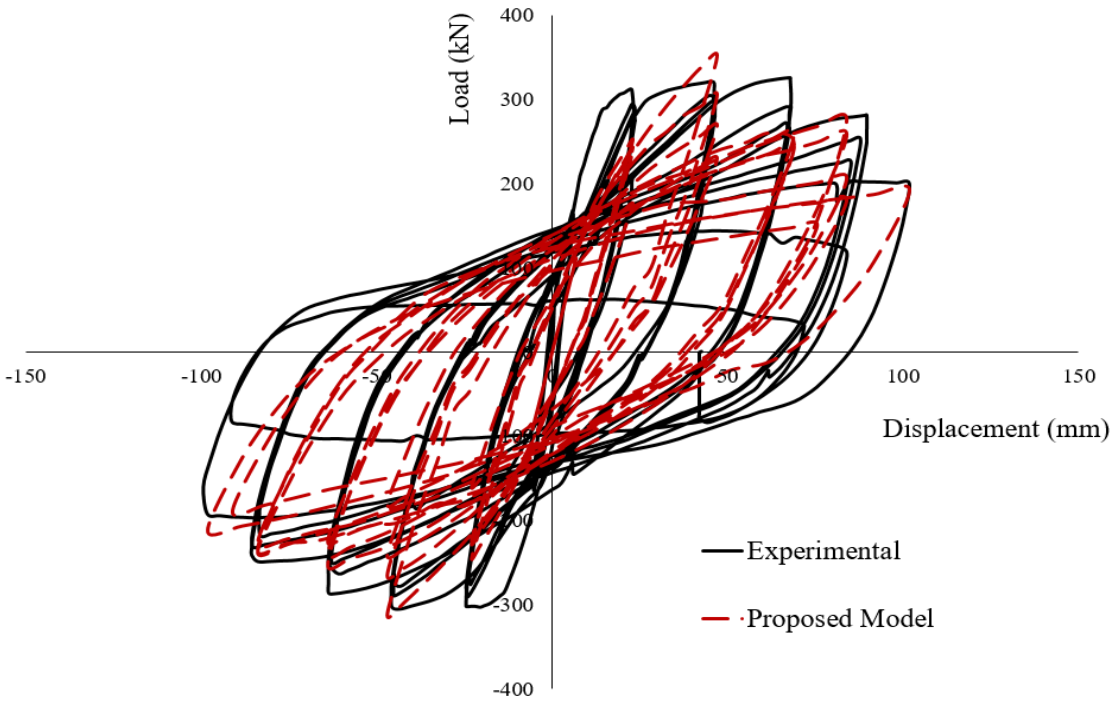

Fig. 9.15 RC Column. Comparison between numerical and experimental results.

Table 9.10 and 9.11 show the comparison of the numerical and experimental results in terms of dissipating energy and load carrying capacity, respectively. The displacement level of the first three cycles was the yield displacement of the column section as a whole and was recorded during the test, where the rate of strain variation was very high at relatively constant loads.

Table 9.10 Comparison of the dissipated energy between experimental results and the numerical model.

RC Column	Dissipated Energy Experimental (kN mm)	Dissipated Energy Predicted (kN mm)	Divergence from experimental (%)
4th Cycle	8921.82	3521.09	60.53
5th Cycle	6680.65	3521.09	47.29
6th Cycle	5893.46	3587.74	39.12
7th Cycle	21679.26	13221.18	39.01
8th Cycle	19298.80	14151.39	26.67
9th Cycle	18600.37	13836.27	25.61
10th Cycle	4508.34	3861.10	14.36
11th Cycle	34293.16	24124.29	29.65
12th Cycle	31069.46	25390.41	18.28
13th Cycle	27697.69	24537.60	11.41
14th Cycle	12729.03	12980.82	1.98
15th Cycle	44082.07	33610.14	23.76
16th Cycle	40108.10	32898.84	17.97
17th Cycle	37092.32	28281.42	23.75
		Average	27.10

Experimentally the structure presents a hysteretic behavior with a dissipated energy close to 700 kN·mm, which represents a mere 7.8% of the dissipated energy reported for the 4th loading

cycle as shown in Table 9.10. In this case, the numerical model behaved elastically during the first three cycles, which represents a stiffer behavior. Table 9.10, shows that the numerical curves capture the corresponding experimental ones in terms of dissipating energy of the 4-17 cycles by an average value of 27%. It is also interesting to note here that, the deviation of the predicted energy dissipation drops to a 19% when accounting the last 9 loading cycles, where the damage level of the specimen is the highest. Furthermore, Table 9.11 shows that the load carrying capacity of the structural member was accurately predicted by an average value of 11%.

Table 9.11 Comparison of the horizontal load of each cycle between experimental and numerical results of the proposed model.

RC Column	Horizontal Load Experimental (kN)		Horizontal Load Predicted Proposed (kN)		Divergence from Experimental	
	Positive	Negative	Positive	Negative	Positive (%)	Negative (%)
4th Cycle	311.90	-303.30	252.35	-245.88	19.09	-18.93
5th Cycle	294.60	-290.80	243.11	-228.47	17.48	-21.44
6th Cycle	283.00	-276.50	239.42	-224.31	15.40	-18.87
7th Cycle	321.00	-305.50	352.17	-312.87	9.71	-2.41
8th Cycle	304.60	-289.90	305.64	-265.86	0.34	-8.29
9th Cycle	298.40	-278.60	269.18	-241.86	9.79	-13.19
10th Cycle	205.50	-178.30	176.02	-161.20	14.34	-9.59
11th Cycle	325.90	-287.20	259.60	-252.98	20.34	-11.91
12th Cycle	291.60	-263.70	260.05	-240.97	10.82	-8.62
13th Cycle	271.40	-250.20	243.41	-225.34	10.31	-9.94
14th Cycle	204.30	-185.50	230.03	-181.40	12.59	-2.21
15th Cycle	281.50	-249.00	258.33	-235.07	8.23	-5.60
16th Cycle	253.50	-230.90	275.88	-227.43	8.83	-1.50
17th Cycle	226.50	-217.80	206.60	-237.85	8.79	-9.20
				Average	11.86	-10.12

During the last cycles, the numerical model exhibits failure of the longitudinal reinforcement, which also indicates the discrepancies of the last cycles in terms of dissipative energy. Nevertheless, the numerically predicted stiffness degradation is in a good agreement with the experimentally obtained curve.

The required Newton-Raphson internal iterations per displacement increment that resulted from the analysis of the RC column model are shown in Fig. 9.16. Once more, all displacement increments required a relatively low number of internal iterations to reach convergence despite the intense nonlinear behavior of the structure due to excessive shear cracking and rebar yielding. The iterative method in this case also used an energy convergence tolerance of 10^{-4}. As it can be observed in Fig. 9.16, 71% of the displacement increments required less than 15 internal iterations. The computational time for the nonlinear solution procedure of 780 displacement increments was 95 seconds (see Table 9.12). This numerical performance further confirms the computational efficiency of the developed algorithm.

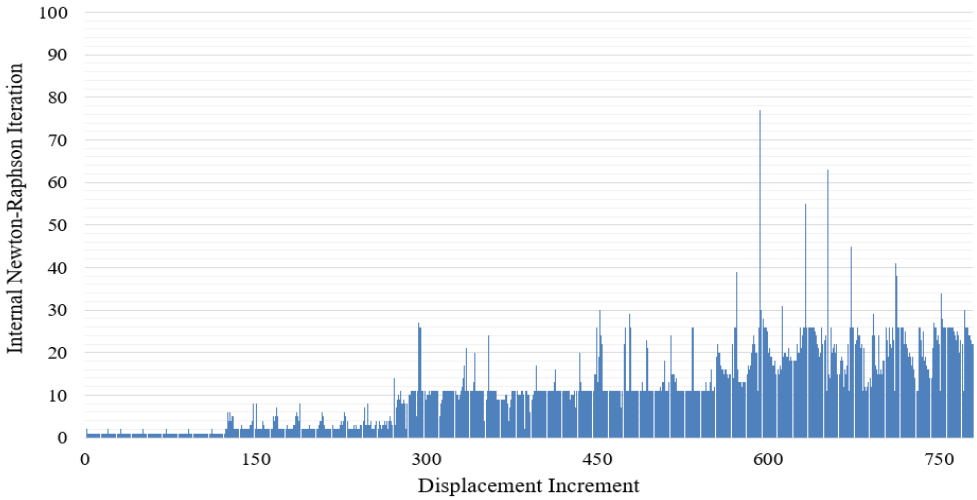

Fig. 9.16 RC Column. Required Newton-Raphson internal iteration per displacement increment.

Table 9.12 CPU time for different tasks of the nonlinear analysis for RC Column.

Task	CPU Time (s)
Embedded rebar element mesh generation	0.02
Nonlinear incremental-iterative solution	94.3
Total Time	94.32

9.7 Numerical Validation of the Proposed Model for Dynamic Analysis

9.7.1 Two-Storey RC frames

A numerical verification of the accuracy and computational efficiency of the proposed numerical method under dynamic loading will be performed on two two-storey RC frames (L30 and H30) that have been tested experimentally by Carydis [40]. The convergence tolerance was once more set to 10^{-4} for the Newton-Raphson iterations, while the nonlinear implicit Newmark integration method was used for the dynamic solution of the equations of motion. The steel rebars were simulated as embedded beam elements within the hexahedral concrete elements.

These two-storey frames were experimentally investigated by performing dynamic tests in an attempt to verify the validity of the European code provisions for the design of earthquake-resistant structures (Carydis [40]). The geometric and reinforcement details are shown in Fig. 9.17. The cylindrical specimen's uniaxial compressive strength of concrete (f_c) was 50 MPa and the yielding stress (f_y) of the steel reinforcement was 500 MPa. Additional masses of 2.87 and 2.62 tons were applied at the lower and upper levels, respectively.

Frame L30 was designed to exhibit moderately low ductility by using a behavioral factor of q = 2.5, whereas the frame H30 was designed to exhibit a higher ductility factor of q = 5. The frames were subjected to horizontal motions applied at their base, as denoted by the green vectors in Fig. 9.18. The base motions were sine-like acceleration records along the plane of the frames as illustrated in Fig. 9.19a and Fig. 9.19b. The accelerograms exhibit a maximum magnitude of approximately one and two times the magnitude of the design ground acceleration of the frames, which was 0.30g. Furthermore, the response spectrum diagram of each earthquake simulation of L30 and H30 specimens is illustrated in Fig. 9.19c and Fig. 9.19d, respectively. In order to show the severity of the ground motion (maximum ground acceleration was 0.75g), the spectra used for the design of the specimens (Eurocode 8 [41], soil type B) are

also plotted in Fig. 9.19c and Fig. 9.19d . The maximum spectral accelerations for L30 are 2.164g and 4.374g for test1 and test2, respectively. For specimen H30, the corresponding maximum spectral accelerations are 2.153g, 4.373g and 4.514g for test1, test2 and test3, respectively (test: is every sinusoidal acceleration motion as depicted in Fig. 9.19).

For the modeling requirements, the concrete and rebars were modeled as described in section 9.6, whereas the full finite element mesh can be seen in Fig. 9.18. It is worth noting that the beam elements used to discretize the rebars have the exact location and direction of the actual reinforcement reported in [40]. The concrete mesh consists of 224 hexahedral finite elements (10cm x 15cm x 15.5cm) and 1,891 steel embedded beam rebar elements that were used to model the reinforcement of the L30 specimen. For the second specimen (H30), a total of 2,384 embedded rebar beam elements were used and the same number of hexahedral elements was used to discretize the concrete domain. For the discretization of the RC slabs, 128 8-noded hexahedral elements were used (red elements in Fig. 9.18), where the mass density of the elements was set accordingly in order to account for the additional mass placed on the structure.

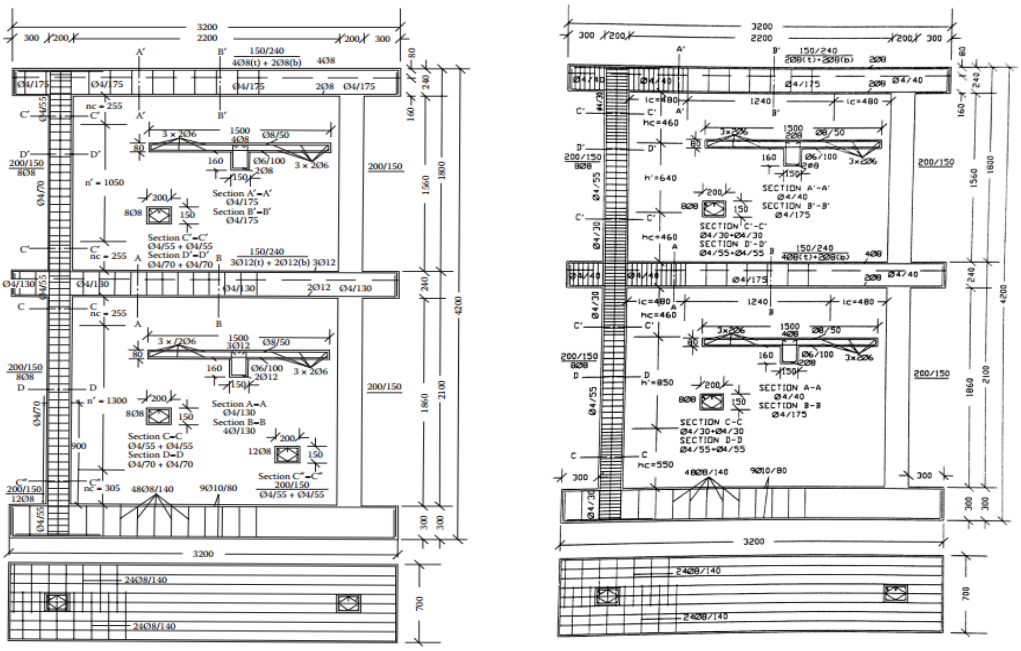

(a) (b)

Fig. 9.17 Geometric and reinforcement details of specimens of the RC-frames. (a) L30 and (b) H30. [40]

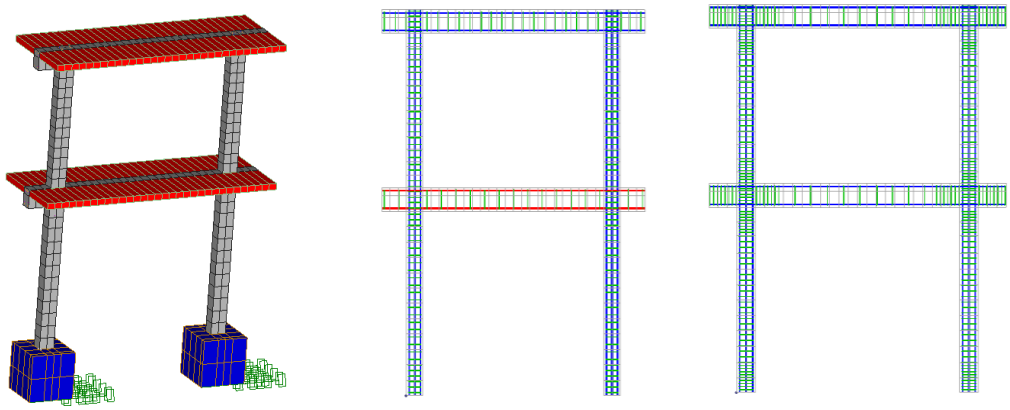

(a) (b)

Fig. 9.18 3D view of the FE mesh of 8-noded hexahedral and embedded rebar elements (a) L30 and (b) H30.

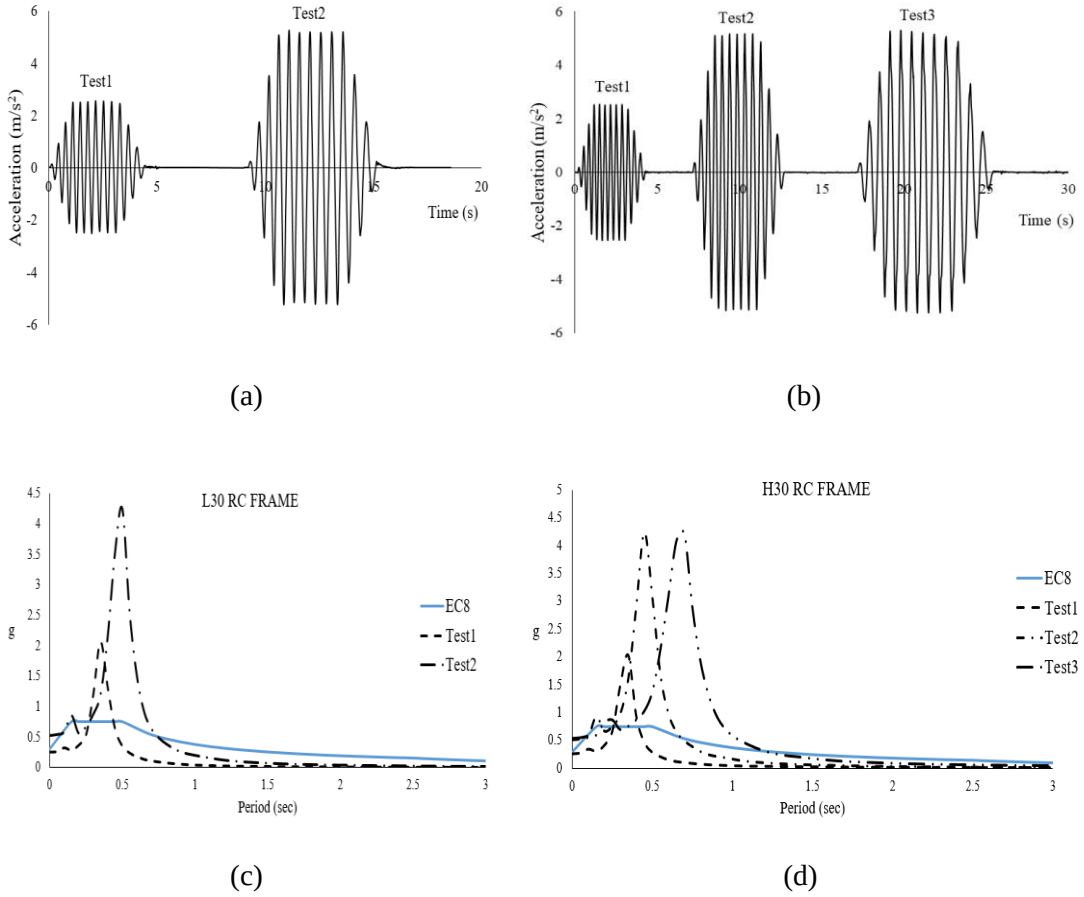

Fig. 9.19 Base acceleration that were subjected during the experiments [40] *and the numerical analyses of specimens (a) L30 and (b) H30. Spectrum acceleration diagrams of (c) L30 and (d) H30 loading histories.*

For the dynamic analysis the time step was set to $\Delta T = 0{,}007746$ s. In order to further verify the performance of the numerical simulation, the natural frequencies for the first two modes were computed and found to be equal to $f_1 = 2.93$ Hz and $f_2 = 9.7$ Hz (computed at the first time steps of the analysis). These values were very close to the experimental ones reported in [40] $f_{1exp} = 3.05$ Hz and $f_{2exp} = 9.8$ Hz. Furthermore, a constant damping ratio of 2% was applied in order to take into account other dissipating mechanisms during the nonlinear dynamic analysis.

The numerically obtained curves, for the case of specimen L30, were compared with the experimental data as shown in Fig. 9.20-Fig. 9.22. It is easy to observe that the numerical model managed to capture adequately the dynamic response of the structure in terms of storey displacement time histories (see Fig. 9.20-Fig. 9.22), demonstrating the ability of the proposed modeling method in capturing the dynamic behavior of this low ductility frame well after the 8^{th} second, where it had developed significant damages. Fig. 9.22 also shows a good agreement between the numerically computed and experimentally measured base shear of the frame.

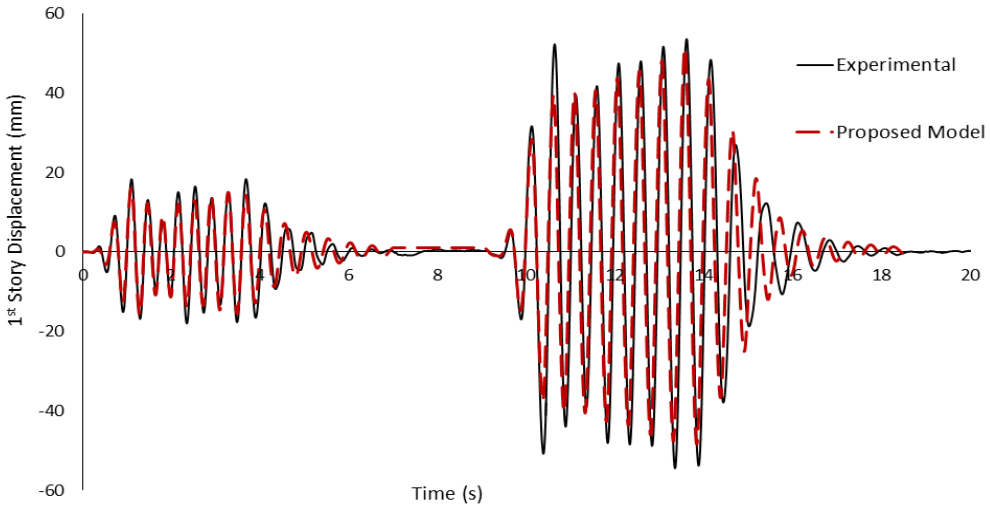

Fig. 9.20 L30 frame. Comparison between the numerical and experimental results of the 1st storey displacement response.

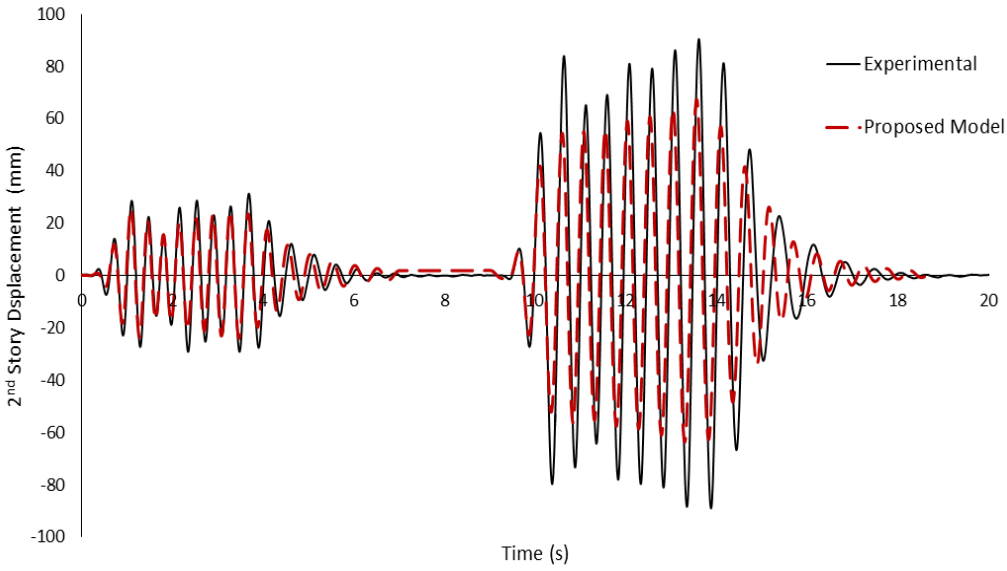

Fig. 9.21 L30 frame. Comparison between the numerical and experimental results of the 2nd storey displacement response.

In an attempt to further investigate the proposed damage factors presented in this work, the L30 RC frame has been also analyzed with the "initial model" without activating the proposed damage factors. Another formulation of the proposed concrete damage factor was also explored in this numerical experiment by assuming a linear correlation between the damage factor D_{CL} and the parameters a, f_{CC}, ε_{cr}, ε_{max} (Eq. (9.11)). This model is referred to as "linear reduction".

$$D_{cl} = \left[1 - \frac{1-a}{f_{cc}}\right] = \left[1 - \frac{\varepsilon_{cr}}{\varepsilon_{\max} \cdot f_{cc}}\right] \tag{9.11}$$

In Fig. 9.23, the numerical results for this parametric investigation are presented for the case of the three different models that were analyzed. It can be seen that, the model with the linear reduction damage factor exhibited higher damages, thus lower base shear, in comparison to the

corresponding model with the proposed concrete damage factor of Eq. (9.1). Hence, the "linear reduction" model derived a lower load-carrying capacity with a decreased hysteretic behavior. However, the numerical model without the damage factors exhibited a stiffer behavior during the first three dynamic cycles in comparison to the corresponding experimental results [40]. As a result, this model presented an excessive cracking at the beginning of the test, leading to premature damages that affected the overall dynamic behavior of the structure. This is attributed to the numerical inability of the model to absorb the developed energy that is generated during the initial dynamic cycles of the test. As a consequence, this led to discrepancies in terms of stiffness and displacements of the numerically predicted structural dynamic response.

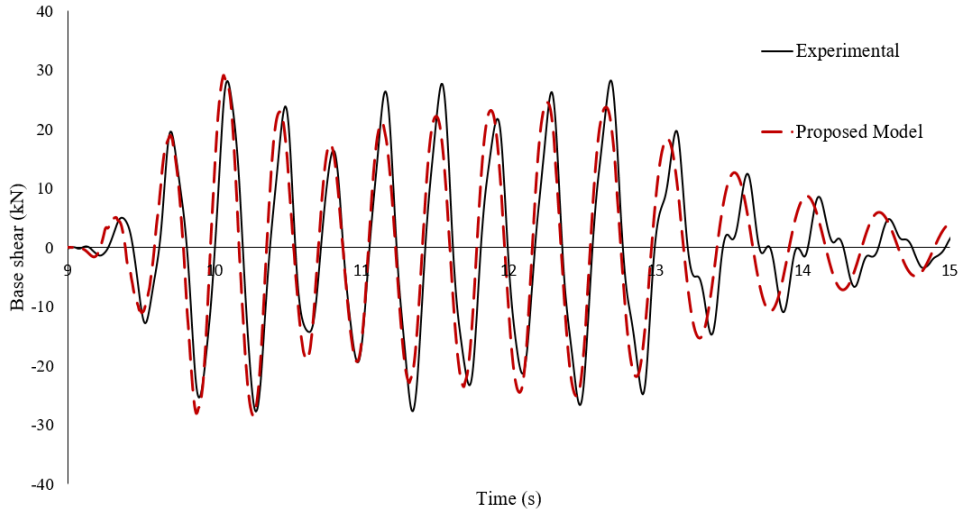

Fig. 9.22 L30 frame. Comparison between the numerical and experimental results of the base shear-time history during test 1.

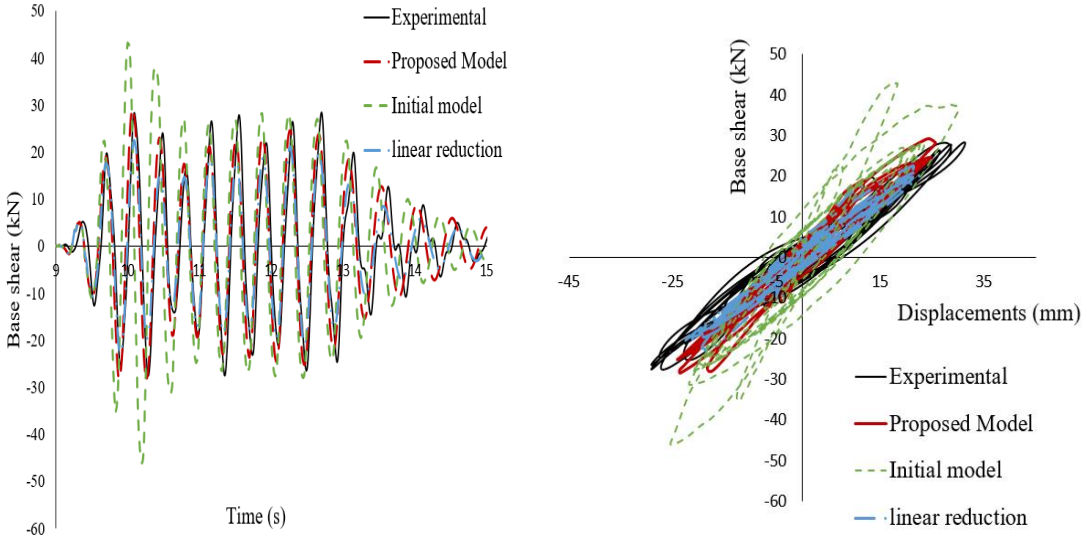

Fig. 9.23 L30 frame. Comparison between the numerical and experimental results of the base shear-time history for three different concrete damage factor formulations.

The second test case was performed on the H30 RC frame of Fig. 9.17b, which was designed in order to exhibit a more ductile behavior by adding more stirrups to the frame in comparison to the L30 specimen. The experimental and numerical tests revealed that, the frame developed excessive cracking, which occurred at the first dynamic cycles of the excitation (first 3 s of the

experiment, see Fig. 9.24). This led to significant strength degradations mainly during the third round of dynamic loading (t > 17 s) as well as due to the yielding and fracture of the longitudinal reinforcement at the base of the frame, which was a behavior also observed during the experiment [40]. The numerically computed displacements of the first and the second floor slabs of the RC frame are compared with the experimental data in Fig. 9.24 and Fig. 9.25, respectively.

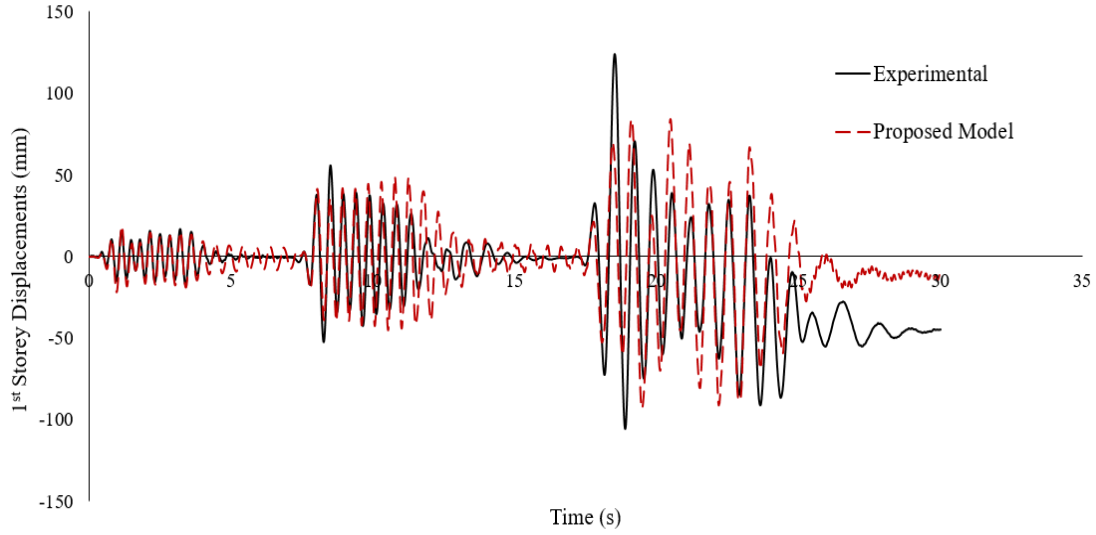

Fig. 9.24 H30 frame. Comparison between the numerical and experimental results of the 1st storey displacement response.

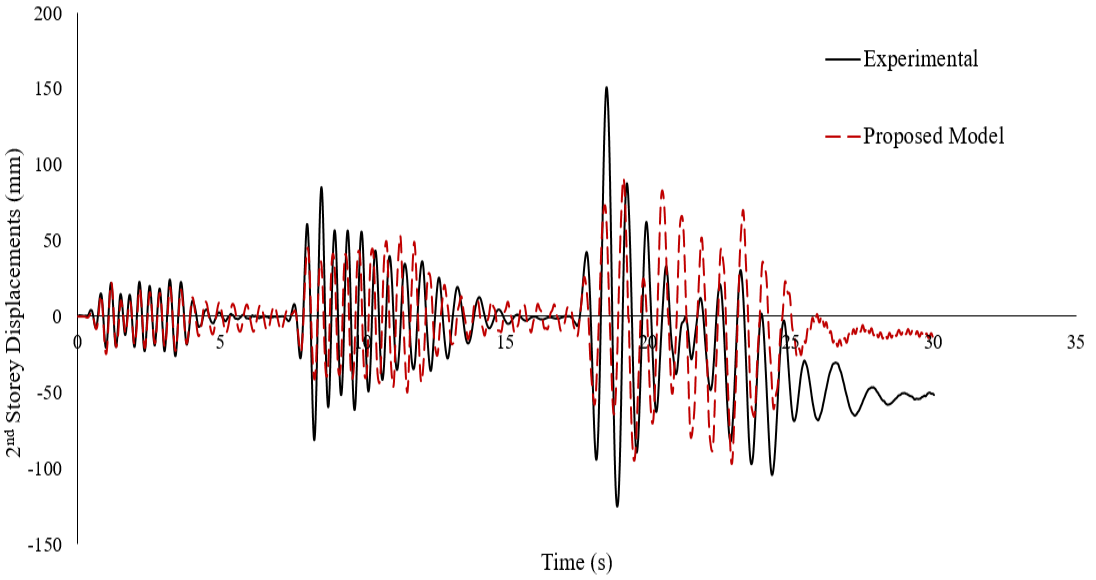

Fig. 9.25 H30 frame. Comparison between the numerical and experimental results of the 2nd storey displacement response.

The numerical findings indicate that the proposed model managed to model the complete dynamic displacement history satisfactorily. It can be observed that during the first two sinusoidal acceleration events the response of the RC frame was predicted fairly accurately, while during the third sinusoidal acceleration event the experimental test exhibited a relatively stiffer behavior. Based on the experimental findings reported in [40], the frame developed severe damages at the base, thus the specimen practically failed due to excessive cracking and rebar failures. This was also the reason of the remaining deformation that can be noted during the last 5 seconds of the experiment (see Fig. 9.24 and Fig. 9.25). It is evident that the dynamic

behavior of the H30 RC frame was governed, at that point, by extreme nonlinearities that forced the development of large horizontal deformations. Nevertheless, the numerical model manages to describe the overall behavior in an accurate manner, without any numerical instabilities.

It should be mentioned that, the same time step was used (ΔT = 0,007746 s) for the nonlinear dynamic analysis. The natural frequencies computed for the first and second modes were found to be equal to f_1 = 3.11 Hz and f_2 = 14.31 Hz, respectively. These values were found to be close to the experimental ones reported in [40]: f_{1exp} = 3.28 Hz and f_{2exp} = 10.72 Hz.

The required internal iterations, for both L30 and H30 numerical models, are shown in the Fig. 9.26a and Fig. 9.26b. Throughout the numerical experiments, all the dynamic step increments required a minimal number of iterations to achieve convergence regardless the degree of nonlinear behavior of the structures. From the computed numerical results, it was found that the required internal iterations per dynamic step during the solution procedure were limited to an average of 2 to 3, underlining the numerical stability of the proposed modeling method. For the L30 model, 87% of the dynamic steps require less than 2 internal Newton-Raphson iterations, while for the case of H30 a 78% of the dynamic steps required less than 5 internal iterations to achieve convergence. This increase is mainly attributed to the fact that during the 3rd sinusoidal acceleration event the analysis was governed by excessive nonlinearities due to significant cracking, rebar yielding and failure that were observed during the numerical analysis.

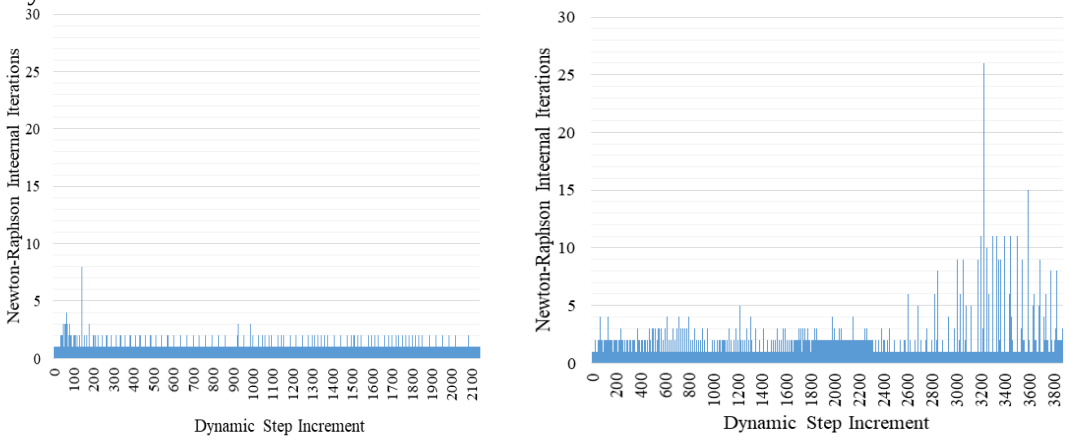

(a) (b)

Fig. 9.26 Required Newton-Raphson internal iterations per dynamic step increment of models (a) L30 and (b) H30.

The computational times for the two nonlinear solution procedures are given in Table 9.13, which refer to the solution of 2,041 and 3,826 dynamic time increments for the test cases of L30 and H30, respectively. The total required time for solving the nonlinear dynamic problems was 319.5 s for L30 and 565.8 s for the case of H30.

Table 9.13 CPU time for different tasks of the nonlinear analysis for L30 and H30.

Task	L30	H30
	CPU Time (s)	CPU Time (s)
Embedded rebar element mesh generation	0.51	0.94
Nonlinear incremental-iterative solution	318.97	564.82
Total Time	319.48	565.76

Finally, Fig. 9.27 shows the crack patterns that were formed at the end of test 3 of the H30 frame. Based on the experimental observations [40], the cracks were mainly formed at the joints and the columns of the specimen. The cracks were larger and denser at the base of the frame, with significant inclination at the base of the first level. In this area, the experimentally observed damages were associated with intense concrete spalling. Similarly, intense inclination of the

cracks appeared at the beam-column joints of the first level of the frame (ground floor). It can be seen that, there is a good agreement on the distribution, the location and the direction of the cracks, which are predicted by the numerical model compared to the corresponding crack patterns of the experimental test. However, the numerically predicted crack patterns appear to be denser than the experiment ones, which is again attributed to the adopted smeared crack approach.

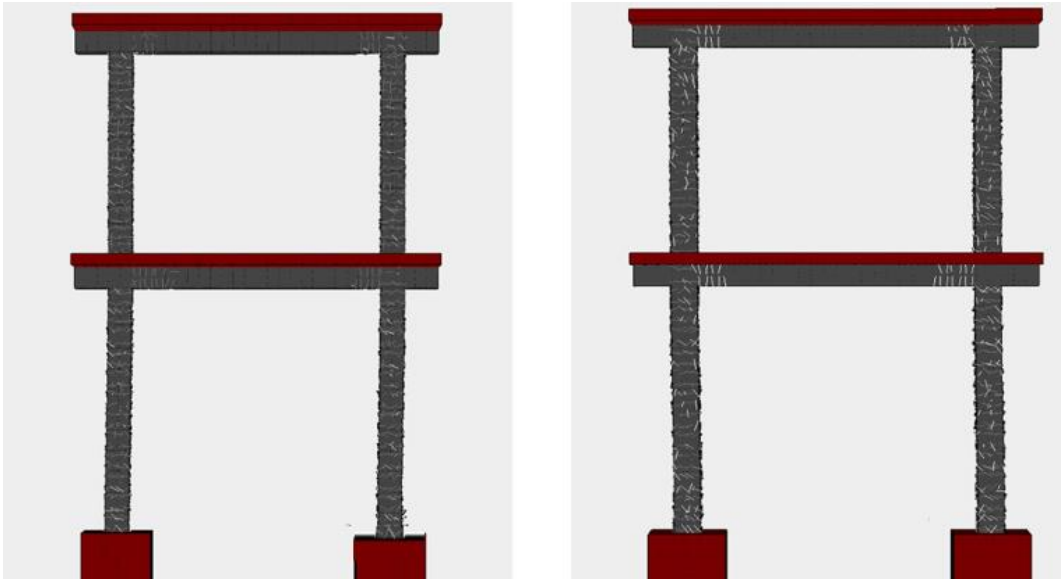

(a)

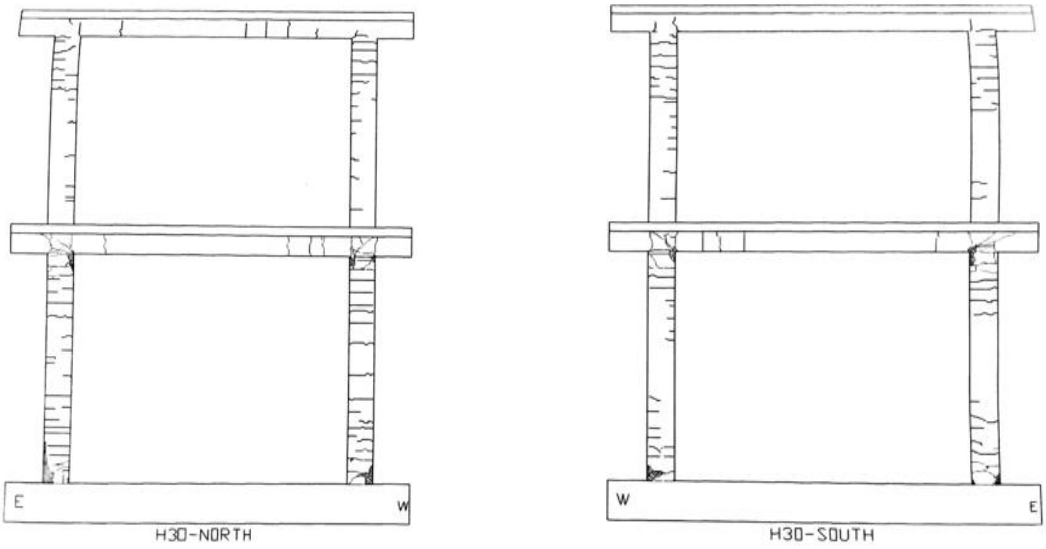

(b)

Fig. 9.27 H30 frame. Comparison between (a) numerical and (b) experimental [40] *obtained crack patterns at the end of test.*

9.7.1.1 Parametric investigation on the type of embedded element

In this section, a comparison between the use of beam and rod embedded elements for the simulation of steel reinforcement will be presented. The numerical model H30 is used to

investigate the case where the rebars are modeled as embedded rods and compared to the numerical results obtained when beam elements are used for the rebar modeling. The same number of finite elements was used in constructing the new model, whereas the material properties for both steel and concrete materials were also kept the same.

The comparison between the numerical results and the experiment, for the displacements of the second floor, is shown in Fig. 9.28. It can be observed that the model with the rod elements developed larger deformations due to the damage that was concentrated at the base of the structure during the 2nd sinusoidal acceleration event (t = 17 s). Therefore, the numerically predicted response during the 3rd sinusoidal acceleration event significantly deviate from the experimental results. As an overall conclusion in the case of this highly nonlinear dynamic problem, the use of beam elements provides additional numerical stability and accuracy to the dynamic simulation of the RC specimen.

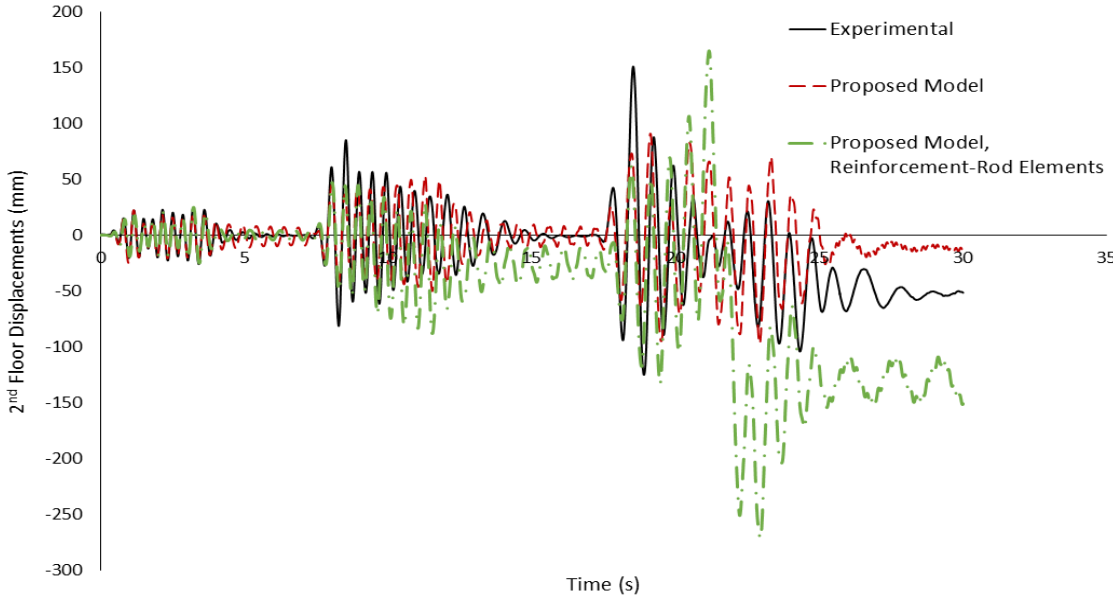

Fig. 9.28 H30 frame. Comparison between the numerical models that use rod and beam elements for modeling the rebars. Second storey displacement history.

Table 9.14 CPU time for the nonlinear dynamic analysis of the H30 frame by using beam and rod elements for modeling the steel reinforcement.

Task	H30 Frame: Beam element	H30 Frame: Rod element
	CPU Time (s)	CPU Time (s)
Embedded rebar element mesh generation	0.94	0.71
Nonlinear incremental-iterative solution	564.82	534.36
Total Time	565.76	535.07

Table 9.14 shows the corresponding computational time required by the two models to solve the complete dynamic problem. As it can be seen, the model with rod elements is only 5% faster than the corresponding model with the beams. This illustrates the numerical efficiency of the developed algorithm, where the additional computational cost with the beam finite element is practically negligible.

9.7.1.2 Investigation of a modified crack closure criterion

The crack closure algorithm applied in Chapter 5 performs the computation of the strains at a cracked GP, where the corresponding strain is computed along the norm of the crack's plane without closing the other cracks existed at the same GP. A modified criterion is examined in this section, where all cracks are assumed to close when the crack-closure condition is satisfied at any cracked direction. In this way, more stiffness is induced in the numerical model when one of the two cracks is closing at a given double cracked GP.

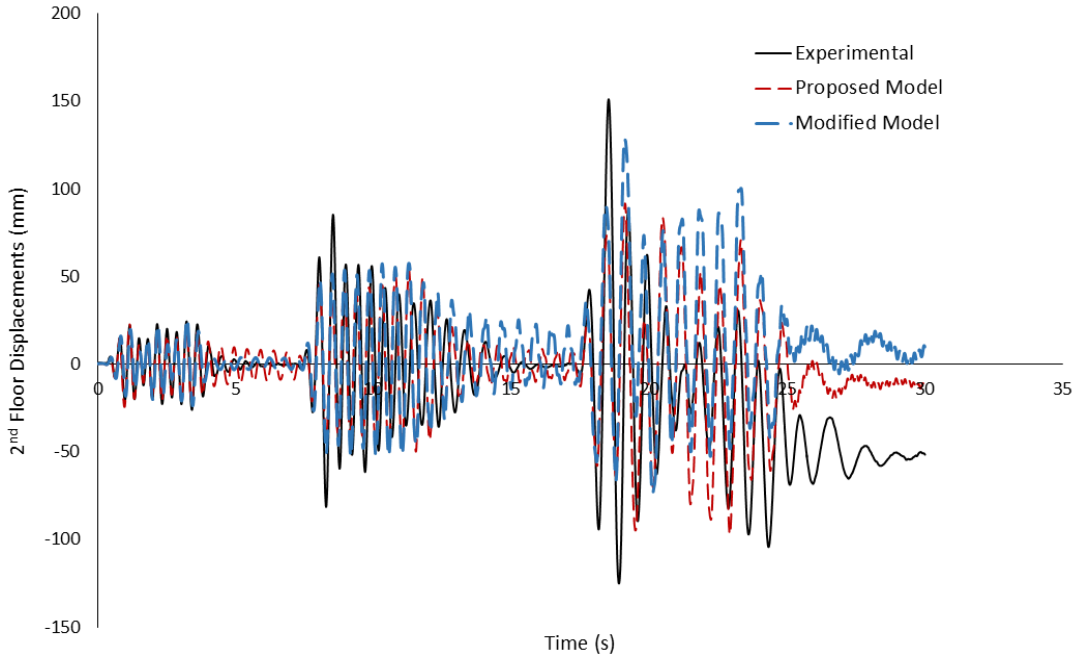

Fig. 9.29 H30 frame. Comparison between the numerical and experimental results of the second story displacement history of the proposed model and the modified model.

Fig. 9.29 shows the results from the dynamic analysis performed with the H30 frame, where the second storey displacement history is depicted. The graph compares the curves that occurred from the use of the new crack-closure assumption described above and the model with the closing criterion described in Chapter 5. The use of the modified criterion, exhibits a similar dynamic behavior with that obtained when using the standard crack-closure criterion, for the case of the first two sinusoidal acceleration events. The main changes are noted at the transition stage between the 2nd and 3rd events (see Fig. 9.29), where the stiffer numerical model (modified model) exhibits a deviation from the experimental data due to the additional stiffness added to the system. At this point, it is evident that the stiffer model (modified model) delivers significantly larger deformations in comparison to the model that uses the standard crack-closure criterion. During the dynamic analysis, it was also found that areas with lower crack numbers managed to close faster when unloading occurred, thus attracting more stiffness in comparison to other areas that did not manage to have their cracks closed. This numerical phenomenon had as a consequence the redistribution of the internal stresses between the cracked and uncracked regions of the structure, which forced the frame to develop larger damages at the base of the frame during the 3rd and final cycle. Nevertheless, both models managed to capture the experimental results in a satisfactory manner, demonstrating the algorithm's ability to simulate complicated and challenging nonlinear dynamic problems.

9.7.1.3 Mesh-sensitivity Analysis

In order to examine the mesh sensitivity of the proposed modeling approach, four additional meshes were developed to model the L30 RC frame as shown in Fig. 9.30. The four meshes that were additionally developed for the needs of this parametric investigation (a, b, c and d in Fig. 9.30), consisted of 294, 318, 512 and 576 hexahedral elements, respectively. The numerical results were compared with the experimental data and the numerical results that derived from the model presented in Fig. 9.17, which consisted of 392 hexahedral elements.

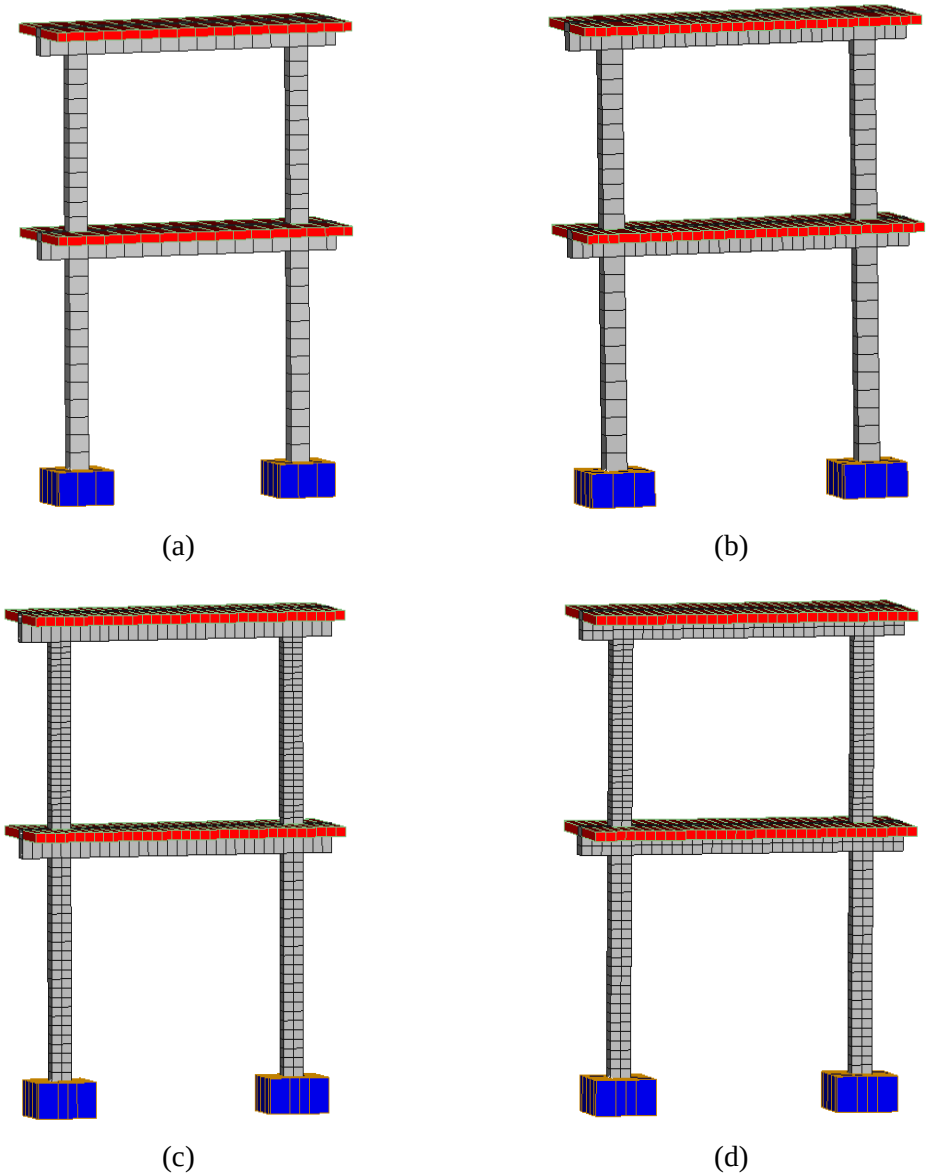

Fig. 9.30 3D view of the FE mesh of the L30 RC frame which consists (a) 294, (b) 318, (c) 512, (d) 576 hexahedral elements.

After the dynamic analyses were performed, the obtained displacement curves were compared as it is illustrated in Fig. 9.31, where the numerically derived horizontal deformations of the second storey were plotted for the case of each developed mesh. It is easy to observe that the variations between the displacement responses that resulted numerically by the four different meshes are minimal, whereas all models managed to solve the complete nonlinear dynamic problem without any numerical instabilities. Furthermore, it is also easy to observe that, they all managed to capture the experimental data with a satisfactory accuracy. It is well known that,

when a finer finite element mesh is used the overall nonlinear numerical behavior of a model is accordingly affected, a numerical phenomenon that can be also seen in Fig. 9.30, thus explains the small variations in terms of displacements between the different numerical models.

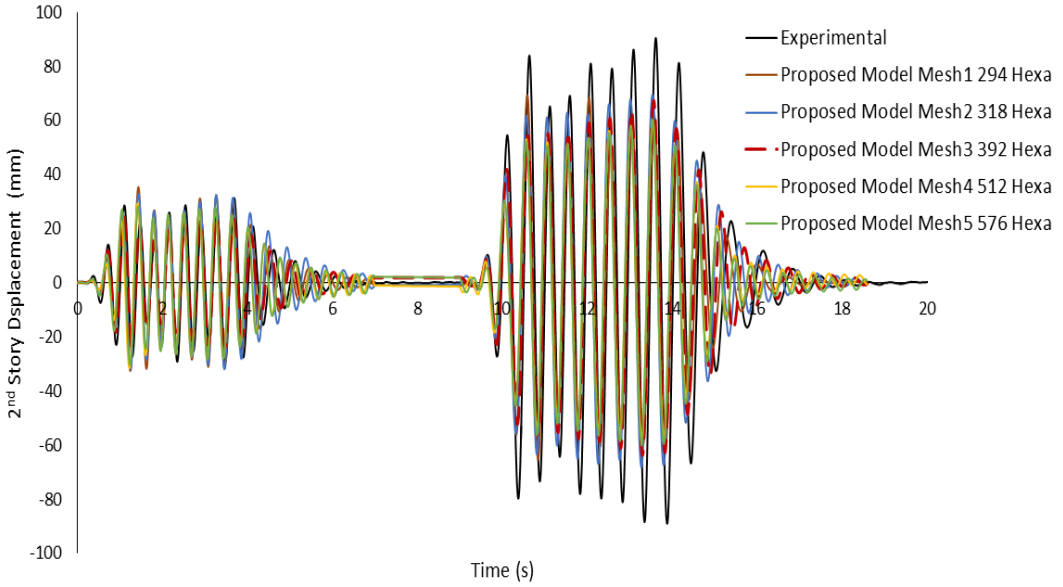

Fig. 9.31 Comparison between numerical and experimental results of the second storey's displacement response for the different mesh discretizations.

It is evident that the first two models, which consist of 294 and 318 hexahedral elements, present slightly larger horizontal displacements given that their meshes foresee the discretization of the column section by using a single hexahedral element. Due to the coarser meshes adopted in these models (see Fig. 9.30a and Fig. 9.30b), the obtained numerical results exhibit a slightly larger stiffness due to the larger elements that are used to discretize the RC frame's columns, hence their dynamic response at the beginning of the dynamic excitation leads to the development of damages at an earlier stage in comparison to the models that adopt a finer mesh (crack openings). This phenomenon leads to a more brittle behavior, which eventually causes a relatively higher accumulated damage and consequently larger deformations during the dynamic excitation. However, it is safe to conclude that the numerical models derived negligible discrepancies, capturing the experimental results with an acceptable accuracy. It is also noteworthy to state at this point that the use of smaller finite element sizes in an attempt to further refine the RC frame's mesh would eventually add significant computational demand without any numerical merit. As it can be seen in Table 9.15, the computational demand to solve the complete nonlinear dynamic problem when the mesh with the largest number of finite elements is used, it requires approximately four times more computational time (13 min) than the model with the coarser mesh (3.3 min). This highlights the importance of developing a method that will be able to use a coarser mesh when dealing with a full-scale structure, without significantly decreasing its numerical accuracy. As it was previously stated, all numerical models were analyzed by using a standard computer system with a CPU power of 2,50 GHz.

So as to further investigate the numerical response that derives when the mesh size adopted for discretizing the RC frame changes, the first two natural frequencies were also computed herein and compared with the experimental data. Table 9.16, shows the natural frequencies that resulted from the five numerical models that were used in this mesh sensitivity study, where it can be seen that the maximum variation was 17.57% and 46.73% for mode 1 and 2, respectively. Both variation values derived from the coarser mesh, as it can be seen in the

relevant table. This numerical phenomenon is attributed to the fact that the two models with the coarser meshes derive a stiffer numerical response at the beginning of the excitation and therefore they result higher natural frequency values. However, the overall average computed error values for the first two modes were equal to 0.5% and 15.3%, respectively, a numerical finding that shows the ability of the proposed numerical method to reproduce the experimental data in a satisfactory manner.

Table 9.15 Computational demand resulted through the sensitivity analysis of the L30 frame.

Model	Number of Hexahedral Elements	CPU Time		
		Embedded rebar mesh generation (s)	Nonlinear Solution Procedure (s)	Total Time (s)
Mesh 1	294	0.37	198.1	198.47
Mesh 2	318	0.46	212.36	212.82
Mesh 3	392	0.51	318.97	319.48
Mesh 4	512	0.87	608.02	608.89
Mesh 5	576	0.99	774.33	775.32

Table 9.16 Natural frequencies resulted through the sensitivity analysis of the L30 frame.

Model	f_1 (Hz)	f_2 (Hz)	$\frac{f_1 - f_{1,exp}}{f_{1,exp}}$ (%)	$\frac{f_2 - f_{2,exp}}{f_{2,exp}}$ (%)
Experimental	3.05	9.8	-	-
Mesh 1	3.59	14.38	17.57	46.73
Mesh 2	3.30	14.11	8.33	44.00
Mesh 3	2.93	9.70	-3.93	-1.02
Mesh 4	2.80	9.31	-8.26	-5.04
Mesh 5	2.71	9.02	-11.24	-7.95
Average			0.5	15.3

The numerical pathology of developing mesh-dependent constitutive models arises from the use of softening characteristics in the constitutive laws. Models usually use the smeared crack approach for simulating cracking thus avoid mesh discontinuities and remeshing procedures. This way, the models simulate the geometrical discontinuity through the assumption of displacement continuity. This procedure introduces excessive strains along the cracked areas. The constitutive models, which describe the post-peak behavior with descending branches, present some stiffness in these cracked areas that is not realistic (take for instance a tensile crack; along that direction the stiffness is zero but the descent branch assumes the contrary). A general numerical deficiency of the smeared crack approach, based on the Rots and Blaauwendraad work [130], is the possibility of developing stress-locking when smeared softening laws are applied, a numerical problem that is alleviated herein due to the brittle concrete behavior assumption. In continuation to that, Bazant and Oh [14] reported that excessive stress and strain concentrations in cracked areas lead to mesh-dependent procedures, thus the load needed to reach the strength limit strongly depends on the choice of element size and incorrectly converges to zero. Once again, this numerical phenomenon is not affecting the proposed method due to the fact that it does not foresee the use of a softening branch.

Most researchers proposed crack band models introducing the fracture energy [14], which is considered to be a material parameter. Additionally, nonlocal techniques have been investigated [165] which are usually combined to damage models. Finally, second-order gradient-based methods have also been proposed. Rots et al. [206] replaced the softening diagram of the

constitutive laws to a saw-tooth diagram of positive slopes. A series of limiter analyses ("event-by-event strategy) replace the incremental Newton-method and led to robust results, as it was reported by the authors [206]. On the other hand, the proposed material model of this work, describes the concrete behavior as a brittle material with an abrupt loss of its caring capacity when the failure criterion is satisfied during the nonlinear dynamic analysis. Therefore, the numerical model manages to discharge the cracked areas from the prementioned excessive stress concentrations by releasing them to the surrounding uncracked areas, thus, the numerical instabilities are in this case prevented, hence the proposed method leads to a mesh-independent numerical procedure.

In addition to the above, it was also observed that during the nonlinear dynamic analysis of the L30 RC frame, in some cases where finer meshes were used so as to numerically study the dynamic response of the specimen, the sections of the columns that are found at the base of the frame developed significant cracking due to the large bending moments that were developed during the numerical experiment. The steel-reinforcement elements take in this case the role of the post-cracking behavior of concrete within the hexahedral elements that have embedded rebars, while the hexahedral elements that do not contain any embedded rebars are called to resist to the external forces without the tensile resistance capacity of the steel rebars. This phenomenon is presented when finer meshes are used which may lead to local failures and divergence of the iteration solution procedure from an early stage of the analysis. This is a numerical phenomenon that is common when 3D detailed modeling is used to solve problems that are expected to exhibit extreme nonlinearities [196], where the effect of cracks are modeled either through the use of the smeared crack approach or through damage models. Additionally, a more extensive mesh sensitivity investigation was performed and presented in [196], where deep RC beams without stirrups were modeled under monotonic loading conditions.

According to the numerical investigation performed and presented in this section, it was found that the use of 10-20 cm hexahedral elements ensure a reliable element size that can be used for establishing numerical efficiency, robustness and accuracy. In addition to that, the overall numerical findings discussed in this section show that by developing a numerical method that exhibits numerical accuracy and robustness when coarser meshes are implemented, it further highlights that the nonlinear dynamic simulation of full-scale RC structures with 3D detailed models is now feasible.

9.7.2 RC frame

A final test case shown in Fig. 9.32, was selected to further study the efficiency of the proposed algorithm. The RC space frame denoted as frame W050, was investigated by Minowa et al. [207]. The RC frame consists of four columns, which were fixed on a shake table at their lower-end and monolithically connected to a steel rigid slab at the top. The columns had a height of 850 mm and a square cross section of 130x130 mm. The geometric details of the RC specimen are given in Fig. 9.32. The uniaxial compressive strength (f_c) of concrete is 26 MPa and the yielding stresses (f_y) of the steel reinforcement are 380 and 392 MPa for the 16 and 6 mm in diameter rebars, respectively. The spacing of the stirrups for each of the four columns is 50 mm, where the total mass placed on the roof is 27.8 tons. The RC frame was subjected to one-dimensional excitations along its longitudinal axis of symmetry. The imposed acceleration record at its base is illustrated in Fig. 9.33, where after the 15th second, the structure undergoes accelerations that increase through time, forcing the frame to develop a significant nonlinear behavior [207]. Thus, the numerical results that will be presented herein will therefore concentrate on the dynamic behavior of the structure after the 15th second of the dynamic excitation.

The concrete domain was modeled by 8-noded hexahedral finite elements and the steel reinforcement were modeled with beam elements. The transverse and longitudinal embedded rebar elements had the exact location and direction of the actual reinforcement. The top and the bottom of each RC column are modelled with 96 rigid 8-noded hexahedral elements in order to avoid local failure that maybe developed at these regions. Overall, 48 concrete finite elements (6.75cm x 13cm x 15cm) and 368 embedded rebar elements were used to model the four RC columns.

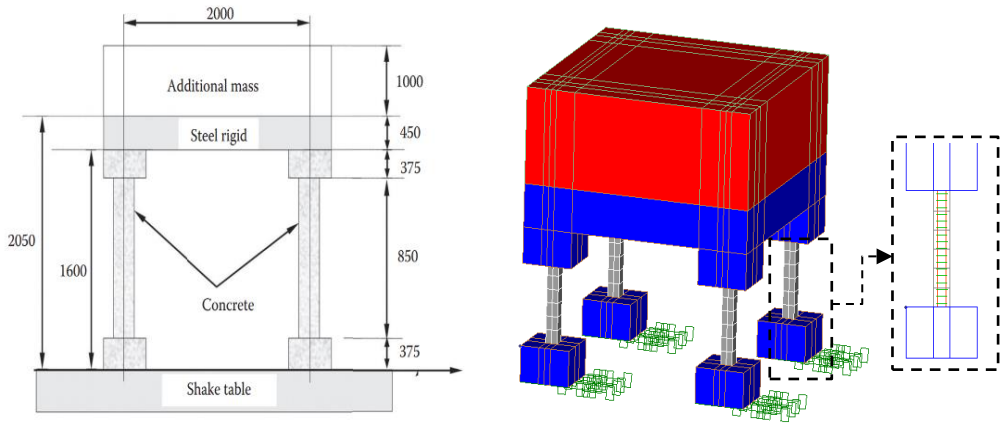

Fig. 9.32 W050 RC frame. Geometric details [207] *and FE mesh with solid and beam finite elements.*

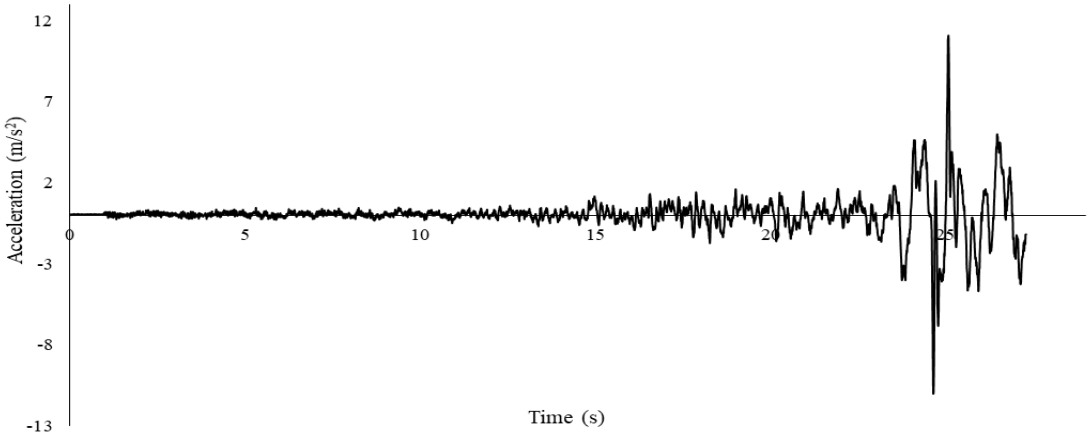

Fig. 9.33 W050 RC frame. Base acceleration of the shake table.

For the steel slab and the additional mass applied at the top of the specimen, 126 hexahedral elements were used to construct the mesh. After performing a modal analysis, it was found that the fundamental period computed by the numerical model was equal to $T_1 = 0.17$ s, a numerical result obtained by using the undamaged properties of the concrete and steel materials. Therefore, the dynamic time integration step was set to $\Delta T = 0.005$ s for the needs of the nonlinear dynamic analysis. The numerical curves are compared with the experimental data in Fig. 9.34 and Fig. 9.35.

The obtained results indicate that the numerically predicted displacements are in a good agreement with the experimental data (Fig. 9.33), while during the final stages of the numerical experiment ($t > 24$ s) the model exhibited high damages at the base of the frame, resulting into larger deformations in comparison to the experiment test [207]. This can be attributed to the highly nonlinear response after the development of significant cracking and spalling at the base

of the structures. By comparing the numerical and experimental base-shear in Fig. 9.35, it can be seen that the numerical model is able to capture the overall behavior of the specimen with a satisfactory accuracy, while the deviation of the curves is more pronounced after the 26th second of the analysis.

It is important to state at this point that the experiment [207] reported significant damages at the columns leading to an actual collapse of the structure. This indicates that the experimental measurements beyond the 24th second of the dynamic excitation could be hindered by a lack of accuracy given the significant nonlinearities that led to the instability of the frame and subsequently to the development of very large deformations. It is widely accepted that measuring accurately the dynamic behavior of any structure which exhibits nonlinear behavior is a challenge on its own, thus many things can affect the final measurements during an experiment. It is therefore impossible for any numerical simulation to be able to capture the experimental results with an absolute accuracy due to numerous reasons, such as lack of additional information regarding the specimen, experimental errors during measurements, external factors that affect the execution of the experiment, as well as the inability of the numerical model to capture additional physical phenomena that take place when rebars start to fail. On the other hand, when dealing with the objectivity and ability of the numerical model to produce the same results when modeling the same specimen, it is evident that the risks involved are significantly lower in comparison to those involved in a physical experiment.

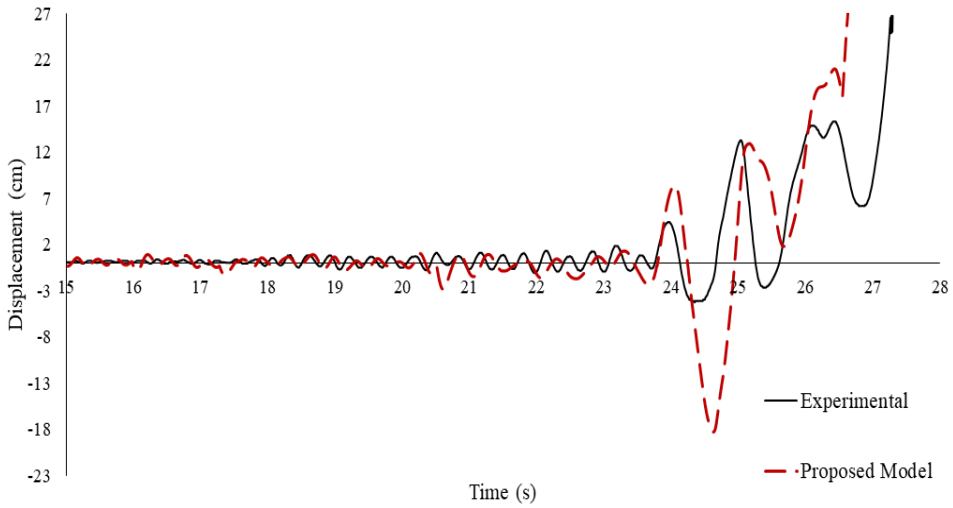

Fig. 9.34 W050 RC frame. Comparison between numerical and experimental results of the displacement response.

In an attempt to further study the proposed algorithm, the RC frame model was also tested with the modified crack-closure procedure that was described in section 9.7.1.2. Fig. 9.36 shows the results of the numerically predicted displacement history. The comparison shows that the modified model derived displacements that were more accurate than the model with the initial crack closure criterion during the dynamic excitation between the 15th and 24th seconds of the numerical test (Fig. 9.36b). This numerical finding occurred due to the excessive cracking that occurs during this period when using the initial crack closure criterion. However, after the 24th second the proposed model managed to capture more realistically the behavior since the vertical displacements were increased significantly and in a similar manner to that of the experiment [207]. On the other hand, the stiffer behavior when the modified model is used, leads to smaller horizontal deformations at the final stage of the dynamic excitation, thus not being able to capture the failure that occurred at the completion of the dynamic excitation. The computational time for solving the complete dynamic problem was measured and presented in Table 9.17.

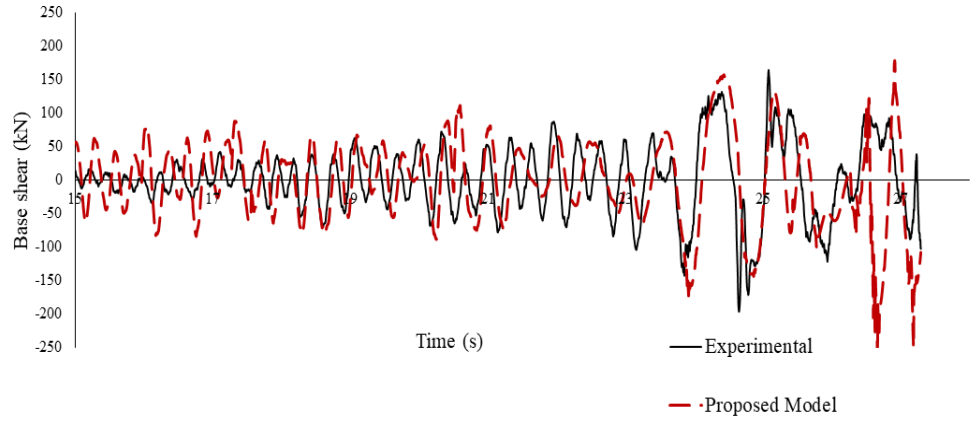

Fig. 9.35 W050 RC frame. Comparison between numerical and experimental results of the base shear response.

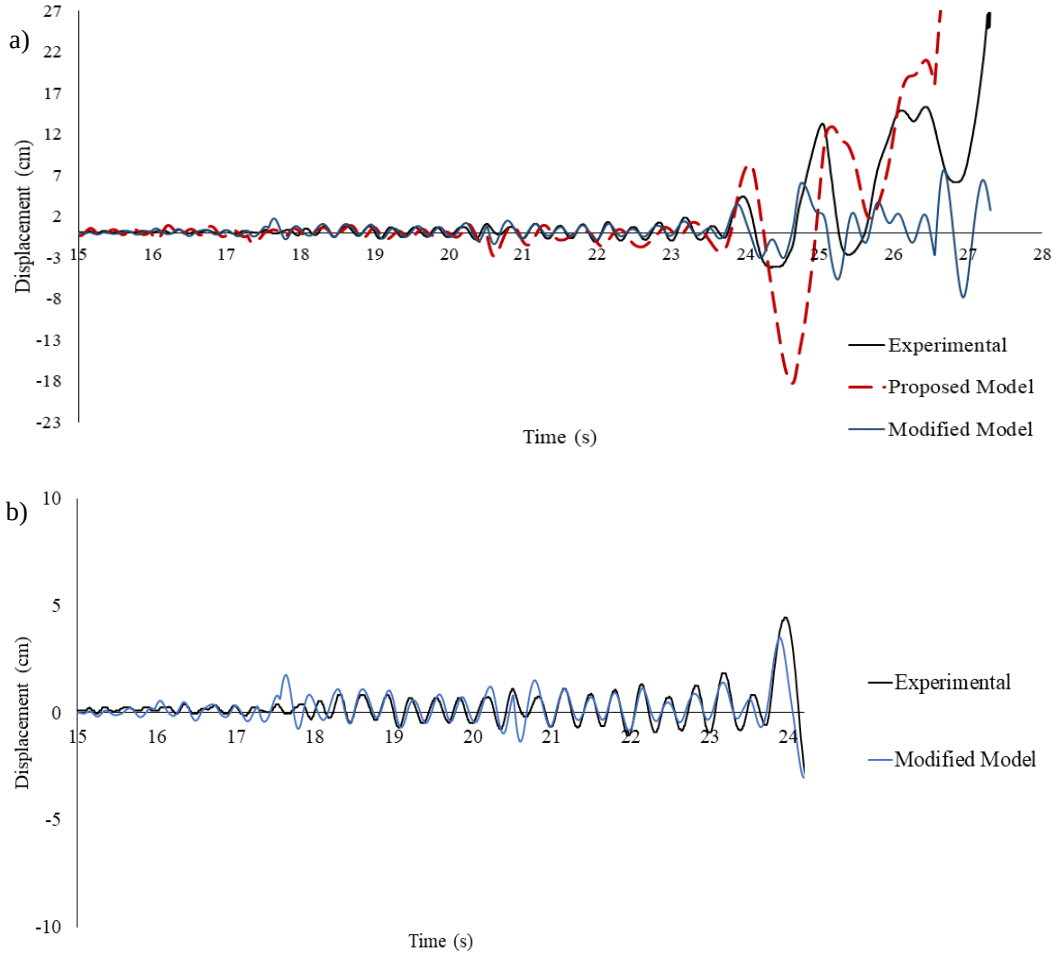

Fig. 9.36 W050 RC frame. a) Comparison between numerical and experimental base shear curve for the case of modified model and the proposed model. b) Comparison between numerical and experimental base shear curve for the case of modified model during the 15th and 24th seconds.

As it can be seen in Table 9.17, the total required time for performing 5,459 dynamic increments, (with a total of 6,636 internal iterations) was 725 seconds, illustrating the computational efficiently of the proposed algorithm. In addition to that, the required internal Newton-Raphson iterations during the solution procedure are given in Fig. 9.37, where it can be observed that most of the increments required a mere 1 to 2 internal iterations to achieve

convergence, demonstrating the numerical stability of the proposed method when dealing with ultimate limit state dynamic loading conditions.

Table 9.17 CPU time for different tasks of the nonlinear analysis for the W050 RC Frame.

Task	CPU Time (s)
Embedded rebar element mesh generation	0.07
Nonlinear incremental-iterative solution	725.30
Total Time	725.37

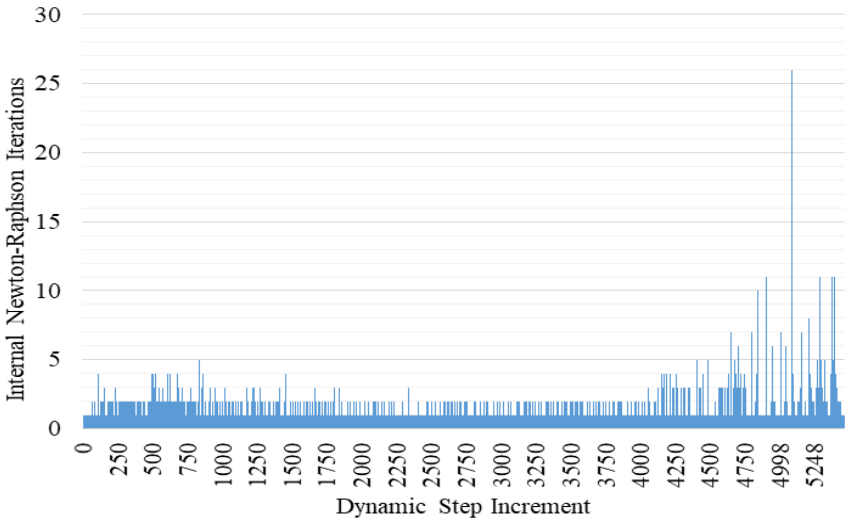

Fig. 9.37 W050 RC frame. Required Newton-Raphson internal iterations per dynamic step increment.

9.7.3 Three-storey, three-bay RC frame subjected to High Intensity Ground Motions

A three-storey, three-bay frame was built and tested at the University of California, Berkeley [208] in order to study the collapse behavior of RC frames with light transverse reinforcement. The geometrical and reinforcement details are illustrated in Fig. 9.38. The RC frame was subjected to a dynamic loading test. The cylinder compressive strength of concrete that was used for the RC frame, was f_c = 24.6 MPa, where the yielding stress of the longitudinal reinforcement was f_y = 445 MPa. Additionally, the beam and column ties were 4.8 and 3.2 mm in diameter with a yielding strength of 558 and 655 MPa, respectively.

Two of the columns, as shown in Fig. 9.38, have been designed according to ACI 318-08 [209] and they were referred to as “ductile” columns with longitudinal reinforcement ratio ρ_l=1.09% and a transverse reinforcement ratio ρ_t=1.1% at the end of the column members. The other two columns were referred to as “older type” columns with longitudinal reinforcement ratio equal to ρ_l=2.45% and a transverse reinforcement ratio of ρ_t=0.15%. Furthermore, the beam’s transverse reinforcement was also designed according to ACI 318-08 [209], while beam-column joint failure was not expected based on the design provisions of the frame.

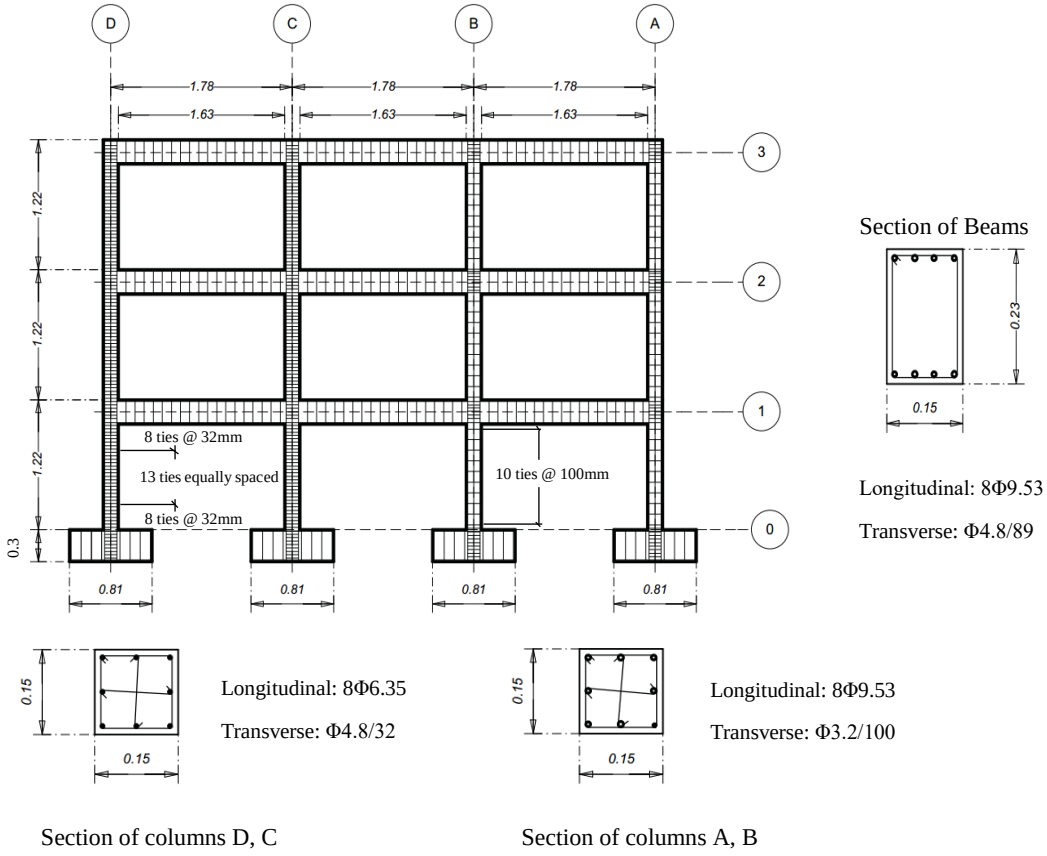

Fig. 9.38 Three-storey, three-bay RC frame. Geometrical and reinforcement details. [208]

Each beam span, has been loaded by four packets of lead weights (6.67 kN per packet). The total load (load packets and weight of concrete frame) of the structure, produced the equivalent amount of load in a typical office building. Additionally, the resulting gravity axial load on the first-storey interior columns was approximately $0.16A_g f_c$, while the axial load of the exterior loads was approximately of $0.08A_g f_c$ (where A_g is the column gross section area). Therefore, every beam span is considered that it has a uniformly distributed load of 16.67 kN/m, which is also used to account for the mass contribution. The ground motion record form the 1985 Chile earthquake at Valparaiso (Llolleo Station, Component 100) was chosen for this dynamic test. The motion was scaled up 4.06 times from its original acceleration amplitudes for the dynamic test and it is illustrated in Fig. 9.39. In addition, the ground motion time scale was divided by a factor of $3^{0.5}$ to satisfy the amplitude requirements.

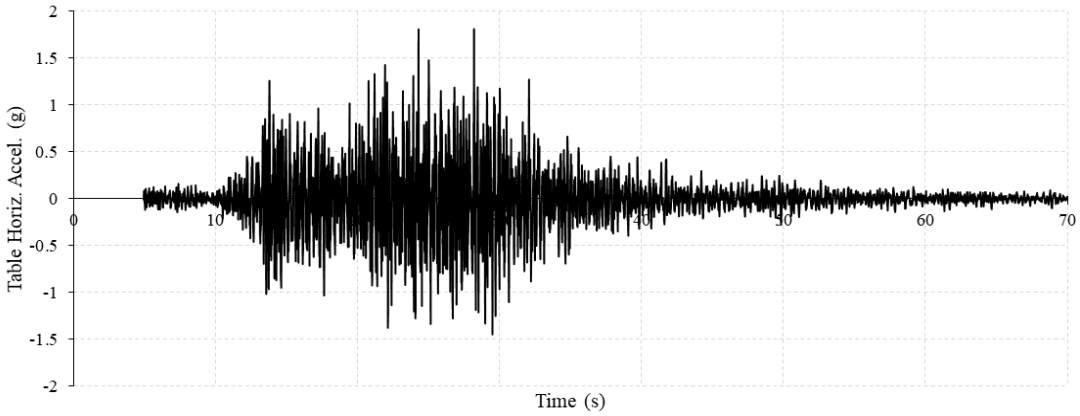

Fig. 9.39 Three-strorey, three-bay RC frame. Acceleration history used during the experiment [210].

For the modeling requirements, the concrete mesh foresaw the use of 336 hexahedral elements and 4,554 steel embedded rebar beam elements that were used to model the reinforcement of the specimen, as shown in Fig. 9.40. Furthermore, 108 hexahedral elements are used (red elements, see Fig. 9.40), where the mass density of the elements was set accordingly in order to account for the additional mass placed on the structure. Finally, 60 hexahedral elements (blue elements, see Fig. 9.40) are used for the support of the columns so as to simulate the boundary conditions of the specimen and to avoid any local failure at the area where the accelerogram is applied.

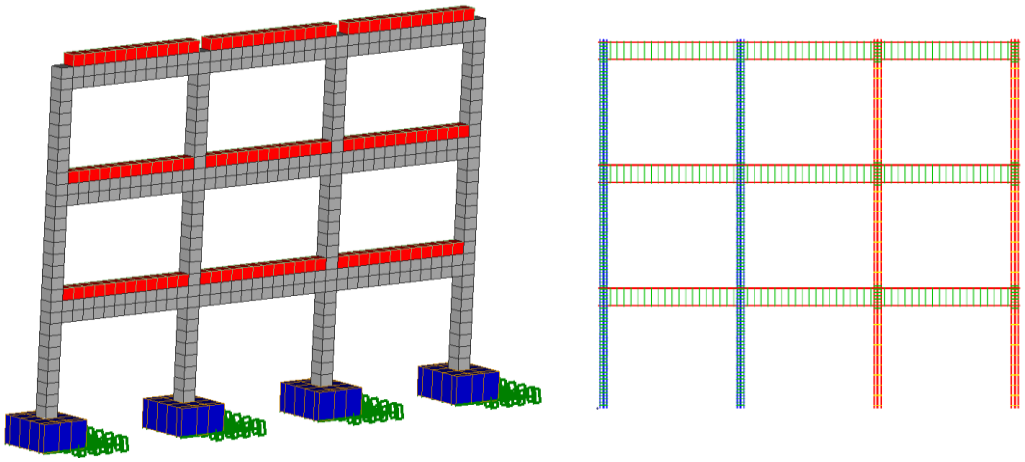

(a) (b)

Fig. 9.40 Three-strorey, three-bay RC frame. 3D view of the FE mesh of 8-noded (a) hexahedral and (b) embedded rebar elements.

The natural periods for the first three modes are compared with the corresponding experimental ones in Table 9.18. The comparison shows that the natural periods that derived from the numerical model, were very close to the experimental ones, where the average computed error was equal to 10%.

Table 9.18 Three-strorey, three-bay RC frame. Comparison between the numerical and the experimental natural periods.

Mode	Experimental period T (s)	Numerical period T (s)	Divergence from experimental (%)
First	0.30	0.30	0
Second	0.10	0.09	10
Third	0.069	0.08	15.94
		Average	8.65

For the nonlinear dynamic analysis, the nonlinear implicit Newmark integration method was used. The convergence tolerance was once more set to 10^{-4} for the Newton Raphson iterations. The time step was set to $\Delta T = 0.002887$ s, which was the time step used for the experimental data. The numerically obtained curves in terms of first-storey displacement histories with the use of different damping ratios ($\xi = 5\%, 7\%, 9\%$) were compared with the experimental data in Fig. 9.41 and Fig. 9.42.

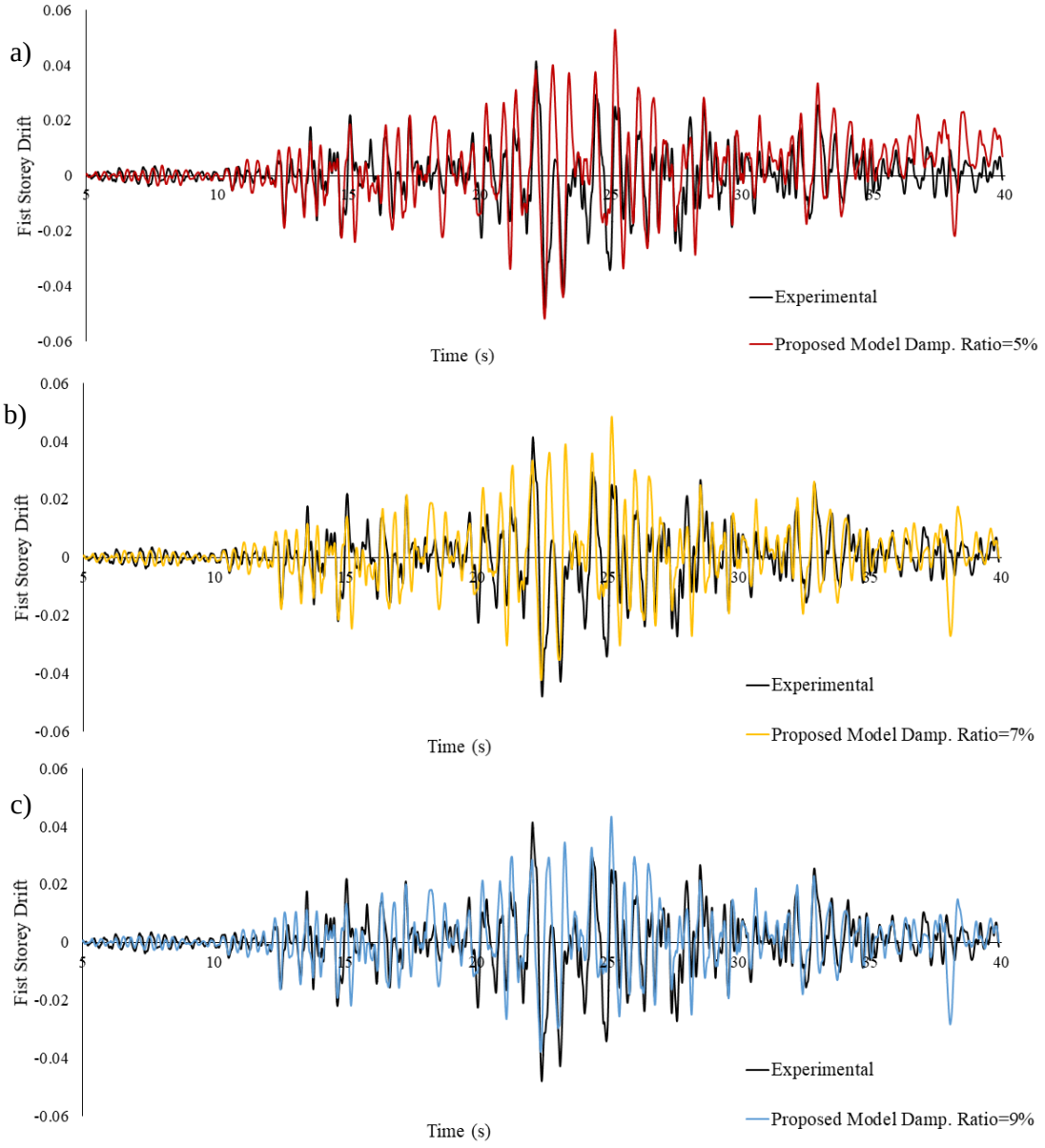

Fig. 9.41 Three-strorey, three-bay RC frame. Comparison between the numerical and experimental results of the first storey displacement response when using damping ratios equal to (a) 5%, (b) 7% and (c) 9%.

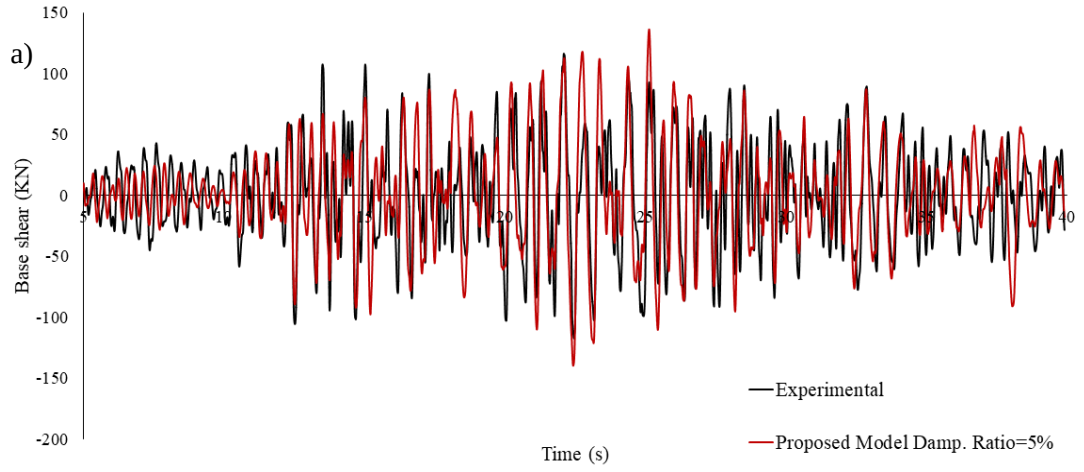

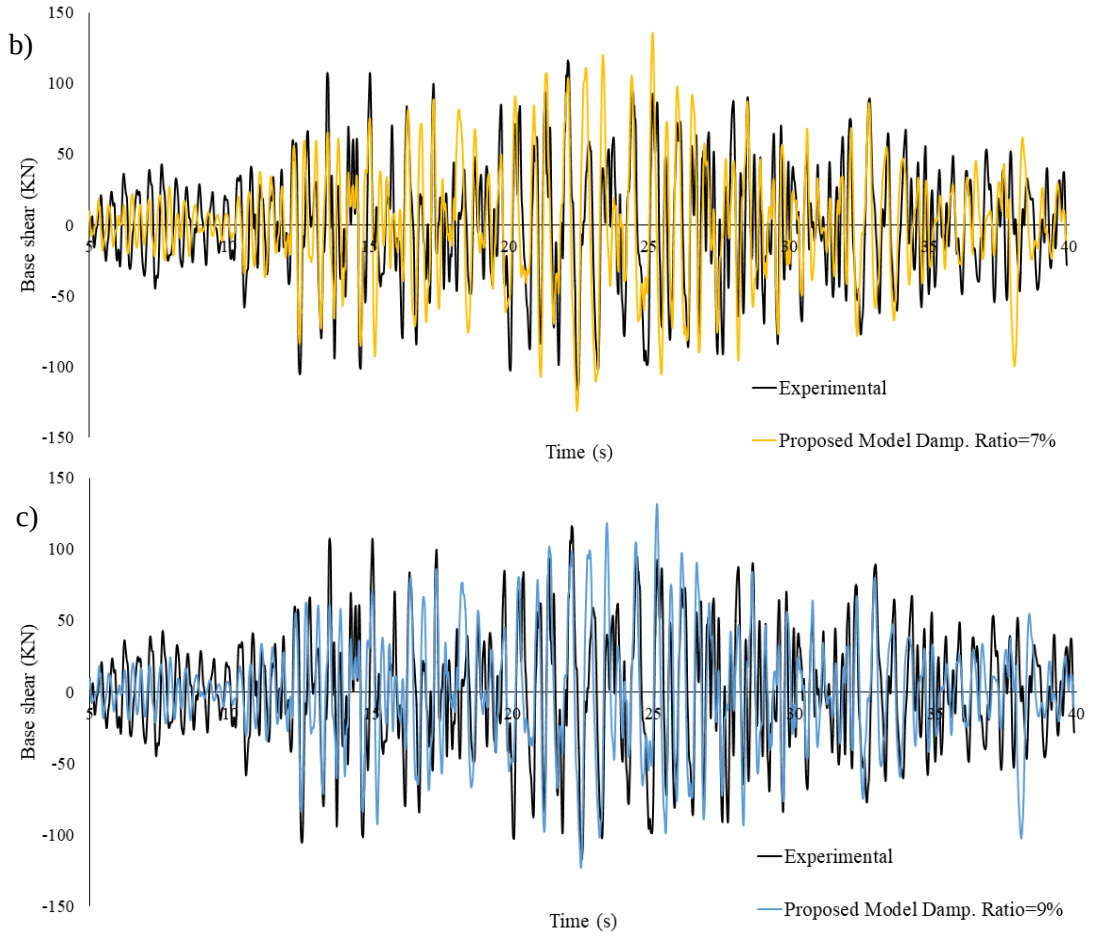

Fig. 9.42 Three-strorey, three-bay RC frame. Comparison between the numerical and experimental results of base shear capacity when using damping ratios equal to (a) 5%, (b) 7% and (c) 9%.

Table 9.19, shows the maximum and minimum derived values for drift and base shear as they resulted from the experiment. The maximum and minimum values of the computed displacements and the corresponding base shear during the 5th to 35th second of the loading history are compare in Table 9.19-9.23. In order to decrease the size of the tables, a time step of 1.5 s was used. Table 9.21 shows that the numerical results capture the experimental results in terms of the first storey displacements, by an average value of 35%, 31% and 30% for the case of the dissipating ratios of 5%, 7% and 9%, respectively. It is easy to observe that the average value is affected by extreme values in the data set. It can be shown that the discrepancy between the numerical and the experimental first-storey maximum displacements for damping ratio of 5%, during the time period of 5s-11s is equal to an average of 20% (14% minimum), while during the 12.4s-20s is equal to 16% (35% minimum). Additionally, it was found that during the 21.4s-24.4s the average deviation is equal to 17% (5% minimum) and during the 27.4s-30.4s this deviation becomes equal to 10% (5% minimum). Furthermore, Table 9.23 shows that the numerical curves capture the experimental results in terms of base shear with an average value of 20% for all damping ratios.

Table 9.19 Three-strorey, three-bay RC frame. Experimental results in terms of first-storey drift and base shear capacity.

Time Step (s)	Experimental First-Storey Displacement Drift		Experimental Base shear (KN)	
	Max	Min	Max	Min
(4.9-6.4)	0.003	- 0.002	36.02	-29.37
(6.4-7.9)	0.004	- 0.004	42.84	-45.03
(7.9-9.4)	0.003	- 0.002	32.86	-29.72
(9.4-10.9)	0.003	- 0.005	41.19	-58.41
(10.9-12.4)	0.005	- 0.003	59.90	-41.97
(12.4-13.9)	0.018	- 0.016	107.39	-105.54
(13.9-15.4)	0.022	- 0.022	107.36	-101.67
(15.4-16.9)	0.014	- 0.016	83.90	-84.42
(16.9-18.4)	0.021	- 0.009	99.71	-55.10
(18.4-19.9)	0.016	- 0.006	84.99	-49.45
(19.9-21.4)	0.017	-0.023	93.65	-102.74
(21.4-22.9)	0.041	- 0.048	116.23	-117.15
(22.9-24.4)	0.029	- 0.043	94.80	-102.45
(24.4-25.9)	0.029	- 0.034	94.89	-99.03
(25.9-27.4)	0.016	- 0.024	72.93	-86.28
(27.4-28.9)	0.027	-0.027	90.23	-91.43
(28.9-30.4)	0.014	-0.019	70.28	-84.11
(30.4-31.9)	0.011	-0.014	62.20	-68.20
(31.9-33.4)	0.026	-0.016	89.34	-77.44
(33.4-34.9)	0.015	-0.010	67.32	-60.43

Table 9.20 Three-strorey, three-bay RC frame. Numerical results in terms of first-storey drift for damping ratios 5%, 7% and 9%.

Time Step (s)	Proposed Model Damp. Ratio=5%		Proposed Model Damp. Ratio=7%		Proposed Model Damp. Ratio=9%	
	Max	Min	Max	Min	Max	Min
(4.9-6.4)	0.001	- 0.002	0.001	- 0.002	0.001	-0.002
(6.4-7.9)	0.004	-0.004	0.003	- 0.003	0.003	-0.003
(7.9-9.4)	0.003	- 0.003	0.003	- 0.003	0.002	-0.003
(9.4-10.9)	0.003	-0.005	0.003	- 0.005	0.002	-0.004
(10.9-12.4)	0.009	- 0.006	0.009	- 0.006	0.008	-0.005
(12.4-13.9)	0.013	- 0.019	0.012	- 0.018	0.011	-0.016
(13.9-15.4)	0.019	-0.024	0.014	- 0.025	0.013	-0.022
(15.4-16.9)	0.018	-0.020	0.017	- 0.018	0.017	-0.015
(16.9-18.4)	0.022	-0.015	0.022	- 0.016	0.020	-0.016
(18.4-19.9)	0.017	-0.022	0.016	- 0.018	0.014	-0.015
(19.9-21.4)	0.031	-0.034	0.032	- 0.030	0.030	-0.027
(21.4-22.9)	0.040	- 0.052	0.036	- 0.042	0.029	-0.038
(22.9-24.4)	0.038	-0.044	0.039	- 0.035	0.035	-0.030
(24.4-25.9)	0.053	-0.034	0.049	- 0.030	0.043	-0.026
(25.9-27.4)	0.032	-0.026	0.030	- 0.024	0.030	-0.022
(27.4-28.9)	0.028	-0.029	0.025	- 0.027	0.021	-0.025
(28.9-30.4)	0.016	-0.018	0.015	- 0.019	0.015	-0.019
(30.4-31.9)	0.022	- 0.008	0.020	- 0.010	0.019	-0.009
(31.9-33.4)	0.034	-0.018	0.026	- 0.019	0.023	-0.018
(33.4-34.9)	0.024	-0.015	0.017	- 0.016	0.014	- 0.013

Table 9.21 Three-strorey, three-bay RC frame. Comparison between numerical and experimental results in terms of first-storey drift for damping ratios 5%, 7% and 9%.

Time Step (s)	Divergence from Experimental data, Damp. Ratio=5%		Divergence from Experimental data, Damp. Ratio=7%		Divergence from Experimental data, Damp. Ratio=9%	
	Max	Min	Max	Min	Max	Min
(4.9-6.4)	46.65	6.10	54.13	11.99	48.51	15.06
(6.4-7.9)	6.04	5.30	10.22	22.99	21.99	31.45
(7.9-9.4)	29.56	45.15	2.63	21.20	16.26	11.67
(9.4-10.9)	4.70	0.30	15.24	12.31	34.41	18.39
(10.9-12.4)	70.00	101.67	62.50	84.98	53.62	63.19
(12.4-13.9)	28.51	16.88	34.12	10.10	36.33	0.66
(13.9-15.4)	14.88	9.46	35.80	11.66	39.03	0.40
(15.4-16.9)	30.56	25.50	19.42	13.04	21.01	0.99
(16.9-18.4)	3.77	71.25	2.40	78.10	4.61	76.03
(18.4-19.9)	6.61	247.79	0.60	179.15	12.74	137.38
(19.9-21.4)	79.27	49.98	82.59	34.77	70.62	17.72
(21.4-22.9)	3.18	7.99	12.85	11.86	29.28	21.15
(22.9-24.4)	31.33	2.87	36.31	17.49	20.78	30.87
(24.4-25.9)	79.70	1.65	64.87	11.12	47.59	25.09
(25.9-27.4)	98.22	10.54	87.12	1.11	83.06	9.28
(27.4-28.9)	5.93	5.33	6.61	0.58	19.81	8.32
(28.9-30.4)	13.88	3.92	6.19	3.71	2.82	3.81
(30.4-31.9)	97.96	40.44	81.86	27.79	69.73	33.39
(31.9-33.4)	31.24	12.60	2.35	25.22	10.28	15.54
(33.4-34.9)	60.68	45.11	8.70	53.29	9.08	27.99
Average	37.13	35.49	31.33	31.62	32.58	27.42

Table 9.22 Three-strorey, three-bay RC frame. Numerical results in terms of base shear capacity for damping ratios 5%, 7% and 9%.

Time Step (s)	Proposed Model Damp. Ratio=5%		Proposed Model Damp. Ratio=7%		Proposed Model Damp. Ratio=9%	
	Max (kN)	Min (kN)	Max (kN)	Min (kN)	Max (kN)	Min (kN)
(4.9-6.4)	18.02	- 21.89	17.93	-20.19	18.30	-19.65
(6.4-7.9)	26.43	-28.19	27.20	-25.08	24.35	-22.11
(7.9-9.4)	24.88	-23.76	22.42	-22.12	17.54	-19.89
(9.4-10.9)	20.94	-34.11	23.23	-34.10	19.48	-31.11
(10.9-12.4)	58.63	-35.14	55.92	-36.80	55.53	-34.15
(12.4-13.9)	66.91	-89.37	65.40	-83.84	62.60	-84.20
(13.9-15.4)	80.26	-97.59	75.31	-92.94	70.45	-92.68
(15.4-16.9)	80.25	-78.16	81.46	-71.52	80.21	-64.79
(16.9-18.4)	86.89	-64.05	88.76	-68.39	86.13	-68.90
(18.4-19.9)	68.83	-83.66	67.58	-76.23	56.94	-66.92
(19.9-21.4)	102.6	- 110.00	107.37	-107.44	101.93	-97.91
(21.4-22.9)	117.8	-139.65	110.87	-131.33	99.24	-123.18
(22.9-24.4)	111.9	-121.15	120.02	-110.58	118.37	-102.02
(24.4-25.9)	136.1	-110.29	135.72	-105.61	131.76	-98.90
(25.9-27.4)	93.13	-86.47	97.88	-90.05	97.43	-89.28
(27.4-28.9)	86.09	-95.29	87.25	-95.80	84.22	-93.51
(28.9-30.4)	53.28	-71.95	56.69	-77.07	56.24	-76.81
(30.4-31.9)	64.49	-47.50	68.10	-49.97	64.07	-46.80
(31.9-33.4)	87.02	-76.41	86.08	-78.37	79.96	-74.86
(33.4-34.9)	60.45	-68.23	55.30	-67.36	47.37	-59.39

Table 9.23 Three-strorey, three-bay RC frame. Comparison between numerical and experimental results in terms of base-shear capacity for damping ratios 5%, 7% and 9%.

Time Step (s)	Divergence from Experimental data, Damp. Ratio=5%		Divergence from Experimental data, Damp. Ratio=7%		Divergence from Experimental data, Damp. Ratio=9%	
	Max	Min	Max	Min	Max	Min
(4.9-6.4)	49.96	25.49	50.22	31.28	49.19	33.09
(6.4-7.9)	38.30	37.41	36.50	44.30	43.16	50.91
(7.9-9.4)	24.27	20.06	31.77	25.56	46.62	33.08
(9.4-10.9)	49.17	41.60	43.61	41.62	52.71	46.74
(10.9-12.4)	2.13	16.27	6.66	12.31	7.30	18.63
(12.4-13.9)	37.69	15.31	39.10	20.55	41.71	20.21
(13.9-15.4)	25.24	4.01	29.85	8.59	34.38	8.84
(15.4-16.9)	4.35	7.42	2.91	15.29	4.39	23.26
(16.9-18.4)	12.86	16.26	10.99	24.14	13.62	25.05
(18.4-19.9)	19.02	69.19	20.48	54.15	33.01	35.32
(19.9-21.4)	9.59	7.06	14.66	4.57	8.84	4.71
(21.4-22.9)	1.39	19.20	4.62	12.10	14.62	5.15
(22.9-24.4)	18.07	18.26	26.60	7.94	24.86	0.41
(24.4-25.9)	43.51	11.36	43.03	6.64	38.85	0.14
(25.9-27.4)	27.70	0.21	34.21	4.37	33.60	3.47
(27.4-28.9)	4.59	4.22	3.30	4.79	6.65	2.28
(28.9-30.4)	24.19	14.46	19.34	8.37	19.98	8.68
(30.4-31.9)	3.69	30.35	9.50	26.74	3.01	31.38
(31.9-33.4)	2.59	1.34	3.64	1.19	10.50	3.34
(33.4-34.9)	10.21	12.90	17.85	11.47	29.64	1.73
Average	20.96	18.92	22.44	18.30	25.83	17.82

Fig. 9.43 shows the force-displacement curves that are compared with the corresponding experimental data. It is found that the two numerical models that adopt damping ratios equal to 7% and 9% produce more accurate results in comparisson to the model with a 5% damping ratio. It important to note at this point that, during the experiment, there was a steel frame that was post-tensioned to the shake table on each side of the concrete frame to restrain the out-of-plain movements. This frame could have had an impact on the stiffness of the specimen and on the damping mechanisms that were developed. This effect was not accounted for during the numerical results.

a)

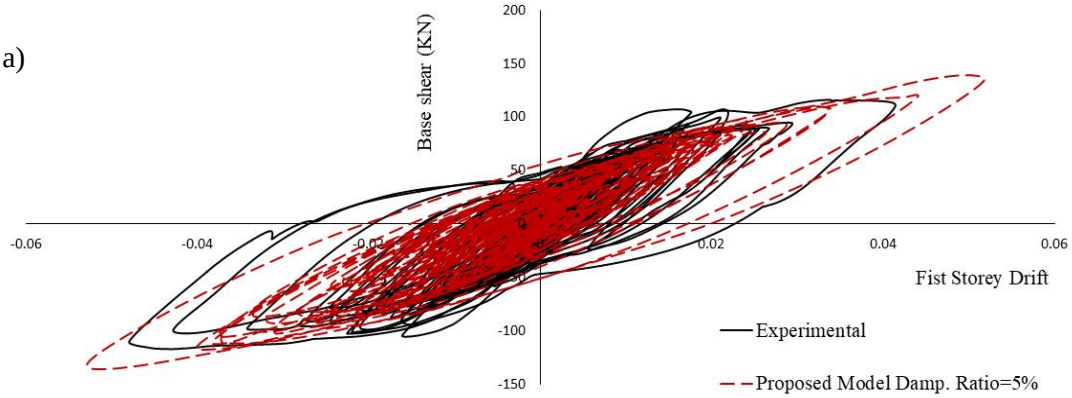

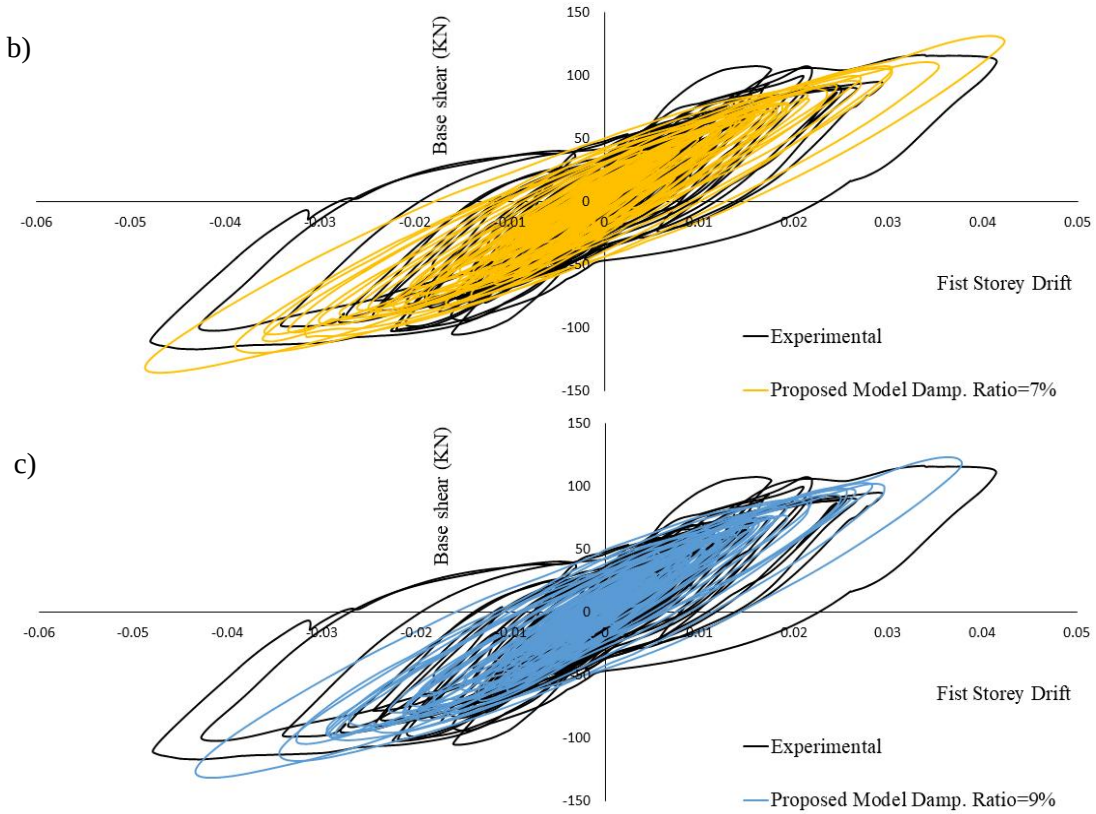

Fig. 9.43 Three-strorey, three-bay RC frame. Comparison between the numerical and experimental results of base shear-fist storey drift curves when using damping ratio equal to (a) 5%, (b) 7% and (c) 9%.

The required Newton-Raphson internal iterations per displacement increment are shown in Fig. 9.43 for the case where the damping ratio was set to 9% (similar results are derived when the use of 5% and 7% damping ratios is adopted). It can be seen that all the displacement increments require a minimal number of iterations to achieve convergence, regardless the degree of nonlinear behavior of the model. As it can be seen, the required internal iterations per dynamic step during the solution procedure were limited to 1 to 2 underlining the numerical stability of the proposed modeling method. The computational time for the nonlinear solution procedure is given in Table 9.24, which refers to the solution of 12,125 dynamic time increments. The total required time for solving the nonlinear dynamic problem was 658.5s with an average error of 1.1×10^{-5}. The CPU used to perform all the analyses had a 3.7 GHz computing power.

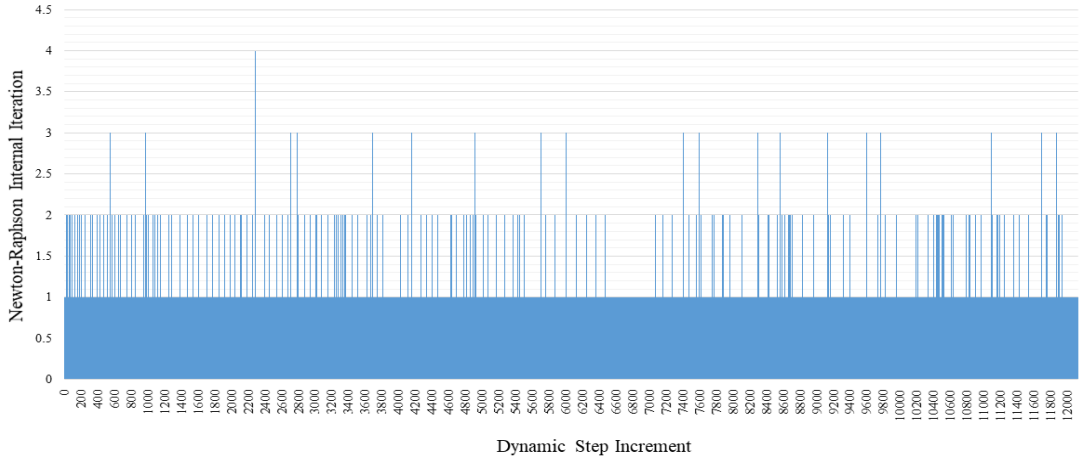

Fig. 9.44 Three-strorey, three-bay RC frame. Number of internal iterations per dynamic step increment.

Table 9.24 Three-strorey, three-bay RC frame. CPU time for different tasks of the nonlinear analysis.

Task	CPU Time (s)
Embedded rebar element mesh generation	0.24
Nonlinear incremental-iterative solution	658.22
Total Time	658.46

9.8 Conclusions

In this chapter, the integration of a 3D detailed solid finite-element model with damage factors related to both concrete and steel reinforcement was proposed for the nonlinear static cyclic and dynamic analysis of RC structures. The concrete material constitutive model combines a realistic assumption of the behavior of concrete, which numerically optimally fits with the smeared crack approach. The numerical model with crack opening and closing introduced in Chapter 5, has been integrated with a proposed concrete damage factor that was formulated by using the characteristics of cracking during the nonlinear cyclic analysis as well as by a damage factor for the steel material model that is also directly connected to the number of opening and closing of concrete cracks, leading to an accurate and numerical efficient algorithmic implementation.

An extensive numerical investigation was performed in order to validate the ability of the proposed modeling framework to capture the cyclic static and dynamic response of RC structures. To achieve this objective, three different experimental setups were modeled and analyzed under ultimate limit state of nonlinear static cyclic loading conditions, while three RC specimens where studied under dynamic loading excitations. All selected experimental setups have been subjected to cyclic loads that forced the structural elements to develop extreme nonlinearities and multiple crack openings and closings.

In the case of structures tested for static cyclic loading, the proposed model was found to be able to capture the level of damage caused by the crack opening and closing, as reported in the various experiments and to predict the overall behavior of the specimens with computational efficiency. The numerical results show that the damage factors provide accuracy to the analysis while the model captures stiffness, strength degradation and pinching mechanisms.

Additionally, the proposed model with the use of the damage factors manages to capture accurately the experimental data of different dynamic loading tests. Similarly the damage factors were found to be crucial for the accuracy and the stability of the nonlinear analysis. Based on the numerical investigation conducted on the RC frame H30, it was concluded that the use of beam elements, is a more optimal simulation approach for the steel reinforcement, which improves the numerical results compared to the experimental data. When the rod embedded rebar elements are used, the H30 frame model was found to develop larger horizontal deformations during the 3rd sinusoidal acceleration event compared to the experimental response. Furthermore, a mesh sensitivity analysis was performed and discussed in section 9.7.1.3 by using the L30 frame model. The analysis concluded that the proposed modeling approach manages to capture the experimental results without any significant mesh sensitivity effects.

A numerical investigation was also performed with a modified crack-closure algorithm, where all cracks were assumed to close when any of the two cracks was found to be closing at a double cracked GP. This modified approach had a negligible effect on the numerical response during the first two sinusoidal acceleration events (H30 RC frames). However, in the 3rd dynamic test the effects of the crack-closure assumption were greater, but still managed to capture the overall dynamic behavior of the under study frame, without any numerical discrepancies. This

sensitivity analysis demonstrates that the proposed algorithm is not affected by modifications related to the crack opening and closing mechanism. The same crack-closure assumption was studied in section 9.7.2 for the W050 RC frame, where the numerical findings indicated that the modified approach was suitable when the structure is heavily cracked but it delivered a stiffer behavior at the end of the experiment. When the structure was subjected to high dynamic excitations and began to fail, the modified approach overestimated the structure's stiffness.

In conclusion, the numerical results presented in this work, demonstrated the ability of the proposed algorithm to capture experimental results with severe nonlinearities, while the numerical model implemented for the simulation of the nonlinear 3D behavior of RC structures was characterized by a reduced computational effort that makes the proposed numerical simulation appealing for the analysis of large-scale structures undergoing excessive cyclic static and dynamic loading [37].

Chapter 10. Capturing the mechanical response of RC members with pinching effects

Contents of Chapter 10

10.1 Pinching characteristics of RC structures 261
10.2 Modified steel reinforcement constitutive law. 266
10.3 Modified concrete constitutive law-concrete crushing 268
10.4 Numerical Implementations 268
10.4.1 RC Beam-Column Joint 269
10.4.2 RC Shear wall SW4 272
10.4.3 RC Column U1 Saatcioglou and Ozcebe 274
10.4.4 RC Beam-Column Joint with Severe Damage and Extreme Slippage 275

10.1 Pinching characteristics of RC structures

The cyclic behavior of RC members describes their energy dissipation based on their mechanisms design. This is a key factor for the seismic behavior of structures that their mechanical response is controlled by plastic displacements and material deterioration that develops during an earthquake excitation. A schematic representation of the hysteretic behavior of a structural member is illustrated in Fig. 10.1. The hysteretic curves exhibit phenomena such as pinching, stiffness degradation, load degradation and sliding. The slip that occurs in plastic regions has a significant influence on the behavior of RC structures subjected to cyclic loading conditions. The slip in plastic regions ("hinges") causes the reduction of the energy dissipation in the post-yielding hysteretic response. This phenomenon is called "pinching effect". Furthermore, the cyclic loading causes the opening of many cracks, which leads to a reduction of slope and a reduction of the maximum loading capacity. These two characteristics are referred to as stiffness and load degradation. Finally, during the opening and closing of cracks, the crack faces slide over each other, leading to the development of deformations without the development of considerable shear resistance. The phenomenon of sliding occurs in regions where severe cracking takes place. The horizontal part that occurs in the beginning of the hysteretic curves as illustrated in Fig. 10.1, describes the effect of sliding.

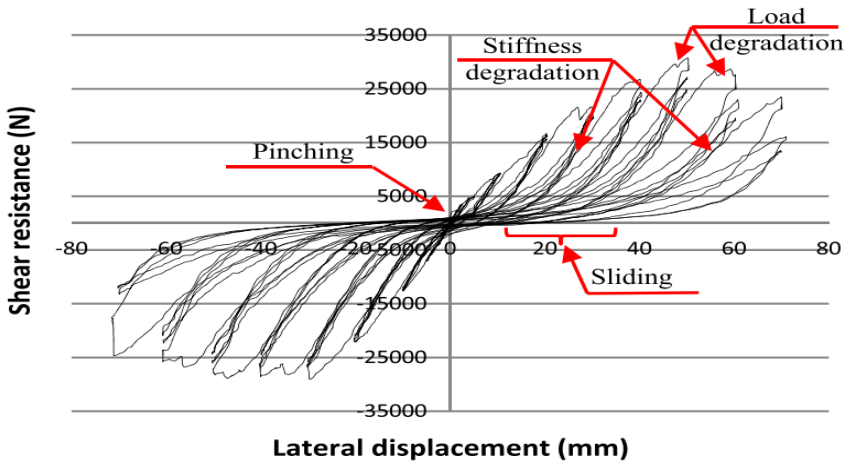

Fig. 10.1 Schematic representation of load-deflection hysteretic loops as presented by Zeynalian et al. [211].

Generally, the pinching phenomenon usually occurs in shear dominated structural members, where they have a small span to depth ratio, as illustrated in Fig. 10.2. Therefore, the effect of shear plays an important role in the hysteretic behavior of the structure.

The level of the pinching effect decreases with increasing axial load in the cases of RC joints as stated in D'Ambrisi and Filippou [212]. As observed by Atalay and Penzien [213], severe stiffness deterioration and pinching effects are appeared in members that are subjected to cyclic shear loading combined with constant axial load. The phenomenon is more noticeable when the applied axial load is relatively low. In this case, the flexural and shear cracks, formed during the previous half cycle, are open when the subjected load is close to zero. Therefore, the shear resistance mechanisms, such as aggregate interlocking and friction along cracks are ineffective. When the cracks are closed, the shear stiffness starts increasing with the contribution of aggregate interlocking and friction. On the other hand, high values of axial load can have a favorable effect on the seismic behavior of the structure. The axial load may cause the closing of the inclined cracks and diminish the effect of shear deformations, reducing the pinching

characteristics of concrete causing more flexural responses. Generally, depending on the intensity, the compressive axial load may have favorable or unfavorable effects on ductility, strength and stiffness degradation throughout the seismic response of a structural member [214].

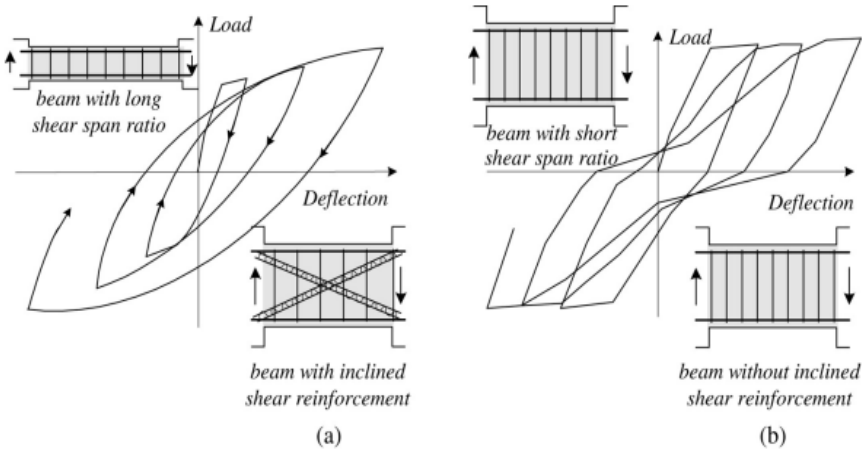

Fig. 10.2 Load deflection curves of RC beams with (a) long shear span ration (no pinching effects), (b) with short shear span ratio (pinching effects). [215]

Fig. 10.3 shows three force-displacement curves of three specimens of a RC joint with the same geometry with different steel-reinforcement configurations. The specimen J1 is designed according to ACI Committee 318M-11 requirements. The specimens exhibits ductile-displacement hysteretic response without pinching effects or stiffness or load deterioration. This is explained by the fact that the seismically designed specimen was designed in order to produce flexural yielding behavior avoiding shear failure. On the other hand, for specimens J2 and J3, the shear failure occurred before the beam-section reached its flexural yield. Therefore their (J2 and J3) is characterized hysteretic behavior by considerable pinching and continuous stiffness and strength degradation.

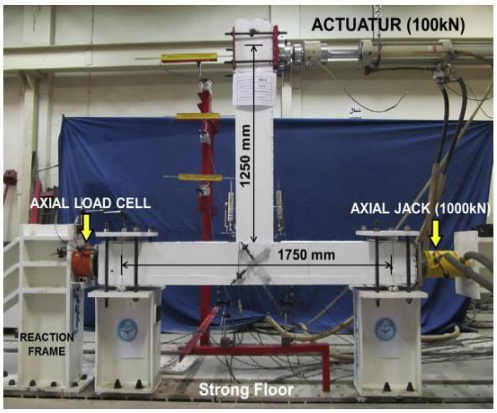

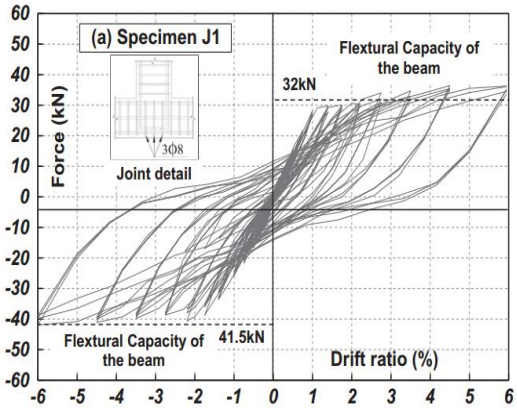

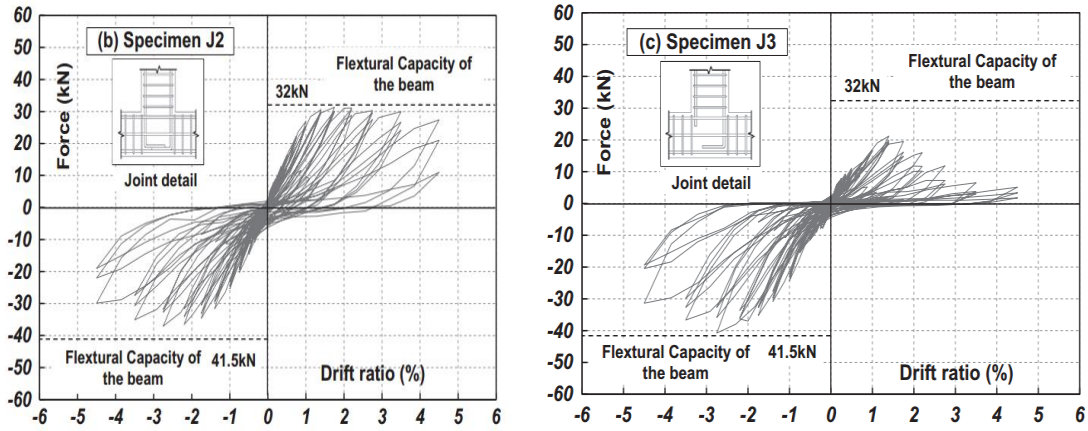

Fig. 10.3 Load displacement curves of RC joint (experimental setup –photo up and left) with (a) confined joint according to ACI 318-08 code [216], *(b) Unconfined joint with no transverse reinforcement and (c) Unconfined joint and inadequate anchorage length of beam bottom bars* [217].

In addition to the above observations, when dealing with RC walls, squat walls appear to produce highly pinched hysteretic curves with little dissipated energy. On the other hand, the slender shear walls produce more flexure-dominant responses with negligible pinching effects as illustrated in Fig. 10.4. In Salonikios et al. [218], it is observed that the axial load and the use of bidiagonal bars have a favorable effect in the hysteretic behavior of the shear wall with shear ratio 1.0 and 1.5. The hysteretic loops have elastoplastic shape with negligible shear phenomena such as pinching effects.

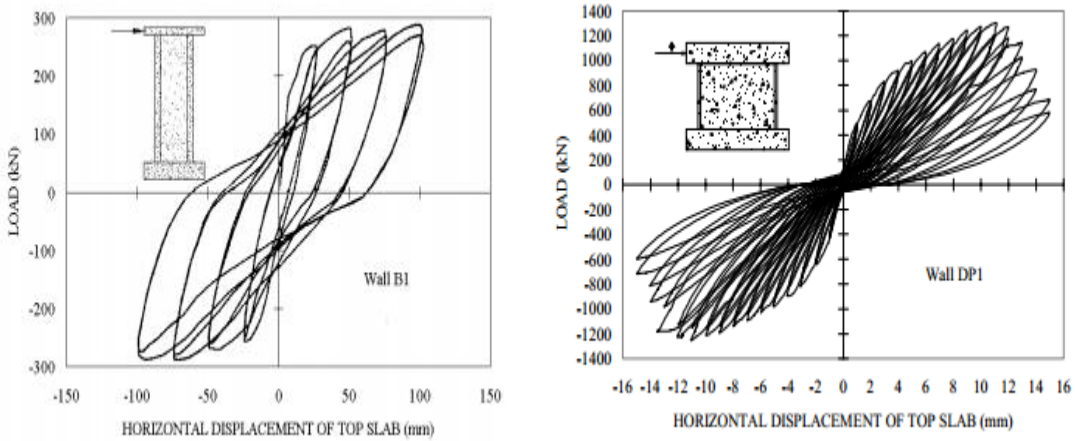

(a) (b)

Fig. 10.4 Load displacement hysteretic curves of (a) Slender RC shear wall (b) Squat RC shear wall, taken from [219].

Finally, Mansour et al. [215] examined the presence of the pinching effect in shear panels with different orientation of steel grids. It was found that when the steel grid was set in the direction of the principle applied stresses, the undesirable pinching effect is eliminating causing the increase of the energy dissipation capacity and ductility of the RC structural elements. In figure Fig. 10.5 [215], two shear panels with (a) 45° and (b) 0° steel grid orientation are shown. The panels are subjected to cyclic shear (applied stresses: σ_h, σ_V) and both vertical and horizontal cracks are open. It is illustrated that by neglecting the cracked concrete, the steel bars have to resist the applied stresses. Therefore, in the case of 45° steel grid orientation, the stresses that

are developed in the steel bars are cancelled out leading to zero shear resistance, while the shear deformation is increasing (pinching effect). In the case of the 0° steel grid orientation, the compressive and tensile stresses the developed in the steel bars are resisting the applied stresses providing shear resistance of the structural member.

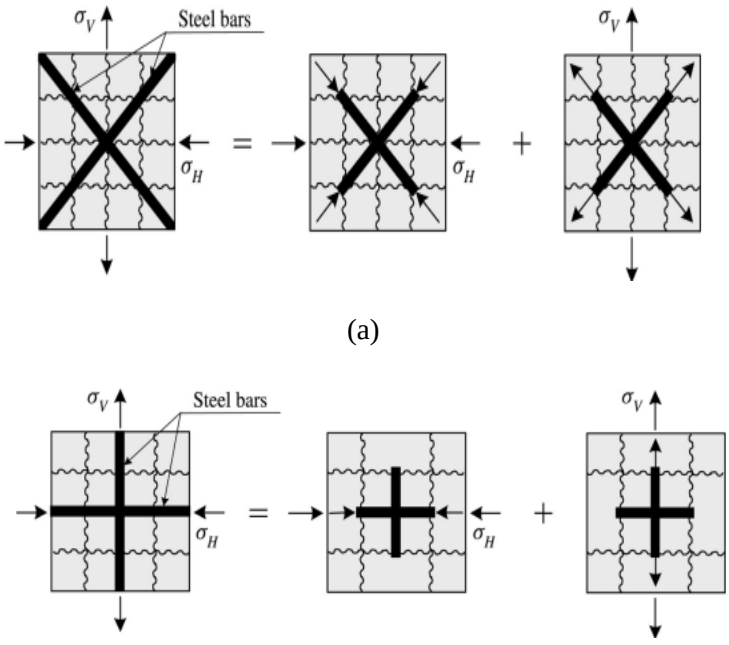

Fig. 10.5 Schematic representation of the stress development in steel bars in a concrete RC panel with (a) 45 steel grid orientation and (b) 0 steel grid orientation. (Mansour et al. [215]*)*

Furthermore, the presence of the pinching effect was also attribute to the deterioration of bonding between the steel bars and concrete medium. According to ACI Committee 408 [220], the compressive strength of concrete, concrete cover, bar size and transverse rib geometry, anchorage length, yield stress of the reinforcing bar, confinement due to transverse reinforcement and the type, and rate of cyclic loading are the main factors that affect the deterioration of bond strength. Several bond-slip models have been introduced in order to predict the behavior at the interface of concrete with steel reinforcement. Several experimental data are provided from Eligehausen et al. [221] and Viwathanatepa et al. [222], who tested the cyclic pull-out response of steel bars embedded in concrete blocks. A thorough literature review can be found in CEB [105], ACI-ASCE Committee 408 [220] and in fib Bulletin no. 10 [223], about bond stress-slip models and the characteristics of bond stress-slip behavior during cyclic loading conditions. Briefly the works of Morita and Kaku [224], Tassios [225], Viwathanatepa et al. [222], Ciampi et al. [226], Eligehausen [221], Hawkins et al. [227], Pochanart and Harmon [228], and Balàzs [229] describe the currently most well-known bond stress-slip models. The model of Eligehousen et al. [10] can describe the local bond stress-slip relationship for arbitrary slip histories as illustrated in Fig. 10.6 which is characterized with simplicity and it has been successfully integrated in many numerical models.

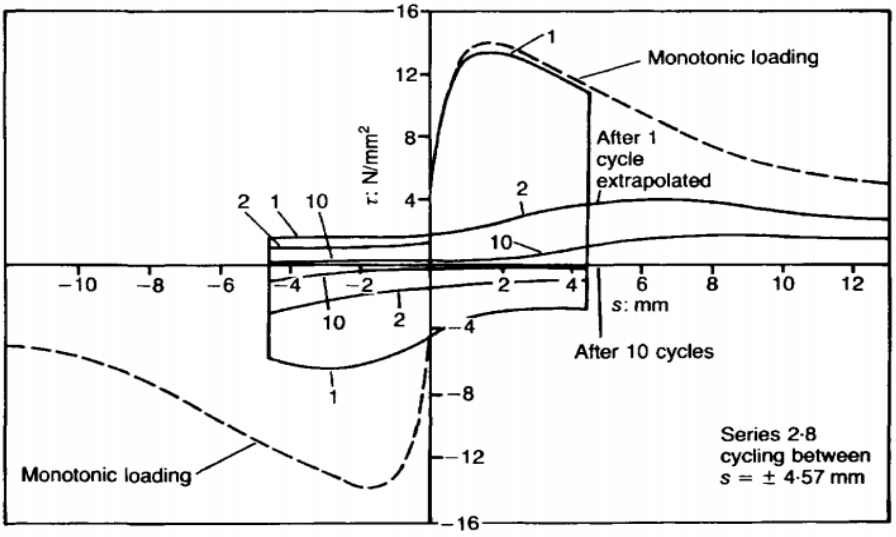

Fig. 10.6 Cyclic bond-slip model from Eligehausen et al. [221]

When dealing with the analysis of RC structural members under cyclic loading, the bond slip model is usually modelled by introducing an additional dof at each rebar of every reinforcement bar (Girard and Bastien [19], Lykidis and Spiliopoulos [27]). Lowes [103] and Fleury et al. [179] used bond elements with zero width for modeling the bond-slip effect of steel bars in RC Joints in 2D analysis. In Monti and Spacone [230], Limkatanyu and Spacone [231] and Ayoub [232], a fiber element which allows for bar slipping for RC columns was presented. Au and Bai [21] modeled the bond-slip effect by adopting a contact elements proposed by Hoshino [233] and Schaefer [234], and subsequently modified by Dinges [235]. Eligehausen et al. [10] assumed a 1D nonlinear spring with a bond-slip relationship, while Melo et al. [24] used a zero-length section element in order to model the bond-slip effect.

The "pinching" effect becomes a very significant factor for the inelastic behavior of RC members in order to predict accurately the energy dissipation of the structure. The phenomenon has to be introduced into the numerical model in a proper way in order to provide accuracy and computational efficiency.

According to the above discussion, the phenomenon of the pinching effect is connected with the crack opening and closure, the crack width, the bonding between steel and concrete, and generally the shear-resistance mechanism of cracked concrete (i.e. aggregate interlock and dowel action). Therefore, when a shear dominated structure is subjected to cyclic loading, in the case of unloading and close to zero applied load, the cracked RC member provides negligible resistance.

The proposed modeling approach which was presented in Chapter 5 and Chapter 9, treats cracking with the smeared crack approach with an abrupt loss of caring capacity when the failure criterion is satisfied. Therefore, the stiffness of concrete members in the direction of the maximum principle tensile stress is set to zero. The shear stiffness of cracked concrete structure is modelled to have a relatively small value which is controlled by the parameter β (shear retention factor, see Chapter 6) which is set to 0.05. The modeling of the crack-closing phenomenon plays an important role to the computational accuracy and numerical efficiency of the model as explained in Chapter 5. Taking into advantage the parameter that controls the level of crack width and forms the crack-closing criterion, a damage factor for concrete was introduced as described in Chapter 9. In this way, the evolution of damage during the static cyclic and dynamic loading process is modelled efficiently describing accurately the strength

and stiffness degradation. The pinching effect, is a phenomenon which appears abruptly and as explained before there are several reasons which can cause it. One main reason that was found to play a controlling role was therefore, a damage factor for steel reinforcement was also introduced the rebar steel response accounting for the crack opening and closing of procedure near the steel reinforcement. It is evident that the number of opening and closing of cracks, and the width of crack opening enhance the slipping of steel bars and deteriorate the shear capacity of the concrete domain. The effect of closing and opening cracks are also observed experimentally in [35]-[36]. Kwak and Kim [20] proposed a modification of the constitutive law of steel reinforcement in order to predict the pinching effect. This approach is also used in this work.

The reduction of shear-stiffness near the "zero applied load" can indirectly be taken into account by modifying the steel reinforcement constitutive law. In this way, a reduced stiffness contribution of the steel reinforcement by defining the accumulated damage due to the crack opening/closure effect can be considered as a result of the loss of bonding mechanism. Consequently, this reduction can also be characterized as the loss of bonding between steel reinforcement and the surrounding damaged concrete without introducing new dofs, which will add computational cost. It must be noted at this point that, the introduction of a dof for each steel reinforcement for integrating them with a bond stress-slip law has been proposed by Lykidis and Spiliopoulos [27]. The model could capture the slipping phenomena of steel bars but it did not show the numerical ability of capturing the pinching effect. In order to overcome previous constraints in capturing the pinching effect characteristics, two modification are proposed herein applied on the steel reinforcement constitutive law, thus, making the capture of the pinching effect numerically feasible.

10.2 Modified steel reinforcement constitutive law.

The steel reinforcement is modelled through the use of the Menegotto-Pinto [34] model that takes into account the Bauschinger effect. The stress-strain relation is described by the Eqs. (5.93) and (5.94). In shear dominated areas of a RC structure, the severe inclined cracking leads to significant strength deterioration of steel reinforcement thus affecting the hysteretic loops of the entire RC member leading to pinching characteristics. The level of damage that occurs due to the opening of cracks can be expressed by the reduction factor introduced in Chapter 9 (Eqs. (9.8)-(9.10)).

As it was mentioned in section 9.4, the material deterioration is applied when $\sigma_s \cdot \varepsilon_s < 0$, which describes the situations when crack closures and re-openings occur and the pinching phenomena are excessive. The σ-ε curves of the Menegotto-Pinto material model that uses the proposed steel damage factor (described in section 9.4) is shown in Fig. 10.7 with different values of the damage factor D_s. The proposed modification of the steel Menegotto-Pinto model is an indirect way of capturing this phenomenon by taking into account the level of cracking that occurred in the surrounding area of the steel rebar, which in this case is the hexahedral element that hosts the embedded rebar. An alternative way of introducing the pinching effect through the stress-strain law of steel reinforcement, is by reducing the parameter R (Eq. (5.94)) of the Menegotto-Pinto [34]. Therefore, by using the same reduction factor the parameter R' is calculated though the following expression:

$$R' = (1 - D_R)R \text{ where } D_R = D_s \tag{10.1}$$

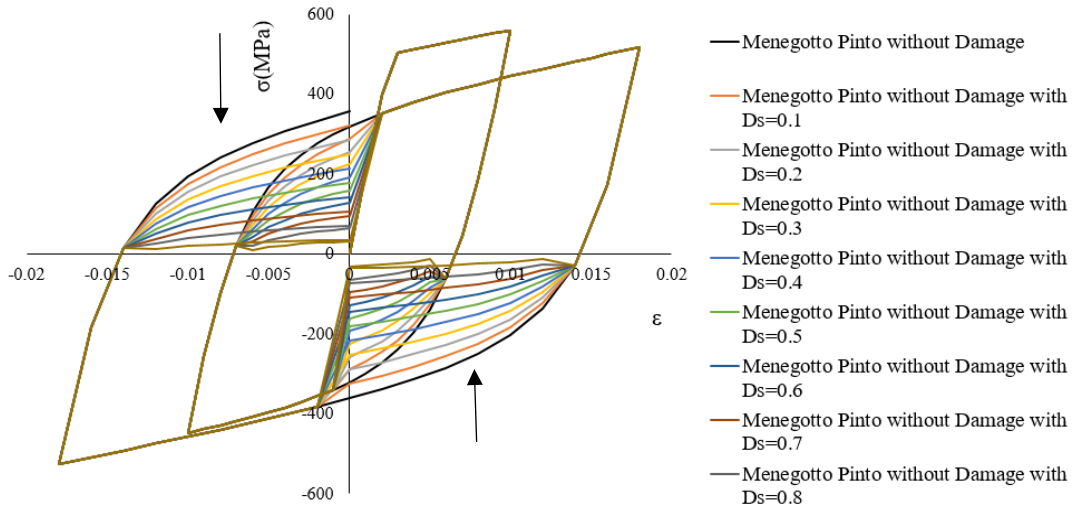

Fig. 10.7 Menegotto-Pinto steel model that uses the modified formulation for parameters E´ (Eq. (9.10) for different values of the damage factor D_S.

Similarly, the material deterioration is applied when $\sigma_s \cdot \varepsilon_s < 0$, which describes the situations when crack closures and re-openings occur and the pinching phenomena are excessive. The σ-ε curves of the Menegotto-Pinto material model that uses the modified steel damage factor is shown in Fig. 10.8 for different values of the damage factor D_R.

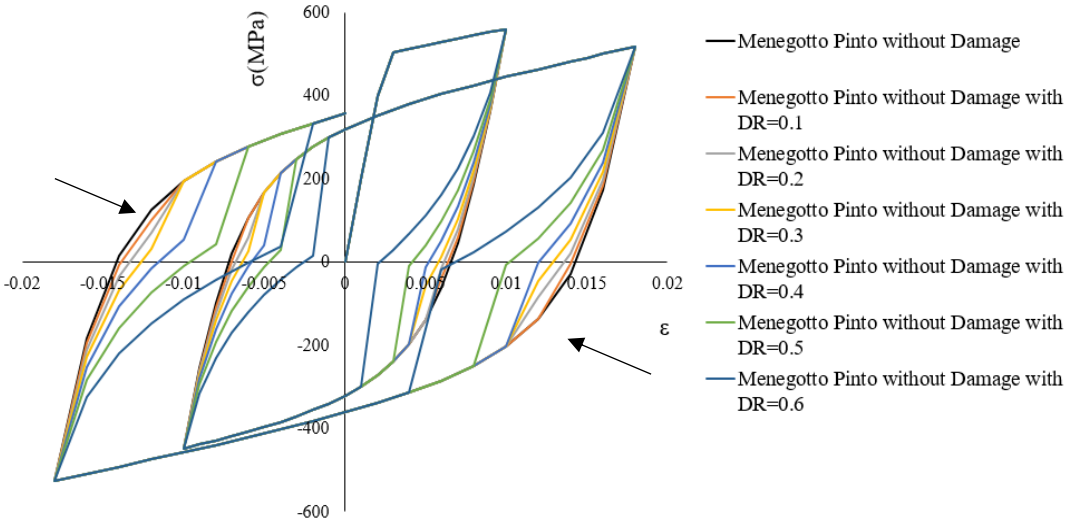

Fig. 10.8 Menegotto-Pinto steel model that uses the modified formulation for parameter R´ (Eq. (10.1)) due to the opening and closure of cracks with different values of the damage factor D_R.

It was also found that, the combination of both damage factors D_S (Eq. (9.10)) and D_R (Eq. (10.1)) could enhance the pinching characteristics of the hysteretic loops. The σ-ε curves of the Menegotto-Pinto material model that uses the modified steel damage factors *(D_s* and *D_R)* are shown in Fig. 10.9 with different values of the damage factors D_s and D_R.

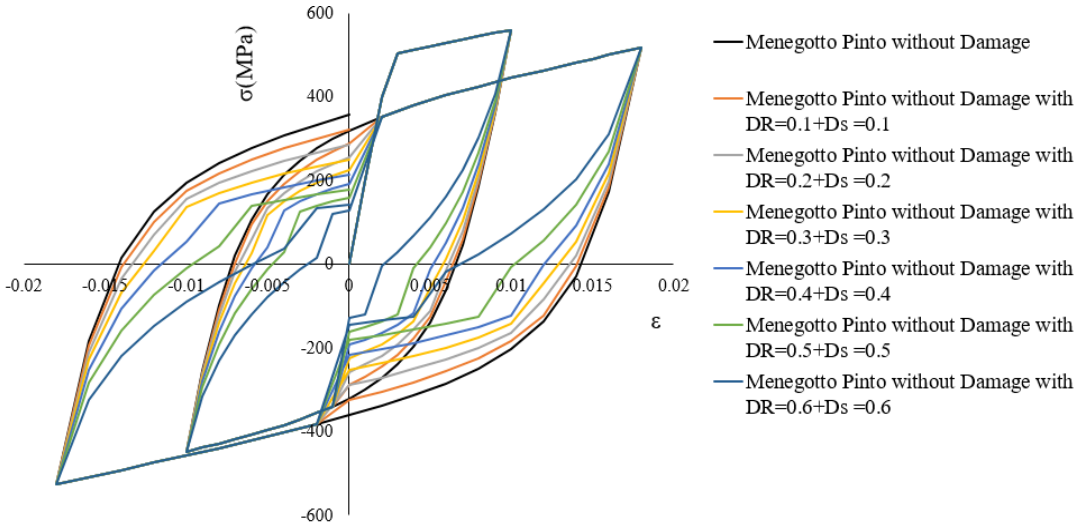

Fig. 10.9 Menegotto-Pinto steel model that uses the modified formulation for parameters E´(Eq. (9.10), R´(Eq. (10.1)) with different values of the damage factor D_R and D_S.

10.3 Modified concrete constitutive law-concrete crushing.

When the concrete failure at a GP is satisfied due to the fact that concrete is under triaxial compression, it is assumed that the concrete is crushed and numerically it is treated as a GP that has completely lost its resistance. This assumption could lead to an underestimation of the capacity of the cracked concrete under compression. Therefore, a small amount of stiffness can be assumed, which can be connected with the width of cracking and the parameter *a* (Eq. (5.89)).

Following the approach of introducing damage factors in Chapter 9, the constitutive matrix of the GP, which is under a crushing stress state is calculated through the following diagonal matrix:

$$C_l^* = \begin{bmatrix} \beta_c\cdot(1-D_c)\cdot(2G_t+\mu) & 0 & 0 & 0 & 0 & 0 \\ 0 & \beta_c\cdot(1-D_c)\cdot(2G_t+\mu) & 0 & 0 & 0 & 0 \\ 0 & 0 & \beta_c\cdot(1-D_c)\cdot(2G_t+\mu) & 0 & 0 & 0 \\ 0 & 0 & 0 & \beta_c\cdot(1-D_c)\cdot\beta\cdot G_t & 0 & 0 \\ 0 & 0 & 0 & 0 & \beta_c\cdot(1-D_c)\cdot\beta\cdot G_t & 0 \\ 0 & 0 & 0 & 0 & 0 & \beta_c\cdot(1-D_c)\cdot\beta\cdot G_t \end{bmatrix} \quad (10.2)$$

Where $\beta_c = 0.025$, a parameter similar to the shear retention factor β and D_c is the damage factor introduced in Chapter 9. The GP is assumed to have lost its resistance, but due to the newly developed constitutive matrix of Eq. (10.2), it is assumed that it has the ability to develop a resistance that is decreasing as the compressive cracks are increasing. Therefore, the cracks of a crushed GP cannot close but do maintain a low stiffness resistance, a numerical approach that does not introduce any instabilities. Furthermore, for the case of RC structures that are subjected to high axial compressive loading, this numerical approach provides the analysis with the required stability in cases of excessive concrete crushing.

10.4 Numerical Implementations

In this section, the numerical validation of the proposed model will be presented in order to predict the pinching characteristics of the hysteretic behavior of structural members for the case

of static cyclic analysis under ultimate limit state loading conditions. It must be noted at this point that all the numerical tests presented in this section have been performed by using a computer with a processing power of 2.50 GHz.

10.4.1 RC Beam-Column Joint

Two beam-column joints shown in Fig. 10.10, were tested by Shiohara and Kusuhara [38] under static cyclic loading. The uniaxial compressive concrete strength was reported to be equal to *fc* = 28.3 MPa and the yielding stress of the steel reinforcement was 456 MPa for the 13 mm diameter bars found in the beam section, while the yielding stress of the bars, placed within the column section, was reported to be equal to E_S = 176 GPa. For the stirrup reinforcement, 6 mm in diameter rebars were used with a yielding stress of 326 MPa and a Young modulus of elasticity equal to 151 GPa.

The frame joint was subjected to different cyclic loading sets according to the experiment [38]. The loading history that was numerically applied in this work, is presented in the form of 15 cycles of imposed displacements as shown in Fig. 9.8 (the same as A2 in Chapter 9). The concrete domain was discretized with 8-noded hexahedral finite elements and the steel reinforcement was discretized with beam finite elements. A total number of 128 concrete (23cm x 15cm x 15cm) and 888 steel NBCFB elements were used to discretize the entire frame joint, following the same approach as described in Chapter 9 for the analysis of specimen A2 [38]. Specimen A1 is simulated as an interior beam-column joint, while specimen A3 simulated the conditions of an exterior corner joint.

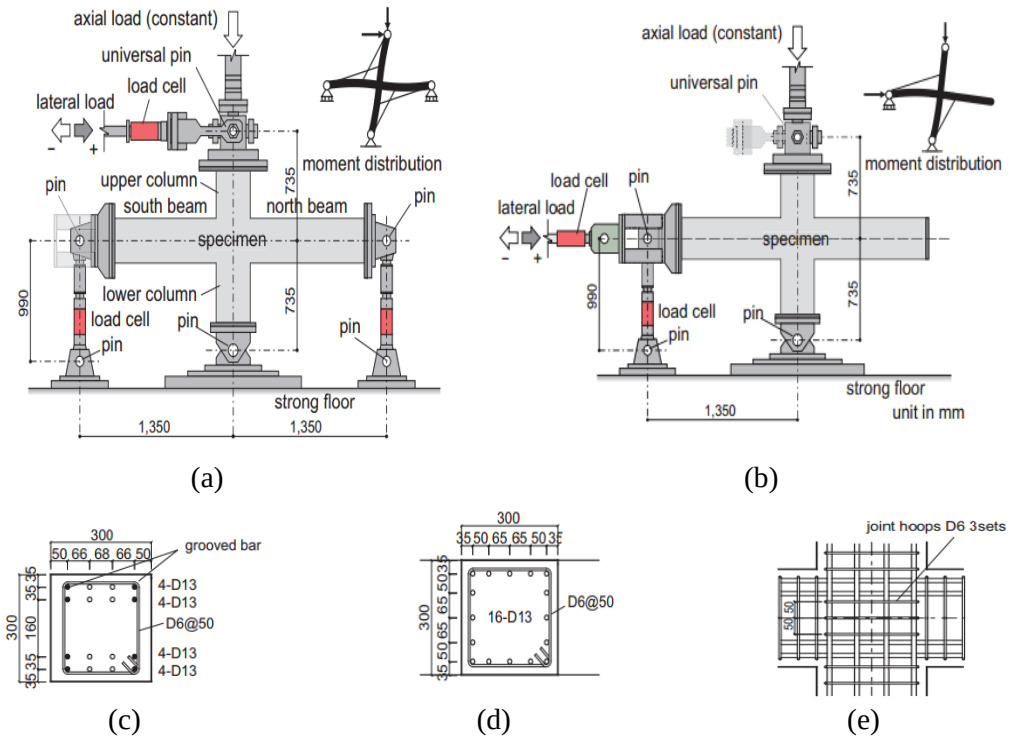

Fig. 10.10 Beam Column joints. Geometry of (a) A1 and (b) A3 specimens, and reinforcement details of the (c) beam, (d) column and (e) joint section. [38]

The boundary conditions of the numerical model can be seen in Fig. 10.11, where the displacements were imposed at the top section of the column for specimen A1 and at the left edge of the beam for specimen A3. A 216 kN compressive force was applied at the top section

of the column for both specimens. Additionally, 8-noded hexahedral finite elements were used at the support and at the sections where displacements are imposed to simulate the metallic plates, that were placed in order to avoid local failure.

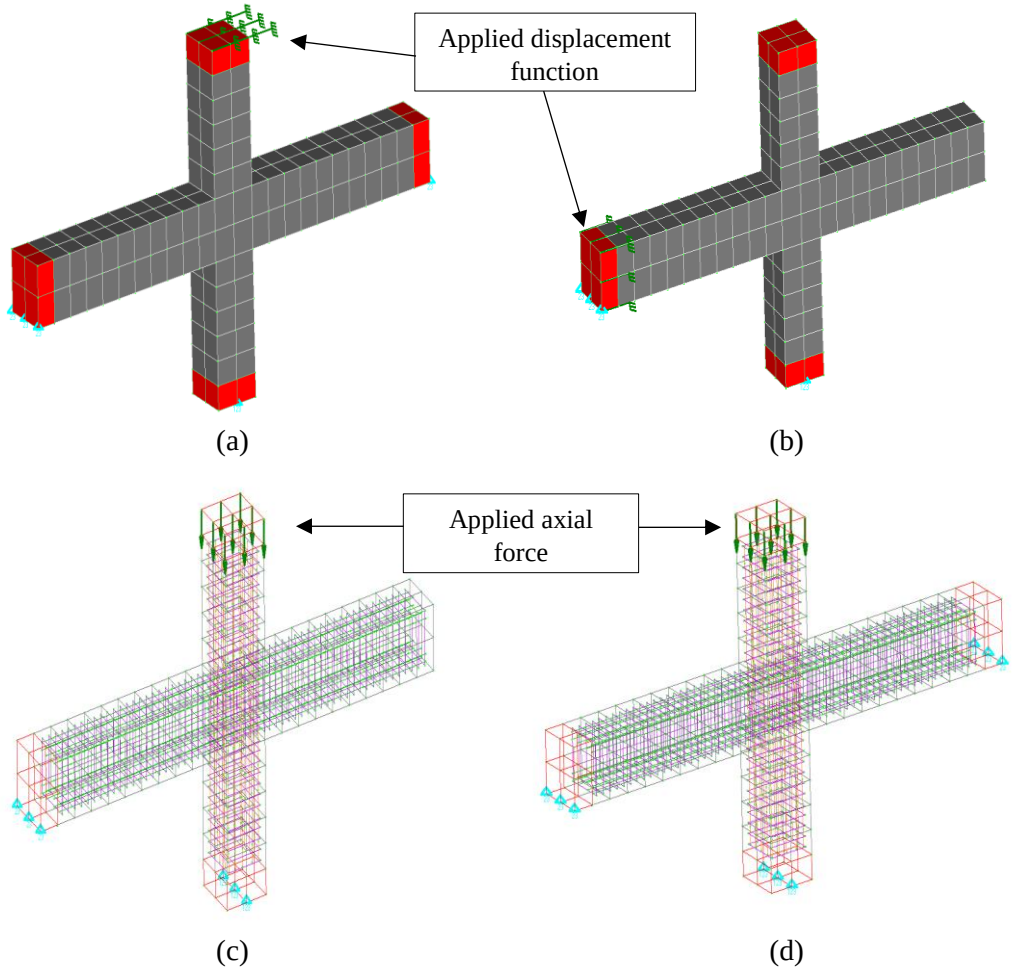

Fig. 10.11 RC beam-column frame joint. FE concrete mesh with imposed displacements for specimen a) A1 and (b) A2. Steel reinforcement mesh and applied axial loads for specimen a) A1 and (b) A2.

The computed force-displacement curves are compared with the corresponding experimental data in Fig. 10.12. As can be seen, the numerical results match very well with the experimental data, where the stiffness and the resulted load-carrying capacity of the specimen were predicted in an accurate manner. Furthermore, the numerical energy dissipation values are very close to the experimental ones. Fig. 10.13 also shows the force-displacement curve when the proposed damage factors for concrete and for steel reinforcement are not applied when modeling specimen A1. The numerical results show that the concrete damage factors manage to capture the stiffness and load-capacity degradation. Furthermore, the pinching characteristics are captured through the use of the modified Menegotto-Pinto model (see Fig. 10.13b). Nevertheless, the pinching effect is observed to be smaller than the experimental one. This is probably attributed to the sliding effect which is shown in the experimental data (Fig. 10.12) due to slipping of steel reinforcement.

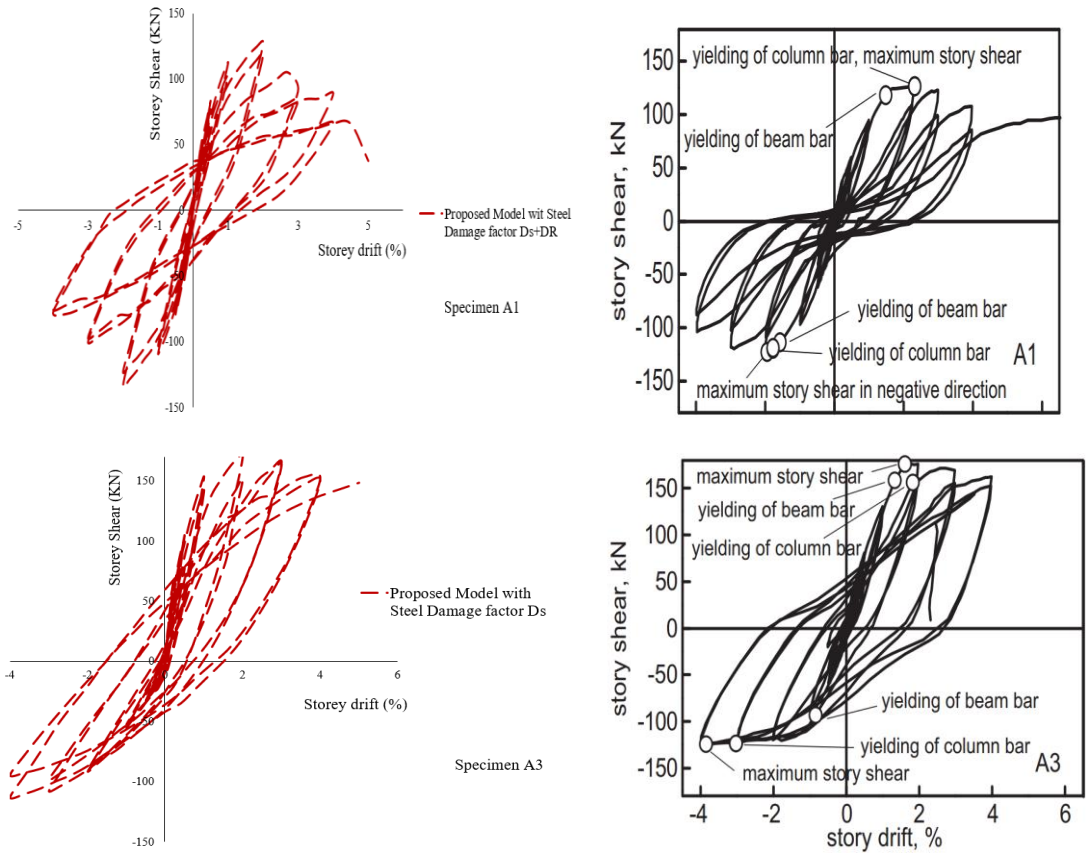

Fig. 10.12 Beam-Column frame joint. Comparison between numerical and experimental results. Complete force-displacement history for specimens A1 (up) and A3 (down).

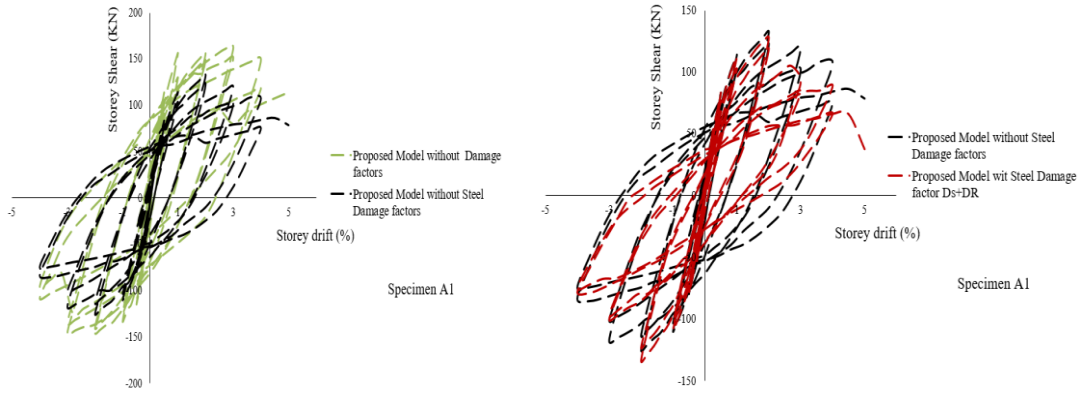

(a) (b)

Fig. 10.13 Beam-Column frame joint. Comparison between numerical results that consider for the (a) concrete damage factor and (b) concrete and steel reinforcement damage factors.

Additionally, as it resulted from the numerical investigation, the hysteretic loops of specimen A3 produce more flexural behavior which is also observed at the experimental results (Fig. 10.13). The numerical results show that they are not affected significantly by the consideration of the damage factor D_s, which is a realistic aspect of the at hand problem given the fact that the experimental behavior presents negligible pinching effects. Nevertheless, the experimental unloading branches of the last cycles, present a considerable small stiffness which is probably attributed to the loss of bond of the steel reinforcement. Table 10.1, shows the comparison of

the maximum predicted storey shear and the experimental data. The comparison shows that the discrepancy between the numerical and experimental data is lower than 10%.

Table 10.1 Beam-Column frame joint. Comparison of the maximum storey shear between experimental and numerical results.

Column-Joint		Maximum Storey Shear		Divergence from Experiment (%)
		Experimental (kN)	Numerical (kN)	
A1	(+)	126.6	127.84	0.98
	(-)	-122.8	-134.12	-9.21
A3	(+)	176.4	171.16	-2.97
	(-)	-124.5	-112.98	9.25

10.4.2 RC Shear wall SW4

The RC shear wall investigated by Pilakoutas and Elnashai [236], was also analyzed by using the modified model. The shear wall was denoted as SW4 and it is rectangular with 1.2 m height and 0.6 m length and 0.06 m thickness as showed in Fig. 10.14 . The material properties are shown in Table 10.2.

Table 10.2 Material properties of Shear wall SW4

Region	Concrete		Horizontal Reinforcement		Vertical Reinforcement		Confining Reinforcement	
	f_c (MPa)	E_c (MPa)	ρ (%)	f_y (MPa)	ρ (%)	f_y (MPa)	ρ (%)	f_y (MPa)
Web	36.9	35240	0.39	545	0.5	545	-	-
Boundary	36.9	35240	0.79	545	6.86	470	0.43	545

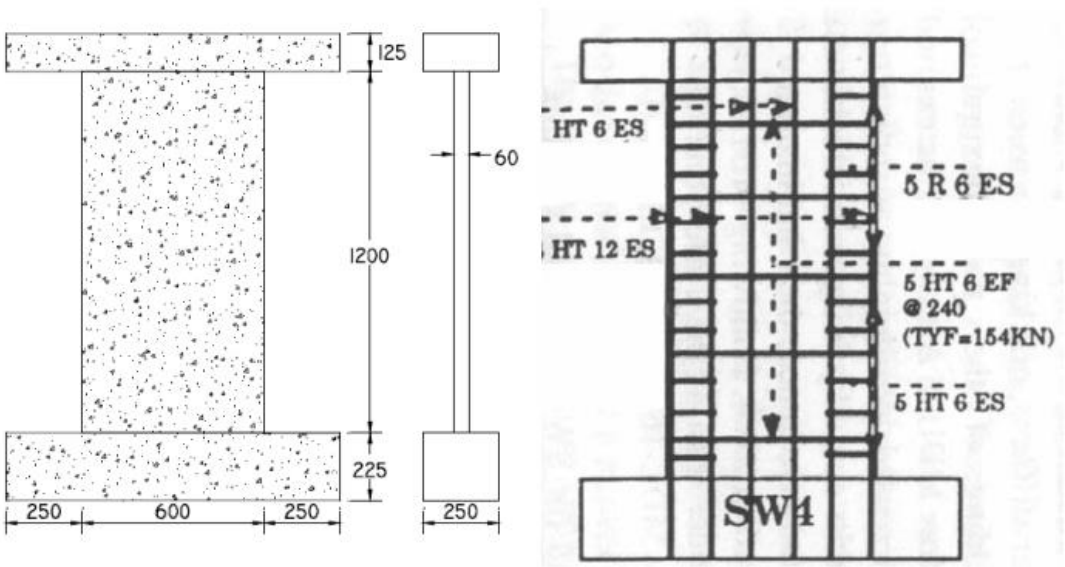

Fig. 10.14 Geometric and reinforcement details of Shear wall SW4 [236].

The shear wall was subjected to different cyclic loading sets according to the according experimental setup [236]. The loading history represents extreme conditions experienced during a severe earthquake and it is illustrated in Fig. 10.15. The concrete domain was discretized with 8-noded hexahedral finite elements and the steel reinforcement was discretized with NBCFB elements. A total number of 50 concrete (23cm x 15cm x 15cm) and 250 steel

reinforcement elements were used to discretize the entire shear wall as illustrated in Fig. 10.16. Additionally, rigid hexahedral elements were used to simulate the metal plates near the boundary condition in order to avoid local failure (red elements in Fig. 10.16).

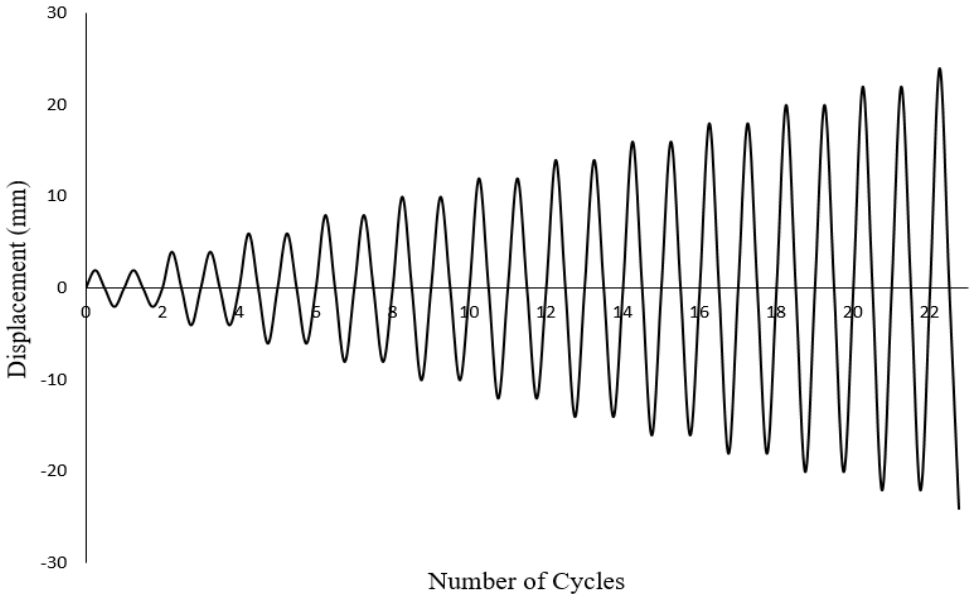

Fig. 10.15 Loading history subjected to SW4

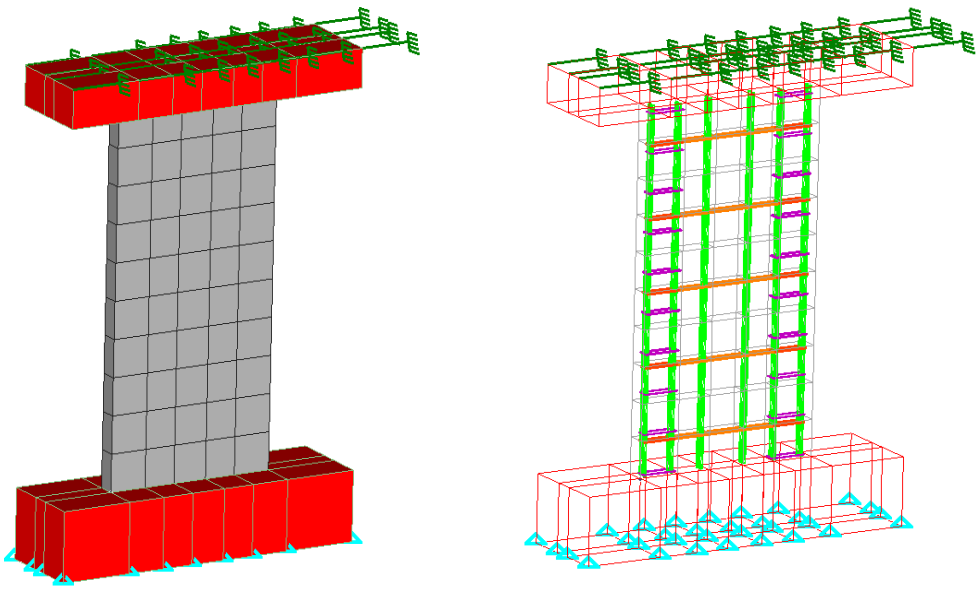

Fig. 10.16 Shear wall SW4. 3D views of the FE mesh of concrete and embedded steel rebar elements.

The numerically curves are compared with the corresponding experimental data in Fig. 10.17. As it can be seen, the numerical results match very well with the experimental data, where the stiffness and the load-carrying capacity of the specimen were predicted in an accurate manner. Furthermore, the numerical energy dissipation of the structure was found to be very close to the experimental one. In addition, the experimental results show a more flexible behavior in terms of structural response without significant pinching effect characteristics. The same mechanical behavior was captured from the numerical results that also did not indicate for any significant pinching behavior.

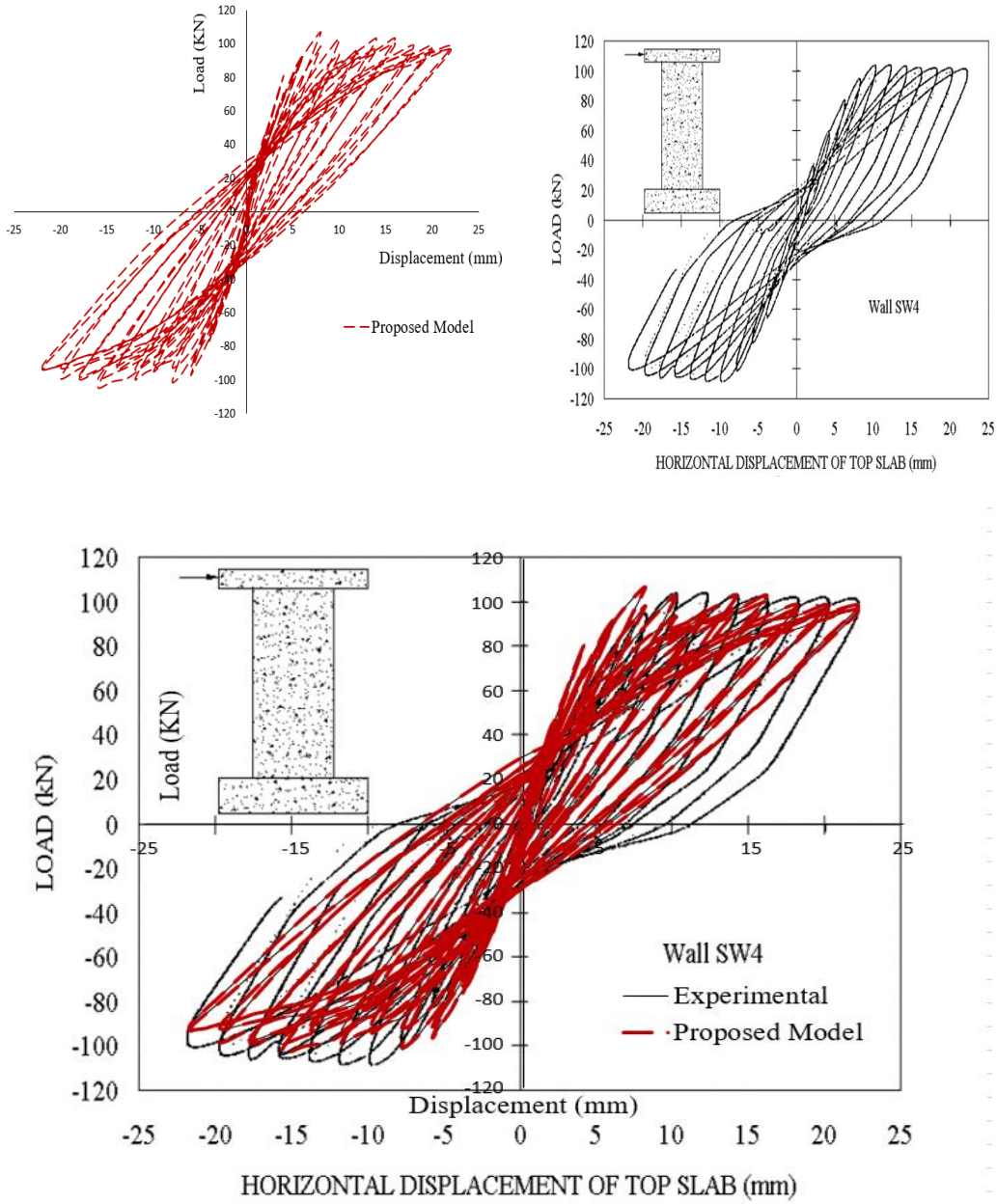

Fig. 10.17 Shear Wall SW4. Comparison between numerical and experimental results in terms of the force-deflection curves.

10.4.3 RC Column U1 Saatcioglou and Ozcebe

Another structural member, which was numerically investigated with the modified model, is a RC column that was subjected to ultimate limit state cyclic loading conditions. This column was experimentally investigated by Saatcioglou and Ozcebe [39] and it was denoted as U1. The uniaxial compressive concrete strength was reported to be equal to f_c = 43.6 MPa and the yielding stress of the steel reinforcement was 430 MPa for the 25 mm rebars used to reinforce the beam section, while the yielding stress for the 10 mm rebars found in the column section was 470 MPa. The geometry, reinforcement details and the mesh of the finite element model U1 as can be seen in Fig. 9.13 in Chapter 9. The stirrups of the specimen U1 have distance 150 mm (Φ10/15cm). The loading cyclic history that was applied on specimen U1, was the same with the specimen's U4, as shown in Fig. 9.14. It must be noted here that specimen U1 was not subjected to any static compressive force during the cyclic test.

The computed force-displacement curves are compared with the corresponding experimental data in Fig. 10.18. As it can be seen, the numerical results without the use of steel damage factors, exhibit larger dissipating energy comparing to the experimental results. The hysteretic curves were predicted with a satisfying accuracy, in terms of loading capacity, stiffness and energy dissipation when the proposed D_s (see Eqs. (9.10)) damage factors are used. The numerical results, when the damage factors are activated (D_s), manage to describe in a realistic manner the experimental results, capturing accurately the strength, stiffness degradation and pinching characteristics. However, specimen U1 suffered from severe damage with significant concrete spalling along the height of the column as it was reported in [39]. The numerical model exhibited larger stiffness than the experimental during the last 3 cycles. However, the experimental results show that the strength and stiffness of the specimen was significantly diminished probably due to compressive failure which the model could not capture during the last 3 cycles.

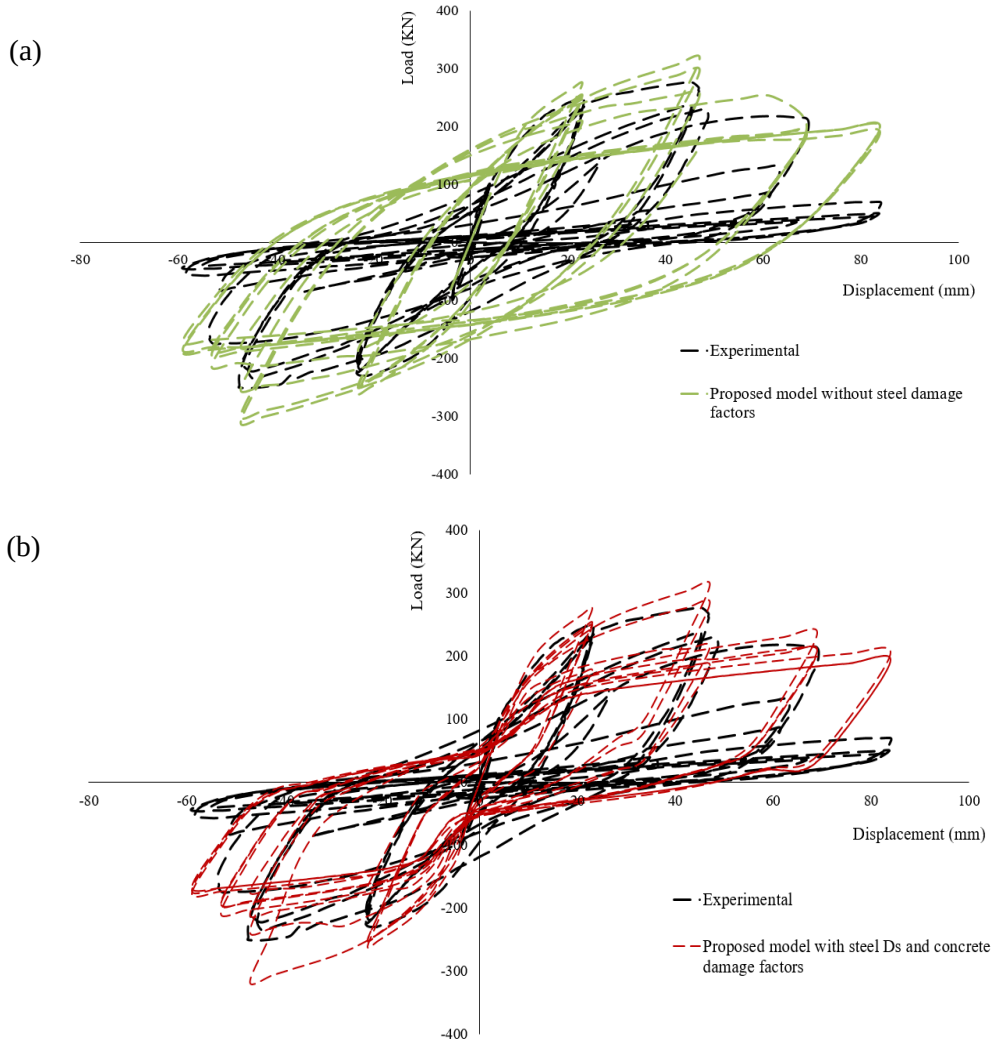

Fig. 10.18 RC column U1. Comparison between numerical results considering damage factors for (a) concrete (b) considering damage factors for both concrete and steel reinforcement.

10.4.4 RC Beam-Column Joint with Severe Damage and Extreme Slippage

An exterior joint was tested by Garcia et al. [237] by applying cyclic loading. The column had

a cross-section of 260 x 260 mm and the longitudinal reinforcement were 16-mm in diameter. The beam had a cross section of 260 x 400 mm and was also reinforced with 16-mm rebars, as illustrated in Fig. 10.19.

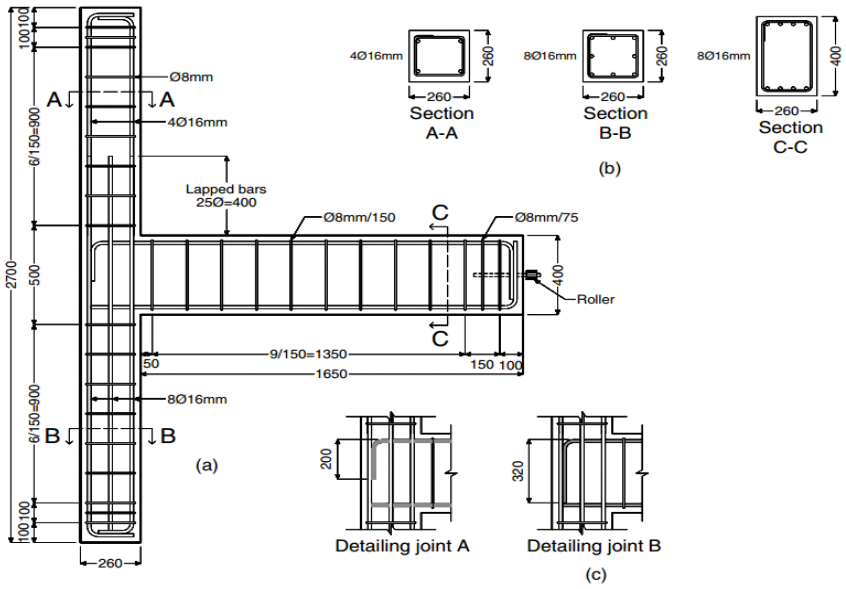

Fig. 10.19 Geometric and reinforcement details of the beam-column joints tested in Garcia et al. [237].

Two types of bar anchorage detailing were examined for the top beam reinforcement as shown in Fig. 10.19c. Therefore, two specimens JA2 and JB2 with different anchorage details were examined .The beam reinforcement of type A and B (Fig. 10.19c) are anchored into the joint for a length of 220 mm (approximately $14d_b$) with no hooks or bends. This short anchorage is assumed insufficient to develop the full capacity of the 16-mm bars according to current design recommendations. Furthermore, the flexural strength of column was designed to be the same as the beam not following the design philosophy of strong column-weak beam. The specimens were designed to fail at the core where there are not any confining stirrups. In order to avoid the shear failure outside the core of the joint, 8-mm transverse stirrups were provided at the column and the beam members spaced every 150 mm. The mean concrete compressive strength was 32 MPa and 31.3 MPa for specimens JA2 and JB2, respectively, and the respective tensile splitting strength was 2.44 MPa and 2.41 MPa for the two specimens. The yield and tensile strength of steel reinforcement were reported to be f_y = 612 MPa and f_u = 726 MPa for the 8 mm bars and f_y = 551 MPa and f_u = 683 MPa for the 16 mm bar respectively. Additionally, the elastic modulus was equal to E_s = 209 GPa.

The frame joints were subjected to different cyclic loading sets according to experiment configuration and design. The loading history is consisted of three push-pull cycles at drift ratios of ±0.25%, ±0.5%, ±0.75%, ±1.0%, ±1.5%, ±2.0%, ±3.0%, ±4.0% and ±5.0%. Furthermore, a second actuator applied a constant axial load N = 150 kN on the column as illustrated in Fig. 10.20.

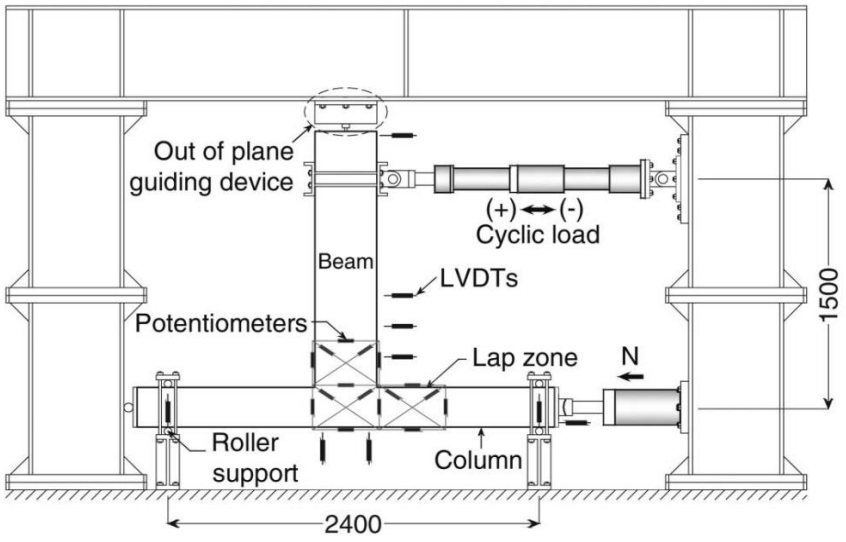

Fig. 10.20 Test setup (units: mm) and instrumentation of RC joints. [237]

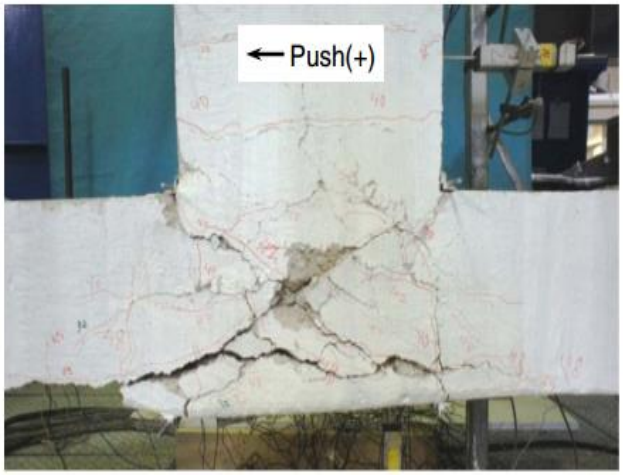

Fig. 10.21 Failure of JB2 specimen [237].

The specimens suffered from severe damages where excessive diagonal cracking and partial concrete spalling in the core had been observed as shown in Fig. 10.21. For the needs of this research work, specimen JB2 was studied through the use of the proposed numerical model that uses the modified damage factors for concrete and steel reinforcement. So as to study the mechanical behavior of specimen JB2, the concrete domain was discretized with 8-noded hexahedral finite elements and the steel reinforcement was discretized with NBCFB elements. A total number of 174 concrete and 324 steel elements were used to discretize the RC joint while 18 hexahedral steel elements (red color) were used at the areas of the boundary conditions in order to prevent local failure, as illustrated in Fig. 10.22.

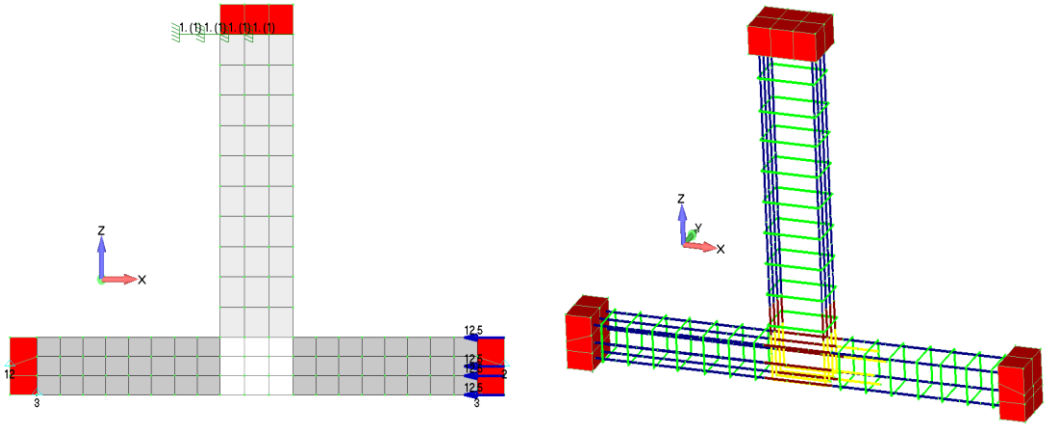

Fig. 10.22 RC joint JB2. (Left) Hexahedral and (Right) embedded rebar finite elements.

The computed force-displacement curves are compared with the corresponding experimental data in Fig. 10.23. As it can be seen, the numerical results match very well with the experimental data, where the stiffness and the resulted load-carrying capacity of the specimen were predicted in an accurate manner. The numerical results show that the concrete damage factors manage to capture the stiffness and load-capacity degradation, where, the pinching characteristics are captured through the use of modified Menegotto-Pinto model by using the damage factors D_s and D_R given in Eqs. (9.10) and (10.1), respectively.

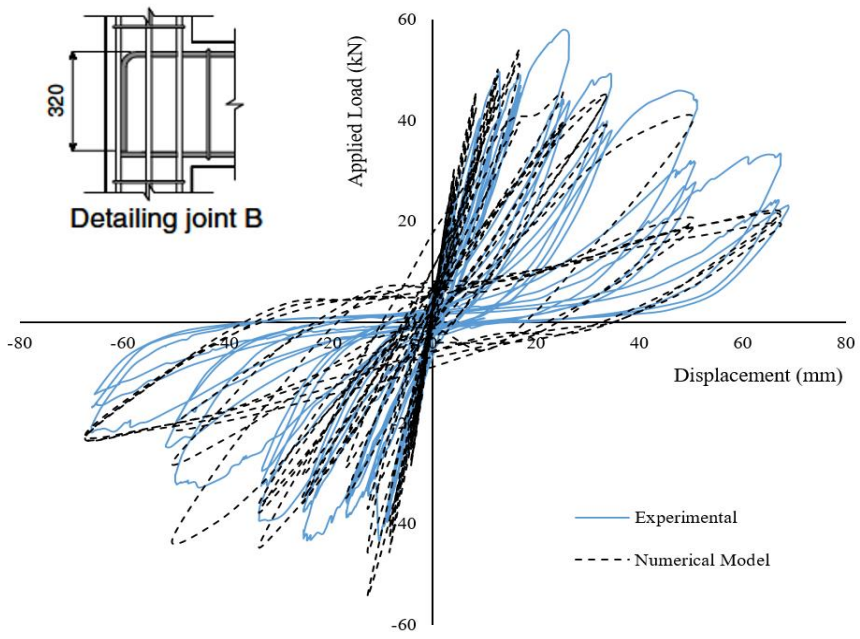

Fig. 10.23 JB2 Joint. Comparison between the numerical and experimental results.

Chapter 11. Conclusions and Future work

Contents of Chapter 11

11.1 Original contribution 281
11.2 Conclusions 282
11.3 Limitations of the proposed model 284
11.4 Future work 286

11.1 Original contribution

The original contribution of the research work presented in this dissertation can be summarized as follows:

1. Development of an innovative and modeling strategy to describe the mechanical response of RC structural members subjected to cyclic loading. The model is characterized by two basic features:

   a. Numerical Accuracy

      The proposed concrete model introduces a new criterion of crack closing which was found to be a crucial feature for the numerical response of RC structures subjected to cyclic loading conditions. Additionally, the numerical accuracy of the proposed model is demonstrated by comparing the numerical results with numerous experimental data with different mechanical behaviors that were found in the literature.

   b. Computational efficiency

      The proposed model prevents the excessive concentrations of stresses in the cracked areas which may lead to numerical instabilities. Additionally, the use of a novel crack closing criterion provides stability in the nonlinear analysis even when the loading is close to load carrying-capacity levels of the specimens. Furthermore, the use of the NBCFB element for steel reinforcement modeling under cyclic loading conditions was found to increase the numerical stability of the nonlinear iterative procedure due to its advanced formulation features. Finally, the ability to capture the 3D cyclic behavior of reinforced concrete members with a small number of hexahedral elements keep the computational demand low, a numerical feature that is significant when dealing with large-scale models.

2. Combine the computationally efficient constitutive modeling (1) with a hybrid simulation methodology presented in Markou and Papadrakakis [37]. Extend the proposed numerical method to model full-scale RC structures under cyclic loading conditions. Furthermore, a complete numerical investigation of a full-scale nonlinear cyclic modeling of the four-storey RC building, which foresaw the use of retrofitting interventions, was performed. As it was presented in this work, the numerical model managed to solve all three different loading sets by using the same mesh (presented for the first time in the international literature). Thereafter, the study of the retrofitting methods and the overall behavior of the building under the three loading events with the use of detailed modeling, was presented herein, while the importance of the developed numerical methods in taking into account the accumulated damage was also presented.

3. Introducing new damage factors for capturing special characteristics of RC behavior subjected to a large number of loading cycles under ultimate limit state conditions, was also an innovative contribution of this work. The concrete and steel material damage factors utilize the propose modeling method with the ability to capture the accumulated damage during the cyclic analysis of RC structures.

4. Extend the proposed modeling procedure for performing dynamic analysis of RC structures. An extensive parametric investigation was also presented on the proposed damage factors when used for the dynamic analysis of RC structures.

5. Two retrofitting techniques (CFRP and RC infill wall) were modelled and investigated throughout the analysis of the four-storey RC building. In this work, different retrofitting configuration of infill wall were tested, which provides new knowledge of practical interest.

6. A modal analysis algorithm was developed that was used to further study the mechanical behavior of the four HYMOD meshes presented in Chapter 8. This is the first time in the international literature that eigenmodes are computed by using HYMOD meshes.
7. Modify the damage factor of steel in order to capture some extreme states of concrete members with excessive cracking and loss of bonding between crack regions and steel reinforcement bars. The proposed modeling method was able to capture the cyclic behavior of RC structures with pinching, without the introduction of additional dofs that would have incorporated significant computational load to the model.
8. All the developed algorithms were integrated within Reconan research software.

11.2 Conclusions

Concrete Material Modeling

The proposed constitutive law for modeling the material of concrete is based on the Markou and Papadrakakis [31] model which was an extension of the Kotsovos and Pavlovic [29] model. This constitutive law foresees that the mechanical behavior of concrete is brittle with an intense nonlinear behavior that is affected by triaxial phenomena. The concrete domain is simulated by 8- or 20-noded isoparametric hexahedral elements with no restriction on the number of cracks.

The concrete material constitutive model combines a realistic assumption of the behavior of concrete, which is numerically integrated with the smeared crack approach. The proposed model was also integrated with a new closing/opening algorithm. The developed modeling algorithm was used to study the behavior of RC specimens under ultimate limit state cycling loading conditions. Based on the numerical findings, the flexible crack closing criterion provides stability in the iterative nonlinear analysis, thus alleviates the numerical problems that did not allow researchers to perform their type of extensive analyses. The use of the proposed innovative crack closing criterion, led to a significant increase of the computational efficiency (very small number of required internal iterations), thus areas that developed large nonlinearities were found to have a small effect on the overall stability of the solution algorithm.

The integration of a 3D detailed solid finite-element model with damage factors related to both concrete and the steel reinforcement was proposed for the nonlinear static cyclic and dynamic analysis of RC structures. The concrete numerical model was integrated by using the characteristics of cracking during the nonlinear cyclic analysis, whereas a damage factor for the steel material model was presented (also directly connected to the number of opening and closing of concrete cracks).

Based on the numerical findings, the overall contribution of the proposed damage factors was found to provide the modeling method with the ability to capture the pinching effect. The numerical study revealed that the steel damage factor was significant in the case of static cyclic loading, where for the dynamic tests performed it was found that the proposed damage factors play a crucial role during the dynamic response of the structures contributing to the ability of the proposed modeling approach to predict in a realistic manner the experimental data.

Finally, the proposed modeling approach manages to capture the experimental results without any significant mesh sensitivity effects. Based on a relevant numerical investigation, it was also concluded that the developed algorithm managed to solve all nonlinear dynamic problems without any numerical instabilities and at the same time exhibited high computational efficiency, which is an important characteristic when dealing with the solution of large-scale structures.

Steel reinforcement-embedded rebar modeling

The use of embedded NBCFB elements developed by Markou [4] for steel reinforcement modeling under monotonic loading conditions, was found to increase the numerical stability of the analysis and lead to more accurate simulations of the hysteric response of RC structural members subjected to cyclic loading. The proposed method demonstrated an overall numerical response that was efficient and robust for the case of different experimental setups (shear walls, deep beams, interior and exterior frame joints), where it managed to capture successfully different mechanical behaviors. The use of embedded truss elements for modeling the steel reinforcement rebars, was found to underestimate the dissipating energy of the RC structural members especially when the structure faces excessive cracking and steel-reinforcement yielding.

Similarly, based on the numerical investigation conducted on RC frames subjected to dynamic analysis, it was concluded that the use of NBCFB element is a more appropriate approach for the steel reinforcement compared to the truss element. This is attributed to the fact that the use of NBCFB embedded elements, improves the numerical results compared to the experimental data due to the shear contribution of the beam element. When the truss embedded elements are used, the RC frame models were found to develop larger horizontal deformations during the acceleration event compared to the experimental response. Therefore, it is recommended to use the NBCFB embedded rebar element when this type of analysis is performed.

Hybrid modeling

The proposed HYMOD approach was found to be capable to accurately predict the nonlinear response of RC structural members under cyclic loading conditions, with a reduced computational effort. The proposed formulation was also found to be computationally robust since it does not require any special algorithmic procedure for its implementation. The integration of the HYMOD algorithm with the cyclic concrete material model further fortified the numerical method with additional numerical stability, which is essential when the cracks begin to open and close. The numerical results revealed that the proposed simulation manages to retain a low ratio of internal iterations per displacement increment, thus further reducing the computational demand of the nonlinear analysis. Furthermore, the mesh sensitivity investigation showed that the proposed modeling approach manages to maintain its accuracy and ability in capturing the mechanical behavior of RC structural members that are tested under cyclic loading conditions for cases in which the mesh size is modified within a recommended margin of 10–25 cm. Additionally, it was concluded that the proposed method's numerical ability to capture the experimental data is not significantly affected when different reduction levels are implemented.

The developed proposed modeling approach managed to overcome the computational limitations and simulate a full-scale four-storey RC building for three loading tests without any numerical problems. Furthermore, the proposed modeling approach did not foresee for any simplification assumptions, thus the geometry of the entire building, its retrofitting domains and the steel reinforcement were modeled in an exact manner, while the material properties that were defined during the model construction complied with the values reported in the experimental report. This highlights the practicality, numerical simplicity and objectivity of the proposed modeling approach, when dealing with the assessment of RC retrofitted structures by using cyclic nonlinear ultimate limit state analysis. The numerical investigation also revealed that the proposed modeling method managed to capture accurately the experimental results that were obtained during the three consecutive loading tests, while maintaining a low ratio of internal iterations per displacement increment. Based on the numerical findings, the main strain concentrations and damages on the frame were found to be located at the structure's joints and

RC shear walls; a numerical finding that complied with the experimental results reported in [42].

Modeling of the Infill Walls for Retrofitting of RC Structures

The HYMOD model was used to perform a numerical investigation of different infill RC wall retrofitting configurations. The initial HYMOD mesh was used to construct three new models by rearranging the infill RC wall elements accordingly. Based on the numerical findings, it was concluded that the model that foresaw the use of RC infill walls throughout the height of the structure, derived the highest shear capacity and energy dissipation enhancements. Its overall energy dissipation, due to the infill RC walls, was found to increase by 500% in comparison to the bare frame model. Additionally, it was concluded that there could be cases where the placing of more infill walls during the strengthening design procedure of a RC frame, will not always translate into a proportional enhancement of the overall shear capacity and energy dissipation. The numerical investigation revealed that local damage accumulation could result into a premature failure of the structure due to excessive damage concentrations at the structural members found at higher floors that were not retrofitted (i.e. for cases where the infill walls are placed only at the ground floor and the remaining floors are left without any strengthening interventions). Therefore, full-scale nonlinear analyses should be performed so as to allocate potential weak areas of the framing system, thus establish an optimum and cost-effective retrofitting design.

The CFRP jacketing that was discretized and incorporated within the HYMOD mesh, was found to affect the stress-strain distribution at a local level, therefore, taking into account the confinement due to this retrofitting technique during the nonlinear cyclic analysis was found to be important when numerically investigating the mechanical response of the retrofitted frame.

Furthermore, Reconan FEA was integrated with a modal analysis algorithm that was used to compute the eigenmodes and their corresponding values by using the four structural configurations. The use of HYMOD meshes in modal analysis was presented here for the first time in the international literature. Based on the modal analysis findings, it was concluded that the two models that were not retrofitted by using infill walls throughout the frame's height, incorporated an irregular stiffness distribution along their height that translated into an irregular deformation between their retrofitted and bare floors. Based on this finding, it is advisable to avoid placing infill RC walls that will not cover the full height of the structure (whenever this is architecturally feasible). The obtained numerical response of the developed modal analysis algorithm was found to be computationally efficient and numerically accurate.

11.3 Limitations of the proposed model

Constitutive relationships within thermodynamic standards

The constitutive relationships used in this study are based on the experimental findings of Kotsovos and Newman [238], which derived from tests on specimens subjected to triaxial loading by using techniques capable of both inducing definable states of stress in the specimens and measuring reliably the deformational response of concrete. The constitutive relations have been derived by regression analysis of experimental data. This material model is not based on a thermodynamic framework in order to dissipate energy based on the laws of loading-reloading respective behavior. The model describes the fracture process of concrete as an evolution of microcracking and macrocracking derived by experimental evidence.

It is important to note at this point that, many constitutive models implemented in structural members are not based on a thermodynamic framework. The elasticity and the elastoplasticity models are based on uniaxial constitutive laws of Popovics [156] and Saenz [155], which are derived by experimental data and it is well known that these models may violate the laws of

thermodynamics. Additionally, empirical models have been widely accepted for modeling concrete structures. The scope of these models, is to conduct a feasible numerical implementation with realistic assumptions and few material parameters. Bergan and Holand [239], indicated that concrete is a highly heterogeneous material whose behavior is mainly influenced by disintegration processes in form of micro- and macro-cracking. These concepts do not fit with the constitutive relations, which are based on the framework of homogenous solids following the laws of thermodynamics. Furthermore, Jirasek and Rolshoven [240] noted that no real material can be assumed as an ideal continuum medium and the effects of heterogeneity are increased on a sufficiently small scale.

The damage material models usually are based on thermodynamic laws. These models build a constitutive model based on the first and the second law of thermodynamics. These models usually use many material parameters and energy functions in order to describe the behavior of concrete (like all models they sometimes manage to capture the mechanical behavior of concrete and some others they fail to do so). These material parameters that are needed when using this type of material models have derived from the thermodynamic framework and their physical interpretation is not very clear. In addition, these models present many numerical problems, which make it difficult to be used for the analysis of full-scale RC structures. In the international literature review, it is easy to observe that the damage models are mainly implemented for modeling concrete specimens and RC structural members under monotonic loading (due to computational restrains and numerical instabilities).

Each material approach has its advantages and disadvantages and of course the selection of the appropriate model depends on the particular characteristic of the problems at hand. The aim of the proposed model, is to describe a 3D material constitutive model with realistic assumptions which can be easily implemented in every structural concrete member and for simulating large structures such as multi-storey buildings and bridges. The simplicity and the computational efficiency in conjunction with the achieved accuracy are the most important features in order to show the practical use of any model. Therefore, a model which is based on experimental findings appears to be more appropriate to serve this goal, so far.

Ductility-brittle behavior

As stated before, the model is based on the assumption of a brittle behavior of concrete material with an abrupt loss of the caring capacity when the failure criterion is satisfied. Therefore, the model does not describe any post-cracking material properties, which are characterized by uncertainty when it comes to their physical interpretation. Despite the fact that this approach provides objectivity, it leads the numerical RC models to develop a brittle failure. In shear dominated structural members, this procedure fits perfectly with the experimental behavior and as described before it can lead to a numerical accurate and computationally efficient constitutive modeling. On the other hand, in cases when flexural behavior dominates, the model seems sometimes to underestimate the structure's strength and the accumulated dissipating energy of the RC structures. Nonetheless, this is in favor of safety.

Crack patterns

The proposed model treats cracking through the smeared crack approach to avoid mesh discontinuities. This way, the models simulate the geometrical discontinuity by the assumption of displacement continuity. Therefore, the numerical procedure does not model crack extensions, whereas it accounts for the crack openings and closures at GPs. The combination of the smeared crack approach with the brittle behavior of concrete leads to more heavily cracked areas than the experimental ones. Although the numerical crack patterns are more heavily cracked (smeared cracks), there is always a good agreement on the location and the direction of the cracks.

11.4 Future work

— ***Dynamic analysis of full-scale structures.***

The HYMOD approach combined with the innovative material modeling will be used for the dynamic analysis of full-scale structures such as RC multi-storey buildings and RC bridges. The use of 3D detailed modeling for the dynamic analysis of full-scale structures is a very interesting task for both scientists and professional engineers. The 3D detailed accurate modeling can allow the investigation of the behavior of structures, which is very difficult and extremely costly to study experimentally.

— ***Prestress and time-dependent characteristics.***

The model can be used for the analysis of prestresses concrete structures. An algorithm has already been developed in ReConAn FEA that takes into account the tendons by introducing prestress forces, as illustrated in Fig. 11.1.

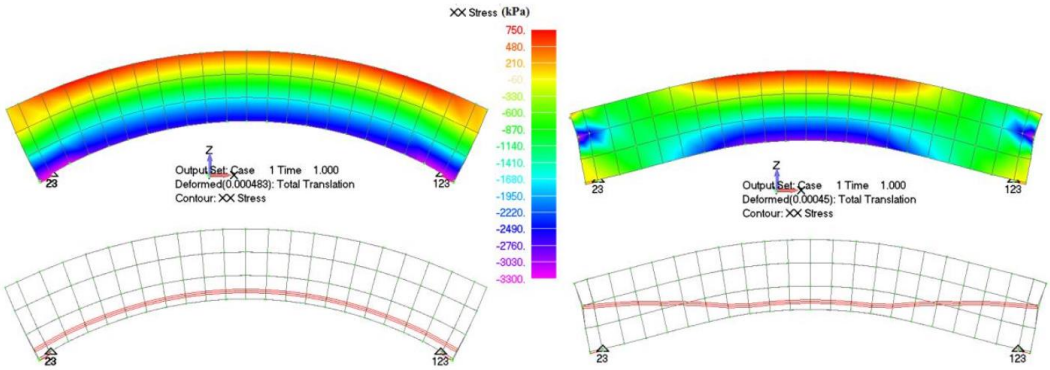

Fig. 11.1 Stress contour and deformed shape of the two RC beam models caused by posttensioning force [241].

In order to investigate accurately the behavior of prestressed concrete structures, time-dependent analysis should be considered concerning the loss of prestress due to creep and shrinkage of concrete and relaxation of the prestressing tendons.

— ***Soil-structure interaction.***

An important feature that has to be investigated is the interaction of the RC structure foundations with the soil as shown in Fig. 11.2. The use of HYMOD modeling for the superstructure and solid finite element discetization of the soil can accurately model the structure response with a realistic representation of the boundary conditions. The study of soil-structure interaction is feasible through the HYMOD method and it has to be tested under dynamic loading conditions.

— ***Parallel solvers.***

A parallel algorithm by using the OpenMP specifications in order to distribute the computational work to cores was investigated for the embedded rebar mesh generation of large-scale RC models[242]. Furthermore, a future objective is to integrate ReConAn FEA with a parallel solver that will use subdomain decomposition procedures in order to solve large-scale models. A subdomain decomposition algorithm is already under development as shown in Fig. 11.3.

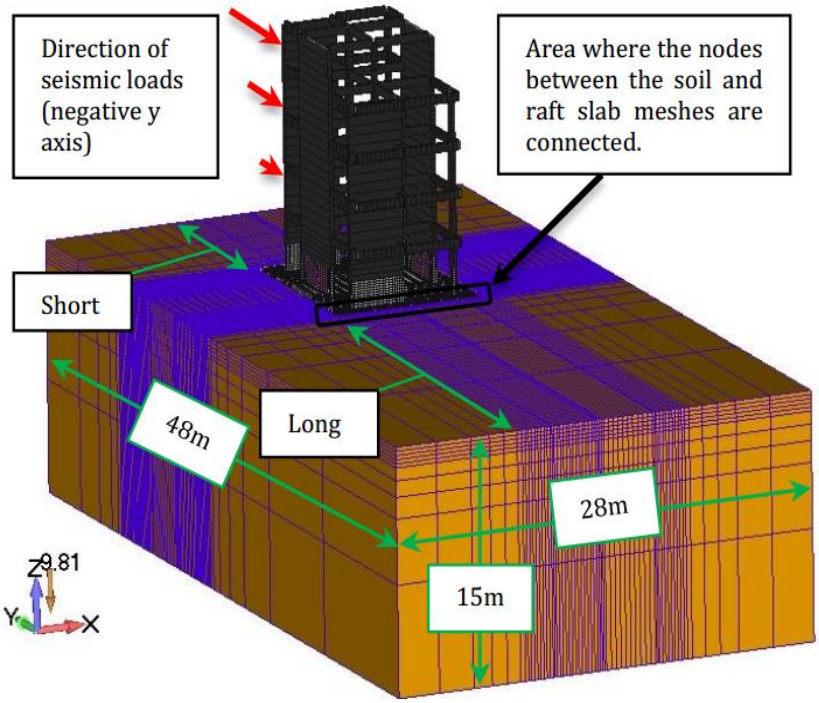

Fig. 11.2 Hymod method with soil mesh.[243]

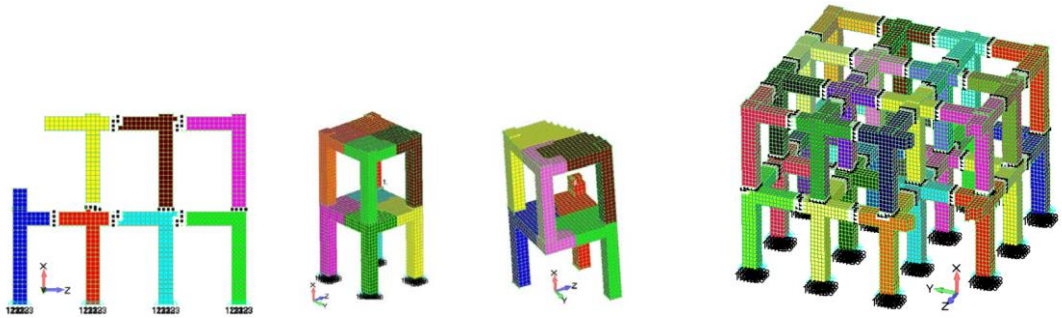

Fig. 11.3 Subdomains developed by ReConAn Paarallilo

— ***Test different retrofitting techniques.***

Adding new shear walls, steel bracing and jacketing are classical methods of retrofitting a RC structure. Furthermore, jacketing with CFRP sheets is a common intervention technique for RC structure rehabilitation and strengthening. These retrofitting techniques can now be modelled through the proposed modeling approach and test their efficiency thus derive an optimum configuration design for strengthening full-scale RC structures.

— ***Comparison with other 3D detailed nonlinear finite element models.***

It's very important to compare the proposed numerical model which is based on experimental tests and appropriate algorithmic design with other models that are derived from plasticity-fracture and damage modeling-thermodynamic laws. Thus, the comparison can give a clear distinction of the limits, the advantages and the disadvantages of each theory. A relevant in-depth numerical investigation has to be performed for the numerical parameters that are used by each modeling approach.

References

[1] "Eurocode 2 (EC2), Design of concrete structures". 2004.

[2] Sezen H, Elwood K, Whittaker A, Mosalam K, Wallace J, Stanton J. "Structural engineering reconnaissance of the August 17, 1999, Kocaeli (Izmit), Turkey, earthquake". PEER Report 2000/09, Pacific Earthquake Engineering Research Center, University of California, Berkeley: 2000.

[3] Kotsovos MD. "Finite-Element Modelling of Structural Concrete: Short-Term Static and Dynamic Loading Conditions". CRC Press; 2015.

[4] Markou G. "Detailed Three-Dimensional Nonlinear Hybrid Simulation for the Analysis of Large-Scale Reinforced Concrete Structures". PhD thesis. National Technical University of Athens., 2011.

[5] Cervenka V. "Inelastic finite element analysis of reinforced concrete panels under in–plane loads". PhD thesis.Boulder, Colorado: University of Colorado, 1970.

[6] Darwin D, Pecknold DA. "Analysis of cyclic loading of plane RC structures". Computers & Structures, Vol. 7(1), pp. 137–47, 1977.

[7] Agrawal AB, Jaeger LG, Mufti AA. "Elastoplastic material model for nonlinear analysis of planar RC structures under cyclic loadings". Canadian Journal of Civil Engineering, Vol. 7(2), pp. 294–303, 1980.

[8] Rule WK, Rowlands RE. "Predicting Behavior of Cyclically Loaded RC Structures". Journal of Structural Engineering, Vol. 118(2), pp. 603–16, 1992.

[9] Ožbolt J, Bažant ZP. "Microplane Model for Cyclic Triaxial Behavior of Concrete". Journal of Engineering Mechanics, Vol. 118(7), pp. 1365–86, 1992.

[10] Eligehausen R, Genesio G, Ozbolt J, Pampanin S. "3D analysis of seismic response of RC beam-column exterior joints before and after retrofit". 2nd ICCRRR, , Cape Town, South Africa.Vol. I, 2008, p. 407–8.

[11] López Cela JJ. "Analysis of reinforced concrete structures subjected to dynamic loads with a viscoplastic Drucker–Prager model". Applied Mathematical Modelling, Vol. 22(7), pp. 495–515, 1998.

[12] Vecchio FJ. "Towards Cyclic Load Modeling of Reinforced Concrete". ACI Structural Journal, Vol. 96(2), pp. 193–202, 1999.

[13] Ile N, Reynouard JM. "Nonlinear Analysis of Reinforced Concrete Shear Wall under Earthquake Loading". Journal of Earthquake Engineering, Vol. 4(2), pp. 183–213, 2000.

[14] Bažant ZP, Oh BH. "Crack band theory for fracture of concrete". Matériaux et Constructions, Vol. 16(3), pp. 155–77, 1983.

[15] Kwan W-P, Billington SL. "Simulation of Structural Concrete under Cyclic Load". Journal of Structural Engineering, Vol. 127(12), pp. 1391–401, 2001.

[16] Balan TA, Filippou FC, Popov EP. "Constitutive Model for 3D Cyclic Analysis of Concrete Structures". Journal of Engineering Mechanics, Vol. 123(2), pp. 143–53, 1997.

[17] Kwon M, Spacone E. "Three-dimensional finite element analyses of reinforced

concrete columns". Computers & Structures, Vol. 80(2), pp. 199–212, 2002.

[18] Palermo D, Vecchio FJ. "Behavior of Three-Dimensional Reinforced Concrete Shear Walls". ACI Structural Journal, Vol. 99(1), pp. 81–9, 2002.

[19] Girard C, Bastien J. "Finite-Element Bond-Slip Model for Concrete Columns under Cyclic Loads". Journal of Structural Engineering, Vol. 128(12), pp. 1502–10, 2002.

[20] Kwak H-G, Kim D-Y. "Material nonlinear analysis of RC shear walls subject to cyclic loadings". Engineering Structures, Vol. 26(10), pp. 1423–36, 2004.

[21] Au FTK, Bai ZZ. "Two-dimensional nonlinear finite element analysis of monotonically and non-reversed cyclically loaded RC beams". Engineering Structures, Vol. 29(11), pp. 2921–34, 2007.

[22] He W, Wu Y-F, Liew KM. "A fracture energy based constitutive model for the analysis of reinforced concrete structures under cyclic loading". Computer Methods in Applied Mechanics and Engineering, Vol. 197(51–52), pp. 4745–62, 2008.

[23] To NHT, Sritharan S, Ingham JM. "Strut-and-Tie Nonlinear Cyclic Analysis of Concrete Frames". Journal of Structural Engineering, Vol. 135(10), pp. 1259–68, 2009.

[24] Melo J, Fernandes C, Varum H, Rodrigues H, Costa A, Arêde A. "Numerical modelling of the cyclic behaviour of RC elements built with plain reinforcing bars". Engineering Structures, Vol. 33(2), pp. 273–86, 2011.

[25] Richard B, Ragueneau F, Cremona C, Adelaide L. "Isotropic continuum damage mechanics for concrete under cyclic loading: Stiffness recovery, inelastic strains and frictional sliding". Engineering Fracture Mechanics, Vol. 77(8), pp. 1203–23, 2010.

[26] Yuchuan L, Shaoqian X, Xuechao G. "An Energy-based Damage Model for Concrete Structures under Cyclic Loading". Procedia Engineering, Vol. 14, pp. 460–9, 2011.

[27] Lykidis GC, Spiliopoulos K V. "3D Solid Finite-Element Analysis of Cyclically Loaded RC Structures Allowing Embedded Reinforcement Slippage". Journal of Structural Engineering, Vol. 134(4), pp. 629–38, 2008.

[28] Lykidis GC, Spiliopoulos K V. "An efficient numerical simulation of the cyclic loading experiments on RC structures". Computers and Concrete, Vol. 13(3), pp. 343–59, 2014.

[29] Kotsovos MD, Pavlovic M. "Structural concrete : finite-element analysis for limit-state design". T. Telford; 1995.

[30] Markou G, Papadrakakis M. "An efficient generation method of embedded reinforcement in hexahedral elements for reinforced concrete simulations". Advances in Engineering Software, Vol. 45(1), pp. 175–87, 2012.

[31] Markou G, Papadrakakis M. "Computationally efficient 3D finite element modeling of RC structures". Computers and Concrete, Vol. 12(4), pp. 443–98, 2013.

[32] Kotsovos MD, Spiliopoulos KV. "Modelling of crack closure for finite-element analysis of structural concrete". Computers & Structures, Vol. 69(3), pp. 383–

98, 1998.

[33] Willam K, Warnke EP. “Constitutive model for the triaxial behavior of concrete”. Seminar on concrete structures subjected to triaxial stresses, Instituto Sperimentale Modeli e Strutture, Bergamo, Paper III-1., 1974.

[34] Menegotto M, Pinto PE. “Method of analysis for cyclically loaded reinforced concrete plane frames including changes in geometry and non-elastic behavior of elements under combined normal force and bending.”. Proceedings, IABSE Symposium on Resistance and Ultimate Deformability of Structures Acted on by Well Defined Repeated Loads, Lisbon, Portugal, 15–22., 1973.

[35] Kinugasa H, Nomura S. “Failure Mechanism under Reversed Cyclic Loading after Flexural Yielding”. Concrete Research and Technology, Vol. 5(2), pp. 21–32, 1994.

[36] Fenwick RC, Megget LM, Wuu P. “Load deflection characteristics of plastic hinges in ductile concrete beams”. In Proceedings 11th WCEE, 1996.

[37] Markou G, Papadrakakis M. “A simplified and efficient hybrid finite element model (HYMOD) for non-linear 3D simulation of RC structures”. Engineering Computations, Vol. 32(5), pp. 1477–524, 2015.

[38] Shiohara H, Kusuhara F. “Benchmark Test for Validation of Mathematical Models for Nonlinear and Cyclic Behaviour of R/C Beam–Column Joints”. Department of Architecture, School of Engineering, University of Tokyo: 2006.

[39] Saatcioglu M, Ozcebe G. “Response of Reinforced Concrete Columns to Simulated Seismic Loading”. ACI Structural Journal, Vol. 86(1), pp. 3–12, 1989.

[40] Carydis P. “European Commision – “Human Capital and Mobility” Programme, Prenormative Research in Support of Eurocode 8, Shaking Table Tests of Reinforced Concrete Frames”. Report No, 8: 1997.

[41] “Eurocode 8 (EC8), Design of structures for earthquake resistance”. 2003.

[42] Poljanšek M, Taucer F, Molina Ruiz J, Chrysostomou C, Kyriakides N, Onoufriou T, et al. “Seismic retrofitting of RC frames with RC infilling (SERFIN project)”. JRC Scientific and Policy Report, Publications Office of the European Union, Luxembourg, Doi:10.2788/630: 2014.

[43] “KANEPE. Code for Intervention in Reinforced Concrete Buildings, Earthquake Planning and Protection Organization (OASP)”. 2012.

[44] Rombach GA. “Finite element design of concrete structures : practical problems and their solution”. Thomas Telford Ltd; 2004.

[45] Argyris J. “Continua and discontinua.”. Oppening address to the International conference on matrix methods of structural mechanics, Dayton, Ohio, Wright-Patterson U.S.A.F. Base: 1965, p. 1–198.

[46] Argyris JH, Scharpf DW. “Some General Considerations on the Natural Mode Technique”. The Aeronautical Journal, Vol. 73(699), pp. 218–26, 1969.

[47] Argyris J, Tenek L. “Natural Mode Method: A Practicable and Novel Approach to the Global Analysis of Laminated Composite Plates and Shells”. Applied Mechanics Reviews, Vol. 49(7), pp. 381–9, 1996.

[48] Argyris J, Tenek L. “Recent Advances in Computational Thermostructural

Analysis of Composite Plates and Shells With Strong Nonlinearities". Applied Mechanics Reviews, Vol. 50(5), pp. 285–306, 1997.

[49] Tenek LT, Argyris J. "Finite Element Analysis for Composite Structures". vol. 59. Dordrecht: Springer Netherlands; 1998.

[50] Fédération internationale du béton. Task Group 4.4. "Practitioners' guide to finite element modelling of reinforced concrete structures : State-of-art report". International Federation for Structural Concrete; 2008.

[51] Clough R, Johnston S. "Effects of stiffness degradation on earthquake ductility requirements.". Transactions of Japan Earthquake Engineering Symposium, Tokyo: 1966, p. 195–8.

[52] Takizawa H. "Notes on Some Basic Problems in Inelastic Analysis of Planar RC Structures". Transactions of the Architectural Institute of Japan, 1976.

[53] Filippou FC, Issa A. "Nonlinear Analysis of Reinforced Concrete Frames under Cyclic Load Reversals". EERC Report 88-12, Earthquake Engineering.Research Center, Berkeley: 1988.

[54] Giberson MF. "The response of nonlinear multistory structures subjected to earthquake excitation". PhD thesis, California Institute of Technology, Pasadena, Calif., 1967.

[55] Salari MR, Spacone E. "Finite element formulations of one-dimensional elements with bond-slip". Engineering Structures, Vol. 23(7), pp. 815–26, 2001.

[56] Schulz M, Filippou FC. "Non-linear spatial Timoshenko beam element with curvature interpolation". International Journal for Numerical Methods in Engineering, Vol. 50(4), pp. 761–85, 2001.

[57] Limkatanyu S, Spacone E. "Reinforced Concrete Frame Element with Bond Interfaces. I: Displacement-Based, Force-Based, and Mixed Formulations". Journal of Structural Engineering, Vol. 128(3), pp. 346–55, 2002.

[58] Limkatanyu S, Spacone E. "Reinforced Concrete Frame Element with Bond Interfaces. II: State Determinations and Numerical Validation". Journal of Structural Engineering, Vol. 128(3), pp. 356–64, 2002.

[59] Papaioannou I, Fragiadakis M, Papadrakakis M. "Inelastic analysis of framed structures using the fiber approach". Proceedings of the 5th International Congress on Computational Mechanics (GRACM 05), Limassol, Cyprus: 2005, p. 231–8.

[60] Argyris JH, Balmer H, Doltsinis JS, Dunne PC, Haase M, Kleiber M, et al. "Finite element method — the natural approach". Computer Methods in Applied Mechanics and Engineering, Vol. 17–18(PART 1), pp. 1–106, 1979.

[61] Mazars J, Kotronis P, Ragueneau F, Casaux G. "Using multifiber beams to account for shear and torsion: Applications to concrete structural elements". Computer Methods in Applied Mechanics and Engineering, Vol. 195(52), pp. 7264–81, 2006.

[62] Marini A, Spacone E. "Analysis of Reinforced Concrete Elements Including Shear Effects". ACI Structural Journal, Vol. 103(5), pp. 645–55, 2006.

[63] Mata P, Oller S, Barbat AH. "Static analysis of beam structures under nonlinear geometric and constitutive behavior". Computer Methods in Applied Mechanics

and Engineering, Vol. 196(45–48), pp. 4458–78, 2007.

[64] Papachristidis A, Fragkiadakis, M. Papadrakakis M. “Modeling of the inelastic response of RC structures accounting for shear strains”. 16th Conference of Concrete, Paphos, Cyprus: 2009.

[65] Klinkel S, Govindjee S. “Using finite strain 3D-material models in beam and shell elements”. Engineering Computations, Vol. 19(3), pp. 254–71, 2002.

[66] Valipour HR, Foster SJ. “Nonlinear reinforced concrete frame element with torsion”. Engineering Structures, Vol. 32(4), pp. 988–1002, 2010.

[67] Spacone E, Ciampi V, Filippou FC. “A Beam Element For Seismic Damage Analysis”. Report No. UCB/EERC-92/07, College of Engineering, University of California, Berkeley: 1992.

[68] Mahasuverachai M, Powell GH. “Inelastic Analysis of Piping and Tubular Structures”. EERC Report 82/27, Earthquake Engineering Research Center, University of California, Berkeley: 1982.

[69] Argyris J, Tenek L, Olofsson L. “TRIC: a simple but sophisticated 3-node triangular element based on 6 rigid-body and 12 straining modes for fast computational simulations of arbitrary isotropic and laminated composite shells”. Computer Methods in Applied Mechanics and Engineering, Vol. 145(1–2), pp. 11–85, 1997.

[70] Software SP. “World-class finite element analysis (FEA) solution for theWindows desktop”, 2009.

[71] Barzegar F, Maddipudi S. “Generating Reinforcement in FE Modeling of Concrete Structures”. Journal of Structural Engineering, Vol. 120(5), pp. 1656–62, 1994.

[72] de Borst R, Crisfield MA, Remmers JJC, Verhoosel C V. “Non-Linear Finite Element Analysis of Solids and Structures”. Chichester, UK: John Wiley & Sons, Ltd; 2012.

[73] Riks E. “An incremental approach to the solution of snapping and buckling problems”. International Journal of Solids and Structures, Vol. 15(7), pp. 529–51, 1979.

[74] Crisfield MA. “A fast incremental/iterative solution procedure that handles “snap-through””. Computers & Structures, Vol. 13(1–3), pp. 55–62, 1981.

[75] Carr J. “RUAUMOKO theory manual”, 2007.

[76] Hall JF. “Problems encountered from the use (or misuse) of Rayleigh damping”. Earthquake Engineering & Structural Dynamics, Vol. 35(5), pp. 525–45, 2006.

[77] Jehel P, Léger P, Ibrahimbegovic A. “Initial versus tangent stiffness-based Rayleigh damping in inelastic time history seismic analyses”. Earthquake Engineering and Structural Dynamics, Vol. 43(3), pp. 467–84, 2013.

[78] Puthanpurayil AM, Lavan O, Carr AJ, Dhakal RP. “Elemental damping formulation: an alternative modelling of inherent damping in nonlinear dynamic analysis”. Bulletin of Earthquake Engineering, Vol. 14(8), pp. 2405–34, 2016.

[79] Charney FA. “Unintended Consequences of Modeling Damping in Structures”. Journal of Structural Engineering, Vol. 134(4), pp. 581–92, 2008.

[80] Lin RM, Zhu J. “On the relationship between viscous and hysteretic damping models and the importance of correct interpretation for system identification”. Journal of Sound and Vibration, Vol. 325(1–2), pp. 14–33, 2009.

[81] Zareian F, Medina RA. “A practical method for proper modeling of structural damping in inelastic plane structural systems”. Computers & Structures, Vol. 88(1–2), pp. 45–53, 2010.

[82] Zhang H, Wang J, Zhang X, Liu G. “Effects of viscous damping models on a single-layer latticed dome during earthquakes”. Structural Engineering and Mechanics, Vol. 62(4), pp. 455–64, 2017.

[83] Bathe KJ. “Solution Methods for Large Generalized Eigenvalue Problems in Structural Engineering”. Report UCSESM 71-20, Department of Civil Engineering, University of California, Berkeley: 1971.

[84] Bathe K-J. “Finite element procedures”. Prentice Hall Engineering, Science, Mathematics, New York: Prentice Hall; 1996.

[85] Aslani F, Jowkarmeimandi R. “Stress–strain model for concrete under cyclic loading”. Magazine of Concrete Research, Vol. 64(8), pp. 673–85, 2012.

[86] Karsan ID, Jirsa JO. “Behavior of Concrete Under Compressive Loadings”. Journal of the Structural Division, Vol. 95(12), pp. 2543–64, 1969.

[87] Sinha BP, Gerstle KH, Tulin LG. “Stress-Strain Relations for Concrete Under Cyclic Loading”. ACI Journal Proceedings, Vol. 61(2), pp. 195–212, 1964.

[88] van Mier JGM, Shah SP, Arnaud M, Balayssac JP, Bascoul A, Choi S, et al. “Strain-softening of concrete in uniaxial compression”. Materials and Structures, Vol. 30(4), pp. 195–209, 1997.

[89] van Mier JGM. “Multiaxial strain-softening of concrete - Part II: Load-histories”. Materials and Structures, Vol. 19(3), pp. 190–200, 1986.

[90] Ahmad SH, Shah SP. “Complete stress–strain curve of concrete and nonlinear design”. Proceedings CSCE-ASCE-ACI-CEB International Symposium on Nonlinear Design of Concrete Structures, University of Waterloo, Ontario, pp. 61–81, 1979.

[91] Wang PT, Shah SP, Naaman AE. “Stress-Strain Curves of Normal and Lightweight Concrete in Compression”. ACI Journal, Vol. 75(11), pp. 603–11, 1978.

[92] Newman K, Lachance L. “The testing of brittle materials under uniaxial compressive stress”. Proceedings of ASTM, Vol. 64, pp. 1044–1067, 1964.

[93] Gerstle KB, Zimmerman RM, Winkler H, Traina LA, Taylor MA, Schickert G, et al. “Behavior of Concrete under Multiaxial Stress States”. Journal of the Engineering Mechanics Division, Vol. 106(6), pp. 1383–403, 1980.

[94] Shah SP, Sankar R. “Internal Cracking and Strain Softening Response of Concrete Under Uniaxial Compression”. ACI Materials Journal, Vol. 84(3), pp. 200–12, 1987.

[95] Li J, Ren X. “Stochastic damage model for concrete based on energy equivalent strain”. International Journal of Solids and Structures, Vol. 46(11–12), pp. 2407–19, 2009.

[96] Kupfer H, Hilsdorf HK, Rusch H. “Behavior of Concrete Under Biaxial Stresses”. ACI Journal Proceedings, Vol. 66(8), pp. 656–66, 1969.

[97] Yin WS, Su ECM, Mansur MA, Hsu TTC. “Biaxial tests of plain and fiber concrete”. ACI Materials Journal, Vol. 86(3), pp. 236–43, 1989.

[98] van Mier JGM. “Fracture Propagation in Concrete under Complex Stress”. Fracture of Concrete and Rock, Springer, New York, NY; 1989, p. 362–75.

[99] Launay P, Gachon H. “Strain and Ultimate Strength of Concrete Under Triaxial Stress”. Special Publication, Journal of American Concrete Institute, Vol. 34, pp. 269–82, 1972.

[100] Brace WF, Bombolakis EG. “A note on brittle crack growth in compression”. Journal of Geophysical Research, Vol. 68(12), pp. 3709–13, 1963.

[101] Hoek E, Bieniawski ZT. “Brittle Rock Fracture Propagation In Rock Under Compression Brittle Rock Fracture Propagation in Rock Under Compression”. International Journal of Fracture Mechanics, Vol. 1(3), pp. 137–55, 1965.

[102] Duda H. “Bruchmechanisches Verhalten von Beton unter monotoner und zyklischer Zugbeanspruchung”. Deutscher Ausschuß Für Stahlbeton, Heft 419, Beuth, Berlin: 1991.

[103] Lowes LN. “Finite element modeling of reinforced concrete beam-column bridge connections.”. Ph.D. thesis, University of California, Berkeley, 1999.

[104] Reinhardt HW, Cornelissen HAW, Hordijk DA. “Tensile Tests and Failure Analysis of Concrete”. Journal of Structural Engineering, Vol. 112(11), pp. 2462–77, 1986.

[105] CEB. “RC Elements under Cyclic Loading”. Thomas Telford Publishing; 1996.

[106] Vintzeleou EN, Tassios TP. “Behavior of Dowels Under Cyclic Deformations”. ACI Structural Journal, Vol. 84(1), pp. 18–30, 1987.

[107] Lea FM, Desch CH. “The chemistry of cement and concrete.”. 2nd editio. London: 1956.

[108] Sakata K, Shimomura T. “Recent Progress in Research on and Code Evaluation of Concrete Creep and Shrinkage in Japan”. Journal of Advanced Concrete Technology, Vol. 2(2), pp. 133–40, 2004.

[109] Ross AD, England GL, Suan RH. “Prestressed concrete beams under a sustained temperature crossfall”. Magazine of Concrete Research, Vol. 17(52), pp. 117–26, 1965.

[110] England GL. “Steady-state stresses in concrete structures subjected to sustained temperatures and loads: Part I. Cases of uniaxial stress”. Nuclear Engineering and Design, Vol. 3(1), pp. 54–65, 1966.

[111] Browne RD. “Properties of Concrete in Reactor Vessels”. Conference on Prestressed Concrete Pressure Vessels at Church House, Westminster SW1, 13-17 March 1967, The Institution of Civil Engineers, London,.

[112] Lykidis GC. “Time dependent analysis of prestressed concrete structures under a change of statically indeterminate form”. MSc Dissertation , Imperial College, London, 2001.

[113] Wittmann FH. “Creep and Shrinkage Mechanisms”. In: Bazant ZP, Wittmann

FH, editors. Creep and Shrinkage in Concrete Structures, John Wiley & Sons Ltd.; 1982, p. 129–61.

[114] Mahin SA, Bertero VV, Atalya MB, Rea. D. “Rate of Loading Effects on Uncracked and Repaired Reinforced Concrete Members”. Report UCB/EERC-72/09.Berkeley: EERC, University of California: 1972.

[115] Ross CA, Tedesco JW, Kuennen ST. “Effects of Strain Rate on Concrete Strength”. ACI Materials Journal, Vol. 92(1), pp. 37–47, 1995.

[116] Ross CA, Jerome DM, Tedesco JW, Hughes ML. “Moisture and Strain Rate Effects on Concrete Strength”. ACI Materials Journal, Vol. 93(3), pp. 293–300, 1996.

[117] Yon J-H, Hawkins NM, Kobayashi AS. “Strain-Rate Sensitivity of Concrete Mechanical Properties”. ACI Materials Journal, Vol. 89(2), pp. 146–53, 1992.

[118] Hughes BP, Watson AJ. “Compressive strength and ultimate strain of concrete under impact loading”. Magazine of Concrete Research, Vol. 30(105), pp. 189–99, 1978.

[119] Lemaitre J, Marquis D. “Modeling Complex Behavior of Metals by the “State-Kinetic Coupling Theory””. Journal of Engineering Materials and Technology, Vol. 114(3), pp. 250, 1992.

[120] Bažant ZP, Prat PC. “Microplane Model for Brittle-Plastic Material: I. Theory”. Journal of Engineering Mechanics, Vol. 114(10), pp. 1672–88, 1988.

[121] Bažant ZP, Caner FC, Carol I, Adley MD, Akers SA. “Microplane Model M4 for Concrete. I: Formulation with Work-Conjugate Deviatoric Stress”. Journal of Engineering Mechanics, Vol. 126(9), pp. 944–53, 2000.

[122] Ngo D, Scordelis AC. “Finite Element Analysis of Reinforced Concrete Beams”. ACI Journal Proceedings, Vol. 64(3), pp. 152–63, 1967.

[123] Nilson AH. “Nonlinear Analysis of Reinforced Concrete by the Finite Element Method”. ACI Journal Proceedings, Vol. 65(9), pp. 757–66, 1968.

[124] Miguel PF. “A discrete-crack model for the analysis of concrete structures.”. Proc. 2nd Int. Conf. Zell-am-See, n.d., p. 897–908.

[125] Gupta AK, Maestrini SR. “Post-Cracking Behavior of Membrane Reinforced Concrete Elements Including Tension-Stiffening”. Journal of Structural Engineering, Vol. 115(4), pp. 957–76, 1989.

[126] Goodman RE, Taylor RL, Brekke TL. “A Model for the Mechanics of Jointed Rock”. Journal of the Soil Mechanics and Foundations Division, Vol. 94(3), pp. 637–60, 1968.

[127] Choun Y-S, Park J. “Evaluation of seismic shear capacity of prestressed concrete containment vessels with fiber reinforcement”. Nuclear Engineering and Technology, Vol. 47(6), pp. 756–65, 2015.

[128] Rashid YR. “Ultimate strength analysis of prestressed concrete pressure vessels”. Nuclear Engineering and Design, Vol. 7(4), pp. 334–44, 1968.

[129] Valliappan S, Doolan TF. “Nonlinear Stress Analysis of Reinforced Concrete”. Journal of the Structural Division, Vol. 98(4), pp. 885–98, 1972.

[130] Rots JG, Blaauwendraad J. “Crack Models for Concrete, Discrete or Smeared?

Fixed, Multi-Directional or Rotating?". HERON, 34 (1), 1989, 1989.

[131] Rots JG, Nauta P, Kusters GM. "Variable reduction factor for the shear stiffness of cracked concrete". Rep B1-84-33, Inst TNO for Building Mat and Struct,Delft, 1984.

[132] Crisfield MA, Wills J. "Analysis Of R/C Panels Using Different Concrete Models". Journal of Engineering Mechanics, Vol. 115(3), pp. 578–97, 1989.

[133] Barzegar F. "Analysis of RC Membrane Elements With Anisotropic Reinforcement". Journal of Structural Engineering, Vol. 115(3), pp. 647–65, 1989.

[134] Wang QB, Van Der Vorm PLJ, Blaauwendraad J. "Failure of reinforced concrete panels — how accurate the models must be. Computer aided analysis and design of concrete structures". Computer aided analysis and design of concrete structures, Proc. 2nd Int. Conf. Zell-am-See, n.d., p. 153–63.

[135] Bathe K-J, Walczak J, Welch A, Mistry N. "Nonlinear analysis of concrete structures". Computers & Structures, Vol. 32(3–4), pp. 563–90, 1989.

[136] Hibbitt D, Karlsson B, Sorensen P. "ABAQUS Manuals: V.I: User's Manual; V.2: Theory Manual; V.3: Example Problems: V.4: System's Manual'", 1989.

[137] Gupta AK, Akbar H. "Cracking in Reinforced Concrete Analysis". Journal of Structural Engineering, Vol. 110(8), pp. 1735–46, 1984.

[138] Bažant ZP. "Comment on Orthotropic Models for Concrete and Geomaterials". Journal of Engineering Mechanics, Vol. 109(3), pp. 849–65, 1983.

[139] Hillerborg A, Modéer M, Petersson P-E. "Analysis of crack formation and crack growth in concrete by means of fracture mechanics and finite elements". Cement and Concrete Research, Vol. 6(6), pp. 773–81, 1976.

[140] Hentz S, Daudeville L, Donzé F-V. "Discrete Element Modelling of a Reinforced Concrete Structure". 16 th ASCE Engineering Mechanics Conference, Seattle, University of Washington.: 2003, p. 1–14.

[141] Rousseau J, Frangin E, Marin P, Daudeville L. "Multidomain finite and discrete elements method for impact analysis of a concrete structure". Engineering Structures, Vol. 31(11), pp. 2735–43, 2009.

[142] Azevedo NM, Lemos JV, de Almeida JR. "Influence of aggregate deformation and contact behaviour on discrete particle modelling of fracture of concrete". Engineering Fracture Mechanics, Vol. 75(6), pp. 1569–86, 2008.

[143] Oñate E, Zárate F, Miquel J, Santasusana M, Celigueta MA, Arrufat F, et al. "A local constitutive model for the discrete element method. Application to geomaterials and concrete". Computational Particle Mechanics, Vol. 2(2), pp. 139–60, 2015.

[144] Sinaie S, Ngo TD, Nguyen VP. "A discrete element model of concrete for cyclic loading". Computers & Structures, Vol. 196, pp. 173–85, 2018.

[145] Belytschko T, Lu Y, Gu L. "Element-free Galerkin methods". International Journal for Numerical Methods in Engineering, Vol. 37(2), pp. 229–56, 1994.

[146] Babuska I, Melenk J. "The partition of unity method". International Journal for Numerical Methods in Engineering, Vol. 40(4), pp. 727–758, 1997.

[147] Rabczuk T, Belytschko T. “A three-dimensional large deformation meshfree method for arbitrary evolving cracks”. Computer Methods in Applied Mechanics and Engineering, Vol. 196(29–30), pp. 2777–99, 2007.

[148] Camacho GT, Ortiz M. “Computational modelling of impact damage in brittle materials”. International Journal of Solids and Structures, Vol. 33(20–22), pp. 2899–938, 1996.

[149] Ortiz M, Pandolfi A. “Finite-deformation irreversible cohesive elements for three-dimensional crack-propagation analysis”. International Journal for Numerical Methods in Engineering, Vol. 44(9), pp. 1267–82, 1999.

[150] Zhou F, Molinari JF. “Dynamic crack propagation with cohesive elements: a methodology to address mesh dependency”. International Journal for Numerical Methods in Engineering, Vol. 59(1), pp. 1–24, 2004.

[151] Belytschko T, Gracie R. “On XFEM applications to dislocations and interfaces”. International Journal of Plasticity, Vol. 23(10–11), pp. 1721–38, 2007.

[152] Verhoosel C V., Scott MA, de Borst R, Hughes TJR. “An isogeometric approach to cohesive zone modeling”. International Journal for Numerical Methods in Engineering, Vol. 87(1–5), pp. 336–60, 2011.

[153] Hognestad E. “A Study of Combined Bending and Axial Load in Reinforced Concrete Members”. Bulletin Series No 399, pp. 128, 1951.

[154] Vecchio FJ, Collins MP. “Compression Response of Cracked Reinforced Concrete”. Journal of Structural Engineering, Vol. 119(12), pp. 3590–610, 1993.

[155] Saenz LP. “Discussion of Equation for The Stress - Strain Curve of Concrete - By Desayi and Krishnan”. Journal of the American Concrete Institute, Vol. 61(9), pp. 1229–35, 1964.

[156] Popovics S. “A numerical approach to the complete stress-strain curve of concrete”. Cement and Concrete Research, Vol. 3(5), pp. 583–99, 1973.

[157] Gerstle KH. “Simple Formulation of Triaxial Concrete Behavior”. ACI Journal Proceedings, Vol. 78(5), pp. 382–7, 1981.

[158] Sfakianakis MG, Fardis MN. “Nonlinear finite element for modeling reinforced concrete columns in three-dimensional dynamic analysis”. Computers & Structures, Vol. 40(6), pp. 1405–19, 1991.

[159] Pagnoni T, Slater J, Ameur-Moussa R, Buyukozturk O. “A nonlinear three-dimensional analysis of reinforced concrete based on a bounding surface model”. Computers & Structures, Vol. 43(1), pp. 1–12, 1992.

[160] Moharrami M, Koutromanos I. “Finite element analysis of damage and failure of reinforced concrete members under earthquake loading”. Earthquake Engineering & Structural Dynamics, Vol. 46(15), pp. 2811–29, 2017.

[161] Belletti B, Cerioni R, Iori I. “Physical Approach for Reinforced-Concrete (PARC) Membrane Elements”. Journal of Structural Engineering, Vol. 127(12), pp. 1412–26, 2001.

[162] Belletti B, Scolari M, Vecchi F. “PARC_CL 2.0 crack model for NLFEA of reinforced concrete structures under cyclic loadings”. Computers & Structures, Vol. 191, pp. 165–79, 2017.

[163] Jason L, Huerta A, Pijaudier-Cabot G, Ghavamian S. “An elastic plastic damage formulation for concrete: Application to elementary tests and comparison with an isotropic damage model”. Computer Methods in Applied Mechanics and Engineering, Vol. 195(52), pp. 7077–92, 2006.

[164] Richard B, Ragueneau F. “Continuum damage mechanics based model for quasi brittle materials subjected to cyclic loadings: Formulation, numerical implementation and applications”. Engineering Fracture Mechanics, Vol. 98(1), pp. 383–406, 2013.

[165] Pijaudier-Cabot G, Bažant ZP. “Nonlocal Damage Theory”. Journal of Engineering Mechanics, Vol. 113(10), pp. 1512–33, 1987.

[166] Vassaux M, Richard B, Ragueneau F, Millard A. “Regularised crack behaviour effects on continuum modelling of quasi-brittle materials under cyclic loading”. Engineering Fracture Mechanics, Vol. 149, pp. 18–36, 2015.

[167] Gkimousis IA. “Modeling Reinforced Concrete Structures under Severe Cyclic Loading Incorporating Plasticity and Damage Models”. National Technical Universityof Athens, 2017.

[168] Reissner E. “On a Variational Theorem in Elasticity”. Journal of Mathematics and Physics, Vol. 29(1–4), pp. 90–5, 1950.

[169] Feist C, Hofstetter G. “An embedded strong discontinuity model for cracking of plain concrete”. Computer Methods in Applied Mechanics and Engineering, Vol. 195(52), pp. 7115–38, 2006.

[170] Roth SN, Léger P, Soulaïmani A. “A combined XFEM-damage mechanics approach for concrete crack propagation”. Computer Methods in Applied Mechanics and Engineering, Vol. 283, pp. 923–55, 2015.

[171] Le J-L, Bažant ZP, Bazant MZ. “Unified nano-mechanics based probabilistic theory of quasibrittle and brittle structures: I. Strength, static crack growth, lifetime and scaling”. Journal of the Mechanics and Physics of Solids, Vol. 59(7), pp. 1291–321, 2011.

[172] Skarzyski L, Tejchman J. “Determination of representative volume element in concrete under tensile deformation”. Computers & Concrete, Vol. 9(1), pp. 35–50, 2012.

[173] Kotsovos MD. “Concrete. A brittle fracturing material”. Matériaux et Constructions, Vol. 17(2), pp. 107–15, 1984.

[174] González-Vidosa F, Kotsovos MD, Pavlović MN. “On the numerical instability of the smeared-crack approach in the non-linear modelling of concrete structures”. Communications in Applied Numerical Methods, Vol. 4(6), pp. 799–806, 1988.

[175] Vidosa FG, Kotsovos MD, Pavlović MN. “Nonlinear finite-element analysis of concrete structures: Performance of a fully three-dimensional brittle model”. Computers & Structures, Vol. 40(5), pp. 1287–306, 1991.

[176] Spiliopoulos K V., Lykidis GC. “An efficient three-dimensional solid finite element dynamic analysis of reinforced concrete structures”. Earthquake Engineering & Structural Dynamics, Vol. 35(2), pp. 137–57, 2006.

[177] Lefas ID, Kotsovos MD. “Strength and Deformation Characteristics of

Reinforced Concrete Walls Under Load Reversals". ACI Structural Journal, Vol. 87(6), pp. 716–26, 1990.

[178] Del Toro Rivera R. "Behavior of reinforced concrete beam column joints under alternated loading". Ph.D. thesis, Ecole Nationale des Ponts et Chaussées, Paris, 1988.

[179] Fleury F, Reynouard JM, Merabet O. "Finite element implementation of a steel-concrete bond law for nonlinear analysis of beam-column joints subjected to earthquake type loading". Structural Engineering and Mechanics, Vol. 7(1), pp. 35–52, 1999.

[180] Luiki M. "Rahmenecke als netzbewehrte Schubscheibe.". MSc thesis, Institute for Structural Concrete, TU-Graz, Graz, 199AD.

[181] Hartl H. "Development of a continuum mechanics based tool for 3D FEA of RC Structures and application to problems of soil structure interaction.". Ph.D. thesis, Faculty of Civil Engineering, Graz Univ. of Technology, 2002.

[182] Červenka J, Papanikolaou VK. "Three dimensional combined fracture–plastic material model for concrete". International Journal of Plasticity, Vol. 24(12), pp. 2192–220, 2008.

[183] Papanikolaou VK, Kappos AJ. "Numerical study of confinement effectiveness in solid and hollow reinforced concrete bridge piers: Methodology". Computers & Structures, Vol. 87(21–22), pp. 1427–39, 2009.

[184] Formaggia L, Gerbeau JF, Nobile F, Quarteroni A. "On the coupling of 3D and 1D Navier–Stokes equations for flow problems in compliant vessels". Computer Methods in Applied Mechanics and Engineering, Vol. 191(6–7), pp. 561–82, 2001.

[185] Urquiza SA, Blanco PJ, Vénere MJ, Feijóo RA. "Multidimensional modelling for the carotid artery blood flow". Computer Methods in Applied Mechanics and Engineering, Vol. 195(33–36), pp. 4002–17, 2006.

[186] Blanco PJ, Feijóo RA, Urquiza SA. "A unified variational approach for coupling 3D–1D models and its blood flow applications". Computer Methods in Applied Mechanics and Engineering, Vol. 196(41–44), pp. 4391–410, 2007.

[187] Huang J. "Numerical solution of the elastic body-plate problem by nonoverlapping domain decomposition type techniques". Mathematics of Computation, Vol. 73(245), pp. 19–34, 2004.

[188] Nazarov SA. "Junctions of singularly degenerating domains with different limit dimensions 1". Journal of Mathematical Sciences, Vol. 80(5), pp. 1989–2034, 1996.

[189] Nazarov SA. "Junctions of singularly degenerating domains with different limit dimensions. II". Journal of Mathematical Sciences, Vol. 97(3), pp. 4085–108, 1999.

[190] Kozlov VA. "Fields in Non-Degenerate 1D-3D Elastic Multi-Structures". The Quarterly Journal of Mechanics and Applied Mathematics, Vol. 54(2), pp. 177–212, 2001.

[191] Blanco PJ, Feijóo RA, Urquiza SA. "A variational approach for coupling kinematically incompatible structural models". Computer Methods in Applied

Mechanics and Engineering, Vol. 197(17–18), pp. 1577–602, 2008.

[192] Mata P, Barbat AH, Oller S. “Two-scale approach for the nonlinear dynamic analysis of RC structures with local non-prismatic parts”. Engineering Structures, Vol. 30(12), pp. 3667–80, 2008.

[193] Bournival S, Cuillière J-C, François V. “A mesh-geometry based method for coupling 1D and 3D elements”. Advances in Engineering Software, Vol. 41(6), pp. 838–58, 2010.

[194] Cuillière J-C, Bournival S, François V. “A mesh-geometry-based solution to mixed-dimensional coupling”. Computer-Aided Design, Vol. 42(6), pp. 509–22, 2010.

[195] Kyriakides N, Chrysostomou CZ, Kotronis P, Georgiou E, Roussis P. “Numerical simulation of the experimental results of a RC frame retrofitted with RC Infill walls”. Earthquakes and Structures, Vol. 9(4), pp. 735–52, 2015.

[196] Markou G, AlHamaydeh M. “3D Finite Element Modeling of GFRP-Reinforced Concrete Deep Beams without Shear Reinforcement”. International Journal of Computational Methods, Vol. 15(02), pp. 1850001, 2018.

[197] “New Greek Seismic Code (NEAK), Athens”. 2000.

[198] “ACI318-14, Building Code Requirements for Structural Concrete and Commentary, ACI Committee 318”. 2014.

[199] Inoue N, Yang K, Shibata A. “Dynamic non-linear analysis of reinforced concrete shear wall by finite element method with explicit analytical procedure”. Earthquake Engineering & Structural Dynamics, Vol. 26(9), pp. 967–86, 1997.

[200] Han TS, Billington SL, Ingraffea AR. “Simulation Strategies to Predict Seismic Response of RC Structures”. Special Publication, Journal of American Concrete Institute, Vol. 205, pp. 191–214, 2001.

[201] Mirzabozorg H, Ghaemian M. “Non-linear behavior of mass concrete in three-dimensional problems using a smeared crack approach”. Earthquake Engineering & Structural Dynamics, Vol. 34(3), pp. 247–69, 2005.

[202] Mazars J, Kotronis P, Davenne L. “A new modelling strategy for the behaviour of shear walls under dynamic loading”. Earthquake Engineering & Structural Dynamics, Vol. 31(4), pp. 937–54, 2002.

[203] Faria R, Oliver J, Cervera M. “Modeling Material Failure in Concrete Structures under Cyclic Actions”. Journal of Structural Engineering, Vol. 130(12), pp. 1997–2005, 2004.

[204] Cotsovos DM. “Cracking of RC beam/column joints: Implications for the analysis of frame-type structures”. Engineering Structures, Vol. 52, pp. 131–9, 2013.

[205] Mansour M, Hsu TTC. “Behavior of Reinforced Concrete Elements under Cyclic Shear. II: Theoretical Model”. Journal of Structural Engineering, Vol. 131(1), pp. 54–65, 2005.

[206] Rots JG, Belletti B, Invernizzi S. “Robust modeling of RC structures with an “event-by-event” strategy”. Engineering Fracture Mechanics, Vol. 75(3–4), pp. 590–614, 2008.

[207] Minowa C, Ogawa N, Hayashida T, Kogoma I, Okada T. “Dynamic and static collapse tests of reinforced-concrete columns”. Nuclear Engineering and Design, Vol. 156(1–2), pp. 269–76, 1995.

[208] Ghannoum WM, Moehle JP. “Experimental Collapse of a Lightly Reinforced Concrete Frame Subjected to High Intensity Ground Motions”. 14th World Conference on Earthquake Engineering, vol. 12-01-0052, Beijing, China: 2008, p. 12–7.

[209] ACI Committee 318. “Building Code Requirements for Structural Concrete (ACI 318-95) and Commentary”. American Concrete Institute, Farmington Hills, MI: 1995.

[210] Ghannoum WM, Moehle JP. “Shake-Table Tests of a Concrete Frame Sustaining Column Axial Failures”. ACI Structural Journal, Vol. 109(3), pp. 393–402, 2012.

[211] Zeynalian M, Ronagh HR, Dux P. “Analytical Description of Pinching, Degrading, and Sliding in a Bilinear Hysteretic System”. Journal of Engineering Mechanics, Vol. 138(11), pp. 1381–7, 2012.

[212] D’Ambrisi A, Filippou FC. “Modeling of Cyclic Shear Behavior in RC Members”. Journal of Structural Engineering, Vol. 125(10), pp. 1143–50, 1999.

[213] Atalay M, Penzien J. “Behavior of critical regions of reinforced concrete components as influenced by moment, shear, and axial force”. Rep. UCB/EERC-75/19, Earthquake Engrg. Res. Ctr., University of California, Berkeley, Calif.: 1975.

[214] Costa J. “Reinforced concrete under large seismic action”. Report BYG.DTUR-076. Danmarks Tekniske Universitet.: 2003.

[215] Mansour MY, Lee JY, Hindi R. “Analytical prediction of the pinching mechanism of RC elements under cyclic shear using a rotation-angle softened truss model”. Engineering Structures, Vol. 27(8), pp. 1138–50, 2005.

[216] “ACI Committee 318M-11. Building code requirements for structural concrete (ACI 318m-11) and commentary”, 2011.

[217] Shafaei J, Zareian MS, Hosseini A, Marefat MS. “Effects of joint flexibility on lateral response of reinforced concrete frames”. Engineering Structures, Vol. 81, pp. 412–31, 2014.

[218] Thomas N. Salonikios Ioannis A. Tegos, and Georgios G. Penelis AJK. “Cyclic Load Behavior of Low-Slenderness Reinforced Concrete Walls: Failure Modes, Strength and Deformation Analysis, and Design Implications”. ACI Structural Journal, Vol. 97(1), pp. 132–41, 2000.

[219] Oesterle RG, Fiorato AE, Johal LS, Carptenter, J. E. R, G. H, et al. “Earthquake-Resistant Structural Walls-Tests of Isolated Walls”. Report to National Science Foundation, Construction Technology Laboratories, Portland Cement Association, Skokie, Ill,: 1976.

[220] ACI-ASCE Committee 408. “Report on steel reinforcing bars under cyclic loads”. American Concrete Institute; 2012.

[221] Eligehaousen R, Popov IEP, Bertero V V. “Local bond stress slip relationship of deformed bars under generalized excitations”. EERC Report 83-23, Earthquake

Engineering Research Center (EERC), University of California, Berkeley: 1983.

[222] Viawanthanatepa S, Popov EP, Bertero V V. “Effects of Generalized Loading on Bond of Reinforced Bars Embedded in Confined Concrete Blocks”. Tech. Rep. UCB/EERC-79/22, Earthquake Engineering Research Center (EERC), University of California, Berkeley: UCB/EERC; 1979.

[223] Fédération internationale du béton. “Bond of reinforcement in concrete : state-of-art report”. International Federation for Structural Concrete; 2000.

[224] Morita S, Kaku T. “Local bond stress-slip relationship under repeated loading. Resistance and ultimate deformability of structures acted on by well-defined repeated loads”. Proceedings of the IABSE Symposium, Lisbon, Portugal, 1973, p. 221–227.

[225] Tassios TP. “Properties of bond between concrete and steel under load cycles idealising seismic actions”. Bulletin d’information No131 of the Commite Euro-International Du Beton, pp. 65–122, 1979.

[226] Ciampi V, Rolf Eligehausen I, Bertero V V, Popov EP. “Analytical Model for Concrete Anchorages of Reinforcing Bars under Generalized Excitations”. Report No. EERC82-83, Earthquake Engineering Research Center (EERC), Berkeley, CA: 1982.

[227] Hawkins N, Lin I, Jeang F. “Local bond strength of concrete for cyclic reversed actions”. Bond in Concrete, pp. 151–161, 1982.

[228] Pochanart S, Harmon T. “Bond-Slip Model for Generalized Excitations Including Fatigue”. ACI Materials Journal, Vol. 86(5), pp. 465–74, 1989.

[229] Balazs GL. “Fatigue of Bond”. ACI Materials Journal, Vol. 88(6), pp. 620–30, 1992.

[230] Monti G, Spacone E. “Reinforced Concrete Fiber Beam Element with Bond-Slip”. Journal of Structural Engineering, Vol. 126(6), pp. 654–61, 2000.

[231] Limkatanyu S, Spacone E. “Effects of reinforcement slippage on the nonlinear response under cyclic loadings of RC frame structures.”. Earthquake Engineering & Structural Dynamics, Vol. 32(15), pp. 2407–2424, 2003.

[232] Ayoub A. “Nonlinear Analysis of Reinforced Concrete Beam–Columns with Bond-Slip”. Journal of Engineering Mechanics, Vol. 132(11), pp. 1177–86, 2006.

[233] Hoshino M. “Ein Beitrag zur Untersunchung des Spannumgszustandes an Arbeitsfugen mit Spannglied–Kopplungen von abschnittsweise in Ortbeton hergestellten Spannbetonbrucken”. Dissertation presented to Technischeltoch Schale, Darmstadt, Germany in partial fulfilment of the requirements for the degree of Doctor of Philosophy, 1974.

[234] Schäfer H. “A contribution to the solution of contact problems with the aid of bond elements”. Computer Methods in Applied Mechanics and Engineering, Vol. 6(3), pp. 335–53, 1975.

[235] Dinges D. “Untersuchung verschiedener Elementsteifigkeitsmatrizen auf ihre Eignung zur Berechnung von Stahlbetonkonstruktionen”. Final Research Report: 1985.

[236] Elnashai AS, Pilakoutas K, Ambraseys NN. “Experimental behaviour of

reinforced concrete walls under earthquake loading". Earthquake Engineering & Structural Dynamics, Vol. 19(3), pp. 389–407, 1990.

[237] Garcia R, Jemaa Y, Helal Y, Guadagnini M, Pilakoutas K. "Seismic Strengthening of Severely Damaged Beam-Column RC Joints Using CFRP". Journal of Composites for Construction, Vol. 18(2), pp. 04013048, 2014.

[238] Kotsovos MD, Newman JB. "Behavior of Concrete Under Multiaxial Stress". ACI Journal Proceedings, Vol. 74(9), pp. 213–23, 1977.

[239] Bergan PG, Holand I. "Nonlinear finite element analysis of concrete structures". Computer Methods in Applied Mechanics and Engineering, Vol. 17–18, pp. 443–67, 1979.

[240] Jirásek M, Rolshoven S. "Comparison of integral-type nonlocal plasticity models for strain-softening materials". International Journal of Engineering Science, Vol. 41(13–14), pp. 1553–602, 2003.

[241] Markou G. "Numerical Investigation of a Full-Scale RC Bridge Through 3D Detailed Nonlinear Limit-State Simulations". SEECCM III 3 rd South-East European Conference on Computational Mechanics- an ECCOMAS and IACM Special Interest Conference, Kos Island, Greece, 12-14 June, 2013.

[242] Markou G. "A Parallel Algorithm for the Embedded Reinforcement Mesh Generation of Large-Scale Reinforced Concrete Models". 9th GRACM International Congress on Computational Mechanics, pp. 211-218, Chania, 4-6 June, 2018.

[243] Markou G, Sabouni R, Suleiman F, El-Chouli R. "Full-Scale Modeling of the Soil-Structure Interaction Problem Through the use of Hybrid Models (HYMOD)". International Journal of Current Engineering and Technology, Vol. 5(2), pp. 885–92, 2015.

Author's References

Journal Papers:

[CM1]. Mourlas Ch, Papadrakakis M, Markou G. "A computationally efficient model for the cyclic behavior of reinforced concrete structural members". Engineering Structures, Vol. 141, pp. 97–125, 2017.

[CM2]. Markou G, Mourlas Ch, Papadrakakis M. "Cyclic nonlinear analysis of large-scale finite element meshes through the use of hybrid modeling (HYMOD)". International Journal of Mechanics, Vol. 11, pp. 218–25, 2017.

[CM3]. Markou G, Mourlas Ch, Papadrakakis M. "A hybrid finite element model (HYMOD) for the non-linear 3D cyclic simulation of RC structures". International Journal of Computational Methods, Vol. 16(01), pp. 1850125 , 2018.

[CM4]. G. Markou, C. Mourlas, H. Bark, and M. Papadrakakis. "Simplified HYMOD non-linear simulations of a full-scale multistory retrofitted RC structure that undergoes multiple cyclic excitations – An infill RC wall retrofitting study". Engineering Structures, Vol. 176, pp. 892–916, Dec. 2018.

[CM5]. C. Mourlas, G. Markou, and M. Papadrakakis. "Accurate and computationally efficient nonlinear static and dynamic analysis of reinforced concrete structures considering damage factors". Engineering Structures, Vol. 178, pp. 258–285, Jan. 2019.

Conference Papers:

[CM6]. Mourlas Ch, Papadrakakis M., Markou G, "Accurate and Efficient modelling for the Cyclic Behavior of RC structural Members". ECCOMAS congress, VII European congress on computational methods in applied sciences and engineering, Crete Island, Greece, 5–10 June 2016.

[CM7]. Bark H, Markou G, Mourlas Ch, Papadrakakis M. "Seismic assessment of a 5-storey retrofitted RC building". ECCOMAS congress, VII European congress on computational methods in applied sciences and engineering, Crete Island, Greece, 5–10 June 2016.

[CM8]. Mourlas Ch, Markou G, Papadrakakis M., "3D nonlinear constitutive modeling for dynamic analysis of reinforced concrete structural members". Procedia Engineering 199, pp. 729-734, September 2017.

[CM9]. Mourlas Ch, Markou G, Papadrakakis M., "Accumulated Damage in Nonlinear Cyclic Static and Dynamic Analysis of Reinforced Concrete Structures Through 3D Detailed Modeling". 9th GRACM International Congress on Computational Mechanics, Crete Island, Greece, 4–6 June 2018.